UNIVERSITY OF SOUTHAMPTON
Faculty of Engineering and Applied Science
Department of Electronics and Computer Science
Southampton, S017 1BJ, UK

Multi-Carrier Code Division Multiple Access

by
Byoung Jo Choi
BSc, MSc

A Doctoral Thesis submitted in partial fulfillment of the requirements for the award of Doctor of Philosophy at the University of Southampton

March 15, 2002

SUPERVISOR: Professor Lajos Hanzo
Dipl Ing, MSc, PhD, SMIEEE
Chair of Telecommunications
Department of Electronics and Computer Science
University of Southampton

UNIVERSITY OF SOUTHAMPTON

ABSTRACT

Faculty of Engineering and Applied Science
Department of Electronics and Computer Science

Doctor of Philosophy

Multi-Carrier Code Division Multiple Access

by Byoung-Jo CHOI

Multi-Carrier Code Division Multiple Access (MC-CDMA) exploits the joint benefits of Direct-Sequence (DS) CDMA and Orthogonal Frequency Division Multiplexing (OFDM). Hence, MC-CDMA exhibits high spectral efficiency and substantial benefits from the frequency diversity provided by frequency selective fading channels. This dissertation investigates several aspects of MC-CDMA. Firstly, the Peak-to-Average Power Ratio (PAPR) of the MC-CDMA signal is analysed. It was shown that the PAPR is characterised by the aperiodic correlation properties of the spreading sequences employed. Several orthogonal spreading codes were investigated in terms of their PAPR and it was found that the PAPR can be upper bounded by 3dB when employing orthogonal complementary codes in the context of low number of sub-carriers. Secondly, the application of adaptive modulation to MC-CDMA was studied. The optimum mode switching levels for generic adaptive modulation schemes were derived first and then, the performance of adaptive-modulation assisted MC-CDMA was analysed for transmission over various propagation scenarios. When space-time block codes were combined with adaptive-modulation assisted MC-CDMA, as expected the SNR gains of adaptive modulation over fixed-mode modems were found to decrease. Lastly, three types of reduced-complexity despreading schemes were proposed with an application to MC-CDMA in mind and the BER performance as well as the achievable complexity reduction were investigated.

Acknowledgment

I would like to thank my supervisor Professor Lajos Hanzo for his continual encouragement and enthusiasm, which have made my research thoroughly enjoyable. Even when I thought I had no hope of finishing my research, he made it absolutely sure that a failure was not an option for "us". Without his emotional and practical help, I would have never finished this work. My sincere thanks go to LG Electronics (LGE), Korea, and the British Council. They have supported my work financially. Specifically, Mr Yong-Il Choi and Dr Kyong-Kuk Lee in LGE provided me with the opportunity of pursuing research in the United Kingdom. I also would like to thank Dr Nak-Myeong Kim, who had taught and trained me as a capable engineer. This work was only possible with the aid of my friends in the Communications Research Group. Thomas Keller helped me understand the intricacies of the OFDM technique and provided me with practical assistance. I am also indebted to Jason Woodard for giving me invaluable advice. Ee Lin Kuan introduced me to various Joint Detection (JD) receivers and answered all my ignorant questions. Choong Hin Wong introduced me to Linux and helped me in numerous practical ways. Bee Leong Yeap contributed tremendously to making our research more fun. Tong Hooi Liew has provided valuable advice on channel coding and space-time coding. I am also indebted to Peter Cherriman, Stephan Weiss, Lie Liang Yang, Xing Yao Wu, Minoru Okada, Chee Siong Lee, Kai Yen, Mong Suan Yee, Hee Thong How, Matthias Münster, Spyros Vlahoyiannatos, Soon Xin Ng, Ahmad Samingan, Hafizal Mohamad, Nurul Nadia Ahmad, Mohamad Yusoff Alias and Jason Wee Peng Ng for their wonderful friendship and their warm encouragement. Professor Joong Hooi Cho and Dong Min Lim encouraged me and gave me invaluable advice, while they were staying in Southampton as visiting scholars. Denis Harvey helped me understand English culture with never-ending humour and with her charm, while providing practical day-to-day assistance.

Without my patient, lovely wife, I would not have 'survived' these years. My two daughters, Soona and Sena, have provided me with a lot of joy over these years. My parents, my brother and sisters always supported me with regular 'survival' packages and warm messages. My sincere thanks are also due for the wonderful friendship of all members of Swaythling Baptist Church, where my family felt at home. I would like to express my special thanks to Robin, who was ever so kind to my family and who explained to me all about 'cricket' by taking me to the Lord's Stadium, the home of cricket. Now I know what 'Googley' is!

List of Publications

1. Byoung-Jo Choi, Ee-Lin Kuan and Lajos Hanzo, "Crest-factor study of MC-CDMA and OFDM," *Proc. IEEE VTC'99 Fall*, vol. 1, pp. 233–237, September 1999

2. Byoung-Jo Choi and Lajos Hanzo, "Crest factors of Shapiro-Rudin sequences based multi-code MC-CDMA signals," *Submitted to Journal of Selected Areas in Communications*

3. Byoung-Jo Choi and Lajos Hanzo, "Crest factors of Shapiro-Rudin sequences based multi-code MC-CDMA signals," *Submitted to IEEE VTC'02 Spring*

4. Byoung-Jo Choi, Matthias Münster, Lie-Liang Yang and Lajos Hanzo, "Performance of Rake receiver assisted adaptive-modulation based CDMA over frequency selective slow Rayleigh fading channel," *Electronics Letters*, vol. 37, pp. 247–249, February 2001

5. Byoung-Jo Choi and Lajos Hanzo, "Rake receiver detection of adaptive modulation aided CDMA over frequency selective channels," *Proc. IEEE VTC'01 Fall*, vol. 3, pp. 1653–1657, October 2001

6. Byoung-Jo Choi, Tong-Hooi Liew and Lajos Hanzo, "Concatenated space-time block coded and turbo coded symbol-by-symbol adaptive OFDM and multi-carrier CDMA systems," *Proc. IEEE VTC'01 Spring*, vol. 2, pp. 776–780, May 2001

7. Byoung-Jo Choi and Lajos Hanzo, "Optimum mode-switching assisted adaptive modulation," *Proc. IEEE Globecom'01*, vol. 6, pp. 3316–3320, November 2001

8. Byoung-Jo Choi and Lajos Hanzo, "Optimum mode-switching assisted constant-power single- and multi-carrier adaptive modulation," *Submitted to Transactions on Vehicular Technology*

9. Tong-Hooi Liew, Byoung-Jo Choi and Lajos Hanzo, "Comparative study of concatenated turbo coded and space-time block coded as well as space-time trellis coded OFDM," *Proc. IEEE VTC'01 Spring*, vol. 2, pp. 781–785, May 2001

Contents

Chapter 1

Introduction

In 1993, a number of hybrid transmission techniques employing Code Division Multiple Access (CDMA) and Orthogonal Frequency Division Multiplexing (OFDM) were proposed [1, 2]. These combined techniques are expected to outperform the pure CDMA and OFDM techniques. The aim of this treatise is to examine various aspects of these techniques.

Since multi-carrier CDMA techniques rely on both CDMA and OFDM, the two conventional techniques will be reviewed briefly. The concept of multi-carrier CDMA will be presented next. The outline of the thesis will be given at the end of this chapter.

1.1 Overview of DS-CDMA

Direct-Sequence (DS) CDMA is a spread-spectrum communication technique. Spread-spectrum techniques were developed originally for military guidance and communications systems [3]. During the second World War, radar engineers used spread-spectrum techniques for mitigating intentional jamming and for achieving high resolution ranging. During the late 1970s, the employment of spread-spectrum techniques was proposed for efficient cellular communication [4]. It is interesting to note that [4] addressed most essential issues involved in DS-CDMA cellular communications at such an early stage, although the proposed scheme was based on frequency hopping spread-spectrum communication. For a detailed historical review of spread-spectrum based communications, the reader is referred to the overview papers by *Scholtz* [3], by *Yue* [5] or to Chapter 2 of [6] by *Simon*, *Omura*, *Scholtz* and *Levitt*.

In CDMA systems, users share the same broad bandwidth all the time, using different spreading codes. This unique feature of CDMA results in a soft capacity limit [4], while conventional Frequency Division Multiple Access (FDMA) and Time Division Multiple Access (TDMA) have hard capacity limits, since they use a finite number of orthogonal resources. The limiting factor of the capacity of CDMA systems is self interference and Multi User Interferences (MUI). The effects of these interference sources depend on the channel's characteristics and on the properties of the spreading codes used. Since any method which reduces the interference is capable of increasing the overall user capacity in CDMA, significant research efforts have been invested in reducing the interference [7]. Several simple

techniques, such as spatial isolation of users by cell sectorisation and discontinuous transmission relying on voice activity detection or on the burstiness of the information source, were shown to increase the user capacity [8]. Other sophisticated techniques employing interference cancellation [9], joint detection [10, 11] and adaptive antenna arrays [12] are realistic at the time of writing and offer further capacity gains.

One of the important merits of CDMA in a cellular environment is its potentially unity frequency reuse factor [8]. In TDMA and FDMA systems, the same frequency could be reused in different cells only beyond a sufficiently hight reuse distance, where the effects of interference between users of the same channel became negligible [13–15]. By contrast, in CDMA systems, the adjacent cells can use the same frequency in conjunction with unique cell-specific spreading sequences assigned for each cell site. Frequency planning is not required any more, while cell planning still remains an important issue, for example, for reasons of transmit power reduction [16]. An obvious advantage of the universal frequency reuse is the substantial potential increase in user capacity per unit bandwidth in comparison to 7-cell clusters. Another important advantage is the ability to use soft hand-off [8]. When a mobile roams across a cell boundary, its communication channel has to be handed over to a more suitable base station [13, 14]. In conventional multiple access systems often this means an abrupt RF channel change. Hence the communication link typically experiences a short discontinuity, while this RF channel change takes place. This is referred to as hard hand-off or hard hand-over [14]. In CDMA systems all base stations may use the same frequency. So-called Rake receivers [17, 18] used in the mobile stations for combining the signals from the two base stations involved in the hand-over [16]. This soft hand-off makes seamless communications possible [19]. The soft hand-off also mitigates the multi-path fading effects during the hand over period with the aid of cell site diversity [16].

In mobile communication the transmitted signal passes through multiple paths generally exhibiting different path lengths. The arrival time of the signals at a receiver spans from several tens of ns to several tens of μs, depending on the environment. The channel impulse response characterises the scattering of the transmitted energy in the time domain. The associated time-domain description results in Inter-Symbol Interference (ISI), where each impulse response component is exposed to fast Rayleigh fading. In conventional FDMA and TDMA systems complex channel equalizers are required for combating dispersion. As the transmission rate is increased, the number of ISI-contaminated adjacent symbols is proportionately increased [13]. Ironically, CDMA communication systems intentionally use significantly higher transmission rates, or chip rates, in order to take advantage of these scattered multi-path signals. Rake receivers [17, 18] are capable of resolving each delayed signal component with an accuracy of a chip period. Each demodulated component is combined by the Rake receivers in order to make effective use of the channel-induced multi-path diversity. A system having a shorter chip period or wider bandwidth is capable of resolving lower delay differences and hence may benefit from higher-order diversity. This characteristic together with the demands of higher data transfer rates render wide-band CDMA more attractive than the existing Pan-American narrow-band CDMA system known as IS-95 [20].

DS-CDMA systems typically suffer from so-called near/far problem [21, 22]. This problem is often more acute in the up link due to its asynchronous nature, than in the synchronous down link [16]. The

base station's receiver will experience excessive multi-user interferences resulting from the undesirable non-zero asynchronous cross correlation between the spreading sequences. This is so, even when the asynchronous cross correlations of the sequences employed are low, due to the effects of the multi-path channel. Thus, a mobile station near the base station should lower its transmit power so that all the reverse link signals at the base station's receiver can be received at equal power, independent of their geographical locations. In open-loop power control schemes [22] a mobile measures the power of the signal received from the base station for determining its required transmit power, assuming that the transmit path and the receiving path have approximately equal attenuations. Sometimes this is not the case, especially in frequency division duplex (FDD) CDMA systems. Thus closed-loop power control is required. In closed-loop power control schemes [23, 24] the base station sends power adjustment commands to each mobile station based on several measures, such as the received signal strength, the ratio of signal energy per bit to noise density (E_b/N_o) and the Bit Error Ratio (BER). Stability problems may arise in closed-loop power control and hence the global stability of the system has to be ensured [23]. Control latency and power adjustment levels are two key parameters in designing a closed-loop power control system [22].

Although power control is typically capable of tracking the power variation due to slow fading, it is almost impossible to compensate for the effects of fast Rayleigh fading, simply because the actual power variation speed exceeds the power control speed. In this case, interleaving combined with channel coding can support the operation of the power control in attaining the target performance. It is desirable to design the interleaver such that the originally consecutive symbols become separated in time by more than the channel's coherence time at the output of interleaver [22]. This implies that a higher interleaver depth is desirable for mobile stations traveling at lower speed for example. However, a higher interleaver depth implies a longer processing delay, which is undesirable for example in interactive voice communications.

CDMA systems use a significantly higher bandwidth than the modulating signal's bandwidth by spreading the original signal with the aid of high rate spreading sequences. The noise-like spreading sequences play an important role in characterising a CDMA communication system. In frequency selective multi-path fading environments ensuring low off-peak auto-correlation of the spreading sequences is necessary for reducing the Inter-Symbol Interference (ISI) and for combining the energy scattered in the time domain using Rake receivers. In multi-user environments additionally a low cross-correlation of the different user's sequences is required for distinguishing the desired users' signals. The family of various spreading sequences will be reviewed in Chapter 2.

1.2 Overview of OFDM

Orthogonal Frequency Division Multiplexing (OFDM) constitutes a specific form of multi carrier modulation technique [25]. The basic approach of OFDM [26–28] is to group serial message symbols and transmit each message symbol on a different frequency domain carrier at a reduced signalling rate. The conventional Frequency Division Multiplexing (FDM) technique requires guard bands between adjacent channels, since the receivers make use of band-pass filters for isolating each channel's signal. However,

OFDM exploits the orthogonality of the subcarrier signals, although the actual frequency spectra of the different subchannels partially overlap with each other. The receiver in OFDM systems makes use of the orthogonality between the subcarriers for recovering the symbols mapped on to a given subcarrier.

The complex baseband equivalent of the OFDM signal $s(t)$ in a symbol duration can be represented as [29] :

$$s(t) = \sum_{k=0}^{N-1} c_k \, e^{j2\pi \frac{k}{T} t} \, , \tag{1.1}$$

where N is the number of carriers and T is the subchannel signaling interval, while c_k is the symbol modulating the subcarrier k. In the next signaling interval a new set of symbols c_k is transmitted. At the receiver, the received signal is multiplied by $e^{-j2\pi \frac{n}{T} t}$ and integrated over a symbol duration in order to recover c_n. The resultant signal becomes, assuming perfect carrier frequency and symbol time recovery over an ideal channel:

$$\frac{1}{T} \int_0^T s(t) e^{-j2\pi \frac{n}{T} t} dt \;\; = \;\; \frac{1}{T} \sum_{k=0}^{N-1} c_k \int_0^T e^{j2\pi \frac{k}{T} t} e^{-j2\pi \frac{n}{T} t} dt = c_n \, . \tag{1.2}$$

In order to implement directly the transmitter and the receiver of an OFDM system, N oscillators are required.

Weinstein and Ebert [30] presented a method involving the Discrete Fourier Transform (DFT) for performing baseband modulation and demodulation, which spurred the development of OFDM systems with the advent of efficient of real-time Digital Signal Processing (DSP) technology. By sampling N times during an OFDM symbol at instants of $t = \frac{m}{N} T$, (1.1) becomes :

$$s(\frac{m}{N} T) = \sum_{k=0}^{N-1} c_k e^{j2\pi \frac{km}{N}} \, , \; (\text{for } m \; = \; 0, \; 1, \; \cdots \, , \; N-1) \, . \tag{1.3}$$

Since $s(\frac{m}{N} T)$ depends only on m, it can be represented as s_m in discrete form, and (1.3) can also be written as :

$$s_m = N \cdot \text{IDFT}(\{c_k\}) \, , \; (\text{for } m \; = \; 0, \; 1, \; \cdots \, , \; N-1), \tag{1.4}$$

where IDFT represents the Inverse Discrete Fourier Transform operator. The efficient implementation of the IDFT is the Inverse Fast Fourier Transform (IFFT). The overall structure of the OFDM transmitter is shown in Figure 1.1. The N message sequences, $c_0, \; c_1, \; \cdots \, , \; c_{N-1}$, form a frame, which is converted into a parallel form, where c_k is modulating the kth carrier. The IFFT module takes the parallel data and calculates N sampled time domain complex signals, $s_0, \; s_1, \; \cdots \, , \; s_{N-1}$, which are low-pass filtered for generating the continuous time domain I and Q signal components. These I and Q components are modulated by sine and cosine waveforms and then they are combined for forming an Intermediate Frequency (IF) signal. The block labled 'LPF' in Figure 1.1 carries out this low-pass filtering, I/Q modulation and I/Q combining. Then this IF signal is upconverted to a carrier frequency and then transmitted with the aid of an antenna. The IFFT eliminates the requirement of employing N oscillators and renders the OFDM transmitter implementationally attractive [29].

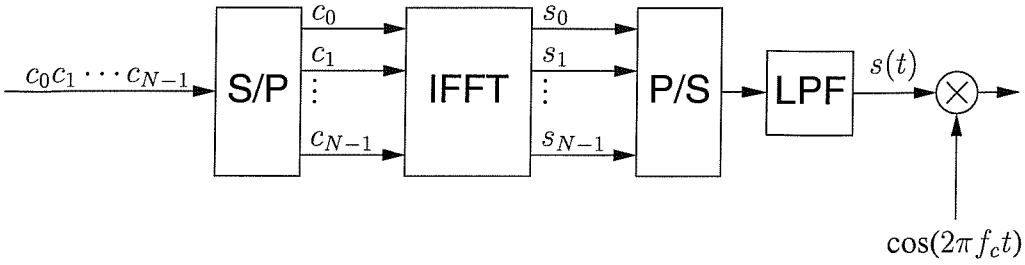

Figure 1.1: OFDM transmitter schematic

At the OFDM receiver, the reverse action takes place. The down-converted received signal is sampled at a rate of N/T and converted into a parallel stream of N values. Then, the FFT is applied in order to recover the desired frequency components, *i.e.* the information symbols, c_k.

In mobile channel environments the transmitted signals experience reflection and refraction [13]. This results in different path delays ranging from several ns to tens of μs, depending on the environments encountered. The receiver has to have a channel equalizer in order to cope with the time dispersion of the received signals. OFDM reduces this requirement by increasing the signaling interval duration. However, it needs a guard time between the OFDM signaling intervals in order to reduce the ISI. Instead of a passive guard space, insertion of a quasi-periodically repeated cyclic prefix is used for removing inter-symbol interference [25]. Let us assume that the channel impulse response, $h(t)$, spans $(\nu+1)\,\frac{T}{N}$, where $\nu \ll N$ and the corresponding discrete channel impulse response, h_n, $0 \leq n \leq \nu$, is $h(\frac{n}{N}T)$. Let $s_{i,n}$ be the nth transmitted symbol in the ith frame as defined in (1.4). The cyclic prefix consists of $s_{i,N-\nu}$, $s_{i,N-\nu+1}$, $\cdots$, $s_{i,N-1}$, which is inserted before $s_{i,0}$, $s_{i,1}$, $\cdots$, $s_{i,N-1}$. Then, the sampled baseband received signal, $r_{i,n}$, for $n = -\nu,\ -\nu+1,\ \cdots,\ -1,\ 0,\ 1,\ 2,\ \cdots,\ N-1$, becomes

$$
\begin{aligned}
r_{i,-\nu} &= h_0 s_{i,N-\nu} + h_1 s_{i-1,N-1} + h_2 s_{i-1,N-2} + \cdots + h_\nu s_{i-1,N-\nu} \\
r_{i,-\nu+1} &= h_0 s_{i,N-\nu+1} + h_1 s_{i,N-\nu} + h_2 s_{i-1,N-1} + \cdots + h_\nu s_{i-1,N-\nu+1} \\
&\vdots \quad\quad \vdots \\
r_{i,-1} &= h_0 s_{i,N-1} + h_1 s_{i,N-2} + h_2 s_{i,N-1} + \cdots + h_\nu s_{i-1,N-1} \\
r_{i,0} &= h_0 s_{i,0} + h_1 s_{i,N-1} + h_2 s_{i,N-2} + \cdots + h_\nu s_{i,N-\nu} \\
r_{i,1} &= h_0 s_{i,1} + h_1 s_{i,0} + h_2 s_{i,N-1} + \cdots + h_\nu s_{i,N-\nu+1} \\
&\vdots \quad\quad \vdots \\
r_{i,\nu} &= h_0 s_{i,\nu} + h_1 s_{i,\nu-1} + h_2 s_{i,\nu-2} + \cdots + h_\nu s_{i,0} \\
&\vdots \quad\quad \vdots \\
r_{i,N-1} &= h_0 s_{i,N-1} + h_1 s_{i,N-2} + h_2 s_{i,N-3} + \cdots + h_\nu s_{i,N-\nu+1}\,.
\end{aligned}
$$

The first ν samples are discarded and the remaining N samples are processed by FFT in the receiver.

The remaining N samples can be represented in a more compact form:

$$r_{i,n} = \sum_{j=0}^{\nu} h_j s_{i,(n-j \bmod N)} \text{ for } n = 0, \cdots, N-1 . \tag{1.5}$$

The recovered data symbol, $\hat{c}_{i,k}$, becomes,

$$\hat{c}_{i,k} = \sum_{n=0}^{N-1} r_{i,n} e^{-j2\pi \frac{n}{N} k} \tag{1.6}$$

$$= c_{i,k} \sum_{n=0}^{\nu} h_n e^{-j2\pi \frac{n}{N} k} \tag{1.7}$$

$$= c_{i,k} H_k , \tag{1.8}$$

where H_k is the frequency domain channel transfer function and $c_{i,k} = \sum_{n=0}^{N-1} s_{i,n} e^{-j2\pi \frac{n}{N} k}$ was used to arrive at Equation 1.7. Equation 1.8 states that the original symbol, $c_{i,k}$, can be recovered without inter-frame interference or inter-subcarrier interference given the knowledge of $\{H_k\}$, which can be estimated.

The frequency spectrum of an OFDM signal using no pulse shaping is presented in Figure 1.2. The

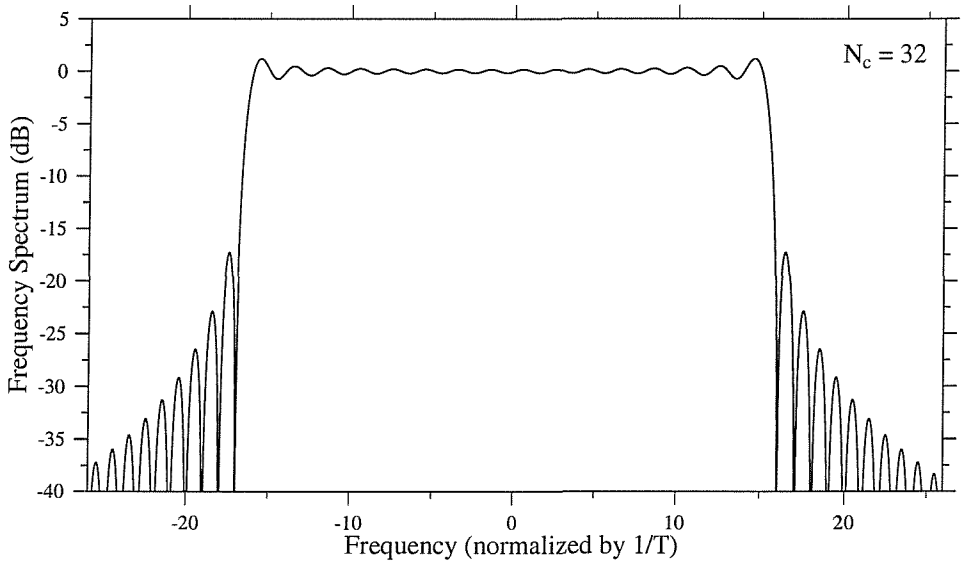

Figure 1.2: Power spectrum of OFDM signal using 32 carriers, without any pulse shaping

required bandwidth is approximately $N \times \frac{1}{T}$, which is the minimum bandwidth imposed by *Nyquist's sampling theorem*. Since the first spectral sidelobes are only about -17.3dB below the passband level, various pulse shaping and wavelet based transform methods were proposed for suppressing the sidelobes [25], which potentially result in adjacent channel interference.

One of the main drawbacks of the above OFDM system is the "peaky" time domain signal, which requires amplifiers having a high dynamic range [31, 32]. This issue will be discussed in more depth in Chapter 4. Another impediment is that OFDM systems are more sensitive to carrier frequency drift, than single carrier [33, 34] systems.

1.3 Multi-Carrier CDMA

A range of novel techniques combining DS-CDMA and OFDM have been presented in the literature [1, 2, 35–37].

A DS-CDMA system applies spreading sequences in the time domain and uses Rake receivers for optimally combining the time-dispersed energy in order to combat the effects of multi-path fading. However, in indoor wireless environments the time dispersion is low, on the order of nano seconds, and hence a high chip rate, on the order of tens of MHz, is required for resolving the multi-path components. This implies a high clock-rates, high power consumption as well as implementation difficulties. In order to overcome these difficulties, several techniques have been proposed, which combine DS-CDMA and multi-carrier modulation, such as MC-CDMA [1, 2, 35], MC-DS-CDMA [36] and Multi-Tone CDMA (MT-CDMA) [37]. This overview is mainly based on references [38, 39] by Prasad and Hara, [40] by Scott, Grant, McLaughlin, Povey and Cruickshank.

1.3.1 MC-CDMA

In MC-CDMA, instead of applying spreading sequences in the time domain, we can apply them in the frequency domain, mapping a different chip of a spreading sequence to an individual OFDM subcarrier. Hence each OFDM subcarrier has a data rate identical to the original input data rate and the multicarrier system 'absorbs' the increased rate due to spreading in a wider frequency band. The transmitted signal of the ith data symbol of the jth user $s_i^j(t)$ is written as [1, 41] :

$$s_i^j(t) = \sum_{k=0}^{K-1} b_i^j \, c_k^j \cos\{2\pi(f_0 + kf_d)t\} \, p(t - iT) \; , \tag{1.9}$$

where

- K is the number of subcarriers,
- b_i^j is the ith message symbol of the jth user,
- c_k^j represents the kth chip, $k = 0, \; \cdots, K-1$, of the spreading sequence of the jth user,
- f_0 is the lowest subcarrier frequency,
- f_d is the subcarrier separation and

- $p(t)$ is a rectangular signalling pulse shifted in time given by :

$$p(t) \triangleq \begin{cases} 1 & \text{for } 0 \leq t \leq T \\ 0 & \text{otherwise .} \end{cases} \tag{1.10}$$

If $1/T$ is used for f_d, the transmitted signal can be generated using the IFFT, as in the case of an OFDM system. The overall transmitter structure can be implemented by concatenating a DS-CDMA spreader and an OFDM transmitter, as shown in Figure 1.3. At the spreader, the information bit, b_i^j, is spread in

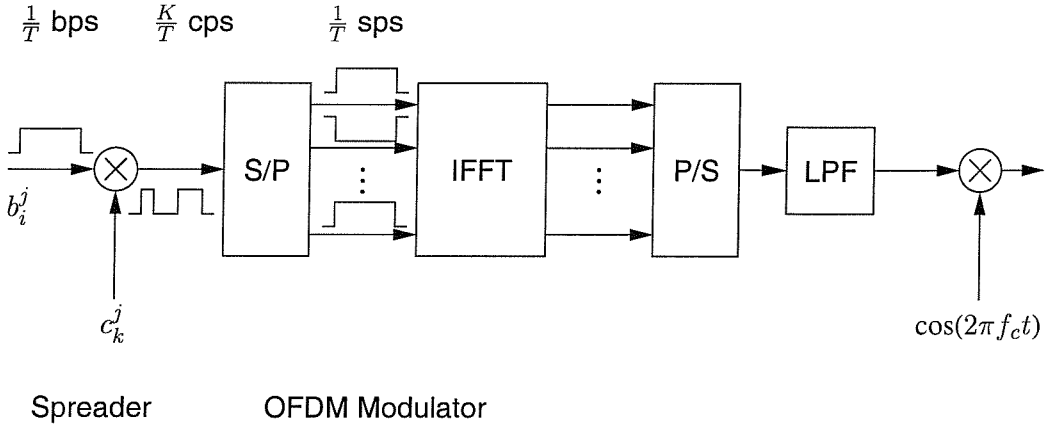

Figure 1.3: Transmitter schematic of MC-CDMA

the time domain by the jth user's spreading sequence, c_k^j, $k = 0, \cdots, K-1$. In this implementation, high speed operations are required at the output of the spreader in order to carry out the chip-related operations. The spread chips are fed into the serial-to-parallel (S/P) block and IFFT is applied to these K parallel chips. The output values of the IFFT in Figure 1.3 are time domain samples in parallel form. After parallel to serial (P/S) conversion these time domain samples are low-pass-filtered, in order to obtain the continuous time domain signal. The signal modulates the carrier and is transmitted to the receiver.

Figure 1.4 shows another implementation, which removes the time domain spreader. In this implementation, the spreading sequence is applied directly to the identical parallel input bits. Hence, the high speed spreading operation is not required.

The spreading sequences in MC-CDMA separate other users' signals from the desired signal, provided that their spreading sequences are orthogonal to each other. Orthogonal codes have zero cross correlation and hence they are particularly suitable for MC-CDMA. Walsh codes and orthogonal Gold codes are well known such codes, which will be examined in Chapter 2.

At the MC-CDMA receiver shown in Figure 1.5 each carrier's symbol, *i.e.* the corresponding chip c_k^j of user j, is recovered using FFT after sampling at a rate of K/T samples/sec and the recovered chip sequence is correlated with the desired user's spreading code in order to recover the original information,

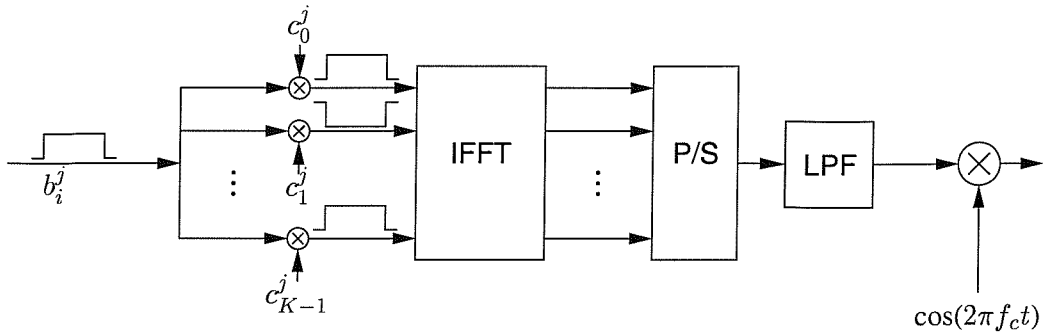

Figure 1.4: Alternative transmitter schematic of MC-CDMA

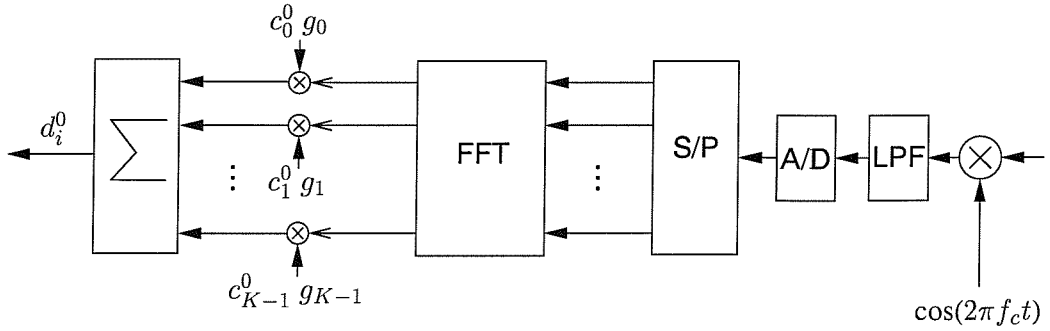

Figure 1.5: Receiver schematic of MC-CDMA

b_i^j. Let us define the ith received symbol at the kth carrier in the downlink as :

$$r_{k,i} = \sum_{j=0}^{J-1} H_k\, b_i^j\, c_k^j + n_{k,i}\,, \tag{1.11}$$

where J is the number of users, H_k is the frequency response of the kth subcarrier and $n_{k,i}$ is the corresponding noise sample. The MC-CDMA receiver of the 0-th user multiplies $r_{k,i}$ of (1.11) by its spreading sequence chip, c_k^0, as well as by the gain, g_k, which is given by the reciprocal of the estimated channel transfer factor of subcarrier k, for each received subcarrier symbol for $k = 0, \cdots, K-1$. It sums all these products, in order to arrive at the decision variable, d_i^0, which is given by :

$$d_i^0 = \sum_{k=0}^{N-1} c_k^0\, g_k\, r_{k,i}\,. \tag{1.12}$$

Without the frequency domain equalization of the received subcarrier symbols, the orthogonality between the different users cannot be maintained. Several methods have been proposed for choosing g_k [1, 38, 41]. The associated BER analysis was performed using various equalization methods over both the Rayleigh channels and Rician channels by Yee and Linnartz [1]. The comparative summary of numerical results for various equalization strategies was given, for example, by Prasad and Hara [38, 39].

1.3.2 MC-DS-CDMA

In order to be able to transmit high-rate data, while maintaining a sufficiently high processing gain, the chip rate of the corresponding DS-CDMA system may have to become significantly higher, than the processing speed of state-of-the-art electronics. In this case, parallel transmission of DS-CDMA signals using the OFDM structure [36, 38] can be a solution. Figure 1.6 shows the transmitter structure of a MC-DS-CDMA system. The K consecutive input bits of the jth user, b_i^j, $i = 0 \cdots K-1$, are serial-

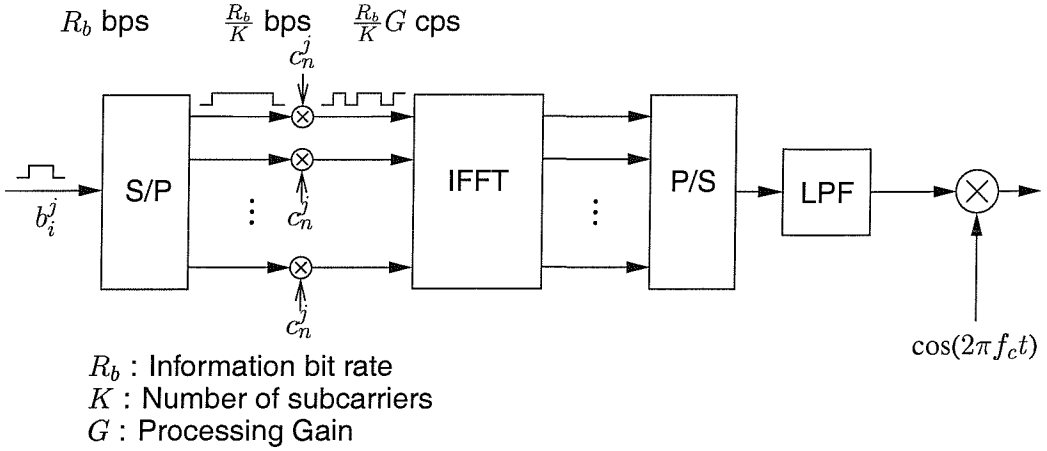

Figure 1.6: Transmitter schematic of MC-DS-CDMA

to-parallel converted first. Then, each bit b_i^j is spread by the jth user's spreading sequence in the time domain. The other operations are identical to those of MC-CDMA. In other words, in the MC-CDMA scheme of Figure 1.3 the data bits arriving at a rate of $1/T$ are first spread and hence have a rate of K/T, before reducing the rate again to $1/T$. By contrast, in the MC-DS-CDMA scheme of Figure 1.6 the bit rate of R_b is first reduced to R_b/K and then we produce the rate R_bG/K using spreading.

Figure 1.7(a) shows the typical spectrum of the MC-DS-CDMA signal operated using the schematic of Figure 1.6. The subcarrier separation, f_d, meets the orthogonality condition [38] of:

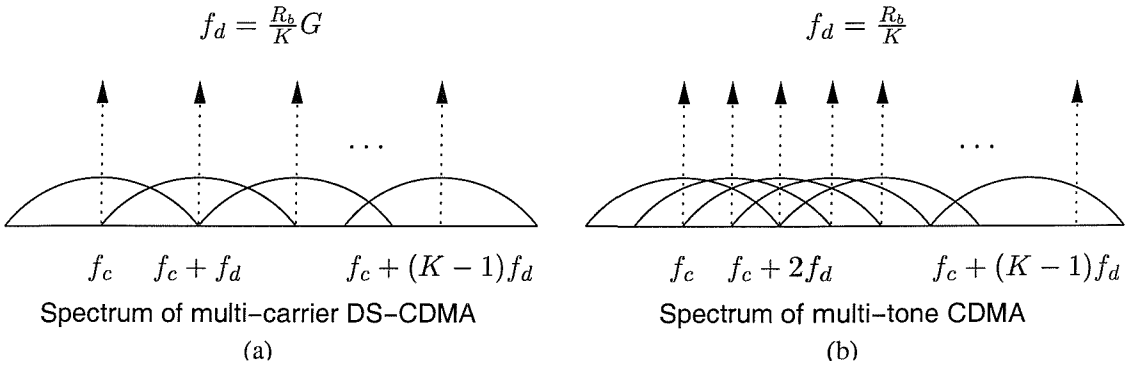

Figure 1.7: Typical power spectra of MC-DS-CDMA and MT-CDMA

$$f_d = \frac{R_b}{K} G \,, \tag{1.13}$$

where R_b is the source bit rate, K is the number of subcarriers and G is the processing gain. When K is equal to G, the MC-DS-CDMA spectrum [36] has the same shape, as that of an MC-CDMA system [1]. While the spectra of MC-CDMA signals [1] and MC-DS-CDMA signals [36] exhibit orthogonality between the subcarriers, that of the MT-CDMA scheme of Figure 1.7(b) does not maintain orthogonality between the subcarriers.

The transmitted signal $s_i^j(t)$ of the jth user during the ith signalling interval is written as :

$$s_i^j(t) = \sum_{k=0}^{K-1} \sum_{g=0}^{G-1} b_{k,i}^j c_g^j \, p(t - iT_s - gT_c) \cos\{2\pi(f_0 + kf_d)t\} \,, \tag{1.14}$$

where $b_{k,i}^j$ is the ith bit of the jth user modulating the kth subcarrier after serial-to-parallel conversion, c_g^j, $g = 0 \cdots G-1$ represents the jth user's spreading sequence, $T_s = \frac{K}{R_b}$ is the signalling interval, $T_c = \frac{T_s}{G}$ is the chip duration and $p(t)$ is defined in Equation 1.10.

1.3.3 MT-CDMA

MT-CDMA is a combined technique employing time domain spreading and a similar multicarrier transmission scheme to that of the MC-DS-CDMA scheme of Figure 1.6. However, the time domain spreading is applied after the IFFT stage. Figure 1.8 represents a simple block diagram of the transmitter structure.

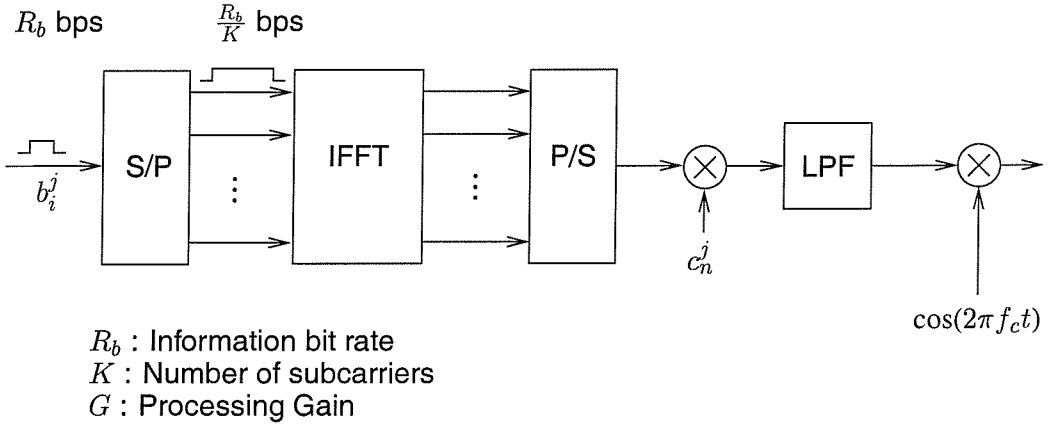

Figure 1.8: Transmitter schematic of MT-CDMA

The required operations are the same as in OFDM, but spreading takes place after the IFFT stage. In this way, the system has a multiple access capability. The corresponding power spectrum is shown in Figure 1.7(b). Each subcarrier's spectrum overlaps with other subcarriers' spectra. The subcarrier frequency spacing is given by [38] :

$$f_d = \frac{R_b}{K} \,, \tag{1.15}$$

which does not retain the subcarriers' orthogonality. The main intention of this operation is to increase the processing gain within a given bandwidth.

1.3.4 Summary

We have briefly investigated three types of multi-carrier spread-spectrum schemes combining DS-CDMA and OFDM techniques, namely MC-CDMA [1, 2, 35], MC-DS-CDMA [36] and MT-CDMA [37]. While MC-CDMA employs frequency domain spreading, the other two schemes, *i.e.* the MC-DS-CDMA and MT-CDMA schemes, employ time domain spreading. Hence, MC-CDMA is capable of exploiting frequency diversity in an explicit manner, since the energy of a symbol is spread over several subcarriers. On the other hand, since all the energy of a symbol is confined to one subcarrier in the MC-DS-CDMA and MT-CDMA schemes, the frequency diversity provided by the different subcarriers cannot be exploited, unless a channel coding scheme is employed in conjunction with cross-subcarrier interleaving [38].

Compared to MC-DS-CDMA requiring the same frequency spectrum band, MT-CDMA is capable of providing a significantly higher spreading factor than that of MC-DS-CDMA, resulting in lower self-interference and in a better suppression of the Multiple Access Interference (MAI) [37]. However, MT-CDMA suffers from inter-subcarrier interference due to the fact that the subcarriers are not orthogonal to each other. Since MC-DS-CDMA is capable of providing backward compatibility with the existing IS-95 DS-CDMA system, a specific form of MC-DS-CDMA has been chosen as one of the Third Generation (3G) mobile communication standards [42].

Prasad and Hara reported that MC-CDMA employing Minimum Mean Square Error Combining (MMSEC) shows the lowest BER amongst the three above-mentioned multi-carrier spread-spectrum schemes in a downlink scenario [39]. The performance of MC-CDMA in a downlink scenario will be investigated in more depth in Chapter 3.

1.4 Outline of the Thesis

Since the properties of spreading sequences are as important in multicarrier CDMA as in DS-CDMA, the properties of various spreading sequences are reviewed in the next chapter. Chapter 3 reviews some of the detection schemes available for MC-CDMA operating in a synchronous environment. Single user detectors as well as multi-user detectors are investigated. One of the main problems associated with the implementation of multi-carrier communication systems is their high Peak-to-Mean Envelope-Power Ratio (PMEPR), requiring highly linear power amplifiers. The envelope power of the MC-CDMA signal is analysed in Chapter 4. Several orthogonal spreading sequences are examined, in order to assess their ability to maintain low PMEPR of the transmitted signal. The effects of reduced PMEPR are investigated in terms of the BER performance and the out-of-band frequency spectrum. In Chapter 5 an adaptive modulation assisted MC-CDMA technique is investigated using both analyses as well as simulation-based studies. Several mode switching schemes are compared and the optimum switching levels are derived for a generic adaptive modulation scheme. Chapter 6 deals with three different types of reduced complexity despreading methods that can be used at the receiver. Their BER performance as well as their computational complexity reductions are presented. Chapter 7 concludes this thesis with a summary of results and lists a number of areas which require further investigations.

The novel contributions of the thesis are as follows.

Chapter 4

- The envelope power of the multi-code MC-CDMA signal was analysed and it was shown that the correlation properties of the spreading codes employed predetermines the envelope power [43].
- A multi-code MC-CDMA scheme employing a certain family of subcomplementary sequences as its spreading sequences was shown to exhibit a Peak-to-Mean Envelope Power Ratio (PMEPR) bounded by 3dB.

Chapter 5

- The mode-switching levels of an adaptive modulation assisted MC-CDMA scheme were optimised on a per-SNR basis, in order for achieving a constant target average BER, while providing the highest possible average Bits Per Symbol (BPS) throughput [44].
- A closed form expression for the average BER and BPS throughput was derived for a so-called two dimensional Rake assisted adaptive QAM scheme and its performance employing the per-SNR optimised mode-switching levels was investigated numerically [45].
- A concatenated turbo coded and space-time coded scheme was amalgamated with the per-SNR optmised adaptive modulation assisted MC-CDMA arrangement and its performance was investigated with the aid of simulations [46, 47]
- A set of globally optimum mode-switching levels was obtained for a generic adaptive modulation scheme operating over a Nakagami fading channel employing the Lagrangian optimisation method [48].
- The performance of a globally optimum mode-switching level assisted adaptive MC-CDMA scheme was analysed, when communicating over frequency selective slow Rayleigh fading channels [49]

Chapter 6

- The performance of a novel reduced complexity despreading detector employed in a fully loaded MC-CDMA scheme was analysed for transmission over both an AWGN channel and an impulse-noise contaminated AWGN channel.

Chapter 2

Basic Spreading Sequences

A spread spectrum communication system spreads the original information signal using user-specific signature sequences. The receiver then correlates the synchronized replica of the signature sequences with the received signal, in order to recover the original information. Due to the noise-like properties of the spreading sequences, 'eavesdropping' is not straightforward. DS-CDMA exploits the code's auto-correlation properties in order to combine the multi-path signals of a particular user. By contrast, the different users' codes exhibit a low cross-correlation, which can be exploited for separating each user's signal. MC-CDMA also relies on this cross-correlation property in supporting multi-user communications. The characteristics of the spreading sequences play an important role in terms of the achievable system performance and hence the properties of several sequences will be examined in this chapter.

2.1 PN Sequences

Pseudo-Noise (PN) sequences are binary sequences, which exhibit noise-like properties. Maximal length sequences (m-sequences), Gold sequences and Kasami sequences are well-known PN sequences. Other important PN sequences are considered in reference [6].

2.1.1 Maximal Length Sequences

Various pseudo-random codes can be generated using Linear Feedback Shift Registers (LFSR). The so-called generator polynomial or LFSR connection polynomial governs all the characteristics of the generator. For a given generator polynomial, there are two ways of implementing LFSRs [6, 50]. The sequence generator shown in Figure 2.1 uses only the LFSR's output bits for feeding information back into several intermediate stages of the shift register, which is attractive for high speed hardware as well as software implementations. The other implementation known as the Fibonacci feedback generator [50], which is shown in Figure 2.2, is capable of generating several delayed versions of the same sequence without any additional logic, at the output of each shift register. Note that the connection position is reversed in Figure 2.2, in order to generate the same sequences as the Galois implementation of [50] as shown in Figure 2.1. Shift-register sequences having the maximum possible repetition period of

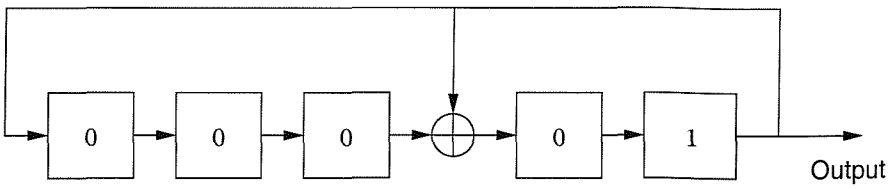

Figure 2.1: Galois feedback implementation of the m-sequence generator. The generator polynomial of $g(x) = 1 + x^2 + x^5$ determines the positions of the non-zero feedback taps.

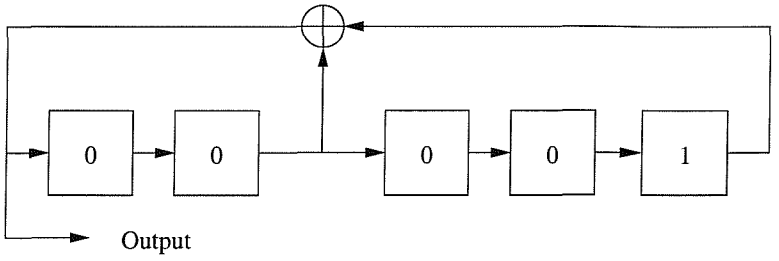

Figure 2.2: Fibonacci feedback implementation of the m-sequence generator. The same generator polynomial was employed as in Figure 2.1.

$2^r - 1$ for an r-stage shift register are referred to as maximal-length sequences or m-sequences. A so-called primitive generator polynomial [50] always yields an m-sequence. The m-sequences have three important properties, namely the so-called balance property, the run-length property as well as the shift-and-add property [51]. The periodic auto-correlation function $R_a(k)$ of the sequence $\{a_n\}$ is defined as :

$$R_a(k) \triangleq \frac{1}{N} \sum_{n=0}^{N-1} a_n a_{n+k} \,, \tag{2.1}$$

where N is the period of the sequence. The periodic auto-correlation function of an m-sequence is given by :

$$R_a(k) = \begin{cases} 1.0 & k = lN \\ -\frac{1}{N} & k \neq lN \,, \end{cases} \tag{2.2}$$

where l is an integer and N is the period of the m-sequence. The excellent auto-correlation property manifested by the high ratio of these two $R_a(k)$ values is a consequence of the above-mentioned first and third properties, as justified in references [6, 50, 51]. The above-mentioned good auto-correlation features justify the employment of m-sequences for example in the Pan-American IS-95 standard CDMA system [20]. Moreover, as the cross-correlation property of these sequences is relatively poor compared to that of the family of Gold codes, usually the same sequences with different offsets are employed for different users or for different base stations in IS-95 based networks.

2.1.2 Gold Codes

Certain pairs of m-sequences having the same degree can be used for generating the so-called Gold codes by linearly combining two m-sequences associated with different offsets, where the operations are defined over the so-called finite Galois field [6, 50, 52]. Not all pairs of m-sequences yield Gold codes and those which do are referred to as *preferred pairs*. The auto-correlations and cross-correlations of Gold codes may exhibit the legitimate values of $\{-1, -t(m), t(m) - 2\}$, where

$$t(m) = \begin{cases} 2^{(m+1)/2} + 1 & \text{for odd } m \\ 2^{(m+2)/2} + 1 & \text{for even } m \,. \end{cases} \tag{2.3}$$

It is worth mentioning that Gold codes do not exist for some value of m [52]. Gold codes exhibit lower peak cross-correlations, than m-sequences, as shown in Table 13-2-1 of [25] and hence they differentiate amongst different users more confidently or distinctively. Furthermore, the cross-correlation function of Gold codes exhibits numerous '-1' values, which is the lowest value among the three possible cross-correlation values. By contrast, Kasami sequences exhibit a lower proportion of '-1's in their cross-correlation functions, while exhibiting a peak cross-correlation, which is half of that of the Gold codes.

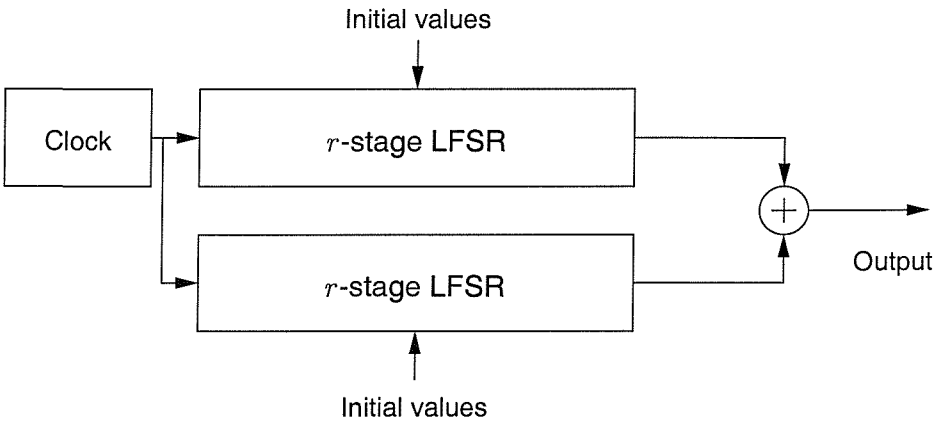

Figure 2.3: Schematic of a Gold code generator

The generation of Gold codes is straightforward. The simple block diagram of a Gold code generator is shown in Figure 2.3. Using two preferred m-sequence generators of degree r, in conjunction with a set of r initial values in the upper LFSR where at least one value is non-zero, 2^r number of different Gold codes can be obtained by changing the set of r initial values of the bottom LFSR according to the range of 0 to $2^r - 1$. Another Gold sequence can be obtained by setting the contents of the upper LFSR to all zeros, which results in a Gold sequence that is identical to the second m-sequence itself, which is generated from the bottom LFSR of Figure 2.3. Hence in total, $2^r + 1$ Gold codes can be obtained from a Gold code generator, which is characterised by a pair of preferred m-sequences.

2.1.3 Kasami Sequences

Kasami sequences have optimal cross-correlation values, reaching the so called Welch lower bound [6, 25]. The lower bound on the cross-correlation between any pair of binary sequences of period n in a set of M sequences is [25] :

$$\phi_{max} \geq n\sqrt{\frac{M-1}{Mn-1}}. \tag{2.4}$$

Kasami sequences can be generated by the following procedure [6]. For the m-sequence $\mathbf{a}$, the so-called decimated sequence of $\mathbf{a}$ is obtained by taking every qth bit of $\mathbf{a}$, which is denoted by $\mathbf{a[q]}$. By choosing $q = 2^{r/2} + 1$, where r is the degree of sequence $\mathbf{a}$, having retained every qth bit of $\mathbf{a}$, $\mathbf{a[q]}$ is periodic with the period of $2^{r/2} - 1$. By repeating $\mathbf{a[q]}$ q times, a new sequence $\mathbf{b}$ of length $2^r - 1$ is obtained. With the aid of $\mathbf{a}$ and $\mathbf{b}$, we form a new set of sequences by module-two adding $\mathbf{a}$ and the $2^{r/2} - 2$ number of cyclically shifted versions of the sequence $\mathbf{b}$. Including $\mathbf{a}$ and $\mathbf{b}$, we get a total of $2^{r/2}$ number of sequences. These sequences are the so-called Kasami sequences [6]. The hardware implementation of Kasami sequences is daunting, because the decimation process requires a high clock frequency. Fortunately, the decimated sequence itself is an m-sequence [6] of order $r/2$ and this fact can be exploited for implementing Kasami sequence generators, as shown in Figure 2.4. The m-sequence

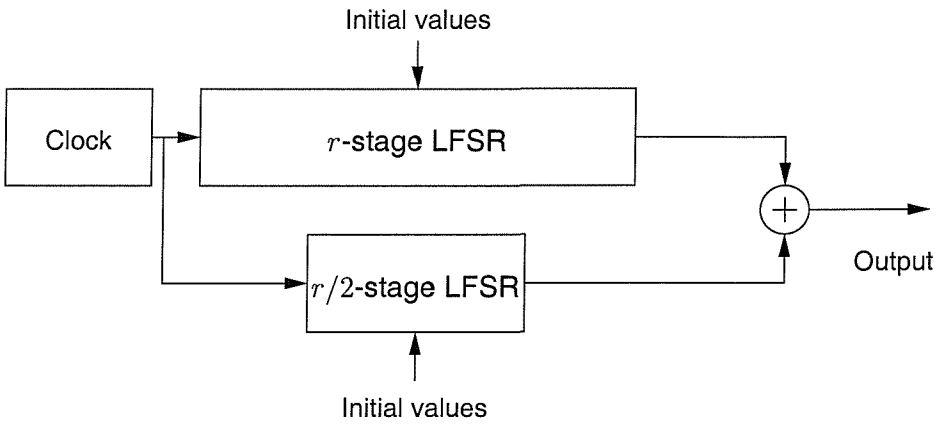

Figure 2.4: Schematic of a Kasami sequence generator

generated by the r-stage LFSR and the other m-sequence output by the $r/2$-stage LFSR are added in the binary Galois field in order to form a Kasami sequence.

2.2 Orthogonal Codes

Orthogonal codes have zero cross-correlation. They may appear attractive in terms of replacing PN codes, which have non-zero cross-correlations. However, the cross-correlation value is zero only when there is no offset between the codes. In fact, they exhibit higher cross-correlations at non-zero offsets, than PN codes. Their auto-correlation properties are usually not attractive either. Nonetheless, orthog-

onal codes have found application for example in perfectly synchronized environments, such as in the down-link of mobile communications.

There are several so-called code expansion techniques that can be used in order to generate orthogonal codes. Probably the Hadamard transform [50] is the best known technique. A modified Hadamard transform also appeared in the literature [53], which is essentially constituted by the Hadamard transform using a different transform coefficient indexing. Orthogonal Gold codes, which will be detailed in Section 2.2.2, show reasonable cross-correlation and off-peak auto-correlation values, while providing perfect orthogonality in the zero-offset case. Lastly, the multi-rate orthogonal codes of Section 2.2.3 are attractive, since they can provide variable spreading factors depending on the information rate to be supported.

2.2.1 Walsh Codes

Walsh codes are generated by applying the Hadamard transform [50] to an one by one zero matrix repeatedly. The Hadamard transform is defined as [50] :

$$\begin{aligned} \mathbf{H}_1 &= [0] \\ \mathbf{H}_{2n} &= \begin{bmatrix} \mathbf{H}_n & \mathbf{H}_n \\ \mathbf{H}_n & \overline{\mathbf{H}}_\mathbf{n} \end{bmatrix}. \end{aligned} \tag{2.5}$$

This transform gives us a Hadamard matrix, $\mathbf{H}_n$, only for $n = 2^i$, where i is an integer. The Hadamard matrix is a symmetric square-shaped matrix. Each column or row corresponds to a Walsh code of length n. Every row of $\mathbf{H}_n$ is orthogonal to all other rows.

As an example, let us consider the case of n = 8. We can generate 8-bit Walsh codes, $\mathbf{H}_8$, applying the transform continuously from $\mathbf{H}_1$ three times repeatedly. The resultant matrix is as follows :

$$\mathbf{H}_8 = \begin{bmatrix} 0 & 0 & 0 & 0 & 0 & 0 & 0 & 0 \\ 0 & 1 & 0 & 1 & 0 & 1 & 0 & 1 \\ 0 & 0 & 1 & 1 & 0 & 0 & 1 & 1 \\ 0 & 1 & 1 & 0 & 0 & 1 & 1 & 0 \\ 0 & 0 & 0 & 0 & 1 & 1 & 1 & 1 \\ 0 & 1 & 0 & 1 & 1 & 0 & 1 & 0 \\ 0 & 0 & 1 & 1 & 1 & 1 & 0 & 0 \\ 0 & 1 & 1 & 0 & 1 & 0 & 0 & 1 \end{bmatrix} \tag{2.6}$$

The first column is the all-zero sequence and the second one is an alternating sequence of '0' and '1'. This is true for all Hadamard matrices. Let $\mathbf{H}_8[i]$ and $\mathbf{H}_8[j]$, $i,\ j\ = 0 \cdots 7$, be two sequences formed from the ith and the jth rows of $\mathbf{H}_8$. Then, we can verify that $\mathbf{H}_8[i]$ and $\mathbf{H}_8[j]$ are orthogonal to each other. Let us refer to i and j as the indexes of $\mathbf{H}_8$.

A possible hardware implementation of $\mathbf{H}_8$ Walsh code is shown in Figure 2.5. It comprises two T-flipflops, a clock generator, three AND gates denoted as $\otimes$ and one XOR gate denoted as $\oplus$. The clock source generates the $010101\cdots$ sequence, which corresponds to $\mathbf{H}_8[1]$. After the first T-flipflop,

the sequence becomes $00110011\cdots$, which is $\mathbf{H}_8[2]$, since the T-flipflop simply halves the clock rate. The output sequence of the second T-flipflop becomes $00001111\cdots$, which represents $\mathbf{H}_8[4]$. In fact, these three sequences, namely $\mathbf{H}_8[1]$, $\mathbf{H}_8[2]$ and $\mathbf{H}_8[4]$, form bases so that the remaining rows of $\mathbf{H}_8$ can be generated by the linear combination of these three sequences. The desired Walsh code index is described by u_2, u_1, u_0, which is a binary bit-based representation of the index. For example, we can set $u_2 = 0$, $u_1 = 1$, $u_0 = 1$, in order to obtain the $\mathbf{H}_8[3]$ sequence. This can be verified by showing

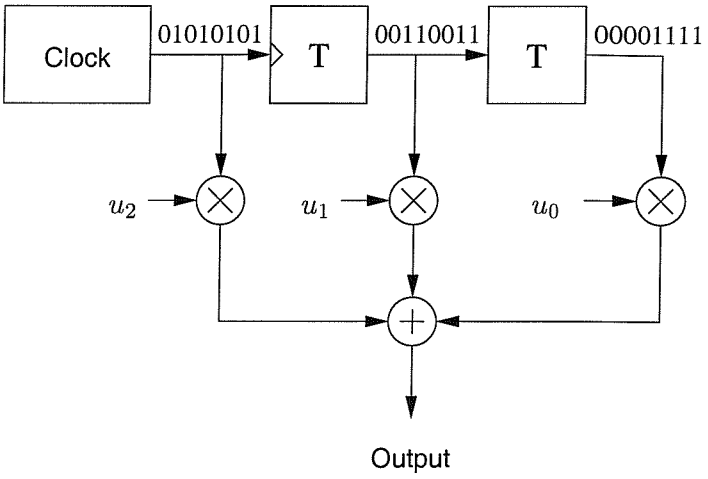

Figure 2.5: Implementation of a Walsh code generator of length=2^3 [50, Figure 9-8, page 542]

that $\mathbf{H}_8[1] \oplus \mathbf{H}_8[2]$ actually yields $\mathbf{H}_8[3]$. A specific disadvantage of this implementation, however, is that the total delay of generating a specific code is proportional to the length of the Walsh code to be generated.

2.2.2 Orthogonal Gold Codes

Experiments show that the cross-correlation values of the Gold codes of Section 2.1.2 are '-1' for many code offsets. This suggests that it may be possible to render the cross-correlation values associated with these offsets '0' by attaching an additional '0' to the original Gold codes. In fact, 2^r orthogonal codes can be obtained by this simple zero-padding from a preferred pair of two r-stage LFSR. These codes are referred to as orthogonal Gold codes.

As an example, let us consider a Gold code characterized by a preferred pair of m-sequences, which are denoted by $g_0(x) = 1 + x + x^3$ and $g_1(x) = 1 + x^2 + x^3$ of order three. We can obtain eight Gold codes of length 7 with the aid of the schematic of Figure 2.3 by changing the initial values of the upper LFSR from '000' to '111', while maintaining the bottom LFSR's initial values as '001'. We arrive at

eight orthogonal Gold codes by attaching a '0' at the tails, which are given below :

$$\mathbf{G}_8 = \begin{bmatrix} 1 & 0 & 1 & 1 & 1 & 0 & 0 & 0 \\ 0 & 1 & 0 & 1 & 0 & 0 & 0 & 0 \\ 1 & 1 & 0 & 0 & 1 & 1 & 0 & 0 \\ 0 & 0 & 1 & 0 & 0 & 1 & 0 & 0 \\ 1 & 0 & 0 & 0 & 0 & 0 & 1 & 0 \\ 0 & 1 & 1 & 0 & 1 & 0 & 1 & 0 \\ 1 & 1 & 1 & 1 & 0 & 1 & 1 & 0 \\ 0 & 0 & 0 & 1 & 1 & 1 & 1 & 0 \end{bmatrix} . \tag{2.7}$$

The ith row of $\mathbf{G}_8$, namely $\mathbf{G}_8[i]$, is the ith orthogonal Gold code of length 8. Let us define an n by n dimensional *cross-correlation matrix* $\mathbf{C}(\mathbf{G})$ of an n by n dimensional code matrix $\mathbf{G}$, where each row is a code of length n, defined as $\mathbf{G}\mathbf{G}^T$, and the operations take place after replacing '0' and '1' with '1' and '-1', respectively. Then, the element in the ith row of the jth column, namely $\mathbf{C}_{ij}$, is the cross-correlation between the two codes, $\mathbf{G}[i]$ and $\mathbf{G}[j]$. Let us also define an n by n dimensional *auto-correlation matrix* $\mathbf{A}(\mathbf{G})$, which comprises $\mathbf{A}_{ij}$, the element in the ith row of the jth column, defined as the auto-correlation value of $\mathbf{G}[i]$ with offset j. Now we get the cross-correlation matrices of $\mathbf{H}_8$ in (2.6) and $\mathbf{G}_8$ in (2.7) as :

$$\mathbf{C}(\mathbf{H}_8) = 8\,\mathbf{I}_8 \tag{2.8}$$

$$\mathbf{C}(\mathbf{G}_8) = 8\,\mathbf{I}_8\,, \tag{2.9}$$

where $\mathbf{I}_8$ is the 8 by 8 dimensional identity matrix. Equations (2.8) and (2.9) show that there is no difference between the Walsh codes and the orthogonal Gold codes in terms of their cross-correlations. However, their auto-correlation properties are different. The auto-correlation matrix, which was defined above, of the Walsh codes of length 8 is shown below:

$$\mathbf{A}(\mathbf{H}_8) = \begin{bmatrix} 8 & 8 & 8 & 8 & 8 & 8 & 8 & 8 \\ 8 & -8 & 8 & -8 & 8 & -8 & 8 & -8 \\ 8 & 0 & -8 & 0 & 8 & 0 & -8 & 0 \\ 8 & 0 & -8 & 0 & 8 & 0 & -8 & 0 \\ 8 & 4 & 0 & -4 & -8 & -4 & 0 & 4 \\ 8 & -4 & 0 & 4 & -8 & 4 & 0 & -4 \\ 8 & 4 & 0 & -4 & -8 & -4 & 0 & 4 \\ 8 & -4 & 0 & 4 & -8 & 4 & 0 & -4 \end{bmatrix} . \tag{2.10}$$

Let us compare (2.10) with the auto-correlation matrix of the orthogonal Gold codes of length 8 formu-

lated as :

$$\mathbf{A}(\mathbf{G}_8) = \begin{bmatrix} 8 & 0 & 0 & -4 & 0 & -4 & 0 & 0 \\ 8 & 0 & 4 & 0 & 0 & 0 & 4 & 0 \\ 8 & 0 & -8 & 0 & 8 & 0 & -8 & 0 \\ 8 & 0 & 0 & 4 & 0 & 4 & 0 & 0 \\ 8 & 0 & 4 & 0 & 0 & 0 & 4 & 0 \\ 8 & -4 & 0 & 0 & 0 & 0 & 0 & -4 \\ 8 & 0 & 0 & 4 & 0 & 4 & 0 & 0 \\ 8 & 4 & 0 & -4 & -8 & -4 & 0 & 4 \end{bmatrix} . \tag{2.11}$$

Observe in (2.11) that $\mathbf{A}(\mathbf{H}_8)$ has 24 number of '$\pm$8's and 16 number of '0's at the various offsets, while $\mathbf{A}(\mathbf{G}_8)$ has 4 number of '$\pm$8's and 36 number of '0's. Both have sixteen '$\pm$4's. Hence, the orthogonal Gold codes exhibit better characteristics, than the Walsh codes in terms of their auto-correlations. We can conclude that orthogonal Gold codes are desirable in some applications, where the codes' auto-correlations have to be low, which is desirable, in order to be able to avoid falsely registering the main peak of the autocorrelation function.

2.2.3 Multi-rate Orthogonal Gold Codes

State-of-the-art wireless communication systems are expected to support multi-rate transmissions. CDMA systems can use multi-rate orthogonal codes for supporting this feature. Despite the terminology 'multi-rate', typically a constant physical chip rate is maintained during variable bit rate transmissions and it is the number of chips per information bit, *i.e.* the spreading factor, which is varied, as it will be described during our further discourse. Generating multi-rate orthogonal codes is fairly straightforward. Commencing from any orthogonal code set, multi-rate codes can be obtained by applying one of the orthogonal transformation techniques described in [50]. Using the Walsh code generator of Figure 2.5 and the orthogonal Gold code generator of Section 2.2.2, one can readily implement multi-rate orthogonal code generators, as shown in Figure 2.6. The clock rate of the Walsh code generator is R_c/L, where R_c is the chip rate and L is the length of the orthogonal Gold code. In other words, the Walsh code generator is clocked once per orthogonal Gold code word. The maximum Walsh code length, n, is given by :

$$n = \frac{SF_{max}}{L} , \tag{2.12}$$

where SF_{max} is the maximum spreading factor and the orthogonal Gold code generator is clocked at the chip-rate of R_c, where SF_{max} is given by $SF_{max} = R_c/R_b$, and R_b is the lowest transmission symbol rate of the multi-rate system. The Walsh code index, $(u_{n-1}, \cdots u_1, u_0)_2$ of Figure 2.6, has to be assigned carefully, in order to preserve the orthogonality between the spread multi-rate data symbols [54]. For the lowest-rate bit stream any free Walsh code index can be assigned from the range of 0 to $n-1$. However, for a $2^k \cdot R_b$-rate data stream, a total of 2^k free Walsh code indices has to be assigned corresponding to the codes $\{W_j\}$, $j = u + \frac{n}{2^k}v$, where u is selected from the set of $\{0, \cdots, \frac{n}{2^k} - 1\}$ and v from the set of $0, \cdots, 2^k - 1$. From the above set of indices only the first assigned index associated with $v = 0$ should be actually used.

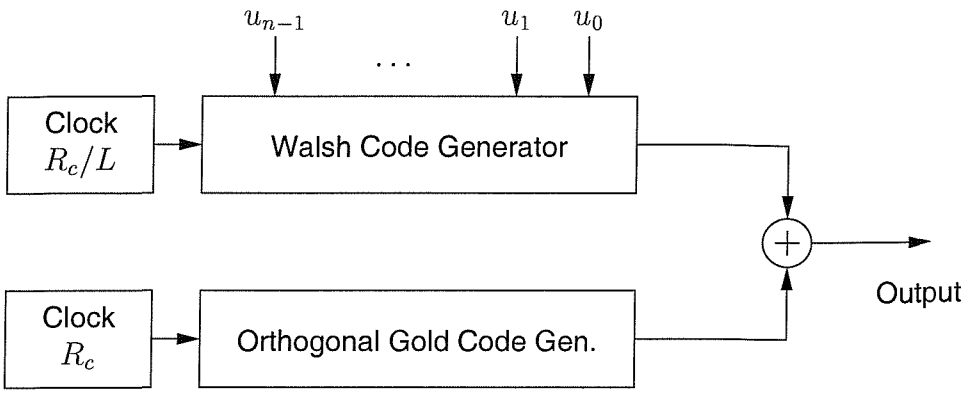

Figure 2.6: A multi-rate orthogonal Gold code generator. L is the length of the orthogonal Gold code, R_c is the chip rate and n is the length of Walsh code.

In order to augment the concept of index assignment, let us now consider a simple example. Let us assume that we have to design a multi-rate CDMA system, which supports two rates, namely 8 kbps and 16 kbps, and that the chip rate, R_c, is 256 kcps. The maximum spreading factor is given by :

$$SF_{max} = R_c/R_b = 256\,kcps/8\,kbps = 32\ , \tag{2.13}$$

where we used R_b = 8kbps as the lowest transmission symbol rate. Let us select $L = 8$, so that we can use $\mathbf{G}_8$ of (2.7). According to (2.12), the maximum Walsh code length n, is $SF_{max}/L = 32/8 = 4$. Thus, we use the 4 by 4 dimensional matrix $\mathbf{H}_4$, given as :

$$\mathbf{H}_4 = \begin{bmatrix} 0 & 0 & 0 & 0 \\ 0 & 1 & 0 & 1 \\ 0 & 0 & 1 & 1 \\ 0 & 1 & 1 & 0 \end{bmatrix}\ , \tag{2.14}$$

according to the schematic of Figure 2.6 for expanding $\mathbf{G}_8$, in order to generate the multi-rate orthogonal Gold code of dimension 32, $\mathbf{M}_{32}$, by using $\mathbf{G}_8$ of (2.7) in its original form in those positions of $\mathbf{H}_4$ in (2.14), where there is a '0' and its complementary form in the positions, where there is '1', yielding :

$$\mathbf{M_{32}} = \begin{bmatrix} \mathbf{G}_8 & \mathbf{G}_8 & \mathbf{G}_8 & \mathbf{G}_8 \\ \mathbf{G}_8 & \overline{\mathbf{G}_8} & \mathbf{G}_8 & \overline{\mathbf{G}_8} \\ \mathbf{G}_8 & \mathbf{G}_8 & \overline{\mathbf{G}_8} & \overline{\mathbf{G}_8} \\ \mathbf{G}_8 & \overline{\mathbf{G}_8} & \overline{\mathbf{G}_8} & \mathbf{G}_8 \end{bmatrix}\ . \tag{2.15}$$

Let us now consider the properties of $\mathbf{M}_{32}$. Each row of $\mathbf{M}_{32}$ is orthogonal to other rows. The codes $\mathbf{M}_{32}[0]$, $\mathbf{M}_{32}[8]$, $\mathbf{M}_{32}[16]$ and $\mathbf{M}_{32}[24]$ are expanded from $\mathbf{G}_8[0]$. In general, $\mathbf{M}_{32}[i]$, $\mathbf{M}_{32}[8+i]$, $\mathbf{M}_{32}[16+i]$ and $\mathbf{M}_{32}[24+i]$, where i spans the range of 0, $\cdots$, 7, are generated from $\mathbf{G}_8[i]$ and hence they are not orthogonal, when they are used for multi-rate spreading. This lack of orthogonality is a consequence of the fact that when supporting a high transmission rate, while fixing the chip-rate,

the number of chips per data bit has to be reduced. For example, when doubling the bit-rate, the number of chips per bit is halved, which inevitably halves the number of orthogonal sequences available. Hence a double bit-rate user has to be assigned two orthogonal codes, which otherwise could be assigned to two basic-rate users. Figure 2.7 shows this concept more explicitly. Since $\mathbf{H}_4[0]$ and $\mathbf{H}_4[2]$ are not orthogonal

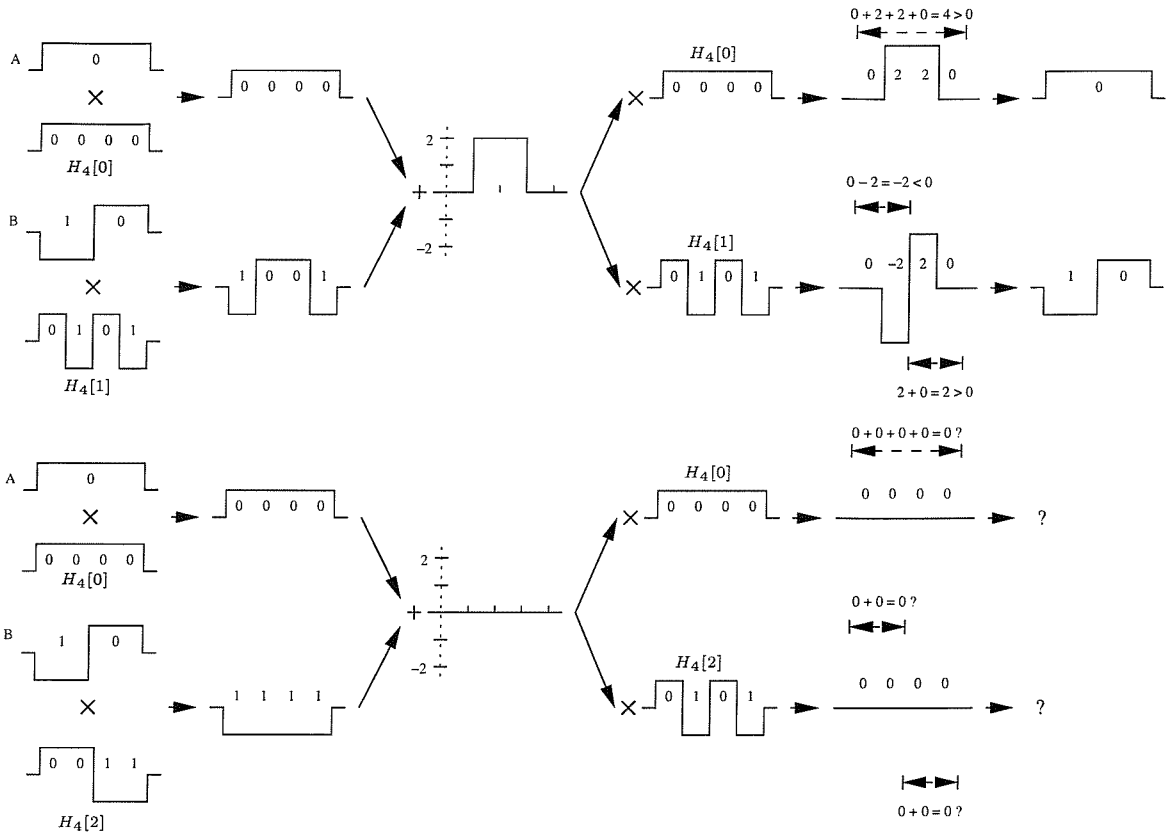

Figure 2.7: A conceptual diagram for multi-rate spreading: 'A' transmits at half the rate of the transmission rate of 'B'. 'A' uses $\mathbf{H}_4[0]$ and 'B' $\mathbf{H}_4[1]$ in the upper graph, which results in perfect information recovery at the receiver. In the lower graph, 'B' uses $\mathbf{H}_4[2]$, which breaks the orthogonality and makes information recovery impossible.

in a multi-rate environment, the receiver may not be able to recover the original symbols from the received signal, as shown in the graph at the bottom of Figure 2.7. In order to prevent this, two free Walsh codes have to be assigned to user 'B', transmitting at twice the transmission rate of user 'A' although effectively only one of these codes is transmitted. More explicitly, this potential non-orthogonality problem only arises in conjunction with the codes, which have the same generating orthogonal Gold code.

2.3 Summary and Conclusions

This chapter examined the correlation properties of a set of PN sequences, specifically those of the m-sequences, Gold codes and Kasami codes, as well as the correlation properties of a set of orthogonal sequences, namely those of Walsh codes, orthogonal Gold codes and multi-rate orthogonal Gold codes. The schematic diagram of each sequence generator was presented in Figure 2.1 through Figure 2.6. Based on these schematics, a sequence generator library[1] was written in C in order to aid future numerical and simulation studies.

It was observed in Section 2.2.2 that orthogonal Gold codes result in lower auto-correlation values, than those of the Walsh codes studied in Section 2.2.1. The effects of the different autocorrelation values of the spreading sequences on the envelope power of the corresponding MC-CDMA signal employing those sequences will be examined in Section 4.5.2.

Specifically, when studying the structure of multi-rate orthogonal Gold codes in Section 2.2.3, we observed that 2^k times higher bit-rate users have to be assigned 2^k number of code indices, even though only one is actually used, in order to preserve the code's orthogonality with respect to the lower bit-rate user's spread signal.

[1] `http://www-mobile.ecs.soton.ac.uk/bjc97r/pnseq/index.html`

Chapter 3

MC-CDMA in Synchronous Environments

In wireless environments the transmitted signals may travel through different propagation paths having different lengths and hence these multi-paths components arrive at the receiver with different delays. This time-dispersive nature of the channel causes Inter-Symbol Interference (ISI) and frequency selective fading [14]. The *RMS delay spread* or multi-path spread, τ_{rms}, of the channel determines the amount of ISI inflicted and the gravity of the channel-induced linear distortions. The reciprocal of the delay spread, namely $1/\tau_{rms} = (\Delta f)_c$, is referred to as the *coherence bandwidth* of the channel [13]. If the total signal bandwidth is wider than $(\Delta f)_c$, the signal experiences *frequency selective* fading [25]. Typically, this is the case, when high rate data is transmitted in a wide signal bandwidth.

In highly frequency selective channels the ISI becomes a major problem in serial modems and hence usually complex channel equalisers are required. In OFDM systems the ISI becomes negligible, as long as a sufficiently high number of guard symbols is introduced [55]. However, due to the frequency selective nature of the channel, each subcarrier has a different bit error ratio (BER). In order to combat this phenomenon several techniques have been used in OFDM, such as error correction coding in conjunction with frequency domain interleaving [34] and adaptive frequency domain loading [55].

Another traditional method of combating the effect of fading is to involve diversity techniques [25]. The main benefit of MC-CDMA in comparison to other OFDM based multiple access methods [56] is the inherent provision of frequency diversity. By contrast, a disadvantage of MC-CDMA is the Multi-User Interference (MUI) encountered. These key factors predetermine the performance of MC-CDMA.

When the MC-CDMA signal experiences severe channel fades, the receiver is likely to make a wrong decision concerning the bit carried by the signal. Diversity techniques arrange for generating several replicas of the signal arriving at the receiver over independent fading paths. From the family of various diversity techniques, frequency diversity, time diversity and antenna diversity are most widely used [25]. Although both MC-CDMA and DS-CDMA use frequency diversity, their receiver structures differ in many aspects. DS-CDMA systems use so called Rake receivers [17] and the number of fingers in the Rake receiver determines the number of diversity paths exploited. In most cases, the number of fingers in DS-CDMA Rake receivers is limited due to their affordable complexity and size. MC-CDMA systems, on the other hand, use a simpler approach, since they transmit the same information on several subcarriers

in order to achieve diversity. The number of subcarriers transmitting the same information determines the order of diversity.

However, the maximum achievable order of frequency diversity, L, in a specific channel is approximately given by [25, 57]

$$L \approx \frac{W}{(\Delta f)_c}, \tag{3.1}$$

where W is the total bandwidth of the channel and $(\Delta f)_c$ is its coherence bandwidth. Hence, spreading a symbol over more than this number of subcarriers is expected to have no more benefits in terms of diversity gain.

In this chapter, the performance of the various diversity techniques and the multi-user interference reduction techniques applicable to MC-CDMA are investigated over a frequency selective indoor fading channel, assuming that all users' signals are synchronous, which is typically the case in the down link.

3.1 The Frequency Selective Channel Model

A narrow-band fading channel can be modeled as a Rayleigh process associated with a specific Doppler spectrum [13]. This channel model is based on the worst case scenario, assuming that no line-of-sight path is available between the transmitter and the receiver. On the other hand, a wideband fading channel can be modeled as a sum of several differently delayed, independent Rayleigh fading processes. The corresponding channel impulse response is described as

$$h(t,\tau) = \sum_{p=1}^{P} a_p \cdot R_p(t) \cdot \delta(\tau - \tau_p), \tag{3.2}$$

where a_p is the normalised amplitude such that $\sum_{p=1}^{P} a_p^2 = 1.0$, $R_p(t)$ is the Rayleigh fading process with $E[R_p^2] = 1.0$ and τ_p is the delay of the p-th path. For computer simulation purposes, τ_p is given in units of the sampling interval duration.

An indoor channel model is considered for investigating the performance of MC-CDMA in synchronous environments. It is a shortened Wireless Asynchronous Transfer Mode (W-ATM) channel model used for example in [13]. The impulse response and frequency domain response of the channel are shown in Figure 3.1. The impulse response was derived by simple ray-tracing in a warehouse-type room of $100 \times 100 \times 3\text{m}^3$ [13] . The main system parameters and channel parameters of the system investigated are summarised in Table 3.1.

3.2 The System Model

The MC-CDMA system considered here employs N subcarriers and each user transmits M bits during a signaling interval, leading to the spreading factor or, synonymously, to the processing gain, G, of N/M [38, 57]. Figure 3.2 shows the transmitter structure of the system model. The data stream of user u is converted into M parallel streams and each stream is spread with the aid of orthogonal spreading

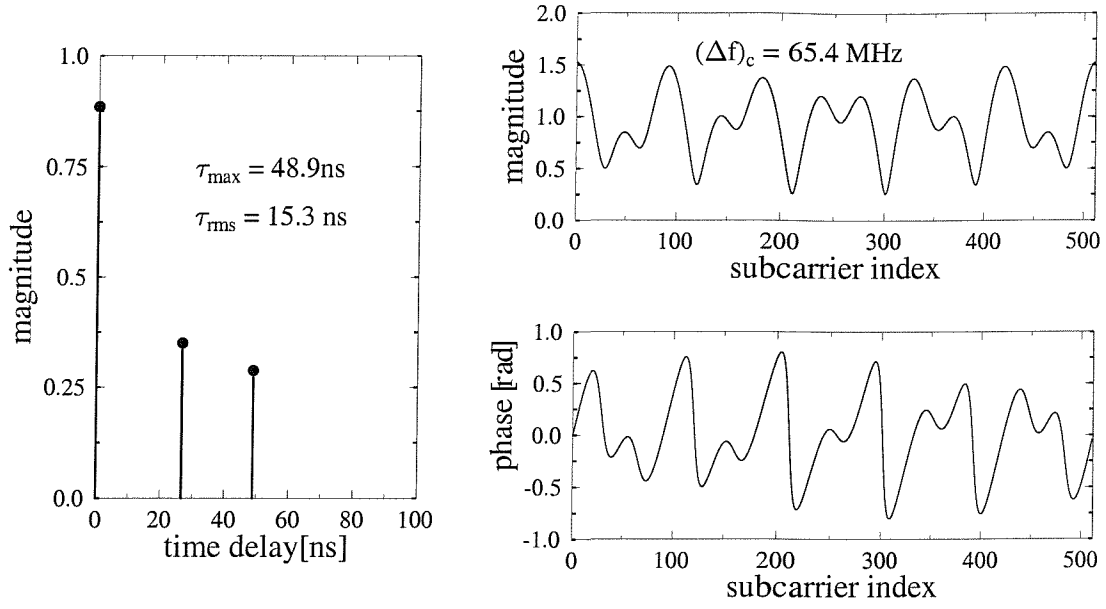

(a) impulse response

(b) frequency response

Figure 3.1: The shortened W-ATM channel model, where τ_{max} is the longest delay, τ_{rms} is the RMS delay spread and $(\Delta f)_c$ is the coherence bandwidth of the channel

parameters	Shortened W-ATM
Carrier frequency, f_c	60 GHz
Sampling rate, $1/T_s$	225 MHz
BPSK data rate, R_b	155 Mbps
Max. speed of mobile, v_{max}	50 Km/h [1]
Max. Doppler frequency, $f_{d,max}$	2277.8 Hz
Normalised Doppler freq., $f_{n,max}$	$1.23 \cdot 10^{-5}$
Max. delay spread, τ_{max}	11 samples
RMS delay spread, τ_{rms}	15.3 ns
Coherence bandwidth, $(\Delta f)_c$	65.4 MHz
No. of subcarriers, N	512
No. of guard symbols, N_g	64

Table 3.1: Main system parameters of the considered W-ATM system and the channel parameters

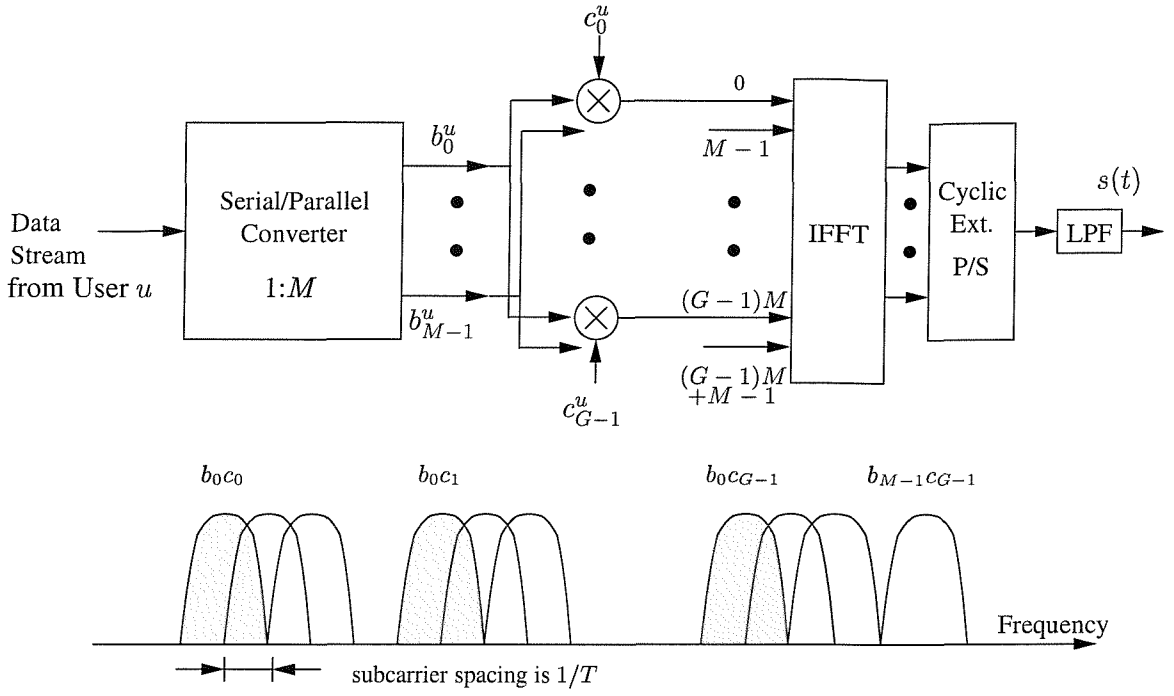

Figure 3.2: MC-CDMA transmitter model and its spectrum for a single user

sequences of Section 2.2, which maps the same bit to G number of subcarriers. The subcarrier spacing between the subcarriers conveying the same bit is set to M, in order to minimise the correlation of the fading of these subcarriers. For simplicity, only a single user is depicted in the figure, but a number of users up to G can be incorporated. The uth user's spreading sequence, c_g^u, $g = 0, 1, \cdots, G-1$, is orthogonal to other users' spreading sequences. The Walsh codes and the orthogonal Gold codes described in Section 2.2 can be used as the spreading sequences. In this model, each user transmits its data at the rate of M/T bps, where T is the frame duration. If the transmission rate can be lowered, the maximum number of users, U, can be increased such that the data streams generated by the M users replace the $1 : M$ serial-to-parallel converter in Figure 3.2 [57]. In this case, the total number of users supported can reach the total number of subcarriers, yielding $U = N$. Bearing this in mind, in our discourse, only the configuration shown in Figure 3.2 will be considered.

The complex baseband representation of the transmitted signal, $s(t)$, in a certain signalling interval can be written as :

$$s(t) = \sum_{u=0}^{U-1} \sum_{m=0}^{M-1} \sum_{g=0}^{G-1} \sqrt{E_c}\, b_m^u\, c_g^u\, e^{j2\pi \frac{1}{T}(gM+m)t}\,, \tag{3.3}$$

where

U is the number of users, which has a maximum of G,

M is the number of bits transmitted per user,

G is the spreading factor or the processing gain given as N/M, where N is the number of

subcarriers,

E_c is the energy per subcarrier, or chip, and $E_c = E_b/N$, where E_b is the energy per bit before spreading,

T is the signalling interval, during which M number of bits per user are transmitted and $1/T$ is equal to the spacing between adjacent subcarriers,

$b_m^u \in \{\pm 1\}$ is the mth bit of user u and

$c_g^u \in \{\pm 1\}$ is the gth chip of the uth user's spreading sequence.

3.3 Single User Detection

In the receiver the mth bit of user u is detected independently from the m'th bits, where $m' \neq m$, for all users. Furthermore assume that there is no inter-subcarrier interference. Thus, without loss of generality, the subscript m can be omitted and the G subcarriers conveying the same bit can be considered for the detection of a bit. In view of (1.8), the demodulated received symbol r_g of the gth subcarrier can be expressed as :

$$r_g = \sum_{u=0}^{U-1} \sqrt{E_c}\, b^u\, c_g^u\, H_g + n_g \,, \tag{3.4}$$

where H_g is the $(gM + m)$th subcarrier's frequency domain channel transfer factor, and n_g is a discrete AWGN process having zero mean and a one-sided power spectral density of N_o. The decision variable of the u'th user's bit, $d^{u'}$, is given for a single user detector as :

$$d^{u'} = \sum_{g=0}^{G-1} q_g\, c_g^{u'}\, r_g \,, \tag{3.5}$$

where q_g is a frequency domain equalisation gain factor, which is dependent upon the diversity combining scheme employed. The decision variable $d^{u'}$ can be expanded with the aid of (3.4) and (3.5) as :

$$\begin{aligned} d^{u'} &= \sum_{g=0}^{G-1} q_g\, c_g^{u'} \left(\sum_{u=0}^{U-1} \sqrt{E_c}\, b^u\, c_g^u\, H_g + n_g \right) \\ &= \sqrt{E_c}\, b^{u'} \sum_{g=0}^{G-1} H_g\, q_g + \sqrt{E_c} \sum_{u=0, u\neq u'}^{U-1} b^u \sum_{g=0}^{G-1} c_g^u\, c_g^{u'}\, H_g\, q_g + \sum_{g=0}^{G-1} c_g^{u'}\, n_g\, q_g \\ &= \alpha + \zeta + \eta \,, \end{aligned} \tag{3.6}$$

where α is the desired signal component given by

$$\alpha = \sqrt{E_c} b^{u'} \sum_{g=0}^{G-1} H_g q_g \,, \tag{3.7}$$

ζ is the MUI given by

$$\zeta = \sqrt{E_c} \sum_{u=0, u\neq u'}^{U-1} b^u \sum_{g=0}^{G-1} c_g^u c_g^{u'} H_g q_g \,, \tag{3.8}$$

and η is the noise component given by

$$\eta = \sum_{g=0}^{G-1} c_g^{u'} n_g q_g \,. \tag{3.9}$$

These three signal components predetermine the performance of the single user detector considered.

3.3.1 Maximal Ratio Combining

In Maximal Ratio Combining (MRC) [1, 25] a stronger signal is assigned a higher weight by the diversity combiners, than a weaker signal, since its contribution is more 'reliable'. The corresponding equalisation gain, q_g, introduced in (3.5) is given as :

$$q_g = H_g^* \,. \tag{3.10}$$

This equalisation gain attempts to accentuate and de-rotate the fading-induced attenuation and phase rotation. The corresponding user's received signal component, α, is given by :

$$\alpha = \sqrt{E_c}\, b^{u'} \sum_{g=0}^{G-1} |H_g|^2 \,. \tag{3.11}$$

On the other hand, the MUI associated with MRC is given by :

$$\zeta = \sqrt{E_c} \sum_{u=0, u\neq u'}^{U-1} b^u \sum_{g=0}^{G-1} c_g^u\, c_g^{u'}\, |H_g|^2 \,. \tag{3.12}$$

Finally, the noise term, η, of (3.9) can be calculated as :

$$\eta = \sum_{g=0}^{G-1} c_g^{u'}\, n_g\, H_g^* \,. \tag{3.13}$$

The effect of MRC is equivalent to that of matched filtering, where the filtering is matched to the channel's transfer function. Matched filtering constitutes the optimal receiver, which maximises the SNR at the output of the decision device [25]. The single user performance of MRC has been widely studied for transmission over Rayleigh fading channel having L-independent propagation paths and the achievable bit error rate, P_e, is given by [25] :

$$P_e = \left[\frac{1}{2}(1-\mu)\right]^L \sum_{k=0}^{L-1} \binom{L-1+k}{k} \left[\frac{1}{2}(1+\mu)\right]^k \,, \tag{3.14}$$

where μ is defined as

$$\mu \triangleq \sqrt{\frac{\overline{\gamma}_b}{L+\overline{\gamma}_b}} \,, \tag{3.15}$$

and $\overline{\gamma}_b$ is the average energy per bit, $\overline{E}_b$, divided by the noise power spectral density, N_o. The associated BER curves for $L = 1, \cdots, 4$ are shown in Figure 3.3 . More specifically, the simulation results for a

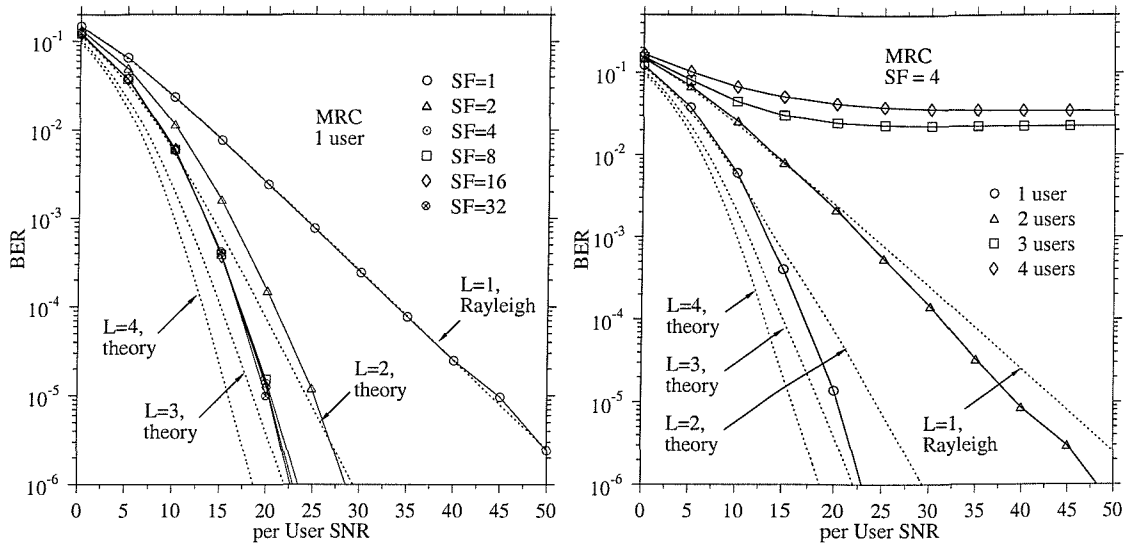

(a) single user

(b) multiple users for SF=4

Figure 3.3: BER of synchronous MC-CDMA for the downlink in conjunction with MRC for transmission over W-ATM channel. The theoretical curves were evaluated from (3.14).

single-user scenario are shown in Figure 3.3(a). The available diversity order, L, is given in (3.1). For the shortened W-ATM channel, we have $225MHz/65.4MHz = 3.44$. Hence, a system having a spreading factor of 4 is expected to reach the diversity-assisted performance enhancement limit. When a spreading factor of 1 is employed corresponding to no spreading, the BER performance of MC-CDMA was identical to the BER of single carrier scheme operating over Rayleigh fading channel. As the spreading factor was increased, the BER performance was improved. However, as it can be seen in Figure 3.3(a), the systems having a Spreading Factor (SF) in excess of 4 did not improve the achievable bit error rate. As the SNR increased, the simulation-based BER approached the theoretical BER associated with $L = 3$ which was evaluated from (3.14) under the assumption of independent fadings over L paths . The discrepancy between the simulation-based and theoretical results was due to the presence of correlated fading over G number of subcarriers [25].

It is interesting to observe the effects of the number of users on the bit error rate, when MRC is used. Figure 3.3(b) shows our simulation results for the spreading factor of four. As the number of users was increased, the bit error rate increased significantly due to the increased amount of MUI. We can view the frequency domain spreading as a form of repetition coding. Thus, the two-user scenario employing SF=4 in MC-CDMA corresponds to a half rate encoder, since 2 information bits are transmitted using a total of 4 symbols. If we compare the BER curves of this two-user system with that of the single-user scenario in MC-CDMA in conjunction with SF=2, where the code rate can also be regarded as $1/2$, we can conclude that the latter scheme performs significantly better. However, in general, more complex channel coding techniques will perform better, than this simple repetition code [25].

In so-called fully loaded conditions when the number of users is equal to the SF, the multi-user

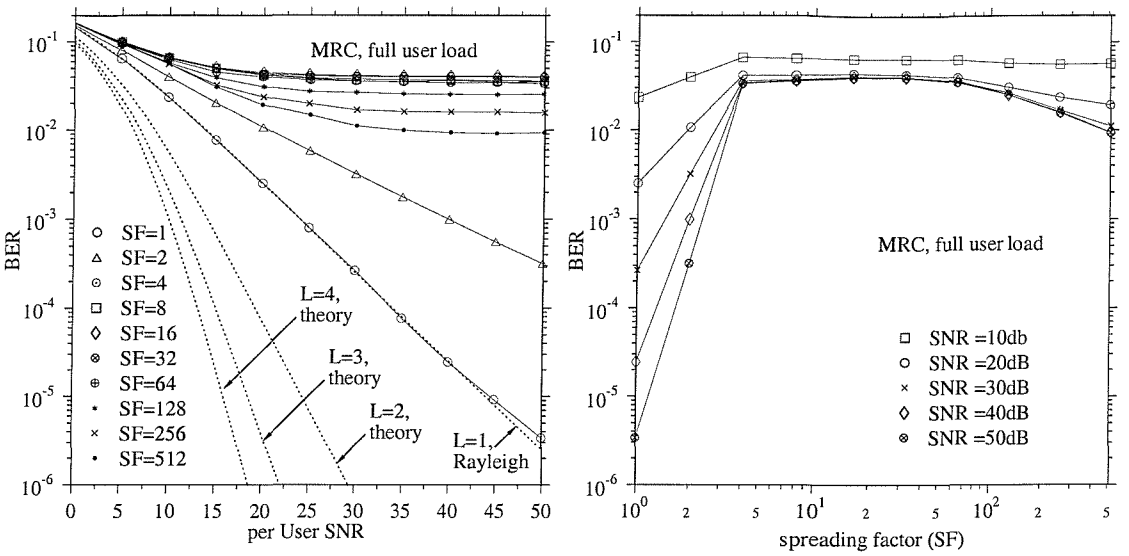

(a) BER vs SNR

(b) BER vs spreading factor (SF)

Figure 3.4: BER of the synchronous MC-CDMA downlink using MRC for full user load over W-ATM channel described in Figure 3.1. SF is the spreading factor and L represents the diversity order.

interference as opposed to the noise component dominates the system's performance, which becomes poor. The corresponding simulation results are given in Figure 3.4. The BER performance of fully loaded MC-CDMA is worse, than that of OFDM, which corresponds to having SF=1. In Figure 3.4(b) it can be observed that the BER increased to a certain limit and then decreased across the SNR range spanning from 20dB to 50dB, as the spreading factor was increased. In order to investigate this phenomenon, we have to consider the statistical properties of α and ζ given in (3.11) and (3.12), respectively.

As the total power of the Channel's Impulse Response (CIR) is normalised such that $\sum_{n=0}^{N-1} |h_n|^2 = 1.0$, the frequency domain channel response satisfies $\sum_{n=0}^{N-1} |H_n|^2 = N$ according to the discrete form of Parseval's theorem [58]. Hence we can assume that $E\left[\sum_{g=0}^{G-1} |H_g|^2\right]$ becomes G. Thus, the average signal power, $E\left[\alpha^2\right]$ becomes [25, pp.43]:

$$\begin{aligned} E\left[\alpha^2\right] &\simeq E_c \cdot (G + G^2) \\ &= E_b \cdot (G + 1)\,, \end{aligned}$$

where E_b is the signal energy per bit during the bit interval. If we assume that subcarrier channel transfer factor H_g obey an independent identically distributed (iid) Rayleigh process with $E\left[|H_g|^2\right] = 2\sigma^2 = 1$ and $c_g^u c_g^{u'}$ has an equal probability of $+1$ or -1, then Equation 3.12 can be regarded as a zero mean Gaussian process, provided that U and G are sufficiently high. The variance, $E\left[\zeta^2\right]$ becomes [25, pp.43]:

$$\begin{aligned} E\left[\zeta^2\right] &= E_c\,(U-1)\,G \times \frac{3}{2} \\ &= E_b\,(U-1)\,\frac{3}{2}\,. \end{aligned}$$

In high SNR scenarios supporting a full user load of $U = G$, the bit error probability, P_e, can be approximated as

$$\begin{aligned} P_e &\simeq \frac{1}{2}\text{efrc}\left(\sqrt{\frac{E[\alpha^2]}{E[\zeta^2]}}\right) \\ &= \frac{1}{2}\text{efrc}\left(\sqrt{\frac{2E_b \cdot (G+1)}{3E_b(U-1)}}\right) \\ &= \frac{1}{2}\text{efrc}\left(\sqrt{\frac{2 \cdot (G+1)}{3(G-1)}}\right) . \end{aligned}$$

This approximate analysis is supported by Figure 3.4. Specifically, we can observe that the BER when $G = 4$ is around 0.07. Figure 3.4(b) is a plot of the BER versus the spreading factor. As the spreading factor was increased beyond 64, the associated bit error ratios were reduced. This can be interpreted as follows. The MUI defined in (3.12) is reduced, when the channel transfer factors $\{H_g\}$ are correlated, which is the case for high SFs, when the subcarriers conveying the same bit are close to each other.

In conclusion, we observed that the channel exhibits a limited amount of diversity and the MUI plays a major role in terms of determining the BER, when MRC is used as the diversity combining method.

3.3.2 Equal Gain Combining

Although the spreading codes are orthogonal, due to the differently delayed multi-path components received their orthogonality is destroyed. The MRC scheme, which is characterised by the equalisation gain given by (3.10), optimally combines these multi-path components in an effort to maximise the SNR, but at the same time it may further impair the orthogonality of the codes. In order to avoid this problem, Equal Gain Combining (EGC) attempts to correct the channel-induced phase rotations [14], leaving the faded magnitudes uncorrected [1]. In this case, the equalisation gain, q_g, is given by:

$$q_g = \frac{H_g^*}{|H_g|} . \tag{3.16}$$

The corresponding three signal components defined in (3.7) to (3.9) are given as :

$$\alpha = \sqrt{E_c}\, b^{u'} \sum_{g=0}^{G-1} |H_g| \tag{3.17}$$

$$\zeta = \sqrt{E_c} \sum_{u=0, u\neq u'}^{U-1} b^u \sum_{g=0}^{G-1} c_g^u c_g^{u'} |H_g| \tag{3.18}$$

$$\eta = \sum_{g=0}^{G-1} c_g^{u'} n_g \frac{H_g^*}{|H_g|} . \tag{3.19}$$

Our simulation results are shown in Figure 3.5. In the single user case shown in Figure 3.5(a), the BER curves approached the theoretical ones, but overall EGC performed slightly worse than MRC. No

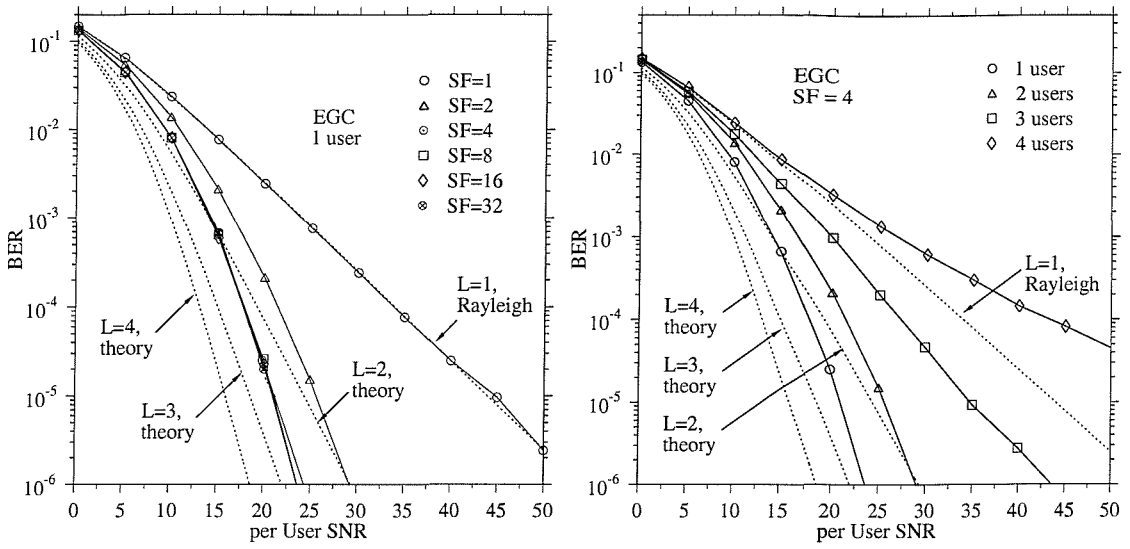

(a) single user

(b) multiple users for SF=4

Figure 3.5: BER performance of the synchronous MC-CDMA downlink using EGC over W-ATM channel. SF is a spreading factor and L is the diversity order.

further improvement was observed for the systems having a SF higher than four, as in the case of MRC. When the number of users was increased for the system employing SF=4, the performance was degraded but remained better, than that of MRC. This results corroborates the BER comparison reported in [1].

When all users are transmitting, the multi-user interference increases significantly, eroding the benefits of the frequency diversity and the performance becomes worse than that of OFDM, corresponding to SF=1. The corresponding simulation results are given in Figure 3.6. As in the case of MRC, the bit error ratio curve converged to a BER floor, when the SNR was high. The BER floor was dependent on the spreading factor. The worst BER floor was observed for SF=16. As the spreading factor increases beyond SF=16, the BER floor is reduced. This can be interpreted using the similar arguments to those in Section 3.3.1 .

3.3.3 Orthogonality Restoring Combining

As argued before, frequency selective fading destroys the orthogonality of the different users' spreading codes. The drawback of the MRC and the EGC scheme is that they inflict MUI due to the above mentioned lack of orthogonality, which is not desirable. If we cancel the effect of the channel transfer function by estimating it and reversing its effects, the orthogonality of the different users can be maintained. This is the aim of Orthogonality Restoring Combining (ORC) or Zero Forcing (ZF) equalisation, which uses the equalisation gain, q_g, given by :

$$q_g = \frac{H_g^*}{|H_g|^2}. \tag{3.20}$$

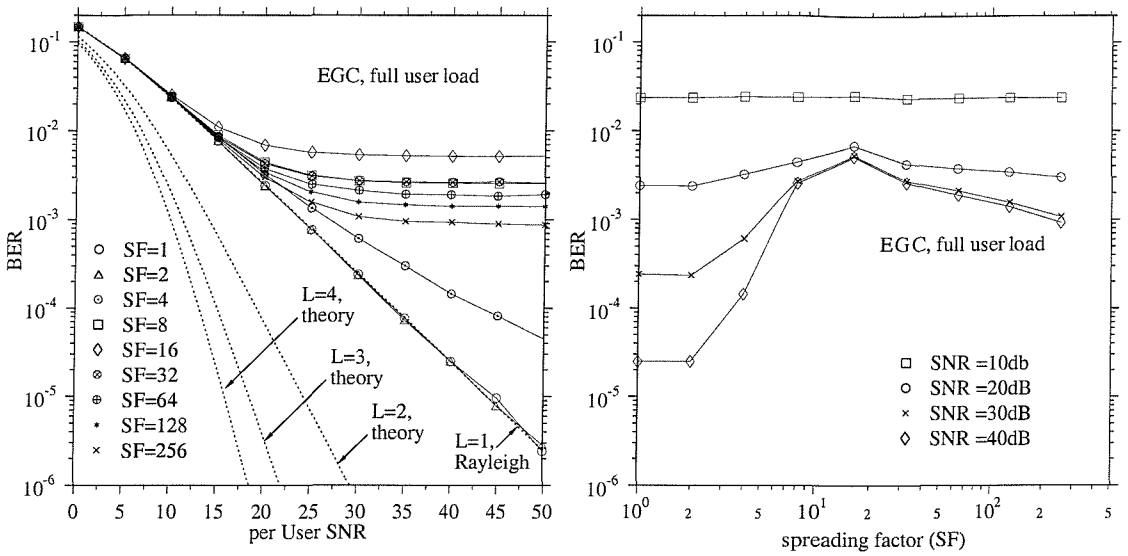

(a) BER vs SNR

(b) BER vs spreading factor (SF)

Figure 3.6: BER performance of the synchronous MC-CDMA downlink using EGC for a full user load. SF is a spreading factor and L is the diversity order.

We have only two components in the decision variable of (3.6) as $\zeta = 0$, which are given by :

$$\alpha = \sqrt{E_c}\, G\, b^{u'} = \sqrt{E_b G}\, b^{u'} \tag{3.21}$$

$$\eta = \sum_{g=0}^{G-1} c_g^{u'}\, n_g\, \frac{H_g^*}{|H_g|^2}\,. \tag{3.22}$$

Figure 3.7 shows our simulation results for the various spreading factors, when ORC is applied in our MC-CDMA scheme. The MC-CDMA system using various spreading factors, *i.e.* different-order diversity schemes, performed worse than the single-user OFDM scheme associated with SF=1, when the average per user SNR, $\overline{\gamma}_b$, was less than 25dB. In fact, as the the spreading factors was increased, the performance degraded, since the ORC scheme using perfect channel estimation already removed the frequency selectivity of the channel transfer function, leaving no room for improvement with the aid of frequency domain diversity. The source of performance degradation in comparison to OFDM was the noise enhancement, particularly at lower SNR values. More specifically, when the fading was severe for a specific subcarrier, the value of n_g/H_g became high, inevitably amplifying both the signal and the noise. As the spreading factor increased, it became more likely that $\{H_g\}$ encountered deep frequency-domain fades, leading to an excessive noise enhancement. This effect is less significant at high SNRs. In order to combat to the noise enhancement problem, the technique of Controlled Equalisation (CE) was proposed by Yee and Linnartz [41], which uses a subset of subcarriers for the ORC scheme, associated with the channel transfer factors that are above a certain threshold.

No noticeable differences were observed between the BERs for the various number of users, as shown in Figure 3.7(b). This result is consistent with the fact that no MUI exists, when ORC is employed.

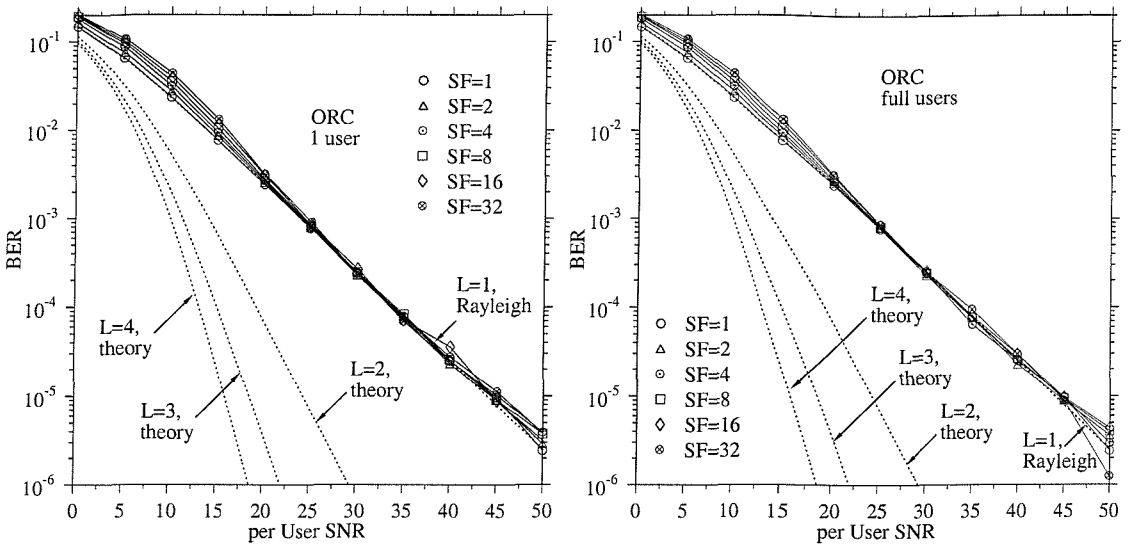

(a) single user

(b) full users

Figure 3.7: BER of the synchronous MC-CDMA downlink using ORC for a single user over W-ATM channel

3.3.4 Minimum Mean Square Error Combining

In the previous section we observed that the ORC scheme effectively reduces the MUI, but introduces noise enhancement at the frequencies where the frequency domain channel transfer funcion response has a low value. Minimum Mean Square Error Combining (MMSEC) reduces this undesirable noise enhancement, while endeavouring to reduce MUI at the same time. The equalisation gain q_g of the MMSEC scheme is given by [38]:

$$q_g = \frac{E_c H_g^*}{E_c|H_g|^2 + \sigma^2}. \tag{3.23}$$

The corresponding three signal components defined in (3.7) to (3.9), upon applying (3.23), can be represented as:

$$\alpha = \sqrt{E_c}\, b^{u'} \sum_{g=0}^{G-1} \frac{E_c|H_g|^2}{E_c|H_g|^2 + \sigma^2} \tag{3.24}$$

$$\zeta = \sqrt{E_c} \sum_{u=0, u\neq u'}^{U-1} b^u \sum_{g=0}^{G-1} c_g^u c_g^{u'} \frac{E_c|H_g|^2}{E_c|H_g|^2 + \sigma^2} \tag{3.25}$$

$$\eta = \sum_{g=0}^{G-1} c_g^{u'} n_g \frac{E_c H_g^*}{E_c|H_g|^2 + \sigma^2}. \tag{3.26}$$

When the received signal strength is considerably higher than the noise variance σ^2, *ie* we have $E_c|H_g|^2 \gg \sigma^2$, then the term $(E_c|H_g|^2 + \sigma^2)$ in (3.24) and (3.25) can be approximated as $E_c|H_g|^2$. In this case the above components become equivalent to those of the ORC scheme characterised by (3.21) through

(3.22) and hence the MUI component is effectively reduced. On the other hand, when the received signal strength is relatively weak compared to the noise variance, *ie* we have $E_c|H_g|^2 \ll \sigma^2$, the noise term becomes:

$$\eta \simeq \sum_{g=0}^{G-1} c_g^{u'} n_g \frac{E_c H_g^*}{\sigma^2} \tag{3.27}$$

and the noise enhancement is prevented, unlike in case of employing ORC. Refer to [38] for the corresponding performance results of MMSEC scheme.

3.4 Multi User Detection

The detection methods of Section 3.3 exploited single user information only, thus the performance was interference limited except in the case of ORC. Moreover, using all the available information at the receiver, such as the spreading codes of all users and their CIRs, the performance can be improved with the aid of Multi-User Detection (MUD). The Maximum Likelihood Detection (MLD) is briefly investigated in the next section followed by MMSE Joint Detection schemes.

3.4.1 Maximum Likelihood Detection

In this scheme the receiver constructs all possible combinations of the transmitted signals of all users and applies their estimated channel transfer functions in order to generate the expected received signals [57]. Explicitly, the receiver chooses the legitimate transmitted signal, which has the smallest Euclidean distance from the received signal.

Let $\mathbf{C}$ be a $G \times U$-dimensional matrix containing the uth user's spreading code in column u, $u = 1, 2, \cdots, U$, $\mathbf{b}$ be a column vector, $(b^0\ b^1\ \cdots\ b^{U-1})^T$ comprised of the possible source bits combination. If we define the channel's transfer factor matrix, $\mathbf{H}$, as a $G \times G$-dimensional diagonal matrix having H_g at $\mathbf{H}_{gg}$, then the expected received column vector $\hat{\mathbf{r}}$ is given by $\hat{\mathbf{r}} = \sqrt{E_c}\mathbf{HCb} + \mathbf{n}$. The Euclidean distance, $\mathcal{D}$, between the actually received signal vector $\mathbf{r}$ containing r_g, $g = 1, 2, \cdots, G$ of (3.4), and the received vector candidate $\hat{\mathbf{r}}$, is given by:

$$\mathcal{D} = || \mathbf{r} - \hat{\mathbf{r}} ||^2 . \tag{3.28}$$

Our simulation results characterising this MUD are given in Figure 3.8. As it can be seen from Figure 3.8(a), the BER curve approached the theoretical BER curve of the single-user scenario for $L = 3$. As the number of users was increased, the performance degraded, but nonetheless remained better than the OFDM BER associated with SF=1. The effect of MUI was considerably reduced compared to the MRC and EGC assisted scenario. Figure 3.8(b) shows the simulation results for the 'fully loaded' MC-CDMA system using the MLD. Even in this condition, the BER was lower than that of OFDM. This implies that MC-CDMA systems employing the MLD are superior to the conventional OFDM scheme in terms of their bit error ratio, while providing the same spectral efficiency. In Section 3.3.1 we observed

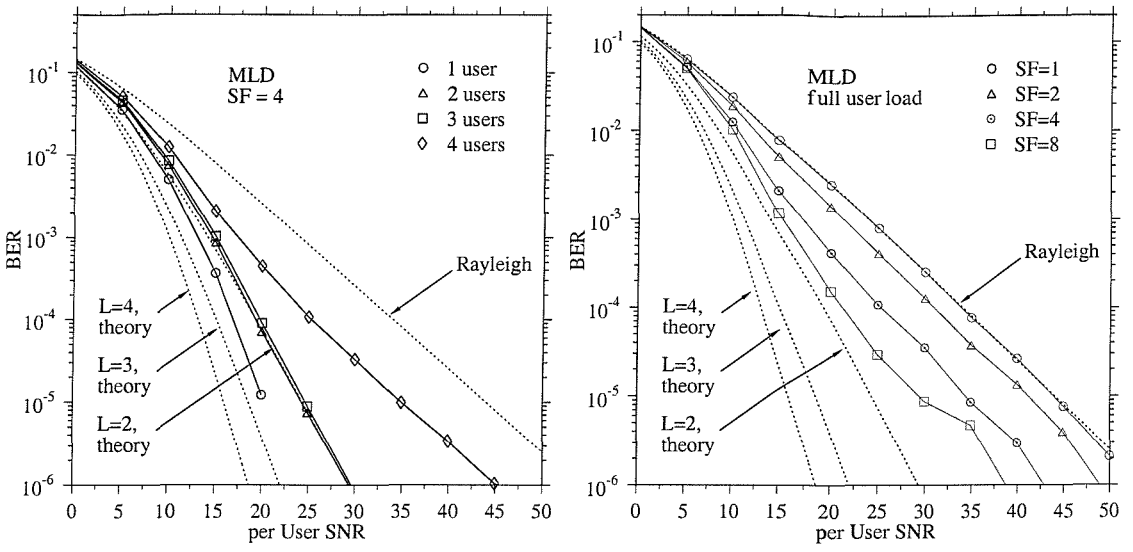

(a) SF=4, users=1,2,3 and 4

(b) full user load

Figure 3.8: BER of MC-CDMA downlink with MLD

that spreading a bit to more subcarriers than the available diversity order of the channel does not improve the performance of single user detection schemes. However, Figure 3.8(b) suggests that in a multi-user scenario spreading the same bit to more subcarriers than the available diversity order of the channel can improve the bit error ratio due to both the reduced MUI and the better exploitation of the available diversity.

3.4.2 Minimum Mean Square Error Joint Detection

Since Minimum Mean Square Error Joint Detection (MMSE-JD) receivers will be used in Chapter 4 and 5, they are described here briefly. The detailed operation of these schemes and their performance was characterised in [59, 60].

In the previous section the received MC-CDMA signal was represented by a vector notation as:

$$\mathbf{r} = \sqrt{E_c}\,\mathbf{HCb} + \mathbf{n}\,, \tag{3.29}$$

where again, E_c is the energy per chip, $\mathbf{H}$ is the $G \times G$ dimensional diagonal frequency domain channel transfer matrix, $\mathbf{C}$ is the $G \times U$ dimensional spreading matrix, $\mathbf{b}$ is the $U \times 1$ dimensional message vector and $\mathbf{n}$ is the $G \times 1$ dimensional noise vector. The system parameter G is the spreading gain and U is the number of simultaneous users. An MMSE Block Linear Equalised (BLE) JD receiver performs the following matrix calculations for generating the estimate of the U number of message vectors $\hat{\mathbf{d}}_{MMSE-BLE}$ [59, 60]:

$$\hat{\mathbf{d}}_{MMSE-BLE} = \left(\mathbf{C}^H\mathbf{H}^H\mathbf{HC} + \sigma^2/E_c\,\mathbf{I}\right)^{-1}\mathbf{H}^H\mathbf{r} \tag{3.30}$$

$$= \sqrt{E_c}\left(\mathbf{F} + \sigma^2/E_c\,\mathbf{I}\right)^{-1}\mathbf{Fb} + \left(\mathbf{F} + \sigma^2/E_c\,\mathbf{I}\right)^{-1}\mathbf{C}^H\mathbf{H}^H\mathbf{n}\,, \tag{3.31}$$

where $\mathbf{A}^H$ represents the Hermitian or the conjugate transpose of the matrix $\mathbf{A}$, $\mathbf{F} \triangleq \mathbf{C}^H\mathbf{H}^H\mathbf{H}\mathbf{C}$ is a $U \times U$ dimensional real symmetric matrix and $\mathbf{I}$ is a $U \times U$ dimensional identity matrix. The desired signal component α, the MUI component ζ and the noise component η of this MMSE-BLE JD receiver can be represented by:

$$\alpha = \sqrt{E_c}\,\mathrm{diag}\left\{\left(\mathbf{F} + \sigma^2/E_c\,\mathbf{I}\right)^{-1}\mathbf{F}\right\}\,\mathbf{b} \tag{3.32}$$

$$\zeta = \sqrt{E_c}\,\overline{\mathrm{diag}}\left\{\left(\mathbf{F} + \sigma^2/E_c\,\mathbf{I}\right)^{-1}\mathbf{F}\right\}\,\mathbf{b} \tag{3.33}$$

$$\eta = \left(\mathbf{F} + \sigma^2/E_c\,\mathbf{I}\right)^{-1}\mathbf{C}^H\mathbf{H}^H\mathbf{n}\,, \tag{3.34}$$

where $\mathrm{diag}\{\mathbf{A}\}$ represents a diagonal matrix having the diagonal elements of $\mathbf{A}$ and $\overline{\mathrm{diag}}\{\mathbf{A}\}$ represents a matrix having only off-diagonal elements of $\mathbf{A}$, *ie* $\overline{\mathrm{diag}}\{\mathbf{A}\} = \mathbf{A} - \mathrm{diag}\{\mathbf{A}\}$.

The MMSE Block Decision Feedback Equalised (BDFE) JD receiver [59] is another MMSE based JD receiver, which operates in a similar fashion to a Successive Interference Canceller (SIC) [7]. The message symbols already detected are fed back to the receiver for reducing the effects of MUI and hence for obtaining more reliable decision statistics for the remaining message symbols. Assuming the absence of error propagation due to incorrect decisions concerning the previous message symbols, the vector of estimated message symbols $\hat{\mathbf{d}}_{MMSE-BDFE}$ produced by the MMSE-BDFE JD receiver can be represented as [59, 60]:

$$\hat{\mathbf{d}}_{MMSE-BDFE} = \sqrt{E_c}\left(\mathbf{I} - \mathbf{D}^{-1}\mathbf{L}^{-1}(\sigma^2/E_c)\right)\mathbf{b} + \mathbf{D}^{-1}\mathbf{L}^{-1}\mathbf{C}^H\mathbf{H}^H\mathbf{n}\,, \tag{3.35}$$

where a $U \times U$-dimensional lower triangular matrix $\mathbf{L}$ is given by the Cholesky decomposition [58] of

$$\mathbf{C}^H\mathbf{H}^H\mathbf{H}\mathbf{C} + (\sigma^2/E_c)\mathbf{I} = \mathbf{L}\mathbf{L}^T \tag{3.36}$$

and $\mathbf{D}$ is the $U \times U$-dimensional diagonal matrix having the diagonal elements of $\mathbf{L}$. Again, for a detailed portrayal of the MMSE-BDFE JD receiver, we refer to [59, 60]:

3.5 Summary and Conclusions

The BER performance of synchronous MC-CDMA in the downlink was investigated in Section 3.3 using simulation studies. In Section 3.3 we employed single-user detectors, namely MRC, EGC and ORC, while in Section 3.4 an MLD multi-user detector operating over the W-ATM channel was used. It was observed in Section 3.3.1 that while MRC is the optimum detector in a single-user scenario, its BER performance was the worst among the three single-user detector investigated in a fully loaded scenario. Neither the EGC nor the ORC assisted MC-CDMA performed better than OFDM in a fully loaded scenario over the specific propagation scenario considered. However, in the same scenario the MLD multi-user detector assisted MC-CDMA scheme of Section 3.4.1 exhibited SNR gains of 5dB, 10dB and 15dB for SF=2, 4 and 8, respectively, in comparison to OFDM, when viewed at the BER of 10^{-6}. We can conclude that the employment of multi-user detectors is essential for MC-CDMA in order to successfully support numerous users at the same time.

Chapter 4

Peak Factor Reduction Techniques

4.1 Introduction

Many practically important absolutely integrable signals can be decomposed into the sum of trigonometric series. These signals have various applications in radars, communications, measurements and so on. They exhibit perfect band-pass nature in the frequency domain. However, they often exhibit a large dynamic range in terms of their amplitude variations in the time domain.

The transmitted signals of multi-carrier modulation systems comprise sums of trigonometric series. These techniques are amenable to transmission over highly time-dispersive channels and they are capable of approaching 2 Baud (Bd)/Hz bandwidth efficiency limit stipulated by Shannon. The main drawback of these techniques is their high peak-to-mean envelope power fluctuation or, synonymously, high crest-factor, which is common to the sums of trigonometric series. In simple terms, this statement implies that the higher the number of OFDM/MC-CDMA subcarriers, the higher the dynamic range of their sum. Hence expensive linear high power amplifiers [13] having a large dynamic range are required in order to reduce the nonlinear distortion of the signals. Multi-carrier CDMA systems inevitably inherit this drawback.

Historically, there have been numerous efforts dedicated to reducing these amplitude variations, in order to mitigate the associated amplifier linearity requirements, the spurious out-of-band (OOB) emissions or the required signal level reduction, termed also as amplifier 'back-off', necessary for preventing amplifier's saturation at high peaks [13]. In this chapter, an overview of past research in this field is given, with an emphasis on several crest-factor reduction techniques applicable to OFDM signals. For MC-CDMA systems, the relationship between the crest-factor and the spreading sequences employed will be analysed and the effects of the crest-factor on the system performance will be investigated.

As mentioned above, OFDM signals are based on the sum of trigonometric series. OFDM is a parallel transmission technique [13], which uses orthogonal subcarriers modulated by the information symbols. The complex time domain baseband representation, $s(t)$, of the OFDM signal is given by

$$s(t) = \sqrt{\frac{1}{N}} \sum_{k=1}^{N} c_k e^{j2\pi \frac{k}{T} t} , \tag{4.1}$$

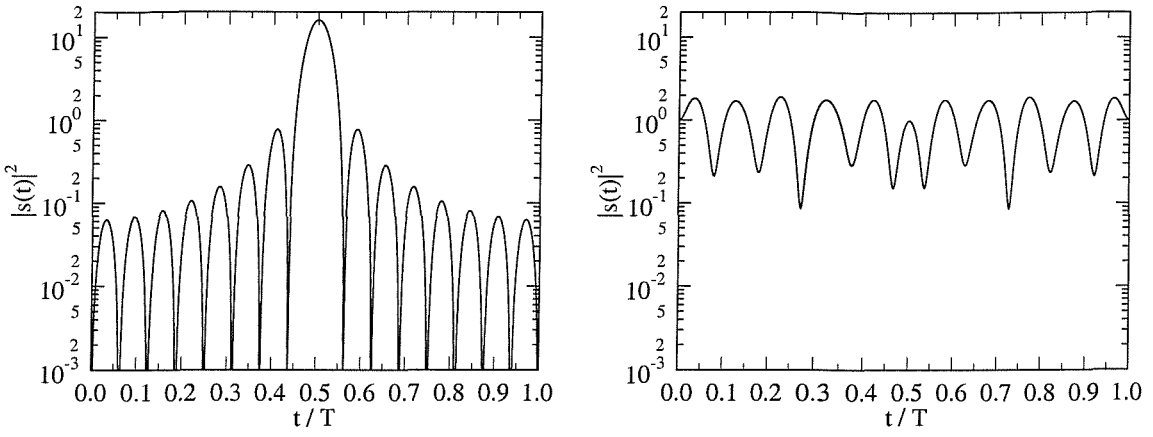

(a) All zero sequence

(b) *Shapiro-Rudin* sequence

Figure 4.1: Examples of normalized envelope power waveforms plotted in a logarithmic scale for 16-carrier BPSK modulated OFDM signals, transmitting (a) the all zero sequence, (b) the Shapiro-Rudin sequence, which will be introduced in Section 4.3.1. The differences in dynamic ranges are quite noticeable.

where N is the number of subcarriers, T is the OFDM signaling interval and c_k is the information symbol modulating the frequency domain subcarriers. For a specific application of multicarrier transmission the following modulated signal representation is proposed by Schroeder [61]:

$$s'(t) = \sqrt{\frac{2}{N}} \sum_{k=1}^{N} \cos(2\pi \frac{k}{T} t + \theta_k) \,, \tag{4.2}$$

where θ_k is the initial phase of the kth subcarrier. We can observe that $s'(t)$ of (4.2) corresponds to the real part of $s(t)$ in (4.1), while having the same average power. Both $s(t)$ and $s'(t)$ are normalized signals, having average powers of unity. Depending on the specific values of c_k or θ_k, $s(t)$ or $s'(t)$ may have a high dynamic range. Figure 4.1 shows $|s(t)|^2$ versus time for two representative information sequences $\{c_k\}$ in the context of 16-carrier BPSK modulated OFDM systems. Fig. 4.1(a) corresponds to the all zero sequence, whereas Fig. 4.1(b) to the so called *Shapiro-Rudin* sequences, which will be introduced in Section 4.3.1. The unmodulated signal associated with the all zero information sequence can be readily visualised, since the associated 16 unity-valued OFDM/BPSK subcarriers represent a 16-subcarrier rectangular frequency-domain window function. Hence, the corresponding time-domain modulated signal generated by the IFFT [13] is a sinc-shaped function, which exhibits the logarithmic power-envelope versus time function seen in Figure 4.1(a). These figures illustrate that the power envelope versus time function changes dramatically, depending also on the specific codes used for mapping the modulating information sequence on to the subcarriers, while having the same total power.

4.2 Measures of Peakiness

A measure of the amplitude variation of $s(t)$ or $s'(t)$ versus time is required for the sake of a quantitative analysis. Various authors [61–63] defined the measure as "peak factor", "crest factor" and so on, sometimes using the same terminology associated with different meanings. "Peak-factor (PF_1)", introduced by *Schroeder* [61], appeared to be the first terminology in various publications. It was defined as the difference between the maximum and minimum amplitudes of a signal divided by its Root-Mean-Square (RMS) value. In reference [61], the "relative peak-factor", defined as $PF_1/(2\sqrt{2})$, was also proposed as a normalized measure, which becomes 1.0 for sine waves. $PF_1/2$ was referred to as the "crest factor (CF_2)" later in reference [62] . In 1981, *Greenstein* and *Fitzgerald* [63] used the same term, namely "peak factor (PF_2)", for the peak-to-average power (PAP [64–67]) ratio (PAPR [68–70]), which is also referred to as the peak-to-mean envelope-power ratio (PMEPR [31, 71]). *Boyd* [72] defined "crest factor (CF_1)" as the ratio of the peak to the RMS amplitude, $||s||_\infty/||s||_2$, which also enjoyed wide-spread use [64, 69].

In this treatise the terminology "crest factor (CF_1)" and "peak factor (PF_2)" will be used, in order to avoid unnecessary confusion, which are defined as the ratio of the peak to the RMS amplitude:

$$\mathrm{CF}_1 \triangleq \frac{||s||_\infty}{||s||_2}, \tag{4.3}$$

where $||s||_\infty = \max_t |s(t)|$ and $||s||_2 = \sqrt{\int_T |s(t)|^2 dt}$, while:

$$\mathrm{PF}_2 \triangleq \frac{\text{Peak Power}}{\text{Average Power}} = \frac{||s||_\infty^2}{||s||_2^2}, \tag{4.4}$$

which is equivalent to the ratio of the peak power to the average power given by $(\mathrm{CF}_1)^2$.

One should note that the crest factors of $s(t)$ and $s'(t)$ are not the same in terms of their values. In fact, the nature of the associated two crest factors is different as well. Let the subscript m represent the index of the sequence applied, as in $s_m(t)$ and $s'_m(t)$. Then, in general, the statement

$$\mathrm{CF}_1[s_m(t)] > \mathrm{CF}_1[s_n(t)] \rightarrow \mathrm{CF}_1[s'_m(t)] > \mathrm{CF}_1[s'_n(t)] \tag{4.5}$$

is not true. Below we illustrate this with the aid of a counter-example. Figure 4.2 compares $|s(t)|$ and $|s'(t)|$ for the data sequences $\{00010\}$ and $\{01001\}$. The former is the so-called *Barker* sequence, which will be introduced in Section 4.3.5, of length 5 and the latter is the fragment of an m-sequence derived using the octally represented generator polynomial of $g = (013)_o$ [50, Table3-5], with the aid of the initial seed of $(06)_o$). In terms of $|s'(t)|$, the partial m-sequence shows the lower CF_1 of 1.79, while the Barker sequence exhibits $\mathrm{CF}_1 = 1.90$. However, as shown in Fig. 4.2(b), this crest factor relationship is reversed in terms of $|s(t)|$, where $\mathrm{CF}_1 = 1.342$ for the Barker sequence and $\mathrm{CF}_1 = 1.637$ for the partial m-sequence, when they are applied to $s(t)$. Thus, in general, a rank ordering according to CF_1 changes, depending on the application and/or on the specific formulation of the time-domain modulated signal, as seen for $s(t)$ and $s'(t)$ in (4.1) and (4.2).

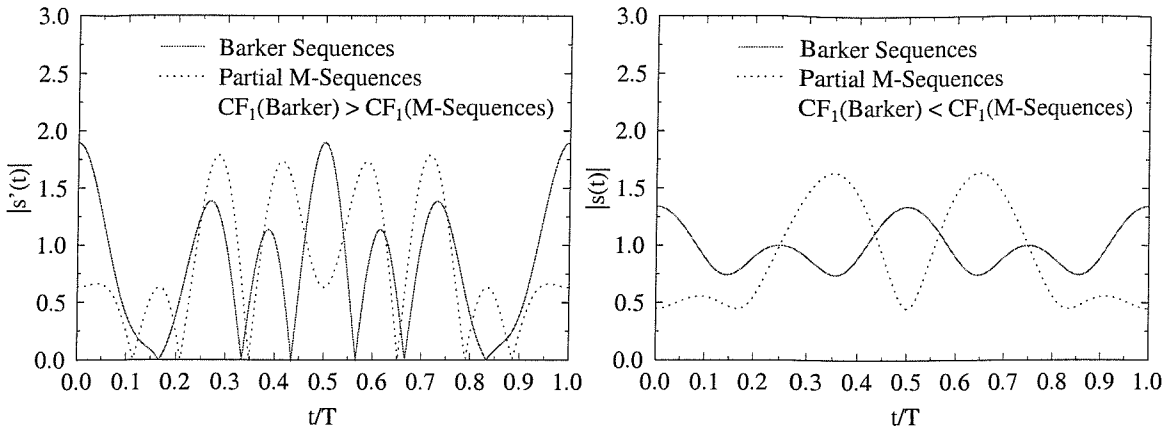

(a) Magnitude of $s'(t)$, $|s'(t)|$ (b) Magnitude of $s(t)$, $|s(t)|$

Figure 4.2: A counter example of (4.5) comparing $|s'(t)|$ and $|s(t)|$ for $\{00010\}$, a Barker sequence, and $\{01001\}$, a sub-sequence of a 7-bit m-sequence

4.3 Special Sequences for Reducing Amplitude Variations

There have been numerous efforts dedicated to reducing the envelope variations of $s(t)$ or $s'(t)$, which were reported for example in [61, 65, 68, 71, 73–75]. A specific approach is to encode the information sequences, $\{c_k\}$, of Equation (4.1) or to adjust $\{\theta_k\}$ in Equation (4.2) so that the resultant signal can exhibit low peak factors. In this section, these efforts will be highlighted.

4.3.1 *Shapiro-Rudin* Sequences

Shapiro [76] and Rudin [73] were interested in trigonometric polynomials having coefficients of ± 1, which correspond to $s(t)$ given in (4.1), as early as in the 1950s. Specifically, Rudin [73] mentioned the existence of the apparent lower bound for $||s||_\infty$ using *Parseval*'s theorem, which is formulated as:

$$\frac{1}{T}\int_T f^2(t)dt = \sum_{k=-\infty}^{\infty} |c_k|^2 , \tag{4.6}$$

where $\{c_k\}$ are the complex frequency domain Fourier series coefficients of the periodic signal $f(t)$. Using (4.6), the average power of $s(t)$ becomes

$$\begin{aligned} \frac{1}{T}\int_T s^2(t)dt &= \sum_{k=-\infty}^{\infty} |c_k|^2 \\ &= \sum_{n=1}^{N} |c_k|^2 \\ &= N . \end{aligned} \tag{4.7}$$

Using the inequality of $\frac{1}{T}\int_T(||s||_\infty)^2dt \geq \frac{1}{T}\int_T s^2(t)dt$ we may conclude that[1]:

$$||s||_\infty \geq \sqrt{N}\,. \tag{4.8}$$

Then Rudin [73] introduced the problem of finding an upper bound for $||s||_\infty$, an absolute constant A having the property that for each N one can find $\{c_k; c_k \in (\pm 1)\}$, satisfying

$$||s||_\infty \leq A\sqrt{N}. \tag{4.9}$$

He also invoked *Shapiro*'s result [76] that $A = \sqrt{2}$ for $N = 2^n$, otherwise $A = 2 + \sqrt{2}$. Their proposed sequences, which satisfy the equality in (4.9) were later referred to as *Shapiro-Rudin* sequences or phases [72]. This remarkable early work in mathematics has not been widely recognized in the communications community until 1981 [63] and it was after 1986 [72], when the work was explained comprehensively. *Shapiro-Rudin* sequences, later were shown to constitute a specific case of *Golay's complementary sequences* [75, 77].

In their original formulation [73], *Shapiro-Rudin* sequences can be constructed using a pair of recursive polynomial relationships, which is given by:

$$\begin{aligned} P_0(x) &= Q_0(x) = x\,, \\ P_{k+1}(x) &= P_k(x) + x^{2^k} Q_k(x)\,, \\ Q_{k+1}(x) &= P_k(x) - x^{2^k} Q_k(x)\,, \end{aligned}$$

and the sign of each term x^n forms the individual components of the sequences. Following several recursive steps commencing from $k = 0$ reveals that the sequence is of length 2^k and that the above relation can be stated more directly [72]:

> Starting with the string $p = 11$ and repeatedly concatenating to p a copy of p with its second half negated, we arrive at the set of *Shapiro-Rudin* sequences.

The first 32-bit sequence is given by

$$1110\ 1101\ 1110\ 0010\ 1110\ 1101\ 0001\ 1101\,,$$

where 1 represents a 1 and 0 stands for -1. As mentioned before, Figure 4.1(b) represents the associated power envelope waveform for 16-carrier BPSK OFDM, when *Shapiro-Rudin* sequences are applied. The peak-factor PF_2 of (4.4) for this case is 1.9 (2.8dB), while the worst case PF_2 associated with using no CF-reduction coding, seen in Figure 4.1(a), is 16 (12.0dB). Shepherd *et al.* [78] proposed half-rate precoding for QPSK OFDM using the *Shapiro-Rudin* sequences of length 8 for 4 message bits, in order to reduce the peak factor. However, the associated halving of the effective throughput is unacceptable in most practical applications.

[1] This sets the minimum CF_1 to unity.

4.3.2 *Golay* Codes

Golay found in 1961 a set of complementary series [77], while he was working on the optical problem of spectrometry. Let $\{a_i\}$ and $\{b_i\}$ be two *Golay* complementary series of length N, and let their aperiodic autocorrelations A_k and B_k be defined by

$$A_k \triangleq \sum_{i=1}^{N-k} a_i a_{i+k} \;, \quad k = 0,\ 1,\ \cdots,\ N-1 \tag{4.10}$$

and

$$B_k \triangleq \sum_{i=1}^{N-k} b_i b_{i+k} \;, \quad k = 0,\ 1,\ \cdots,\ N-1 \;, \tag{4.11}$$

where the terminology "aperiodic" implies that the sequences are not used cyclically in the auto-correlation calculation process. Then, the following property holds:

$$A_k + B_k = 0 \;\forall\, k,\ k \neq 0 \;, \tag{4.12}$$

$$A_0 + B_0 = 2N \;. \tag{4.13}$$

The aperiodic autocorrelations of the transmitted sequence $s(t)$ given in Equation 4.1 play a major role [61, 70, 79] in deciding the peak factor of the signal. However, Equations (4.12) and (4.13) do not say anything about the aperiodic autocorrelations of individual series. Golay found several transforms of the sequences, which do not alter their properties, and hence were shown to be invariant in terms of the peak factors.

It was Popović, who showed in 1991 that PF_2 of $s(t)$ employing any *Golay* complementary series for $\{c_k\}$ is bounded by two (or 3dB) [75]. This is also true when representing $\{c_k\}$ with the aid of complex complementary sequences [80–82]. Popović also noted that *Shapiro-Rudin* sequences belong to a large family of Golay sequences of length 2^k. *Davis* and *Jedwab* [71] reported that Golay sequences can be used as a precoder for OFDM in order to bound the PF_2 within a ratio of two (or 3dB) as well as additionally to provide some error correction capability. The code rate, R, is given [71] by

$$R = \frac{\lfloor \log_2(m!/2) \rfloor + m + 1}{2^m} \;, \tag{4.14}$$

where 2^m is the length of the Golay codes used. Figure 4.3 shows the code rate versus the number of carriers. As the number of carriers increases, the code rate becomes too low to be applicable to OFDM. For $N > 16$, the coding rates are below $1/2$, which is unacceptable in most applications and hence it is better to use amplifier-back-off or other error correction codes [83] .

4.3.3 M-Sequences

Maximal-length sequences were already discussed in Section 2.1.1, which exhibit randomness properties, also known as the "balance property", "run-length property" and "shift-and-add property" [51]. Their periodic autocorrelations $R_a(k)$, defined as $R_a(k) \triangleq \sum_{i=1}^{N} c_i c_{i+k}$, are given as:

$$R_a(k) = \begin{cases} N & k = lN \\ -1 & k \neq lN \;, \end{cases} \tag{4.15}$$

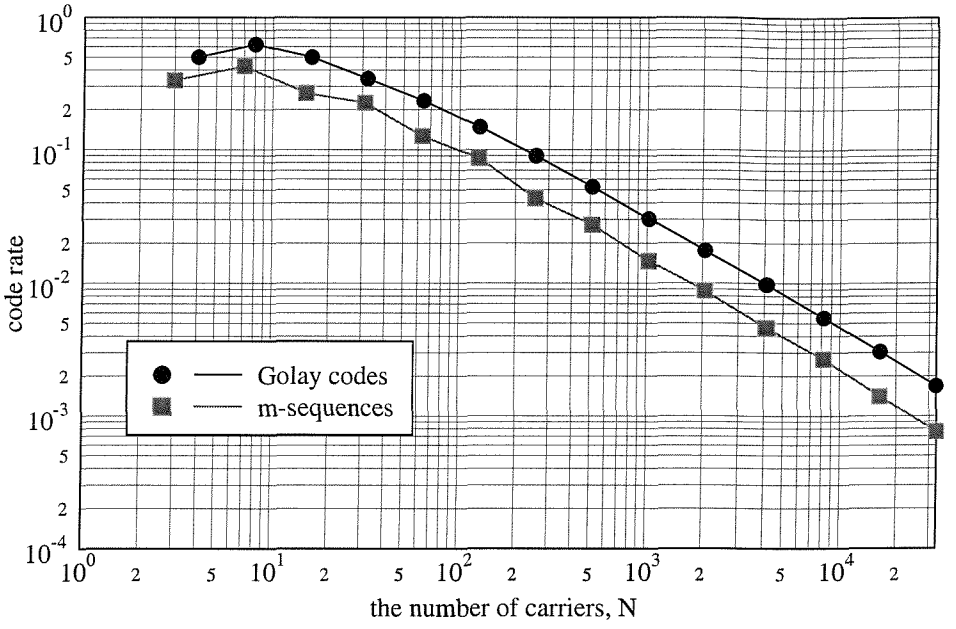

Figure 4.3: The coding rate of Golay sequences and m-sequences used in OFDM

where l is an integer and N is the period of the m-sequence. The excellent auto-correlation property manifested by the high ratio of these two $R_a(k)$ values accrues from the "balance property" and "shift-and-add property", an issue detailed in references [6, 50, 51]. Since the definition of aperiodic auto-correlation given in (4.10) is similar to that of the periodic auto-correlation provided in (4.15), $s(t)$ of (4.1) employing an m-sequence for c_k may result in a low crest factor. Li and Ritcey [65] proposed a precoding scheme using m-sequences for OFDM, in order to reduce the peak factors, claiming to have achieved very low PF_2 values, which were later shown to be optimistic [66, 67]. The CF_1 values of $s'(t)$ and $s(t)$, when encoded by m-sequences, appear in Figures 4.4 and 4.5, respectively, in conjunction with a range of other schemes, which will be described at a later stage in the forthcoming sections. The coding rate R is given by:

$$R = \frac{\lfloor \log_2 N + \log_2 N_p \rfloor}{N}, \tag{4.16}$$

where N_p is the number of primitive polynomials of degree r, given by [51]:

$$N_p = \frac{2^r - 1}{r} \prod_{j=1}^{J} \frac{p_j - 1}{p_j}, \tag{4.17}$$

where p_j, $j = 1, 2, \cdots, J$ are prime factors of the period $N = 2^r - 1$ and J is the number of the prime factors. Figure 4.3 also shows the corresponding code rate R of (4.16). Compared with the code

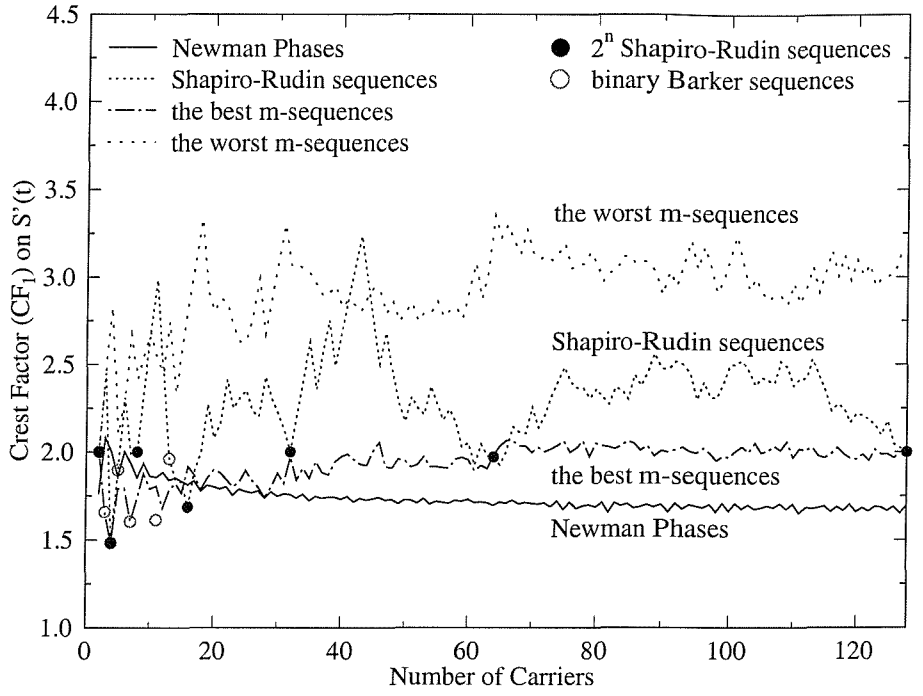

(a) CF_1 of $s'(t)$ up to $N = 128$

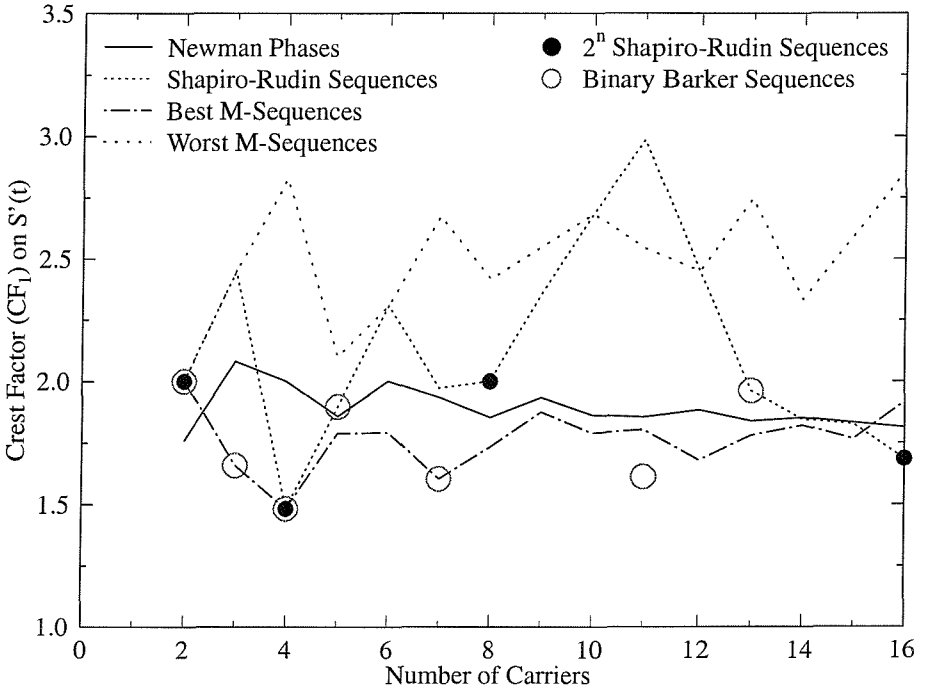

(b) CF_1 of $s'(t)$ up to $N = 16$

Figure 4.4: The comparison of CF_1 of $s'(t)$ defined in (4.2) using various CF-reduction schemes

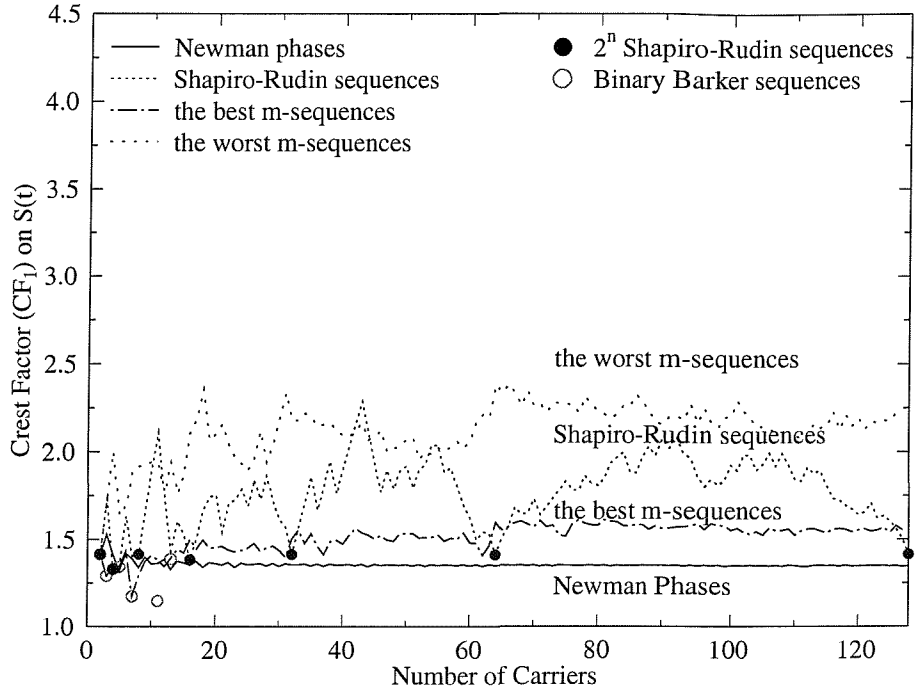

(a) CF_1 of $s(t)$ up to $N = 128$

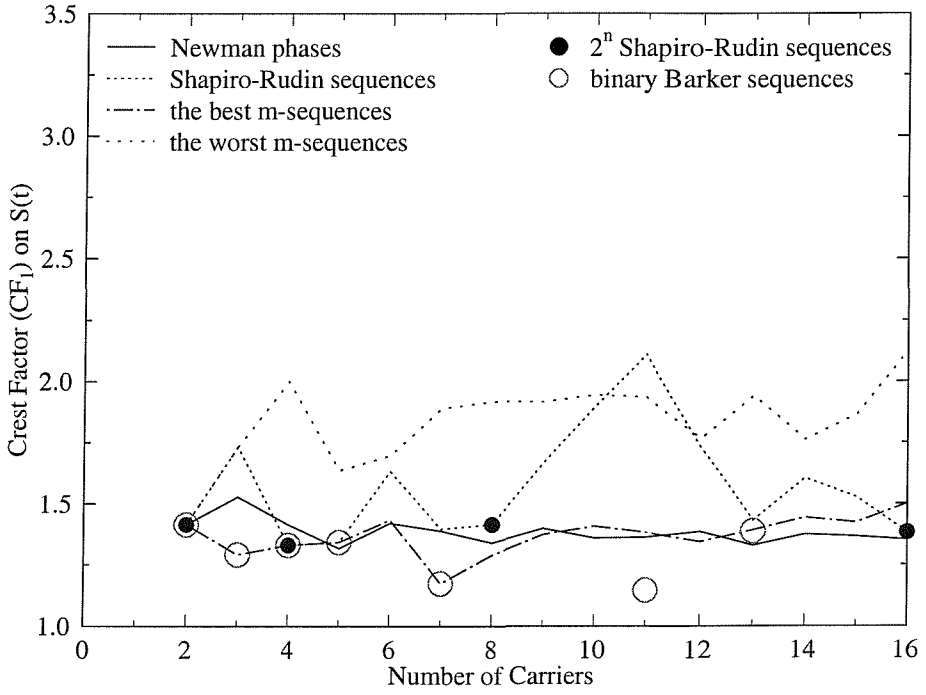

(b) CF_1 of $s(t)|$ up to $N = 16$

Figure 4.5: The comparison of CF_1 of $s(t)$ defined in (4.1) using various CF-reduction schemes

rate of the Golay codes given in (4.14) of Section 4.3.2, m-sequences require a lower code rate, while the peak factors of the Golay codes lie between the those of the worst case and the best case of the m-sequences. This implies that m-sequences are impractical for peak factor reduction motivated coding in most applications.

4.3.4 *Newman* Phases and *Schroeder* Phases

In 1965 Newman [74] suggested, a formula for adjusting the phases, while he was aiming for maximising the so-called L^1 norm representing the absolute value of trigonometric polynomials. The Newman phases are given by [74]:

$$\theta_k^{(Newman)} = \frac{\pi(k-1)^2}{N}, \tag{4.18}$$

where the denominator N is the number of subcarriers. An application of $\{\theta_k^{(Newman)}\}$ given in (4.18) for the choice of $\{\theta_k\}$ of $s'(t)$ defined in (4.2) was reported by *Boyd* [72] together with the achievable CF_1 results.

While *Newman* constructed the set of low crest factor phases $\{\theta_k^{(Newman)}\}$ purely mathematically, *Schroeder* [61] used engineering arguments for deriving similarly advantageous, low-CF phases. Based on the observation that Frequency Modulation (FM) signals have constant envelopes and that there is a relationship between the instantaneous frequencies of FM signals and their power spectra, Schroeder derived the phase sequences, $\{\theta_k^{(Schroeder)}\}$, given by [61, Eq.11]

$$\theta_k^{(Schroeder)} = \theta_1 - \frac{\pi k(k-1)}{N}, \tag{4.19}$$

which are similar to the *Newman* phases of (4.18). Specifically, assuming $\theta_1 = -\frac{\pi}{N}$, and a time shift of $T/(2N)$ together with time reversal yields an $s'(t)$ function identical to that upon using the Newman phases of (4.18). Figure 4.6 shows the $s'(t)$ functions using both *Newman* phases and *Schroeder* phases for $N = 16$ number of harmonics. A time translation of $T/(2N) = T/32$ and time reversal of $s'(t)$ with respect to the original *Schroeder* phases results the same $s'(t)$ function generated using *Newman* phases. The CF_1 value in this case is 1.813 (5.17dB), while the worst case is $\sqrt{2N} = 4\sqrt{2}$ (15.05dB).

Greenstein and Fitzgerald [63] proposed a similar phasing scheme in 1981. Narahashi and Nojima [68] also reported a similar phasing scheme, given by:

$$\theta_k^{(Narahashi)} = \frac{(k-1)(k-2)}{N-1}\pi. \tag{4.20}$$

These phases were derived by setting $\rho_1 = 0$, where ρ_1 is the aperiodic autocorrelation coefficient at a displacement of one, which is given by $\rho_1 = \sum_{i=1}^{N-1} c_i c_{i+1}^*$. The achievable crest factor reduction is similar to that attained with the aid of *Newman* phases.

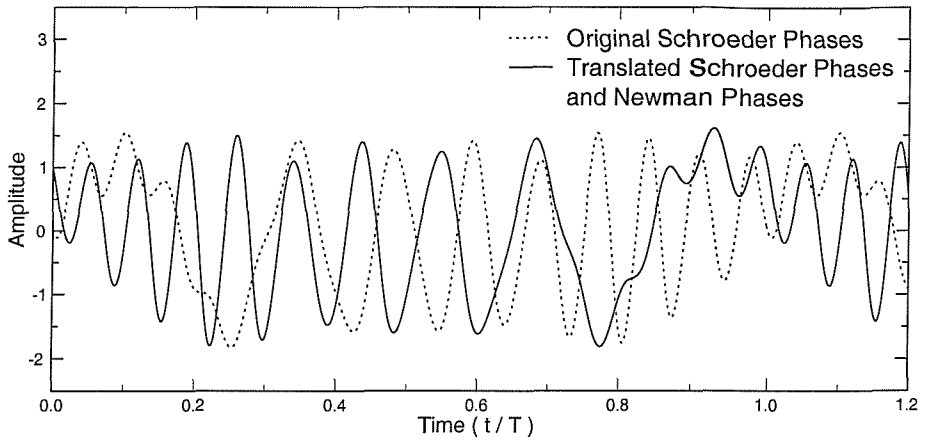

Figure 4.6: The function $s'(t)$ of (4.2) when *Newman* phases [74] and *Schroeder* phases [61] are used

4.3.5 *Barker* Codes

According to Schroeder [61, Eq.18][2] the envelope power of $s(t)$ can be written as: as:

$$s^2(t) = 1 + \frac{2}{N} \sum_{k=1}^{N-1} \rho_k \cos(k\omega t) \,, \tag{4.21}$$

where ρ_k are the aperiodic autocorrelations defined by $\rho_k = \sum_{i=1}^{N-k} c_i c_{i+k}^*$ and ω is the fundamental angular frequency. It is apparent that a low $\{\rho_k\}$ value is desirable for attaining low peak factors. In this sense, *Barker* codes [84, 85] are optimal. More specifically, *Barker* codes are defined as arbitrary binary sequences (or complex sequences for generalized Barker codes) of length N, for which the aperiodic autocorrelations, ρ_k, satisfy [84, 85]:

$$|\rho_k| \begin{cases} = N & \text{for} \quad k = 0 \,, \\ \leq 1 & \text{for} \quad k = 1, 2, \cdots, N-1 \,, \\ = 0 & \text{for} \quad k \geq N \,. \end{cases} \tag{4.22}$$

Unfortunately, only few binary Barker sequences [86] are known, which are summarised in Table 4.1. In Table 4.1, 1 represents +1 and 0 corresponds to -1. In the case of $N = 4$, the two codes are also *Golay* complementary sequences. Other than those listed above, no binary *Barker* sequences seem to exist [86, 87]. However, the generalized *Barker* sequences [87], which allow c_k to have unit magnitude complex values, exist for an arbitrary value of N.

[2]This relation appeared again in the recent literature [70, 79].

N	Codes	CF_1 for $s(t)$
2	11	2.00
3	110	1.66
4	1110, 1101	1.48
5	11101	1.90
7	1110010	1.60
11	11100010010	1.61
13	1111100110101	1.96

Table 4.1: All the known binary *Barker* sequences [86]

4.3.6 Comparison of Various Schemes

Having introduced a range of CF reduction techniques, it is interesting to compare their crest-factors (CF_1). Figure 4.4 and Table 4.2 show the crest factors (CF_1) of the various schemes, when they are applied to $s'(t)$ of (4.2).

Sequences	N=2	4	8	16	32	64	128
Binary Barker	2.00	1.48	-	-	-	-	-
Newman phases	1.76	2.00	1.85	1.81	1.76	1.69	1.69
The best partial m-sequences	2.00	1.48	1.73	1.92	1.97	1.98	2.00
Shapiro-Rudin sequences	2.00	1.48	2.00	1.69	2.00	1.97	2.00
The worst partial m-sequences	2.00	2.83	2.42	2.86	3.06	3.35	3.14

Table 4.2: CF_1 values of $s'(t)$ defined in (4.2) for certain sequence length N using various CF-reduction schemes

For the range of sequence lengths N that we studied, *Newman* phases show the lowest crest factors (CF_1). For N values up to 15 shown in Figure 4.4(b), the best case of partial m-sequences or the binary *Barker* sequences show the lowest CF_1 values. The partial m-sequences show a large range of CF_1 values, depending on the polynomial used and the initial seed applied. Broadly speaking, *Shapiro-Rudin* sequences and thus *Golay* complementary codes exhibit crest factors between those of the worst-case and best-case m-sequences. The crest factors of all the investigated sequences fall well below four (or 6dB), regardless of the sequence length N. Beside the schemes investigated, there is a numerically near-optimal solution [62], which appears to be the best known solution at the time of writing, since its crest factor approaches $\sqrt{2}$.

Figure 4.5 and Table 4.3 show the crest factors (CF_1) of the various CF reduction schemes, when they are applied to $s(t)$ of (4.1) . In Section 4.2, we showed that the rank ordering based on CF_1 was not the same for $s(t)$ and $s'(t)$. For $s(t)$ the *Barker* sequences of Table 4.1 show the best results amongst the binary sequences considered. However, it is interesting to note that the *Newman* phases of (4.18) exhibit

Sequences	N=2	4	8	16	32	64	128
Binary Barker	1.41	1.33	-	-	-	-	-
Newman phases	1.41	1.41	1.34	1.35	1.35	1.35	1.35
The best m-sequences	1.41	1.33	1.29	1.50	1.50	1.60	1.55
Shapiro-Rudin sequences	1.41	1.33	1.41	1.38	1.41	1.41	1.41
The worst m-sequences	1.41	2.00	1.92	2.12	2.18	2.38	2.24

Table 4.3: CF_1 values of $s(t)$ defined in (4.1) for certain sequence lengths N using various CF-reduction schemes

lower CF_1 values than *Barker* sequences, when considering $N = 5$ and 13. This suggests that some complex sequences, such as generalized *Barker* sequences [87], may be exhibit lower crest factors, than those of binary Barker sequences.

4.4 Crest Factor Reduction Mapping Schemes for OFDM

4.4.1 Some Properties of the Peak Factors in OFDM

The *normalized* complex envelope $s(t)$ of the transmitted waveform of BPSK-modulated OFDM signal can be written as [66]:

$$s(t) = \frac{1}{\sqrt{N}} \sum_{k=0}^{N-1} c_n \, e^{j2\pi \frac{kt}{T}} , \tag{4.23}$$

where N is the number of carriers, $c_k \in \{-1, +1\}$ is the information bearing frequency domain modulating symbol transmitting by the kth subcarrier and T is the OFDM symbol duration. Applying Parseval's theorem to (4.23), we find that the average power of $s(t)$ is unity. Hence the peak-to-mean envelope power ratio (*PMEPR* = PF_2) is simply given by the maximum value of the envelope power, $|s(t)|^2$, over the OFDM symbol period.

As an example, let us examine the 4-carrier BPSK modulated OFDM scenario. There are 2^4 possible message sequences. The sequences can be represented by their decimal values, from 0, 1, $\cdots$, 15, corresponding to the messages of '0000', '0001', $\cdots$, '1111'. Figure 4.7 shows the normalized envelope power waveforms, $|s(t)|^2$, of all possible message sequences of 4-carrier BPSK modulated OFDM, where each graph has two waveforms, which have the same *PMEPR*. All the waveforms in Figure 4.7 have the same average power, namely unity. Furthermore all the waveforms are symmetric to $0.5t/T$, since the power envelopes can be represented with the sums of cosine harmonics, as shown in Equations (A.3), (A.4) and (A.5) in the Appendix. The dotted lines represent the waveforms that can be generated with the aid of shifting the solid lines by $0.5t/T$ and have the same *PMEPR* as their counterparts shown using solid lines. The waveforms in the top graph are more desirable in CF terms than the others, since they show the lowest power variations and the lowest *PMEPR*. Eight message symbols corresponding to the decimal notations of 1, 7, 8, 14 and 2, 4, 11, 13, belong to this category. By contrast, the sub-figure

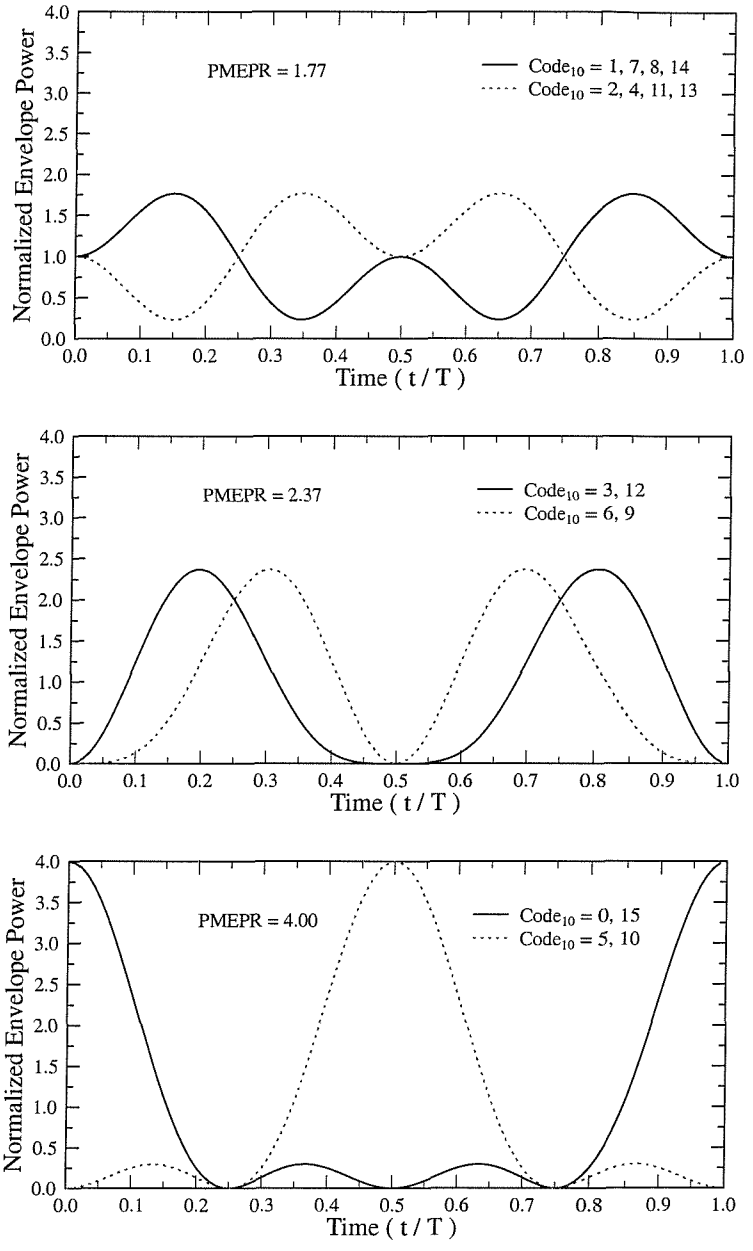

Figure 4.7: Normalized envelope power waveforms, $|s(t)|^2$, for 4-carrier BPSK modulated OFDM signals for the message symbols (top: *PMEPR* = 1.77, middle: *PMEPR* = 2.37 and bottom: *PMEPR* = 4.00), where each frequency domain sample is represented by its corresponding decimal value, hence Code_{10}, for example $\text{Code}_{10} = 1$ denotes a message sequence of '0001' and $\text{Code}_{10} = 7$ '0111'.

at the bottom shows the worst case amongst the three possible *PMEPR* values, which is associated with $PMEPR = 4$.

The power envelope waveforms are dependent on the characteristics of the corresponding message sequences, but some sequences yield exactly the same power envelopes and some others show shifted envelopes. This observation led us to investigate the underlying nature of the sequences employed. Appendix A.2 provides a detailed analysis of the *PMEPR* for BPSK modulated OFDM signals. The *PMEPR* of a message symbol is shown to be dependent on its aperiodic autocorrelation values defined in (4.10). Based on this observation, the message symbols can be grouped in terms of their *PMEPR*. It is shown in Appendix A.2 that irrespective of the number of subcarriers, in BPSK modulated OFDM there are at least four message symbols, which yield an identical *PMEPR*. These four messages can be obtained by three distinctive transformations of one message. It is also shown that in certain conditions another four messages also yield the same *PMEPR* and hence form an equivalent class. In general, four or eight message groups belong to a *PMEPR* group.

For QPSK-modulated OFDM signals, the normalized complex envelope waveform, $s(t)$, can be written as [32]

$$s(t) = \frac{1}{\sqrt{2N}} \sum_{k=0}^{N-1} (c_{2k} + jc_{2k+1})\ e^{j2\pi \frac{kt}{T}}\ , \tag{4.24}$$

where N is the number of carriers, c_{2k} and c_{2k+1} are the in-phase symbol and the quadrature phase symbol, respectively, mapped to the kth subcarrier, while $c_i \in \{-1, +1\}$ and T is the OFDM symbol duration. Van Eetvelt, Shepherd and Barton [32] presented an excellent analysis of QPSK modulated multi-carrier systems and showed that 16 messages form a so-called coset, in which messages yield the same *PMEPR*. They also presented an algorithm, which can be used for finding equivalent classes from a given coset leader and tabulated the equivalence classes up to $N = 5$ carriers. Although their results are useful, Algorithm 2 of [32, page 91] does not give the results claimed [32, Table 4, page 94] for the 5-carrier case. Table A.4 shows the correct equivalent groupings for 5-carrier QPSK OFDM.

4.4.2 CF-Reduction Block Coding Scheme

An important observation concerning the peak factor distributions of multi-carrier systems is that there are not many message symbols which yield high peak factors. Figure 4.8 presents the Cumulative Probability Distributions (CDF) for 4-, 6- and 8-carrier OFDM signals. The graph at the left of Figure 4.8 represents BPSK modulated OFDM and the right one is for QPSK modulated OFDM signals. The cumulative distributions presented in Figure 4.8 for QPSK exhibit twice as many steps, as those related to BPSK, since there are twice as many legitimate symbols for the same number of carriers. The distributions of the real and imaginary amplitudes of $s(t)$ for a high number of subcarriers N were shown to be approximated by the Gaussian distribution [88, 89].

Jones, Wilkinson and Barton [31] proposed a simple block coding scheme for eliminating those message symbols from the coded message symbol set, which yield high peak factors. For example, in the case of 8-carrier BPSK modulated OFDM, the cumulative distribution reaches 50% at a *PMEPR* of 2.8, which is shown in Table 4.4. This means that the worst case *PMEPR* can be reduced from 8.0 to 2.8

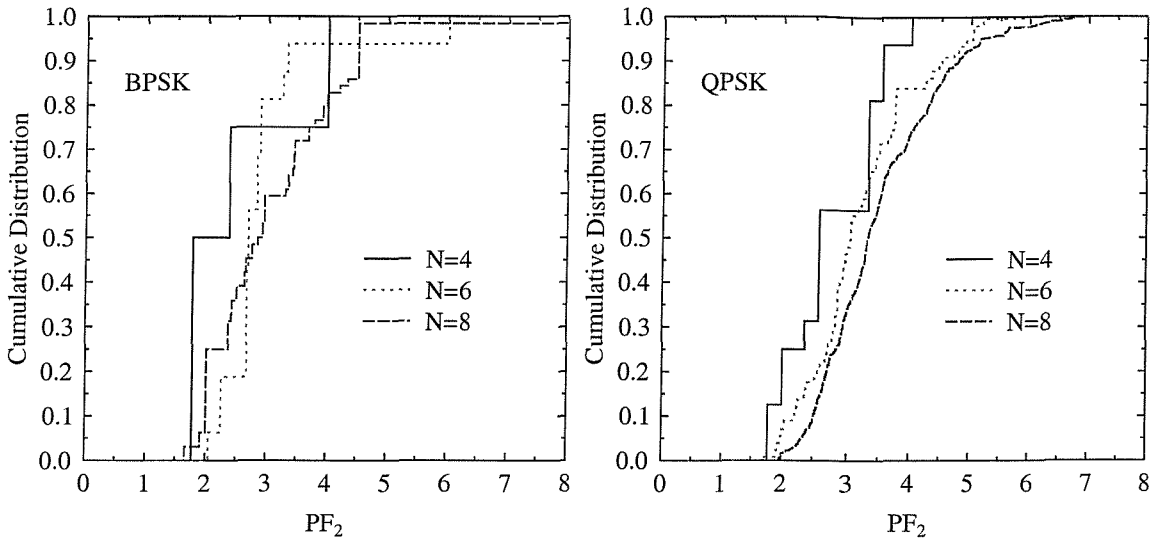

Figure 4.8: Cumulative distributions of the peak factor PF_2 of (4.4) for BPSK modulated OFDM (left) and QPSK modulated OFDM (right) using 4, 6 and 8 carriers.

by employing an (8,7) block code at the cost of a throughput loss of $1/8$. This scheme achieves a low worst case peak factor in a simple manner with the aid of high-rate block codes. By employing lower-rate block codes, even lower peak factors can be obtained [31] at the cost of further effective throughput loss. For example, a (4,3) block code is capable of reducing the PF_2 of (4.4) further, down to 2.0 for an 8-carrier BPSK OFDM system. The same method can be used for QPSK modulated OFDM [32, 90]. The main drawback of this scheme is that the encoding and decoding processes rely on look-up tables, since no structured or algorithmic description of the block coding method concerned is known [65].

A half rate coding method was proposed by *Friese* [69], which can be regarded as a non-structured block coding method. According to this scheme, the phase difference of a pair of subcarriers is dependent on the message symbol they carry. Thus, there is a degree of freedom in choosing the phase differences between the consecutive pairs of carriers. *Friese* proposed to optimize the phase differences of adjacent subcarriers using the algorithm given in [62]. He reported a considerable reduction in terms of the achievable crest factors. However, the computational complexity inherent in the algorithm hinders its real-time application for a high number of subcarriers N and in the context of high speed data transmission.

Some structured block coding methods appeared in the literature as well. Shepherd, Eetvelt, Millington and Barton [78] proposed the employment of *Shapiro-Rudin* codes for block coding. Davis and Jedwab [71] proposed a block coding scheme based on *Golay* codes. However, the code rates of these structured block coding methods were typically low , as seen in Figure 4.3.

PF_2	1.7	1.9	2.0	2.4	2.5	2.6	2.7
PDF	0.031	0.031	0.188	0.109	0.031	0.031	0.031
CDF	0.031	0.063	0.250	0.359	0.391	0.422	0.453
PF_2	2.8	2.9	3.0	3.3	3.4	3.5	3.7
PDF	0.047	0.063	0.031	0.016	0.078	0.031	0.031
CDF	0.500	0.563	0.594	0.609	0.688	0.719	0.750
PF_2	3.8	3.9	4.0	4.2	4.3	4.5	8.0
PDF	0.016	0.031	0.031	0.016	0.016	0.125	0.016
CDF	0.766	0.797	0.828	0.844	0.859	0.984	1.000

Table 4.4: Probability Density Functions (PDF) and Cumulative Distribution Functions (CDF) of the peak factors in BPSK-OFDM using 8 subcarriers: The PF_2 value of (4.4) at CDF=0.5 is 2.8, which is the worst-case peak factor, when an (8,7) nonlinear block code is used for eliminating half of the message codes, yielding higher values of PF_2 than 2.8 or 4.47dB.

4.4.3 Selected Mapping Based CF-Reduction

In 1996, Bäuml, Fischer and Huber [64] proposed a new mapping algorithm for reducing peak factors in OFDM. One of the advantages of the scheme advocated in [64, 91] is that it has a low transmission overhead. In their scheme, the best mapping resulting in the lowest CF is selected from a set of n random mapping attempts, which map $\{c_k\}$ to $\{c_k^{(i)}\}$, $i = 1, \cdots, n$. As n increases, there is a reduced chance that the selected mapping exhibits a high worst-case crest factor. The problem is in the context as to select the best mapping efficiently in real time. A crude approach is to calculate all the crest factors associated with the n different tentative mapping attempts, which requires a considerable computational effort.

Eetvelt, Wade and Tomlinson [70] proposed a heuristic measure for identifying possible message codes yielding high crest factors. The corresponding measure was defined as:

$$SF = \frac{|W_H - N|^2 + |R_1|2}{2N^2}, \tag{4.25}$$

where W_H is the Hamming weight of the message codes and $R_1 = \sum_{i=1}^{N-1} c_{i-1}/c_i$, which has high values for structured sequences exhibiting high crest factors. The smaller SF, the more likely that the message code has low peak factors. Eetvelt, Wade and Tomlinson [70] also proposed a scrambling scheme based on m-sequences for deriving the suggested random mapping method.

Mestdagh and Spruyt [88] analyzed a specific version of the 'selected mapping' method of [64] in conjunction with fixed peak-clipping in the amplifier. It was shown that there exists an optimal clipping level in terms of the achievable SNR gain for the given D/A or A/D precision and for the given number of random mapping trials used for finding the best mapping.

4.4.4 Partial Transmit Sequences

A different approach within the frame work of the mapping concept is to use partial transmit sequences [92]. The problem associated with using the selected mapping based techniques of the previous section is that the selection functions may require n implementationally demanding IFFT operations for arriving at n different mapping choices. Müller and Huber [92] reduced the number of IFFT operations required to $\log_2 \sqrt{n}$, where n is the number of mapping choices available. In their scheme the legitimate information symbol set $\{c_k\}$ is partitioned into V number of sets. The V number of partitioned sets are subjected to IFFT, in order to generate V number of time-domain 'Partial Transmit Sequences (PTS)' and the transmitted signal is represented as a linear combination of these PTS. The optimization of the peak factor is performed using V number of independent multiplication factors for each PTS. Allowing $\{\pm 1, \pm j\}$ for each multiplication factor, 4^V legitimate choices are presented and the best one is selected for transmission. Müller and Huber also compared the amplitude distributions associated with their scheme to those of the selected mapping schemes of Section 4.4.3. The authors claimed that their scheme was more efficient in terms of reducing the peak factors, than the selected mapping based method of Section 4.4.3 for the same number of IFFT operations, namely when assuming $V = n$, where again V indicates the number of PTS and n is the number of tentative CF-reducing mapping attempts in the context of the selected mapping scheme. However, since their calculation of the peak factors was not based on the continuous time domain signal, but on the discrete values generated by the IFFT, the corresponding peak factors were lower, than the actual peak factors. Furthermore, their assumption of $V = n$ resulted in 4^V number of PTS based choices, requiring 4^V number of CF calculating operations, while the number of mapping choices for the selected mapping method remained V. In general, comparisons have to be carried out under the assumption of constant computational efforts. In this sense, using effective selection functions [70, 93] for identifying low crest-factor messages is of salient importance.

4.5 Peak Factors in Multi-Carrier CDMA

In order to capitalise on the joint benefits of direct-sequence code division multiple access (DS-CDMA) and orthogonal frequency division multiplexing (OFDM), multi-carrier CDMA (MC-CDMA) was proposed [1, 2] and has drawn significant research interests in recent years. DS-CDMA spreads the original spectrum of the information signal over wide bandwidth and hence even if certain frequencies are faded, it is capable of exploiting frequency diversity using Rake receivers, where the number of fingers in the Rake receiver determines the maximum achievable diversity gain. OFDM, on the other hand, is resilient to frequency selective fading since it effectively converts a high-rate single carrier scheme to numerous parallel low-rate schemes. Furthermore, OFDM asymptotically approaches the theoretically highest 2Bd/Hz Shannonian bandwidth efficiency. One of the main drawbacks of OFDM is that the envelope power of the transmitted signal fluctuates widely, requiring a highly linear RF power amplifier. Since our advocated MC-CDMA system spreads a message symbol across the frequency domain and uses an OFDM transmitter for conveying each spread bit with the aid of each subcarrier, its transmitted signal also exhibits a high CF.

In this section, we analyse the characteristics of the envelope power of the MC-CDMA signal and establish the relationship between the envelope power and certain properties of the spreading sequences employed. The associated crest factors of several spreading sequences are examined and the results are discussed. In order to investigate the effects of the different crest factors on the performance of MC-CDMA systems, the bit error rate and the power spectrum are also studied, employing a specific solid-state transistor amplifier (SSTA) model. Finally, a range of practical solutions are presented for mitigating the crest factor problem in the context of MC-CDMA communication systems.

4.5.1 System Model and Envelope Power

The simplified transmitter structure of a multi-code MC-CDMA system is portrayed in Figure 4.9, where L symbols $\{b_l \mid 0 \leq l < L\}$ are transmitted simultaneously using L orthogonal spreading sequences $\{\mathbf{C}_l \mid 0 \leq l < L\}$, each constituted by N chips according to $\mathbf{C}_l = \{c_l[n] \mid 0 \leq n < N\}$. Since the L number of N-chip parallel spreading codes seen in Figure 4.9 are orthogonal, their superposition can be decomposed into L parallel message symbols at the receiver. Observe in Figure 4.9 that the superposition of the L parallel messages is modulated with the aid of the IFFT block in a single step, as in OFDM. Throughout this section, we use a subscript for the spreading code index, a square bracket $[\cdot]$ for a discrete index to time, frequency or sequence, and a round bracket for a continuous index to time. The number of parallel symbols L mapped to L N-chip orthogonal codes can be adjusted on a frame-by-frame basis, in order to accommodate the channel quality variations and for supporting variable-rate sources. In other words, this structure is suitable for the transmission of variable bit rate (VBR) data as well as constant bit rate (CBR) data. Both base-stations and mobile terminals can employ this structure. Various multiple access schemes such as FDMA, TDMA and CDMA can be incorporated for supporting multiple users. Blind transmission-rate detection can be readily employed in the corresponding receivers. When $L = N$, the N-point IFFT of Figure 4.9 conveys N message symbols and hence the spectral efficiency of the multi-code MC-CDMA system is the same as that of OFDM, with the additional advantage of attaining frequency diversity gain, since the information symbols are spread using the N-chip spreading codes.

Although the more attractive family of Quadrature Amplitude Modulation (QAM) schemes [13] can be readily used for generating the information symbols $\{b_l\}$ from the source data bits, here we limit the symbol mapping scheme to M-ary phase shift keying (MPSK) for the rest of this section. Furthermore, we limit our choice of the spreading sequences to those having elements satisfying $|c_l[n]| = 1$. The normalised complex envelope of an MPSK modulated multi-code MC-CDMA signal may be represented for the duration of a symbol period T as:

$$s(t) = \frac{1}{\sqrt{N}} \sum_{l=0}^{L-1} \sum_{n=0}^{N-1} b_l \, c_l[n] \, e^{j2\pi F n \frac{t}{T}} \, , \tag{4.26}$$

where F is the subcarrier separation parameter [1] invoked for mapping the spread information symbol to N subcarriers that are sufficiently far apart in the frequency domain, in order to experience independent fading over different subcarriers. We assume the idealistic condition that the system is operated in a synchronous environment, which is always the case in the downlink scenario.

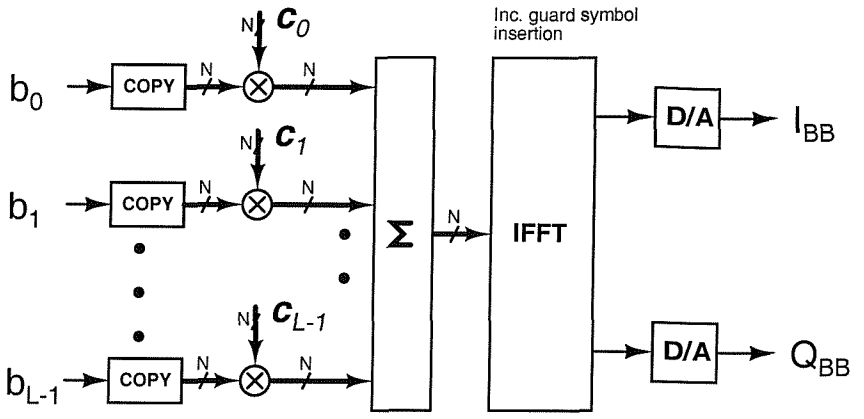

Figure 4.9: MC-CDMA transmitter model: $\mathbf{b_i}$ and $\mathbf{C_i}$ are the i-th message symbol and spreading sequence, respectively.

The spreading sequences are orthogonal to each other and satisfy :

$$\sum_{n=0}^{N-1} c_i[n]\, c_j^*[n] = N\delta_{i,j}\ , \tag{4.27}$$

where c^* is the complex conjugate of c and $\delta_{i,j}$ is the Kronecker delta function.

Having established the system model, let us now analyse the envelope power of the signal. Let us define the combined complex symbol mapped to n-th subcarrier $d[n]$ as ;

$$d[n] \triangleq \sum_{l=0}^{L-1} b_l\, c_l[n]\ . \tag{4.28}$$

Then, following the approach used by Schroeder [61] and Tellambura [79], the envelope power, $|s(t)|^2$, may be expressed as:

$$\begin{aligned} |s(t)|^2 &= s(t)s^*(t) \\ &= \left(\frac{1}{\sqrt{N}}\sum_{n=0}^{N-1} d[n]e^{j2\pi Fn\frac{t}{T}}\right)\cdot\left(\frac{1}{\sqrt{N}}\sum_{n=0}^{N-1} d[n]^* e^{-j2\pi Fn\frac{t}{T}}\right) \\ &= \frac{1}{N}\sum_{n=0}^{N-1}|d[n]|^2 + \frac{2}{N}\mathrm{Re}\left\{\sum_{n=1}^{N-1} D[n]e^{j2\pi Fn\frac{t}{T}}\right\}\ , \end{aligned} \tag{4.29}$$

where $D[n]$ is:

$$D[n] = \sum_{i=0}^{N-n-1} d[i]d^*[i+n] \tag{4.30}$$

and Re[·] represents the real part of a signal.

The first term in (4.29) is the DC component, which is constant over time, and the second term is the AC components, which has an average of zero over the signaling interval duration of T. Thus, the

average power of $s(t)$ is given by the first term in (4.29), which turns out to be L, regardless of the spreading sequences employed, as it is shown below.

The term $|d[n]|^2$ in (4.29) can be expanded as:

$$\begin{aligned} |d[n]|^2 &= \left(\sum_{l=0}^{L-1} b_l\, c_l[n]\right) \cdot \left(\sum_{l=0}^{L-1} b_l^*\, c_l^*[n]\right) \\ &= \sum_{l=0}^{L-1} |b_l|^2\, |c_l[n]|^2 + \sum_{l=0}^{L-1} \sum_{l'=0,l'\neq l}^{L-1} b_l b_{l'}^*\, c_l[n] c_{l'}^*[n] \\ &= L + \sum_{l=0}^{L-1} \sum_{l'=0,l'\neq l}^{L-1} b_l b_{l'}^*\, c_l[n] c_{l'}^*[n]\,. \end{aligned} \tag{4.31}$$

Thus, the first term in (4.29), which is the average power during the signaling interval T, becomes:

$$\begin{aligned} \frac{1}{N}\sum_{n=0}^{N-1} |d[n]|^2 &= \frac{1}{N}\sum_{n=0}^{N-1} L + \frac{1}{N}\sum_{n=0}^{N-1} \left(\sum_{l=0}^{L-1} \sum_{l'=0,l'\neq l}^{L-1} b_l b_{l'}^*\, c_l[n] c_{l'}^*[n]\right) \\ &= L + \frac{1}{N}\sum_{l=0}^{L-1} \sum_{l'=0,l'\neq l}^{L-1} \left(b_l b_{l'}^* \sum_{n=0}^{N-1} c_l[n] c_{l'}^*[n]\right)\,. \end{aligned} \tag{4.32}$$

Considering the orthogonality condition of (4.27) defined for the different spreading codes, the last term in (4.32) becomes zero. Thus, the average transmitted power becomes:

$$\frac{1}{N}\sum_{n=0}^{N-1} |d[n]|^2 = L\,, \tag{4.33}$$

where again, L is the number of simultaneously used spreading codes.

Let us now concentrate our attention on the second term of (4.29). The n-th harmonic component $D[n]$, of the instantaneous power $|s(t)|^2$, which is defined in (4.30), is constituted by the terms, $d[i]d^*[i+n]$, which can be expanded as:

$$\begin{aligned} d[i]d^*[i+n] &= \left(\sum_{l=0}^{L-1} b_l\, c_l[i]\right) \cdot \left(\sum_{l=0}^{L-1} b_l^*\, c_l^*[i+n]\right) \\ &= \sum_{l=0}^{L-1} |b_l|^2 c_l[i]\, c_l^*[i+n] + \sum_{l=0}^{L-1} \sum_{l'=0,l'\neq l}^{L-1} b_l\, b_{l'}^*\, c_l[i]\, c_{l'}^*[i+n]\,. \end{aligned} \tag{4.34}$$

Upon substituting (4.34) into (4.30), we arrive at:

$$\begin{aligned} D[n] &= \sum_{i=0}^{N-n-1} \left(\sum_{l=0}^{L-1} |b_l|^2\, c_l[i] c_l^*[i+n] + \sum_{l=0}^{L-1} \sum_{l'=0,l'\neq l}^{L-1} b_l b_{l'}^*\, c_l[i] c_{l'}^*[i+n]\right) \\ &= \sum_{l=0}^{L-1} \sum_{i=0}^{N-n-1} c_l[i] c_l^*[i+n] + \sum_{l=0}^{L-1} \sum_{l'=0,l'\neq l}^{L-1} \sum_{i=0}^{N-n-1} b_l b_{l'}^*\, c_l[i] c_{l'}^*[i+n] \\ &= \sum_{l=0}^{L-1} A_l[n] + \sum_{l=0}^{L-1} \sum_{l'=0,l'\neq l}^{L-1} b_l b_{l'}^*\, X_{l,l'}[n]\,, \end{aligned} \tag{4.35}$$

where $A_l[n]$ represents the **aperiodic autocorrelations of the l-th spreading code**, defined by:

$$A_l[n] \triangleq \sum_{i=0}^{N-n-1} c_l[i]\, c_l^*[i+n] \tag{4.36}$$

and $X_{l,l'}[n]$ represents the **aperiodic cross-correlations between the l-th and l'-th spreading codes**, defined by:

$$X_{l,l'}[n] \triangleq \sum_{i=0}^{N-n-1} c_l[i]\, c_{l'}^*[i+n]\,, \tag{4.37}$$

where the term 'aperiodic' indicates that the correlation is calculated as if the sequences are one-shot sequence followed by all-zero sequences. We introduce $A[n]$ and $X[n]$, which are the collective forms of the correlations, defined as:

$$A[n] \triangleq \sum_{l=0}^{L-1} A_l[n] \;\text{ for } n \neq 0,\; A[0] \triangleq NL/2 \tag{4.38}$$

$$X[n] \triangleq \sum_{l=0}^{L-1} \sum_{l'=0, l' \neq l}^{L-1} b_l b_{l'}^*\, X_{l,l'}[n]\,. \tag{4.39}$$

The collective aperiodic autocorrelation $A[n]$ is message independent, *i.e.* independent of b_l, while the collective aperiodic crosscorrelation $X[n]$ is message dependent. Upon applying Equations (4.33), (4.35), (4.38) and (4.39), we can represent the envelope power $|s(t)|^2$ as:

$$|s(t)|^2 = L + \frac{2}{N}\mathrm{Re}\left[\sum_{n=1}^{N-1} (A[n] + X[n])\, e^{j2\pi F n \frac{t}{T}}\right] \tag{4.40}$$

$$= \frac{2}{N}\mathrm{Re}\left[\sum_{n=0}^{N-1} (A[n] + X[n])\, e^{j2\pi F n \frac{t}{T}}\right]\,, \tag{4.41}$$

since $A[0] = NL/2$ and $X[0] = 0$.

Ideally $|s(t)|^2$ should be constant. A trivial case exists for BPSK MC-CDMA with $N = 2$ and $L = 2$, where $\{c_0[n]\} = \{1, 1\}$ and $\{c_1[n]\} = \{1, -1\}$. In this case, both $A[n]$ and $X[n]$ become zero, leaving $|s(t)|^2 = 2$. For other values of N and L, there does not seem to be any ideal choices of the spreading sequences in terms of producing a constant envelope. However, some spreading sequences produce lower envelope fluctuation, than others and this issue will be addressed in the next two subsections.

The envelope may also be expressed as:

$$|s(t)|^2 = \sum_{l=0}^{L-1} |s_l(t)|^2 + \mathrm{Re}\left[\sum_{l=0}^{L-1} \sum_{l'=0, l' \neq l}^{L-1} b_l b_{l'}^* \frac{2}{N} \sum_{n=1}^{N-1} X_{l,l'}[n] e^{j2\pi F n \frac{t}{T}}\right]\,, \tag{4.42}$$

where $|s_l(t)|^2$ is the envelope power of the lth information bearing signal, which is given by [79]:

$$|s_l(t)|^2 = 1 + \frac{2}{N}\mathrm{Re}\sum_{n=1}^{N-1} A_l[n] e^{j2\pi F n \frac{t}{T}}\,, \tag{4.43}$$

which is a rephrased version of the well-known autocorrelation theorem [94]. Equation (4.42) suggests that the total envelope power is the sum of the power of L single-code MC-CDMA transmit signal envelopes, plus a term that depends on the aperiodic crosscorrelations of the lth and l'th spreading codes defined in (4.37) multiplied by the transmitted bits $b_l b_{l'}$. It can be observed in (4.43) that for the single-code case corresponding to $L = 1$ the above crosscorrelation terms do not contribute to the envelope power. However, as L increases, the crosscorrelation terms given in (4.37) play an increasingly dominant role.

4.5.2 Spreading Sequences and Crest Factors

In the previous section, we observed that the envelope power of a multi-code MC-CDMA signal is characterised by the aperiodic autocorrelations and crosscorrelations of the spreading sequences employed. Hence, low values of $A[n]$ and $X[n]$ are desirable in (4.42) and (4.43) in order for a set of spreading codes to exhibit a low crest factor. In this section, we introduce several well-known sequences and investigate their crest factor properties based on their correlation characteristics.

4.5.2.1 Single-code Signal

For a single-code MC-CDMA signal the envelope power is entirely characterised by the aperiodic autocorrelations of the employed spreading sequence, as shown in (4.43) [61, 79]. The Walsh codes of Section 2.2.1 and orthogonal Gold codes (OGold) of Section 2.2.2 are well-known binary orthogonal codes. There exist complex orthogonal sequences as well, such as the family of Frank codes [95–97] and Zadoff-Chu codes [98, 99], which have been applied for multi-carrier CDMA systems [100, 101].

A. Frank codes

A Frank code [95–97] is defined as:

$$s[k + iM] = e^{j2\pi pki/M}, \tag{4.44}$$

where $M^2 = N$ is the length of the codes, $0 \leq k,\ i < M$, and p is relatively prime with respect to M, *i.e.* they do not have a common divisor. Here, we set p to 1 for simplicity. A Frank code has perfect periodic autocorrelation, implying that

$$\sum_{n=0}^{N-1} s[n]s^*[n+k] = \begin{cases} N & \text{if } k = 0 \\ 0 & \text{otherwise.} \end{cases} \tag{4.45}$$

Hence, a Frank code and its $N - 1$ circularly shifted versions form a set of N complex orthogonal sequences [95, 96].

Popović [102] as well as Antweiler and Bömer [103] recognised that there exist $\lceil M/2 \rceil$ distinct magnitude sets $\{|A_l[n]|\}$ of aperiodic autocorrelations for the set of N Frank sequences, hence $\lceil M/2 \rceil$ number of corresponding crest factors. In general, from Equation (4.43) we can observe that the envelope

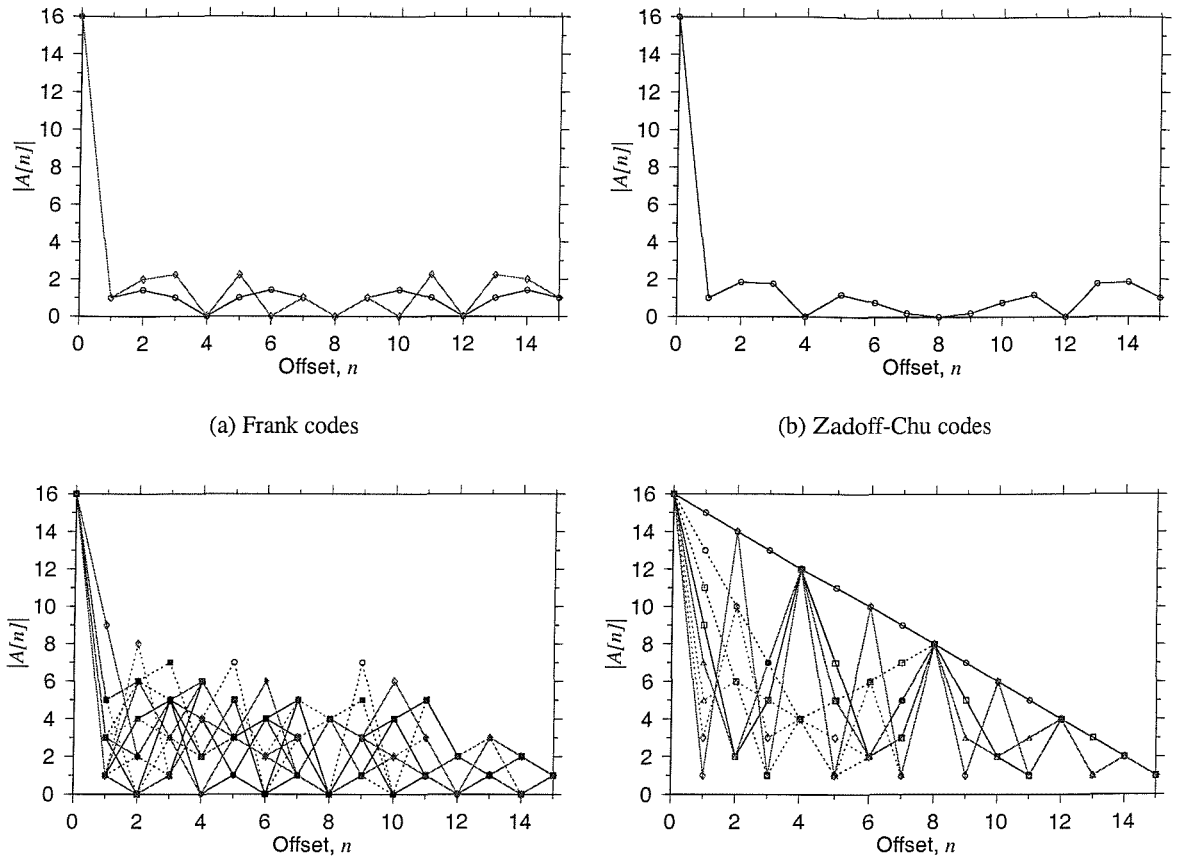

(a) Frank codes

(b) Zadoff-Chu codes

(c) Orthogonal Gold codes

(d) Walsh codes

Figure 4.10: The magnitude $|A[n]|$ of the aperiodic autocorrelation functions defined in (4.36) for various spreading sequences having a length of $N = 16$ and for a single code of $L = 1$.It can be shown and it is also demonstrated by the sub-figures that there are 2, 1, 16 and 8 sets of magnitudes for the Frank, Zadoff-Chu, orthogonal Gold and Walsh codes, respectively.

power waveform $|s'_l(t)|^2$ having $\{A_l[n]e^{j\alpha n}\}$ instead of $\{A_l[n]\}$ becomes:

$$\begin{aligned} |s'(t)|^2 &= 1 + \frac{2}{N}\mathrm{Re}\sum_{n=1}^{N-1} A_l[n]e^{j\alpha n}\, e^{j2\pi F n\frac{t}{T}} \\ &= 1 + \frac{2}{N}\mathrm{Re}\sum_{n=1}^{N-1} A_l[n]e^{j2\pi F n\frac{1}{T}\left(t+\frac{T\alpha}{2\pi F}\right)} \\ &= \left|s\left(t+\frac{T\alpha}{2\pi F}\right)\right|^2, \end{aligned} \tag{4.46}$$

which is a time-shifted version of the original envelope power waveform. Figure 4.10 depicts the magnitudes $\{|A[n]|\}$ of the autocorrelations of four different classes of spreading sequences having a length of $N = 16$. In case of Frank codes, only two sets of autocorrelation magnitudes $\{|A[n]|\}$ appear in Figure 4.10(a). This was expected, since $M^2 = N$, yielding $M = 4$ for $N = 16$ and according to

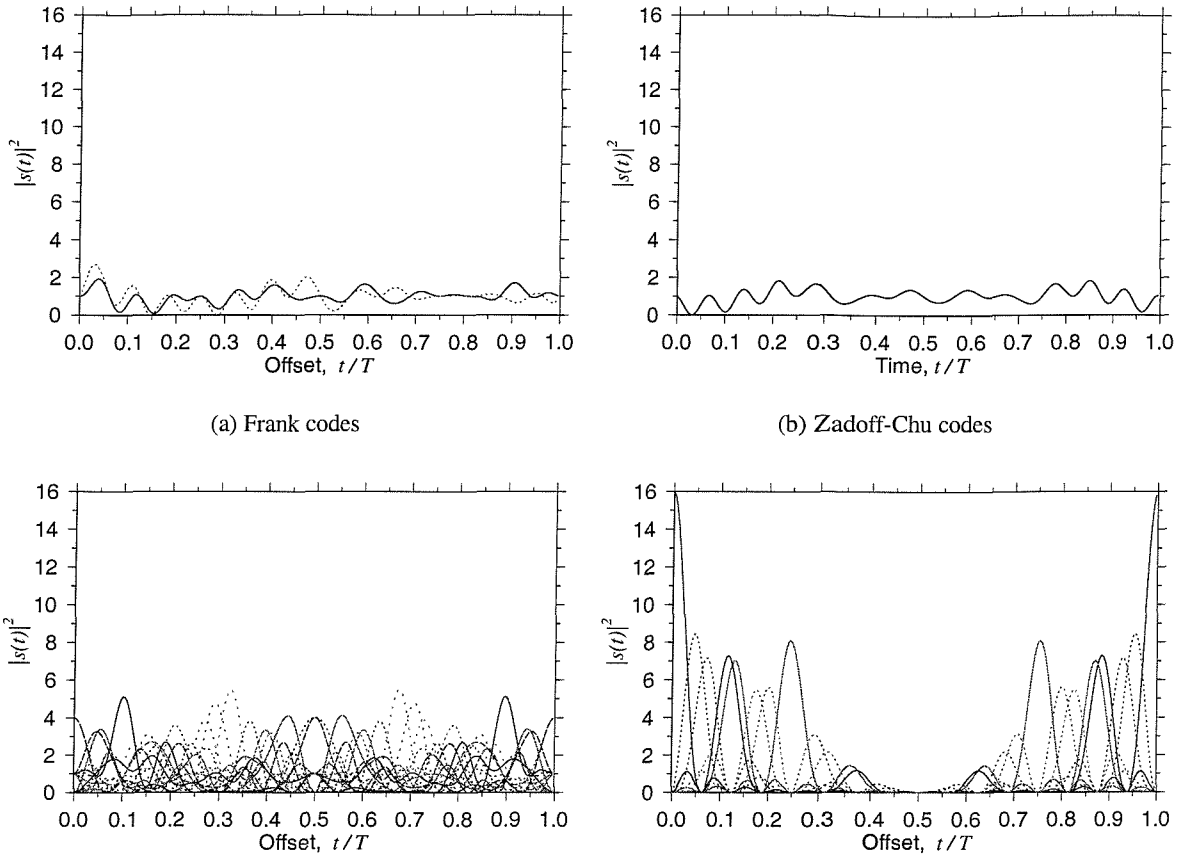

(a) Frank codes

(b) Zadoff-Chu codes

(c) Orthogonal Gold codes

(d) Walsh codes

Figure 4.11: The envelope power $|s(t)|^2$ of single-code MC-CDMA signals employing various spreading sequences with the length N of 16 : Only unique waveforms over time-shifting were displayed. There are 2, 1, 16 and 8 sets of unique waveforms for Frank, Zadoff-Chu, orthogonal Gold and Walsh codes respectively.

[102, 103] there exist $\lceil 4/2 \rceil = 2$ magnitude sets. Furthermore, we can observe in Figure 4.10(a) that the off-peak autocorrelation magnitude $|A[n]|$ of Frank codes shows symmetry around $n = 8$. This is because $A[n] = -A[N - n]$ for any code satisfying (4.45) [104]. Frank codes exhibit low off-peak autocorrelations, which is typically quantified in terms of their so-called merit factor (MF) [102–104], defined as:

$$\text{MF} \triangleq A^2[0]/(2\sum_{n=1}^{N-1}|A[n]|^2)\ . \tag{4.47}$$

A high value of MF is beneficial in terms of low PF as well as of reliable code-acquisition at the beginning of establishing synchronisation between the transmitter and receiver. Half of Frank codes exhibit a MF of 8, while we have MF=4 for the other half of the set of codes. By contrast, all of the Zadoff-Chu codes exhibit MF=6.7. The merit factors of orthogonal Gold codes lie between 0.6 and 1.8, except for one of

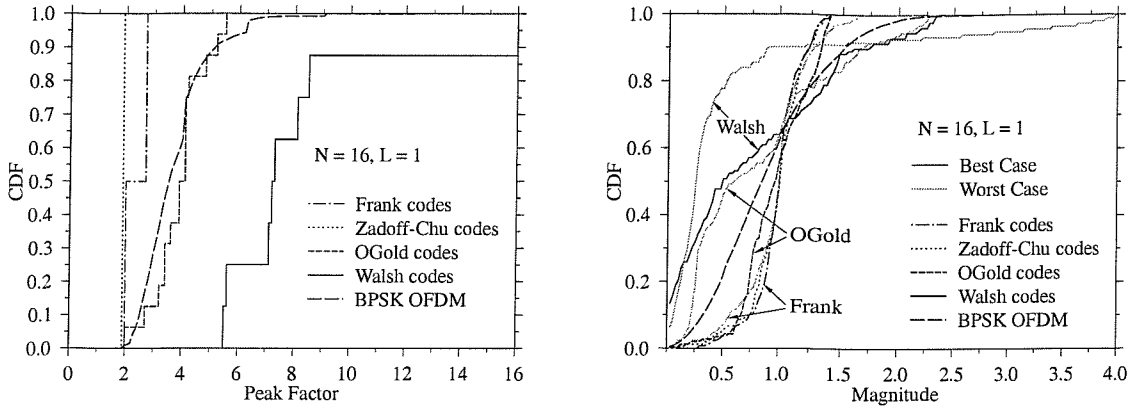

(a) CDF of PF (CF^2)

(b) CDF of $|s(t)|$

Figure 4.12: The crest factor and magnitude cumulative distribution function (CDF) of BPSK MC-CDMA and BPSK OFDM for the spreading factor of $N = 16$ and for the number of simultaneously used codes $L = 1$

them, which is 4.0, and those for Walsh codes are below 0.52.

The time domain power envelope waveforms of the four codes characterised in terms of $|A[n]|$ in Figure 4.10 are shown in Figure 4.11. Only the power envelope waveforms are depicted in the Figure which cannot be mapped to each other by time-shifting. Similarly to the observation made in terms of the autocorrelation magnitudes $\{|A[n]|\}$, there are two unique power envelope waveforms for Frank codes. Both waveforms fluctuate less dramatically, than those of the binary OGold and Walsh codes shown in Figure 4.11(c) and 4.11(d). The CDF of the crest factors shows a two-step distribution function for the Frank codes in Figure 4.12(a), since there are two different power envelope waveforms for the MC-CDMA signals employing N-different Frank codes.

B. Zadoff-Chu Codes

The family of Zadoff-Chu code [98, 99] is defined as:

$$s[k] = \begin{cases} e^{j\pi k^2 p/N} & \text{for even } N \\ e^{j\pi k(k+1)p/N} & \text{for odd } N, \end{cases} \tag{4.48}$$

where N is the length of the code, $0 \leq k < N$ and p is relatively prime with respect to N, and we set p to 1 again. Similarly to Frank codes, Zadoff-Chu codes have perfect periodic autocorrelations. Hence, we can generate $N - 1$ further Zadoff-Chu sequences $s_l[k] = s[k + l]$, $1 \leq l \leq N - 1$, by circularly shifting a Zadoff-Chu code. It can be shown that the family of Zadoff-Chu codes defined in (4.48) is similar to the set of Newman phases [74], Schroeder phases [61], Greenstein phases [63] and Narahashi phases [68], which were introduced in (4.18), (4.19) and (4.20) of Section 4.3.1 . It is interesting to note that various researchers have found closely related codes independently, using different methods over a time-span of 30 years.

All the Zadoff-Chu codes of length $N = 16$ showed the same aperiodic correlation magnitude sets, as seen in Figure 4.10(b), hence a single unique power envelope waveform is shown in Figure 4.11(b),

which becomes also explicit in terms of the crest factor CDF of Figure 4.12(a). This is because the aperiodic autocorrelations of Zadoff-Chu codes are given as:

$$\begin{aligned} A_l[n] &= \sum_{i=0}^{N-n-1} s_l[i]s_l^*[i+n] \\ &= \sum_{i=0}^{N-n-1} e^{j\pi\frac{(i+l)^2}{N}} e^{-j\pi\frac{(i+l+n)^2}{N}} \\ &= e^{-j\pi\frac{n^2+2nl}{N}} \sum_{i=0}^{N-n-1} e^{-j\pi\frac{2ni}{N}} \\ &= e^{-j2\pi\frac{nl}{N}} A_0[n] \,. \end{aligned} \tag{4.49}$$

Substituting (4.49) into (4.43), we have

$$|s_l(t)|^2 = \left| s_0\left(t - \frac{Tl}{NF}\right)\right|^2 , \tag{4.50}$$

which states that the lth user's power envelope waveform is a time-shifted version of the first user's power envelope, retaining all the magnitude statistics.

The magnitudes of the aperiodic autocorrelation of Zadoff-Chu codes also exhibit a symmetry around $n = 8$ due to their perfectly periodic autocorrelation function. The crest factor of Zadoff-Chu codes was the lowest among the investigated four spreading sequences. Furthermore, the high peak-to-sidelobe ratio of the autocorrelation function of Figure 4.10(b) is advantageous in terms of reliable code acquisition.

C. Orthogonal Gold codes

As it was mentioned in Section 2.2.2, orthogonal Gold (OGold) code [52] are derived from binary pseudo-random codes. It was observed in Figure 4.10(c) that each of the 16 OGold code has different autocorrelation magnitude sets $\{|A[n]|\}$. Accordingly, the 16 envelope power waveforms seen in Figure 4.11(c) are all different. However, four codes of the 16 codes happen to have the same crest factor and some further codes exhibit similar crest factors. This explains the various steps in the crest factor distribution of OGold codes in Figure 4.12(a). The crest factor distribution is similar to that of BPSK OFDM using no spreading codes, which corresponds to random codes, since all 2^{16} message sequences were encountered. It is interesting to see that some of the orthogonal Gold codes have low crest factors, approaching those of Frank codes and Zadoff-Chu codes. This implies that we can employ a specific code assignment scheme for reducing the crest factor of each uplink signal in synchronous MC-CDMA systems employing orthogonal Gold codes, when the number of simultaneously transmitting mobiles is low and hence low-CF sequences can be invoked. This is however not the case, when a large user population has to be supported using short codes of a limited-sized set.

D. Walsh codes

The family of Walsh codes was introduced in Section 2.2.1. Members of this code family exhibit some structure and this contributes to the high values of their aperiodic autocorrelations seen in Figure 4.10(d). In fact, the all-zero sequence, $\{W_0[k]\}$, which is the first sequence in any Walsh code set, gives us the

highest possible autocorrelation magnitude set for $\{|A[n]|\} = N - n$ and hence yields the highest possible crest factor of $\sqrt{N}$ or a peak factor of N. In Figure 4.10(d), 4.11(d) and 4.12(a), we can observe that there are $N/2$ different autocorrelation magnitude values $\{|A[n]|\}$ for the N Walsh codes of length N and hence $N/2$ different unique power envelope waveforms $|s(t)|^2$ and crest factors are observed. This can be explained as follows. Observing (2.6) in Section 2.2.1, we find:

$$W_{2m+1}[k] = W_{2m}[k]\, e^{j\pi k}\,, \tag{4.51}$$

where $m = 0, \cdots, N/2 - 1$. In other words, the odd-indexed Walsh sequence can be obtained by changing the sign of every other element. The corresponding aperiodic autocorrelations of (4.36) results in:

$$A_{2m+1}[n] = A_{2m}[n]\, e^{-j\pi n}\,, \tag{4.52}$$

where $m = 0, \cdots, N/2 - 1$, and hence the envelope power waveform of the $(2m + 1)$-th Walsh code is a time-shifted version of that of the $(2m)$-th Walsh code, retaining all the same magnitude statistics. Figure 4.12(a) shows the 8-step distribution function of the crest factors for the Walsh-spread MC-CDMA signals using $N = 16$. Even the lowest crest factor of the Walsh codes is higher than the highest crest factor of OGold codes.

Figure 4.12(b) depicts the magnitude distributions of single-code MC-CDMA signals employing four different spreading codes, where the "best case" and the "worst case" represent the specific codes of having the lowest crest factor and the highest crest factor, respectively, for the particular class of spreading sequences. Desired magnitude distributions are expected to exhibit a steep CDF curve around the average magnitude, indicating the predominance of the average magnitudes. The Frank, Zadoff-Chu and the best-case OGold sequences exhibited this desirable tendency.

We conclude that the Zadoff-Chu sequences are the most attractive ones from the set of four spreading sequences investigated in the context of synchronous single-code MC-CDMA systems in terms of their low crest factors.

So far, we implicitly considered a synchronous uplink scenario, where different mobiles use different orthogonal spreading codes transmitting using the same set of subcarriers. In a downlink scenario or in a uplink scenario, where different mobiles are assigned non-overlapping sets of subcarriers, we do not need N orthogonal sequences for spreading a message symbol over N subcarriers. We only need one spreading sequence. If this is the case, we are free to choose any sequence producing a low crest factor, such as a poly-phase code based on the Newman phases of Section 4.3.4 [74] or a Golay code of Section 4.3.2 [77], also known as a complementary code. *Popović* [75] showed that in this context the crest factor of the single-code MC-CDMA signal employing any Golay codes is bounded by 3dB.

4.5.2.2 Shapiro-Rudin-based Spreading Sequences

Multi-code MC-CDMA signals are transmitted by the base-station transmitter in the downlink or by mobile terminals in the uplink, when more than one symbols have to be transmitted simultaneously. As we

have shown in Section 4.5.1, the power envelope of the transmitted signal depends on the sum of the aperiodic autocorrelations $A[n]$ given in (4.38) and on the modulated sum of the aperiodic crosscorrelations $X[n]$ given in (4.39). In this section, we will consider a range of specific special sequences, which exhibit zero or small values of $A[n]$ and $X[n]$.

While studying an absolute bound for a sum of trigonometric polynomials having binary coefficients, *Shapiro*, then an MSc student, found [73] a pair of binary sequences having a low bound. These sequences are referred to as Shapiro-Rudin sequences, which are defined recursively as:

$$\mathbf{s}_0 = \mathbf{c}_0 = 1 \,, \tag{4.53}$$

$$\mathbf{s}_{n+1} = \mathbf{s}_n \mathbf{c}_n \,, \tag{4.54}$$

$$\mathbf{c}_{n+1} = \mathbf{s}_n \bar{\mathbf{c}}_n \,, \tag{4.55}$$

where the sequence $\mathbf{ab} = (a_1 a_2 \cdots a_{N-1} b_1 b_2 \cdots b_{N-1})$ represents a concatenation of sequences $\mathbf{a} = (a_1 a_2 \cdots a_{N-1})$ and $\mathbf{b} = (b_1 b_2 \cdots b_{N-1})$, and $\bar{\mathbf{a}} = (-a_1 - a_2 \cdots - a_{N-1})$ a negation of the original sequence $\mathbf{a}$. Later it was recognised [75] that Shapiro-Rudin sequences constitute a special case of *Golay*'s complementary sequences [77]. A pair of equally long sequences is said to be a complementary pair, if their combined aperiodic autocorrelation defined in (4.38) for $L = 2$ is zero except at zero shift. As we mentioned before, this is the property we want to retain in order to maintain low crest factors.

In our forthcoming discourse, we use $\otimes$ as the aperiodic correlation operator, $\phi_{a,b}$ as the aperiodic cross-correlation sequence $\phi_{a,b}[n] \triangleq (\mathbf{a} \otimes \mathbf{b})[n]$, $n = 0, 1, \cdots, N-1$ and $\Upsilon(\mathbf{a})$ as a specific version of $\mathbf{a}$ that was shifted to the left by one, *i.e.* $\Upsilon(\mathbf{a})[n] = \mathbf{a}[n+1]$, $n = 0, 1, 2, \cdots, N-1$. We also use $\vec{\mathbf{a}}$ to denote the sequence $\mathbf{a}$ that was shifted by the length of $\mathbf{a}$, *i.e.* $\vec{\mathbf{a}}[n] = \mathbf{a}[n-N]$, $n = N, N+1, \cdots, 2N-1$. Furthermore, $\tilde{\mathbf{a}}$ represents a version of the sequence $\mathbf{a}$ which is reverse-ordered, *i.e.* $\tilde{\mathbf{a}}[n] = \mathbf{a}[N-1-n]$, $n = 0, 1, \cdots, N-1$. Finally, we denote the concatenated sequence of the sequences $\mathbf{a}$ and $\mathbf{b}$ as $\mathbf{ab}$.

The following relationship regarding the cross-correlation sequence is useful in deriving the crest-factor properties of multi-code MC-CDMA signals:

$$\begin{aligned} \mathbf{a} \otimes \vec{\mathbf{b}} &= \left\{ \sum_{i=0}^{n-1} a_{N-n+i} b_i \mid 0 \le n < N \right\} \left\{ \sum_{i=0}^{N-n-1} a_i b_{i+n} \mid 0 \le n < N \right\} \\ &= \Upsilon(\phi_{b,a})\ \phi_{a,b} \,. \end{aligned} \tag{4.56}$$

In other words, the aperiodic crosscorrelation sequence created from the sequence $\mathbf{a}$ and the sequence $\vec{\mathbf{b}}$, which is the N times right-shifted version of $\mathbf{b}$, is given by the concatenated sequence of $\Upsilon(\phi_{b,a}) = \Upsilon(\mathbf{b} \otimes \mathbf{a}$ and $\phi_{a,b} = \mathbf{a} \otimes \mathbf{b}$. This can be readily verified by the direct calculation of the aperiodic crosscorrelation function of $\mathbf{a}$ and $\vec{\mathbf{b}}$.

The next theorem is required for characterising the crest-factor property of MC-CDMA signals employing a pair of Shapiro-Rudin sequences.

Theorem 4.1 *Let $\mathbf{s}_n$ and $\mathbf{c}_n$ be a pair of Shapiro-Rudin sequences [73] of length $N = 2^n$. With the aid of these sequence, we derive four half-length sequences defined as $\{\mathbf{u}_{n-1}[k] = \mathbf{s}_n[2k]\}$, $\{\mathbf{v}_{n-1}[k] = \mathbf{s}_n[2k+1]\}$, $\{\mathbf{x}_{n-1}[k] = \mathbf{c}_n[2k]\}$ and $\{\mathbf{y}_{n-1}[k] = \mathbf{c}_n[2k+1]\}$, where $0 \le k < N/2$. Then, $\mathbf{u}$ and $\mathbf{v}$ form a complementary pair, and so do $\mathbf{x}$ and $\mathbf{y}$.*

For example, we can derive two complementary pairs of length 8, hence in total of four sequences, from a pair of complementary sequence pair of length 16.

Proof: From the definition of the Shapiro-Rudin sequences [73], we can derive the recursive relationships between the new decimated sequences:

$$\mathbf{u}_0 = s_0 \qquad \mathbf{u}_n = \mathbf{u}_{n-1}\,\mathbf{x}_{n-1} \tag{4.57}$$

$$\mathbf{v}_0 = c_0 \qquad \mathbf{v}_n = \mathbf{v}_{n-1}\,\mathbf{y}_{n-1} \tag{4.58}$$

$$\mathbf{x}_0 = s_0 \qquad \mathbf{x}_n = \mathbf{u}_{n-1}\,\overline{\mathbf{x}}_{n-1} \tag{4.59}$$

$$\mathbf{y}_0 = \overline{c}_0 \qquad \mathbf{y}_n = \mathbf{v}_{n-1}\,\overline{\mathbf{y}}_{n-1}\,. \tag{4.60}$$

It will be shown that:

$$\phi_{u_n}[k] + \phi_{v_n}[k] = \phi_{x_n}[k] + \phi_{y_n}[k] = 2^{n+1}\delta[k]\,. \tag{4.61}$$

For $n = 0$, this is trivial. For $n = 1$, $\mathbf{u}_1 = [s_0 s_0]$, $\mathbf{v}_1 = [c_0 \overline{c}_0]$, $\mathbf{x}_1 = [s_0 \overline{s}_0]$ and $\mathbf{y}_1 = [c_0 c_0]$. The sums of the autocorrelations associated with $n = 1$ are given as:

$$\mathbf{u}_1 \otimes \mathbf{u}_1 + \mathbf{v}_1 \otimes \mathbf{v}_1 = [+2\ +1] + [+2\ -1] = [+4\ 0] \tag{4.62}$$

$$\mathbf{x}_1 \otimes \mathbf{x}_1 + \mathbf{y}_1 \otimes \mathbf{y}_1 = [+2\ -1] + [+2\ +1] = [+4\ 0]\,. \tag{4.63}$$

Therefore Equation 4.61 is true for $n = 0$ and $n = 1$. Let us now assume that (4.61) holds for $n = m-2$ and $n = m-1$. Then, $\phi_{u_m}[k] + \phi_{v_m}[k]$ is given as:

$$\begin{aligned}
\phi_{u_m}[k] + \phi_{v_m}[k] &= \mathbf{u}_m \otimes \mathbf{u}_m + \mathbf{v}_m \otimes \mathbf{v}_m \\
&= (\mathbf{u}_{m-1}\mathbf{x}_{m-1}) \otimes (\mathbf{u}_{m-1}\mathbf{x}_{m-1}) + (\mathbf{v}_{m-1}\mathbf{y}_{m-1}) \otimes (\mathbf{v}_{m-1}\mathbf{y}_{m-1}) \\
&= \mathbf{u}_{m-1} \otimes \mathbf{u}_{m-1} + \mathbf{x}_{m-1} \otimes \mathbf{x}_{m-1} + \mathbf{u}_{m-1} \otimes \vec{\mathbf{x}}_{m-1} + \vec{\mathbf{x}}_{m-1} \otimes \mathbf{u}_{m-1} \\
&\quad + \mathbf{v}_{m-1} \otimes \mathbf{v}_{m-1} + \mathbf{y}_{m-1} \otimes \mathbf{y}_{m-1} + \mathbf{v}_{m-1} \otimes \vec{\mathbf{y}}_{m-1} + \vec{\mathbf{y}}_{m-1} \otimes \mathbf{v}_{m-1} \\
&= 2^m\delta[k] + 2^m\delta[k] + \mathbf{u}_{m-1} \otimes \vec{\mathbf{x}}_{m-1} + \mathbf{v}_{m-1} \otimes \vec{\mathbf{y}}_{m-1} \\
&= 2^{m+1}\delta[k] + \mathbf{S}_{m-1}\,,
\end{aligned} \tag{4.64}$$

where $\mathbf{S}_{m-1} = \mathbf{u}_{m-1} \otimes \vec{\mathbf{x}}_{m-1} + \mathbf{v}_{m-1} \otimes \vec{\mathbf{y}}_{m-1}$. Applying (4.56), $\mathbf{S}_{m-1}$ in the last term of (4.64) can be further expanded as:

$$\begin{aligned}
\mathbf{S}_{m-1} &= \mathbf{u}_{m-1} \otimes \vec{\mathbf{x}}_{m-1} + \mathbf{v}_{m-1} \otimes \vec{\mathbf{y}}_{m-1} \\
&= \Upsilon\left(\phi_{x_{m-1},u_{m-1}}\right)\ \phi_{u_{m-1},x_{m-1}} + \Upsilon\left(\phi_{y_{m-1},v_{m-1}}\right)\ \phi_{v_{m-1},y_{m-1}} \\
&= \Upsilon\left(\mathbf{x}_{m-1} \otimes \mathbf{u}_{m-1}\right)\ \mathbf{u}_{m-1} \otimes \mathbf{x}_{m-1} + \Upsilon\left(\mathbf{y}_{m-1} \otimes \mathbf{v}_{m-1}\right)\ \mathbf{v}_{m-1} \otimes \mathbf{y}_{m-1} \\
&= \Upsilon\left([\mathbf{u}_{m-2}\,\overline{\mathbf{x}}_{m-2}] \otimes [\mathbf{u}_{m-2}\,\mathbf{x}_{m-2}]\right)\ \left([\mathbf{u}_{m-2}\,\mathbf{x}_{m-2}] \otimes [\mathbf{u}_{m-2}\,\overline{\mathbf{x}}_{m-2}]\right) \\
&\quad + \Upsilon\left([\mathbf{v}_{m-2}\,\overline{\mathbf{y}}_{m-2}] \otimes [\mathbf{v}_{m-2}\,\mathbf{y}_{m-2}]\right)\ \left([\mathbf{v}_{m-2}\,\mathbf{y}_{m-2}] \otimes [\mathbf{v}_{m-2}\,\overline{\mathbf{y}}_{m-2}]\right) \\
&= \Upsilon\left(\mathbf{u}_{m-2} \otimes \vec{\mathbf{x}}_{m-2} + \mathbf{v}_{m-2} \otimes \vec{\mathbf{y}}_{m-2}\right)\ \left(-\mathbf{u}_{m-2} \otimes \vec{\mathbf{x}}_{m-2} - \mathbf{v}_{m-2} \otimes \vec{\mathbf{y}}_{m-2}\right) \\
&= \Upsilon\left(\mathbf{S}_{m-2}\right)\ \left(\mathbf{S}_{m-2}\right)\,.
\end{aligned} \tag{4.65}$$

Upon exploiting that $\mathbf{S}_0 = \mathbf{u}_0 \otimes \vec{\mathbf{x}}_0 + \mathbf{v}_0 \otimes \vec{\mathbf{y}}_0 = [0\ 0]$, we get:

$$\mathbf{S}_{m-1} = \mathbf{0} \tag{4.66}$$

When substituting (4.66) into (4.64), we arrive at:

$$\phi_{u_m}[k] + \phi_{v_m}[k] = 2^{m+1}\,\delta[k]\,. \tag{4.67}$$

Hence, we can conclude that Equation (4.61) holds for any integer $n \geq 0$. ¶

Corollary 4.2 *The autocorrelation ϕ_s of any Shapiro-Rudin sequence $\mathbf{s}$ satisfies that:*

$$\phi_s[2k] = 0 \qquad \textit{for any } k \geq 1 \tag{4.68}$$

Proof: Let $\mathbf{u}_{n-1}$ and $\mathbf{v}_{n-1}$ be the even indexed sequence and the odd indexed sequence of $\mathbf{s}_n$, as defined in Theorem 4.1. Then,

$$\begin{aligned} \phi_{s_n}[2k] &= \phi_{u_{n-1}}[k] + \phi_{v_{n-1}}[k] \\ &= 2^n \delta[k]\,, \end{aligned} \tag{4.69}$$

as given in (4.61). ¶

We are now ready for introducing a crest factor property of the family of Shapiro-Rudin sequences in the context of MC-CDMA systems.

Theorem 4.3 *If we apply a pair of Shapiro-Rudin sequences [73, 75, 77, 105] as the spreading sequences for a two-code BPSK modulated MC-CDMA transmitter having $N = 2^m$ $(m = 1, 2, 3, \cdots)$ subcarriers, then the crest factor is bounded by 3dB.*

For example, a pair of Shapiro-Rudin sequences of length $N = 8 = 2^3$, $\mathbf{a} = (+1{+}1{+}1{-}1{+}1{+}1{-}1{+}1)$ and $\mathbf{b} = (+1 + 1 + 1 - 1 - 1 - 1 + 1 - 1)$, are orthogonal to each other and hence can be used as spreading sequences of a two-code MC-CDMA scheme.

Proof: Let $\mathbf{s}_m = \mathbf{s}_{m-1}\mathbf{c}_{m-1}$ and $\mathbf{c}_m = \mathbf{s}_{m-1}\bar{\mathbf{c}}_{m-1}$ be a pair of Shapiro-Rudin sequences of length $N = 2^m$, where the pair $\mathbf{s}_{m-1}$ and $\mathbf{c}_{m-1}$ is constituted by a pair of Shapiro-Rudin sequence of length $N/2$. It is well-known that Shapiro-Rudin sequences are complementary and hence:

$$A_m^{(2)}[n] = \mathbf{s}_m \otimes \mathbf{s}_m + \mathbf{c}_m \otimes \mathbf{c}_m = 0 \qquad \text{for } n \geq 1, \tag{4.70}$$

where the superscript (2) represents the number of codes used for supporting multiple users or multiple bits per symbol. On the other hand, the aperiodic crosscorrelations are given as:

$$\begin{aligned} \mathbf{s}_m \otimes \mathbf{c}_m &= (\mathbf{s}_{m-1}\mathbf{c}_{m-1}) \otimes (\mathbf{s}_{m-1}\bar{\mathbf{c}}_{m-1}) \\ &= \mathbf{s}_{m-1} \otimes \mathbf{s}_{m-1} - \mathbf{s}_{m-1} \otimes \vec{\mathbf{c}}_{m-1} + \vec{\mathbf{c}}_{m-1} \otimes \mathbf{s}_{m-1} - \mathbf{c}_{m-1} \otimes \mathbf{c}_{m-1} \end{aligned} \tag{4.71}$$

$$\begin{aligned} \mathbf{c}_m \otimes \mathbf{s}_m &= (\mathbf{s}_{m-1}\bar{\mathbf{c}}_{m-1}) \otimes (\mathbf{s}_{m-1}\mathbf{c}_{m-1}) \\ &= \mathbf{s}_{m-1} \otimes \mathbf{s}_{m-1} + \mathbf{s}_{m-1} \otimes \vec{\mathbf{c}}_{m-1} - \vec{\mathbf{c}}_{m-1} \otimes \mathbf{s}_{m-1} - \mathbf{c}_{m-1} \otimes \mathbf{c}_{m-1} \end{aligned} \tag{4.72}$$

The combined aperiodic crosscorrelation $X_m^{(2)}[n]$ becomes:

$$\begin{aligned} X_m^{(2)}[n] &= b_0 b_1(\mathbf{s}_m \otimes \mathbf{c}_m) + b_1 b_0(\mathbf{c}_m \otimes \mathbf{s}_m) \\ &= 2b_0 b_1(\mathbf{s}_{m-1} \otimes \mathbf{s}_{m-1}) - 2b_1 b_0(\mathbf{c}_{m-1} \otimes \mathbf{c}_{m-1}) \\ &= 4b_0 b_1(\mathbf{s}_{m-1} \otimes \mathbf{s}_{m-1}) \\ &= 4b_0 b_1 A_{m-1}^{(1)}[n]\,, \end{aligned} \tag{4.73}$$

where b_0 and b_1 are the information bits. Applying (4.70) and (4.73) to (4.40), we can establish the relationships between the two envelope powers $|s_m^{(2)}(t)|^2$ and $|s_{m-1}^{(1)}(t)|^2$, one for $L = 2$ and N number of subcarriers, and another one for $L = 1$ and $N/2$ number of subcarriers. Firstly, let us consider the case for $b_0 b_1 = 1$.

$$\begin{aligned} \left|s_m^{(2)}(t)\right|^2 &= 2 + \frac{2}{N}\mathrm{Re}\left[\sum_{n=1}^{N/2-1} 4A_{m-1}^{(1)}[n]e^{j2\pi Fn\frac{t}{T}}\right] \\ &= 2 + 2\frac{2}{N/2}\mathrm{Re}\left[\sum_{n=0}^{N/2-1} A_{m-1}^{(1)}[n]e^{j2\pi Fn\frac{t}{T}}\right] \\ &= 2\left|s_{m-1}^{(1)}(t)\right|^2 . \end{aligned} \tag{4.74}$$

When $b_0 b_1 = -1$, $X_m^{(2)}[n]$ becomes $-4A_{m-1}^{(1)}[n]$, which is equivalent to $4A_{m-1}^{(1)}[n]e^{j\pi n}$ due to Corollary 4.2 . Then the envelope power becomes:

$$\begin{aligned} \left|s_m^{(2)}(t)\right|^2 &= 2 + \frac{2}{N}\mathrm{Re}\left[\sum_{n=1}^{N/2-1} 4A_{m-1}^{(1)}[n]e^{j\pi n}e^{j2\pi Fn\frac{t}{T}}\right] \\ &= 2 + 2\frac{2}{N/2}\mathrm{Re}\left[\sum_{n=0}^{N/2-1} A_{m-1}^{(1)}[n]e^{j2\pi Fn\frac{1}{T}(t+\frac{T}{2F})}\right] \\ &= 2\left|s_{m-1}^{(1)}\left(t+\frac{T}{2F}\right)\right|^2 . \end{aligned} \tag{4.75}$$

Since the average power of $s_m^{(2)}(t)$ is 2, and the peak factor is defined as the ratio of the maximum value of $s_m^{(2)}(t)$ to the average value, the peak factor remains the same for $s_m^{(2)}(t)$ as in $s_{m-1}^{(1)}(t)$. Considering that the peak factor of $s_{m-1}^{(1)}(t)$ is at most 2 [75], we can conclude that a pair of Shapiro-Rudin sequences produces a crest factor of less than or equal to 3dB for a two-code BPSK modulated MC-CDMA system. ¶

It is interesting to note that the combined crosscorrelation of the two constituent codes of a pair of Shapiro-Rudin sequences exhibits the property of so-called sub-complementarity [105]. Sivaswamy introduced sub-complementary sequences in [105]. A pair of sequences of length $N = 2^k N_o$, $k \geq 1$, is called a sub-complementary pair, if the combined aperiodic autocorrelation $A[n]$ of (4.38) is zero for $n > N_o$. A method of constructing sub-complementary pairs was also given in [105] as follows. Let

$\mathbf{s}_{m-1}$ be any sequence of length $N/2$. Then, a pair of sequences $\mathbf{s}_m$ and $\hat{\mathbf{s}}_m$, constructed as [105]:

$$\mathbf{s}_m = \mathbf{s}_{m-1}\mathbf{s}_{m-1} \tag{4.76}$$

$$\hat{\mathbf{s}}_m = \mathbf{s}_{m-1}\overline{\mathbf{s}}_{m-1}\,, \tag{4.77}$$

is known to form a sub-complementary pair [105]. Sivaswamy's sub-complementary pairs exhibit similar crest factor characteristics to those of Shapiro-Rudin sequences in the context of two-code BPSK modulated MC-CDMA systems.

Theorem 4.4 *If we apply a Shapiro-Rudin sequence [73] of length $N/2$ as the base sequence $\mathbf{s}_{m-1}$, then the sub-complementary pair [105] $\mathbf{s}_m$ and $\hat{\mathbf{s}}_m$ of (4.76) and (4.77) produces a crest factor less than or equal to 3dB, provided that they are applied in two-code BPSK modulated MC-CDMA systems.*

For example, the sequence $\mathbf{a} = (+1+1+1-1+1+1-1+1)$ in the previous example for Theorem 4.3 can be used as the base sequence of a pair of sub-complementary sequences. According to the generation methods defined in (4.76) and (4.77), a pair of sub-complementary sequences $\mathbf{s}$ and $\hat{\mathbf{s}}$, given as:

$$\mathbf{s} = (+1+1+1-1+1+1-1+1+1+1+1-1+1+1-1+1) \tag{4.78}$$

$$\hat{\mathbf{s}} = (+1+1+1-1+1+1-1+1-1-1-1+1-1-1+1-1) \tag{4.79}$$

can be used for a two-code MC-CDMA system, since they are inherently orthogonal to each other owing to the Walsh code like definition of (4.76) and (4.77).
Proof: the aperiodic autocorrelations can be formulated as:

$$\begin{aligned}\mathbf{s}_m \otimes \mathbf{s}_m &= (\mathbf{s}_{m-1}\mathbf{s}_{m-1}) \otimes (\mathbf{s}_{m-1}\mathbf{s}_{m-1}) \\ &= \mathbf{s}_{m-1} \otimes \mathbf{s}_{m-1} + \mathbf{s}_{m-1} \otimes \vec{\mathbf{s}}_{m-1} + \vec{\mathbf{s}}_{m-1} \otimes \mathbf{s}_{m-1} + \mathbf{s}_{m-1} \otimes \mathbf{s}_{m-1} \qquad (4.80)\\ \hat{\mathbf{s}}_m \otimes \hat{\mathbf{s}}_m &= (\mathbf{s}_{m-1}\overline{\mathbf{s}}_{m-1}) \otimes (\mathbf{s}_{m-1}\overline{\mathbf{s}}_{m-1}) \\ &= \mathbf{s}_{m-1} \otimes \mathbf{s}_{m-1} - \mathbf{s}_{m-1} \otimes \vec{\mathbf{s}}_{m-1} - \vec{\mathbf{s}}_{m-1} \otimes \mathbf{s}_{m-1} + \mathbf{s}_{m-1} \otimes \mathbf{s}_{m-1}\,. \qquad (4.81)\end{aligned}$$

Thus the combined aperiodic autocorrelation $A_m^{(2)}[n]$ defined in (4.38) becomes:

$$\begin{aligned}A_m^{(2)}[n] &= \mathbf{s}_m \otimes \mathbf{s}_m + \hat{\mathbf{s}}_m \otimes \hat{\mathbf{s}}_m \\ &= 4(\mathbf{s}_{m-1} \otimes \mathbf{s}_{m-1}) = 4A_{m-1}^{(1)}[n]\,, \qquad (4.82)\end{aligned}$$

where $A_{m-1}^{(1)}[n]$ is the aperiodic autocorrelation of the Shapiro-Rudin sequence $\mathbf{s}_{m-1}$. On the other hand, the aperiodic crosscorrelations defined in (4.37) are given as:

$$\begin{aligned}\mathbf{s}_m \otimes \hat{\mathbf{s}}_m &= (\mathbf{s}_{m-1}\mathbf{s}_{m-1}) \otimes (\mathbf{s}_{m-1}\overline{\mathbf{s}}_{m-1}) \\ &= \mathbf{s}_{m-1} \otimes \mathbf{s}_{m-1} - \mathbf{s}_{m-1} \otimes \vec{\mathbf{s}}_{m-1} + \vec{\mathbf{s}}_{m-1} \otimes \mathbf{s}_{m-1} - \mathbf{s}_{m-1} \otimes \mathbf{s}_{m-1} \qquad (4.83)\\ \hat{\mathbf{s}}_m \otimes \mathbf{s}_m &= (\mathbf{s}_{m-1}\overline{\mathbf{s}}_{m-1}) \otimes (\mathbf{s}_{m-1}\mathbf{s}_{m-1}) \\ &= \mathbf{s}_{m-1} \otimes \mathbf{s}_{m-1} + \mathbf{s}_{m-1} \otimes \vec{\mathbf{s}}_{m-1} - \vec{\mathbf{s}}_{m-1} \otimes \mathbf{s}_{m-1} - \mathbf{s}_{m-1} \otimes \mathbf{s}_{m-1}\,. \qquad (4.84)\end{aligned}$$

The combined aperiodic crosscorrelation $X_m^{(2)}[n]$ becomes:

$$\begin{aligned} X_m^{(2)}[n] &= b_0 b_1 (\mathbf{s}_m \otimes \hat{\mathbf{s}}_m) + b_1 b_0 (\hat{\mathbf{s}}_m \otimes \mathbf{s}_m) \\ &= 0 \,. \end{aligned} \tag{4.85}$$

Upon substituting (4.82) and (4.85) in (4.40), we can conclude that:

$$\left| s_m^{(2)}(t) \right|^2 = 2 \left| s_{m-1}^{(1)}(t) \right|^2 , \tag{4.86}$$

which is identical to (4.74) . Therefore, we reached the same conclusion, as stated in Theorem 4.3, namely that the corresponding crest factor is bounded by 3dB. ¶

It is interesting to see in (4.85) that the combined aperiodic crosscorrelation of Sivaswamy's sub-complementary pair vanishes, and hence we conclude that the envelope power waveform does not depend on the message sequences. Considering that a pair of Shapiro-Rudin sequences has zero off-peak combined aperiodic autocorrelation since it is a specific case of complementary pair, the Shapiro-Rudin and the Sivaswamy's sub-complementary families of pairs are dual.

So far we have concentrated our attention on the cases, when two symbols had to be transmitted simultaneously. We found that the crest factors of MC-CDMA signals employing the Shapiro-Rudin sequence pairs of (4.54) and (4.55) or the Sivaswamy sub-complementary pairs of (4.76) and (4.76) are bounded by 3dB. Let us now extend our discussions to the scenario where more than two spreading sequences are used for supporting multiple symbols generated by a single user or for supporting multiple users.

Tseng and Liu [80] introduced a wider range of complementary sets of sequences. A set of sequences of equal length is said to be a complementary set, if the sum of autocorrelations of all the sequences in that set is zero, except for the peak term in zero-shift position [80]. Sivaswamy [105] proposed a method for constructing a complementary set of 2^{n+1} number of sequences of length $2^n N$, where $n \geq 1$ and N is the length of the base complementary pair. When $n = 1$, we can obtain a complementary set of four sequences of length N from a base complementary pair $\mathbf{s}_0$ and $\mathbf{c}_0$ of length $N/2$ using the following method [105]:

$$\mathbf{S}_1 = \mathbf{s}_0 \mathbf{s}_0 \tag{4.87}$$

$$\mathbf{S}_2 = \mathbf{s}_0 \bar{\mathbf{s}}_0 \tag{4.88}$$

$$\mathbf{S}_3 = \mathbf{c}_0 \mathbf{c}_0 \tag{4.89}$$

$$\mathbf{S}_4 = \mathbf{c}_0 \bar{\mathbf{c}}_0 \,. \tag{4.90}$$

Theorem 4.5 *If we apply a pair of Shapiro-Rudin sequence [73] of length $N/2$ as the base sequences $\mathbf{s}_0$ and $\mathbf{c}_0$, the set of four complementary sequences, given by (4.87) - (4.90), produces a crest factor less than or equal to 3dB, provided that the sequences $\mathbf{S}_1$, $\mathbf{S}_2$, $\mathbf{S}_3$ and $\mathbf{S}_4$ are applied to four-code BPSK modulated MC-CDMA systems.*

For example, a pair of Shapiro-Rudin sequences of length $N/2 = 4$, $\mathbf{a} = (+1 + 1 + 1 - 1)$ and $\mathbf{b} = (+1 + 1 - 1 + 1)$, can be used to generate $\mathbf{S}_1 = (+1 + 1 + 1 - 1 + 1 + 1 + 1 - 1)$, $\mathbf{S}_2 =$

$(+1+1+1-1-1-1-1+1), \mathbf{S}_3 = (+1+1-1+1+1+1-1+1)$ and $\mathbf{S}_4 = (+1+1-1+1-1-1+1-1)$. We can readily verify that they form an orthogonal set and hence these four sequences can be used as the spreading sequences of four-code BPSK modulated MC-CDMA systems.

Proof: Sivaswamy [105] showed that the set of four sequences form a complementary set and hence we have:

$$A[n] = 4N\delta[n] \,. \tag{4.91}$$

The crosscorrelations between all possible combinations of pairs are given as follows:

$$\mathbf{S}_1 \otimes \mathbf{S}_2 = \mathbf{s}_0 \otimes \mathbf{s}_0 - \mathbf{s}_0 \otimes \mathbf{s}_0 - \mathbf{s}_0 \otimes \vec{\mathbf{s}}_0 + \vec{\mathbf{s}}_0 \otimes \mathbf{s}_0 = -\mathbf{s}_0 \otimes \vec{\mathbf{s}}_0 \tag{4.92}$$

$$\mathbf{S}_2 \otimes \mathbf{S}_1 = \mathbf{s}_0 \otimes \mathbf{s}_0 - \mathbf{s}_0 \otimes \mathbf{s}_0 + \mathbf{s}_0 \otimes \vec{\mathbf{s}}_0 - \vec{\mathbf{s}}_0 \otimes \mathbf{s}_0 = \mathbf{s}_0 \otimes \vec{\mathbf{s}}_0 \tag{4.93}$$

$$\mathbf{S}_1 \otimes \mathbf{S}_3 = \mathbf{s}_0 \otimes \mathbf{c}_0 + \mathbf{s}_0 \otimes \mathbf{c}_0 + \mathbf{s}_0 \otimes \vec{\mathbf{c}}_0 + \vec{\mathbf{s}}_0 \otimes \mathbf{c}_0 = 2\mathbf{s}_0 \otimes \mathbf{c}_0 + \mathbf{s}_0 \otimes \vec{\mathbf{c}}_0 \tag{4.94}$$

$$\mathbf{S}_3 \otimes \mathbf{S}_1 = \mathbf{c}_0 \otimes \mathbf{s}_0 + \mathbf{c}_0 \otimes \mathbf{s}_0 + \mathbf{c}_0 \otimes \vec{\mathbf{s}}_0 + \vec{\mathbf{c}}_0 \otimes \mathbf{s}_0 = 2\mathbf{c}_0 \otimes \mathbf{s}_0 + \mathbf{c}_0 \otimes \vec{\mathbf{s}}_0 \tag{4.95}$$

$$\mathbf{S}_1 \otimes \mathbf{S}_4 = \mathbf{s}_0 \otimes \mathbf{c}_0 - \mathbf{s}_0 \otimes \mathbf{c}_0 - \mathbf{s}_0 \otimes \vec{\mathbf{c}}_0 + \vec{\mathbf{s}}_0 \otimes \mathbf{c}_0 = -\mathbf{s}_0 \otimes \vec{\mathbf{c}}_0 \tag{4.96}$$

$$\mathbf{S}_4 \otimes \mathbf{S}_1 = \mathbf{c}_0 \otimes \mathbf{s}_0 - \mathbf{c}_0 \otimes \mathbf{s}_0 + \mathbf{c}_0 \otimes \vec{\mathbf{s}}_0 - \vec{\mathbf{c}}_0 \otimes \mathbf{s}_0 = \mathbf{c}_0 \otimes \vec{\mathbf{s}}_0 \tag{4.97}$$

$$\mathbf{S}_2 \otimes \mathbf{S}_3 = \mathbf{s}_0 \otimes \mathbf{c}_0 - \mathbf{s}_0 \otimes \mathbf{c}_0 + \mathbf{s}_0 \otimes \vec{\mathbf{c}}_0 - \vec{\mathbf{s}}_0 \otimes \mathbf{c}_0 = \mathbf{s}_0 \otimes \vec{\mathbf{c}}_0 \tag{4.98}$$

$$\mathbf{S}_3 \otimes \mathbf{S}_2 = \mathbf{c}_0 \otimes \mathbf{s}_0 - \mathbf{c}_0 \otimes \mathbf{s}_0 - \mathbf{c}_0 \otimes \vec{\mathbf{s}}_0 + \vec{\mathbf{c}}_0 \otimes \mathbf{s}_0 = -\mathbf{c}_0 \otimes \vec{\mathbf{s}}_0 \tag{4.99}$$

$$\mathbf{S}_2 \otimes \mathbf{S}_4 = \mathbf{s}_0 \otimes \mathbf{c}_0 + \mathbf{s}_0 \otimes \mathbf{c}_0 - \mathbf{s}_0 \otimes \vec{\mathbf{c}}_0 - \vec{\mathbf{s}}_0 \otimes \mathbf{c}_0 = 2\mathbf{s}_0 \otimes \mathbf{c}_0 - \mathbf{s}_0 \otimes \vec{\mathbf{c}}_0 \tag{4.100}$$

$$\mathbf{S}_4 \otimes \mathbf{S}_2 = \mathbf{c}_0 \otimes \mathbf{s}_0 + \mathbf{c}_0 \otimes \mathbf{s}_0 - \mathbf{c}_0 \otimes \vec{\mathbf{s}}_0 - \vec{\mathbf{c}}_0 \otimes \mathbf{s}_0 = 2\mathbf{c}_0 \otimes \mathbf{s}_0 - \mathbf{c}_0 \otimes \vec{\mathbf{s}}_0 \tag{4.101}$$

$$\mathbf{S}_3 \otimes \mathbf{S}_4 = \mathbf{c}_0 \otimes \mathbf{c}_0 - \mathbf{c}_0 \otimes \mathbf{c}_0 - \mathbf{c}_0 \otimes \vec{\mathbf{c}}_0 + \vec{\mathbf{c}}_0 \otimes \mathbf{c}_0 = -\mathbf{c}_0 \otimes \vec{\mathbf{c}}_0 \tag{4.102}$$

$$\mathbf{S}_4 \otimes \mathbf{S}_3 = \mathbf{c}_0 \otimes \mathbf{c}_0 - \mathbf{c}_0 \otimes \mathbf{c}_0 + \mathbf{c}_0 \otimes \vec{\mathbf{c}}_0 - \vec{\mathbf{c}}_0 \otimes \mathbf{c}_0 = \mathbf{c}_0 \otimes \vec{\mathbf{c}}_0 \tag{4.103}$$

The combined crosscorrelation defined in (4.39), assuming BPSK modulation, is given by:

$$\begin{aligned} X[n] =& b_1 b_2 \left(\mathbf{S}_1 \otimes \mathbf{S}_2 + \mathbf{S}_2 \otimes \mathbf{S}_1\right) + b_1 b_3 \left(\mathbf{S}_1 \otimes \mathbf{S}_3 + \mathbf{S}_3 \otimes \mathbf{S}_1\right) \\ &+ b_1 b_4 \left(\mathbf{S}_1 \otimes \mathbf{S}_4 + \mathbf{S}_4 \otimes \mathbf{S}_1\right) + b_2 b_3 \left(\mathbf{S}_2 \otimes \mathbf{S}_3 + \mathbf{S}_3 \otimes \mathbf{S}_2\right) \\ &+ b_2 b_4 \left(\mathbf{S}_2 \otimes \mathbf{S}_4 + \mathbf{S}_4 \otimes \mathbf{S}_2\right) + b_3 b_4 \left(\mathbf{S}_3 \otimes \mathbf{S}_4 + \mathbf{S}_3 \otimes \mathbf{S}_4\right) \,, \end{aligned} \tag{4.104}$$

where again b_1, b_2, b_3 and b_4 are the four information bits to be transmitted. Considering that $\mathbf{S}_1 \otimes \mathbf{S}_2 + \mathbf{S}_2 \otimes \mathbf{S}_1 = 0$ and $\mathbf{S}_3 \otimes \mathbf{S}_4 + \mathbf{S}_4 \otimes \mathbf{S}_3 = 0$, $X[n]$ can be reduced to:

$$\begin{aligned} X[n] =& b_1 b_3 \left(\mathbf{S}_1 \otimes \mathbf{S}_3 + \mathbf{S}_3 \otimes \mathbf{S}_1\right) + b_1 b_4 \left(\mathbf{S}_1 \otimes \mathbf{S}_4 + \mathbf{S}_4 \otimes \mathbf{S}_1\right) \\ &+ b_2 b_3 \left(\mathbf{S}_2 \otimes \mathbf{S}_3 + \mathbf{S}_3 \otimes \mathbf{S}_2\right) + b_2 b_4 \left(\mathbf{S}_2 \otimes \mathbf{S}_4 + \mathbf{S}_4 \otimes \mathbf{S}_2\right) . \end{aligned} \tag{4.105}$$

Firstly, let us assume that $b_1 b_4 = b_2 b_3$, which implies that $b_1 b_3 = b_2 b_4$ holds as well. It can be shown that eight messages out of the $s^L = 2^4 = 16$ possible 4-bit messages satisfy this condition. In this case, $X[n]$ becomes:

$$X[n] = \pm 4 \left(\mathbf{s}_0 \otimes \mathbf{c}_0 + \mathbf{c}_0 \otimes \mathbf{s}_0\right) \,. \tag{4.106}$$

Since $\{\mathbf{s}_0, \mathbf{c}_0\}$ constitutes a Shapiro-Rudin pair, the sequences can be written as $\mathbf{s}_0 = \mathbf{ab}$ and $\mathbf{c}_0 = \mathbf{a}\overline{\mathbf{b}}$, where $\mathbf{a}$ and $\mathbf{b}$ are also Shapiro-Rudin sequences of length $N/4$. Then, as we observed in (4.71), (4.72) and (4.73), $X[n]$ becomes:

$$X[n] = \pm 16\, \mathbf{a} \otimes \mathbf{a}\,. \tag{4.107}$$

According to (4.42) the normalised power envelope is given by:

$$\frac{|(s(t)|^2}{4} = 1 + \frac{2}{4N}\mathrm{Re}\left[\sum_{n=1}^{N/4-1} \pm 16\, \mathbf{a} \otimes \mathbf{a}\, e^{j2\pi F n \frac{t}{T}}\right] \tag{4.108}$$

$$= \begin{cases} 1 + \frac{2}{N/4}\mathrm{Re}\left[\sum_{n=1}^{N/4-1} \mathbf{a} \otimes \mathbf{a}\, e^{j2\pi F n \frac{t}{T}}\right] & \text{for } b_1 b_4 = 1 \\ 1 + \frac{2}{N/4}\mathrm{Re}\left[\sum_{n=1}^{N/4-1} \mathbf{a} \otimes \mathbf{a}\, e^{j2\pi F n \frac{1}{T}\left(t + \frac{T}{2F}\right)}\right] & \text{for } b_1 b_4 = -1 \end{cases} \tag{4.109}$$

$$\leq 2\,. \tag{4.110}$$

Let us now assume that $b_1 b_4 = -b_2 b_3$, which also implies that $b_1 b_3 = -b_2 b_4$. Depending on the signs of $b_1 b_4$ and $b_1 b_3$, we get:

$$X[n] = \begin{cases} \pm 4\, \mathbf{s}_0 \otimes \vec{\mathbf{c}}_0 & \text{for } b_1 b_4 = -b_2 b_3 \\ \pm 4\, \mathbf{c}_0 \otimes \vec{\mathbf{s}}_0 & \text{for } b_1 b_4 = b_2 b_3\,. \end{cases} \tag{4.111}$$

Considering that:

$$\mathbf{s}_0\mathbf{c}_0 \otimes \mathbf{s}_0\mathbf{c}_0 = \mathbf{s}_0 \otimes \mathbf{s}_0 + \mathbf{c}_0 \otimes \mathbf{c}_0 + \mathbf{s}_0 \otimes \vec{\mathbf{c}}_0 + \vec{\mathbf{c}}_0 \otimes \mathbf{s}_0 = N\delta[n] + \mathbf{s}_0 \otimes \vec{\mathbf{c}}_0\,, \tag{4.112}$$

we can express $\mathbf{s}_0 \otimes \vec{\mathbf{c}}_0$ of (4.111) as $\mathbf{s}_0\mathbf{c}_0 \otimes \mathbf{s}_0\mathbf{c}_0$. In a similar manner, $\mathbf{c}_0 \otimes \vec{\mathbf{s}}_0$ can be replaced by $\mathbf{c}_0\mathbf{s}_0 \otimes \mathbf{c}_0\mathbf{s}_0$. We note that $\mathbf{s}_1 = \mathbf{s}_0\mathbf{c}_0$ and $\mathbf{s}_0\overline{\mathbf{c}}_0$ form a complementary pair of length N and so do $\mathbf{s}_1' = \mathbf{c}_0\mathbf{s}_0$ and $\overline{\mathbf{c}}_0\mathbf{s}_0$. Therefore, when $b_1 b_4 = -b_2 b_3$, the normalised power envelope can be formulated as:

$$\frac{|(s(t)|^2}{4} = 1 + \frac{2}{4N}\mathrm{Re}\left[\sum_{n=1}^{N-1} \pm 4\, \mathbf{s}_1 \otimes \mathbf{s}_1\, e^{j2\pi F n \frac{t}{T}}\right] \tag{4.113}$$

$$= \begin{cases} 1 + \frac{2}{N}\mathrm{Re}\left[\sum_{n=1}^{N-1} \mathbf{s}_1 \otimes \mathbf{s}_1\, e^{j2\pi F n \frac{t}{T}}\right] & \text{for } b_1 b_4 = 1 \\ 1 + \frac{2}{N}\mathrm{Re}\left[\sum_{n=1}^{N-1} \mathbf{s}_1 \otimes \mathbf{s}_1\, e^{j2\pi F n \frac{1}{T}\left(t + \frac{T}{2F}\right)}\right] & \text{for } b_1 b_4 = -1 \end{cases} \tag{4.114}$$

$$\leq 2\,. \tag{4.115}$$

In a similar manner, the normalised power envelope associated with $b_1 b_4 = b_2 b_3$ can be shown to be less than or equal to 2. Hence, the corresponding crest factors are always bounded by 3dB. ¶

Figure 4.13 depicts the peak-factors of some of Sivaswamy's complementary sets constituted by $L = 4$ sequences. As shown in Theorem 4.5, there can be three different magnitude distributions for the specific sequence length of $N = 2^n$, depending on the message bits. The marker $\circ$ in Figure 4.13 represents the peak factor of the signal, when $X[k] = \pm 16\, \mathbf{a} \otimes \mathbf{a}$, which is the case for half the number of

message bits from the set of 16 possible message bits. The marker □ represents the peak factors, when $X[k] = \pm 4\,\mathbf{s}_0 \otimes \mathbf{c}_0$, and the marker ⋆ when $X[k] = \pm 4\,\mathbf{c}_0 \otimes \mathbf{s}_0$, both of which occur for 4 message bits from the set of $2^L = s^4 = 16$ possible message bits. We can observe in Figure 4.13 that the peak factors associated with marker ○ are the lowest among the three values when the sequence length N is $2^2 = 4$, $2^4 = 16$ or $2^6 = 64$. An ideal peak factor of 1 was achieved for the sequence length of $N = 1^2 = 4$, representing a constant power envelope. The fact that all the peak factors in Figure 4.13 are bounded by 2 corroborates Theorem 4.5 .

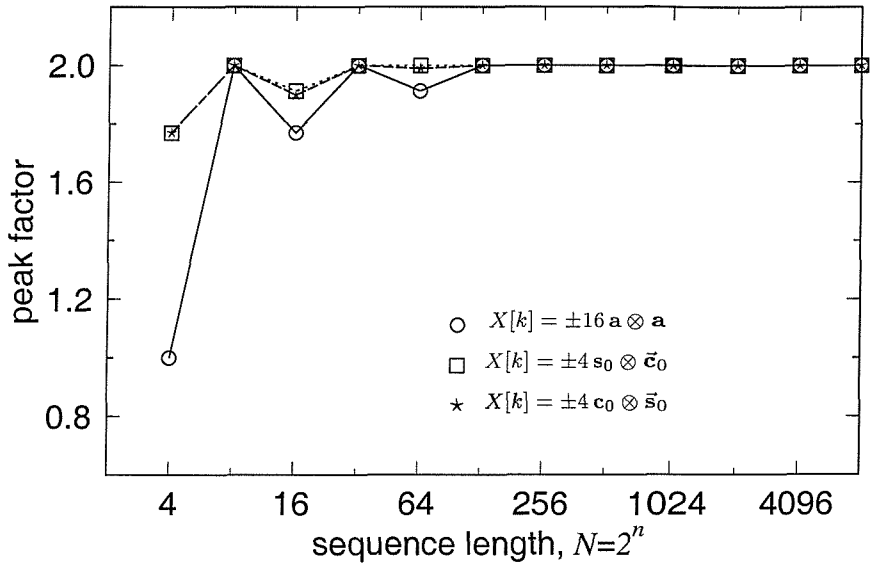

Figure 4.13: The peak-factors of Sivaswamy's complementary set of sequences. The number of simultaneously used sequences is $L = 4$ and the sequence length of $N = 2^n$ is between $2^2 = 4$ and $= 2^{13} = 8192$.

4.5.2.3 Peak Factor Distribution of Multi-Code MC-CDMA

In this section, we investigate the peak factor distribution of multi-code BPSK MC-CDMA. Two binary sequences, namely Walsh codes and orthogonal Gold codes, along with two so-called root-unity polyphase sequences, namely the so-called Frank codes [96] and Zadoff-Chu codes[98, 99] - are considered as the orthogonal spreading codes for our BPSK modulated MC-CDMA scheme. We assumed that the number of subcarriers, N, is 16. However, the results shown in this section apply also to MC-CDMA schemes with $16 \times F$ subcarriers, where the originally adjacent chips are F-subcarriers apart, in order to achieve independent fading on each subcarrier, which improves the achievable diversity gain.

When L number of codes are used simultaneously from the set of N available spreading codes, there are $\binom{N}{L}$ possible choices of selecting a specific spreading codes. If there are no other constraints to be satisfied, when selecting the codes, maintaining a low worst case peak factor can be a selection criterion. We can observe the effects of the code selection with the aid of the Cumulative Distribution Functions

(CDF) of the worst case peak factors encountered, when choosing the spreading codes. The CDF of a single-code MC-CDMA signal was shown Figure 4.12(a). Figure 4.14 depicts the corresponding CDFs for $L = 2, 4, 8, 15$ number of codes in conjunction with the spreading factor of $N = 16$. When

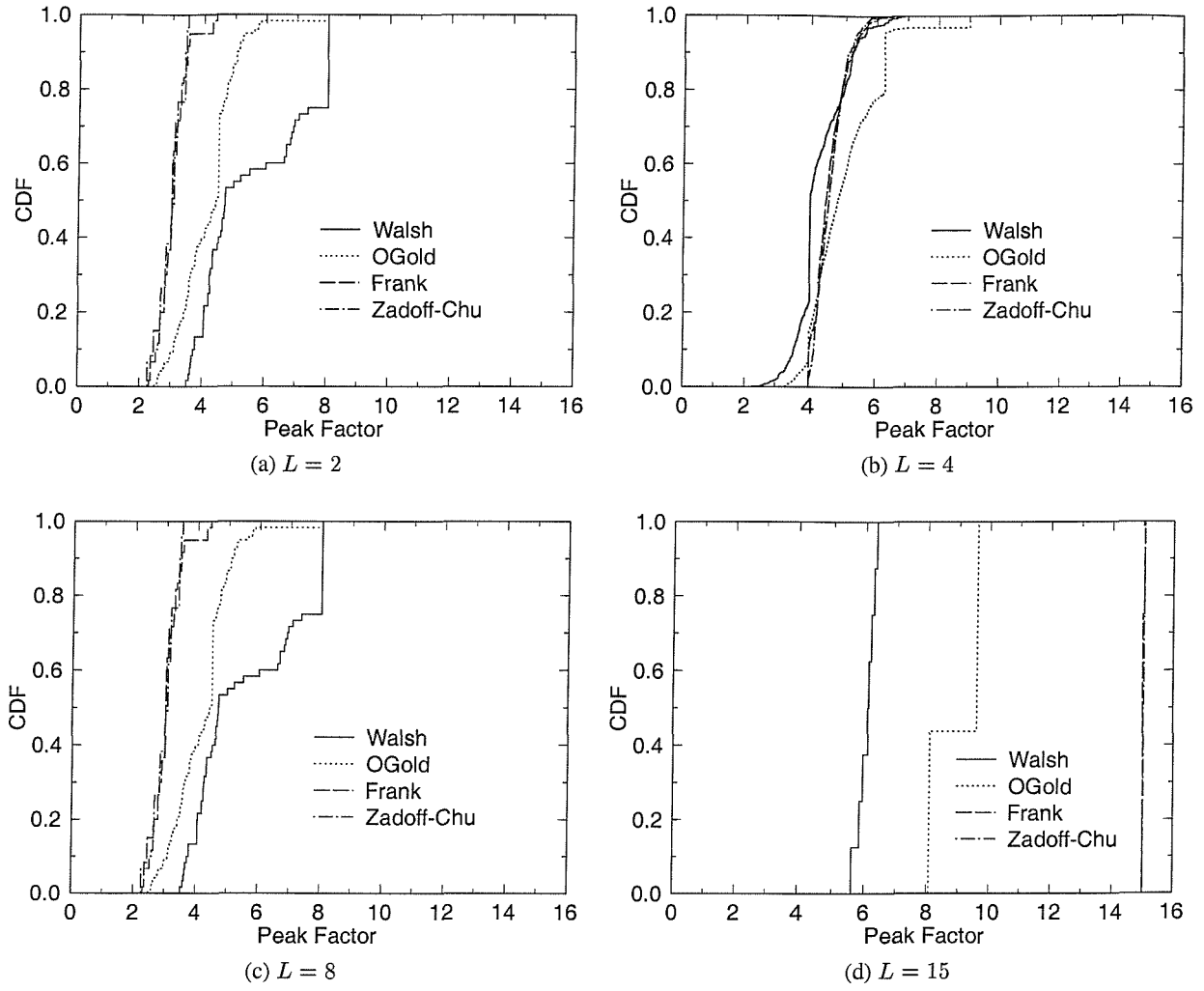

(a) $L = 2$ (b) $L = 4$

(c) $L = 8$ (d) $L = 15$

Figure 4.14: Cumulative Distribution Function (CDF) of the maximum PF (CF^2) for multi-code BPSK modulated MC-CDMA signals. The spreading factor was $N = 16$ and the number of simultaneously used codes was $L = 2, 4, 8, 15$. There exists $\binom{N}{L}$ number of possible code selections for the given value of L. Walsh codes exhibit desirable peak factor distributions for large L values, *i.e.* when either supporting a high number of users or transmitting a high number of bits per symbol, because their combined crosscorrelation term becomes small.

$L = 2$, there are $\binom{16}{2} = 120$ possible pairs of spreading codes, which we can choose. We can observe in Figure 4.14(a) that the peak factors of the Zadoff-Chu code pairs are in the rage of 2.3 to 3.5, depending on the specific pairs selected. The lowest peak factors of the Zadoff-Chu, Frank and OGold codes are similar. A quarter of the Walsh pairs exhibited the highest peak factor of 8, which was extremely undesirable.

However, as the number of codes L increases, the Walsh code sets begin to show more desirable peak factor distributions. This is already evident for $L = 4$, as shown in Figure 4.14(b). The lowest and the highest peak factors were 2.2821 and 6.8595, respectively, for Walsh codes of length $N = 16$ and for $L = 4$ simultaneously employed codes. This implies that the code selection is important in multi-code MC-CDMA, in order to reduce the corresponding peak factor.

For higher number of simultaneously used codes L, the CF advantage of Walsh codes over the other spreading codes considered becomes more pronounced. When $L = 15$, any combination of Walsh codes exhibited lower peak factors, than the best combinations of the other spreading codes investigated, as we can observe in Figure 4.14(d)

Class	$L = 2$	$L = 4$	$L = 8$	$L = 15$
Walsh	0x0480; 3.512	0x03c0; 2.282	0x23cd; 2.786	0xbfff; 5.602
OGold	0x0202; 2.489	0x9208; 3.161	0xf20e; 4.480	0xfbff; 8.067
Frank	0x0900; 2.307	0x04a4; 4.000	0x4d74; 8.000	0xff7f; 15.000
Zadoff	0x4040; 2.262	0x2174; 4.000	0x44de; 8.000	0xff74; 15.001

Table 4.5: The best code combinations and the corresponding peak factors for $L = 2, 4, 8$ and 15 number of simultaneous codes. The code combinations are represented in hexadecimal form, where the index of each contributing code is indicated by a '1' at the corresponding bit position of the equivalent binary bit pattern.

The best code combinations are summarised in Table 4.5 together with the corresponding peak factors for $L = 2, 4, 8, 15$ number of simultaneous codes and for the spreading factor of $N = 16$. In Table 4.5 the code combinations are represented by hexadecimal numbers, where the index of each contributing code is indicated by a '1' at the corresponding bit position of the equivalent binary bit pattern. For example, the best Walsh code combination for $L = 2$ is given by the pair of 8th and 11th Walsh codes, exhibiting the lowest peak factor, which is indicated by a '1' at positions 8 and 11 in the binary pattern of "0x0480 = $(0000\,0100\,1000\,0000)_2$", where "0x" is the hexadecimal notation prefix. The least significant bit represents the first code in the set.

Figure 4.15(a) depicts the maximum peak factors evaluated for the set of all 2^L messages using the best code-combinations, taking into account all possible $\binom{N}{L}$ choices. For our BPSK modulated OFDM modem, (N, L) non-linear PF reduction codes [31] associated with the code rate of L/N were used in order to arrive at the maximum peak factors plotted. The PFs plotted were multiplied by N/L in order to normalise them for the sake of maintaining the same average power as the original uncoded MC-CDMA. Walsh-spread MC-CDMA shows the lowest maximum peak factors for $L \geq 3$ amongst the four MC-CDMA systems studied. In fact, the peak factors of the Walsh-spread MC-CDMA signals approached the practically achievable minimum peak factor for various numbers of simultaneous codes L.

As mentioned before, Jones, Wilkinson and Barton [31] introduced a non-linear block coding scheme for reducing the overall peak factor of OFDM signals, hence we apply the same coding scheme for

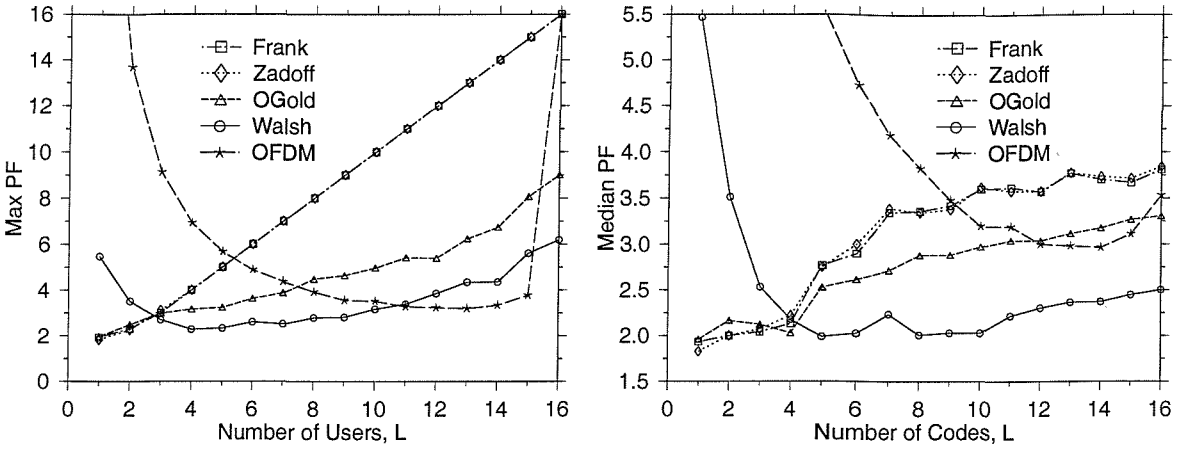

(a) Maximum Peak Factor

(b) Median Peak Factor

Figure 4.15: The maximum and median PF (CF^2) when using various spreading codes for BPSK modulated MC-CDMA. A set of nonlinear peak-factor reduction codes [31] of rate L/N were used for BPSK modulated OFDM and the PFs plotted were normalised by L/N for the sake of maintaining the same average power as the MC-CDMA scheme. The spreading factor was $N = 16$. The reduced PFs seen in this figure in comparison to Figure 4.14 are the consequence of employing the rate L/N nonlinear PF reduction codes.

reducing the peak factors of MC-CDMA signals. Let us eliminate half of the messages which yield high values of peak factors. Then the worst case peak factor corresponds to the median peak factor of the original uncoded MC-CDMA signals. The median peak factor also depends on the spreading sequence combination employed. The best code combination which has the lowest median peak factor may be different from the code combination yielding the lowest maximum peak factor, which was displayed in Table 4.5. Figure 4.15(b) depicts the median peak factors for the best combination of L simultaneous codes for the spreading factor of $N = 16$. We can observe in Figure 4.15(b) that the $15/16$ nonlinear block code used for Walsh spread MC-CDMA reduces the peak factor from 6.18 to 2.50, which is only 1dB higher than the practically achievable minimum peak factor of 3dB. This implies that Walsh-spread MC-CDMA can be viewed as a peak-factor reducing scheme in the context of conventional OFDM, in addition to the inherent diversity gain provided by frequency domain spreading. Figure 4.15(b) suggests that adaptively applying spreading the specific spreading code family, which exhibits the lowest peak factor for the given number of simultaneous codes L in conjunction with a rate of $(L-1)/L$ crest factor reduction coding, we can reduce the overall peak factor below 2.5 for any L, provided that the other system requirements are not violated by the PF reduction motivated spreading code adaptation.

4.5.3 Clipping Amplifier and BER Comparison

Having investigated the peak factor distributions numerically, let us now study the effects of the peak factor on the achievable BER performance, when the MC-CDMA signal is subjected to nonlinear ampli-

fication.

4.5.3.1 Nonlinear Power Amplifier Model

During our forthcoming investigations, we need a tractable model for the power amplifiers to be used in order to study the effects of nonlinear amplification. Most portable wireless devices use Solid-State-Power-Amplifiers (SSPA). The amplitude transfer characteristics or the AM-AM curve $g(x)$ of an SSPA can be modeled as [106–108]:

$$g(x) = \frac{x}{(1 + x^{2p})^{1/2p}}, \tag{4.116}$$

where x is the input magnitude and p is the smoothness factor during its transition from the linear region to the saturation region. Furthermore, it is assumed that the original phase characteristics of MC-CDMA signal are retained by the linear-phase amplifier, implying the absence of phase distortion. Figure 4.16 illustrates the amplitude transger curves for a few different smoothness factors, p, together with the 1dB compression line. Specifically, the 1dB compression point is defined, as the point on the output versus

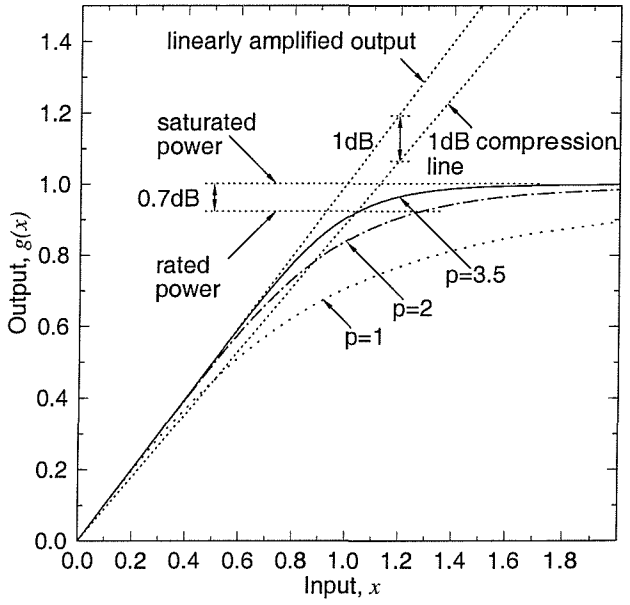

Figure 4.16: AM-AM curves of the SSPA model of (4.116) [106–108]

input curve, where the output level falls 1dB below its expected linearly amplified value. Using simple arithmetic, we can find the 1dB compression point in the form of:

$$\frac{x}{(1 + x^{2p})^{1/2p}} = kx, \tag{4.117}$$

where k is the 1dB compression line's steepness coefficient given as $k = 10^{-1/20}$. The solution of (4.117) for the input level x, where the 1dB output power compression is encountered, is given by $x_{1dB} = (k^{-2p} - 1)^{1/(2p)}$. For typical SSPAs, the output power at the 1dB compression point is about 0.7

dB below the saturation power [3]. Therefore the smoothness factor p in (4.116) should satisfy $g(x_{1dB}) = k(k^{-2p} - 1)^{1/(2p)} = \alpha$, where α is $10^{-0.7/20}$. The value of the smoothness factor p which satisfies this relation is $p = 3.58$. The corresponding value of the input level, where the 1dB compression is encountered, is denoted by x_{1dB}, which becomes $x_{1dB} = 1.035117539$.

More explicitly, the average output power is typically backed-off from the saturation power, in order to reduce the nonlinear distortion of the amplified signal. The 1dB compression point is the typically used reference point specified in terms of the input power. Thus, we get a 0.7 dB lower output power, than the saturation power, when the power amplifier is operating at 0dB back-off. Sometimes, we want to investigate the effects of the nonlinear amplification on the bit error ratio, as well as on the out-of-band frequency response, which determines the amount of out-of-band spurious emissions inflicted on other communication systems operating in the adjacent frequency band.

4.5.3.2 Effects of Clipping on Output Power

We have seen in Section 4.5.2.3 that MC-CDMA signals exhibit a fluctuating envelope power and hence when they are subject to nonlinear amplification, they produce out-of-band spurious emissions. The extreme peaks of the signal inevitably suffer from so-called "clipping effects", when they enter the saturation region of the amplifier, resulting in the loss of effective transmission power as well as the signal distortion, unless the gain of the amplifier is reduced to a level, where the amplifier's maximum output level is sufficiently high for the signal peaks not to be clipped. We have shown in Section 4.5.2.3 that the degree of power envelope variations of a MC-CDMA signal depends on the spreading sequences employed. Therefore, the loss of effective transmission power is also expected to depend on the spreading sequences used. Figure 4.17 depicts the relationship between the input-backoff of the power amplifier and the effective relative output power of the MC-CDMA signals spread by the various spreading sequences employed.

When only one simultaneous spreading code was used, we found that the effective transmission power loss was about 0.7dB for the Frank and Zadoff-Chu spread MC-CDMA signals, while the corresponding losses were 1.3dB, 2.3dB and 4.4dB for a complementary code, a single OGold code and a single Walsh code. A Shapiro-Rudin sequence was used as the complementary code, which was found to exhibit the lowest loss of effective transmission power amongst the three binary spreading sequences compared. Apart from the effects of signal distortion and the associated spurious out-of-band emissions, a high power loss may be encountered, which is a serious impediment in practical systems.

When two simultaneous spreading codes were used as seen in Figure 4.17(b), the MC-CDMA signal employing a complementary pair of Shapiro-Rudin codes showed the lowest power loss of 1.6dB for the set of five spreading codes investigated. A pair of OGold codes and a pair of Frank codes were next, showing an associated power loss of 1.7dB and 1.8dB, respectively. Finally, the Walsh codes and Zadoff-Chu codes exhibited a high power loss of around 3dB at 0dB input back-off. The spreading code pairs were selected on the basis of maintaining the lowest crest-factors for each family of spreading codes. It

[3] http://www.vertexepi.com/brochure/broch3.htm

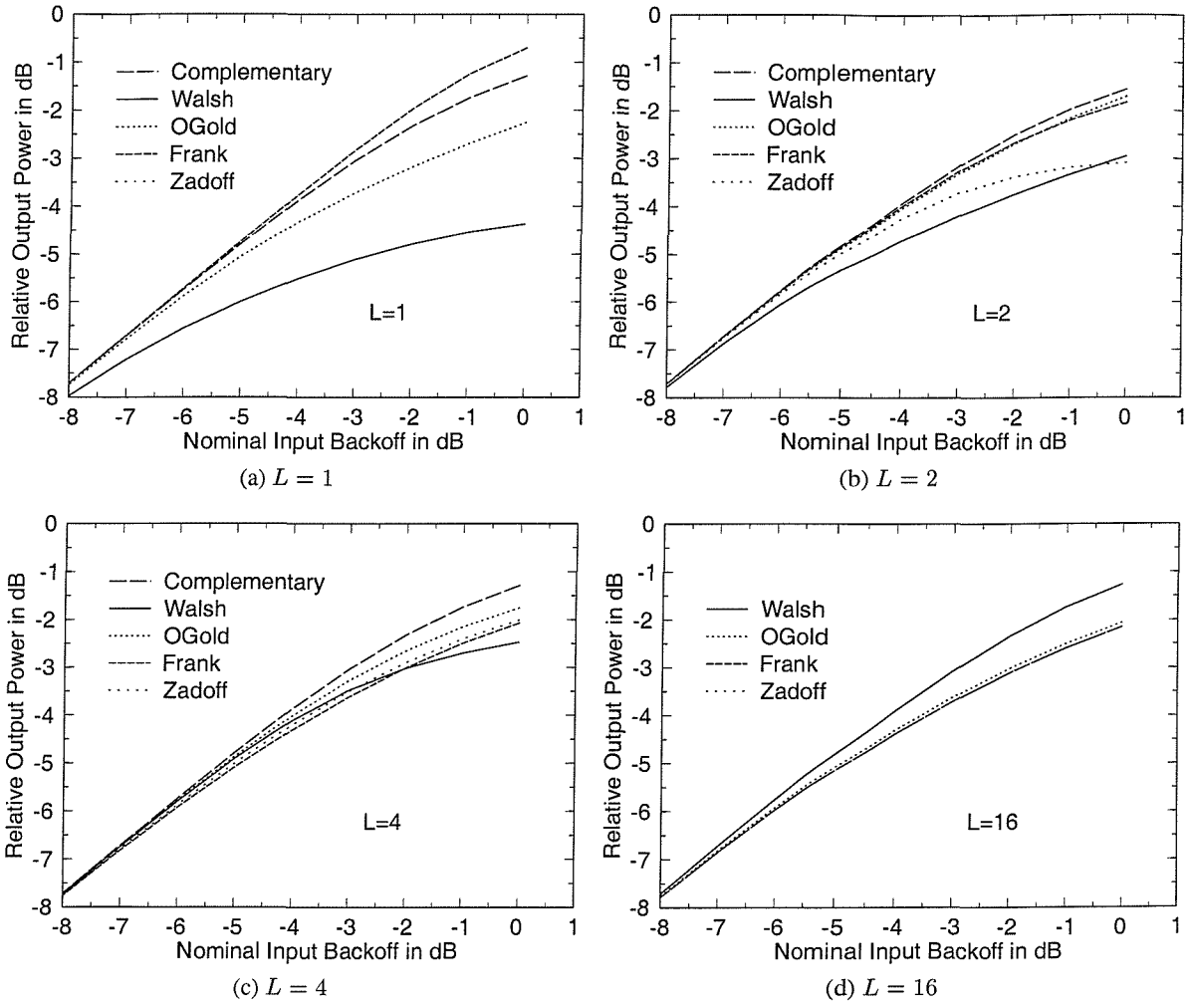

(a) $L = 1$ (b) $L = 2$

(c) $L = 4$ (d) $L = 16$

Figure 4.17: The relative output power versus input back-off in MC-CDMA for various spreading codes. The spreading factor was $N = 16$, while the number of simultaneous codes was $L = 1, 2, 4$ and 16. The corresponding curve for OFDM - although not shown in the figures - was almost identical to that of the Frank and the Zadoff-Chu spreading code based MC-CDMA using $L = 16$ simultaneous codes. Shapiro-Rudin codes were used as the complementary codes.

is interesting to observe that the Frank and Zadoff codes showed nearly identical maximum peak factors, although they exhibited quite a different power loss, as it can be observed in Figure 4.17(b). This is because the power loss depends on the magnitude distribution, rather than on the maximum peak factor of the signal.

When four spreading codes were used simultaneously, as seen in Figure 4.17(c), the effective transmission power losses at 0dB input back-off were 1.3dB for Sivaswamy's complementary set, 1.8dB for OGold codes, 2.0dB for Zadoff-Chu codes, 2.1dB for Frank codes and 2.5dB for Walsh codes. Considering that Walsh codes exhibited the lowest maximum crest factor of 2.28 in Figure 4.15(a) amongst the spreading codes investigated, except for Sivaswamy's complementary set, the Walsh code related high power loss is surprising. This implies that the Walsh-spread quad-code MC-CDMA signal still exhibits a relatively poor magnitude distribution.

The Walsh-spread MC-CDMA signals using the maximum possible number of simultaneous multi-codes of $L = 16$ showed the lowest power loss of 1.3dB amongst the four different spreading codes investigated in the context of MC-CDMA, as seen in Figure 4.17(d). The desirable characteristic of attaining a low effective power loss was observed for Walsh codes, when the number of simultaneous codes L was higher than 8. The power loss curve for OFDM - although not shown explicitly in the figure - was almost identical to those observed for Zadoff-Chu and Frank code spread MC-CDMA signals, as seen in Figure 4.17(d).

We may conclude that the effective transmission power loss is also an important system performance factor, when choosing spreading sequences for multi-code MC-CDMA transmitters, and hence in addition to the crest factor studies further power-loss related investigations are required. In the fully loaded case, when the number of simultaneous codes is $L = 16$, the Walsh-spread MC-CDMA signal showed a lower power loss than OFDM, underlining another advantage of using spreading in comparison to conventional OFDM employing no spreading.

4.5.3.3 Effects of Clipping on the Bit Error Ratio

Simulations were carried out, in order to investigate the effects of nonlinear amplification in the context of BPSK modulated MC-CDMA and BPSK modulated OFDM systems over AWGN channels. When a single spreading code was employed for BPSK MC-CDMA, the effects of nonlinear amplification were moderate, resulting in an almost unimpaired BPSK bit error probability, as it can be observed in Figure 4.18. Since there is little margin for any BER improvement in comparison to a perfectly linearly amplified scenario, neither CF-reduction coding nor input back-off affects the corresponding BER. Only OFDM could achieve some BER improvement with the advent of crest-factor reduction coding, when using an input back-off of 3dB.

When the number of simultaneous codes L was increased to two, as seen in Figure 4.19, Walsh-spread BPSK MC-CDMA showed approximately 1dB SNR loss, as it can be observed in Figure 4.19, due to the associated nonlinear amplification and the high crest factor encountered. The BER of Walsh-spread MC-CDMA could not be improved by crest-factor reduction coding, since all the $2^L = 2^2 = 4$ number of bit combinations result in the same crest-factor distribution. However, involving 3dB input back-off

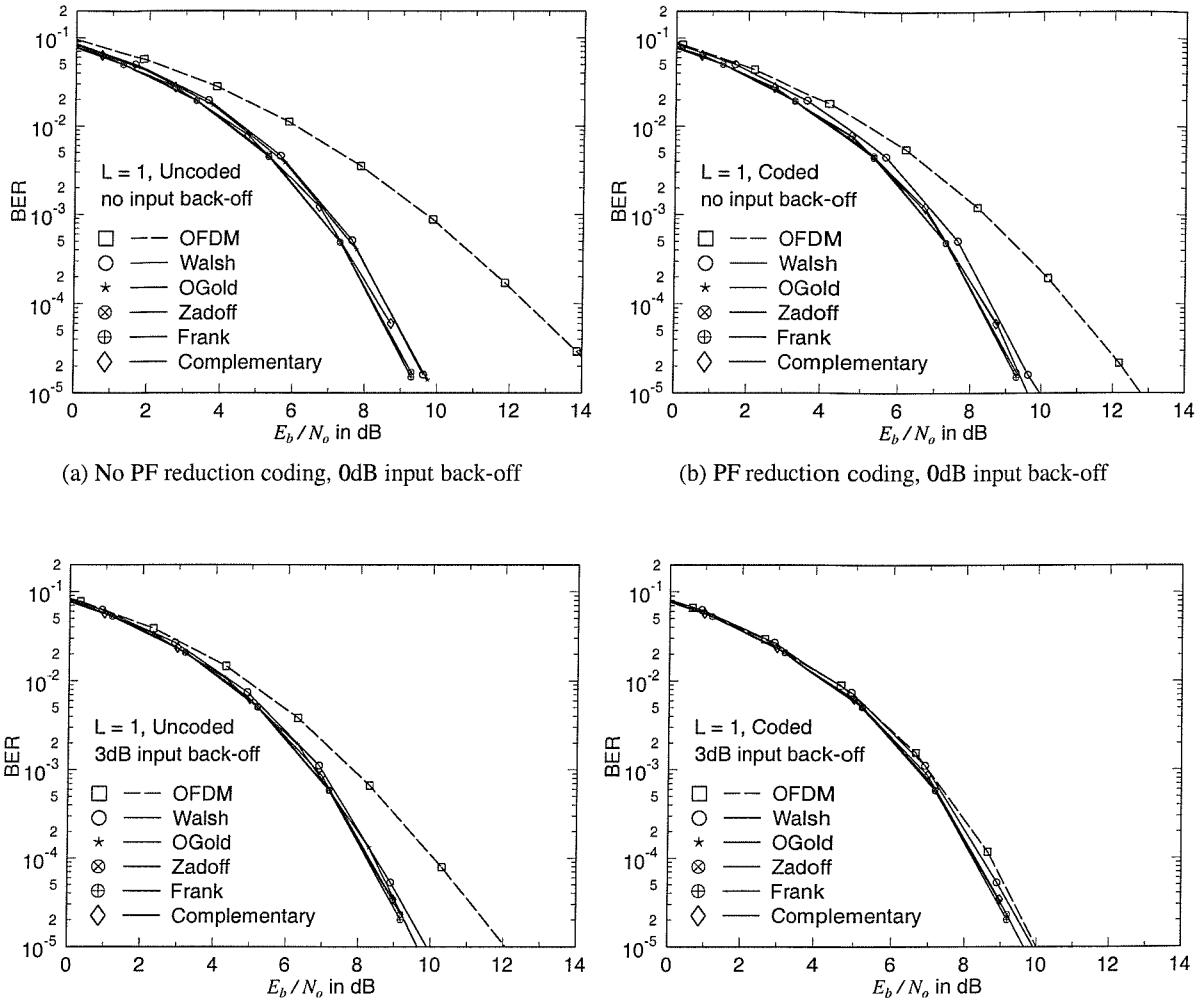

(a) No PF reduction coding, 0dB input back-off

(b) PF reduction coding, 0dB input back-off

(c) No PF reduction coding, 3dB input back-off

(d) PF reduction coding, 3dB input back-off

Figure 4.18: The BER of BPSK modulated MC-CDMA and BPSK modulated OFDM over AWGN channels for a SF of $N = 16$ and for $L = 1$ user.

slightly reduced the BER. The SNR values used in Figure 4.18 to 4.21 are based on the measured received signal powers, hence they do not show the effective output power loss encountered at the transmitter side, which was studied in the previous subsection.

When the number of simultaneous codes L was four as portrayed in Figure 4.20, all the MC-CDMA systems exhibited similar bit error rates. The Frank and Zadoff-Chu based systems exhibited a slightly higher BER, than the other MC-CDMA systems, however the differences became negligible as crest-factor reduction coding or the input back-off of 3dB was applied.

Figure 4.21 depicts the BER curves of the investigated MC-CDMA systems, when the number of simultaneous codes L is 16. For a fully loaded MC-CDMA system, only Walsh spreading showed a better BER, than OFDM at an input back-off of 0dB and without crest-factor reduction coding. Considering

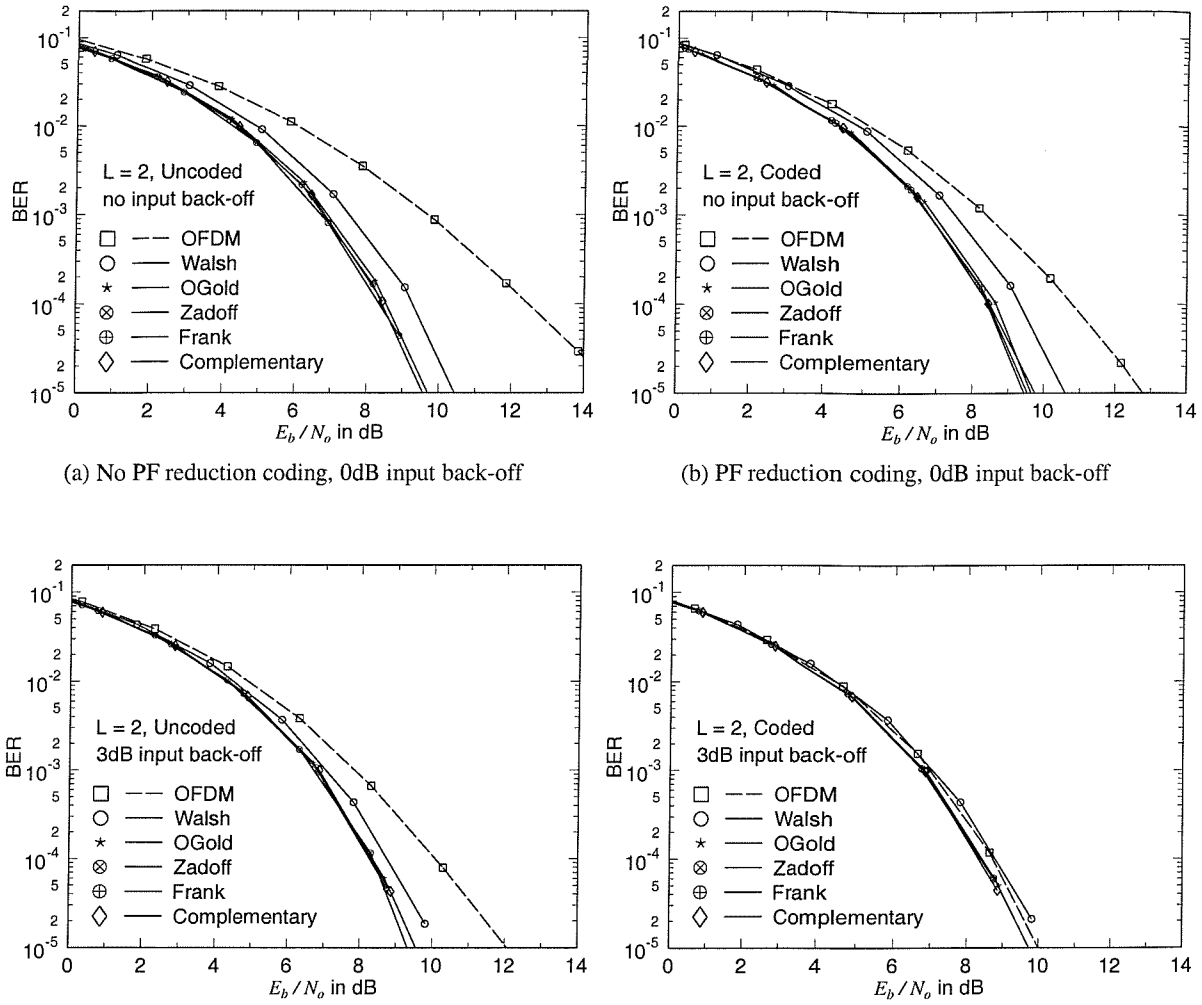

(a) No PF reduction coding, 0dB input back-off

(b) PF reduction coding, 0dB input back-off

(c) No PF reduction coding, 3dB input back-off

(d) PF reduction coding, 3dB input back-off

Figure 4.19: The BER of BPSK modulated MC-CDMA and BPSK modulated OFDM over AWGN channels for a SF of $N = 16$ and for $L = 2$ users.

that Walsh-spread MC-CDMA has an approximately 1dB lower loss of effective transmission power, than that of OFDM, the SNR difference of about 2dB observed at a given BER is deemed to be a significant benefit of Walsh-spread MC-CDMA from a practical point of view. Both crest-factor reduction coding and 3dB input back-off had the potential of reducing the BER of Walsh-spread MC-CDMA to a value near the ideal BER associated with using perfectly linear, infinite dynamic range amplification. When these two techniques were combined, the bit error rates of all the investigated systems approached the ideal BER, as we can observe in Figure 4.21(d) .

The BER performance of MMSE Joint-Detection (JD) assisted MC-CDMA [59] and that of single-user OFDM is shown in Figure 4.22 for transmission over Rayleigh channels, where independent sub-carrier fading and perfect channel channel transfer function estimation were assumed. The independent

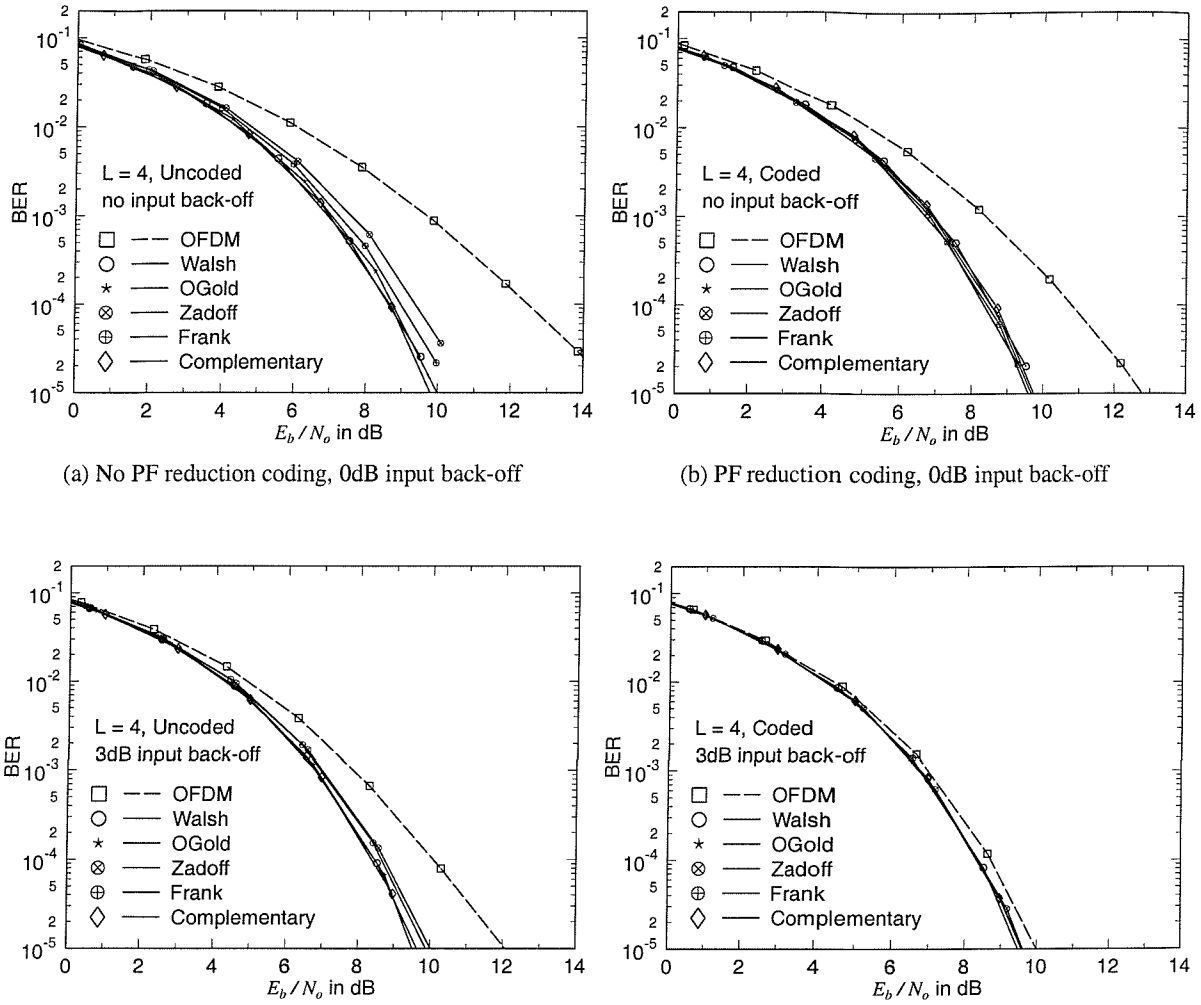

(a) No PF reduction coding, 0dB input back-off

(b) PF reduction coding, 0dB input back-off

(c) No PF reduction coding, 3dB input back-off

(d) PF reduction coding, 3dB input back-off

Figure 4.20: The BER of BPSK modulated MC-CDMA and BPSK modulated OFDM over AWGN channels for a SF of $N = 16$ and for $L = 4$ users.

subcarrier fading can be achieved in a system, where many subcarriers are employed in conjunction with frequency domain interleaving, provided that the number of resolvable multi-path components in the channel is higher than or equal to the spreading gain. Figure 4.22(a) shows the performance advantage of MC-CDMA systems over OFDM. MC-CDMA exhibited a significantly better BER performance than OFDM, while maintaining the same bandwidth efficiency. This was achieved despite supporting $L = 16$ users, while the OFDM scheme supported a single user, which was a benefit of using the Minimum Mean Square Error (MMSE) Block Linear Equalised (BLE) Joint Detector (JD) of Section 3.4.2. This performance trend is only true, however, when there is sufficient diversity gain in order to compensate for the multiple user interference (MUI) or multi-code interference. It was observed in other simulations not included here that a diversity order of two or three is sufficient for MMSE JD-MC-CDMA to overcome

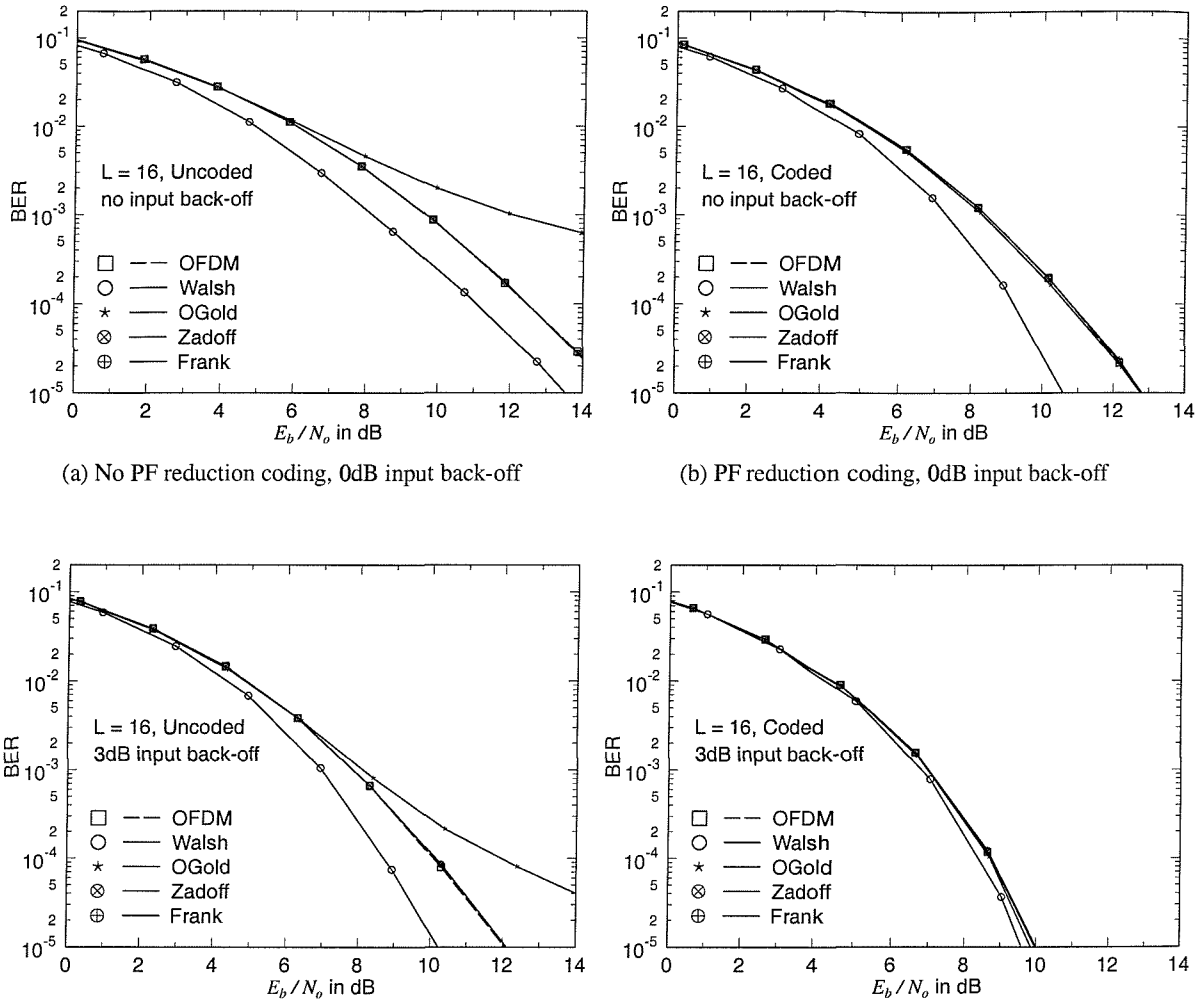

(a) No PF reduction coding, 0dB input back-off

(b) PF reduction coding, 0dB input back-off

(c) No PF reduction coding, 3dB input back-off

(d) PF reduction coding, 3dB input back-off

Figure 4.21: The BER of BPSK modulated MC-CDMA and BPSK modulated OFDM over AWGN channels for a SF of $N = 16$ and for $L = 16$ users.

the MUI. We can also observe however that JD MC-CDMA is more sensitive to amplitude clipping than OFDM. However, Walsh-spread MC-CDMA was not the best performing scheme over Rayleigh channels. Two of the poly-phase codes, namely the Frank and Zadoff-Chu spreading codes, were more effective, than the binary spreading codes, namely the Walsh and OGold codes, in this environment. Considering that the poly-phase-spread signals suffer from higher distortion due to clipping, this result is surprising. It implies that the MUI imposed by the poly-phase-spread systems is lower than that of the binary spreading based systems and this MUI difference plays a more dominant role in determining their BER performance than the clipping-induced distortion. The BER performance of the MMSE JD MC-CDMA and OFDM systems using CF-reduction coding is shown in Figure 4.22(b). The BER improvement was around 1dB for the MC-CDMA systems at a BER of 10^{-5} and at a back-off of 3dB, in

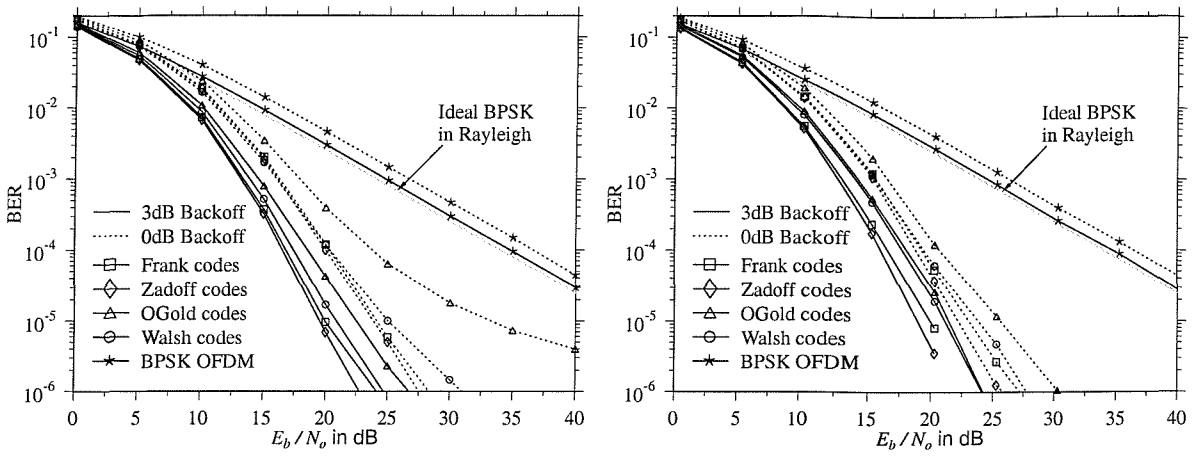

(a) **Without** CF-reduction coding (b) **With** (16,15) CF-reduction coding

Figure 4.22: BER versus E_b/N_o performance of BPSK modulated JD MC-CDMA and that of BPSK modulated OFDM when transmitting over Rayleigh channels for a SF of $N = 16$ and for $L = 16$ users. MMSE Joint Detection was used for MC-CDMA and independent fading of each subcarrier was assumed.

comparison to the uncoded system. This BER improvement was more noticeable at 0dB back-off, where the effects of amplitude clipping are more dramatic.

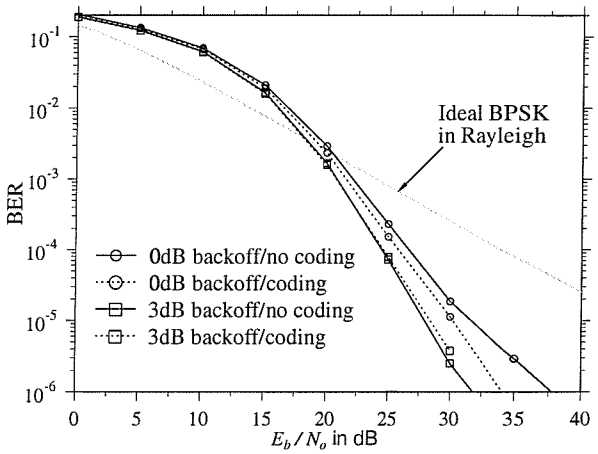

Figure 4.23: The BER of Walsh-spread BPSK modulated MC-CDMA, when a MMSE single-user detector was employed. The crest-factor reduction coding increased the bit error ratio at 3dB back-off. The number of users L and the spreading factor N were both 16.

When MMSE single user detection was employed for our MC-CDMA systems, we found that the CF-reduction coding slightly degraded the BER performance at a 3dB back-off for the Walsh-spread system, as it can be observed in Figure 4.5.3.3. This implies that the CF-reduction coding is not optimal in reducing the overall BER, since it may select the specific message codes, which incur a high MUI, resulting in a degraded BER performance. This is especially true for the case, when there is little margin for crest-factor improvement, such as for example in conjunction with the amplifier having a 3dB back-

off.

4.5.3.4 Clipping Effects on Frequency Spectrum

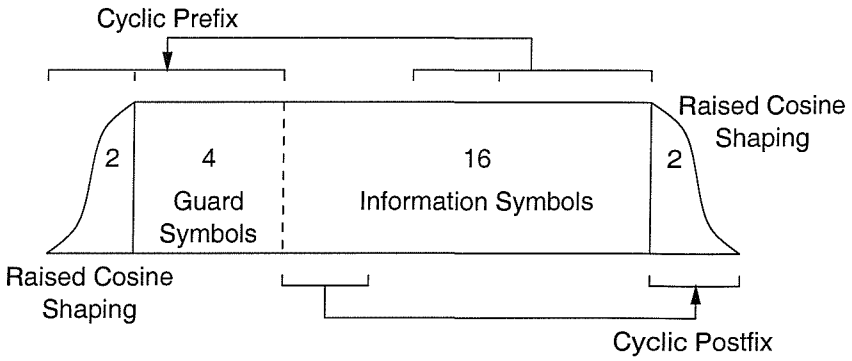

Figure 4.24: The time-domain frame structure of MC-CDMA system. The number of subcarriers was $N = 16$ conveying 16 information symbols.

Since frequency spectrum is a valuable commodity, it has to be effectively shared. The clipping-induced out-of-band emissions result in an increased adjacent channel interference. Multicarrier systems typically exhibit attractive spectral characteristics. In Section 4.5.2.3, we have observed that the crest factors of MC-CDMA signals are dependent on the spreading sequences employed and also found that MC-CDMA signals generated with the aid of the appropriate spreading sequences exhibit lower crest factors, than those of OFDM. Therefore, it is expected that MC-CDMA signals show better spectral characteristics than OFDM signals. The corresponding spectrum is dependent on the time-domain transmission frame structure employed. We used a modified version of the frame structure employed in the IEEE 802.11 high-speed Wireless LAN [109] operated in the 5 GHz band. Figure 4.24 depicts the time-domain frame structure employed in our reference system. The time domain frame consists of 16 information symbols, which are obtained by applying IFFT to 16 frequency domain symbols plus six cyclic prefix and two cyclic postfix symbols. The first and the last two symbols are subjected to time domain raised cosine shaping, in order to prevent abrupt time-domain signal changes.

The spectra shown in Figure 4.25 were obtained by averaging the individual spectra associated with all the possible messages using the best combinations of spreading sequences in terms of attaining the lowest possible crest factors. Specifically, Figure 4.25(a) displays the spectra of BPSK modulated MC-CDMA signals employing a Walsh code and a Zadoff-Chu code. We can observe that the spectrum of MC-CDMA signal employing the Zadoff-Chu spreading code exhibits a lower out-of-band power than that of Walsh code. The spectra corresponding to MC-CDMA signals employing the OGold code, Frank code and complementary code were between those associated with the Walsh and Zadoff-Chu spreading codes. This observation about the spectra is consistent with the comparison of their corresponding crest factors as we have seen in Section 4.5.2.3. When the number of simultaneous codes L was four, the spectrum recorded for a set of four Sivaswamy's complementary sequences showed the lowest out-of-

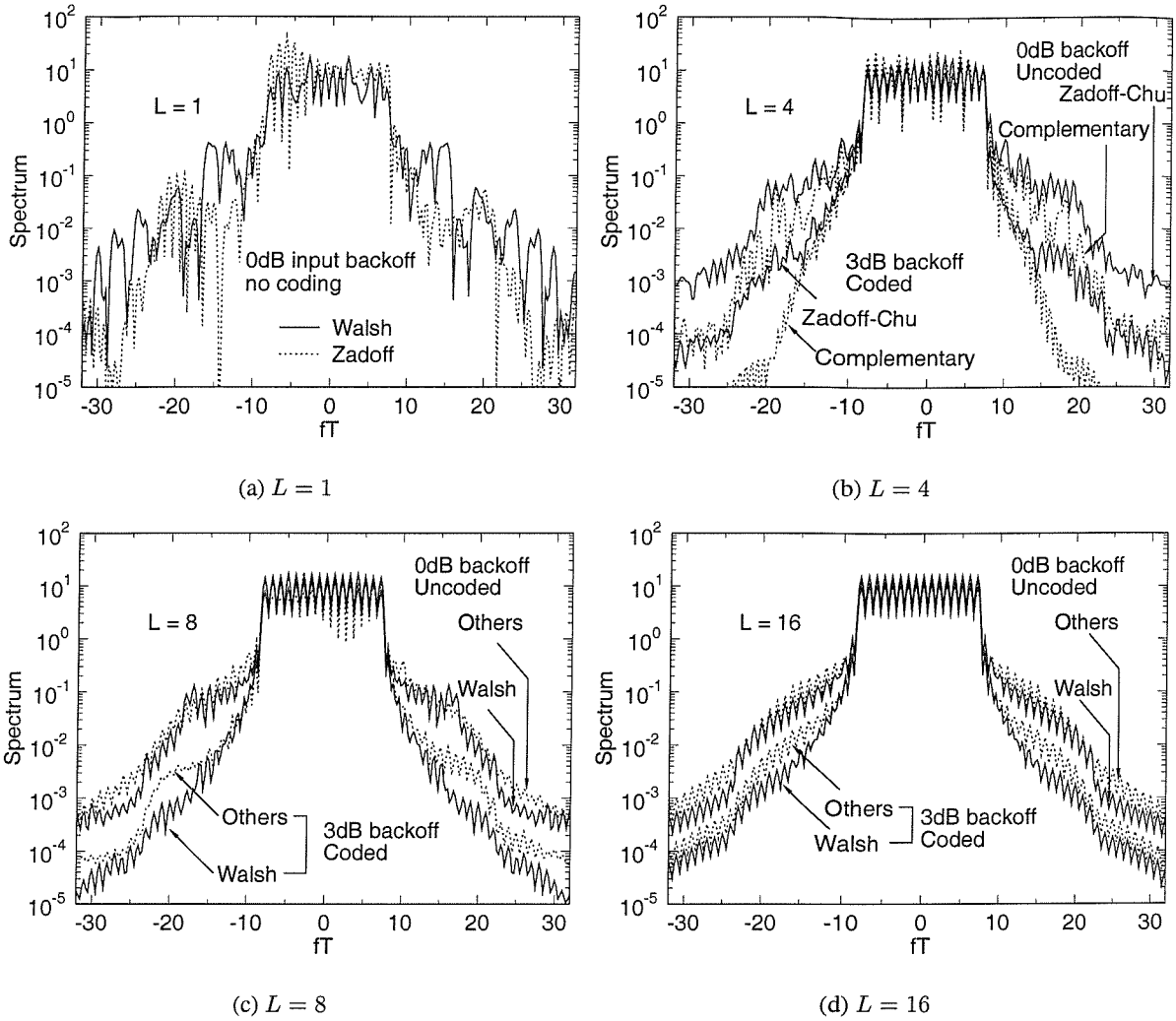

(a) $L = 1$ (b) $L = 4$

(c) $L = 8$ (d) $L = 16$

Figure 4.25: The frequency spectrum of BPSK modulated MC-CDMA signals. The number of subcarriers N was 16 and the nonlinear amplifier model of Section 4.5.3.1 was used. The frequency axis was scaled in terms of the normalised frequency fT, where T denotes the bit duration.

band spurious spillage, which is depicted in Figure 4.25(b) . With the aid of the previously introduced 15/16-rate peak-factor reduction coding and using a 3dB input back-off, the out-of-band spectral spillage was considerably reduced. When the number of simultaneous codes L was higher than eight, the Walsh-spread BPSK modulated MC-CDMA showed scheme exhibited the lowest out-of-band power spillage for the set of investigated systems, as it can be seen in Figure 4.25(c) and Figure 4.25(d). Therefore, we conclude that the Walsh spreading codes are effective in reducing out-of-band spurious emissions and concomitantly in reducing the worst case peak factors.

4.6 Summary and Conclusions

In addition to the more widely recognised benefits of MC-CDMA - such as its substantial frequency diversity gain - we showed in this chapter that MC-CDMA is also capable of mitigating the CF problem. Specifically, in Section 4.5.1 we investigated the relationship between the envelope power and the properties of range of spreading sequences. It was shown in the context of (4.40) that the envelope power is determined by the sums of the aperiodic autocorrelations defined in (4.36) and by the aperiodic cross-correlations of the spreading sequences defined in (4.37). We showed furthermore in Section 4.5.2.1 and 4.5.2.3 that the former property is more important when supporting a low number of users, L, while the latter plays a more dominant role under highly loaded conditions, *i.e.* for a high values of L.

When we consider that the weighted sums of the aperiodic autocorrelations and the aperiodic cross-correlations defined in (4.38) and (4.39) are bounded by a constant [110], it is apparent that there are no 'magic' sequences, which exhibit "good" CF distributions for an arbitrary number of simultaneous codes, namely for all values of L. For example, the family of orthogonal Gold codes is more attractive for low values of L, while Walsh codes are preferred for high L values. The two poly-phase codes considered, namely the Frank and Zadoff-Chu spreading codes, were also found attractive for $L = 1$, while their CF distributions were the least attractive amongst the codes studied for $L = 1$, as we have seen in Section 4.5.2.3.

In Section 4.5.2.2, we found that the crest-factors of a two-code BPSK modulated MC-CDMA signal, employing a pair of Shapiro-Rudin sequences or a pair of sub-complementary sequences based on a Shapiro-Rudin pair, are bounded by 3dB. We also showed in Section 4.5.2.2 that the crest-factor of the four-code BPSK modulated MC-CDMA signal employing Sivaswamy's set of complementary sequences is also bounded by 3dB. Therefore these sequences are preferred spreading sequences for MC-CDMA in terms of low crest-factors, low BERs and attractive spectral characteristics. However, we were unable to find larger set of such sequences which had more than four codes.

When we set L=N, in order to maintain the same spectral efficiency as OFDM, Walsh-spread BPSK modulated MC-CDMA showed a significant peak factor reduction over OFDM in conjunction with the same rate CF-reduction block encoder, when investigating under 'fully loaded' conditions. When a 3dB back-off was applied to the transmitter's power amplifier, the Walsh-spread MC-CDMA system showed an approximately 2dB SNR gain at a BER of 10^{-5} in Figure 4.21 in an AWGN environment, when compared to OFDM. When transmitting over a channel exhibiting independent Rayleigh fading over each subcarrier, MMSE JD MC-CDMA employing Zadoff-Chu spreading codes was found to be the best scheme, as seen in Figure 4.22.

4.6.1 Diversity Considerations

As a possible future research topic, we investigate breifly the frequency domain symbol magnitude of multi-code MC-CDMA system employing the Walsh codes and it's impact on the achievable diversity

gain. The scaled frequency domain symbol magnitude $\sqrt{N}\,|s_n|$ of the n-th subchannel can be given as:

$$\sqrt{N}\,|s_n| = \left| \sum_{l=0}^{L-1} b_l\, c_l[n] \right| , \tag{4.118}$$

where b_l is the lth user's information bit, c_l is the lth user's spreading sequence, L is the number of simultaneous users and N is the spreading factor. Since the scaled frequency domain symbol magnitude $\sqrt{N}\,|s_n|$ is a sum of even number of binary values ± 1, the legitimate values are $\{(L-2i)|i = 0, .., \lfloor L/2 \rfloor\}$. Let us define Q_i as the the number of subchannels, which have the magnitude of a $L-2i$. By definition, the Q_i values are non-negative integers. Additionally, the following two constraints are imposed on $\{Q_i\}$:

$$\sum_{i=0}^{\lfloor L/2 \rfloor} Q_i\,(L-2i)^2 = NL\,, \tag{4.119}$$

$$\sum_{i=0}^{\lfloor L/2 \rfloor} Q_i = N\,, \tag{4.120}$$

where (4.119) simply states that the total power in the frequency domain is equal to the average time domain power given in Equation 4.33 and (4.120) implies that the total number of subcarriers is N.

Let us consider an example, where the number of subcarriers is $N = 16$ and the number of simultaneous codes is $L = 2$. Applying (4.119), we get $Q_0 \times 2^2 = 16 \times 2$ and hence $Q_0 = 8$. From (4.120), we have $Q_0 + Q_1 = 16$, and hence $Q_1 = 8$. In this example, we have only one solution for the set of $\{Q_i\}$ values, namely $\{Q_i\} = \{8,\ 8\}$ for the corresponding magnitude set of $\sqrt{N}|s_n| \in \{2,\ 0\}$.

Below we provide another example for $N = 16$ and $L = 6$. In this scenario, the possible magnitude set is given by $\{6, 4, 2, 0\}$. For this magnitude set, there exist 10 solutions for $\{Q_i\}$, namely $\{0, 3, 12, 1\}$, $\{0, 4, 8, 4\}$, $\{0, 5, 4, 7\}$, $\{0, 6, 0, 10\}$, $\{1, 0, 15, 0\}$, $\{1, 1, 11, 3\}$, $\{1, 2, 7, 6\}$, $\{1, 3, 3, 9\}$, $\{2, 0, 6, 8\}$ and $\{2, 1, 2, 11\}$ depending on the $L = 6$ number of bits b_l in (4.118).

Now a question arises as to "Which set of Q_i will maximise the achievable diversity gain over N independent fading channels?" or "Which set of Q_i is the worst in this respect?". A seemingly good candidate can be found in the second example for $L = 6$. Specifically, the fifth solution, namely $\{1, 0, 15, 0\}$, does not 'waste' any diversity potential, since there is no zero magnitude subcarriers in the frequency domain. By contrast, the other Q_i sets have at least one zero magnitude. For example, the first solution for Q_i given by $\{0, 3, 12, 1\}$ contains a single zero magnitude, while the second solution given by $\{0, 4, 8, 4\}$ has four zero-magnitude subcarriers in the frequency domain.

Having observed that some bit combinations yield a better set of Q_i values, while some do not, we can devise a coding scheme, which eliminates the source bit code words associated with a high number of zero magnitudes in the corresponding Q_i set, in order to more efficiently utilise the frequency diversity potential achievable. However, further investigations are required regarding the statistical distributions associated with the set of Q_i values and the feasiblity of joint code construction methods has to be explored with the aim of reducing the worst case peak factor as well as for the sake of increasing the average diversity order.

Chapter 5

Adaptive Modulation

5.1 Introduction

Mobile communications channels typically exhibit time-variant channel quality fluctuations [14] and hence conventional fixed-mode modems suffer from bursts of transmission errors, even if the system was designed to provide a high link margin. An efficient approach to mitigating these detrimental effects is to adaptively adjust the transmission format based on the near-instantaneous channel quality information perceived by the receiver, which is fed back to the transmitter with the aid of a feedback channel [111]. This scheme requires a reliable feedback link from the receiver to the transmitter and the channel quality variation should be sufficiently slow for the transmitter to be able to adapt. *Hayes* [111] proposed transmission power adaptation, while *Cavers* [112] suggested invoking a variable symbol duration scheme in response to the perceived channel quality at the expense of a variable bandwidth requirement. Since a variable-power scheme increases both the average transmitted power requirements and the level of co-channel interference [113] imposed on other users of the system, instead variable-rate Adaptive Quadrature Amplitude Modulation (AQAM) was proposed by *Steele* and *Webb* as an alternative, employing various star-QAM constellations [113, 114]. With the advent of Pilot Symbol Assisted Modulation (PSAM) [115–117], *Otsuki et al.* [118] employed square constellations instead of star constellations in the context of AQAM, as a practical fading counter measure. Analysing the channel capacity of Rayleigh fading channels [119–121], *Goldsmith et al.* showed that variable-power, variable-rate adaptive schemes are optimum, approaching the capacity of the channel and characterised the throughput performance of variable-power AQAM [120] . However, they also found that the extra throughput achieved by the additional variable-power assisted adaptation over the constant-power, variable-rate scheme is marginal for most types of fading channels [120, 122].

5.2 Increasing the Average Transmit Power as a Fading Counter-Measure

The radio frequency (RF) signal radiated from the transmitter's antenna takes different routes, experiencing refraction, scattering and reflections, before it arrives at the receiver. Each multi-path component

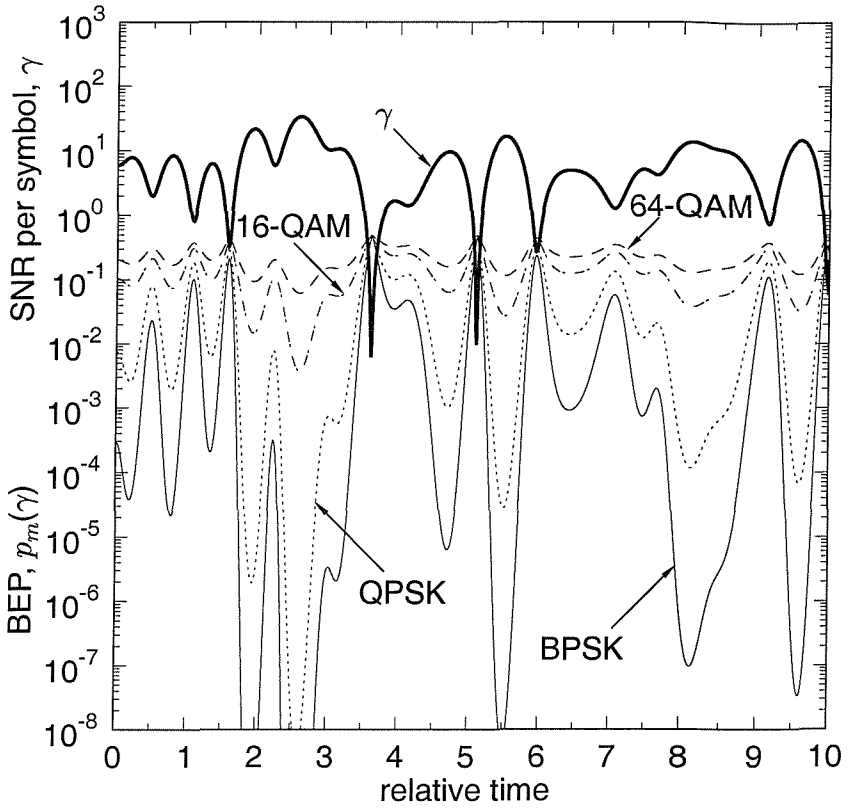

Figure 5.1: Instantaneous SNR per transmitted symbol, γ, in a flat Rayleigh fading scenario and the associated instantaneous bit error probability, $p_m(\gamma)$, of various fixed-mode QAM. The average SNR is $\bar{\gamma} = 10$dB. The fading magnitude plot is based on a normalised Doppler frequency of $f_N = 10^{-4}$ and for the duration of $100ms$, corresponding to a mobile terminal traveling at the speed of $54km/h$ and operating at $f_c = 2GHz$ frequency band at the sampling rate of $1MHz$.

arriving at the receiver simultaneously adds constructively or destructively, resulting in fading of the combined signal. When there is no line-of-sight component amongst these signals, the combined signal is characterised by Rayleigh fading. The instantaneous SNR (iSNR), γ, per transmitted symbol[1] is depicted in Figure 5.1 for a typical Rayleigh fading using the thick line. The Probability Density Function (PDF) of γ is given as [25]:

$$f_{\bar{\gamma}}(\gamma) = \frac{1}{\bar{\gamma}} e^{\gamma/\bar{\gamma}}, \tag{5.1}$$

where $\bar{\gamma}$ is the average SNR and $\bar{\gamma} = 10$dB was used in Figure 5.1.

The instantaneous Bit Error Probability (iBEP), $p_m(\gamma)$, of BPSK, QPSK, 16-QAM and 64-QAM is also shown in Figure 5.1 with the aid of four different thin lines. These probabilities are obtained from the corresponding bit error probability over AWGN channel conditioned on the iSNR, γ, which are given

[1]When no diversity is employed at the receiver, the SNR per symbol, γ, is the same as the channel SNR, γ_c. In this case, we will use the term "SNR" without any adjective.

as [13]:

$$p_m(\gamma) = \sum_i A_i Q(\sqrt{a_i \gamma}) \,, \tag{5.2}$$

where $Q(x)$ is the Gaussian Q-function defined as $Q(x) \triangleq \frac{1}{\sqrt{2\pi}} \int_x^\infty e^{-t^2/2} dt$ and $\{A_i, a_i\}$ is a set of modulation mode dependent constants. For the Gray-mapped square QAM modulation modes associated with $m = 2, 4, 16, 64$ and 256, the sets $\{A_i, a_i\}$ are given as [13, 123]:

$$\begin{array}{lll}
m = 2, & \text{BPSK} & \{(1,2)\} \\
m = 4, & \text{QPSK} & \{(1,1)\} \\
m = 16, & \text{16-QAM} & \left\{\left(\frac{3}{4}, \frac{1^2}{5}\right), \left(\frac{2}{4}, \frac{3^2}{5}\right), \left(-\frac{1}{4}, \frac{5^2}{5}\right)\right\} \\
m = 64, & \text{64-QAM} & \left\{\left(\frac{7}{12}, \frac{1^2}{21}\right), \left(\frac{6}{12}, \frac{3^2}{21}\right), \left(-\frac{1}{12}, \frac{5^2}{21}\right), \left(\frac{1}{12}, \frac{9^2}{21}\right), \left(-\frac{1}{12}, \frac{13^2}{21}\right)\right\} \\
m = 256, & \text{256-QAM} & \left\{\left(\frac{15}{32}, \frac{1^2}{85}\right), \left(\frac{14}{32}, \frac{3^2}{85}\right), \left(\frac{5}{32}, \frac{5^2}{85}\right), \left(-\frac{6}{32}, \frac{7^2}{85}\right), \left(-\frac{7}{32}, \frac{9^2}{85}\right), \right. \\
 & & \left(\frac{6}{32}, \frac{11^2}{85}\right), \left(\frac{9}{32}, \frac{13^2}{85}\right), \left(\frac{8}{32}, \frac{15^2}{85}\right), \left(-\frac{7}{32}, \frac{17^2}{85}\right), \left(-\frac{6}{32}, \frac{19^2}{85}\right), \\
 & & \left.\left(-\frac{1}{32}, \frac{21^2}{85}\right), \left(\frac{2}{32}, \frac{23^2}{85}\right), \left(\frac{3}{32}, \frac{25^2}{85}\right), \left(-\frac{2}{32}, \frac{27^2}{85}\right), \left(-\frac{1}{32}, \frac{29^2}{85}\right)\right\} .
\end{array} \tag{5.3}$$

As we can observe in Figure 5.1, $p_m(\gamma)$ exhibits high values during the deep channel envelope fades, where even the most robust modulation mode, namely BPSK, exhibits a bit error probability $p_2(\gamma) > 10^{-1}$. By contrast even the error probability of the high-throughput 16-QAM mode, namely $p_{16}(\gamma)$, is below 10^{-2}, when the iSNR γ exhibits a high peak. This wide variation of the communication link's quality is a fundamental problem in wireless radio communication systems. Hence, numerous techniques have been developed for combating this problem, such as increasing the average transmit power, invoking diversity, channel inversion, channel coding and/or adaptive modulation techniques. In this section we will investigate the efficiency of employing an increased average transmit power.

As we observed in Figure 5.1, the instantaneous Bit Error Probability (BEP) becomes excessive for sustaining an adequate service quality during instances, when the signal experiences a deep channel envelope fade. Let us define the cut-off BEP p_c, below which the Quality Of Service (QOS) becomes unacceptable. Then the outage probability P_{out} can be defined as:

$$P_{out}(\bar{\gamma}, p_c) \triangleq \Pr[p_m(\gamma) > p_c] \,, \tag{5.4}$$

where $\bar{\gamma}$ is the average channel SNR dependent on the transmit power, p_c is the cut-off BEP and $p_m(\gamma)$ is the instantaneous BEP, conditioned on γ, for an m-ary modulation mode, given for example by (5.2). We can reduce the outage probability of (5.4) by increasing the transmit power, and hence increasing the average channel SNR $\bar{\gamma}$. Let us briefly investigate the efficiency of this scheme.

Figure 5.2(a) depicts the instantaneous BEP as a function of the instantaneous channel SNR. Once the cut-off BEP p_c is determined as a QOS-related design parameter, the corresponding cut-off SNR γ_o can be determined, as shown for example in Figure 5.2(a) for $p_c = 0.05$. Then, the outage probability of (5.4) can be calculated as:

$$P_{out} = \Pr[\gamma < \gamma_o] \,, \tag{5.5}$$

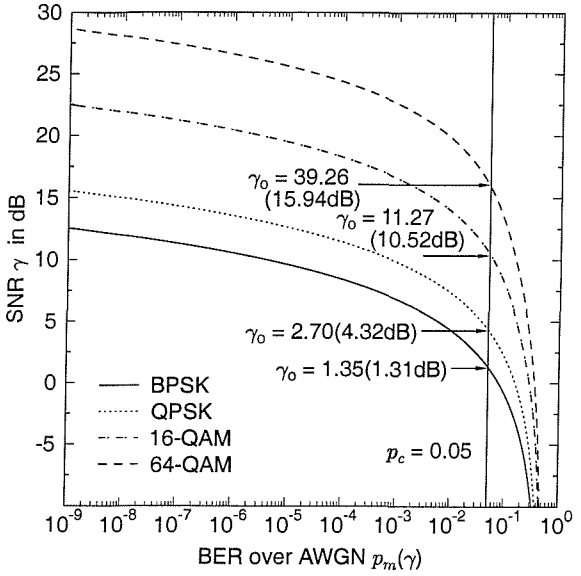

(a) SNR versus BER over AWGN channels

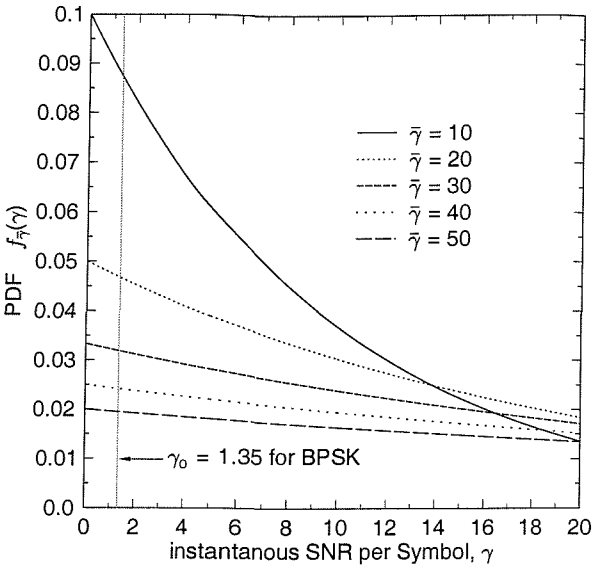

(b) PDF $f_{\bar{\gamma}}(\gamma)$ of the instantaneous SNR γ over Rayleigh channel

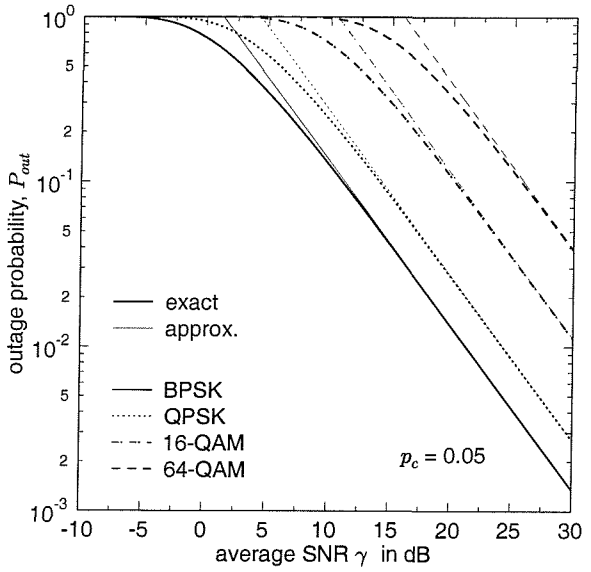

(c) Outage Probability over Rayleigh channel

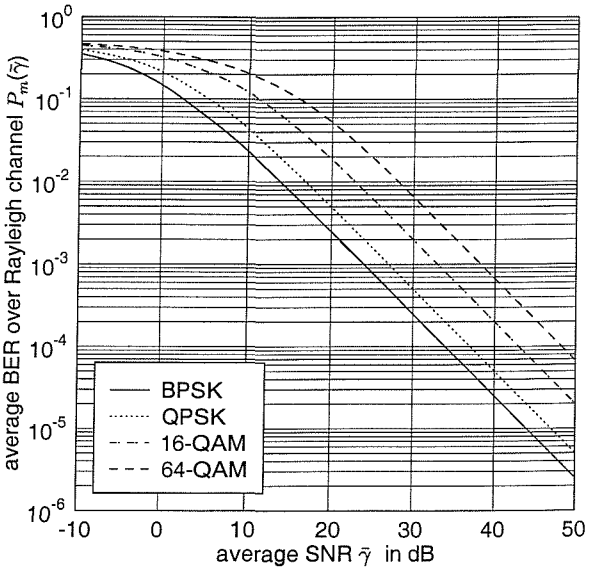

(d) BER over Rayleigh channel

Figure 5.2: The effects of an increased average transmit power. (a) The the cut-off SNR γ_o versus the cut-off BEP p_c for BPSK, QPSK, 16-QAM and 64-QAM. (b) PDF of the iSNR γ over Rayleigh channel, where the outage probability is given by the area under the PDF curve surrounded by the two lines given by $\gamma = 0$ and $\gamma = \gamma_o$. An increased transmit power increases the average SNR $\bar{\gamma}$ and hence reduces the area under the PDF proportionately to $\bar{\gamma}$. (c) The exact outage probability versus the average SNR $\bar{\gamma}$ for BPSK, QPSK, 16-QAM and 64-QAM evaluated from (5.7) confirms this observation. (d) The average BER is also inversely proportional to the transmit power for BPSK, QPSK, 16-QAM and 64-QAM.

and in physically interpreted terms its value is equal to the area under the PDF curve of Figure 5.2(b) surrounded by the left y-axis and $\gamma = \gamma_o$ vertical line. Upon taking into account that for high SNRs the PDFs of Figure 5.2(b) are near-linear, this area can be approximated by $\gamma_o/\bar{\gamma}$, considering that $f_{\bar{\gamma}}(0) = 1/\bar{\gamma}$. Hence, the outage probability is inversely proportional to the transmit power, requiring an approximately 10-fold increased transmit power for reducing the outage probability by an order of magnitude, as seen in Figure 5.2(c). The exact value of the outage probability is given by:

$$P_{out} = \int_0^{\gamma_o} f_{\bar{\gamma}}(\gamma)\, d\gamma \tag{5.6}$$

$$= 1 - e^{-\gamma_o/\bar{\gamma}}\,, \tag{5.7}$$

where we used the PDF $f_{\bar{\gamma}}(\gamma)$ given in (5.1). Again, Figure 5.2(c) shows the exact outage probabilities together with their linearly approximated values for several QAM modems recorded for the cut-off BER of $p_c = 0.05$, where we can confirm the validity of the linearly approximated outage probability[2], when we have $P_{out} < 0.1$.

The average BER $P_m(\bar{\gamma})$ of an m-ary Gray-mapped QAM modem is given by [13, 25, 124]:

$$P_m(\bar{\gamma}) = \int_0^{\infty} p_m(\gamma)\, f_{\bar{\gamma}}(\gamma)\, d\gamma \tag{5.8}$$

$$= \frac{1}{2} \sum_i A_i \{1 - \mu(\bar{\gamma}, a_i)\}\,, \tag{5.9}$$

where a set of constants $\{A_i, a_i\}$ is given in (5.3) and $\mu(\bar{\gamma}, a_i)$ is defined as:

$$\mu(\bar{\gamma}, a_i) \triangleq \sqrt{\frac{a_i\bar{\gamma}}{1 + a_i\bar{\gamma}}}\,. \tag{5.10}$$

In physical terms (5.8) implies weighting the BEP $p_m(\gamma)$ experienced at an iSNR γ by the probability of occurrence of this particular value of γ - which is quantified by its PDF $f_{\bar{\gamma}}(\gamma)$ - and then averaging, *i.e.* integrating, this weighted BEP over the entire range of γ. Figure 5.2(d) displays the average BER evaluated from (5.9) for the average SNR rage of $-10\text{dB} \geq \bar{\gamma} \geq 50\text{dB}$. We can observe that the average BER is also inversely proportional to the transmit power.

In conclusion, we studied the efficiency of increasing the average transmit power as a fading countermeasure and found that the outage probability as well as the average bit error probability are inversely proportional to the average transmit power. Since the maximum radiated powers of modems are regulated in order to reduce the co-channel interference and transmit power, the acceptable transmit power increase may be limited and hence employing this technique may not be sufficiently effective for achieving the desired link performance. We will show that the AQAM philosophy of the next section is a more attractive solution to the problem of channel quality fluctuation experienced in wireless systems.

5.3 System Description

A stylised model of our adaptive modulation scheme is illustrated in Figure 5.3, which can be invoked in conjunction with any power control scheme. In our adaptive modulation scheme, the modulation mode

[2]The same approximate outage probability can be derived by taking the first term of the Taylor series of e^x of (5.7).

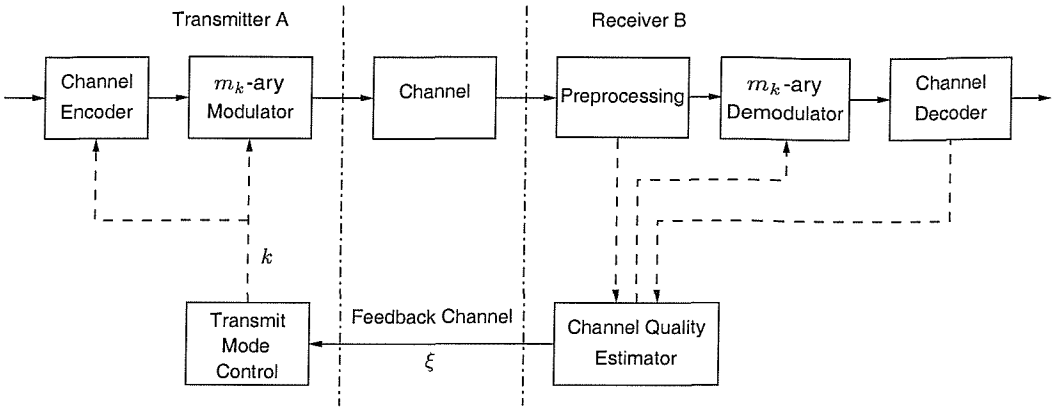

Figure 5.3: Stylised model of near-instantaneous adaptive modulation scheme

used is adapted on a near-instantaneous basis for the sake of counteracting the effects of fading. Let us describe the detailed operation of the adaptive modem scheme of Figure 5.3. Firstly, the channel quality ξ is estimated by the remote receiver B. This channel quality measure ξ can be the instantaneous channel SNR, the Radio Signal Strength Indicator (RSSI) output of the receiver [113], the decoded BER [113], the Signal to Interference-and-Noise Ratio (SINR) estimated at the output of the channel equaliser [125], or the SINR at the output of a CDMA joint detector [126]. The estimated channel quality perceived by receiver B is fed back to transmitter A with the aid of a feedback channel, as seen in Figure 5.3. Then, the transmit mode control block of transmitter A selects the highest-throughput modulation mode k capable of maintaining the target BER based on the channel quality measure ξ and the specific set of adaptive mode switching levels $\mathbf{s}$. Once k is selected, m_k-ary modulation is performed at transmitter A in order to generate the transmitted signal $s(t)$, and the signal $s(t)$ is transmitted through the channel.

The general model and the set of important parameters specifying our constant-power adaptive modulation scheme are described in the next subsection in order to develop the underlying general theory. Then, in Section 5.3.2 several application examples are introduced.

5.3.1 General Model

A K-mode adaptive modulation scheme adjust its transmit mode k, where $k \in \{0, 1 \cdots K-1\}$, by employing m_k-ary modulation according to the near-instantaneous channel quality ξ perceived by receiver B of Figure 5.3. The mode selection rule is given by:

$$\text{Choose mode } k \text{ when } \quad s_k \leq \xi < s_{k+1} \ , \tag{5.11}$$

where a switching level s_k belongs to the set $\mathbf{s} = \{s_k \mid k = 0, 1, \cdots, K\}$. The Bits Per Symbol (BPS) throughput b_k of a specific modulation mode k is given by $b_k = \log_2(m_k)$ if $m_k \neq 0$, otherwise $b_k = 0$. It is convenient to define the incremental BPS c_k as $c_k = b_k - b_{k-1}$, when $k > 0$ and $c_0 = b_0$, which quantifies the achievable BPS increase, when switching from the lower-throughput mode k–1 to mode k.

5.3.2 Examples

5.3.2.1 Five-Mode AQAM

A five-mode AQAM system has been studied extensively by many researchers, which was motivated by the high performance of the Gray-mapped constituent modulation modes used. The parameters of this five-mode AQAM system are summarised in Table 5.1. In our investigation, the near-instantaneous

k	0	1	2	3	4
m_k	0	2	4	16	64
b_k	0	1	2	4	6
c_k	0	1	1	2	2
modem	No Tx	BPSK	QPSK	16-QAM	64-QAM

Table 5.1: The parameters of five-mode AQAM system

channel quality ξ is defined as instantaneous channel SNR γ. The boundary switching levels are given as $s_0 = 0$ and $s_5 = \infty$. Figure 5.4 illustrates operation of the five-mode AQAM scheme over a typical narrow-band Rayleigh fading channel scenario. Transmitter A of Figure 5.3 keeps track of the channel SNR γ perceived by receiver B with the aid of a low-BER, low-delay feedback channel - which can be created for example by superimposing the values of ξ on the reverse direction transmitted messages of transmitter B - and determines the highest-BPS modulation mode maintaining the target BER depending on which region γ falls into. The channel-quality related SNR regions are divided by the modulation mode switching levels s_k. More explicitly, the set of AQAM switching levels $\{s_k\}$ is determined such that the average BPS throughput is maximised, while satisfying the average target BEP requirement, P_{target}. We assumed a target BEP of $P_{target} = 10^{-2}$ in Figure 5.4. The associated instantaneous BPS throughput b is also depicted using the thick stepped line at the bottom of Figure 5.4. We can observe that the throughput varied from 0 BPS, when the no transmission (No-Tx) QAM mode was chosen, to 4 BPS, when the 16-QAM mode was activated. During the depicted observation window the 64-QAM mode was not activated. The instantaneous BEP, depicted as a thin line using the middle trace of Figure 5.4, is concentrated around the target BER of $P_{target} = 10^{-2}$.

5.3.2.2 Seven-Mode Adaptive Star-QAM

Webb and Steele revived the research community's interest on adaptive modulation, although a similar concept was initially suggested by Hayes [111] in the 1960s. Webb and Steele reported the performance of adaptive star-QAM systems [113]. The parameters of their system are summarised in Table 5.2.

5.3.2.3 Five-Mode APSK

Our five-mode Adaptive Phase-Shift-Keying (APSK) system employs m-ary PSK constituent modulation modes. The magnitude of all the constituent constellations remained constant, where adaptive

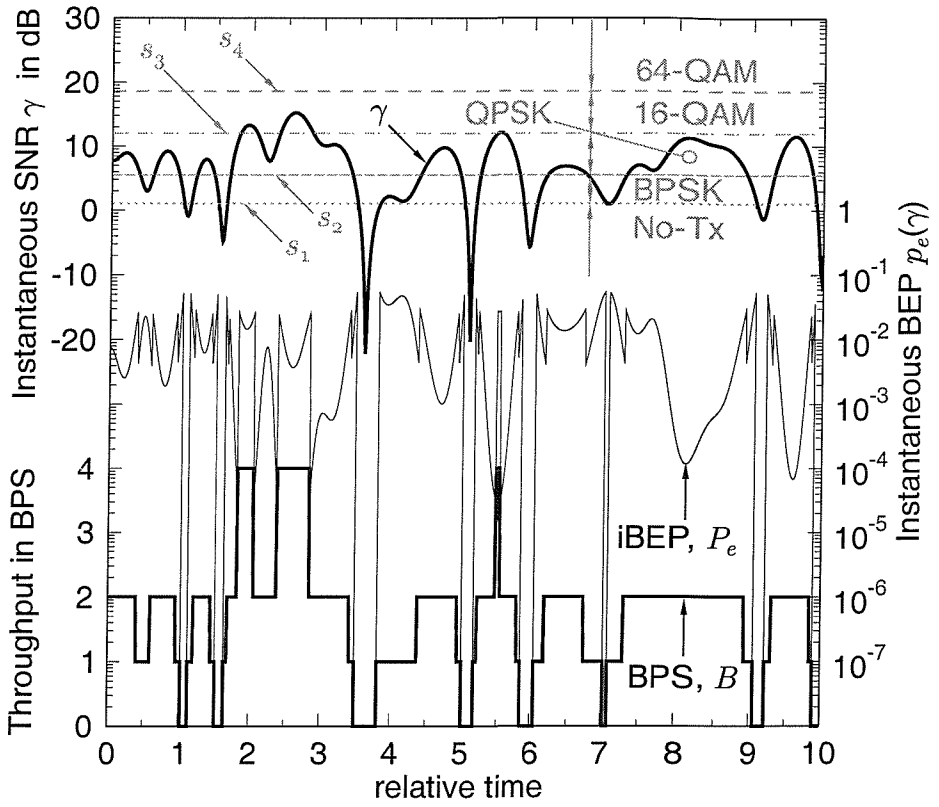

Figure 5.4: The operation of the five-mode AQAM scheme over a Rayleigh fading channel. The instantaneous channel SNR γ is represented as a thick line at the top part of the graph, the associated instantaneous BEP $P_e(\gamma)$ as a thin line at the middle, and the instantaneous BPS throughput $b(\gamma)$ as a thick line at the bottom. The average SNR is $\bar{\gamma} = 10$dB, while the target BER is $P_{target} = 10^{-2}$.

k	0	1	2	3	4	5	6
m_k	0	2	4	8	16	32	64
b_k	0	1	2	3	4	5	6
c_k	0	1	1	1	1	1	1
modem	No Tx	BPSK	QPSK	8-QAM	16-QAM	32-QAM	64-QAM

Table 5.2: The parameters of a seven-mode adaptive star-QAM system [113], where 8-QAM and 16-QAM employed four and eight constellation points allocated to two concentric rings, respectively, while 32-QAM and 64-QAM employed eight and 16 constellation points over four concentric rings, respectively.

modem parameters are summarised in Table 5.3.

k	0	1	2	3	4
m_k	0	2	4	8	16
b_k	0	1	2	3	4
c_k	0	1	1	1	1
modem	No Tx	BPSK	QPSK	8-PSK	16-PSK

Table 5.3: The parameters of the five-mode APSK system

5.3.2.4 Ten-Mode AQAM

Hole, Holm and Øien [127] studied a trellis coded adaptive modulation scheme based on eight-mode square- and cross-QAM schemes. Upon adding the No-Tx and BPSK modes, we arrive at a ten-mode AQAM scheme. The associated parameters are summarised in Table 5.4.

k	0	1	2	3	4	5	6	7	8	9
m_k	0	2	4	8	16	32	64	128	256	512
b_k	0	1	2	3	4	5	6	7	8	9
c_k	0	1	1	1	1	1	1	1	1	1
modem	No Tx	BPSK	QPSK	8-Q	16-Q	32-C	64-Q	128-C	256-Q	512-C

Table 5.4: The parameters of the ten-mode adaptive QAM scheme based on [127], where m-Q stands for m-ary square QAM and m-C for m-ary cross QAM.

5.3.3 Characteristic Parameters

In this section, we introduce several parameters in order to characterise our adaptive modulation scheme. The constituent mode selection probability (MSP) $\mathcal{M}_k$ is defined as the probability of selecting the k-th mode from the set of K possible modulation modes, which can be calculated as a function of the channel quality metric ξ, regardless of the specific metric used, as:

$$\mathcal{M}_k = \Pr[\, s_k \leq \xi < s_{k+1} \,] \tag{5.12}$$

$$= \int_{s_k}^{s_{k+1}} f(\xi)\, d\xi \,, \tag{5.13}$$

where s_k denotes the mode switching levels and $f(\xi)$ is the probability density function (PDF) of ξ. Then, the average throughput B expressed in terms of BPS can be described as:

$$B = \sum_{k=0}^{K-1} b_k \int_{s_k}^{s_{k+1}} f(\xi)\, d\xi \tag{5.14}$$

$$= \sum_{k=0}^{K-1} b_k \mathcal{M}_k \,, \tag{5.15}$$

which in simple verbal terms can be formulated as the weighted sum of the throughput b_k of the individual constituent modes, where the weighting takes into account the probability $\mathcal{M}_k$ of activating the various constituent modes. When $s_K = \infty$, the average throughput B can also be formulated as:

$$B = \sum_{k=0}^{K-1} b_k \int_{s_k}^{s_{k+1}} f(\xi)\, d\xi \tag{5.16}$$

$$= \sum_{k=0}^{K-1} \left[b_k \int_{s_k}^{\infty} f(\xi)\, d\xi - b_k \int_{s_{k+1}}^{\infty} f(\xi)\, d\xi \right] \tag{5.17}$$

$$= b_0 \int_{s_0}^{\infty} f(\xi)\, d\xi + \sum_{k=1}^{K-1} (b_k - b_{k-1}) \int_{s_k}^{\infty} f(\xi)\, d\xi \tag{5.18}$$

$$= \sum_{k=0}^{K-1} c_k \int_{s_k}^{\infty} f(\xi)\, d\xi \tag{5.19}$$

$$= \sum_{k=0}^{K-1} c_k F_c(s_k) \,, \tag{5.20}$$

where $c_k \triangleq b_k - b_{k-1}$ and $F_c(\xi)$ is the complementary Cumulative Distribution Function (CDF) defined as:

$$F_c(\xi) \triangleq \int_{\xi}^{\infty} f(x)\, dx \,. \tag{5.21}$$

Let us now assume that we use the instantaneous SNR γ as the channel quality measure ξ, which implies that no co-channel interference is present. By contrast, when operating in a co-channel interference limited environment, we can use the instantaneous SINR as the channel quality measure ξ, provided that the co-channel interference has a near-Gaussian distribution. In such scenario, the mode-specific average BER P_k can be written as:

$$P_k = \int_{s_k}^{s_{k+1}} p_{m_k}(\gamma)\, f(\gamma)\, d\gamma \,, \tag{5.22}$$

where $p_{m_k}(\gamma)$ is the BER of the m_k-ary constituent modulation mode over the AWGN channel and we used γ instead of ξ in order to explicitly indicate the employment of γ as the channel quality measure. Then, the average BEP P_{avg} of our adaptive modulation scheme can be represented as the sum of the

BEPs of the specific constituent modes divided by the average adaptive modem throughput B, formulated as [128]:

$$P_{avg} = \frac{1}{B} \sum_{k=0}^{K-1} b_k P_k \,, \tag{5.23}$$

where b_k is the BPS throughput of the k-th modulation mode, P_k is the mode-specific average BER given in (5.22) and B is the average adaptive modem throughput given in (5.15) or in (5.20).

The aim of our adaptive system is to transmit as high number of bits per symbol as possible, while providing the required QoS. More specifically, we are aiming for maximising the average BPS throughput B of (5.14), while satisfying the average BEP requirement of $P_{avg} \leq P_{target}$. Hence, we have to satisfy the constraint of meeting P_{target}, while optimising the design parameter of s, which is the set of modulation-mode switching levels. The determination of optimum switching levels will be investigated in Section 5.4. Since the calculation of the optimum switching levels typically requires the numerical computation of the parameters introduced in this section, it is advantageous to express the parameters in a closed form, which is the objective of next section.

5.3.3.1 Closed Form Expressions for Transmission over Nakagami Fading Channels

Fading channels often are modeled as Nakagami fading channels [129]. The PDF of the instantaneous channel SNR γ over a Nakagami fading channel is given as [129]:

$$f(\gamma) = \left(\frac{m}{\bar{\gamma}}\right)^m \frac{\gamma^{m-1}}{\Gamma(m)} e^{-m\gamma/\bar{\gamma}} \,, \quad \gamma \geq 0 \,, \tag{5.24}$$

where the parameter m governs the severity of fading and $\Gamma(m)$ is the Gamma function [130]. When $m = 1$, the PDF of (5.24) is reduced to the PDF of γ over Rayleigh fading channel, which is given in (5.1). As m increases, the fading behaves like Rician fading, and it becomes the AWGN channel, when m tends to ∞. Here we restrict the value of m to be a positive integer. In this case, the Nakagami fading model of (5.24), having a mean of $\bar{\gamma}_s = m\,\bar{\gamma}$, will be used to describe the PDF of the SNR per symbol γ_s in an m-antenna based diversity assisted system employing Maximal Ratio Combining (MRC).

When the instantaneous channel SNR γ is used as the channel quality measure ξ in our adaptive modulation scheme transmitting over a Nakagami channel, the parameters defined in Section 5.3.3 can be expressed in a closed form. Specifically, the mode selection probability $\mathcal{M}_k$ can be expressed as:

$$\mathcal{M}_k = \int_{s_k}^{s_{k+1}} f(\gamma)\, d\gamma \tag{5.25}$$

$$= F_c(s_k) - F_c(s_{k+1}) \,, \tag{5.26}$$

where the complementary CDF $F_c(\gamma)$ is given by:

$$F_c(\gamma) = \int_{\gamma}^{\infty} f(x)\, dx \tag{5.27}$$

$$= \int_{\gamma}^{\infty} \left(\frac{m}{\bar{\gamma}}\right)^m \frac{x^{m-1}}{\Gamma(m)}\, e^{-mx/\bar{\gamma}}\, dx \tag{5.28}$$

$$= e^{-m\gamma/\bar{\gamma}} \sum_{i=0}^{m-1} \frac{(m\gamma/\bar{\gamma})^i}{\Gamma(i+1)}\,. \tag{5.29}$$

In deriving (5.29) we used the result of the indefinite integral of [94]:

$$\int x^n e^{-ax}\, dx = -(e^{-ax}/a) \sum_{i=0}^{n} x^{n-i}/a^i\, n!/(n-i)!)\,. \tag{5.30}$$

In a Rayleigh fading scenario, *i.e.* when $m = 1$, the mode selection probability $\mathcal{M}_k$ of (5.26) can be expressed as:

$$\mathcal{M}_k = e^{-s_k/\bar{\gamma}} - e^{-s_{k+1}/\bar{\gamma}}\,. \tag{5.31}$$

The average throughput B of our adaptive modulation scheme transmitting over a Nakagami channel is given by substituting (5.29) into (5.20), yielding:

$$B = \sum_{k=0}^{K-1} c_k\, e^{-ms_k/\bar{\gamma}} \left\{ \sum_{i=0}^{m-1} \frac{(ms_k/\bar{\gamma})^i}{\Gamma(i+1)} \right\}\,. \tag{5.32}$$

Let us now derive the closed form expressions for the mode specific average BEP P_k defined in (5.22) for the various modulation modes when communicating over a Nakagami channel. The BER of a Gray-coded square QAM constellation for transmission over AWGN channels was given in (5.2) and it is repeated here for convenience:

$$p_{m_k,QAM}(\gamma) = \sum_i A_i\, Q(\sqrt{a_i\gamma})\,, \tag{5.33}$$

where the values of the constants A_i and a_i were given in (5.3). Then, the mode specific average BER $P_{k,QAM}$ of m_k-ary QAM over a Nakagami channel can be expressed in Appendix C as:

$$P_{k,QAM} = \int_{s_k}^{s_{k+1}} p_{m_k,QAM}(\gamma)\, f(\gamma)\, d\gamma \tag{5.34}$$

$$= \sum_i A_i \int_{s_k}^{s_{k+1}} Q(\sqrt{a_i\gamma}) \left(\frac{m}{\bar{\gamma}}\right)^m \frac{\gamma^{m-1}}{\Gamma(m)}\, e^{-m\gamma/\bar{\gamma}}\, d\gamma \tag{5.35}$$

$$= \sum_i A_i \left\{ -e^{-m\gamma/\bar{\gamma}}\, Q(\sqrt{a_i\gamma}) \sum_{j=0}^{m-1} \frac{(m\gamma/\bar{\gamma})^j}{\Gamma(j+1)} \right]_{s_k}^{s_{k+1}} + \sum_{j=0}^{m-1} X_j(\gamma, a_i) \Bigg]_{s_k}^{s_{k+1}} \Bigg\}\,, \tag{5.36}$$

where $g(\gamma)]_{s_k}^{s_{k+1}} \triangleq g(s_{k+1}) - g(s_k)$ and $X_j(\gamma, a_i)$ is given by:

$$X_j(\gamma, a_i) = \frac{\mu^2}{\sqrt{2a_i\pi}} \left(\frac{m}{\bar{\gamma}}\right)^j \frac{\Gamma(j+\frac{1}{2})}{\Gamma(j+1)} \sum_{k=1}^{j} \left(\frac{2\mu^2}{a_i}\right)^{j-k} \frac{\gamma^{k-\frac{1}{2}}}{\Gamma(k+\frac{1}{2})} e^{-a_i\gamma/(2\mu^2)} + \left(\frac{2\mu^2 m}{a_i\bar{\gamma}}\right)^j \frac{1}{\sqrt{\pi}} \frac{\Gamma(j+\frac{1}{2})}{\Gamma(j+1)} \mu\, Q\left(\sqrt{a_i\gamma}/\mu\right) , \quad (5.37)$$

where, again, $\mu \triangleq \sqrt{\frac{a_i\bar{\gamma}}{2+a_i\bar{\gamma}}}$ and $\Gamma(x)$ is the Gamma function.

On the other hand, the high-accuracy approximated BER formula of a Gray-coded m_k-ary PSK scheme ($k \geq 3$) transmitting over an AWGN channel is given as [131]:

$$p_{m_k,PSK} \simeq \frac{2}{k}\left\{Q\left(\sqrt{2\gamma}\sin(\pi/2^k)\right) + Q\left(\sqrt{2\gamma}\sin(3\pi/2^k)\right)\right\} \quad (5.38)$$

$$= \sum_i A_i\, Q(\sqrt{a_i\gamma}) , \quad (5.39)$$

where the set of constants $\{(A_i, a_i)\}$ is given by $\{(2/k,\ 2\sin^2(\pi/m_k)), (2/k,\ 2\sin^2(3\pi/m_k))\}$. Hence, the mode-specific average BEP $P_{k,PSK}$ can be represented using the same equation, namely (5.36), as for $P_{k,QAM}$.

5.4 Optimum Switching Levels

In this section we restrict our interest to adaptive modulation schemes employing the SNR per symbol γ as the channel quality measure ξ. We then derive the optimum switching levels as a function of the target BEP and illustrate the operation of the adaptive modulation scheme. The corresponding performance results of the adaptive modulation schemes communicating over a flat-fading Rayleigh channel are presented in order to demonstrate the effectiveness of the schemes.

5.4.1 Limiting the Peak Instantaneous BEP

The first attempt of finding the optimum switching levels that are capable of satisfying various transmission integrity requirements was made by Webb and Steele [113]. They used the BEP curves of each constituent modulation mode, obtained from simulations over an AWGN channel, in order to find the Signal-to-Noise Ratio (SNR) values, where each modulation mode satisfies the target BEP requirement [13]. This intuitive concept of determining the switching levels has been widely used by researchers [118, 122] since then. The regime proposed by Webb and Steele can be used for ensuring that the instantaneous BEP always remains below a certain threshold BEP P_{th}. In order to satisfy this constraint, the first modulation mode should be "no transmission". In this case, the set of switching levels $\mathbf{s}$ is given by:

$$\mathbf{s} = \{\, s_0 = 0,\ s_k \mid p_{m_k}(s_k) = P_{th}\ \ k \geq 1\} . \quad (5.40)$$

Figure 5.5 illustrates how this scheme operates over a Rayleigh channel, using the example of the five-mode AQAM scheme described in Section 5.3.2.1. The average SNR was $\bar{\gamma} = 10$dB and the instanta-

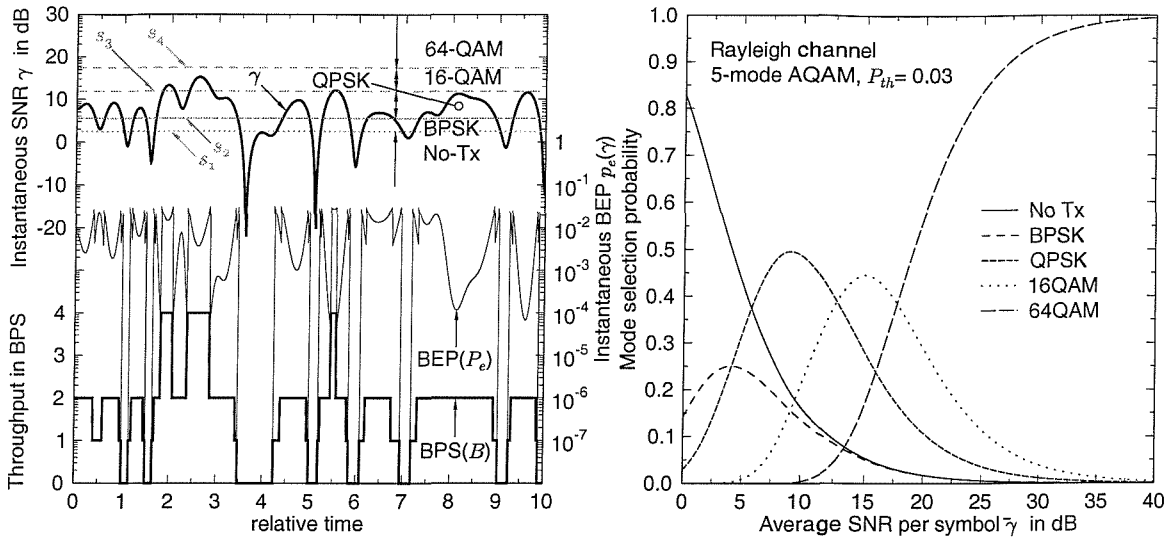

(a) operation of AQAM

(b) mode selection probability

Figure 5.5: Various characteristics of the five-mode AQAM scheme communicating over a Rayleigh fading channel employing the specific set of switching levels designed for limiting the peak instantaneous BEP to $P_{th} = 3 \times 10^{-2}$. (a) The evolution of the instantaneous channel SNR γ is represented by the thick line at the top of the graph, the associated instantaneous BER $p_e(\gamma)$ by the thin line in the middle and the instantaneous BPS throughput $b(\gamma)$ by the thick line at the bottom. The average SNR is $\bar{\gamma} = 10$dB. (b) As the average SNR increases, the higher-order AQAM modes are selected more often.

neous target BEP was $P_{th} = 3 \times 10^{-2}$. Using the expression given in (5.2) for p_{m_k}, the set of switching levels can be calculated for the instantaneous target BEP, which is given by $s_1 = 1.769$, $s_2 = 3.537$, $s_3 = 15.325$ and $s_4 = 55.874$. We can observe that the instantaneous BEP represented as a thin line by the middle of trace of Figure 5.5(a) was limited to values below $P_{th} = 3 \times 10^{-2}$.

At this particular average SNR predominantly the QPSK modulation mode was invoked. However, when the instantaneous channel quality is high, 16-QAM was invoked in order to increase the BPS throughput. The mode selection probability $\mathcal{M}_k$ of (5.26) is shown in Figure 5.5(b). Again, when the average SNR is $\bar{\gamma} = 10$dB, the QPSK mode is selected most often, namely with the probability of about 0.5. The 16-QAM, No-Tx and BPSK modes have had the mode selection probabilities of 0.15 to 0.2, while 64-QAM is not likely to be selected in this situation. When the average SNR increases, the next higher order modulation mode becomes the dominant modulation scheme one by one and eventually the highest order of 64-QAM mode of the five-mode AQAM scheme prevails.

The effects of the number of modulation modes used in our AQAM scheme on the performance are depicted in Figure 5.6. The average BER performance portrayed in Figure 5.6(a) shows that the AQAM schemes maintain an average BEP lower than the peak instantaneous BEP of $P_{th} = 3 \times 10^{-2}$ even in the low SNR region, at the cost of a reduced average throughput, which can be observed in Figure 5.6(b). As the number of the constituent modulation modes employed of the AQAM increases, the SNR regions,

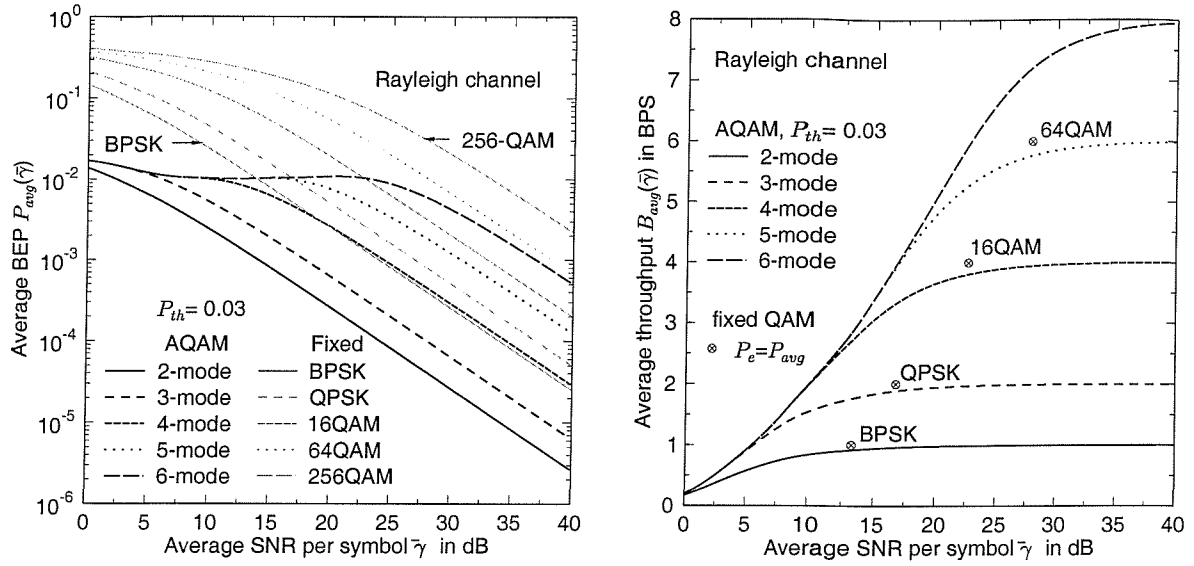

(a) average BER

(b) average throughput

Figure 5.6: The performance of AQAM employing the specific switching levels defined for limiting the peak instantaneous BEP to $P_{th} = 0.03$. (a) As the number of constituent modulation modes increases, the SNR region where the average BEP remains around $P_{avg} = 10^{-2}$ widens. (b) The SNR gains of AQAM over the fixed-mode QAM scheme required for achieving the same BPS throughput at the same average BEP of P_{avg} are in the range of 5dB to 8dB.

where the average BEP is near constant around $P_{avg} = 10^{-2}$ expands to higher average SNR values. We can observe that the AQAM scheme maintains a constant SNR gain over the highest-order constituent fixed QAM mode, as the average SNR increases, at the cost of a negligible BPS throughput degradation. This is because the AQAM activates the low-order modulation modes or disables transmissions completely, when the channel envelope is in a deep fade, in order to avoid inflicting bursts of bit errors.

Figure 5.6(b) compares the average BPS throughput of the AQAM scheme employing various numbers of AQAM modes and those of the fixed QAM constituent modes achieving the same average BER. When we want to achieve the target throughput of $B_{avg} = 1$ BPS using the AQAM scheme, Figure 5.6(b) suggest that 3-mode AQAM employing No-Tx, BPSK and QPSK is as good as four-mode AQAM, or in fact any other AQAM schemes employing more than four modes. In this case, the SNR gain achievable by AQAM is 7.7dB at the average BEP of $P_{avg} = 1.154 \times 10^{-2}$. For the average throughputs of $B_{avg} = 2$, 4 and 6, the SNR gains of the 6-mode AQAM schemes over the fixed QAM schemes are 6.65dB, 5.82dB and 5.12dB, respectively.

Figure 5.7 shows the performance of the six-mode AQAM scheme, which is an extended version of the five-mode AQAM of Section 5.3.2.1, for the peak instantaneous BEP values of $P_{th} = 10^{-1}$, 10^{-2}, 10^{-3}, 10^{-4} and 10^{-5}. We can observe in Figure 5.7(a) that the corresponding average BER P_{avg} decreases as P_{th} decreases. The average throughput curves seen in Figure 5.7(b) indicate that as anticipated the increased average SNR facilitates attaining an increased throughput by the AQAM

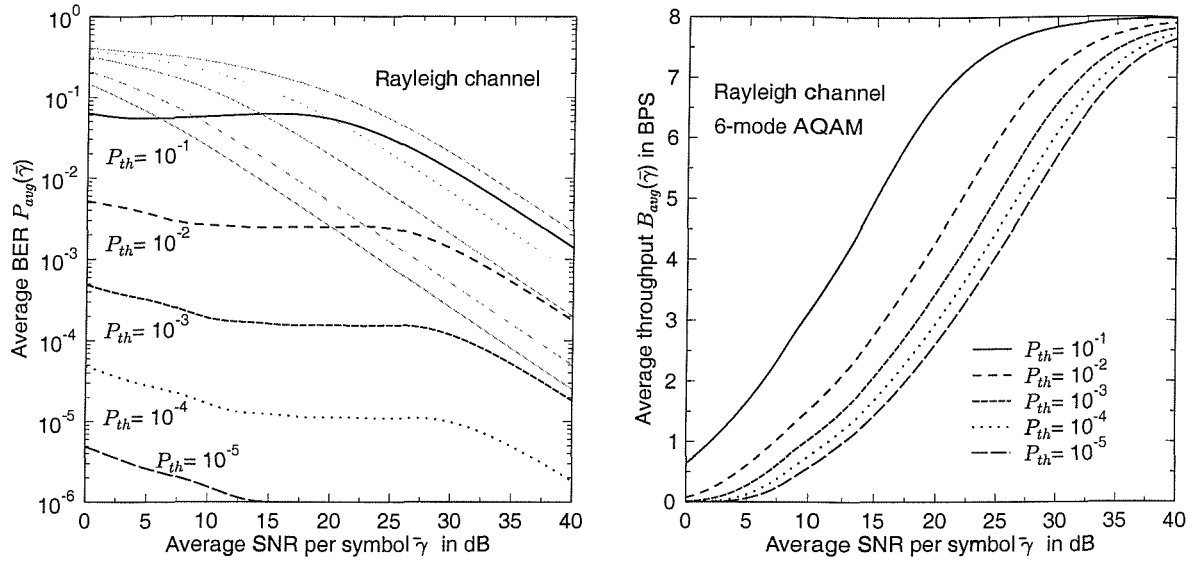

(a) average BER

(b) average throughput

Figure 5.7: The performance of the six-mode AQAM employing the switching levels of (5.40) designed for limiting the peak instantaneous BEP.

scheme and there is a clear design trade-off between the achievable average throughput and the peak instantaneous BEP. This is because predominantly lower-throughput, but more error-resilient AQAM modes have to activated, when the target BER is low. By contrast, higher-throughput but more error-sensitive AQAM modes are favoured, when the tolerable BER is increased.

In conclusion, we introduced an adaptive modulation scheme, where the objective is to limit the peak instantaneous BEP. A set of switching levels designed for meeting this objective was given in (5.40), which is independent of the underlying fading channel and the average SNR. The corresponding average BER and throughput formulas were derived in Section 5.3.3.1 and some performance characteristics of a range of AQAM schemes for transmitting over a flat Rayleigh channel were presented in order to demonstrate the effectiveness of the adaptive modulation scheme using the analysis technique developed in Section 5.3.3.1. The main advantage of this adaptive modulation scheme is in its simplicity regarding the design of the AQAM switching levels, while its drawback is that there is no direct relationship between the peak instantaneous BEP and the average BEP, which was used as our performance measure. In the next section a different switching-level optimisation philosophy is introduced and contrasted with the approach of designing the switching levels for maintaining a given peak instantaneous BEP.

5.4.2 Torrance's Switching Levels

Torrance and Hanzo [132] proposed the employment of the following cost function and applied Powell's optimisation method [58] for generating the optimum switching levels:

$$\Omega_T(\mathbf{s}) = \sum_{\bar{\gamma}=0\text{dB}}^{40\text{dB}} [10\log_{10}(\max\{P_{avg}(\bar{\gamma};\mathbf{s})/P_{th}, 1\}) + B_{max} - B_{avg}(\bar{\gamma};\mathbf{s})] \ , \tag{5.41}$$

where the average BER P_{avg} is given in (5.23), $\bar{\gamma}$ is the average SNR per symbol, $\mathbf{s}$ is the set of switching levels, P_{th} is the target average BER, B_{max} is the BPS throughput of the highest order constituent modulation mode and the average throughput B_{avg} is given in (5.14). The idea behind employing the cost function Ω_T is that of maximising the average throughput B_{avg}, while endeavoring to maintain the target average BEP P_{th}. Following the philosophy of Section 5.4.1, the minimisation of the cost function of (5.41) produces a set of constant switching levels across the entire SNR range. However, since the calculation of P_{avg} and B_{avg} requires the knowledge of the PDF of the instantaneous SNR γ per symbol, in reality the set of switching levels $\mathbf{s}$ required for maintaining a constant P_{avg} is dependent on the channel encountered and the receiver structure used.

Figure 5.8 illustrates the operation of a five-mode AQAM scheme employing *Torrance*'s SNR-independent switching levels designed for maintaining the target average BER of $P_{th} = 10^{-2}$ over a flat Rayleigh channel. The average SNR was $\bar{\gamma} = 10$dB and the target average BEP was $P_{th} = 10^{-2}$. *Powell*'s minimisation [58] involved in the context of (5.41) provides the set of optimised switching levels, given by $s_1 = 2.367$, $s_2 = 4.055$, $s_3 = 15.050$ and $s_4 = 56.522$. Upon comparing Figure 5.8(a) to Figure 5.5(a) we find that the two schemes are nearly identical in terms of activating the various AQAM modes according to the channel envelope trace, while the peak instantaneous BEP associated with Torrance's switching scheme is not constant. This is in contrast to the constant peak instantaneous BEP values seen in Figure 5.5(a). The mode selection probabilities depicted in Figure 5.8(b) are similar to those seen in Figure 5.5(b).

The average BER curves, depicted in Figure 5.9(a) show that *Torrance*'s switching levels support the AQAM scheme in successfully maintaining the target average BEP of $P_{th} = 10^{-2}$ over the average SNR range of 0dB to 20dB, when five or six modem modes are employed by the AQAM scheme. Most of the AQAM studies found in the literature have applied *Torrance*'s switching levels owing to the above mentioned good agreement between the design target P_{th} and the actual BEP performance P_{avg} [133].

Figure 5.9(b) compares the average throughputs of a range of AQAM schemes employing various numbers of AQAM modes to the average BPS throughput of fixed-mode QAM arrangements achieving the same average BEP, *i.e.* $P_e = P_{avg}$, which is not necessarily identical to the target BEP of $P_e = P_{th}$. Specifically, the SNR values required by the fixed mode scheme in order to achieve $P_e = P_{avg}$ are represented by the markers '$\otimes$', while the SNRs, where the target average BEP of $P_e = P_{th}$ is achieved, is denoted by the markers '$\odot$'. Compared to the fixed QAM schemes achieving $P_e = P_{avg}$, the SNR gains of the AQAM scheme were 9.06dB, 7.02dB, 5.81dB and 8.74dB for the BPS throughput values of 1, 2, 4 and 6, respectively. By contrast, the corresponding SNR gains compared to the fixed QAM schemes achieving $P_e = P_{th}$ were 7.55dB, 6.26dB, 5.83dB and 1.45dB. We can observe that the SNR gain of

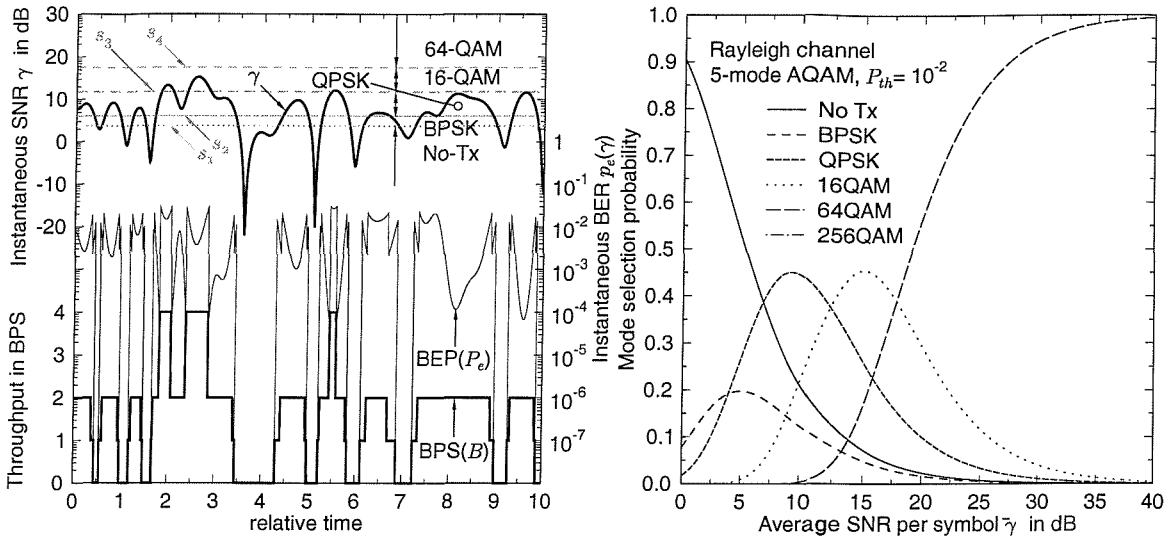

(a) operation of AQAM

(b) mode selection probability

Figure 5.8: Performance of the five-mode AQAM scheme over a flat Rayleigh fading channel employing the set of switching levels derived by Torrance and Hanzo [132] for achieving the target average BEP of $P_{th} = 10^{-2}$. (a) The instantaneous channel SNR γ is represented as a thick line at the top part of the graph, the associated instantaneous BEP $p_e(\gamma)$ as a thin line at the middle, and the instantaneous BPS throughput $b(\gamma)$ as a thick line at the bottom. The average SNR is $\bar{\gamma} = 10$dB. (b) As the SNR increases, the higher-order AQAM modes are selected more often.

the AQAM arrangement over the 64-QAM scheme achieving a BEP of $P_e = P_{th}$ is small compared to the SNR gains attained comparison to the lower-throughput fixed-mode modems. This is due to the fact that the AQAM scheme employing *Torrance*'s switching levels allows the target BER to drop at a high average SNR due to its sub-optimum thresholds, which prevents the scheme from increasing the average throughput steadily to the maximum achievable BPS throughput. This phenomenon is more visible for low target average BERs, as it can be observed in Figure 5.10.

In conclusion, we reviewed an adaptive modulation scheme employing Torrance's switching levels [132], where the objective was to maximise the average BPS throughput, while maintaining the target average BEP. Torrance's switching levels are constant across the entire SNR range and the average BEP P_{avg} of the AQAM scheme employing these switching levels shows good agreement with the target average BEP P_{th}. However, the range of average SNR values, where $P_{avg} \simeq P_{th}$ was limited up to 25dB.

5.4.3 Cost Function Optimisation as a Function of the Average SNR

In the previous section, we investigated *Torrance*'s switching levels [132] designed for achieving a certain target average BEP. However, the actual average BEP of the AQAM system was not constant across the SNR range, implying that the average throughput could potentially be further increased. Hence here we

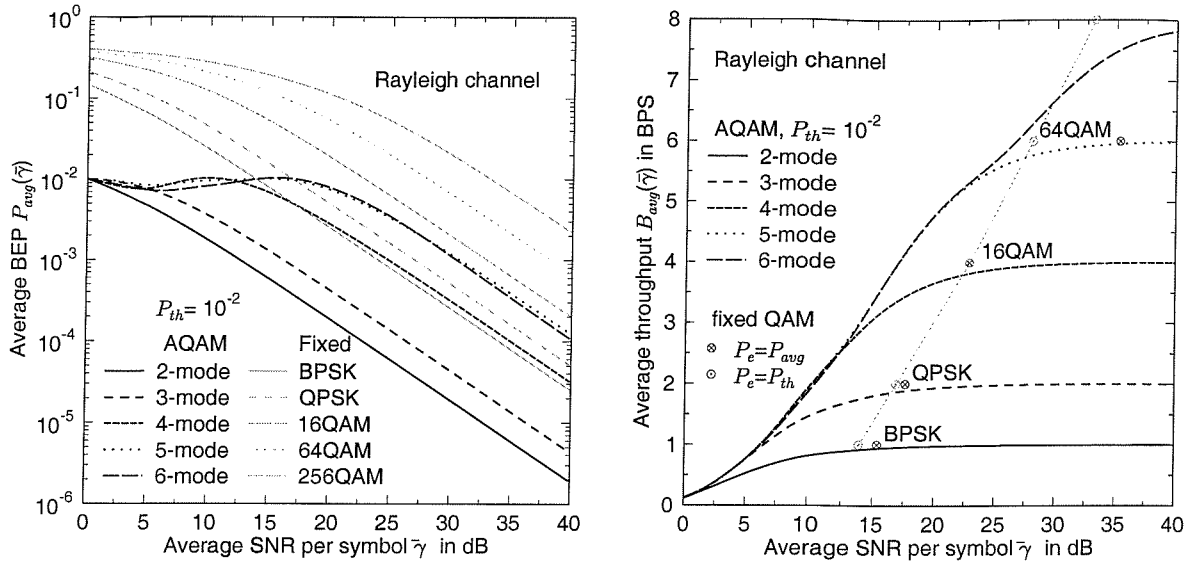

(a) average BER

(b) average throughput

Figure 5.9: The performance of various AQAM systems employing *Torrance*'s switching levels [132] designed for the target average BEP of $P_{th} = 10^{-2}$. (a) The actual average BEP P_{avg} is close to the target BEP of $P_{th} = 10^{-2}$ over an average SNR range which becomes wider, as the number of modulation modes increases. However, the five-mode and six-mode AQAM schemes have a similar performance across much of the SNR range. (b) The SNR gains of the AQAM scheme over the fixed-mode QAM arrangements, while achieving the same throughput at the same average BEP, *i.e.* $P_e = P_{avg}$, range from 6dB to 9dB, which corresponds to a 1dB improvement compared the SNR gains observed in Figure 5.6(b). However, the SNR gains over the fixed mode QAM arrangement achieving the target BEP of $P_e = P_{avg}$ are reduced, especially at high average SNR values, namely for $\bar{\gamma} > 25$dB.

propose a modified cost function $\Omega(\mathbf{s}; \bar{\gamma})$, putting more emphasis on achieving a higher throughput and optimise the switching levels for a given SNR, rather than for the whole SNR range [44]:

$$\Omega(\mathbf{s}; \bar{\gamma}) = 10 \log_{10}(\max\{P_{avg}(\bar{\gamma}; \mathbf{s})/P_{th}, 1\}) + \rho \log_{10}(B_{max}/B_{avg}(\bar{\gamma}; \mathbf{s})) , \quad (5.42)$$

where $\mathbf{s}$ is a set of switching levels, $\bar{\gamma}$ is the average SNR per symbol, P_{avg} is the average BEP of the adaptive modulation scheme given in (5.23), P_{th} is the target average BEP of the adaptive modulation scheme, B_{max} is the BPS throughput of the highest order constituent modulation mode. Furthermore, the average throughput B_{avg} is given in (5.14) and ρ is a weighting factor, facilitating the above-mentioned BPS throughput enhancement. The first term at the right hand side of (5.42) corresponds to a cost function, which account for the difference, in the logarithmic domain, between the average BEP P_{avg} of the AQAM scheme and the target BEP P_{th}. This term becomes zero, when $P_{avg} \leq P_{th}$, contributing no cost to the overall cost function Ω. On the other hand, the second term of (5.42) accounts for the logarithmic distance between the maximum achievable BPS throughput B_{max} and the average BPS throughput B_{avg} of the AQAM scheme, which decreases, as B_{avg} approaches B_{max}. Applying Powell's minimi-

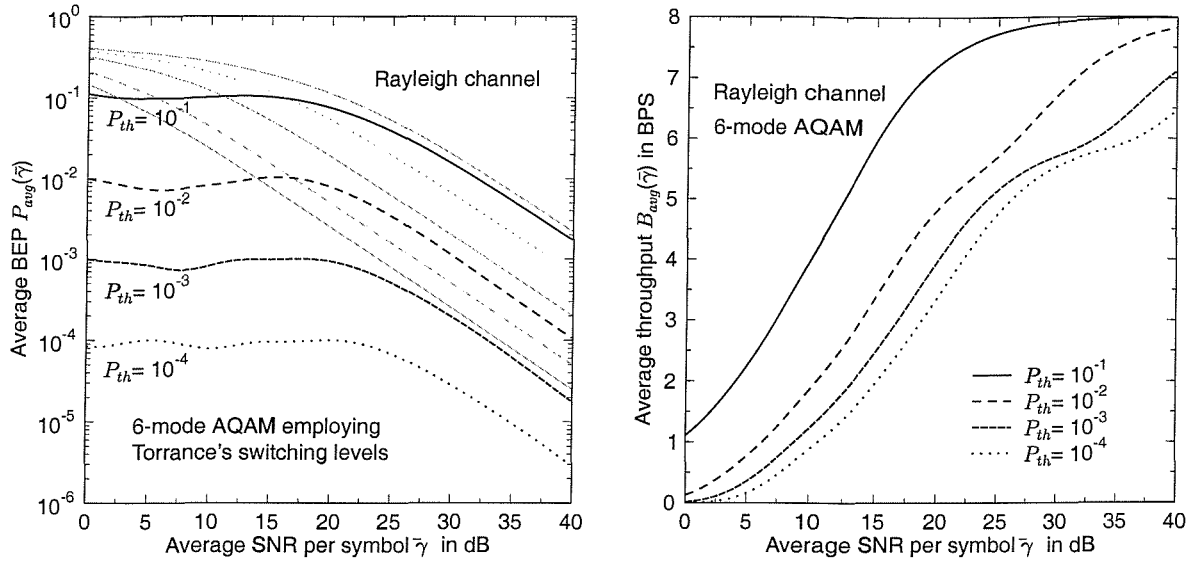

(a) average BER

(b) average throughput

Figure 5.10: The performance of the six-mode AQAM scheme employing Torrance's switching levels [132] for various target average BERs. When the average SNR is over 25dB and the target average BER is low, the average BEP of the AQAM scheme begins to decrease, preventing the scheme from increasing the average BPS throughput steadily.

sation [58] to this cost function under the constraint of $s_{k-1} \leq s_k$, the optimum set of switching levels $\mathbf{s}_{opt}(\bar{\gamma})$ can be obtained, resulting in the highest average BPS throughput, while maintaining the target average BEP.

Figure 5.11 depicts the switching levels versus the average SNR per symbol optimised in this manner for five-mode AQAM scheme achieving the target average BEP of $P_{th} = 10^{-2}$ and 10^{-3}. Since the switching levels are optimised for each specific average SNR value, they are not constant across the entire SNR range. As the average SNR $\bar{\gamma}$ increases, the switching levels decrease in order to activate the higher-order mode modulation modes more often in an effort to increase the BPS throughput. The low-order modulation modes are abandoned one by one, as $\bar{\gamma}$ increases, activating always the highest-order modulation mode, namely 64-QAM, when the average BEP of the fixed-mode 64-QAM scheme becomes lower, than the target average BEP P_{th}. Let us define the *avalanche SNR* $\bar{\gamma}_\alpha$ of a K-mode adaptive modulation scheme as the lowest SNR, where the target BEP is achieved, which can be formulated as:

$$P_{e,m_K}(\bar{\gamma}_\alpha) = P_{th} \ , \tag{5.43}$$

where m_K is the highest order modulation mode, P_{e,m_K} is the average BEP of the fixed-mode m_K-ary modem activated at the average SNR of $\bar{\gamma}$ and P_{th} is the target average BEP of the adaptive modulation scheme. We can observe in Figure 5.11 that when the average channel SNR is higher than the avalanche SNR, *i.e.* $\bar{\gamma} \geq \bar{\gamma}_\alpha$, the switching levels are reduced to zero. Some of the optimised switching level versus SNR curves exhibit glitches, indicating that the multi-dimensional optimisation might result in

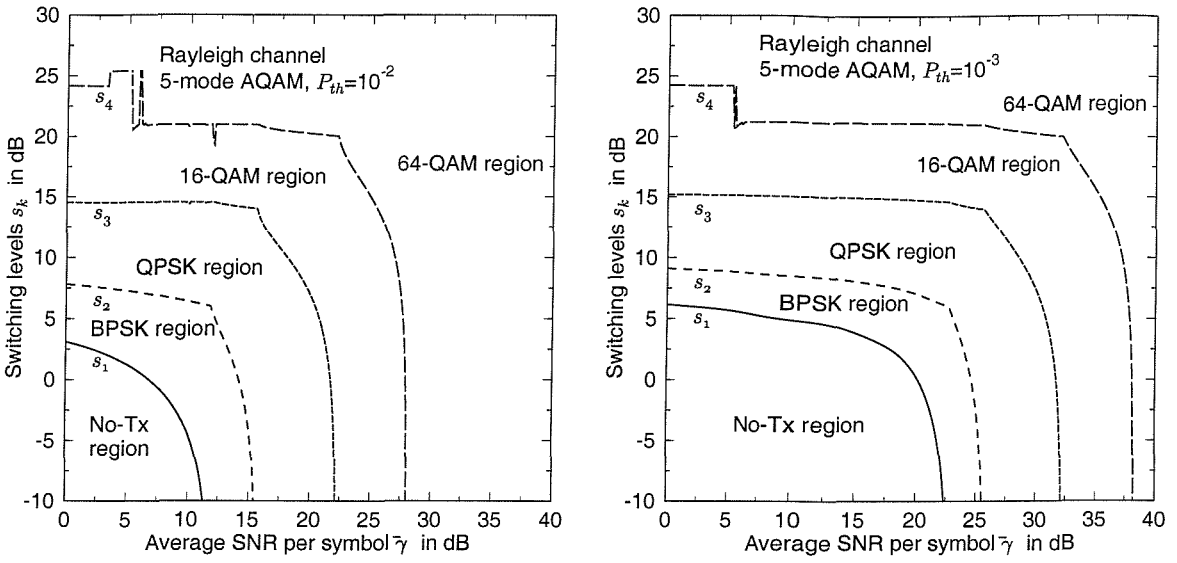

(a) $P_{th} = 10^{-2}$ (b) $P_{th} = 10^{-3}$

Figure 5.11: The switching levels optimised at each average SNR value in order to achieve the target average BER of (a) $P_{th} = 10^{-2}$ and (b) $P_{th} = 10^{-3}$. As the average SNR $\bar{\gamma}$ increases, the switching levels decrease in order to activate the higher-order mode modulation modes more often in an effort to increase the BPS throughput. The low-order modulation modes are abandoned one by one as $\bar{\gamma}$ increases, activating the highest-order modulation mode, namely 64-QAM, all the time when the average BEP of the fixed-mode 64-QAM scheme becomes lower than the target average BEP P_{th}.

local optima in some cases.

The corresponding average BEP P_{avg} and the average throughput B_{avg} of the two to six-mode AQAM schemes designed for the target average BEP of $P_{th} = 10^{-2}$ are depicted in Figure 5.12. We can observe in Figure 5.12(a) that now the actual average BEP P_{avg} of the AQAM scheme is exactly the same as the target BEP of $P_{th} = 10^{-2}$, when the average SNR $\bar{\gamma}$ is less than or equal to the avalanche SNR $\bar{\gamma}_\alpha$. As the number of AQAM modulation modes K increases, the range of average SNRs where the design target of $P_{avg} = P_{th}$ is met extends to a higher SNR, namely to the avalanche SNR. In Figure 5.12(b), the average BPS throughputs of the AQAM modems employing the 'per-SNR optimised' switching levels introduced in this section are represented in thick lines, while the BPS throughput of the six-mode AQAM arrangement employing Torrance's switching levels [132] is represented using a solid thin line. The average SNR values required by the fixed-mode QAM scheme for achieving the target average BEP of $P_{e,m_K} = P_{th}$ are represented by the markers '$\odot$'. As we can observe in Figure 5.12(b) the new per-SNR optimised scheme produces a higher BPS throughput, than the scheme using Torrance's switching regime, when the average SNR $\bar{\gamma} > 20$dB. However, for the range of 8dB $< \bar{\gamma} <$ 20dB, the BPS throughput of the new scheme is lower than that of *Torrance*'s scheme, indicating that the multi-dimensional optimisation technique might reach local minima for some SNR values.

Figure 5.13(a) shows that the six-mode AQAM scheme employing 'per-SNR optimised' switching

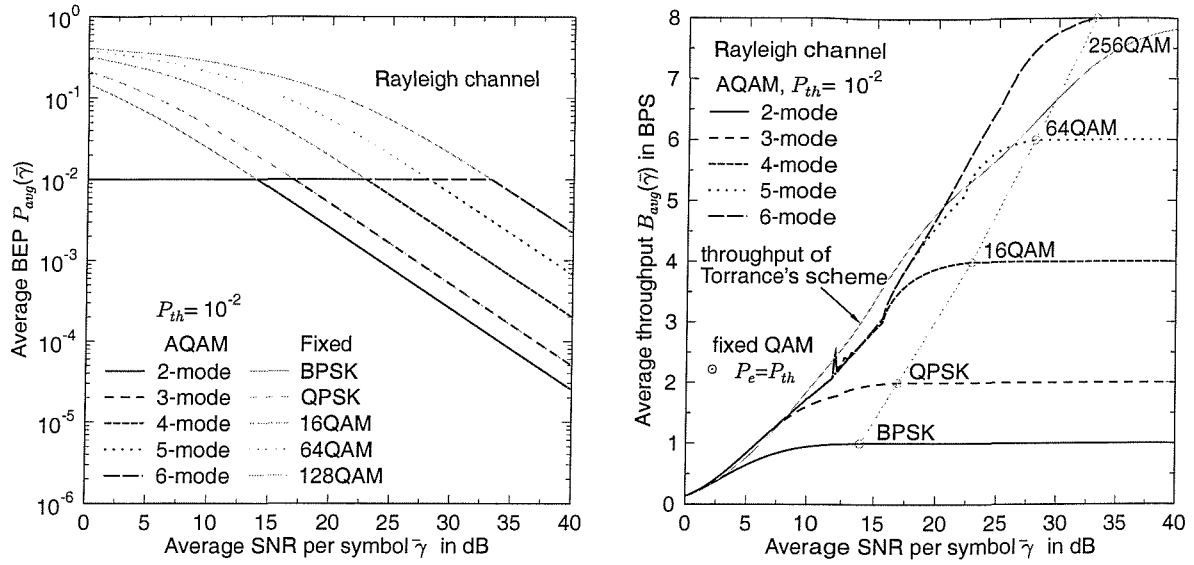

(a) average BEP

(b) average throughput

Figure 5.12: The performance of K-mode AQAM schemes for $K = 2, 3, 4, 5$ and 6, employing the switching levels optimised for each SNR value designed for the target average BEP of $P_{th} = 10^{-2}$. (a) The actual average BEP P_{avg} is exactly the same as the target BER of $P_{th} = 10^{-2}$, when the average SNR $\bar{\gamma}$ is less than or equal to the so-called avalanche SNR $\bar{\gamma}_\alpha$, where the average BEP of the highest-order fixed-modulation mode is equal to the target average BEP. (b) The average throughputs of the AQAM modems employing the 'per-SNR optimised' switching levels are represented in the thick lines, while that of the six-mode AQAM scheme employing Torrance's switching levels [132] is represented by a solid thin line.

levels satisfies the target average BEP values of $P_{th} = 10^{-1}$ to 10^{-4}. However, the corresponding average throughput performance shown in Figure 5.13(b) also indicates that the thresholds generated by the multi-dimensional optimisation were not satisfactory. The BPS throughput achieved was heavily dependent on the value of the weighting factor ρ in (5.42). The glitches seen in the BPS throughput curves in Figure 5.13(b) also suggest that the optimisation process might result in some local minima.

We conclude that due to these problems it is hard to achieve a satisfactory BPS throughput for adaptive modulation schemes employing the switching levels optimised for each SNR value based on the heuristic cost function of (5.42), while the corresponding average BEP exhibits a perfect agreement with the target average BEP.

5.4.4 Lagrangian Method

As argues in the previous section, Powell's minimisation [58] of the cost function often leads to a local minimum, rather than to the global minimum. Hence, here we adopt an analytical approach to finding the globally optimised switching levels. Our aim is to optimise the set of switching levels, $\mathbf{s}$, so that

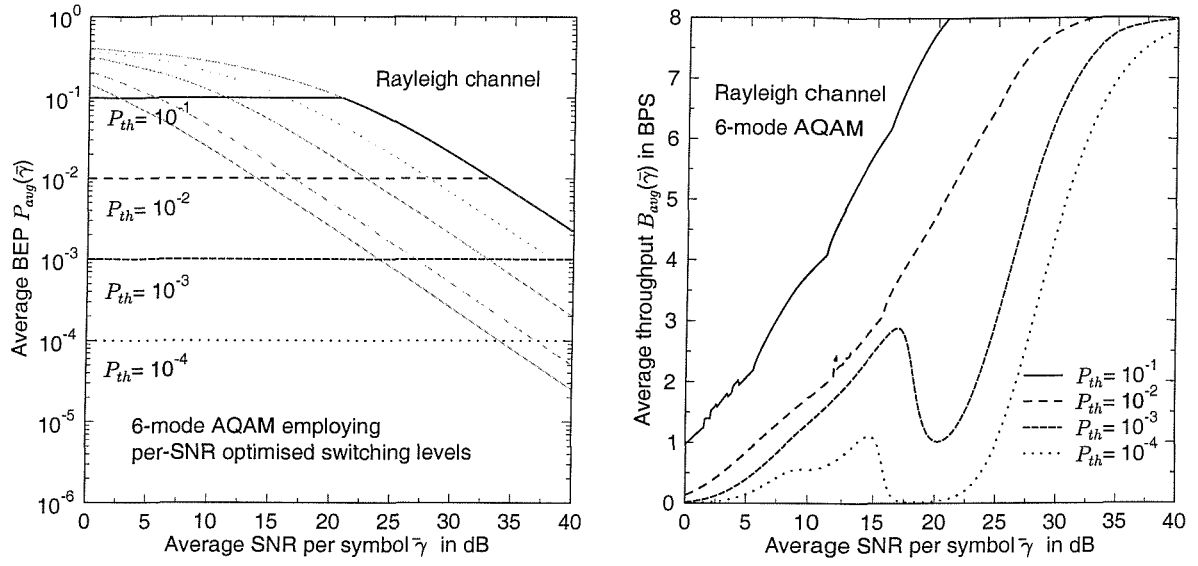

(a) average BER

(b) average throughput

Figure 5.13: The performance of six-mode AQAM employing 'per-SNR optimised' switching levels for various values of the target average BEP. (a) The average BEP P_{avg} remains constant until the average SNR $\bar{\gamma}$ reaches the avalanche SNR, then follows the average BEP curve of the highest-order fixed-mode QAM scheme, *i.e.* that of 256-QAM. (b) For some SNR values the BPS throughput performance of the six-mode AQAM scheme is not satisfactory due to the fact that the multi-dimensional optimisation algorithm becomes trapped in local minima and hence fails to reach the global minimum.

the average BPS throughput $B(\bar{\gamma};\mathbf{s})$ can be maximised under the constraint of $P_{avg}(\bar{\gamma};\mathbf{s}) = P_{th}$. Let us define P_R for a K-mode adaptive modulation scheme as the sum of the mode-specific average BEP weighted by the BPS throughput of the individual constituent mode:

$$P_R(\bar{\gamma};\mathbf{s}) \triangleq \sum_{k=0}^{K-1} b_k \, P_k \, , \tag{5.44}$$

where $\bar{\gamma}$ is the average SNR per symbol, $\mathbf{s}$ is the set of switching levels, K is the number of constituent modulation modes, b_k is the BPS throughput of the k-th constituent mode and the mode-specific average BEP P_k is given in (5.22) as:

$$P_k = \int_{s_k}^{s_{k+1}} p_{m_k}(\gamma) \, f(\gamma) \, d\gamma \, , \tag{5.45}$$

where again, $p_{m_k}(\gamma)$ is the BEP of the m_k-ary modulation scheme over the AWGN channel and $f(\gamma)$ is the PDF of the SNR per symbol γ. Explicitly, (5.45) implies weighting the BEP $p_{m_k}(\gamma)$ by its probability of occurrence quantified in terms of its PDF and then averaging, *i.e.* integrating it over the range spanning from s_k to s_{k+1}. Then, with the aid of (5.23), the average BEP constraint can also be written as:

$$P_{avg}(\bar{\gamma};\mathbf{s}) = P_{th} \iff P_R(\bar{\gamma};\mathbf{s}) = P_{th} \, B(\bar{\gamma};\mathbf{s}) \, . \tag{5.46}$$

Another rational constraint regarding the switching levels can be expressed as:

$$s_k \leq s_{k+1} \,. \tag{5.47}$$

As we discussed before, our optimisation goal is to maximise the objective function $B(\bar{\gamma}; \mathbf{s})$ under the constraint of (5.46). The set of switching levels $\mathbf{s}$ has $K+1$ levels in it. However, considering that we have $s_0 = 0$ and $s_K = \infty$ in many adaptive modulation schemes, we have $K-1$ independent variables in $\mathbf{s}$. Hence, the optimisation task is a $K-1$ dimensional optimisation under a constraint [134]. It is a standard practice to introduce a modified object function using a Lagrangian multiplier and convert the problem into a set of one-dimensional optimisation problems. The modified object function Λ can be formulated employing a Lagrangian multiplier λ [134] as:

$$\Lambda(\mathbf{s}; \bar{\gamma}) = B(\bar{\gamma}; \mathbf{s}) + \lambda \left\{ P_R(\bar{\gamma}; \mathbf{s}) - P_{th}\, B(\bar{\gamma}; \mathbf{s}) \right\} \tag{5.48}$$

$$= (1 - \lambda P_{th})\, B(\bar{\gamma}; \mathbf{s}) + \lambda P_R(\bar{\gamma}; \mathbf{s}) \,. \tag{5.49}$$

The optimum set of switching levels should satisfy:

$$\frac{\partial \Lambda}{\partial \mathbf{s}} = \frac{\partial}{\partial \mathbf{s}} \left(B(\bar{\gamma}; \mathbf{s}) + \lambda \left\{ P_R(\bar{\gamma}; \mathbf{s}) - P_{th}\, B(\bar{\gamma}; \mathbf{s}) \right\} \right) = 0 \quad \text{and} \tag{5.50}$$

$$P_R(\bar{\gamma}; \mathbf{s}) - P_{th}\, B(\bar{\gamma}; \mathbf{s}) = 0 \,. \tag{5.51}$$

The following results are helpful in evaluating the partial differentiations in (5.50) :

$$\frac{\partial}{\partial s_k} P_{k-1} = \frac{\partial}{\partial s_k} \int_{s_{k-1}}^{s_k} p_{m_{k-1}}(\gamma)\, f(\gamma)\, d\gamma = p_{m_{k-1}}(s_k)\, f(s_k) \tag{5.52}$$

$$\frac{\partial}{\partial s_k} P_k = \frac{\partial}{\partial s_k} \int_{s_k}^{s_{k+1}} p_{m_k}(\gamma)\, f(\gamma)\, d\gamma = -p_{m_k}(s_k)\, f(s_k) \tag{5.53}$$

$$\frac{\partial}{\partial s_k} F_c(s_k) = \frac{\partial}{\partial s_k} \int_{s_k}^{\infty} f(\gamma)\, d\gamma = -f(s_k) \,. \tag{5.54}$$

Using (5.52) and (5.53), the partial differentiation of P_R defined in (5.44) with respect to s_k can be written as:

$$\frac{\partial P_R}{\partial s_k} = b_{k-1}\, p_{m_{k-1}}(s_k)\, f(s_k) - b_k\, p_{m_k}(s_k)\, f(s_k) \,, \tag{5.55}$$

where b_k is the BPS throughput of an m_k-ary modem. Since the average throughput is given by $B = \sum_{k=0}^{K-1} c_k\, F_c(s_k)$ in (5.20), the partial differentiation of B with respect to s_k can be written as, using (5.54) :

$$\frac{\partial B}{\partial s_k} = -c_k\, f(s_k) \,, \tag{5.56}$$

where c_k was defined as $c_k \triangleq b_k - b_{k-1}$ in Section 5.3.1. Hence (5.50) can be evaluated as:

$$\left[-c_k(1 - \lambda\, P_{th}) + \lambda \left\{ b_{k-1}\, p_{m_{k-1}}(s_k) - b_k p_{m_k}(s_k) \right\} \right] f(s_k) = 0 \;\text{ for } k = 1, 2, \cdots, K-1 \,. \tag{5.57}$$

A trivial solution of (5.57) is $f(s_k) = 0$. Certainly, $\{s_k = \infty,\ k = 1, 2, \cdots, K-1\}$ satisfies this condition. Again, the lowest throughput modulation mode is 'No-Tx' in our model, which corresponds to no transmission. When the PDF of γ satisfies $f(0) = 0$, $\{s_k = 0,\ k = 1, 2, \cdots, K-1\}$ can also be a solution, which corresponds to the fixed-mode m_{K-1}-ary modem. The corresponding avalanche SNR $\bar{\gamma}_\alpha$ can obtained by substituting $\{s_k = 0,\ k = 1, 2, \cdots, K-1\}$ into (5.51), which satisfies:

$$p_{m_{K-1}}(\bar{\gamma}_\alpha) - P_{th} = 0\,. \tag{5.58}$$

When $f(s_k) \neq 0$, Equation (5.57) can be simplified upon dividing both sides by $f(s_k)$, yielding:

$$-c_k(1 - \lambda P_{th}) + \lambda \left\{ b_{k-1}\, p_{m_{k-1}}(s_k) - b_k p_{m_k}(s_k) \right\} = 0 \ \text{ for } k = 1, 2, \cdots, K-1\,. \tag{5.59}$$

Rearranging (5.59) for $k = 1$ and assuming $c_1 \neq 0$, we have:

$$1 - \lambda P_{th} = \frac{\lambda}{c_1} \left\{ b_0\, p_{m_0}(s_1) - b_1 p_{m_1}(s_1) \right\}. \tag{5.60}$$

Substituting (5.60) into (5.59) and assuming $c_k \neq 0$ for $k \neq 0$, we have:

$$\frac{\lambda}{c_k} \left\{ b_{k-1}\, p_{m_{k-1}}(s_k) - b_k p_{m_k}(s_k) \right\} = \frac{\lambda}{c_1} \left\{ b_0\, p_{m_0}(s_1) - b_1 p_{m_1}(s_1) \right\}. \tag{5.61}$$

In this context we note that the Lagrangian multiplier λ is not zero because substitution of $\lambda = 0$ in (5.59) leads to $-c_k = 0$, which is not true. Hence, we can eliminate the Lagrangian multiplier dividing both sides of (5.61) by λ. Then we have:

$$y_k(s_k) = y_1(s_1) \ \text{ for } k = 2, 3, \cdots K-1\,, \tag{5.62}$$

where the function $y_k(s_k)$ is defined as:

$$y_k(s_k) \triangleq \frac{1}{c_k} \left\{ b_k p_{m_k}(s_k) - b_{k-1}\, p_{m_{k-1}}(s_k) \right\}\,,\ k = 2, 3, \cdots K-1\,, \tag{5.63}$$

which does not contain the Lagrangian multiplier λ and hence it will be referred to as the 'Lagrangian-free function'. This function can be physically interpreted as the normalised BEP difference between the adjacent AQAM modes. For example, $y_1(s_1) = p_2(s_1)$ quantifies the BEP increase, when switching from the No-Tx mode to the BPSK mode, while $y_2(s_2) = 2\,p_4(s_2) - p_2(s_2)$ indicates the BEP difference between the QPSK and BPSK modes. These curve will be more explicitly discussed in the context of Figure 5.14. The significance of (5.62) is that the relationship between the optimum switching levels s_k, where $k = 2, 3, \cdots K-1$, and the lowest optimum switching level s_1 is independent of the underlying propagation scenario. Only the constituent modulation mode related parameters, such as b_k, c_k and $p_{m_k}(\gamma)$, govern this relationship.

Let us now investigate some properties of the Lagrangian-free function $y_k(s_k$ given in (5.63). Considering that $b_k > b_{k-1}$ and $p_{m_k}(s_k) > p_{m_{k-1}}(s_k)$, it is readily seen that the value of $y_k(s_k)$ is always positive. When $s_k = 0$, $y_k(s_k)$ becomes:

$$y_k(0) \triangleq \frac{1}{c_k} \left\{ b_k p_{m_k}(0) - b_{k-1}\, p_{m_{k-1}}(0) \right\} = \frac{1}{c_k} \left\{ \frac{b_k}{2} - \frac{b_{k-1}}{2} \right\} = \frac{1}{2}\,. \tag{5.64}$$

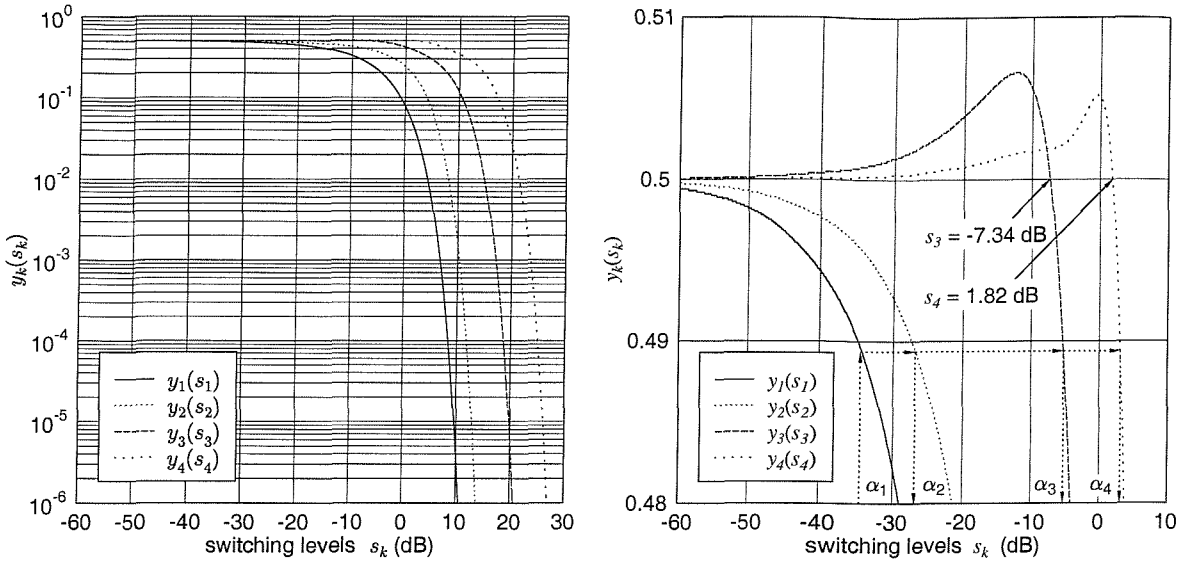

(a) global behaviour

(b) behaviour near 0.5

Figure 5.14: The Lagrangian-free functions $y_k(s_k)$ of (5.66) through (5.69) for Gray-mapped square-shaped QAM constellations. As s_k becomes lower $y_k(s_k)$ asymptotically approaches 0.5. Observe that while $y_1(s_1)$ and $y_2(s_2)$ are monotonic functions, $y_3(s_3)$ and $y_4(s_4)$ cross the $y = 0.5$ line.

The solution of $y_k(s_k) = 1/2$ can be either $s_k = 0$ or $b_k p_{m_k}(s_k) = b_{k-1} p_{m_{k-1}}(s_k)$. When $s_k = 0$, $y_k(s_k)$ becomes $y_k(\infty) = 0$. We also conjecture that

$$\frac{d\,s_k}{d\,s_1} = \frac{y_1'(s_1)}{y_k'(s_k)} > 0 \text{ when } y_k(s_k) = y_1(s_1), \tag{5.65}$$

which states that the k-th optimum switching level s_k always increases, whenever the lowest optimum switching level s_1 increases. Our numerical evaluations suggest that this conjecture appears to be true.

As an example, let us consider the five-mode AQAM scheme introduced in Section 5.3.2.1. The parameters of the five-mode AQAM scheme are summarised in Table 5.1. Substituting these parameters into (5.62) and (5.63), we have the following set of equations.

$$y_1(s_1) = p_2(s_1) \tag{5.66}$$

$$y_2(s_2) = 2\,p_4(s_2) - p_2(s_2) \tag{5.67}$$

$$y_3(s_3) = 2\,p_{16}(s_3) - p_4(s_3) \tag{5.68}$$

$$y_4(s_4) = 3\,p_{64}(s_4) - 2\,p_{16}(s_4) \tag{5.69}$$

The Lagrangian-free functions of (5.66) through (5.69) are depicted in Figure 5.14 for Gray-mapped square-shaped QAM. As these functions are basically linear combinations of BEP curves associated with AWGN channels, they exhibit waterfall-like shapes and asymptotically approach 0.5, as the switching levels s_k approach zero (or $-\infty$ expressed in dB). While $y_1(s_1)$ and $y_2(s_2)$ are monotonic functions, $y_3(s_3)$ and $y_4(s_4)$ cross the $y = 0.5$ line at $s_3 = -7.34$ dB and $s_4 = 1.82$ dB respectively, as it can be

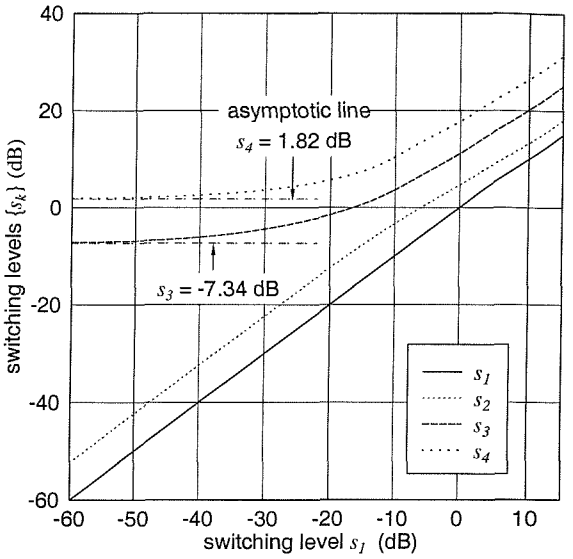

Figure 5.15: Optimum switching levels as a function of s_1. Observe that while the optimum value of s_2 shows a linear relationship with respect to s_1, those of s_3 and s_4 asymptotically approach constant values as s_1 is reduced. A low value of s_1 corresponds to a high value of average SNR.

observed in Figure 5.14(b). One should also notice that the trivial solutions of (5.62) are $y_k = 0.5$ at $s_k = 0$, $k = 1, 2, 3, 4$, as we have discussed before.

For a given value of s_1, the other switching levels can be determined as $s_2 = y_2^{-1}(y_1(s_1))$, $s_3 = y_3^{-1}(y_1(s_1))$ and $s_4 = y_4^{-1}(y_1(s_1))$. Since deriving the analytical inverse function of y_k is an arduous task, we can rely on a graphical or a numerical method. Figure 5.14(b) illustrates an example of the graphical method. Specifically, when $s_1 = \alpha_1$, we first find the point on the curve y_1 directly above the abscissa value of α_1 and then draw a horizontal line across the corresponding point. From the crossover points found on the curves of y_2, y_3 and y_4 with the aid of the horizontal line, we can find the corresponding values of the other switching levels, namely those of α_2, α_3 and α_4. In a numerical sense, this solution corresponds to a one-dimensional (1-D) root finding problem [58, Ch 9]. Furthermore, the $y_k(s_k)$ values are monotonic, provided that we have $y_k(s_k) < 0.5$ and this implies that the roots found are unique. The numerical results shown in Figure 5.15 represent the direct relationship between the optimum switching level s_1 and the other optimum switching levels, namely s_2, s_3 and s_4. While the optimum value of s_2 shows a near-linear relationship with respect to s_1, those of s_3 and s_4 asymptotically approach two different constants, as s_1 becomes smaller. This corroborates the trends observed in Figure 5.14(b), where $y_3(s_3)$ and $y_4(s_4)$ cross the $y = 0.5$ line at $s_3 = -7.34$ dB and $s_4 = 1.82$ dB, respectively. Since the low-order modulation modes are abandoned at high average channel SNRs in order to increase the average throughput, the high values of s_1 on the horizontal axis of Figure 5.15 indicate encountering a low channel SNR, while low values of s_1 suggest that high channel SNRs are experienced, as it transpires for example from Figure 5.11.

Since we can relate the other switching levels to s_1, we have to determine the optimum value of s_1 for the given target BEP, P_{th}, and the PDF of the instantaneous channel SNR, $f(\gamma)$, by solving the

constraint equation given in (5.51). This problem also constitutes a 1-D root finding problem, rather than a multi-dimensional optimisation problem, which was the case in Sections 5.4.2 and 5.4.3 . Let us define the constraint function $Y(\bar{\gamma}; \mathbf{s}(s_1))$ using (5.51) as:

$$Y(\bar{\gamma}; \mathbf{s}(s_1)) \triangleq P_R(\bar{\gamma}; \mathbf{s}(s_1)) - P_{th}\, B(\bar{\gamma}; \mathbf{s}(s_1)), \tag{5.70}$$

where we represented the set of switching levels as a vector, which is the function of s_1, in order to emphasise that s_k satisfies the relationships given by (5.62) and (5.63). More explicitly, $Y(\bar{\gamma}; \mathbf{s}(s_1))$ of (5.70) can be physically interpreted as the difference between $P_R(\bar{\gamma}; \mathbf{s}(s_1))$, namely the sum of the mode-specific average BEPs weighted by the BPS throughput of the individual AQAM modes, as defined in (5.44) and the average BPS throughput $B(\bar{\gamma}; \mathbf{s}(s_1))$ weighted by the target BEP P_{th}. Considering the equivalence relationship given in (5.46), (5.70) reflects just another way of expressing the difference between the average BEP P_{avg} of the adaptive scheme and the target BEP P_{th}. Even though the relationships implied in $\mathbf{s}(s_1)$ are independent of the propagation conditions and the signaling power, the constraint function $Y(\bar{\gamma}; \mathbf{s}(s_1))$ of (5.70) and hence the actual values of the optimum switching levels are dependent on propagation conditions through the PDF $f(\gamma)$ of the SNR per symbol and on the average SNR per symbol $\bar{\gamma}$.

Let us find the initial value of $Y(\bar{\gamma}; \mathbf{s}(s_1))$ defined in (5.70), when $s_1 = 0$. An obvious solution for s_k when $s_1 = 0$ is $s_k = 0$ for $k = 1, 2, \cdots, K-1$. In this case, $Y(\bar{\gamma}; \mathbf{s}(s_1))$ becomes:

$$Y(\bar{\gamma}; 0) = b_{K-1}\,(P_{m_{K-1}}(\bar{\gamma}) - P_{th}), \tag{5.71}$$

where b_{K-1} is the BPS throughput of the highest-order constituent modulation mode, $P_{m_{K-1}}(\bar{\gamma})$ is the average BEP of the highest-order constituent modulation mode for transmission over the underlying channel scenario and P_{th} is the target average BEP. The value of $Y(\bar{\gamma}; 0)$ could be positive or negative, depending on the average SNR $\bar{\gamma}$ and on the target average BEP P_{th}. Another solution exists for s_k when $s_1 = 0$, if $b_k\, p_{m_k}(s_k) = b_{k-1}\, p_{m_{k-1}}(s_k)$. The value of $Y(\bar{\gamma}; 0^+)$ using this alternative solution turns out to be close to $Y(\bar{\gamma}; 0)$. However, in the actual numerical evaluation of the initial value of Y, we should use $Y(\bar{\gamma}; 0^+)$ for ensuring the continuity of the function Y at $s_1 = 0$.

In order to find the minima and the maxima of Y, we have to evaluate the derivative of $Y(\bar{\gamma}; \mathbf{s}(s_1))$ with respect to s_1, which can be expressed as:

$$\frac{dY}{ds_1} = \sum_{k=1}^{K-1} \frac{\partial Y}{\partial s_k} \frac{ds_k}{ds_1} \tag{5.72}$$

$$= \sum_{k=1}^{K-1} \frac{\partial}{\partial s_k} \{P_R - P_{th}\, B\} \frac{ds_k}{ds_1}\,. \tag{5.73}$$

Upon applying (5.52) through (5.56) into (5.73) we have:

$$\begin{aligned}\frac{dY}{ds_1} &= \sum_{k=1}^{K-1} \left\{ b_{k-1}\, p_{m_{k-1}}(s_k) - b_k\, p_{m_k}(s_k) + P_{th}\, c_k \right\} f(s_k)\, \frac{ds_k}{ds_1} \\ &= \sum_{k=1}^{K-1} \left[\frac{c_k}{c_1} \left\{ b_0\, p_{m_0}(s_1) - b_1\, p_{m_1}(s_1) \right\} + P_{th}\, c_k \right] f(s_k)\, \frac{ds_k}{ds_1} \\ &= \frac{1}{c_1} \left\{ b_0\, p_{m_0}(s_1) - b_1\, p_{m_1}(s_1) + P_{th} \right\} \sum_{k=1}^{K-1} c_k\, f(s_k)\, \frac{ds_k}{ds_1} . \end{aligned} \tag{5.74}$$

Considering $f(s_k) \geq 0$ and using our conjecture that $\frac{ds_k}{ds_1} > 0$ given in (5.65), we can conclude from (5.74) that $\frac{dY}{ds_1} = 0$ has roots, when $f(s_k) = 0$ for all k or when $b_1\, p_{m_1}(s_1) - b_0\, p_{m_0}(s_1) = P_{th}$. The former condition corresponds to either $s_i = 0$ for some PDF $f(\gamma)$ or to $s_k = \infty$ for all PDFs. By contrast, when the condition of $b_1\, p_{m_1}(s_1) - b_0\, p_{m_0}(s_1) = P_{th}$ is met, $dY/ds_1 = 0$ has a unique solution. Investigating the sign of the first derivative between these zeros and using the mini-max analysis, which will be described with the aid of (5.75) and (5.82), we can conclude that $Y(\bar{\gamma}; s_1)$ has a global minimum of $Y_{min} < 0$ at $s_1 = \zeta$ such that $b_1\, p_{m_1}(\zeta) - b_0\, p_{m_0}(\zeta) = P_{th}$ and a maximum of Y_{max1} at $s_1 = 0$, as well as another maximum value $Y_{max2} = 0^-$ at $s_1 = \infty$. **This implies that there exist a unique set of optimum switching levels when $Y_{max1} > 0$ at $s_1 = 0$.**

Since $Y(\bar{\gamma}; s_1)$ has a maximum value at $s_1 = \infty$, let us find the corresponding maximum value. Let us first consider $\lim_{s_1 \to \infty} P_{avg}(\bar{\gamma}; \mathbf{s}(s_1))$, where upon exploiting (5.23) and (5.44) we have:

$$\lim_{s_1 \to \infty} P_{avg}(\bar{\gamma}; s_k) = \frac{\lim_{s_1 \to \infty} P_R}{\lim_{s_1 \to \infty} B} \tag{5.75}$$

$$= \frac{0}{0} . \tag{5.76}$$

When applying l'Hopital's rule and using Equations (5.52) through (5.56), we have:

$$\frac{\lim_{s_1 \to \infty} P_R}{\lim_{s_1 \to \infty} B} = \frac{\lim_{s_1 \to \infty} \frac{d}{ds_1} P_R}{\lim_{s_1 \to \infty} \frac{d}{ds_1} B} \tag{5.77}$$

$$= \lim_{s_1 \to \infty} \frac{1}{c_1}\, b_1\, p_{m_1}(s_1) - b_0\, p_{m_0}(s_1) \tag{5.78}$$

$$= 0^+ , \tag{5.79}$$

implying that $P_{avg}(\bar{\gamma}; s_k)$ approaches zero from positive values, when s_1 tends to ∞. Since according to (5.23), (5.44) and (5.70) the function $Y(\bar{\gamma}; \mathbf{s}(s_1))$ can be written as $B(P_{avg} - P_{th})$, we have:

$$\lim_{s_1 \to \infty} Y(\bar{\gamma}; s_1) = \lim_{s_1 \to \infty} B(P_{avg} - P_{th}) \tag{5.80}$$

$$= \lim_{s_1 \to \infty} B(0^+ - P_{th}) \tag{5.81}$$

$$= 0^- , \tag{5.82}$$

Hence $Y(\bar{\gamma}; \mathbf{s}(s_1))$ asymptotically approaches zero from negative values, as s_1 tends to ∞. From the

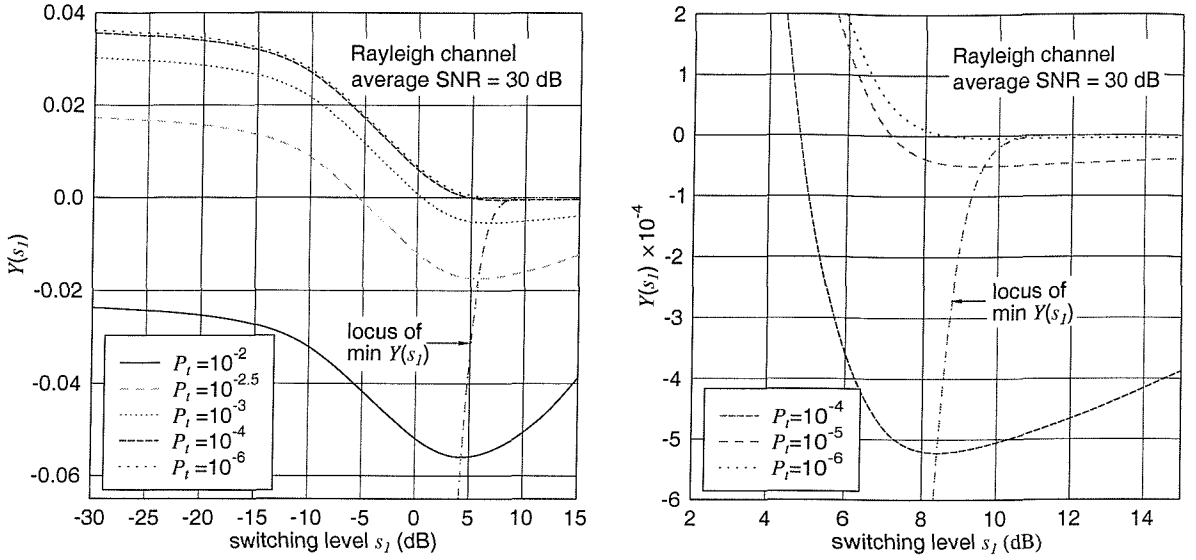

(a) global behaviour

(b) behaviour near $Y(s_1) = 0$

Figure 5.16: The constraint function $Y(\bar{\gamma}; \mathbf{s}(s_1))$ defined in (5.70) for our five-mode AQAM scheme employing Gray-mapped square-constellation QAM operating over a flat Rayleigh fading channel. The average SNR was $\bar{\gamma} = 30$ dB and it is seen that Y has a single minimum value, while approaching 0^-, as s_1 increases. The solution of $Y(\bar{\gamma}; \mathbf{s}(s_1)) = 0$ exists, when $Y(\bar{\gamma}; 0) = 6\{p_{64}(\bar{\gamma}) - P_{th}\} > 0$ and is unique.

analysis of the minimum and the maxima, we can conclude that the constraint function $Y(\bar{\gamma}; \mathbf{s}(s_1))$ defined in (5.70) has a unique zero only if $Y(\bar{\gamma}; 0^+) > 0$ at a switching value of $0 < s_1 < \zeta$, where ζ satisfies $b_1 p_{m_1}(\zeta) - b_0 p_{m_0}(\zeta) = P_{th}$. By contrast, when $Y(\bar{\gamma}; 0^+) < 0$, the optimum switching levels are all zero and the adaptive modulation scheme always employs the highest-order constituent modulation mode.

As an example, let us evaluate the constraint function $Y(\bar{\gamma}; s_1)$ for our five-mode AQAM scheme operating over a flat Rayleigh fading channel. Figure 5.16 depicts the values of $Y(s_1)$ for several values of the target average BEP P_{th}, when the average channel SNR is 30dB. We can observe that $Y(s_1) = 0$ may have a root, depending on the target BEP P_{th}. When $s_k = 0$ for $k < 5$, according to (5.23), (5.44) and (5.70) $Y(s_1)$ is reduced to

$$Y(\bar{\gamma}; 0) = 6(P_{64}(\bar{\gamma}) - P_{th}) , \tag{5.83}$$

where $P_{64}(\bar{\gamma})$ is the average BEP of 64-QAM over a flat Rayleigh channel. The value of $Y(\bar{\gamma}; 0)$ in (5.83) can be negative or positive, depending on the target BEP P_{th}.

We can observe in Figure 5.16 that the solution of $Y(\bar{\gamma}; \mathbf{s}(s_1)) = 0$ is unique, when it exists. The locus of the minimum $Y(s_1)$, *i.e.* the trace curve of points $(Y_{min}(s_{1,min}), s_{1,min})$, where Y has the minimum value, is also depicted in Figure 5.16. The locus is always below the horizontal line of $Y(s_1) = 0$ and asymptotically approaches this line, as the target BEP P_{th} becomes smaller.

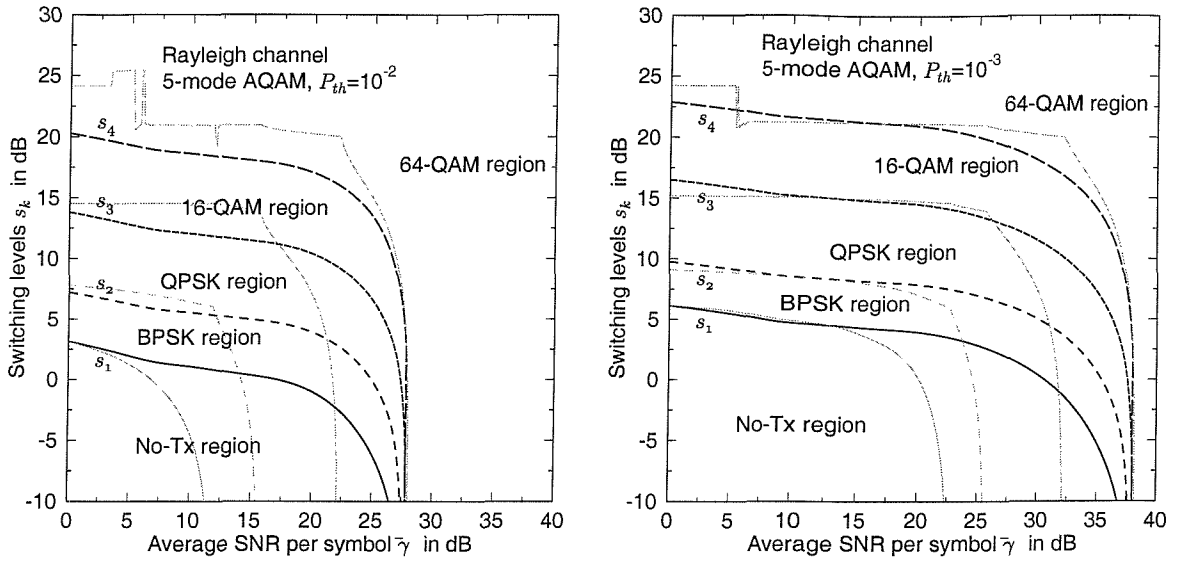

(a) $P_{th} = 10^{-2}$ (b) $P_{th} = 10^{-3}$

Figure 5.17: The switching levels for our five-mode AQAM scheme optimised at each average SNR value in order to achieve the target average BEP of (a) $P_{th} = 10^{-2}$ and (b) $P_{th} = 10^{-3}$ using the Lagrangian multiplier based method of Section 5.4.4. The switching levels based on Powell's optimisation are represented in thin grey lines for comparison.

Figure 5.17 depicts the switching levels optimised in this manner for our five-mode AQAM scheme maintaining the target average BEPs of $P_{th} = 10^{-2}$ and 10^{-3}. The switching levels obtained using Powell's optimisation method in Section 5.4.3 are represented as the thin grey lines in Figure 5.17 for comparison. In this case all the modulation modes may be activated with a certain probability, until the average SNR reaches the avalanche SNR value, while the scheme derived using Powell's optimisation technique abandons the lower throughput modulation modes one by one, as the average SNR increases.

Figure 5.18 depicts the average throughput B expressed in BPS of the AQAM scheme employing the switching levels optimised using the Lagrangian method. In Figure 5.18(a), the average throughput of our six-mode AQAM arrangement using Torrance's scheme discussed in Section 5.4.2 is represented as a thin grey line. The Lagrangian multiplier based scheme showed SNR gains of 0.6dB, 0.5dB, 0.2dB and 3.9dB for a BPS throughput of 1, 2, 4 and 6, respectively, compared to Torrance's scheme. The average throughput of our six-mode AQAM scheme is depicted in Figure 5.18(b) for the several values of P_{th}, where the corresponding BPS throughput of the AQAM scheme employing per-SNR optimised thresholds determined using Powell's method are also represented as thin lines for $P_{th} = 10^{-1}$, 10^{-2} and 10^{-3}. Comparing the BPS throughput curves, we can conclude that the per-SNR optimised Powell method of Section 5.4.3 resulted in imperfect optimisation for some values of the average SNR.

In conclusion, we derived an optimum mode-switching regime for a general AQAM scheme using the Lagrangian multiplier method and presented our numerical results for various AQAM arrangement. Since the results showed that the Lagrangian optimisation based scheme is superior in comparison to

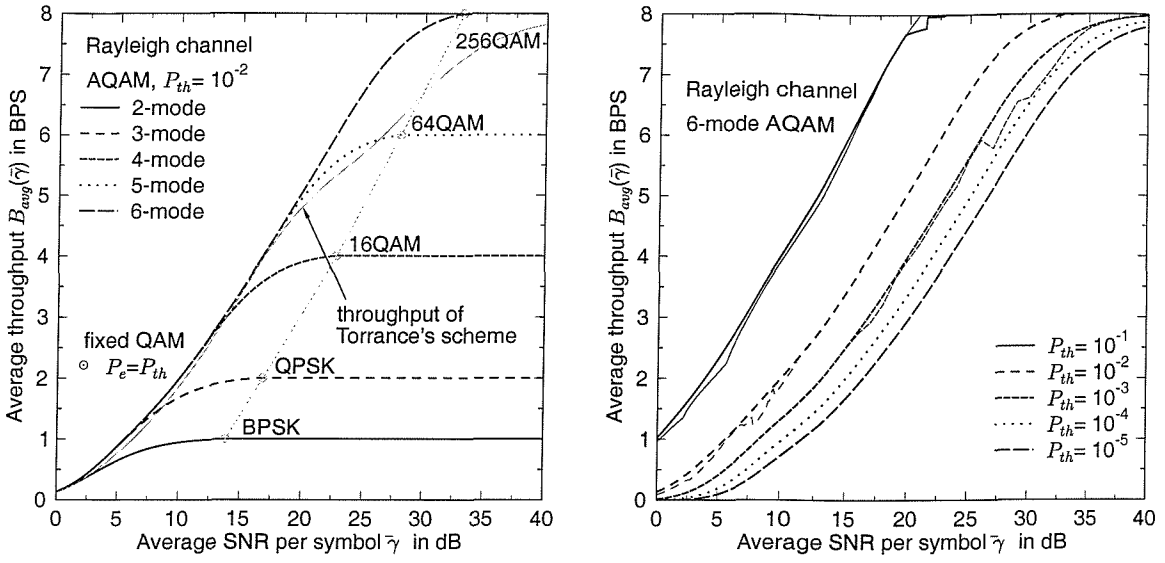

(a) $P_{th} = 10^{-2}$ (b) 6-mode AQAM

Figure 5.18: The average BPS throughput of various AQAM schemes employing the switching levels optimised using the Lagrangian multiplier method (a) for $P_{th} = 10^{-2}$ employing two to six-modes and (b) for $P_{th} = 10^{-2}$ to $P_{th} = 10^{-5}$ using six-modes. The average throughput of the six-mode AQAM scheme using Torrance's switching levels [132] is represented for comparison as the thin grey line in figure (a). The average throughput of the six-mode AQAM scheme employing per-SNR optimised thresholds using Powell's optimisation method are represented by the thin lines in figure (b) for the target average BEP of $P_{th} = 10^{-1}$, 10^{-2} and 10^{-3}.

the other methods investigated, we will employ these switching levels in order to further investigate the performance of various adaptive modulation schemes.

5.5 Results and Discussions

The average throughput performance of adaptive modulation schemes employing the globally optimised mode-switching levels of Section 5.4.4 is presented in this section. The mobile channel is modelled as a Nakagami-m fading channel. The performance results and discussions include the effects of the fading parameter m, that of the number of modulation modes, the influence of the various diversity schemes used and the range of Square QAM, Star QAM and MPSK signalling constellations.

5.5.1 Narrow-band Nakagami-m Fading Channel

The PDF of the instantaneous channel SNR γ of a system transmitting over the Nakagami fading channel is given in (5.24). The parameters characterising the operation of the adaptive modulation scheme were summarised in Section 5.3.3.1.

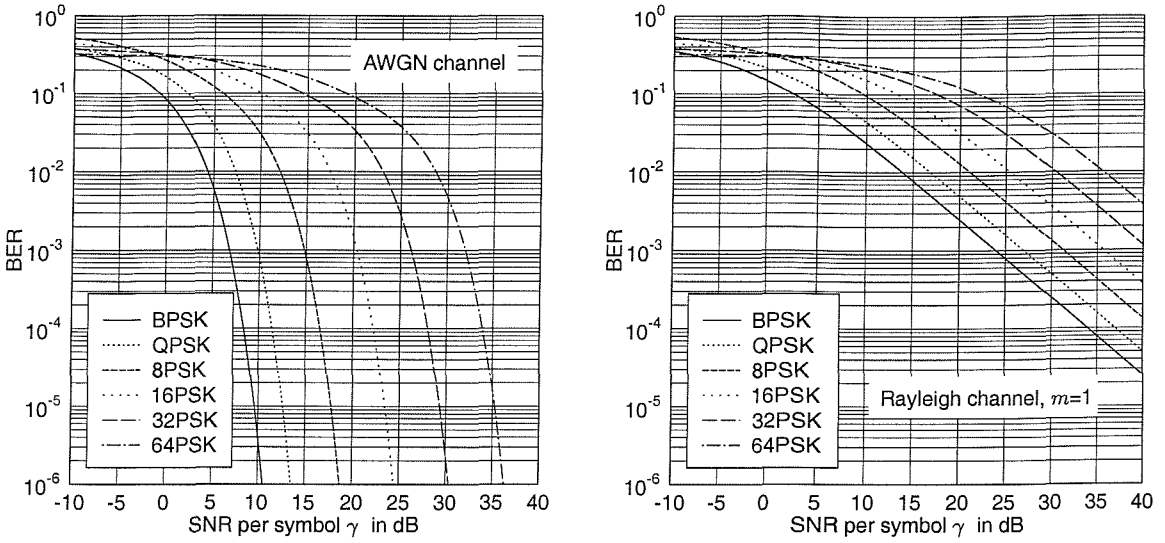

(a) AWGN Channel

(b) Rayleigh Channel, $m = 1$

Figure 5.19: The average BER of various MPSK modulation schemes

5.5.1.1 Adaptive PSK Modulation Schemes

Phase Shift Keying (PSK) has the advantage of exhibiting a constant envelope power, since all the constellation points are located on a circle. Let us first consider the BER of fixed-mode PSK schemes as a reference, so that we can compare the performance of adaptive PSK and fixed-mode PSK schemes. The BER of Gray-coded coherent M-ary PSK (MPSK), where $M = 2^k$, for transmission over the AWGN channel can be closely approximated by [131]:

$$p_{MPSK}(\gamma) \simeq \sum_{i=1}^{2} A_i \, Q(\sqrt{a_i \gamma}\,) \,, \tag{5.84}$$

where $M \geq 8$ and the associated constants are given by [131]:

$$A_1 = A_2 = 2/k \tag{5.85}$$

$$a_1 = 2\sin^2(\pi/M) \tag{5.86}$$

$$a_2 = 2\sin^2(3\pi/M) \,. \tag{5.87}$$

Figure 5.19(a) shows the BER of BPSK, QPSK, 8PSK, 16PSK, 32PSK and 64PSK for transmission over the AWGN channel. The differences of the required SNR per symbol, in order to achieve the BER of $p_{MPSK}(\gamma) = 10^{-6}$ for the modulation modes having a throughput difference of 1 BPS are around 6dB, except between BPSK and QPSK, where a 3dB difference is observed.

The average BER of MPSK schemes over a flat Nakagami-m fading channel is given as:

$$P_{MPSK}(\bar{\gamma}) = \int_0^\infty p_{MPSK}(\gamma)\, f(\gamma)\, d\gamma \,, \tag{5.88}$$

where the BEP $p_{MPSK}(\gamma)$ for a transmission over the AWGN channel is given by (5.84) and the PDF $f(\gamma)$ is given by (5.24). A closed form solution of (5.88) can be readily obtained for an integer m using the results given in [25, (14-4-15)], which can be expressed as:

$$P_{MPSK}(\bar{\gamma}) = \sum_{i=1}^{2} A_i \left[\tfrac{1}{2}(1-\mu_i)\right]^m \sum_{j=0}^{m-1} \binom{m-1+j}{j} \left[\tfrac{1}{2}(1+\mu_i)\right]^j , \tag{5.89}$$

where μ_i is defined as:

$$\mu_i \triangleq \sqrt{\frac{a_i\bar{\gamma}}{2m + a_i\bar{\gamma}}} . \tag{5.90}$$

Figure 5.19(b) shows the average BER of the various MPSK schemes for transmission over a flat Rayleigh channel, where $m = 1$. The BER of MPSK over the AWGN channel given in (5.84) and that over a Nakagami channel given in (5.89) will be used in comparing the performance of adaptive PSK schemes.

The parameters of our nine-mode adaptive PSK scheme are summarised in Table 5.5 following the definitions of our generic model used for the adaptive modulation schemes developed in Section 5.3.1. The models of other adaptive PSK schemes employing a different number of modes can be readily obtained by increasing or reducing the number of columns in Table 5.5. Since the number of modes is

k	0	1	2	3	4	5	6	7	8
m_k	0	2	4	8	16	32	64	128	256
b_k	0	1	2	3	4	5	6	7	8
c_k	0	1	1	1	1	1	1	1	1
mode	No Tx	BPSK	QPSK	8PSK	16PSK	32PSK	64PSK	128PSK	256PSK

Table 5.5: Parameters of a nine-mode adaptive PSK scheme following the definitions of the generic adaptive modulation model developed in Section 5.3.1.

$K = 9$, we have $K + 1 = 10$ mode-switching levels, which are hosted by the vector $\mathbf{s} = \{s_k \mid k = 0, 1, 2, \cdots, 9\}$. Let us assume $s_0 = 0$ and $s_9 = \infty$. In order to evaluate the performance of the nine-mode adaptive PSK scheme, we have to obtain the optimum switching levels first. Let us evaluate the 'Lagrangian-free' functions defined in (5.63), using the parameters given in Table 5.5 and the BER expressions given in (5.84). The 'Lagrangian-free' functions of our nine-mode adaptive PSK scheme are depicted in Figure 5.20. We can observe that there exist two solutions for s_k satisfying $y_k(s_k) = y_1(s_1)$ for a given value of s_1, which are given by the crossover points over the horizontal lines at the various coordinate values scaled on the vertical axis. However, only the higher value of s_k satisfies the constraint of $s_{k-1} \leq s_k$, $\forall\ k$. The enlarged view near $y_k(s_k) = 0.5$ seen in Figure 5.20(b) reveals that $y_4(s_4)$ may have no solution of $y_4(s_4) = y_1(s_1)$, when $y_1(s_1) > 0.45$. One option is to use a constant value of $s_4 = 2.37$dB, where $y_4(s_4)$ reaches its peak value. The other option is to set $s_4 = s_3$, effectively

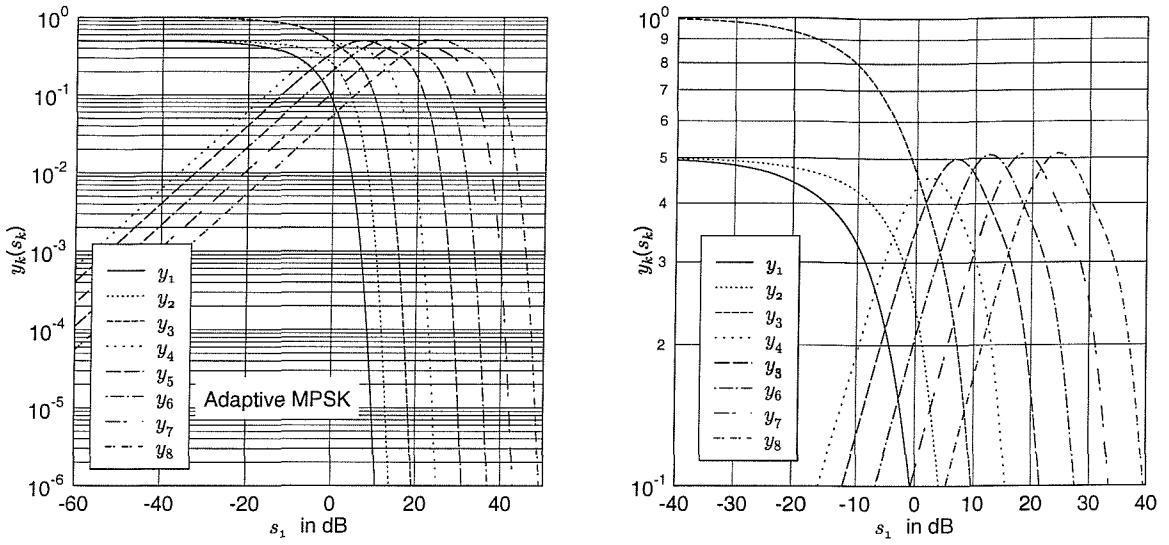

(a) Global Relationship

(b) Near $y_k(s_k) = 0.5$

Figure 5.20: 'Lagrangian-free' functions of (5.63) for a nine-mode adaptive PSK scheme. For a given value of s_1, there exist two solutions for s_k satisfying $y_k(s_k) = y_1(s_1)$. However, only the higher value of s_k satisfies the constraint of $s_{k-1} \leq s_k$, $\forall\, k$.

eliminating 16PSK from the set of possible modulation modes. It was found that both the policies result in the same performance up to four effective decimal digits in terms of the average BPS throughput.

Upon solving $y_k(s_k) = y_1(s_1)$, we arrive at the relationships sought between the first optimum switching level s_1 and the remaining optimum switching levels s_k. Figure 5.21(a) depicts these relationships. All the optimum switching levels, except for s_1 and s_2, approach their asymptotic limit monotonically, as s_1 decreases. A decreased value of s_1 corresponds to an increased value of the average SNR. Figure 5.21(b) illustrates the optimum switching levels of a seven-mode adaptive PSK scheme operating over a Rayleigh channel associated with $m = 1$ at the target BER of $P_{th} = 10^{-2}$. These switching levels were obtained by solving (5.70). The optimum switching levels show a steady decrease in their values as the average SNR increases, until it reaches the avalanche SNR value of $\bar{\gamma} = 35$dB, beyond which always the highest-order PSK modulation mode, namely 64PSK, is activated.

Having highlighted the evaluation of the optimum switching levels for an adaptive PSK scheme, let us now consider the associated performance results. We are reminded that the average BEP of our optimised adaptive scheme remains constant at $P_{avg} = P_{th}$, provided that the average SNR is less than the avalanche SNR. Hence, the average BPS throughput and the relative SNR gain of our APSK scheme in comparison to the corresponding fixed-mode modem are our concern.

Let us now consider Figure 5.22, where the average BPS throughput of the various adaptive PSK schemes operating over a Rayleigh channel associated with $m = 1$ are plotted, which were designed for the target BEP of $P_{th} = 10^{-2}$ and $P_{th} = 10^{-3}$. The markers '$\otimes$' and '$\odot$' represent the required SNR of the various fixed-mode PSK schemes, while achieving the same target BER as the adaptive schemes, op-

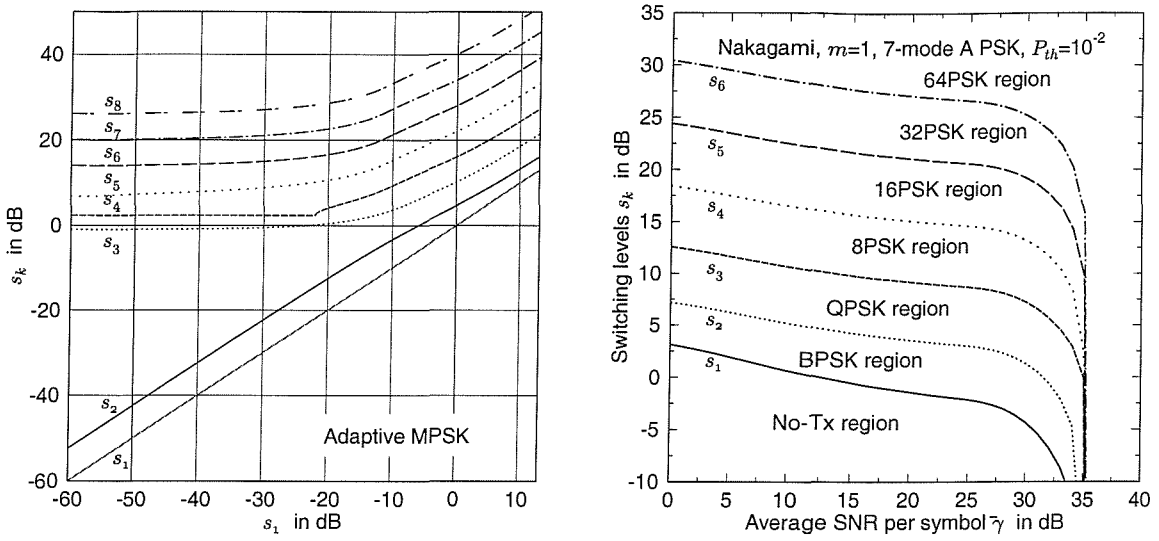

(a) Relationship between the optimum switching levels of adaptive PSK schemes employing up to nine modes

(b) Optimum switching levels of a seven-mode adaptive PSK scheme

Figure 5.21: Optimum switching levels. (a) Relationships between s_k and s_1 in a nine-mode adaptive PSK scheme. (b) Optimum switching levels for 7-mode adaptive PSK scheme operating over a Rayleigh channel at the target BER of $P_{th} = 10^{-2}$.

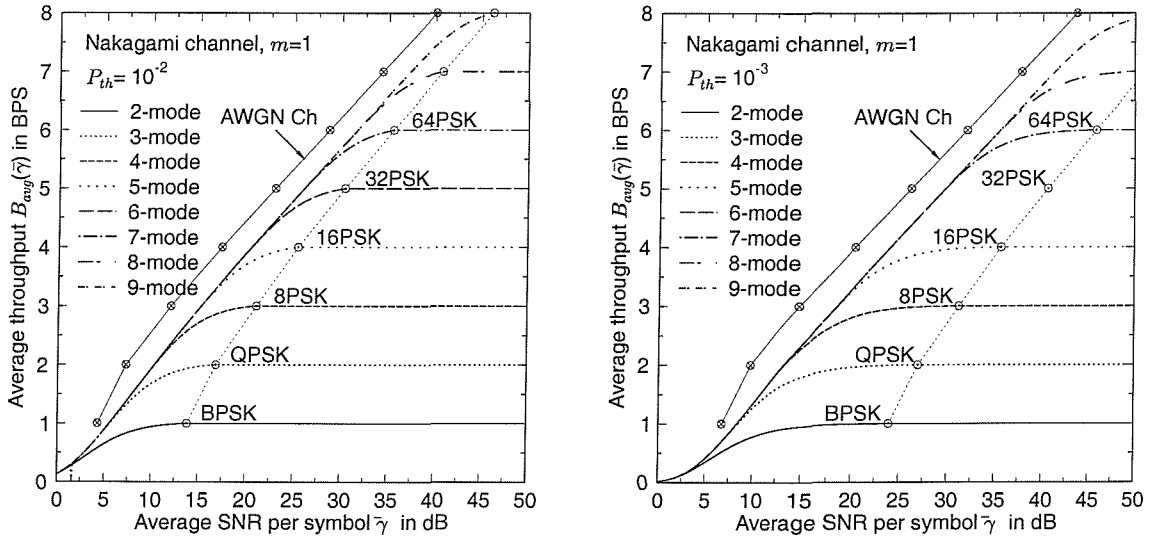

(a) $P_{th} = 10^{-2}$

(b) $P_{th} = 10^{-3}$

Figure 5.22: The average BPS throughput of various adaptive PSK schemes operating over a Rayleigh channel ($m = 1$) at the target BER of (a) $P_{th} = 10^{-2}$ and (b) $P_{th} = 10^{-3}$. The markers '$\otimes$' and '$\odot$' represent the required SNR of the corresponding fixed-mode PSK scheme, while achieving the same target BER as the adaptive schemes, operating over an AWGN channel and a Rayleigh channel, respectively.

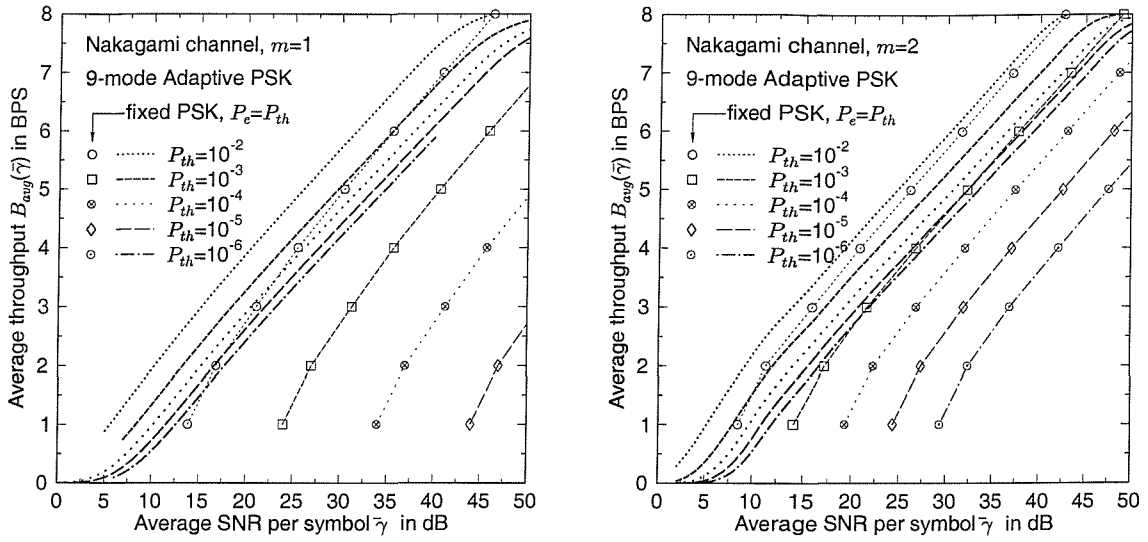

(a) $m = 1$ (b) $m = 2$

Figure 5.23: The average BPS throughput of a nine-mode adaptive PSK scheme operating over a Nakagami fading channel (a) $m = 1$ and (b) $m = 2$. The markers represent the SNR required for achieving the same BPS throughput and the same average BER as the adaptive schemes.

erating over an AWGN channel and a Rayleigh channel, respectively. It can be observed that introducing an additional constituent mode into an adaptive PSK scheme does not make any impact on the average BPS throughput, when the average SNR is relatively low. For example, when the average SNR $\bar{\gamma}$ is less than 10dB in Figure 5.22(a), employing more than four APSK modes for the adaptive scheme does not improve the average BPS throughput. In comparison to the various fixed-mode PSK modems, the adaptive modem achieved the SNR gains between 4dB and 8dB for the target BEP of $P_{th} = 10^{-2}$ and 10dB to 16dB for the target BER of $P_{th} = 10^{-3}$ over a Rayleigh channel. Since no adaptive scheme operating over a fading channel can outperform the corresponding fixed-mode counterpart operating over an AWGN channel, it is interesting to investigate the performance differences between these two schemes. Figure 5.22 suggests that the required SNR of our adaptive PSK modem achieving 1BPS for transmission over a Rayleigh channel is approximately 1dB higher, than that of fixed-mode BPSK operating over an AWGN channel. Furthermore, this impressive performance can be achieved by employing only three modes, namely No-Tx, BPSK and QPSK for the adaptive PSK modem. For other BPS throughput values, the corresponding SNR differences are in the range of 2dB to 3dB, while maintaining the BEP of $P_{th} = 10^{-2}$ and 4dB for the BEP of $P_{th} = 10^{-3}$.

We observed in Figure 5.22 that the average BPS throughput of the various adaptive PSK schemes is dependent on the target BEP. Hence, let us investigate the BPS performances of the adaptive modems for the various values of target BEPs using the results depicted in Figure 5.23. The average BPS throughputs of a nine-mode adaptive PSK scheme are represented as various types of lines without markers depending on the target average BERs, while those of the corresponding fixed PSK schemes are represented as

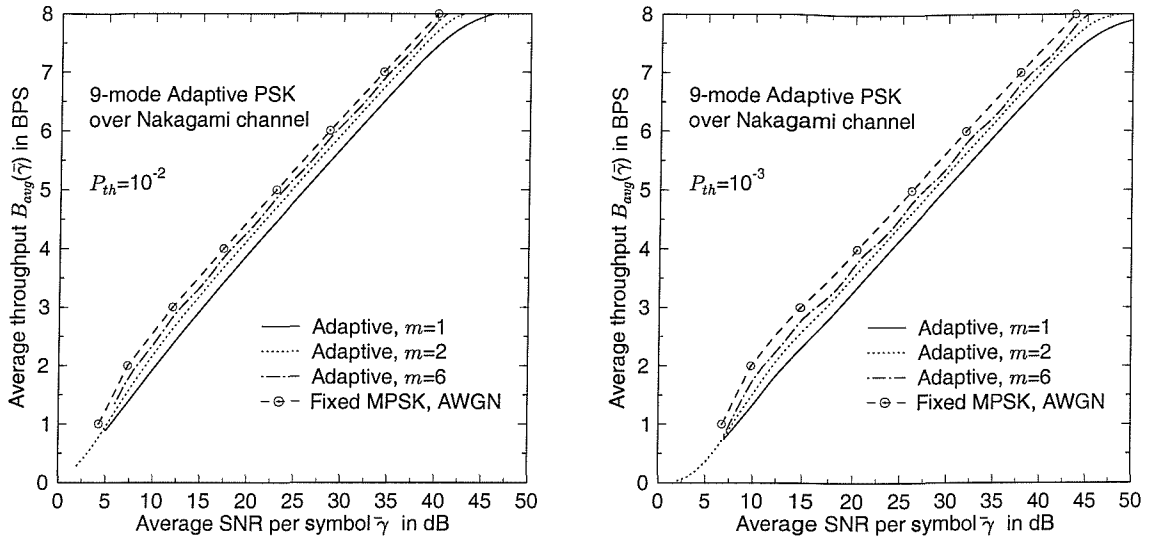

(a) $P_{th} = 10^{-2}$ (b) $P_{th} = 10^{-3}$

Figure 5.24: The effects of the Nakagami fading parameter m on the average BPS throughput of a nine-mode adaptive PSK scheme designed for the target BER of (a) $P_{th} = 10^{-2}$ and (b) $P_{th} = 10^{-3}$. As m increases, the average throughput of the adaptive modem approaches the throughput of fixed PSK modems operating over an AWGN channel.

various types of lines with markers according to the key legend shown in Figure 5.23. We can observe that the difference between the required SNRs of the adaptive schemes and fixed schemes increases, as the target BER decreases. It is interesting to note that the average BPS curves of the adaptive PSK schemes seem to converge to a set of densely packed curves, as the target BEP decreases to values around $10^{-4} \sim 10^{-6}$. In other words, the incremental SNR required for achieving the next target BEP, which is an order of magnitude lower, decreases as the target BER decreases. On the other hand, the incremental SNR for the same scenario of fixed modems seems to remain nearly constant at 10dB. Comparing Figure 5.23(a) and Figure 5.23(b), we find that this seemingly constant incremental SNR of the fixed-mode modems is reduced to about 5dB, as the fading becomes less severe, *i.e.* when the fading parameter becomes $m = 2$.

Let us now investigate the effects of the Nakagami fading parameter m on the average BPS throughput performance of various adaptive PSK schemes by observing Figure 5.24. The BPS throughput of the various fixed PSK schemes for transmission over an AWGN channel is depicted in Figure 5.24 as the ultimate performance limit achievable by the adaptive schemes operating over Nakagami fading channels. For example, when the channel exhibits Rayleigh fading, *i.e.* when the fading parameter becomes $m = 1$, the adaptive PSK schemes show 3dB to 4dB SNR penalty compared to their fixed-mode counterparts operating over the AWGN channel. Compared to fixed-mode BPSK, the adaptive scheme required only a 1dB higher SNR. As the fading becomes less severe, the average BPS throughput of the adaptive PSK schemes approaches that of fixed-mode PSK operating over the AWGN channel. For the target BEP

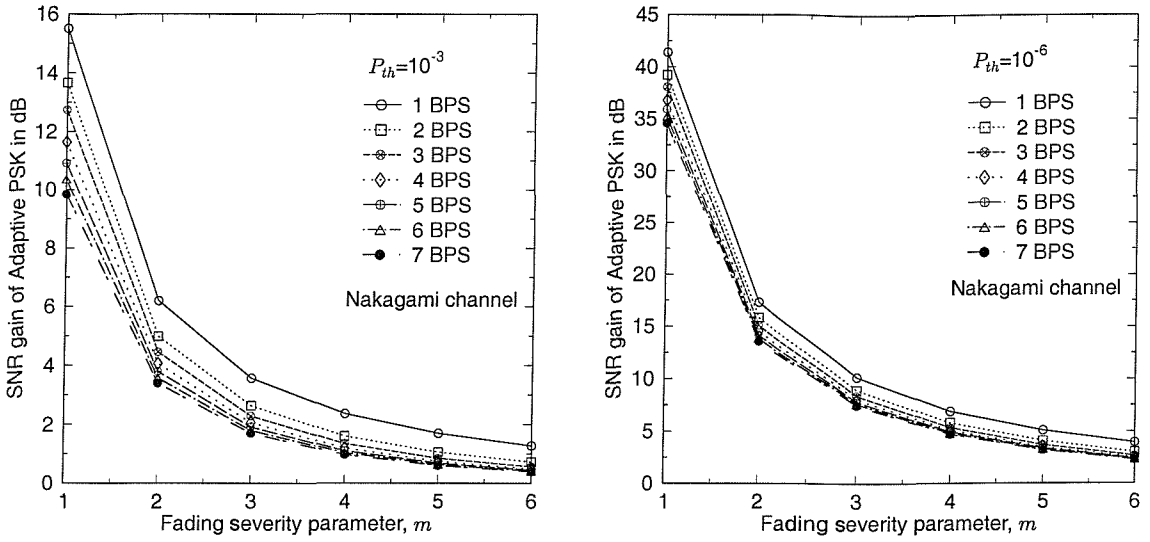

(a) $P_{th} = 10^{-3}$ (b) $P_{th} = 10^{-6}$

Figure 5.25: The SNR gain of adaptive PSK schemes in comparison to the corresponding fixed-mode PSK schemes yielding the same BPS throughput for the target BER of (a) $P_{th} = 10^{-3}$ and (b) $P_{th} = 10^{-6}$. The performance advantage of employing adaptive PSK schemes decreases, as the fading becomes less severe.

of $P_{th} = 10^{-3}$, the SNR gap between the BPS throughput curves becomes higher. The adaptive PSK scheme operating over the Rayleigh channel required 4dB to 5dB higher SNR for achieving the same throughput compared to the fixed PSK schemes operating over the AWGN channel.

Figure 5.25 summarises the relative SNR gains of our adaptive PSK schemes over the corresponding fixed PSK schemes. For the target BEP of $P_{th} = 10^{-3}$ the relative SNR gain of the nine-mode adaptive scheme compared to BPSK changes from 15.5dB to 1.3dB, as the Nakagami fading parameter changes from 1 to 6. Observing Figure 5.25(a) and Figure 5.25(b) we conclude that the advantages of employing adaptive PSK schemes are more pronounced when

1. the fading is more severe,
2. the target BER is lower, and
3. the average BPS throughput is lower.

Having studied the range of APSK schemes, let us in the next section consider the family of adaptive coherently detected Star-QAM schemes.

5.5.1.2 Adaptive Coherent Star QAM Schemes

In this section, we study the performance of adaptive coherent QAM schemes employing Type-I Star constellations [13]. Even though non-coherent Star QAM (SQAM) schemes are more popular owing

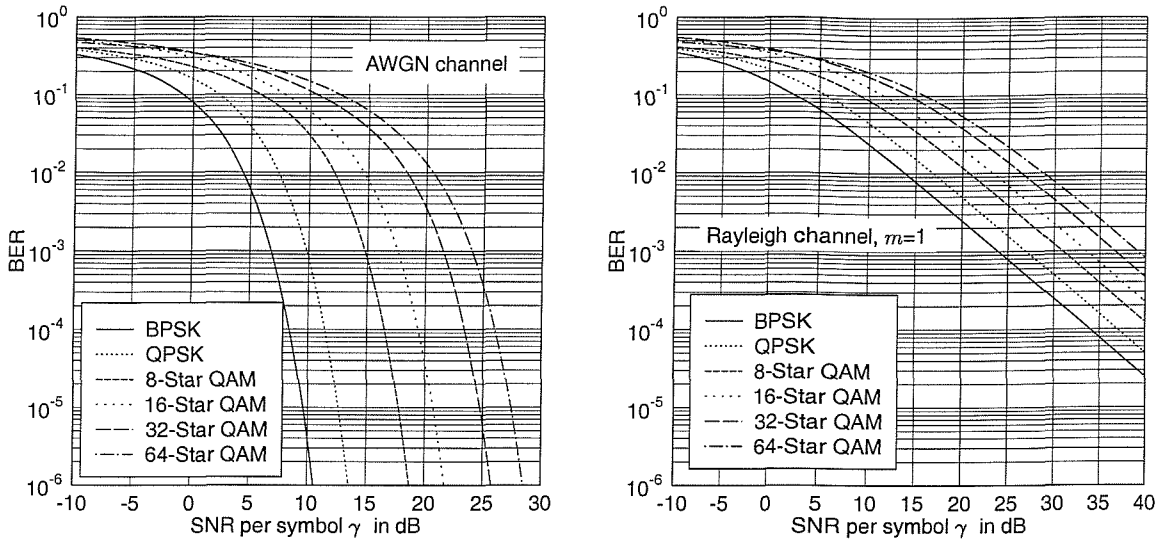

(a) AWGN Channel

(b) Rayleigh Channel, $m = 1$

Figure 5.26: The average BER of various SQAM modulation schemes

to their robustness to fading without requiring pilot symbol assisted channel estimation and Automatic Gain Control (AGC) at the receiver, the results provided in this section can serve as benchmark results for non-coherent Star QAM schemes and the coherent Square QAM schemes.

The BER of coherent Star QAM over an AWGN channel is derived in Appendix D. It is shown that their BER can be expressed as:

$$p_{SQAM}(\gamma) \simeq \sum_i A_i \, Q(\sqrt{a_i \gamma}\,), \tag{5.91}$$

where A_i and a_i are given in Appendix D for 8-Star, 16-Star, 32-Star and 64-Star QAM. The SNR-dependent optimum ring ratios were also derived in Appendix D for these Star QAM modems. Figure 5.26(a) shows the BER of BPSK, QPSK, 8-Star QAM, 16-Star QAM, 32-Star QAM and 64-Star QAM employing the optimum ring ratios over the AWGN channel. Comparing Figure 5.19(a) and Figure 5.26(a), we can observe that 16-Star QAM, 32-Star QAM and 64-Star QAM are more power-efficient than 16 PSK, 32 PSK and 64 PSK, respectively. However, the envelope power of the Star QAM signals is not constant, unlike that of the PSK signals. Following an approach similar to that used in (5.88) and (5.89), the average BEP of the various SQAM schemes over a flat Nakagami-m fading channel can be expressed as:

$$P_{SQAM}(\bar{\gamma}) = \sum_i A_i \left[\tfrac{1}{2}(1-\mu_i)\right]^m \sum_{j=0}^{m-1} \binom{m-1+j}{j} \left[\tfrac{1}{2}(1+\mu_i)\right]^j, \tag{5.92}$$

where μ_i is defined as:

$$\mu_i \triangleq \sqrt{\frac{a_i \bar{\gamma}}{2m + a_i \bar{\gamma}}}\,. \tag{5.93}$$

Figure 5.26(b) shows the average BEP of various SQAM schemes for transmission over a flat Rayleigh channel, where $m = 1$. It can be observed that the 16-Star, 32-Star and 64-Star QAM schemes exhibit SNR advantages of around 3.5dB, 4dB, and 7dB compared to 16-PSK, 32-PSK and 64-PSK schemes at a BEP of 10^{-2}. The BEP of SQAM for transmission over the AWGN channel given in (5.91) and that over a Nakagami channel given in (5.92) will be used in comparing the performance of the various adaptive SQAM schemes.

k	0	1	2	3	4	5	6
m_k	0	2	4	8	16	32	64
b_k	0	1	2	3	4	5	6
c_k	0	1	1	1	1	1	1
mode	No Tx	BPSK	QPSK	8-Star	16-Star	32-Star	64-Star

Table 5.6: Parameters of a seven-mode adaptive Star QAM scheme following the definitions developed in Section 5.3.1 for the generic adaptive modulation model

The parameters of a seven-mode adaptive Star QAM scheme are summarised in Table 5.6 following the definitions of the generic model developed in Section 5.3.1 for adaptive modulation schemes. Since the number of modes is $K = 7$, we have $K + 1 = 8$ mode-switching levels hosted by the vector $\mathbf{s} = \{s_k \mid k = 0, 1, 2, \cdots, 7$. Let us assume that $s_0 = 0$ and $s_7 = \infty$. Then, we have to determine the optimum values for the remaining six switching levels using the technique developed in Section 5.4.4. The 'Lagrangian-free' functions corresponding to a seven-mode Star QAM scheme are depicted in Figure 5.27 and the relationships obtained for the switching levels are displayed in Figure 5.28(a). We can observe that as seen for APSK in Figure 5.20 there exist two solutions for s_6 satisfying $y_6(s_6) = y_1(s_1)$ for a given value of s_1, when $y_1 \leq 0.382$. However, only the higher value of s_k satisfies the constraint of $s_6 \geq s_5$. When $s_1 \leq 7.9$dB, the optimum value of s_6 should be set to s_5, in order to guarantee $s_6 \geq s_5$. Figure 5.28(b) illustrates the optimum switching levels of a seven-mode adaptive Star QAM scheme operating over a Rayleigh channel at the target BER of $P_{th} = 10^{-2}$. These switching levels were obtained by solving (5.70). The optimum switching levels show a steady decrease in their values, as the average SNR increases, until they reach the avalanche SNR value of $\bar{\gamma} = 28.5$dB, beyond which always the highest-order modulation mode, namely 64-Star QAM, is activated.

Let us now investigate the associated performance results. We are reminded that the average BEP of our optimised adaptive scheme remains constant at $P_{avg} = P_{th}$, provided that the average SNR is less than the avalanche SNR. Hence, the average BPS throughput and the SNR gain of our adaptive modem in comparison to the corresponding fixed-mode modems are our concern.

Let us first consider Figure 5.29, where the average BPS throughput of the various adaptive Star QAM schemes operating over a Rayleigh channel associated with $m = 1$ is shown at the target BEP of $P_{th} = 10^{-2}$ and $P_{th} = 10^{-3}$. The markers '$\otimes$' and '$\odot$' represent the required SNR of the corresponding fixed-mode Star QAM schemes, while achieving the same target BEP as the adaptive schemes,

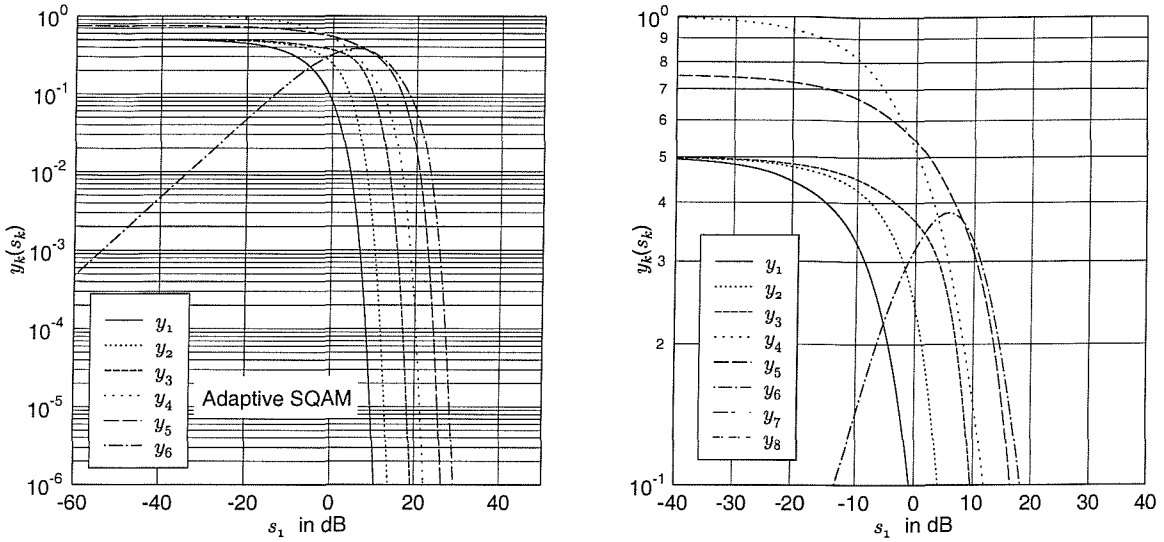

(a) Overall Relationship

(b) Near $y_k(s_k) = 0.5$

Figure 5.27: 'Lagrangian-free' functions of (5.63) for a seven-mode adaptive Star QAM scheme.

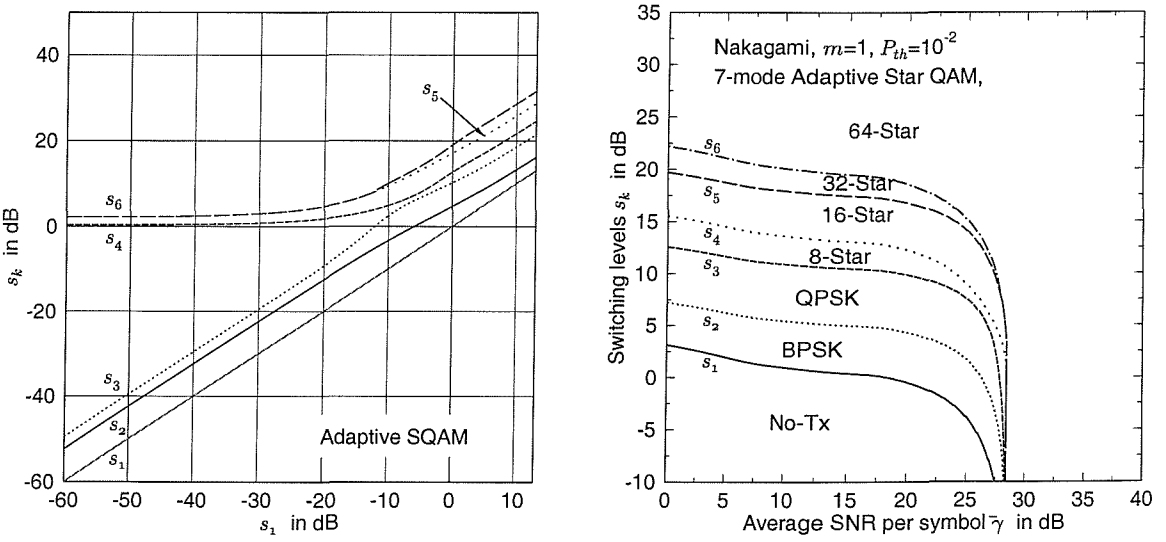

(a) Relationship between the optimum switching levels

(b) Optimum switching levels

Figure 5.28: Optimum switching levels of a seven-mode Adaptive Star QAM scheme. (a) Relationships between s_k and s_1. (b) Optimum switching levels of a seven-mode adaptive Star QAM scheme operating over a Rayleigh channel at the target BER of $P_{th} = 10^{-2}$.

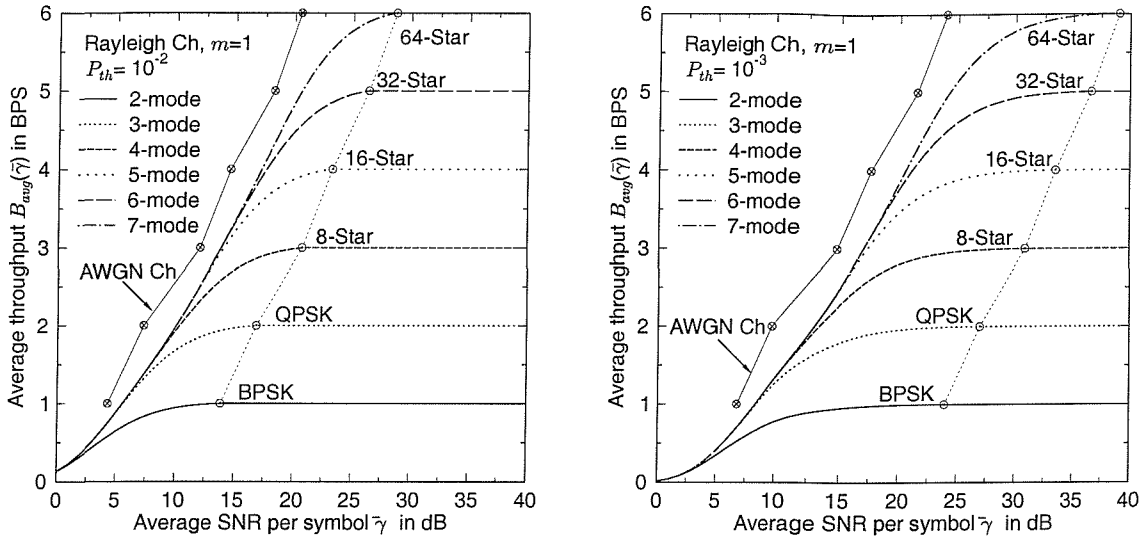

(a) $P_{th} = 10^{-2}$ (b) $P_{th} = 10^{-3}$

Figure 5.29: The average BPS throughput of the various adaptive Star QAM schemes operating over a Rayleigh fading channel associated with $m = 1$ at the target BEP of (a) $P_{th} = 10^{-2}$ and (b) $P_{th} = 10^{-3}$. The markers '⊗' and '⊙' represent the required SNR of the corresponding fixed-mode Star QAM schemes, while achieving the same target BER as the adaptive schemes, operating over an AWGN channel and a Rayleigh channel, respectively.

operating over an AWGN channel and a Rayleigh channel, respectively. Comparing Figure 5.22(a) and Figure 5.29(a), we find that the gradient of the average BPS curves of the adaptive Star QAM schemes is higher than that of adaptive PSK schemes. Explicitly, the gradient of the Star QAM schemes is around 0.3BPS/dB, whereas that of the APSK schemes was 0.18BPS/dB. This is due to the more power-efficient constellation arrangement of Star QAM in comparison to the single-ring constellations of the PSK modulations schemes. In comparison to the corresponding fixed-mode Star QAM modems, the adaptive modem achieved an SNR gain of 6dB to 8dB for the target BEP of $P_{th} = 10^{-2}$ and 12dB to 16dB for the target BEP of $P_{th} = 10^{-3}$ over a Rayleigh channel. Compared to the fixed-mode Star QAM schemes operating over an AWGN channel, our adaptive schemes approached their performance within about 3dB in terms of the required SNR value, while achieving the same target BER of $P_{th} = 10^{-2}$ and $P_{th} = 10^{-3}$.

Since Figure 5.29 suggests that the relative SNR gain of the adaptive schemes is dependent on the target BER, let us investigate the effects of the target BEP in more detail. Figure 5.30 shows the BPS throughput of the various adaptive schemes at the target BEP of $P_{th} = 10^{-2}$ to $P_{th} = 10^{-6}$. The average BPS throughputs of a seven-mode adaptive Star QAM scheme is represented with the aid of the various line types without markers, depending on the target average BERs, while those of the corresponding fixed-mode Star QAM schemes are represented as various types of lines having markers according to the legends shown in Figure 5.30. We can observe that the difference between the SNRs required for the

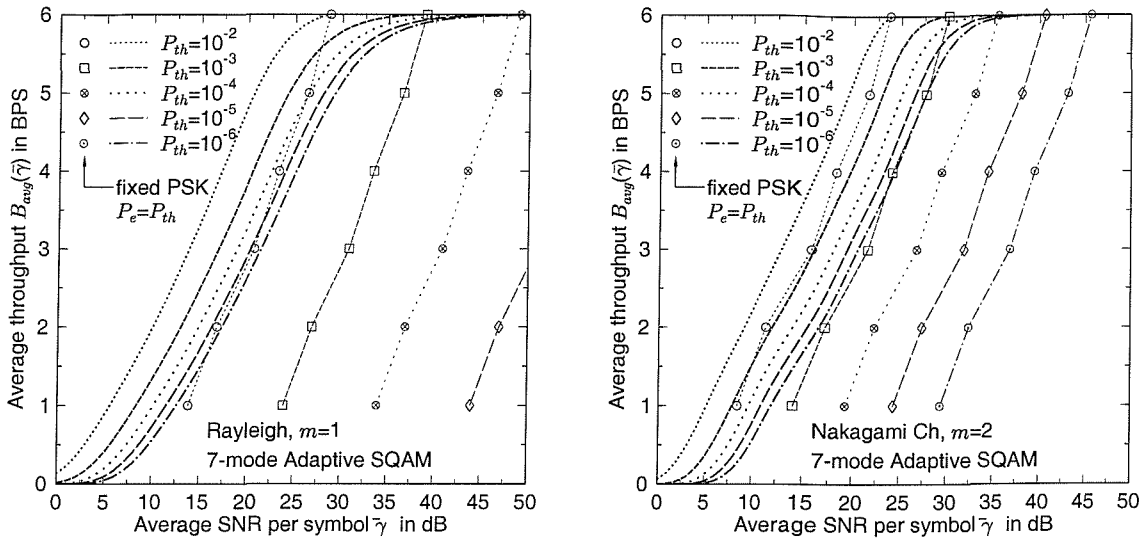

(a) $m = 1$ (b) $m = 2$

Figure 5.30: The average BPS throughput of a seven-mode adaptive Star QAM scheme operating over a Nakagami fading channel (a) $m = 1$ and (b) $m = 2$. The markers represent the SNR required by the fixed-mode schemes for achieving the same BPS throughput and the same average BER as the adaptive schemes.

adaptive schemes and fixed schemes increases, as the target BER decreases. The fixed-mode Star QAM schemes require additional SNRs of 10dB and 6dB in order to achieve an order of magnitude lower BER for the Nakagami fading parameters of $m = 1$ and $m = 2$, respectively. However, our adaptive schemes require additional SNRs of only 1dB to 3dB for achieving the same goal.

Let us now investigate the effects of the Nakagami fading parameter m on the average BPS throughput performance of the various adaptive Star QAM schemes by observing Figure 5.31. The BPS throughput of the fixed-mode Star QAM schemes for the transmission over an AWGN channel is depicted in Figure 5.31 as the ultimate performance limit achievable by the adaptive schemes operating over Nakagami fading channels. As the Nakagami fading parameter m increases from 1 to 2 and to 6, the SNR gap between the adaptive schemes operating over a Nakagami fading channel and the fixed-mode schemes decreases. When the average SNR is less than $\bar{\gamma} \leq$ 6dB, the average BPS throughput of our adaptive schemes decreases, when the fading parameter m increases. The rationale of this phenomenon is that as the channel becomes more and more like an AWGN channel, the probability of activating the BPSK mode is reduced, resulting in more frequent activation of the No-Tx mode and hence the corresponding average BPS throughput inevitably decreases.

The effects of the Nakagami fading factor m on the SNR gain of our adaptive Star QAM scheme can be observed in Figure 5.32. As expected, the relative SNR gain of the adaptive schemes at a throughput of 1 BPS is the highest among the BPS throughputs considered. However, the order observed in terms of the SNR gain of the adaptive schemes does not strictly follow the increasing BPS order at the target BEP

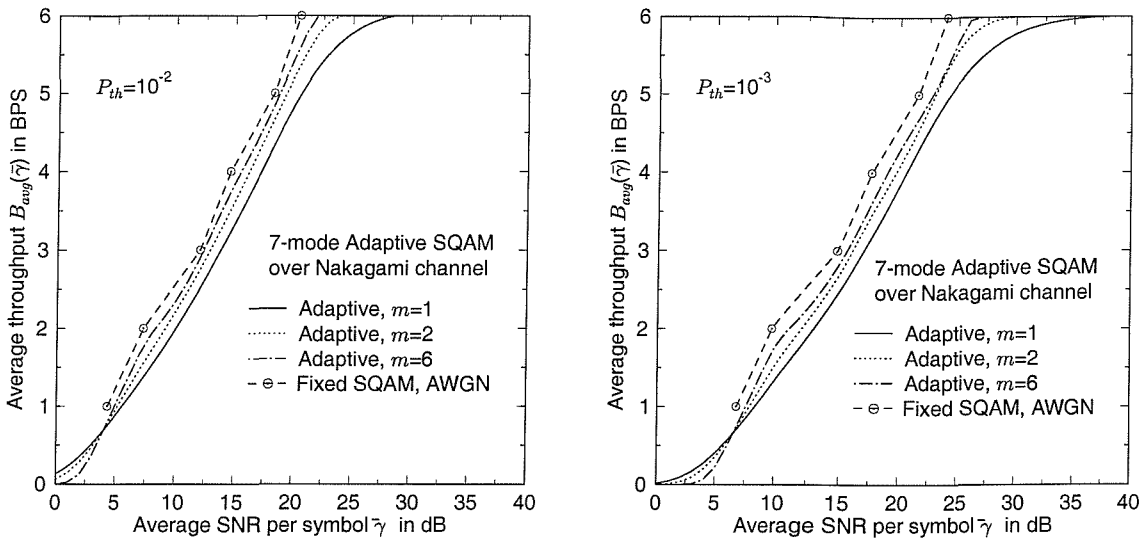

(a) $P_{th} = 10^{-2}$ (b) $P_{th} = 10^{-3}$

Figure 5.31: The effects of the Nakagami fading parameter m on the average BPS throughput of a seven-mode adaptive Star QAM scheme at the target BER of (a) $P_{th} = 10^{-2}$ and (b) $P_{th} = 10^{-3}$. As m increases, the average throughput of the adaptive modem approaches the throughput of the fixed-mode Star QAM modems operating over an AWGN channel.

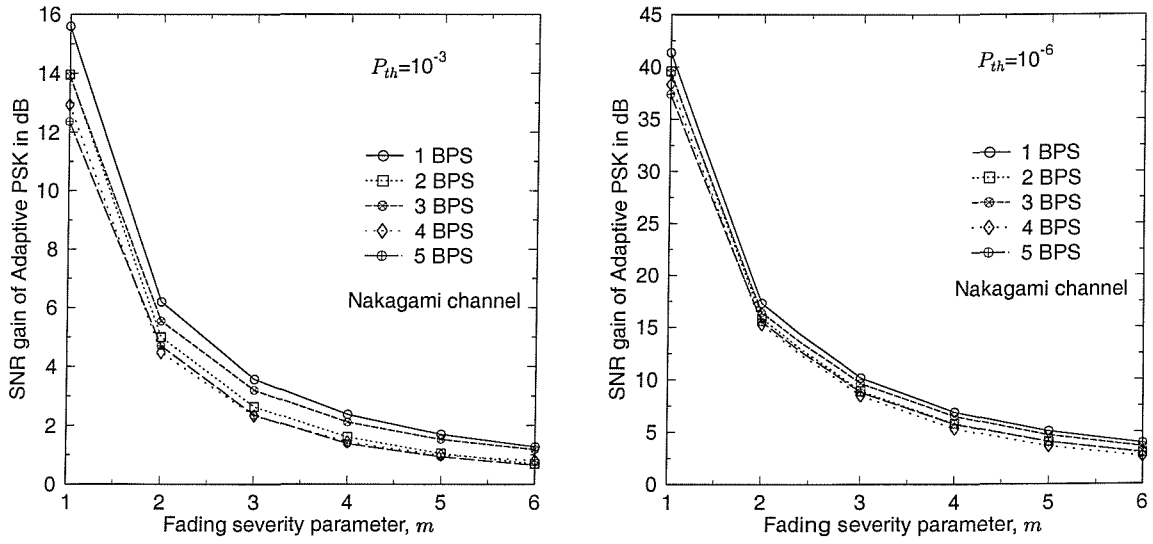

(a) $P_{th} = 10^{-3}$ (b) $P_{th} = 10^{-6}$

Figure 5.32: The SNR gain of the various adaptive Star QAM schemes in comparison to the fixed-mode Star QAM schemes yielding the same BPS throughput at the target BEP of (a) $P_{th} = 10^{-3}$ and (b) $P_{th} = 10^{-6}$. The advantage of the adaptive Star QAM schemes decreases, as the fading becomes less severe.

of $P_{th} = 10^{-3}$ and $P_{th} = 10^{-6}$, as did for the adaptive PSK schemes of Section 5.5.1.1. Even though the adaptive Star QAM schemes exhibit a higher throughput, than the adaptive PSK schemes, the SNR gains compared to their fixed-mode counterparts are more or less the same, showing typically less than 1dB difference, except for the 5 BPS throughput scenario, where the adaptive QAM scheme gained up to 1.3dB more in terms of the required SNR than the adaptive PSK scheme.

Having studied the performance of a range of adaptive Star QAM schemes, in the next section we consider adaptive modulation schemes employing the family of square-shaped QAM constellations.

5.5.1.3 Adaptive Coherent Square QAM Modulation Schemes

Since coherent Square M-ary QAM (MQAM) is the most power-efficient M-ary modulation scheme [13] and the accurate channel estimation becomes possible with the advent of Pilot Symbol Assisted Modulation (PSAM) techniques [115–117], *Otsuki*, *Sampei* and *Morinaga* proposed to employ coherent square QAM as the constituent modulation modes for an adaptive modulation scheme [118] instead of non-coherent Star QAM modulation [113]. In this section, we study the various aspects of this adaptive square QAM scheme employing the optimum switching levels of Section 5.4.4. The closed form BER expressions of square QAM over an AWGN channel can be found in (5.2) and that over a Nakagami channel can be expressed using a similar form given in (5.92). The optimum switching levels of adaptive Square QAM were studied in Section 5.4.4 as an example.

The average BER of our six-mode adaptive Square QAM scheme operating over a flat Rayleigh fading channel is depicted in Figure 5.33(a), which shows that the modem maintains the required constant target BER, until it reaches the BER curve of the specific fixed-mode modulation scheme employing the highest-order modulation mode, namely 256-QAM, and then it follows the BER curve of the 256-QAM mode. The various grey lines in the figure represent the BER of the fixed constituent modulation modes for transmission over a flat Rayleigh fading channel. An arbitrarily low target BER could be maintained at the expense of a reduced throughput.

The average throughput is shown in Figure 5.33(b) together with the estimated channel capacity of the narrow-band Rayleigh channel [119, 120] and with the throughput of several variable-power, variable-rate modems reported in [122]. Specifically, Goldsmith and Chua [122] studied the performance of their variable-power variable-rate adaptive modems based on a BER bound of m-ary Square QAM, rather than using an exact BER expression. Since our adaptive Square QAM schemes do not vary the transmission power, our scheme can be regarded as a sub-optimal policy [122]. However, the throughput performance of Figure 5.33(b) shows that the SNR degradation is within 2dB in the low-SNR region and within half a dB in the high-SNR region, in comparison to the ideal continuously variable-power adaptive QAM scheme employing a range of hypothetical continuously variable-BPS QAM modes [122], represented as the 'Goldsmith 1' scheme in the figure. *Goldsmith* and *Chua* [122] also reported the performance of a variable-power discrete-rate and a constant-power discrete-rate scheme, which we represented as the 'Goldsmith 2' and 'Goldsmith 3' in Figure 5.33(b), respectively. Since their results are based on approximate BER formulas, the average BPS throughput performance of the 'Goldsmith 3' scheme is optimistic, when the average SNR γ is less than 17dB. Considering that our scheme achieves

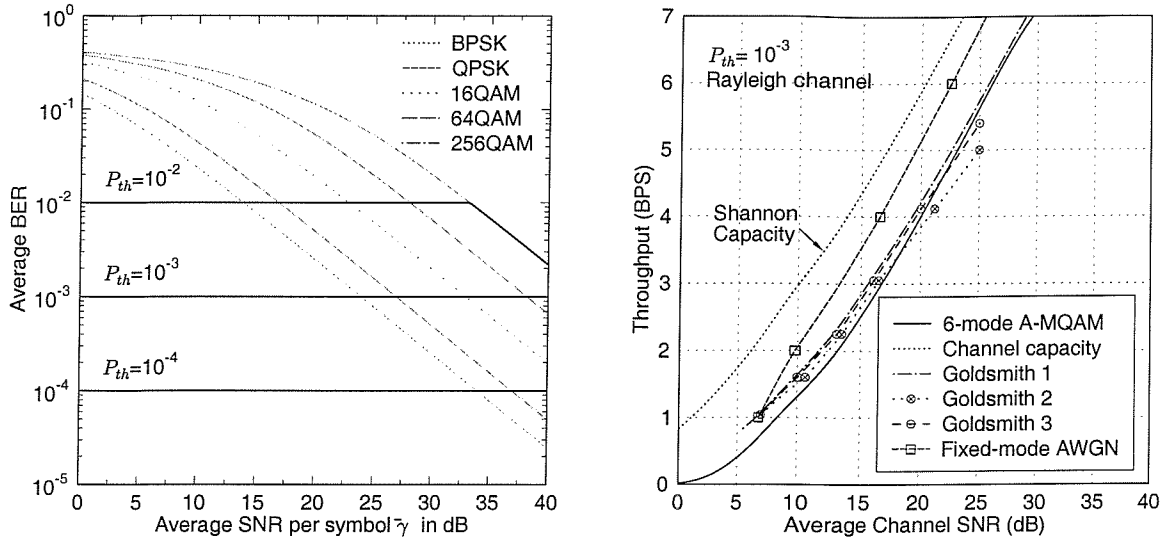

(a) BER

(b) Throughput: $P_t = 10^{-3}$

Figure 5.33: The average BER and average throughput performance of a six-mode adaptive Square QAM scheme operating over a flat Rayleigh channel ($m = 1$). (a) The constant target average BER is maintained over the entire range of the average SNR values up the avalanche SNR. (b) The average BPS throughput of the equivalent constant-power adaptive scheme is compared to to *Goldsmith*'s schemes [122]. The 'Goldsmith 1' and 'Goldsmith 2' schemes represent a variable-power adaptive scheme employing a hypothetical continuously variable-BPS QAM modulation modes and Square QAM modes, respectively. The 'Goldsmith 3' scheme represents the simulation results associated with a constant-power adaptive Square QAM reported in [122].

the maximum possible throughput the given average SNR value with the aid of the globally optimised switching levels, the average throughput of the 'Goldsmith 3' scheme is expected to be lower, than that of our scheme, as is the case when the average SNR γ is higher than 17dB.

Figure 5.34(a) depicts the average BPS throughput of our various adaptive Square QAM schemes operating over a Rayleigh channel associated with $m = 1$ at the target BEP of $P_{th} = 10^{-3}$. Figure 5.34(a) shows that even though the constituent modulation modes of our adaptive schemes do not include 3, 5 and 7-BPS constellations, the average BPS throughput steadily increases without undulations. Comparing to the fixed-mode Square QAM schemes operating over an AWGN channel, our adaptive schemes require additional SNRs of less than 3.5dB, when the throughput is below 6.5 BPS. The comparison of the average BPS throughputs of the adaptive schemes employing PSK, Star QAM and Square QAM modems, as depicted in Figure 5.34(b), confirms the superiority of Square QAM over the other two schemes in terms of the required average SNR for achieving the same throughput and the same target average BEP. Since all these three schemes employ BPSK, QPSK as the second and the third constituent modulation modes, their throughput performance shows virtually no difference, when the average throughput is less than or equal to $B_{avg} = 2$ BPS.

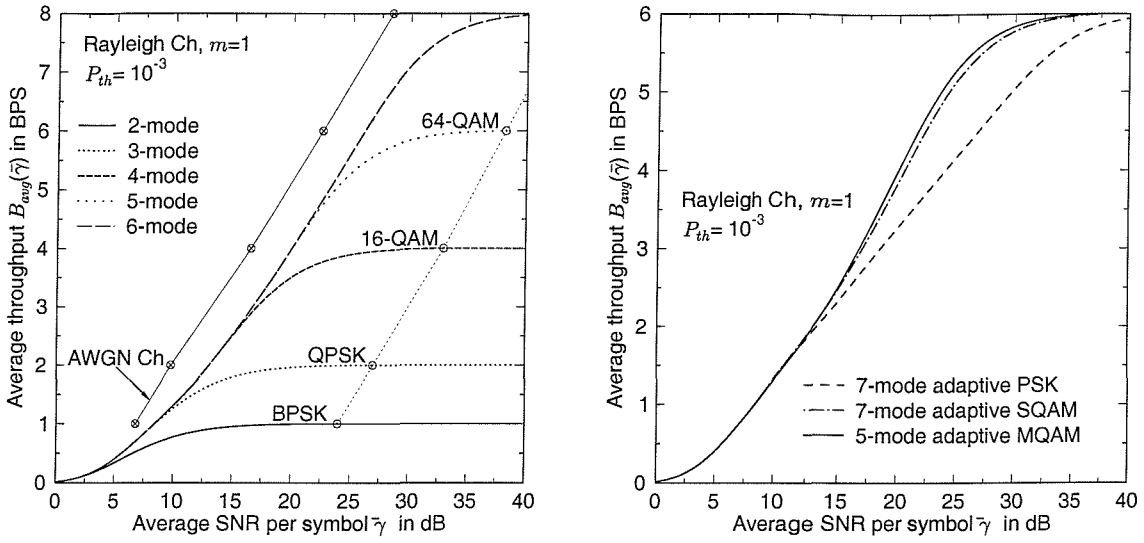

(a) $P_{th} = 10^{-2}$ (b) $P_{th} = 10^{-3}$

Figure 5.34: The average BPS throughput of various adaptive Square QAM schemes operating over a Rayleigh channel ($m = 1$) at the target BEP of $P_{th} = 10^{-3}$. (a) The markers '⊗' and '⊙' represent the required SNR of the corresponding fixed-mode Square QAM schemes achieving the same target BER as the adaptive schemes, operating over an AWGN channel and a Rayleigh channel, respectively. (b) The comparison of the various adaptive schemes employing PSK, Star QAM and Square QAM as the constituent modulation modes.

Let us now investigate the effects of the Nakagami fading parameter m on the average BPS throughput performance of the adaptive Square QAM schemes observing Figure 5.35. The BPS throughput of the fixed-mode Square QAM schemes over an AWGN channel is depicted in Figure 5.35 as the ultimate performance limit achievable by the adaptive schemes operating over Nakagami fading channels. Similar observations can be made for the adaptive Square QAM scheme, like for the adaptive Star QAM arrangement characterised in Figure 5.31. A specific difference is, however, that the average BPS throughput recorded for the fading parameter of $m = 6$ exhibits an undulating curve. For example, an increased m value results in a limited improvement of the corresponding average BPS throughput near the throughput values of 2.5, 4.5 and 6.5 BPS. This is because our adaptive Square QAM schemes do not use 3-, 5- and 7-BPS constituent modems, unlike the adaptive PSK and adaptive Star QAM schemes. Figure 5.36 depicts the corresponding optimum mode-switching levels for the six-mode adaptive Square QAM scheme. The black lines represent the switching levels, when the Nakagami fading parameter is $m = 6$ and the grey lines when $m = 1$. In general, the lower the switching levels, the higher the average BPS throughput of the adaptive modems. When the Nakagami fading parameter is $m = 1$, the switching levels decrease monotonically, as the average SNR increases. However, when the fading severity parameter is $m = 6$, the switching levels fluctuate, exhibiting several local minima around 8dB, 15dB and 21dB. In general, the optimum switching levels become higher, as the average SNR becomes

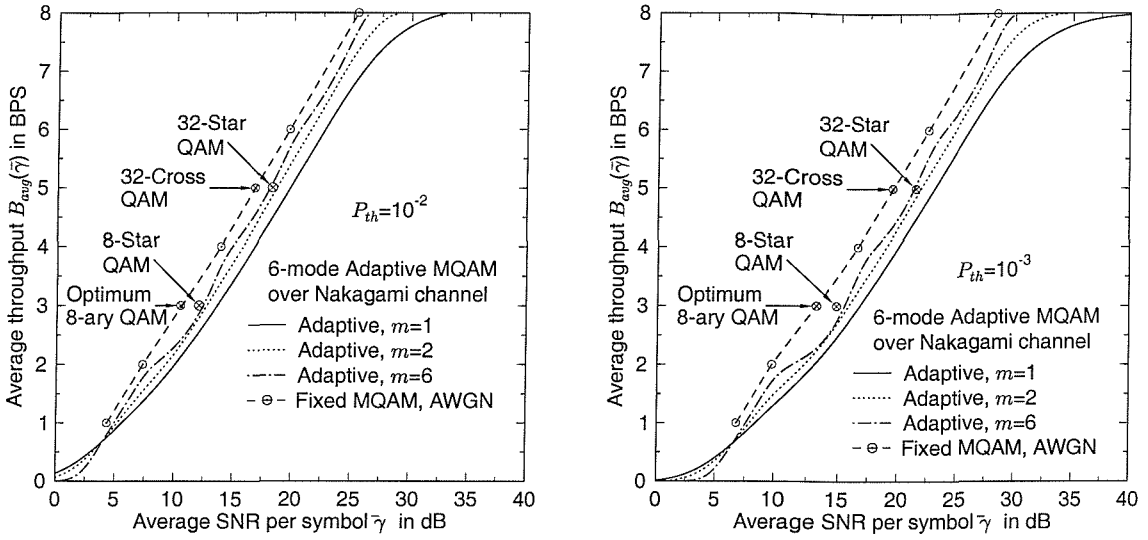

(a) $P_{th} = 10^{-2}$ (b) $P_{th} = 10^{-3}$

Figure 5.35: The effects of the Nakagami fading parameter m on the average BPS throughput of a seven-mode adaptive Square QAM scheme at the target BEP of (a) $P_{th} = 10^{-2}$ and (b) $P_{th} = 10^{-3}$. As m increases, the average throughput of the adaptive modem approaches the throughput of the corresponding fixed Square QAM modems operating over an AWGN channel.

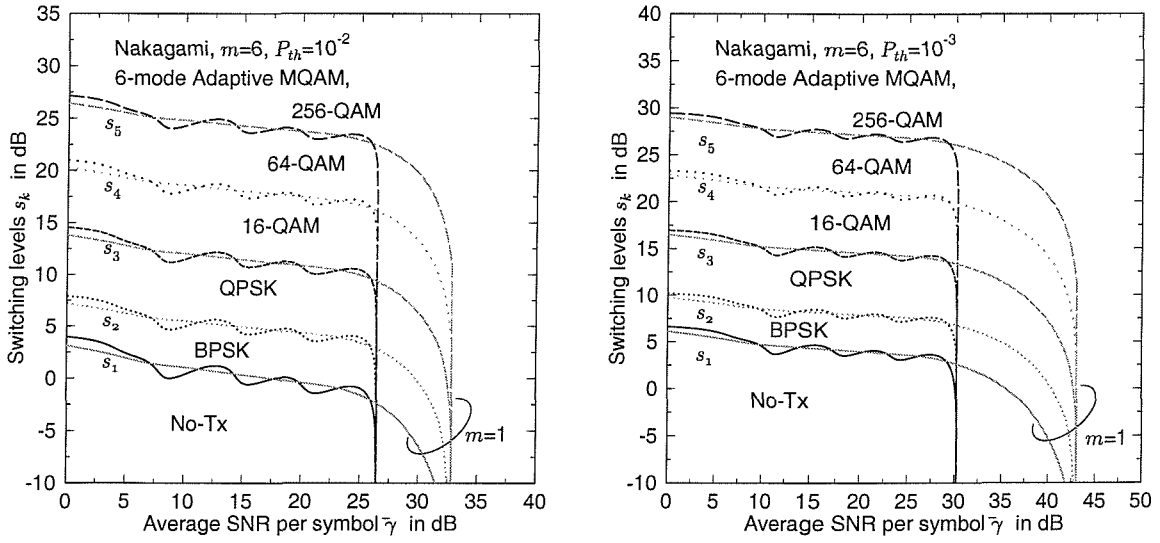

(a) $P_{th} = 10^{-2}$ (b) $P_{th} = 10^{-3}$

Figure 5.36: The switching levels of the six-mode adaptive Square QAM scheme operating over Nakagami fading channels at the target BER of (a) $P_{th} = 10^{-2}$ and (b) $P_{th} = 10^{-3}$. The bold lines are used for the fading parameter of $m = 6$ and the grey lines are for $m = 1$.

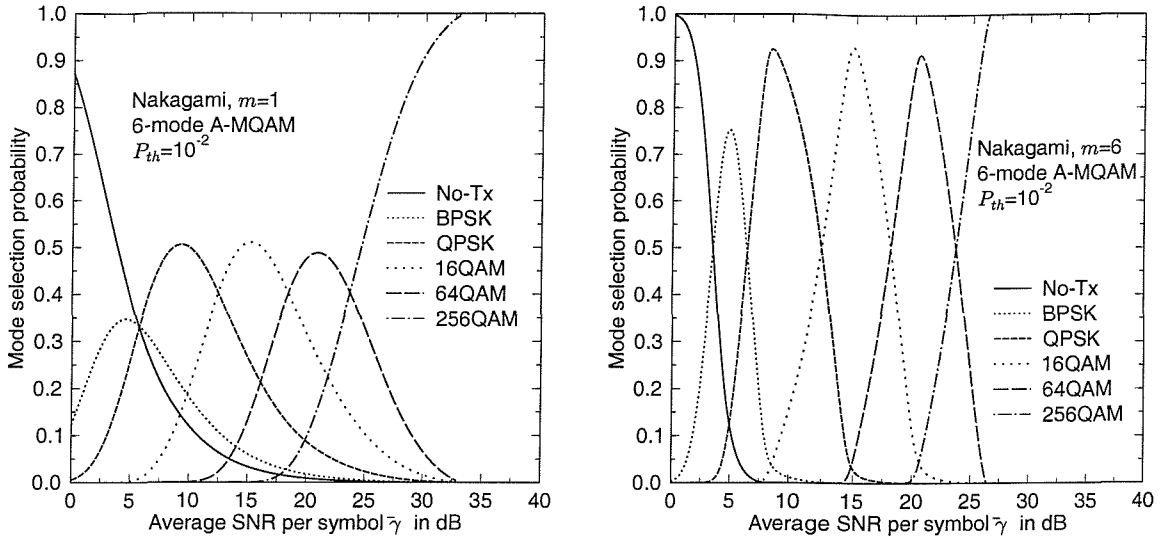

(a) $m = 1$ (b) $m = 6$

Figure 5.37: The mode selection probability of a six-mode adaptive Square QAM scheme operating over Nakagami fading channels at the target BEP of $P_{th} = 10^{-2}$. When the fading becomes less severe, the mode selection scheme becomes more 'selective' in comparison to that for $m = 1$.

higher. However the switching level curves undulate, because as the average SNR becomes higher, the next higher-throughput modulation mode becomes predominantly selected and the average target BER cannot be maintained, unless the swithcing levels are increased. In the extreme case of $m \to \infty$, *i.e.* when operating over an AWGN-like channel, the switching levels would be $s_1 = s_2 = 0$ and $s_k = \infty$ for other k values in the SNR range of 7.3dB $< \bar{\gamma} <$ 14dB, $s_1 = s_2 = s_3 = 0$ and $s_4 = s_5 = \infty$ when we have 14dB $< \bar{\gamma} <$ 20dB, $s_k = 0$ except for $s_5 = \infty$ when the SNR is in the range of 20dB $< \bar{\gamma} <$ 25dB. Finally, we have $s_k = 0$ for $\forall k$, when $\bar{\gamma} >$ 25dB, when considering the fixed-mode Square QAM performance achieved for transmission over an AWGN channel represented by the makers '$\odot$' in Figure 5.35. Observing Figure 5.37, we find that our adaptive schemes become highly 'selective', when the Nakagami fading parameter becomes $m = 6$, exhibiting narrow triangular shapes. As m increases, the shapes will eventually converge to Kronecker delta functions.

A possible approach to reducing the undulating behaviour of the average BPS throughput curve is the introduction of a 3-BPS and a 5-BPS mode as additional constituent modem modes. The power-efficiency of 8-Star QAM and 32-Star QAM is insufficient for maintaining a linear growth of the average BPS throughput, as we can observe in Figure 5.35. Instead, the most power-efficient 8-ary QAM scheme [25, pp 279] and 32-ary Cross QAM scheme [13, pp 236] have a potential of reducing these undulation effects. However, since we observed in Section 5.5.1.1 and Section 5.5.1.2 that the relative SNR advantage of employing adaptive Square QAM rapidly reduces, when the Nakagami fading parameter increases, even though the additional 3-BPS and 5-BPS modes are also used, there seems to be no significant benefit in employing non-square shaped additional constellations.

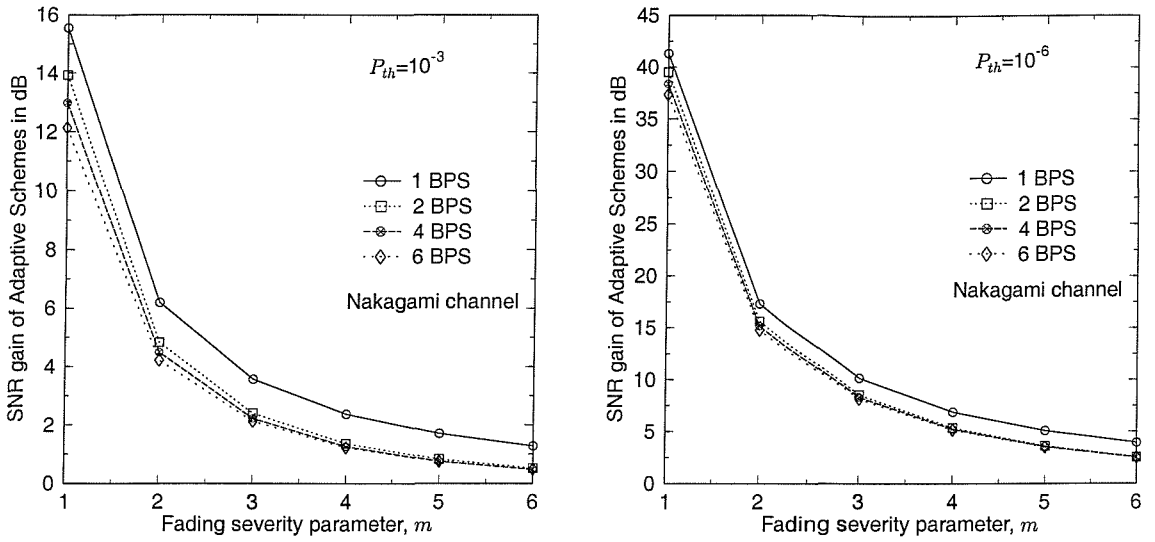

(a) $P_{th} = 10^{-3}$ (b) $P_{th} = 10^{-6}$

Figure 5.38: The SNR gain of the six-mode adaptive Square QAM scheme in comparison to the various fixed-mode Square QAM schemes yielding the same BPS throughput at the target BEP of (a) $P_{th} = 10^{-3}$ and (b) $P_{th} = 10^{-6}$. The performance advantage of the adaptive Square QAM schemes decreases, as the fading becomes less severe.

Again, we can observe in Figure 5.35 that when the average SNR is less than $\bar{\gamma} \leq$ 6dB, the average BPS throughput of our adaptive Square QAM scheme decreases, as the Nakagami fading parameter m increases. As we discussed in Section 5.5.1.2, this is due to the less frequent activation of the BPSK mode in comparison to the 'No-Tx' mode, as the channel variation is reduced.

The effects of the Nakagami fading factor m on the relative SNR gain of our adaptive Square QAM scheme can be observed in Figure 5.38. The less severe the fading, the smaller the relative SNR advantage of employing adaptive Square QAM in comparison to its fixed-mode counterparts. Except for the 1-BPS mode, the SNR gains become less than 0.5dB, when m is increased to 6 at the target BEP of $P_{th} = 10^{-3}$. The trend observed is the same at the target BEP of $P_{th} = 10^{-6}$, showing relatively higher gains in comparison to the $P_{th} = 10^{-3}$ scenario.

5.5.2 Performance over Narrow-band Rayleigh Channels Using Antenna Diversity

In the last section, we observed that the adaptive modulation schemes employing Square QAM modes exhibit the highest BPS throughput among the schemes investigated, when operating over Nakagami fading channels. As we discussed in Section 5.3.3.1, a flat Nakagami fading channel having a fading parameter of m is equivalent to $D = m$ number of independent flat Rayleigh channels, when MRC assisted diversity is employed. Therefore, the results of Section 5.5.1.3 can be invoked for characterising an MRC antenna diversity assisted adaptive Sqaure QAM scheme operating over D independent Rayleigh channels. However, the combined average SNR of the MRC assisted adaptive Square QAM scheme is

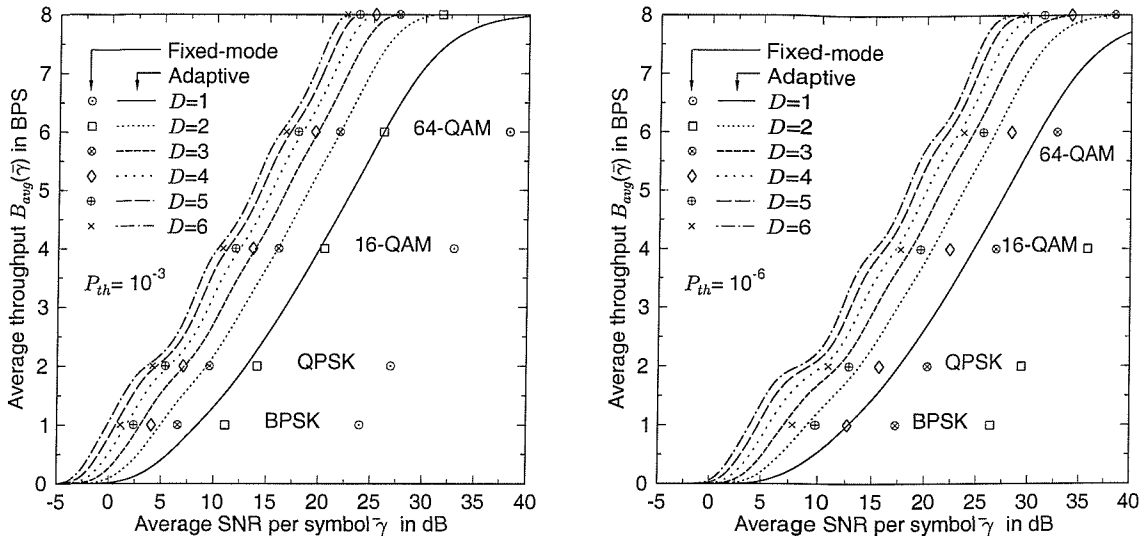

(a) $P_{th} = 10^{-3}$ (b) $P_{th} = 10^{-6}$

Figure 5.39: The average BPS throughput of the MRC-aided antenna-diversity assisted adaptive Square QAM scheme operating over independent Rayleigh fading channels at the target average BEP of (a) $P_{th} = 10^{-3}$ and (b) $P_{th} = 10^{-6}$. The markers represent the corresponding fixed-mode Square QAM performances.

D times higher, than that of the adaptive Square QAM scheme communicating over a flat Nakagami fading channel. Hence, in order to gain an insight into the performance of the MRC antenna diversity assisted adaptive Square QAM scheme communicating over D number of independent Rayleigh fading channels, the related performance is presented in this section without repeating the results similar to those presented in Section 5.5.1.3.

The BEP expression of the fixed-mode coherent BPSK scheme can be found in [25, pp 781] and those of coherent Square QAM can be readily extended using the equations in (5.2) and (5.3). Furthermore, the antenna diversity scheme operating over independent narrow-band Rayleigh fading channels can be viewed as a special case of the two-dimensional (2D) Rake receiver analysed in Appendices B and C. The performance of antenna-diversity assisted adaptive Square QAM schemes can be readily analysed using the technique developed in Section 5.4.4.

Figure 5.39 depicts the average BPS throughput performance of our adaptive schemes employing Maximal Ratio Combining (MRC) aided antenna diversity [135, Ch 5, 6] operating over independent Rayleigh fading channels at the target average BEP of $P_{th} = 10^{-3}$ and $P_{th} = 10^{-6}$. The markers represent the performance of the corresponding fixed-mode Square QAM modems in the same scenario. The average SNRs required achieving the target BEP of the fixed-mode schemes and that of the adaptive schemes decrease, as the antenna diversity order increases. However, the differences between the required SNRs of the adaptive schemes and their fixed-mode counterparts also decrease, as the antenna diversity order increases. The SNRs of both schemes required for achieving the target BEPs of $P_{th} = 10^{-3}$

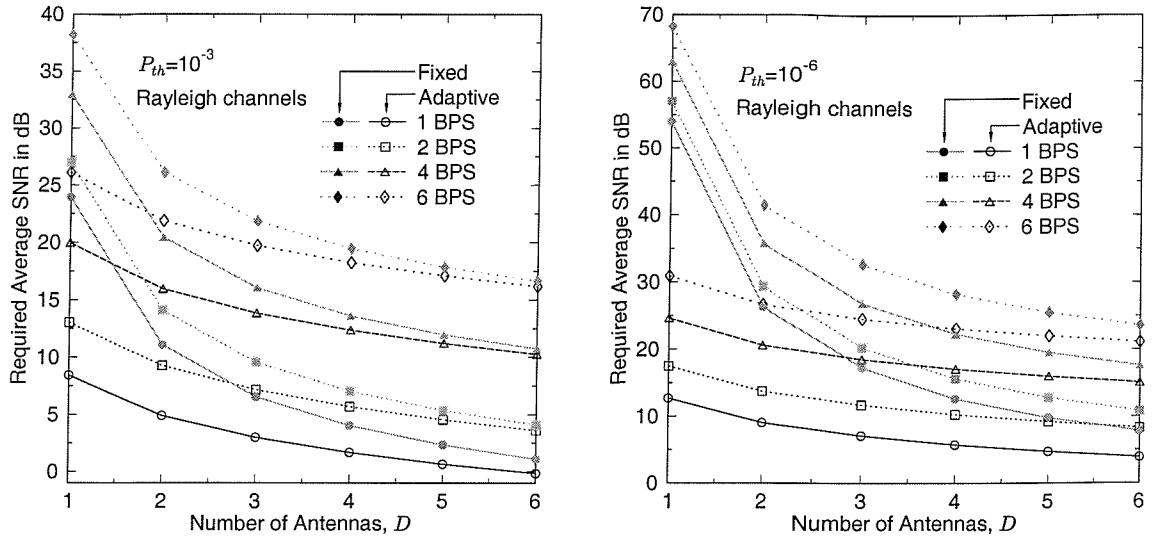

(a) $P_{th} = 10^{-3}$ (b) $P_{th} = 10^{-6}$

Figure 5.40: The SNR required for the MRC-aided antenna-diversity assisted adaptive Square QAM schemes and the corresponding fixed-mode modems operating over independent Rayleigh fading channels at the target average BEP of (a) $P_{th} = 10^{-3}$ and (b) $P_{th} = 10^{-6}$.

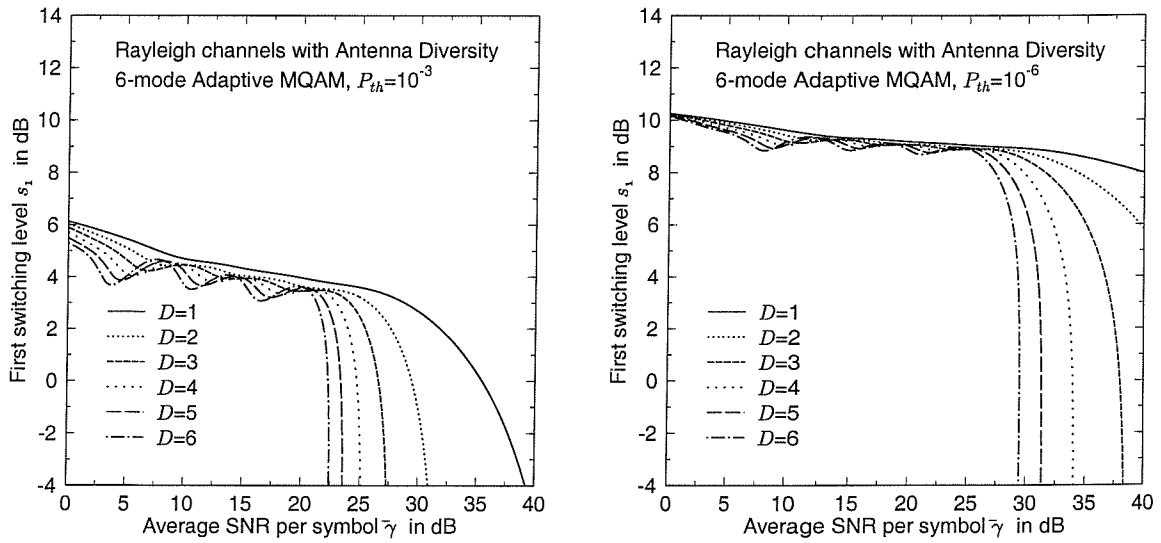

(a) $P_{th} = 10^{-3}$ (b) $P_{th} = 10^{-6}$

Figure 5.41: The first switching level s_1 of the MRC-aided antenna-diversity assisted adaptive Square QAM scheme operating over independent Rayleigh fading channels at the target average BEP of (a) $P_{th} = 10^{-3}$ and (b) $P_{th} = 10^{-6}$.

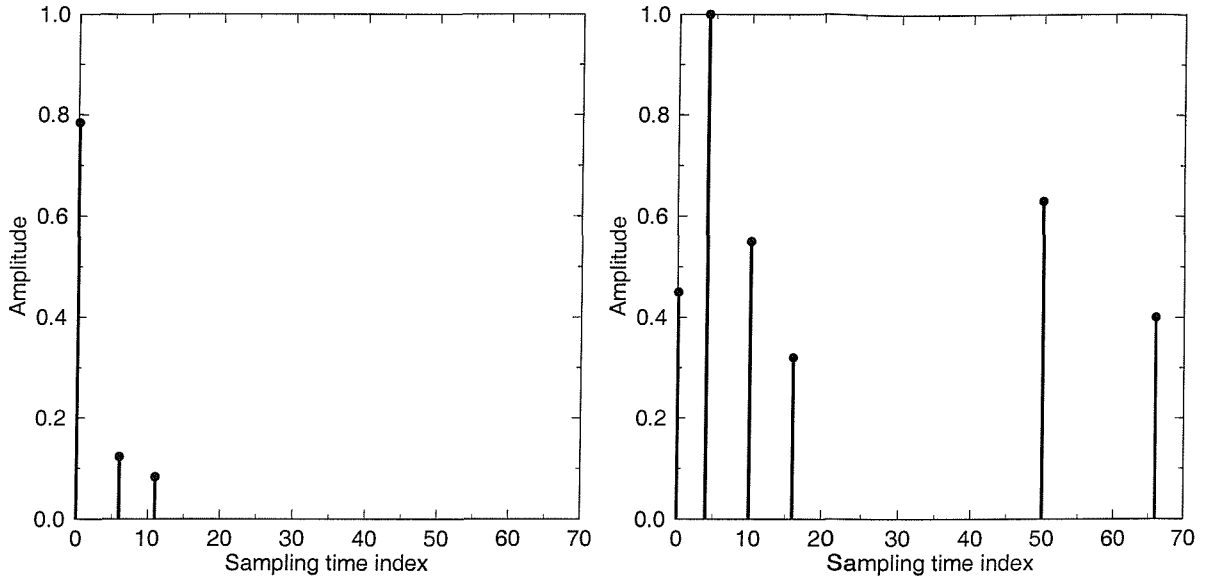

(a) W-ATM Channel

(b) Bad Urban-A Channel

Figure 5.42: Multi-path Intensity Profiles (MIPs) of the Wireless Asynchronous Transfer Mode (W-ATM) indoor channel [13, Ch 20] and that of the Bad-Urban Reduced-model A (BU-RA) channel [136]

and $P_{th} = 10^{-6}$ are displayed in Figure 5.40, where we can observe that dual antenna diversity is sufficient for the fixed-mode schemes in order to obtain half of the achievable SNR gain of the six-antenna aided diversity scheme, whereas triple-antenna diversity is required for the adaptive schemes operating in the same scenario. The corresponding first switching levels s_1 are depicted in Figure 5.41 for different order of antenna diversity up an order of six. As the antenna diversity order increases, the avalanche SNR becomes lower and the switching-threshold undulation effects begins to appear. The required values of the first switching level s_1 are within a range of about 1dB and 0.5dB for the target BEPs of $P_{th} = 10^{-3}$ and $P_{th} = 10^{-6}$, respectively, before the avalanche SNR is reached. This suggests that the optimum mode-switching levels are more dependent on the target BEP, than on the number of diversity antennas.

5.5.3 Performance over Wideband Rayleigh Channels using Antenna Diversity

Wideband fading channels are characterised by their multi-path intensity profiles (MIP). In order to study the performance of the various adaptive modulation schemes, we employ two different MIP models in this section, namely a shortened Wireless Asynchronous Transfer Mode (W-ATM) channel [13, Ch 20] for an indoor scenario and a Bad-Urban Reduced-model A (BU-RA) channel [136] for a hilly urban outdoor scenario. Their MIPs are depicted in Figure 5.42. The W-ATM channel exhibits short-range, low-delay multi-path components, while the BU-RA channel exhibits six higher-delay multi-path components. Again, let us assume that our receivers are equipped with MRC Rake receivers [17], employing a sufficiently higher number of Rake fingers, in order to capture all the multi-path components generated

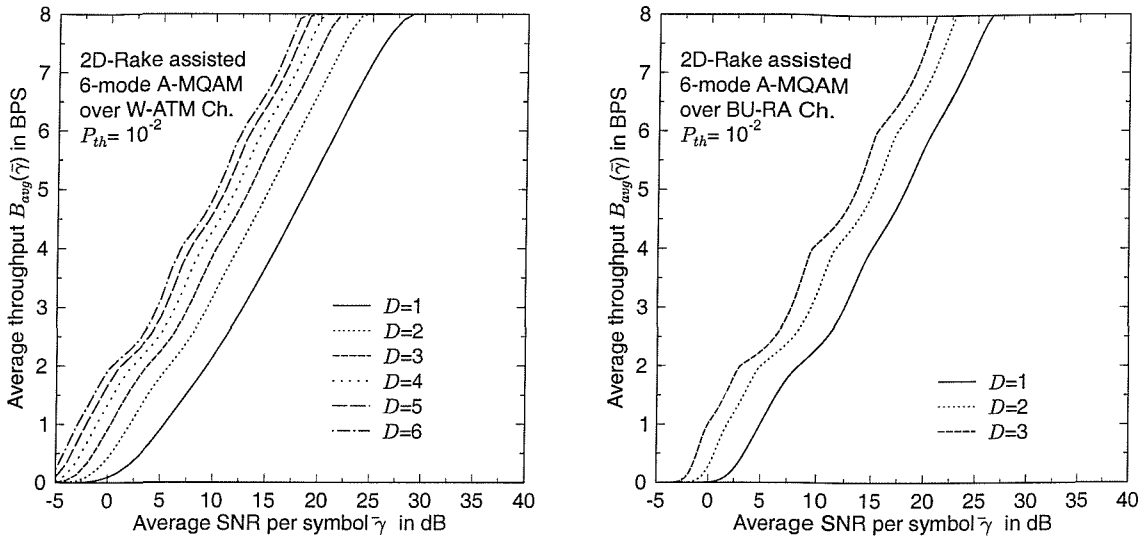

(a) W-ATM Channel

(b) BU-RA Channel

Figure 5.43: The effects of the number of diversity antennas on the average BPS throughput of the 2D-Rake assisted six-mode adaptive Square QAM scheme operating over the wideband independent Rayleigh fading channels characterised in Figure 5.42 at the target BEP of $P_{th} = 10^{-2}$. The the number of diversity antennas is D.

by our channel models. Furthermore, we employ antenna diversity [135, Ch 5] at the receivers. This combined diversity scheme is often referred to as a two-dimensional (2D) Rake receiver [137, pp 263]. The BER of the 2D Rake receiver transmission over wide-band independent Rayleigh fading channels is analysed in Appendix B. A closed-form expression for the mode-specific average BEP of a 2D-Rake assisted adaptive Square QAM scheme is also given in Appendix C. Hence, the performance of our 2D-Rake assisted adaptive modulation scheme employing the optimum switching levels can be readily obtained.

The average BPS throughputs of our 2D-Rake assisted adaptive schemes operating over the two different types of wideband channel scenarios is presented in Figure 5.43 at the target BEP of $P_{th} = 10^{-2}$. The throughput performance depicted corresponds to the upper-bound performance of Direct-Sequence Code Division Multiple Access (DS-CDMA) or Multi-Carrier CDMA employing Rake receivers and the MRC-aided diversity assisted scheme in the absence of Multiple Access Interference (MAI). We can observe that the BPS throughput curves undulate, when the number of antennas D increases. This effect is more pronounced for transmission over the BU-RA channel, since the BU-RA channel exhibits six multi-path components, increasing the available diversity potential of the system approximately by a factor of two in comparison to that of the W-ATM channel. The performance of our adaptive scheme employing more than three antennas for transmission over the BU-RA channel could not be obtained owing to numerical instability, since the associated curves become similar to a series of step-functions, which is not analytic in mathematical terms. A similar observation can be made in the context of Figure 5.44,

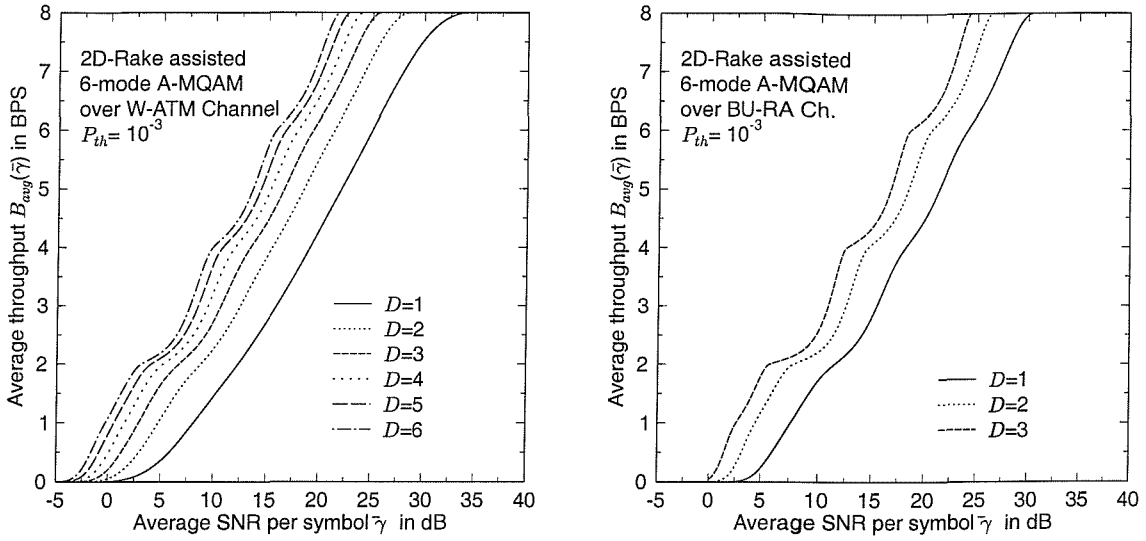

(a) W-ATM Channel

(b) BU-RA Channel

Figure 5.44: The effects of the number of diversity antennas on the average BPS throughput of the 2D-Rake assisted six-mode adaptive Square QAM scheme operating over the wideband independently Rayleigh fading channels characterised in Figure 5.42 at the target BEP of $P_{th} = 10^{-3}$. The the number of diversity antennas is D .

where the target BEP is $P_{th} = 10^{-3}$. Comparing Figure 5.43 and Figure 5.44, we observe that the BPS throughput curves corresponding to $P_{th} = 10^{-3}$ are similar to shifted version of those corresponding to $P_{th} = 10^{-2}$, which are shifted in the direction of increasing SNRs. On the other hand, the BPS throughput curves corresponding to $P_{th} = 10^{-3}$ undulate more dramatically. When the number of antennas is $D = 3$, the BPS throughput curves of the BU-RA channel exhibits a stair-case like shape. The corresponding mode switching levels and mode selection probabilities are shown in Figure 5.45. Again, the switching levels heavily undulate. The mode-selection probability curve of BPSK has a triangular shape, increasing linearly, as the average SNR $\bar{\gamma}$ increases to 2.5dB and decreasing linearly again as $\bar{\gamma}$ increases from 2.5dB. On the other hand, the mode-selection probability curve of QPSK increases linearly and decreases exponentially, since no 3-BPS mode is used. This explains, why the BPS throughput curves increase in a near-linear fashion in the SNR range of 0 to 5dB and in a stair-case fashion beyond that point. We can conclude that the stair-case like shape in the upper SNR range of SNR is a consequence of the absence of the 3-BPS, 5-BPS and 7-BPS modulation modes in the set of constituent modulation modes employed. As we discussed in Section 5.5.1.3, this problem may be mitigated by introducing power-efficient 8 QAM, 32 QAM and 128 QAM modes.

The average SNRs required achieving the target BEP of $P_{th} = 10^{-3}$ by the 2D-Rake assisted adaptive scheme and the fixed-mode schemes operating over wide-band fading channels are depicted in Figure 5.46. Since the fixed-mode schemes employing Rake receivers are already enjoying the diversity benefit of multi-path fading channels, the SNR advantages of our adaptive schemes are less than 8dB

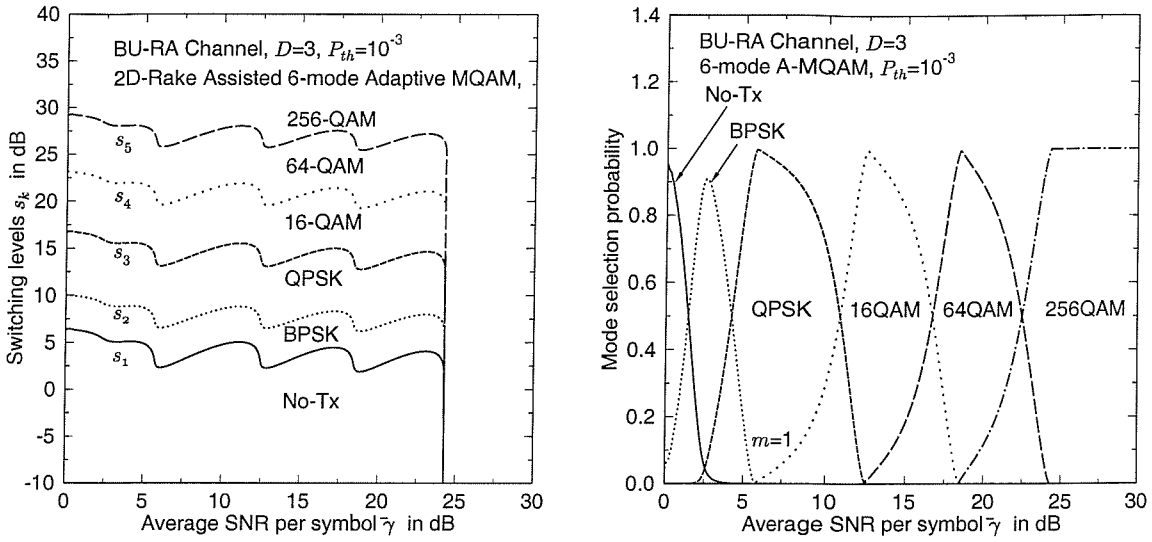

(a) Switching Levels

(b) Mode Selection Probability

Figure 5.45: The mode switching levels and mode selection probability of the 2D-Rake assisted six-mode adaptive Square QAM scheme using $D = 3$ antennas operating over the BU-RA channel characterised in Figure 5.42(b) at the target BEP of $P_{th} = 10^{-3}$.

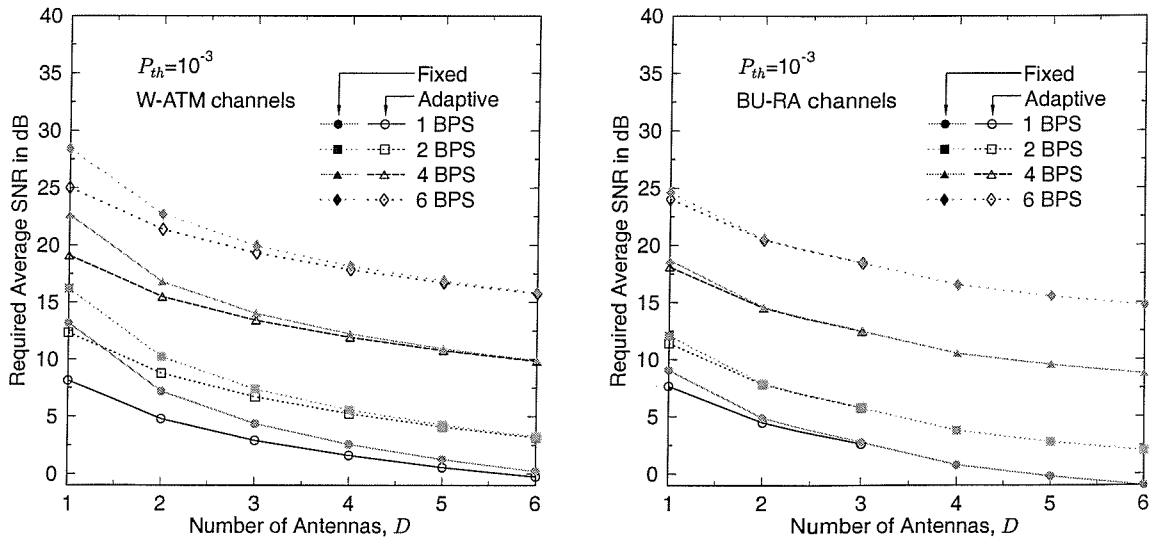

(a) W-ATM Channel

(b) BU-RA Channel

Figure 5.46: The average SNRs required for achieving the target BEP of $P_{th} = 10^{-3}$ by the 2D-Rake assisted adaptive schemes and by the fixed-mode schemes operating over (a) the W-ATM channel and (b) the BU-RA channel

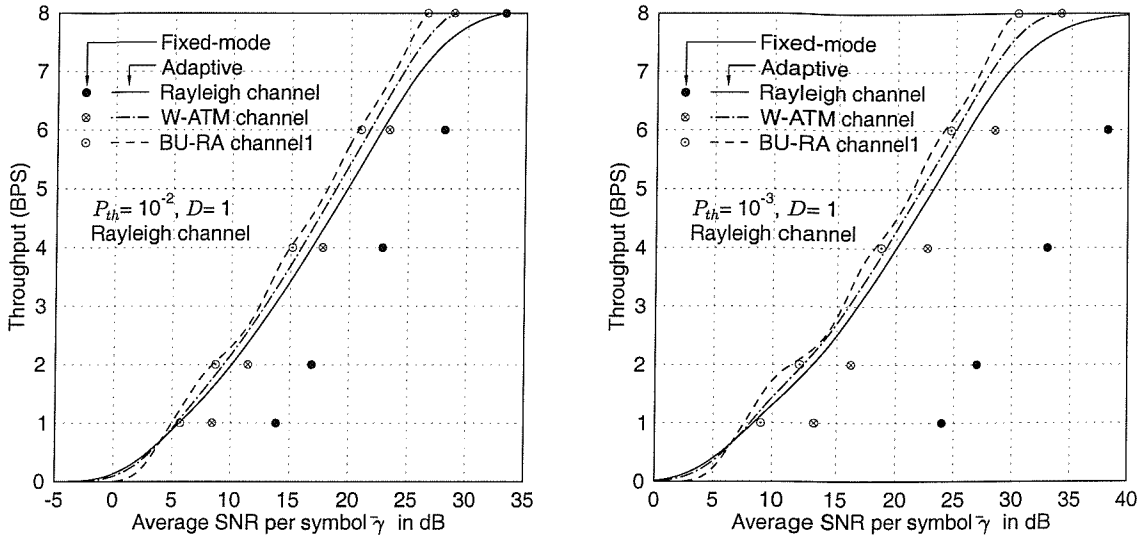

(a) $P_{th} = 10^{-2}$ (b) $P_{th} = 10^{-3}$

Figure 5.47: The average BPS throughput of the adaptive schemes and fixed-mod schemes transmission over a narrow-band Rayleigh channel, the W-ATM channel and BU-RA channel of Figure 5.42 at the target BEP of (a) $P_{th} = 10^{-2}$ and (b) $P_{th} = 10^{-3}$.

and 2.6dB over the W-ATM channel and over BU-RA channel, respectively, even when a single antenna is employed. This relative small SNR gain in comparison to those observed over narrow-band fading channels in Figure 5.40 erode as the number of antennas increases. For example, when the number of antennas is $D = 6$, the SNR gains of the adaptive schemes operating over the W-ATM channel of Figure 5.42(a) become virtually zero, where the combined channel becomes an AWGN-like channel. On the other hand, $D = 3$ number of antennas is sufficient for the BU-RA channel for exhibiting such a behavior, since the underlying multi-path diversity provided by the six-path BU-RA channel is higher than that of the tree-path W-ATM channel.

5.5.4 Uncoded Adaptive Multi-Carrier Schemes

The performance of the various adaptive Square QAM schemes has been studied also in the context of multi-carrier systems [13, 138, 139]. The family of Orthogonal Frequency Division Multiplex (OFDM) [55] systems converts frequency selective Rayleigh channels into frequency non-selective or flat Rayleigh channels for each sub-carrier, provided that the number of sub-carriers is sufficiently high. The power and bit allocation strategy of adaptive OFDM has attracted substantial research interests [13]. OFDM is particularly suitable for combined time-frequency domain processing [139]. Since each sub-carrier of an OFDM system experiences a flat Rayleigh channel, we can apply adaptive modulation for each sub-carrier independently from other sub-carriers. Although a practical scheme would group the sub-carriers into similar-quality sub-bands for the sake of reducing the associated modem mode signaling requirements. The performance of this AQAM assisted OFDM (A-OFDM) scheme is identical to that of

the adaptive scheme operating over flat Rayleigh fading channels, characterised in Section 5.5.2.

MC-CDMA [1, 2] receiver can be regarded as a frequency domain Rake-receiver, where the multiple carriers play a similar role to that of the time-domain Rake fingers. Our simulation results showed that the single-user BER performance of MC-CDMA employing multiple antennae is essentially identical to that of the time-domain Rake receiver using antenna diversity, provided that the spreading factor is higher than the number of resolvable multi-path components in the channel. Hence, the throughput of the Rake-receiver over the three-path W-ATM channel [13] and the six-path BU-RA channel [136] studied in Section 5.5.3 can be used for investigating the upper-bound performance of adaptive MC-CDMA schemes over these channels. Figure 5.47 compares the average BPS throughput performances of these schemes, where the throughput curves of the various adaptive schemes are represented as three different types of lines, depending on the underlying channel scenarios, while the fixed-mode schemes are represented as three different types of markers. The solid line corresponds to the performance of A-OFDM and the marker '•' corresponds to that of the fixed-mode OFDM. On the other hand, the dotted lines correspond to the BPS throughput performance of adaptive MC-CDMA operating over wide-band channels and the markers '⊙' and '⊗' to those of the fixed-mode MC-CDMA schemes.

It can be observed that fixed-mode MC-CDMA has a potential to outperform A-OFDM, when the underlying channel provides sufficient diversity due to the high number of resolvable multi-path components. For example, the performance of fixed-mode MC-CDMA operating over the W-ATM channel of Figure 5.42(a) is slightly lower than that of A-OFDM for the BPS range of less than or equal to 6 BPS, owing to the insufficient diversity potential of the wide-band channel. On the other hand, fixed-mode MC-CDMA outperforms A-OFDM, when the channel is characterised by the BU-RA model of Figure 5.42(b). We have to consider several factors, in order to answer, whether fixed-mode MC-CDMA is better than A-OFDM. Firstly, fully loaded MC-CDMA, which can transmit the same number of symbols as OFDM, suffers from multi-code interference and our simulation results showed that the SNR degradation is about 2-4dB at the BER of 10^{-3}, when the Minimum Mean Square Error Block Decision Feedback Equaliser (MMSE-BDFE) [140] based joint detector is used at the receiver. Considering these SNR degradations, the throughput of fixed-mode MC-CDMA using the MMSE-BDFE joint detection receiver falls just below that of the A-OFDM scheme, when the channel is characterised by the BU-RA model. On the other hand, the adaptive schemes may suffer from inaccurate channel estimation/prediction and modem mode signalling feedback delay [122]. Hence, the preference order of the various schemes may depend on the channel scenario encountered, on the interference effects and other practical issues, such as the aforementioned channel estimation accuracy, feedback delays, etc.

5.5.5 Concatenated Space-Time Block Coded and Turbo Coded Symbol-by-Symbol Adaptive OFDM and Multi-Carrier CDMA[3]

In the previous sections we studied the performance of uncoded adaptive schemes. Since a Forward Error Correction (FEC) code reduces the SNR required for achieving a given target BER at the expense of a

[3]This section was based on collaborative research with the contents of [46].

reduced BPS throughput, it is interesting to investigate the performance of adaptive schemes employing FEC techniques. A variety of FEC techniques has been used in the context of adaptive modulation schemes. In their pioneering work on adaptive modulation, Webb and Steele [113] used a set of binary BCH codes. Vucetic [141] employed various punctured convolutional codes in response to the time-variant channel status. On the other hand, various Trellis Coded Modulation (TCM) [142, 143] schemes were used in the context of adaptive modulation by Alamouti and Kallel [144], Goldsmith and Chua [145], as well as Hole, Holm and Øien [127]. Keller, Liew and Hanzo studied the performance of Redundant Residue Number System (RRNS) codes in the context of adaptive multi-carrier modulation [146, 147]. Various turbo coded adaptive modulation schemes have been investigated also by Liew, Wong, Yee and Hanzo [148–150]. With the advent of space-time (ST) coding techniques [151–153], various concatenated coding schemes combining ST coding and FEC coding can be applied in adaptive modulation schemes. In this section, we investigate the performance of various concatenated space-time block-coded and turbo-coded adaptive OFDM and MC-CDMA schemes.

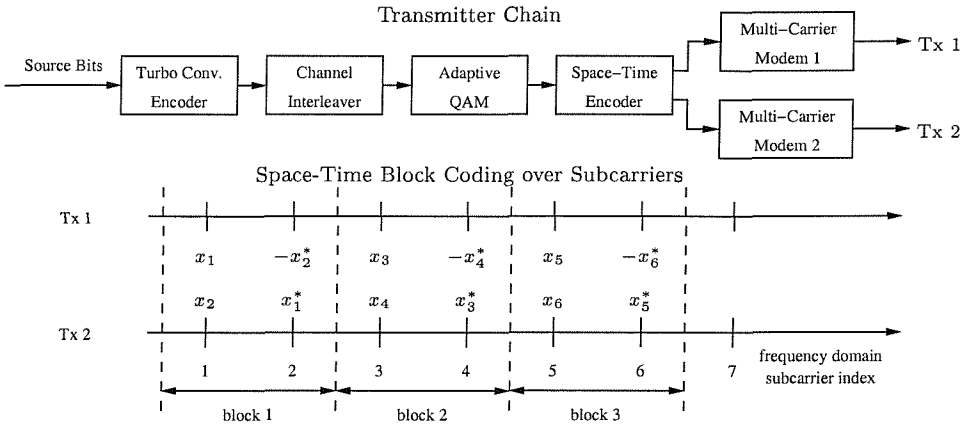

Figure 5.48: Transmitter structure and space-time block encoding scheme

Figure 5.48 portrays the stylised transmitter structure of our system. The source bits are channel coded by a half-rate turbo convolutional encoder [154] using a constraint length of $K = 3$ as well as an interleaver having a memory of $L = 3072$ bits and interleaved by a random block interleaver. Then, the AQAM block selects a modulation mode from the set of no transmission, BPSK, QPSK, 16-QAM and 64-QAM depending on the instantaneous channel quality perceived by the receiver, according to the SNR-dependent optimum switching levels derived in Section 5.4.4. It is assumed that the perfectly estimated channel quality experienced by receiver A is fed back to transmitter B superimposed on the next burst transmitted to receiver B. The modulation mode switching levels of our AQAM scheme determine the average BER as well as the average throughput.

The modulated symbol is now space-time encoded. As seen at the bottom of Figure 5.48, Alamouti's space-time block code [152] is applied across the frequency domain. A pair of the adjacent sub-carriers belonging to the same space-time encoding block is assumed to have the same channel quality. We employed a Wireless Asynchronous Transfer Mode (W-ATM) channel model [13, pp.474] transmitting at a carrier frequency of 60GHz, at a sampling rate of 225MHz and employing 512 sub-carriers. Specif-

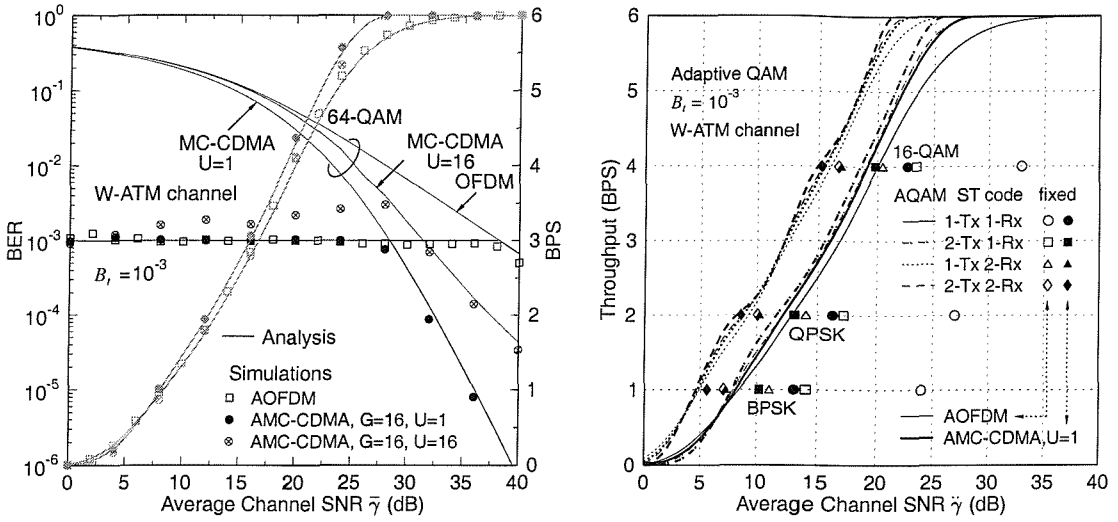

(a) BER and Throughput, No ST coding

(b) Throughput with ST coding

Figure 5.49: Performance of uncoded five-mode AOFDM and AMC-CDMA. The target BER is $B_t = 10^{-3}$ when transmitting over the W-ATM channel [13, pp.474]. (a) The constant average BER is maintained for AOFDM and single user AMC-CDMA, while 'full-user' AMC-CDMA exhibits a slightly higher average BER due to the residual MUI. (b) The SNR gain of the adaptive modems decreases, as ST coding increases the diversity order. The BPS curves appear in pairs, corresponding to AOFDM and AMC-CDMA - indicated by the thin and thick lines, respectively - for each of the four different ST code configurations. The markers represent the SNRs required by the fixed-mode OFDM and MC-CDMA schemes for maintaining the target BER of 10^{-3} in conjunction with the four ST-coded schemes considered.

ically, we used a three-path fading channel model, where the average SNR of each path is given by $\bar{\gamma}_1 = 0.79192\bar{\gamma}$, $\bar{\gamma}_2 = 0.12424\bar{\gamma}$ and $\bar{\gamma}_3 = 0.08384\bar{\gamma}$. The Multi-path Intensity Profile (MIP) of the W-ATM channel is illustrated in Figure 5.42(a) in Section 5.5.3. Each channel associated with a different antenna is assumed to exhibit independent fading.

The simulation results related to our uncoded adaptive modems are presented in Figure 5.49. In Figure 5.49(a) both the continuous black lines and the related markers drawin in continuous lines represent the BERs, while their grey or 'half-tone' counterparts the BPS throughputs. Viewing Figure 5.49(a) from a different perspective, all the lines indicate analytical results, while all the markers correspond to simulation results. The set of three BER curves represented by black lines decreasing as the average SNR becomes higher corresponds to those of fixed-mode OFDM and MC-CDMA schemes. Since we employed the optimum switching levels derived in Section 5.4.4, both our adaptive OFDM (AOFDM) and the adaptive single-user MC-CDMA (AMC-CDMA) modems maintain the constant target BER of 10^{-3} up to the 'avalanche' SNR value, and then follow the BER curve of the fixed-mode 64-QAM mode. However, 'full-user' AMC-CDMA, which is defined as an AMC-CDMA system supporting $U = 16$ users

with the aid of a spreading factor of $G = 16$ and employing the MMSE-BDFE Joint Detection (JD) receiver described in Section 3.4.2, exhibits a slightly higher average BER, than the target of $B_t = 10^{-3}$ due to the fact that residual Multi-User Interference (MUI) of the imperfect joint detector does not strictly follow a Gaussian distribution. Since in Section 5.4.4 we derived the optimum switching levels based on a single-user system, the levels are no longer optimum, when residual MUI does not follow Gaussian distribution. The average throughputs of the various schemes expressed in terms of BPS steadily increase and at high SNRs reach the throughput of 64-QAM, namely 6 BPS. The throughput degradation of 'full-user' MC-CDMA imposed by the imperfect JD was within a fraction of a dB. Observe in Figure 5.49(a) that the analytical and simulation results are in good agreement, which we denoted by the lines and distinct symbols, respectively.

The effects of ST coding on the average BPS throughput are displayed in Figure 5.49(b). Specifically, the thick lines represent the average BPS throughput of our AMC-CDMA scheme, while the thin lines represent those of our AOFDM modem. The four pairs of hollow and filled markers associated with the four different ST-coded AOFDM and AMC-CDMA scenarios considered represent the BPS throughput versus SNR values associated with fixed-mode OFDM and fixed-mode MMSE-BDFE JD assisted MC-CDMA schemes. Specifically, observe for each of the 1, 2 and 4 BPS fixed-mode schemes that the right most markers, namely the circles, correspond to the 1-Tx / 1-Rx scenario, the squares to the 2-Tx / 1-Rx scheme, the triangles to the 1-Tx / 2-Rx arrangement and the diamonds to the 2-Tx / 2-Rx scenarios. First of all, we can observe that the BPS throughput curves of OFDM and single-user MC-CDMA are close to each other, namely within 1 dB for most of the SNR range. This is surprising, considering that the fixed-mode MMSE-BDFE JD assisted MC-CDMA scheme was reported to exhibit around 10dB SNR gain at a BER of 10^{-3} and 30dB gain at a BER of 10^{-6} over OFDM [43]. This is confirmed in Figure 5.49(b) by observing that the SNR difference between the $\circ$ and $\bullet$ markers is around 10dB, regardless whether the 4, 2 or 1 BPS scenario is concerned.

Let us now compare the SNR gains of the adaptive modems over the fixed modems. The SNR difference between the BPS curve of AOFDM and the fixed-mode OFDM represented by the symbol $\circ$ at the same throughput is around 15dB. The corresponding SNR difference between the adaptive and fixed-mode 4, 2 or 1 BPS MC-CDMA modem is around 5dB. More explicitly, since in the context of the W-ATM channel model [13, pp.474] fixed-mode MC-CDMA appears to exhibit a 10dB SNR gain over fixed-mode OFDM, the additional 5dB SNR gain of AMC-CDMA over its fixed-mode counterpart results in a total SNR gain of 15dB over fixed-mode OFDM. Hence ultimately the performance of AOFDM and AMC-CDMA becomes similar.

Let us now examine the effect of ST block coding. The SNR gain of the fixed-mode schemes due to the introduction of a 2-Tx / 1-Rx ST block code is represented as the SNR difference between the two right most markers, namely circles and squares. These gains are nearly 10dB for fixed-mode OFDM, while they are only 3dB for fixed-mode MC-CDMA modems. However, the corresponding gains are less than 1dB for both adaptive modems, namely for AOFDM and AMC-CDMA. Since the transmitter power is halved due to using two Tx antennas in the ST codec, a 3dB channel SNR penalty was already applied to the curves in Figure 5.49(b). The introduction of a second receive antenna instead of a second

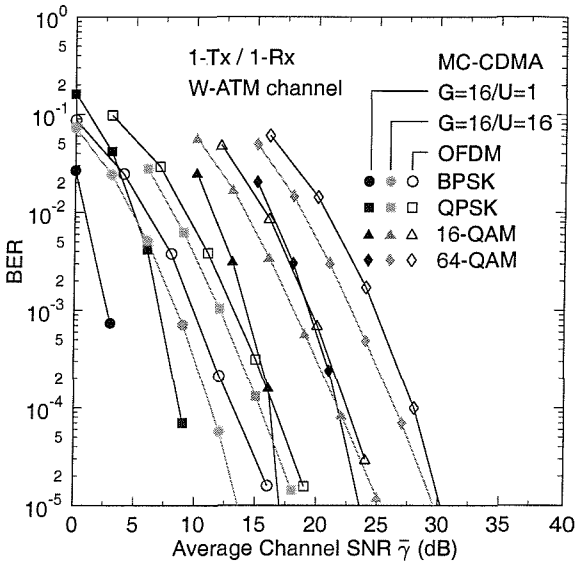

Figure 5.50: Performance of turbo convolutional coded fixed-mode OFDM and MC-CDMA for transmission over the W-ATM channel of [13, pp.474], indicating that JD MC-CDMA still outperforms OFDM. However, the SNR gain of JD MC-CDMA over OFDM is reduced to 1-2dB at a BER of 10^{-4}.

transmit antenna eliminates this 3dB penalty, which results in a better performance for the 1-Tx/2-Rx scheme than for the 2-Tx/1-Rx arrangement. Finally, the 2-Tx / 2-Rx system gives around 3-4dB SNR gain in the context of fixed-mode OFDM and a 2-3dB SNR gain for fixed-mode MC-CDMA, in both cases over the 1-Tx / 2-Rx system. By contrast, the SNR gain of the 2-Tx / 2-Rx scheme over the 1-Tx / 2-Rx based adaptive modems was, again, less than 1dB in Figure 5.49(b). More importantly, for the 2-Tx / 2-Rx scenario the advantage of employing adaptive modulation erodes, since the fixed-mode MC-CDMA modem performs as well as the AMC-CDMA modem in this scenario. Moreover, the fixed-mode MC-CDMA modem still outperforms the fixed-mode OFDM modem by about 2dB. We conclude that since the diversity-order increases with the introduction of ST block codes, the channel quality variation becomes sufficiently small for the performance advantage of adaptive modems to erode. This is achieved at the price of a higher complexity due to employing two transmitters and two receivers in the ST coded system.

When channel coding is employed in the fixed-mode multi-carrier systems, it is expected that OFDM benefits more substantially from the frequency domain diversity than MC-CDMA, which benefitted more than OFDM without channel coding. The simulation results depicted in Figure 5.50 show that the various turbo-coded fixed-mode MC-CDMA systems consistently outperform OFDM. However, the SNR differences between the turbo-coded BER curves of OFDM and MC-CDMA are reduced considerably.

The performance of the concatenated ST block coded and turbo convolutional coded adaptive modems is depicted in Figure 5.51. We applied the optimum set of switching levels designed in Section 5.4.4 for achieving an uncoded BER of 3×10^{-2}. This uncoded target BER was stipulated after observing that it is reduced by half-rate, $K = 3$ turbo convolutional coding to a BER below 10^{-7}, when transmitting over

AWGN channels. However, our simulation results yielded zero bit errors, when transmitting 10^9 bits, except for some SNRs, when employing only a single antenna.

Figure 5.51(a) shows the BER of our turbo coded adaptive modems, when a single antenna is used. We observe in the figure that the BER reaches its highest value around the 'avalanche' SNR point, where the adaptive modulation scheme consistently activates 64-QAM. The system is most vulnerable around this point. In order to interpret this phenomenon, let us briefly consider the associated interleaving aspects. For practical reasons we have used a fixed interleaver length of $L = 3072$ bits. When the instantaneous channel quality was high, the $L = 3072$ bits were spanning a shorter time-duration during their passage over the fading channel, since the effective BPS throughput was high. Hence the channel errors appeared more bursty, than in the lower-throughput AQAM modes, which conveyed the $L = 3072$ bits over a longer time duration, hence dispersing the error bursts over a longer duration of time. The uniform dispersion of erroneous bits versus time enhances the error correction power of the turbo code. On the other hand, in the SNR region beyond the 'avalanche' SNR point seen in Figure 5.51(a) the system exhibited a lower uncoded BER, reducing the coded BER even further. This observation suggests that further research ought to determine the set of switching thresholds directly for a coded adaptive system, rather than by simply estimating the uncoded BER, which is expected to result in near-error-free transmission.

We can also observe that the turbo coded BER of AOFDM is higher than that of AMC-CDMA in the SNR rage of 10-20dB, even though the uncoded BER is the same. This appears to be the effect of the limited exploitation of frequency domain diversity of coded OFDM, compared to MC-CDMA, which leads to a more bursty uncoded error distribution, hence degrading the turbo coded performance. The fact that ST block coding aided multiple antenna systems show virtually error free performance corroborates our argument.

Figure 5.51(b) compares the throughputs of the coded adaptive modems and the uncoded adaptive modems exhibiting a comparable average BER. The SNR gains due to channel coding were in the range of 0dB to 8dB, depending on the SNR region and on the scenarios employed. Each bundle of throughput curves corresponds to the scenarios of 1-Tx/1-Rx OFDM, 1-Tx/1-Rx MC-CDMA, 2-Tx/1-Rx OFDM, 2-Tx/1-Rx MC-CDMA, 1-Tx/2-Rx OFDM, 1-Tx/2-Rx MC-CDMA, 2-Tx/2-Rx OFDM and 2-Tx/2-Rx MC-CDMA starting from the far right curve, when viewed for throughput values higher than 0.5 BPS. The SNR difference between the throughput curves of the ST and turbo coded AOFDM and those of the corresponding AMC-CDMA schemes was reduced compared to the uncoded performance curves of Figure 5.49(b). The SNR gain owing to ST block coding assisted transmit diversity in the context of AOFDM and AMC-CDMA was within 1dB due to the halved transmitter power. Therefore, again, ST block coding appears to be less effective in conjunction with adaptive modems.

In conclusion, the performance of ST block coded constant-power adaptive multi-carrier modems employing optimum SNR-dependent modem mode switching levels were investigated in this section. The adaptive modems maintained the constant target BER stipulated, whilst maximising the average throughput. As expected, it was found that ST block coding reduces the relative performance advantage of adaptive modulation, since it increases the diversity order and eventually reduces the channel quality

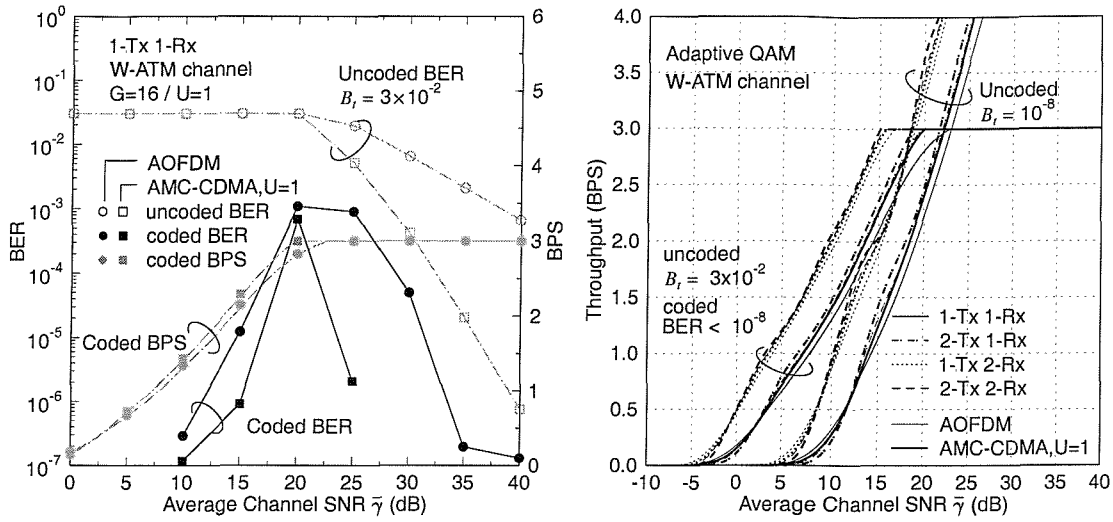

(a) BER

(b) Throughput

Figure 5.51: Performance of the concatenated ST block coded and turbo convolutional coded adaptive OFDM and MC-CDMA systems over W-ATM channel of [13, pp.474]. The uncoded target BER is 3×10^{-2}. The coded BER was less than 10^{-8} for most of the SNR range, resulting in virtually error free transmission. (a) The coded BER becomes higher near the 'avalanche' SNR point, when a single antenna was used. (b) The coded adaptive modems have SNR gains up to 7dB compared to their uncoded counterparts achieving a comparable average BER.

variations. When turbo convolutional coding was concatenated to the ST block codes, near-error-free transmission was achieved at the expense of halving the average throughput. Compared to the uncoded system, the turbo coded system was capable of achieving a higher throughput in the low SNR region at the cost of a higher complexity. The study of the relationship between the uncoded BER and the corresponding coded BER showed that adaptive modems obtain higher coding gains, than that of fixed modems. This was due to the fact that the adaptive modem avoids burst errors even in deep channel fades by reducing the number of bits per modulated symbol eventually to zero.

5.6 Summary and Conclusions

Following a brief introduction to several fading counter-measures, a general model was developed in order to describe several adaptive modulation schemes employing various constituent modulation modes, such as PSK, Star QAM and Square QAM, as one of the attractive fading counter-measures. In Section 5.3.3.1, the closed form expressions were derived for the average BER, the average BPS throughput and the mode selection probability of the adaptive modulation schemes, which were shown to be dependent on the mode-switching levels as well as on the average SNR. After reviewing in Section 5.4.1, 5.4.2 and 5.4.3 the existing techniques devised for determining the mode-switching levels, in Section 5.4.4 the

optimum switching levels achieving the highest possible BPS throughput while maintaining the average target BER were developed based on the Lagrangian optimisation method.

Then, in Section 5.5.1 the performance of uncoded adaptive PSK, Star QAM and Square QAM was characterised, when the underlying channel was a Nakagami fading channel. It was found that an adaptive scheme employing a k-BPS fixed-mode as the highest throughput constituent modulation mode was sufficient for attaining all the benefits of adaptive modulation, while achieving an average throughput of up to $k-1$ BPS. For example, a three-mode adaptive PSK scheme employing No-Tx, 1-BPS BPSK and 2-BPS QPSK modes attained the maximum possible average BPS throughput of 1 BPS and hence adding higher-throughput modes, such as 3-BPS 8-PSK to the three-mode adaptive PSK scheme resulting in a four-mode adaptive PSK scheme did not achieved a better performance across the 1 BPS throughput range. Instead, this four-mode adaptive PSK scheme extended the maximal achievable BPS throughput by any adaptive PSK scheme to 2 BPS, while asymptotically achieving a throughput of 3 BPS as the average SNR increases. On the other hand, the relative SNR advantage of adaptive schemes in comparison to fixed-mode schemes increased as the target average BER became lower and decreased as the fading became less severe. More explicitly, less severe fading corresponds to an increased Nakagami fading parameter m, to an increased number of diversity antennas, or to an increased number of multi-path components encountered in wide-band fading channels. As the fading becomes less severe, the average BPS throughput curves of our adaptive Square QAM schemes exhibit undulations owing to the absence of 3-BPS, 5-BPS and 7-BPS square QAM modes.

The comparisons between fixed-mode MC-CDMA and adaptive OFDM (AOFDM) were made based on different channel models. In Section 5.5.4 it was found that fixed-mode MC-CDMA might outperform adaptive OFDM, when the underlying channel provides sufficient diversity. However, a definite conclusion could not be drawn since in practice MC-CDMA might suffer from MUI and AOFDM might suffer from imperfect channel quality estimation and feedback delays.

Concatenated space-time block coded and turbo convolutional-coded adaptive multi-carrier systems were investigated in Section 5.5.5. The coded schemes reduced the required average SNR by about 6dB-7dB at throughput of 1 BPS achieving near error-free transmission. It was also observed in Section 5.5.5 that increasing the number of transmit antennas in adaptive schemes was not very effective, achieving less than 1dB SNR gain, due the fact that the transmit power per antenna had to be reduced in order to limit the total transmit power for the sake of fair comparison.

Chapter 6

Successive Partial Despreading Based Multi-Code MC-CDMA

6.1 Introduction

In the downlink scenario of spread spectrum systems several spreading codes may be simultaneously assigned to one user in order to support a high data throughput [42]. A specific example of this concept, namely a multi-code MC-CDMA scheme, was introduced in Section 4.5.1. When the number of simultaneously transmitted spreading codes L is equal to the spreading factor N, the system is said to be 'fully loaded'. A fully loaded MC-CDMA scheme was referred to as Walsh Hadamard Transform (WHT) based OFDM in references [155, 156]. More explicitly, the bandwidth requirement of the system is increased by a factor of N, when a spreading factor of N is used. However, under fully loaded conditions this system is capable of transmitting N bits of a single user with the aid of employing N parallel codes. Hence a total of N bits are transmitted in an N times higher bandwidth and therefore we may refer to this scheme as a 'unity-rate coding arrangement'. However, when non-orthogonal spreading codes are used or when the orthogonality of the codes is destroyed by the fading channels, a fully loaded CDMA system suffers from an excessive Multiple Code Interference (MCI). This phenomenon is also referred to as Multiple User Interference (MUI), when the simultaneously transmitted codes are used for supporting different users, as we observed in Section 3.3. In order to effectively cancel the above mentioned MCI or MUI, a multi user detector [157] or a joint detector [59] has to be employed in the receiver. In Section 4.5.3.3 we observed that the BER performance of the Minimum Mean Square Error (MMSE) Joint Detector (JD) assisted fully loaded multi-code MC-CDMA system is better, than that of OFDM, when the channel is independently Rayleigh fading over each subcarrier. However, one of the major obstacles of implementing joint-detection receivers has been their high implementational complexity.

In this chapter, we investigate a reduced-complexity despreading technique involved in the context of fully loaded Walsh-spread multi-code systems employing BPSK modulation, based on a Walsh matrix assisted partitioning. Let us assume that our system model is a BPSK modulated fully loaded multi-code MC-CDMA scheme, which was referred to in [155] as a WHT/OFDM arrangement.

6.2 System Model

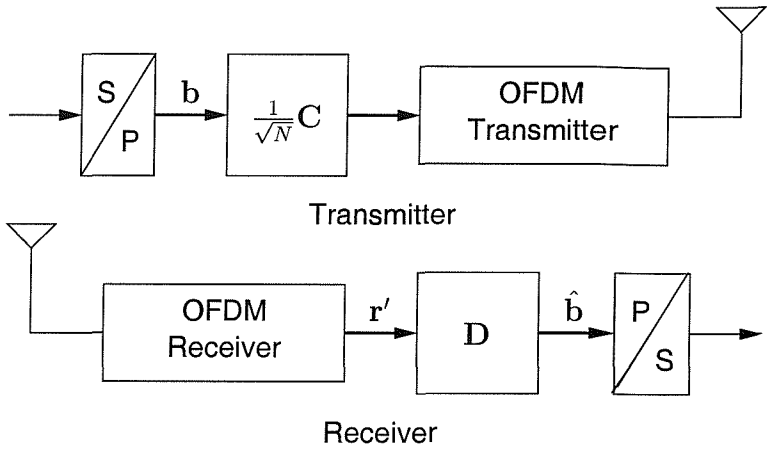

Figure 6.1: A transmitter and a receiver schematic of fully loaded multi-code BPSK modulated MC-CDMA

The transmitter schematic of the investigated fully loaded multi-code BPSK modulated MC-CDMA scheme is depicted in Figure 6.1. The serial-to-parallel converter gathers N number of different consecutive information bits in order to generate a $N \times 1$ dimensional information bit vector $\mathbf{b}$. Then, an $N \times N$ dimensional Walsh spreading matrix, namely $1/\sqrt{N}\,\mathbf{C}$ is for transforming this bit vector $\mathbf{b}$, in order to generate the $N \times 1$ dimensional frequency domain symbol vector $\mathbf{s}$, which is transmitted using a conventional OFDM transmitter [13]. The $N \times 1$ dimensional frequency domain symbol vector $\mathbf{s}$ can be expressed as:

$$\mathbf{s} = \frac{1}{\sqrt{N}}\,\mathbf{C}\,\mathbf{b}\,, \tag{6.1}$$

where N is the spreading factor. The scaling factor of $1/\sqrt{N}$ was introduced in (6.1) for rendering the average power of the transformed message the same as that of the unspread symbol.

The OFDM receiver recovers the $N \times 1$ dimensional frequency domain symbol vector $\mathbf{r}$, which was corrupted by fading and contaminated by noise. Various despreading/detection techniques have been developed for recovering the original symbol $\mathbf{b}$ from the spread symbol $\mathbf{s}$ [50]. However, all techniques are based on applying the despreading matrix, $\mathbf{D}$. This despreading process can be represented as:

$$\hat{\mathbf{b}} = \mathbf{D}\,\mathbf{r}', \tag{6.2}$$

where $\hat{\mathbf{b}}$ is the estimated $N \times 1$ dimensional binary antipodal message vector, the despreading matrix $\mathbf{D}$ is given as $\mathbf{C}^H$ with the superscript ^{H} indicating the Hermitian [94] of the matrix $\mathbf{C}$ and $\mathbf{r}'$ is the fading-compensated received vector. Since the kth estimated bit $\hat{\mathbf{b}}_k$ is obtained by $\hat{\mathbf{b}}_k = \sum_{n=1}^{N} \mathbf{D}_{kn}\,\mathbf{r}'_n$, N number of multiplications and $N-1$ number of additions are required for calculating $\hat{\mathbf{b}}_k$, where $k = 1, \cdots, N$, yielding a total number of multiplications given by N^2 and $N^2 - N$ number of additions for detecting all the bits.

The advantage of this Walsh-spreading based scheme is highlighted here in comparison to a conventional OFDM scheme as follows. When a conventional OFDM scheme experiences frequency-selective fading, the specific bits of the N-bit OFDM symbol conveyed by the highly attenuated subcarriers are virtually obliterated by the fading. By contrast, when invoking the above-mentioned Walsh-spreading scheme, each component of the transformed vector $\mathbf{s}$ is dependent on each of the N bits of the vector $\mathbf{b}$. When a specific component of the N-component vector $\mathbf{s}$ is obliterated by a badly faded OFDM subcarrier, the effects of this are spread to all the N bits of the estimated transmitted vector $\hat{\mathbf{b}}$, but they only fractionally contaminate each of the N bits. Hence there is still a high probability that all N bits can be recovered without an error, despite having a corrupted subcarrier. The same approach can be extended to a scenario, where one or several of the components of the vector $\mathbf{s}$ are simply ignored during the detection process, in an effort to reduce the associated detection complexity.

In Section 2.2.1 we observed that Walsh codes is recursively defined using Walsh-Hadamard transform. Exploiting this recursive structure inherent in Walsh codes, we may be able to reduce the number of operations required for despreading in (6.2). Hence, we propose an alternative approach to the conventional "full despreading", termed as "successive partial despreading" (SPD), for employment in Walsh-spread systems, where only half of the vector components of the fading compensated received signal $\{r'[k]\}$ are used during the first stage detection, while the other half of the vector components are involved for the final detection only if it is deemed necessary. We will see that the proposed technique requires less than half the number of operations, compared to the conventional despreading method. Three types of SPD detection schemes are introduced in Section 6.3. The proposed schemes are analysed, when communicating over the AWGN channel in terms of their achievable BER performance and their implementational complexity in Section 6.4. In a certain scenario, a time domain impulse noise [158, 159] or a narrow-band jamming/interference [160] in the frequency domain can be a dominant channel impairment source. In this situation some chips of the simultaneous codes have to be discarded, since the magnitude of the impulse noise in the time domain is higher than that of the chip concerned. The same action has to be taken as regards to a particular subcarrier, when the magnitude of the narrow-band jamming signal in the frequency domain is higher than that of the subcarrier. Section 6.5 investigates the performance of the proposed SPD scheme, when one of the symbols modulating a specific subcarrier is unavailable due to the above-mentioned impairments. Section 6.6 concludes with a number of observations and future research directions. Following the above conceptual introduction, let us now elaborate on the associated detection philosophy in more depth.

6.3 The Sequential Partial Despreading Concept

The N-dimensional Walsh-Hadamard matrix, $\mathbf{W}_N$, can be represented in its recursive form as [50]:

$$\mathbf{W}_N = \begin{bmatrix} \mathbf{W}_{N/2} & \mathbf{W}_{N/2} \\ \mathbf{W}_{N/2} & \overline{\mathbf{W}}_{N/2} \end{bmatrix}. \tag{6.3}$$

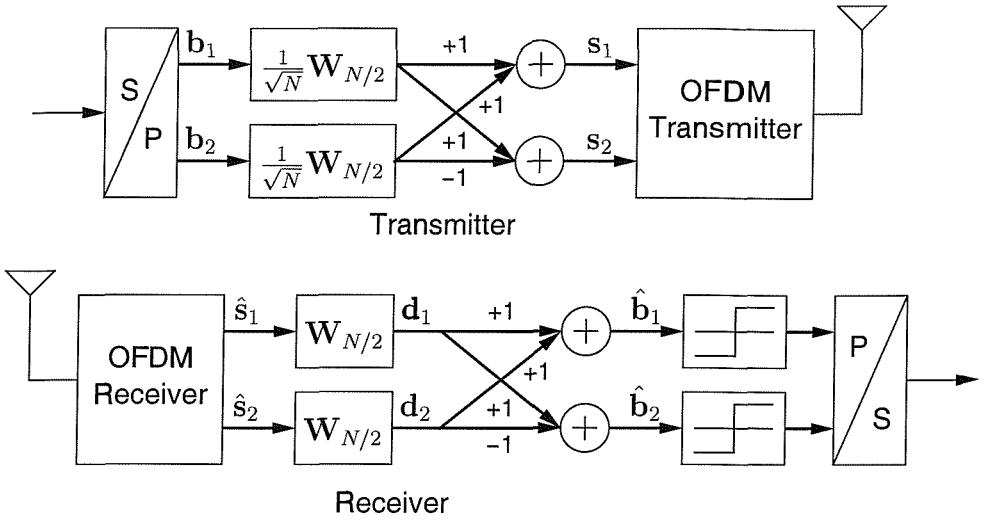

Figure 6.2: Transmitter and receiver schematic of the SPD scheme for fully loaded multi-code BPSK modulated MC-CDMA, where $\mathbf{W}_{N/2}$ is the $N/2$-dimensional Walsh spreading matrix.

Then the spread symbol of (6.1) can be re-written with the aid of the $N/2$-dimensional sub-matrices and sub-vectors as:

$$\begin{bmatrix} \mathbf{s}_1 \\ \mathbf{s}_2 \end{bmatrix} = \frac{1}{\sqrt{N}} \begin{bmatrix} \mathbf{W}_{N/2} & \mathbf{W}_{N/2} \\ \mathbf{W}_{N/2} & \overline{\mathbf{W}}_{N/2} \end{bmatrix} \begin{bmatrix} \mathbf{b}_1 \\ \mathbf{b}_2 \end{bmatrix} , \tag{6.4}$$

where $\mathbf{s}_1$ and $\mathbf{s}_2$ are the $N/2 \times 1$ dimensional sub-vectors of $\mathbf{s}$, and $\mathbf{b}_1$ and $\mathbf{b}_2$ are the $N/2 \times 1$ dimensional antipodal sub-vectors of $\mathbf{b}$ having components of ± 1.

The expression in (6.4) can be decomposed into two equations, one for $\mathbf{s}_1$ and the other for $\mathbf{s}_2$ as follows:

$$\mathbf{s}_1 = \frac{1}{\sqrt{N}}\mathbf{W}_{N/2}\mathbf{b}_1 + \frac{1}{\sqrt{N}}\mathbf{W}_{N/2}\mathbf{b}_2 \tag{6.5}$$

$$\mathbf{s}_2 = \frac{1}{\sqrt{N}}\mathbf{W}_{N/2}\mathbf{b}_1 + \frac{1}{\sqrt{N}}\overline{\mathbf{W}}_{N/2}\mathbf{b}_2 \, . \tag{6.6}$$

The corresponding transmitter and receiver schematics are depicted in Figure 6.2, explicitly showing the decomposed matrix operations. In the proposed SPD scheme, the despreading is performed at the receiver upon multiplying $\mathbf{W}_{N/2}$ by the recovered frequency domain symbol $\hat{\mathbf{s}}_1$ and $\hat{\mathbf{s}}_2$ output by the OFDM receiver, which is expressed as:

$$\mathbf{d}_1 = \mathbf{W}_{N/2}\,\hat{\mathbf{s}}_1 \tag{6.7}$$

$$\mathbf{d}_2 = \mathbf{W}_{N/2}\,\hat{\mathbf{s}}_2 \, . \tag{6.8}$$

For simplicity, let us assume that $\mathbf{s}_1$ and $\mathbf{s}_2$ have been received without any channel impairments and without any noise for the moment. Then, exploiting that $\mathbf{W}_{N/2}\,\mathbf{W}_{N/2} = N/2\,\mathbf{I}_{N/2}$, the two $N/2$

dimensional despread symbol vectors of (6.7) and (6.8) can be expressed as:

$$\mathbf{d}_1 = \frac{\sqrt{N}}{2}(\mathbf{b}_1 + \mathbf{b}_2) \tag{6.9}$$

$$\mathbf{d}_2 = \frac{\sqrt{N}}{2}(\mathbf{b}_1 - \mathbf{b}_2)\,. \tag{6.10}$$

The last operation of the receiver is that of recovering $\mathbf{b}_1$ and $\mathbf{b}_2$ with the aid of:

$$\hat{\mathbf{b}}_1 = \frac{\mathbf{d}_1 + \mathbf{d}_2}{\sqrt{N}} \tag{6.11}$$

$$\hat{\mathbf{b}}_2 = \frac{\mathbf{d}_1 - \mathbf{d}_2}{\sqrt{N}}, \tag{6.12}$$

in order to recover $\hat{\mathbf{b}}$. Explicitly, according to (6.9) and (6.10) in the absence of channel impairments the detection variables $\mathbf{d}_1$ and $\mathbf{d}_2$ are given by the sum and the difference of the two independent $N/2 \times 1$ dimensional message symbols $\mathbf{b}_1$ and $\mathbf{b}_2$. When the kth bits of the subvectors $\mathbf{b}_1$ and $\mathbf{b}_2$, namely $\mathbf{b}_1[k]$ and $\mathbf{b}_2[k]$, have the same value, $\mathbf{d}_1[k]$ in the numerator of (6.11) is sufficient for the detection of both $\mathbf{b}_1$ and $\mathbf{b}_2$, since $\mathbf{d}_2[k] = \sqrt{N}/2\,(\mathbf{b}_1 - \mathbf{b}_2) = 0$ conveys no information. By contrast, in the presence of channel-impairments $\mathbf{b}_1[k] = \mathbf{b}_2[k]$ is indicated on a probablistic basis by $\mathbf{d}_2[k] \approx 0$ according to (6.10). On the other hand, when we have $\mathbf{b}_1[k] = -\mathbf{b}_2[k]$, $\mathbf{d}_1[k] = \sqrt{N}/2\,(\mathbf{b}_1 + \mathbf{b}_2)$ becomes zero and $\mathbf{d}_2[k] = \sqrt{N}/2\,(\mathbf{b}_1 - \mathbf{b}_2)$ is required for the correct detection of both bits.

Let us now consider three types of SPD detection schemes, which we referred to as the Type I, Type II, and Type III SPD schemes. They differ in their philosophy of using the despread symbol vectors $\mathbf{d}_1$ of (6.9) and $\mathbf{d}_2$ of (6.10), when generating the decision variables $\hat{\mathbf{b}}_1$ and $\hat{\mathbf{b}}_2$ for the original message vectors of $\mathbf{b}_1$ and $\mathbf{b}_2$. The noise-contaminated PDFs of $\mathbf{d}_1$ and $\mathbf{d}_2$ are plotted in Figure 6.3, which will be consulted throughout our further discourse.

Type I : The decision variables $\hat{\mathbf{b}}_1[k]$ and $\hat{\mathbf{b}}_2[k]$ are identical to those of the conventional despreading detectors, but due to processing two $N/2$-dimensional vectors instead of an N-dimensional vector the detector requires a reduced number of multiplications and additions, as it will be shown in Section 6.4.1. Upon neglecting the scaling factor of $1/\sqrt{N}$ in (6.11) and (6.12) the associated decision variables are expressed as:

$$\hat{\mathbf{b}}_1[k] = \mathbf{d}_1[k] + \mathbf{d}_2[k] \tag{6.13}$$

$$\hat{\mathbf{b}}_2[k] = \mathbf{d}_1[k] - \mathbf{d}_2[k]\,, \tag{6.14}$$

where $\mathbf{d}_1[k]$ and $\mathbf{d}_2[k]$ are now contaminated by the channel effects and hence they obey the noisy PDFs seen in Figure 6.3.

Type II : If the detector's confidence in $\hat{\mathbf{b}}_1[k] = \hat{\mathbf{b}}_2[k]$ is high, since we have $|\mathbf{d}_1[k]| > V_T$ in Figure 6.3(a), then according to (6.9) we can confidently assume that $\hat{\mathbf{b}}_1[k] = \hat{\mathbf{b}}_2[k]$. By contrast, if the probability of $\hat{\mathbf{b}}_1[k] = \hat{\mathbf{b}}_2[k]$ is low, since a low $|\mathbf{d}_1[k]|$ value is encountered, which is indicative of $\hat{\mathbf{b}}_1[k] = -\hat{\mathbf{b}}_2[k]$, then we make the apposite decision for $\hat{\mathbf{b}}_1[k]$ and $\hat{\mathbf{b}}_2[k]$, namely

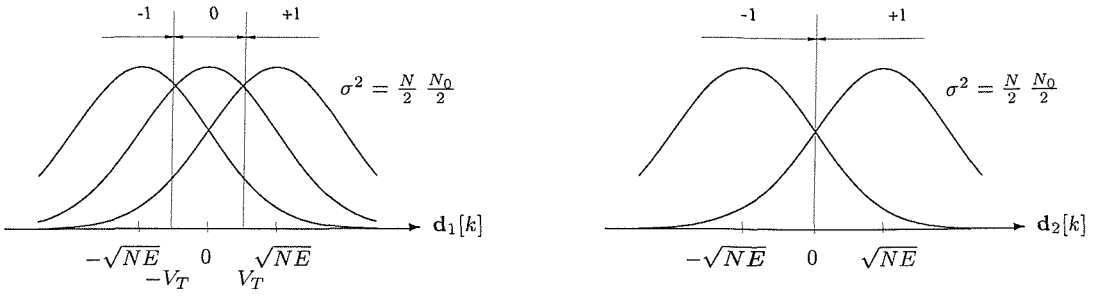

(a) the first stage

(b) the second stage

Figure 6.3: PDF of the detection variables $\mathbf{d}_1[k]$ and $\mathbf{d}_2[k]$ in the AWGN channel and the first as well as second stage decision region, when the SPD based detection is employed. (a) PDF of the noise contaminated component $\mathbf{d}_1[k]$ during the first detection stage. (b) PDF of the noise contaminted component $\mathbf{d}_2[k]$ during the second detection stage when $\mathbf{b}_1[k] = -\mathbf{b}_2[k]$.

$\hat{\mathbf{b}}_1[k] = -\hat{\mathbf{b}}_2[k]$. This detector has the lowest complexity among the three SPD schemes, as it will be shown in Section 6.4.4. The decision variables can be summarised as:

$$\hat{\mathbf{b}}_1[k] = \hat{\mathbf{b}}_2[k] = \mathbf{d}_1[k], \text{ when } |\mathbf{d}_1[k]| > V_T\,, \tag{6.15}$$

$$\hat{\mathbf{b}}_1[k] = -\hat{\mathbf{b}}_2[k] = \mathbf{d}_2[k], \text{ otherwise.} \tag{6.16}$$

Type III : When $\mathbf{d}_1[k] \approx 0$, *i.e.* $|\mathbf{d}_1[k]| \leq V_T$ in Figure 6.3(a), the Type III detector uses Type I decision variables of (6.13) and (6.14). Otherwise, it invokes the Type II detector and hence detects $\hat{\mathbf{b}}_1[k]$ and $\hat{\mathbf{b}}_2[k]$ based on only $\mathbf{d}_1[k]$, requiring no further operations. Accordingly, the decision rule can be summarised as:

$$\hat{\mathbf{b}}_1[k] = \hat{\mathbf{b}}_2[k] = \mathbf{d}_1[k], \text{ when } |\mathbf{d}_1[k]| > V_T\,, \tag{6.17}$$

$$\hat{\mathbf{b}}_1[k] = \mathbf{d}_1[k] + \mathbf{d}_2[k],\ \hat{\mathbf{b}}_2[k] = \mathbf{d}_1[k] - \mathbf{d}_2[k], \text{ otherwise.} \tag{6.18}$$

These three types of detectors will be compared in the following sections in terms of their BER performances and their complexities. Although we proposed the above three types of SPD detectors based on the first order decomposition of the Walsh-Hadamard matrix, a recursive application of these SPD schemes using a higher order decomposition is feasible. In fact, the recursive implementation of Type I despreading detector is known as Fast Walsh-Hadamard Transform [155]. We will observe in Section 6.4 and 6.5 that Type II and Type III detectors require a lower number of operations than Type I detector.

6.4 AWGN Channel

When communicating over the AWGN channel we can not expect any diversity gain and there is not much benefit in employing spreading system. However, the BER analysis of the proposed successive partial despreading schemes in the AWGN channel is a good starting point for comparing them with the conventional scheme.

In the AWGN channel, the decomposed received vectors, $\hat{\mathbf{s}}_1$ and $\hat{\mathbf{s}}_2$ of Figure 6.2, can be expressed as:

$$\hat{\mathbf{s}}_1 = \sqrt{E}\,\mathbf{s}_1 + \mathbf{n}_1 \tag{6.19}$$

$$\hat{\mathbf{s}}_2 = \sqrt{E}\,\mathbf{s}_2 + \mathbf{n}_2, \tag{6.20}$$

where E is the energy per received bit, $\mathbf{s}_1$ and $\mathbf{s}_2$ are given in (6.5) and (6.6), and $\mathbf{n}_i[k]$, $i = 1,\ 2$ and $k = 1,\ \cdots, N/2$ represents the independently and identically distributed (*iid*) zero-mean Gaussian distribution having a variance of $\sigma^2 = N_o/2$. As for the single-carrier DS-CDMA systems, we assume that the PN-based scrambling was removed already, leaving Walsh spreading imposed on the original message bits. As for MC-CDMA, some receiver preprocessing was assumed, such as employing an N component FFT for recovering the frequency domain symbols from the received time domain symbols. Upon applying the $N/2 \times N/2$-dimensional despreading matrix, $\mathbf{W}_{N/2}$, to $\hat{\mathbf{s}}_1$ and $\hat{\mathbf{s}}_2$ as expressed in (6.7) and (6.8), we get the the detection variables $\mathbf{d}_1$ and $\mathbf{d}_2$ formulated as:

$$\mathbf{d}_1 = \frac{1}{2}\sqrt{NE}\,\mathbf{b}_1 + \frac{1}{2}\sqrt{NE}\,\mathbf{b}_2 + \eta_1 \tag{6.21}$$

$$\mathbf{d}_2 = \frac{1}{2}\sqrt{NE}\,\mathbf{b}_1 - \frac{1}{2}\sqrt{NE}\,\mathbf{b}_2 + \eta_2\ , \tag{6.22}$$

where each noise component $\eta_i[k]$, $i = 1,\ 2$ and $k = 1,\ \cdots, N/2$ is also *iid* (owing to the orthogonality between the rows of the Walsh-Hadamard matrix) and has a zero mean Gaussian distribution with $\sigma^2 = (N/2)\,(N_o/2)$, since $\eta_i[k]$ is a sum of $N/2$ number of Gaussian random variables $\mathbf{n}_i[j]$, $j = 1, \cdots, N/2$ having a variance of $N_o/2$. Having obtained the detection variables $\mathbf{d}_1$ and $\mathbf{d}_2$ in the AWGN channel, let us now investigate the BER performance of the three types of SPD detectors described in Section 6.3 .

6.4.1 Type I Detector

As seen in (6.13) and (6.14), in the context of the Type I detector the decision variables become:

$$\hat{\mathbf{b}}_1 = \mathbf{d}_1 + \mathbf{d}_2 \ = \sqrt{NE}\,\mathbf{b}_1 + \eta_1 + \eta_2 \tag{6.23}$$

$$\hat{\mathbf{b}}_2 = \mathbf{d}_1 - \mathbf{d}_2 \ = \sqrt{NE}\,\mathbf{b}_2 + \eta_1 - \eta_2\ . \tag{6.24}$$

The energy per bit becomes N times E after the despreading process, however the noise variance also becomes N times $N_o/2$. Hence, the bit energy per noise power ratio, γ, does not change. The BER is the same as for the conventional despreading detector or the ideal BPSK detector, which is given by:

$$P_{e,I} = \mathrm{Q}(\sqrt{2\gamma})\ . \tag{6.25}$$

The number of multiplications required by the Type I detector is given by:

$$N_I(\times) = \left(\frac{N}{2}\right)^2 + \left(\frac{N}{2}\right)^2 = \frac{N^2}{2}, \tag{6.26}$$

while the number of additions required is given by:

$$N_I(+) = \left(\frac{N}{2} - 1\right)\frac{N}{2} + \left(\frac{N}{2} - 1\right)\frac{N}{2} + N = \frac{N^2}{2}. \tag{6.27}$$

6.4.2 Type II Detector

Type II detector has the lowest complexity among the three SPD detectors. It uses $\mathbf{d}_1[k]$ to make the first stage decision. If the decision is of low confidence, the detector assumes that $\mathbf{b}_1[k] = -\mathbf{b}_2[k]$ and uses $\mathbf{d}_2[k]$ to decide the specific value of the original bits. The PDF of $\mathbf{d}_1[k]$ defined in (6.21) is illustrated in Figure 6.3(a), when communicating over AWGN channels. The figure shows three decision regions for the first stage, namely region '-1', the low-confidence region denoted by '0' and region '+1'. The conditional PDF of $\mathbf{d}_2[k]$ defined in (6.22) when $\mathbf{b}_1[k] = -\mathbf{b}_2[k]$ is also depicted in Figure 6.3(b), where only two decision regions are present, namely those associated with $\mathbf{d}_2[k] = -\sqrt{NE}$ and $\mathbf{d}_2[k] = \sqrt{NE}$. The decision threshold level V_T associated with the first stage detection should lie between 0 and $\sqrt{NE}$, where $\sqrt{NE}$ is the mean of the distribution of $\mathbf{d}_1[k]$ conditioned on $\mathbf{b}_1[k] = \mathbf{b}_2[k]$. If it is too close to zero, the low-confidence region denoted by '0' becomes small and the detector has a problem in confidently detecting the case of $\mathbf{b}_1[k] = -\mathbf{b}_2[k]$. By contrast, if the detection threshold V_T approaches $\sqrt{NE}$, the detection region associated with $\mathbf{d}_1[k] = \pm 1$, *i.e.* with $\mathbf{b}_1[k] = \mathbf{b}_2[k]$ is reduced to a half, which will lead to a poor bit error rate performance. Hence, it is expected that there exists an optimum threshold level V_T for a given signal power.

Firstly, we assume that $\mathbf{b}_1[k]$ was different from $\mathbf{b}_2[k]$, namely that we had $\mathbf{b}_1[k] = -\mathbf{b}_2[k]$. In this case, the random variable $\mathbf{d}_1[k]$ defined in (6.21) results in $\mathbf{d}_1[k] = \eta_1[k]$, having a zero mean Gaussian PDF, as shown in the middle of Figure 6.3(a). In this scenario, provided that $\mathbf{d}_1[k]$ falls in region '-1' or '+1' of Figure 6.3(a) and hence it is outside the region '0', the Type II detector will make a decision of either $\hat{\mathbf{b}}_1[k] = \hat{\mathbf{b}}_2[k] = -1$ or $+1$, respectively, resulting in a decision error concerning the transmission of one of the two bits. Let us define $P_e(A|B)$ as the conditional BEP associated with this scenario, where the detection variable $\mathbf{d}_1[k]$ falls in the region 'A', although it was expected to fall in the region 'B' of Figure 6.3(a), where 'A' and 'B' belong to one of '+1', '0' and '-1'. Let us also define $P_e(B)$ as the conditional BEP, when $\mathbf{d}_1[k]$ is expected to fall in the region 'B' of Figure 6.3(a). For example, $P_e(+1|0)$ denotes the conditional BEP of the Type II detector associated with the scenario, where $\mathbf{d}_1[k]$ falls in the region '+1' owing to a high positive value of the noise, namely when $\mathbf{d}_1[k] = \eta_1[k] > V_T$, and when we had $\mathbf{b}_1[k] = -\mathbf{b}_2[k]$, corresponding to $\mathbf{d}_1[k] = 0$ in a noiseless environment. More explicitly, the probability of error in the specific scenario of encountering a $\mathbf{d}_1[k]$ value in the '+1' region conditioned

on encountering $\mathbf{d}_1[k] = 0$ in the noiseless scenario is denoted by $P_e(+1|0)$, which can be formulated as:

$$P_e(+1|0) = \Pr(\mathbf{d}_1[k] > V_T | \mathbf{b}_1[k] = -\mathbf{b}_2[k]) \cdot \frac{1}{2} \tag{6.28}$$

$$= \mathrm{Q}\left(\frac{V_T}{\sigma}\right) \cdot \frac{1}{2}. \tag{6.29}$$

Similarly, the conditional BEP of $P_e(-1|0)$ in the same scenario, except for the difference that $\mathbf{d}_1[k]$ falls in the region '-1' instead of '+1', namely when we have $\mathbf{d}_1[k] = \eta_1[k] < -V_T$, assumes the same value as $P_e(+1|0)$ given in (6.29). Hence, the combined BEP corresponding to the scenario that $\mathbf{d}_1[k]$ falls outside of the region '0', namely when $|\mathbf{d}_1[k]| > V_T$, which is denoted by $P_e(\pm 1|0)$ can be formulated as:

$$P_e(\pm 1|0) = P_e(+1|0) + P_e(-1|0) \tag{6.30}$$

$$= 2 \cdot \mathrm{Q}\left(\frac{V_T}{\sigma}\right) \cdot \frac{1}{2} \tag{6.31}$$

$$= \mathrm{Q}\left(\frac{V_T}{\sigma}\right), \tag{6.32}$$

where the variance of $\mathbf{d}_1[k]$, and hence also that of the noise component $\eta_1[k]$ is $\sigma^2 = (N/2)(N_o/2)$, as we argued in Section 6.4 on page 165 . On the other hand, when $\mathbf{d}_1[k] = \eta_1[k]$ falls in region '0' as expected, namely when we have $-V_T \leq \mathbf{d}_1[k] = \eta_1[k] \leq +V_T$ owing to a moderate value of the noise, the Type II detector involves the second stage detection variable $\mathbf{d}_2[k]$ in order to arrive at the estimated bits $\hat{\mathbf{b}}_1$ and $\hat{\mathbf{b}}_2$. Since we are considering the scenario of $\mathbf{b}_1[k] = -\mathbf{b}_2[k]$, the detection variable $\mathbf{d}_2[k]$ defined in (6.22) becomes:

$$\mathbf{d}_2[k] = \sqrt{NE}\,\mathbf{b}_1[k] + \eta_2[k], \tag{6.33}$$

and its PDF is depicted in Figure 6.3(b) . When $\mathbf{d}_2[k]$ falls in the region '-1', namely when $\mathbf{d}_2[k] \leq 0$, assuming furthermore that $\mathbf{b}_1 = 1$ and hence $\mathbf{b}_2 = -1$ are transmitted, then the Type II detector will result in an erroneous decision concerning both transmitted bits. In the opposite scenario, namely when $\mathbf{d}_2[k]$ falls in the region '+1', the Type II detector will incur no bit errors, provided that $\mathbf{b}_1 = 1$ and hence $\mathbf{b}_2 = -1$ were transmitted. The associated BEP denoted as $P_e(0|0)$, in the scenario when $\mathbf{d}_1[k]$ of (6.21) falls in the region '0', conditioned on the fact that indeed it was expected to fall in the region '0', since $\mathbf{b}_1[k] = -\mathbf{b}_2[k]$ was transmitted, can be formulated as:

$$P_e(0|0) = \Pr(|\mathbf{d}_1[k]| \leq V_T \mid \mathbf{b}_1[k] = -\mathbf{b}_2[k]) \cdot \Pr(\{\mathbf{d}_2[k] < 0 \mid \mathbf{b}_1[k] = -\mathbf{b}_2[k] = +1\} \text{ or } \{\mathbf{d}_2[k] \geq 0 \mid \mathbf{b}_1[k] = -\mathbf{b}_2[k] = -1\}) \tag{6.34}$$

$$= \left\{1 - 2\mathrm{Q}\left(\frac{V_T}{\sigma}\right)\right\} \left\{\mathrm{Q}\left(\frac{\sqrt{NE}}{\sigma}\right) \cdot \frac{1}{2} + \mathrm{Q}\left(\frac{\sqrt{NE}}{\sigma}\right) \cdot \frac{1}{2}\right\} \tag{6.35}$$

$$= \left\{1 - 2\mathrm{Q}\left(\frac{V_T}{\sigma}\right)\right\} \mathrm{Q}\left(\frac{\sqrt{NE}}{\sigma}\right), \tag{6.36}$$

where the variance σ^2 of $\mathbf{d}_1[k]$ and $\mathbf{d}_2[k]$, and hence that of the noise components $\eta_1[k]$ and $\eta_2[k]$ is $\sigma^2 = (N/2)(N_o/2)$, as we argued in Section 6.4 on page 165. Hence, the bit error probability $P_e(0)$ associated with the case of $\mathbf{b}_1[k] = -\mathbf{b}_2[k]$, namely when $\mathbf{d}_1[k] = 0$ is expected, can be formulated, with the aid of (6.32) and (6.36), as:

$$P_e(0) = P_e(\pm 1|0) + P_e(0|0) \tag{6.37}$$

$$= \mathrm{Q}\left(\frac{V_T}{\sigma}\right) + \left\{1 - 2\mathrm{Q}\left(\frac{V_T}{\sigma}\right)\right\} \mathrm{Q}\left(\frac{\sqrt{NE}}{\sigma}\right)$$

$$= \mathrm{Q}(2\sqrt{\gamma}\upsilon) + \{1 - 2\mathrm{Q}(2\sqrt{\gamma}\upsilon)\}\mathrm{Q}(2\sqrt{\gamma}) \,, \tag{6.38}$$

where γ is the bit energy to noise power ratio, defined as $\gamma = E/N_o$ and υ is the threshold level normalised to $\sqrt{NE}$, defined by $\upsilon = V_T/\sqrt{NE}$.

Let us now assume that the original transmitted bits satisfy $\mathbf{b}_1[k] = \mathbf{b}_2[k]$. In this scenario the detection variable $\mathbf{d}_1[k]$ defined in (6.21) can be expressed as:

$$\mathbf{d}_1[k] = \sqrt{NE}\,\mathbf{b}_1 + \eta_1 \,. \tag{6.39}$$

Specifically, when the bits we have are $\mathbf{b}_1[k] = \mathbf{b}_2[k] = -1$ and $\mathbf{d}_1[k]$ of (6.39) falls in region '+1' of Figure 6.3(a), provided that $\mathbf{d}_1[k]$ is expected to fall in region '-1', it will lead to bit errors for both $\mathbf{b}_1[k]$ and $\mathbf{b}_2[k]$ with a certainty. The associated BEP $P_e(+1|-1)$ can be expressed as:

$$P_e(+1|-1) = \Pr(\mathbf{b}_1[k] = -1 \mid \mathbf{b}_1[k] = \mathbf{b}_2[k]) \cdot \Pr(\mathbf{d}_1[k] > V_T \mid \mathbf{b}_1[k] = \mathbf{b}_2[k] = -1) \tag{6.40}$$

$$= \frac{1}{2} \cdot \mathrm{Q}\left(\frac{\sqrt{NE} + V_T}{\sigma}\right) . \tag{6.41}$$

Likewise, when the bits encountered are $\mathbf{b}_1[k] = \mathbf{b}_2[k] = +1$ and $\mathbf{d}_1[k]$ of (6.39) falls in region '-1' of Figure 6.3(a), provided that $\mathbf{d}_1[k]$ is expected to fall in region '+1', again both bits will be in error. The conditional BEP associated with this scenario, which is denoted by $P_e(-1|+1)$ has the same value as $P_e(+1|-1)$, as given in (6.41). Hence, the combined BEP denoted by $P_e(\mp 1|\pm 1)$, associated with the scenario where $\mathbf{d}_1[k]$ falls in the opposite region with respect to the expected region, when we have $\mathbf{b}_1[k] = \mathbf{b}_2[k]$, can be expressed as:

$$P_e(\mp 1|\pm 1) = P_e(+1|-1) + P_e(-1|+1) \tag{6.42}$$

$$= \mathrm{Q}\left(\frac{\sqrt{NE} + V_T}{\sigma}\right) . \tag{6.43}$$

By contrast, when $\mathbf{d}_1[k]$ of (6.39) falls in region '0' of Figure 6.3(a), namely when we have $|\mathbf{d}_1[k]| \leq V_T$, the Type II detector will incorrectly assume that $\mathbf{b}_1[k] = -\mathbf{b}_2[k]$ was transmitted and will use the second stage detection variable $\mathbf{d}_2[k]$ defined in (6.22) in order to carry out a decision. However, regardless of the decision made in the second stage, the incorrect assumption of $\mathbf{b}_1[k] = -\mathbf{b}_2[k]$ made by the Type II SPD detector will remit in a single bit error for the two transmitted bits, yielding a conditional BEP of $1/2$, since we assumed that the same bits are transmitted. The BEP associated with the scenario that

$\mathbf{b}_1[k] = \mathbf{b}_2[k] = +1$ are transmitted and that the first stage detection variable $\mathbf{d}_1[k]$ of (6.39) falls in the region '0', which is denoted by $P_e(0|+1)$, can be expressed as:

$$P_e(0|+1) = \Pr(\mathbf{b}_1[k] = +1|\mathbf{b}_1[k] = \mathbf{b}_2[k]) \cdot \Pr(|\mathbf{d}_1[k]| \leq V_T \mid \mathbf{b}_1[k] = \mathbf{b}_2[k]) \cdot \frac{1}{2} \tag{6.44}$$

$$= \frac{1}{2} \cdot \left\{ \mathrm{Q}\left(\frac{\sqrt{NE} - V_T}{\sigma} \right) - \mathrm{Q}\left(\frac{\sqrt{NE} + V_T}{\sigma} \right) \right\} \frac{1}{2} \tag{6.45}$$

$$= \frac{1}{4} \left\{ \mathrm{Q}\left(\frac{\sqrt{NE} - V_T}{\sigma} \right) - \mathrm{Q}\left(\frac{\sqrt{NE} + V_T}{\sigma} \right) \right\} . \tag{6.46}$$

Likewise, the BEP associated with the scenario that $\mathbf{b}_1[k] = \mathbf{b}_2[k] = -1$ are transmitted and that the first stage detection variable $\mathbf{d}_1[k]$ of (6.39) falls in the region '0', which is denoted by $P_e(0|-1)$, has the same value as $P_e(0|+1)$ given in (6.46). Hence, the combined BEP associated with the scenario that the first stage detection variable $\mathbf{d}_1[k]$ of (6.39) falls in the region '0', when $\mathbf{b}_1[k] = \mathbf{b}_2[k] = \pm 1$, which is denoted by $P_e(0|\pm 1)$, can be formulated as:

$$P_e(0|\pm 1) = P_e(0|+1) + P_e(0|-1) \tag{6.47}$$

$$= \frac{1}{2} \left\{ \mathrm{Q}\left(\frac{\sqrt{NE} - V_T}{\sigma} \right) - \mathrm{Q}\left(\frac{\sqrt{NE} + V_T}{\sigma} \right) \right\} . \tag{6.48}$$

Therefore, with the aid of (6.43) and (6.48) the conditional BEP $P_e(\pm 1)$ for the case of $\mathbf{b}_1[k] = \mathbf{b}_2[k] = \pm 1$ can be summarised as:

$$P_e(\pm 1) = P_e(\mp 1|\pm 1) + P_e(0|\pm 1) \tag{6.49}$$

$$= \mathrm{Q}\left(\frac{\sqrt{NE} + V_T}{\sigma} \right) + \frac{1}{2} \left\{ \mathrm{Q}\left(\frac{\sqrt{NE} - V_T}{\sigma} \right) - \mathrm{Q}\left(\frac{\sqrt{NE} + V_T}{\sigma} \right) \right\} \tag{6.50}$$

$$= \frac{1}{2} \left\{ \mathrm{Q}\left(2\sqrt{\gamma}(1-\upsilon)\right) + \mathrm{Q}\left(2\sqrt{\gamma}(1+\upsilon)\right) \right\} . \tag{6.51}$$

From (6.38) and (6.51), the total BEP $P_{e,II}$ of the Type II detector may be expressed as:

$$P_{e,II} = \frac{1}{2}\{P_e(0) + P_e(\pm 1)\} \tag{6.52}$$

$$= \frac{1}{2}\mathrm{Q}(2\sqrt{\gamma}\upsilon) + \left\{ \frac{1}{2} - \mathrm{Q}(2\sqrt{\gamma}\upsilon) \right\} \mathrm{Q}(2\sqrt{\gamma}) + \frac{1}{4}\{\mathrm{Q}(2\sqrt{\gamma}(1-\upsilon)) + \mathrm{Q}(2\sqrt{\gamma}(1+\upsilon))\}$$

$$= \frac{1}{4}\left[\mathrm{Q}\left(2\sqrt{\gamma}(1-\upsilon)\right) + \mathrm{Q}\left(2\sqrt{\gamma}(1+\upsilon)\right)\right] + \mathrm{Q}\left(2\sqrt{\gamma}\,\upsilon\right)\left[\frac{1}{2} - \mathrm{Q}\left(2\sqrt{\gamma}\right)\right] + \frac{1}{2}\mathrm{Q}\left(2\sqrt{\gamma}\right) . \tag{6.53}$$

The bit error probability $P_{e,II}$ of (6.53) is illustrated in Figure 6.4(a) as a function of both the normalised threshold υ and the SNR γ. It can be observed that the threshold levels play an important role in determining the bit error rate. When υ is zero, the region '0' in Figure 6.3(a) vanishes. In this case, we see in (6.53) that $P_{e,II}$ becomes $1/4 + 1/2\mathrm{Q}(2\sqrt{\gamma}) \approx 1/4$ for $\gamma \gg$ 0dB. When υ approaches ∞, the region '+1' and '-1' in Figure 6.3(a) vanishes and $P_{e,II}$ becomes $1/4 + 1/2\mathrm{Q}(2\sqrt{\gamma})$, which is the same as for the case of $\upsilon = 0$.

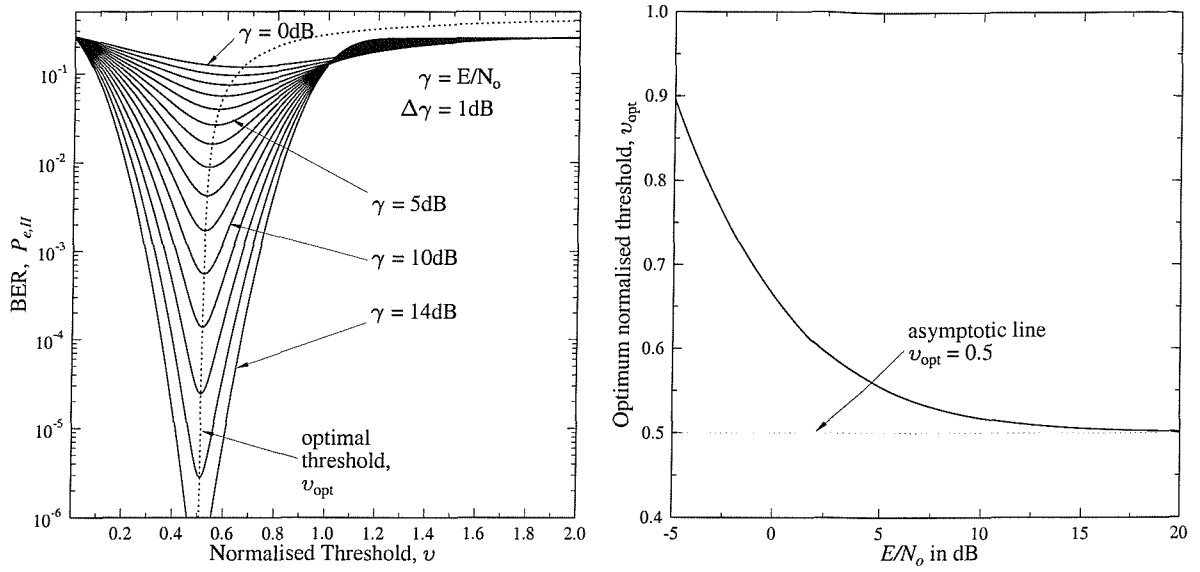

(a) Bit error rates

(b) Optimal threshold level

Figure 6.4: BER characteristics of the Type II detector: (a) BER $P_{e,II}$ of the Type II detector versus the normalised threshold level υ, for several values of SNR $\gamma = E/N_o$ in terms of dB. It can be observed that there exist optimum threshold levels for given E/N_o values. (b) the optimum normalised threshold levels, υ_{opt}, versus E/N_o. υ_{opt} asymptotically approaches $1/2$ as E/N_o becomes large.

The optimal threshold can be obtained by finding υ_{opt} such that $(\partial P_e/\partial \upsilon)\ |_{\upsilon=\upsilon_{opt}} = 0$. Using the following relation regarding a derivative of the Q-function [94]:

$$\frac{\partial \mathrm{Q}(ax+b)}{\partial x} = -\frac{a}{\sqrt{2\pi}} e^{-(ax+b)^2/2} , \tag{6.54}$$

we can derive $\partial P_{e,II}/\partial \upsilon$, which can be expressed as:

$$\frac{\partial P_{e,II}}{\partial \upsilon} = \frac{\sqrt{\gamma}}{2\sqrt{2\pi}} \left[e^{-2\gamma(1-\upsilon)^2} - e^{-2\gamma(1+\upsilon)^2} - \{2 - 4\mathrm{Q}(2\sqrt{\gamma})\} e^{-2\gamma\upsilon^2} \right] . \tag{6.55}$$

Upon equating this expression to zero, the optimum threshold υ_{opt} can be expressed as:

$$\upsilon_{opt} = \frac{1}{4\gamma} \log_e \left(\mu + \sqrt{1+\mu^2} \right) , \tag{6.56}$$

where $\mu = \{1 - 2\mathrm{Q}(2\sqrt{\gamma})\} e^{2\gamma}$. The optimum normalised threshold level, υ_{opt}, as a function of $\gamma = E_b/N_o$ is illustrated in Figure 6.4(b), which asymptotically approaches $1/2$, as γ grows. When $\upsilon_{opt} \simeq 1/2$, $P_{e,II}$ of (6.53) can be simplified to:

$$P_{e,II} \simeq \frac{3}{4}\mathrm{Q}\left(\sqrt{\gamma}\right) + \frac{2}{4}\mathrm{Q}\left(2\sqrt{\gamma}\right) + \frac{1}{4}\mathrm{Q}\left(3\sqrt{\gamma}\right) - \mathrm{Q}\left(\sqrt{\gamma}\right)\mathrm{Q}\left(2\sqrt{\gamma}\right) . \tag{6.57}$$

Having analysed the achievable BEP, let us now examine the complexity of the Type II SPD detector. The probability $P_{II}(0)$ that $\mathbf{d}_1$ falls in the region '0' of Figure 6.3(a), is useful for calculating the number

of operations required by the Type II detector, since this quantifies the probability that the Type II detector has to calculate the second stage detection variable $\mathbf{d}_2[k]$ additionally. The probability $P_{II}(0)$ can be formulated as:

$$
\begin{aligned}
P_{II}(0) &= \Pr(|\mathbf{d}_1| \leq V_T) && (6.58)\\
&= \Pr(\mathbf{b}_1 = \mathbf{b}_2 = +1) \cdot \Pr(|\mathbf{d}_1| \leq V_T \mid \mathbf{b}_1 = \mathbf{b}_2 = +1)\\
&\quad + \Pr(\mathbf{b}_1 = \mathbf{b}_2 = -1) \cdot \Pr(|\mathbf{d}_1| \leq V_T \mid \mathbf{b}_1 = \mathbf{b}_2 = -1)\\
&\quad + \Pr(\mathbf{b}_1 = -\mathbf{b}_2) \cdot \Pr(|\mathbf{d}_1| \leq V_T \mid \mathbf{b}_1 = -\mathbf{b}_2) && (6.59)\\
&= \frac{1}{4}\left\{\mathrm{Q}\left(\frac{\sqrt{NE} - V_T}{\sigma}\right) - \mathrm{Q}\left(\frac{\sqrt{NE} + V_T}{\sigma}\right)\right\}\\
&\quad + \frac{1}{4}\left\{\mathrm{Q}\left(\frac{\sqrt{NE} - V_T}{\sigma}\right) - \mathrm{Q}\left(\frac{\sqrt{NE} + V_T}{\sigma}\right)\right\}\\
&\quad + \frac{1}{2}\left\{1 - 2\mathrm{Q}\left(\frac{V_T}{\sigma}\right)\right\} && (6.60)\\
&= \frac{1}{2}\{1 - 2\mathrm{Q}(2\sqrt{\gamma}\upsilon) + \mathrm{Q}(2\sqrt{\gamma}(1-\upsilon)) - \mathrm{Q}(2\sqrt{\gamma}(1+\upsilon))\}\,. && (6.61)
\end{aligned}
$$

Then, the required number of multiplications, $N_{II}(\times)$, can be expressed as:

$$
N_{II}(\times) = \left(\frac{N}{2}\right)^2 + \left(\frac{N}{2}\right)^2 \cdot P_{II}(0)\,, \tag{6.62}
$$

where the first term indicates the number of multiplications involved in calculating $\mathbf{d}_1$ expressed in (6.7), while the second term quantifies the number of multiplications involved in determining $\mathbf{d}_2$, weighted by the probability that $\mathbf{d}_2$ is required. Upon substituting (6.61) in (6.62), we have:

$$
N_{II}(\times) = \frac{N^2}{8}\{3 - 2\mathrm{Q}(2\sqrt{\gamma}\upsilon) + \mathrm{Q}(2\sqrt{\gamma}(1-\upsilon)) - \mathrm{Q}(2\sqrt{\gamma}(1+\upsilon))\}\,. \tag{6.63}
$$

On the other hand, the number of operations required for deriving $\mathbf{d}_1$ according to (6.7), $(N/2)(N/2-1)$ number of additions are necessitated. Hence, following the approach adopted for calculating $N_{II}(\times)$ above, the number of additions $N_{II}(+)$ required by the Type II detector can be expressed as:

$$
\begin{aligned}
N_{II}(+) &= \frac{N(N-2)}{4}(1 + P_{II}(0))\\
&= \frac{N(N-2)}{8}\{3 - 2\mathrm{Q}(2\sqrt{\gamma}\upsilon) + \mathrm{Q}(2\sqrt{\gamma}(1-\upsilon)) - \mathrm{Q}(2\sqrt{\gamma}(1+\upsilon))\}\,. && (6.64)
\end{aligned}
$$

6.4.3 Type III Detector

In the context of the Type III SPD detector we have to calculate the probability of $\mathbf{d}_1$ falling in the region '0' in Figure 6.3(a), during the first detection stage. Figure 6.3(a) shows the PDF of $\mathbf{d}_1[k]$, where again, the first stage detector has three decision regions denoted by '-1', '0' and '+1'. Firstly, let us assume that $\mathbf{b}_1[k] = -\mathbf{b}_2[k]$ are transmitted. Then, according to (6.21) $\mathbf{d}_1[k]$ becomes $\mathbf{d}_1[k] = \eta_1[k]$, which

falls in the region '0', provided that the noise contribution obeys $|\eta_1[k]| < V_T$. This probability can be expressed as:

$$\Pr(|\eta_1[k]| < V_T) = 1 - 2\mathrm{Q}\left(\frac{V_T}{\sigma}\right) . \tag{6.65}$$

As described in Section 6.3, when $\mathbf{d}_1[k]$ falls in the region '0' of Figure 6.3(a), the Type III detector uses the Type I detection variables of (6.23) and (6.24), which are repeated here for convenience:

$$\hat{\mathbf{b}}_1 = \mathbf{d}_1 + \mathbf{d}_2 = \sqrt{NE}\,\mathbf{b}_1 + \eta_1 + \eta_2 \tag{6.66}$$

$$\hat{\mathbf{b}}_2 = \mathbf{d}_1 - \mathbf{d}_2 = \sqrt{NE}\,\mathbf{b}_2 + \eta_1 - \eta_2 . \tag{6.67}$$

When $\mathbf{b}_1[k] = -1$, $\hat{\mathbf{b}}_1[k]$ of (6.66) becomes $\hat{\mathbf{b}}_1[k] = -\sqrt{NE} + \eta_1 + \eta_2$, which results in a bit error, if $\eta_1 + \eta_2 > \sqrt{NE}$, indicating that the total noise contribution is higher than the signal contribution. The probability of this bit error denoted by $P_e(0|0)$, following the definition given in Section 6.4.2 on page 166, corresponds to the scenario, where $\mathbf{d}_1[k]$ falls in the region '0', when it was expected to fall in the region '0', can be expressed as:

$$\begin{aligned} P_e(0|0) &= \Pr(|\eta_1[k]| < V_T \mid \mathbf{b}_1[k] = -\mathbf{b}_2[k] = -1) \cdot \\ &\quad \Pr(\hat{\mathbf{b}}_1[k] > 0 \mid \mathbf{b}_1[k] = -\mathbf{b}_2[k] = -1,\ |\eta_1[k]| < V_T) && (6.68) \\ &= \Pr(|\eta_1[k]| < V_T \mid \mathbf{b}_1[k] = -\mathbf{b}_2[k] = -1) \cdot \\ &\quad \Pr(\eta_1[k] + \eta_2[k] > \sqrt{NE} \mid \mathbf{b}_1[k] = -\mathbf{b}_2[k] = -1,\ |\eta_1[k]| < V_T) && (6.69) \\ &= \Pr(\eta_1[k] + \eta_2[k] > \sqrt{NE},\ |\eta_1[k]| < V_T \mid \mathbf{b}_1[k] = -\mathbf{b}_2[k] = -1) && (6.70) \end{aligned}$$

In order to calculate $P_e(0|0)$ in (6.70), we need the joint PDF of η_1 and η_2, denoted as f_{η_1,η_2}. Considering that η_1 and η_2 are independent and identical Gaussian random variables, f_{η_1,η_2} can be expressed as:

$$f_{\eta_1,\eta_2} = \frac{1}{2\pi\sigma^2} e^{-\frac{\eta_1^2+\eta_2^2}{2\sigma^2}} , \tag{6.71}$$

where $\sigma^2 = (N/2)(N_o/2)$. The integration region associated with the bit error probability of (6.70) is depicted in Figure 6.5(a). Referring to (6.71) and to Figure 6.5(a), we can express the bit error probability as:

$$\begin{aligned} P_e(0|0) &= \Pr(\eta_1[k] + \eta_2[k] > \sqrt{NE},\ |\eta_1[k]| < V_T \mid \mathbf{b}_1[k] = -\mathbf{b}_2[k] = -1) && (6.72) \\ &= -\sqrt{NE} + \eta_1[k] + \eta_2[k] > 0, |\eta_1[k]| < V_T\} && (6.73) \\ &= \int_{-V_T}^{V_T} \int_{\sqrt{NE}-\eta_1}^{\infty} \frac{1}{2\pi\sigma^2} e^{-(\eta_1^2+\eta_2^2)/(2\sigma^2)} d\eta_2\, d\eta_1 && (6.74) \\ &= \int_{-V_T}^{V_T} \frac{1}{\sqrt{2\pi}\sigma} e^{-\eta_1^2/(2\sigma^2)} \mathrm{Q}\left(\frac{\sqrt{NE}-\eta_1}{\sigma}\right) d\eta_1 && (6.75) \\ &= \frac{1}{\sqrt{2\pi}} \int_{-2\sqrt{\gamma}\upsilon}^{2\sqrt{\gamma}\upsilon} e^{-\eta^2/2} \mathrm{Q}(2\sqrt{\gamma} - \eta) d\eta , && (6.76) \end{aligned}$$

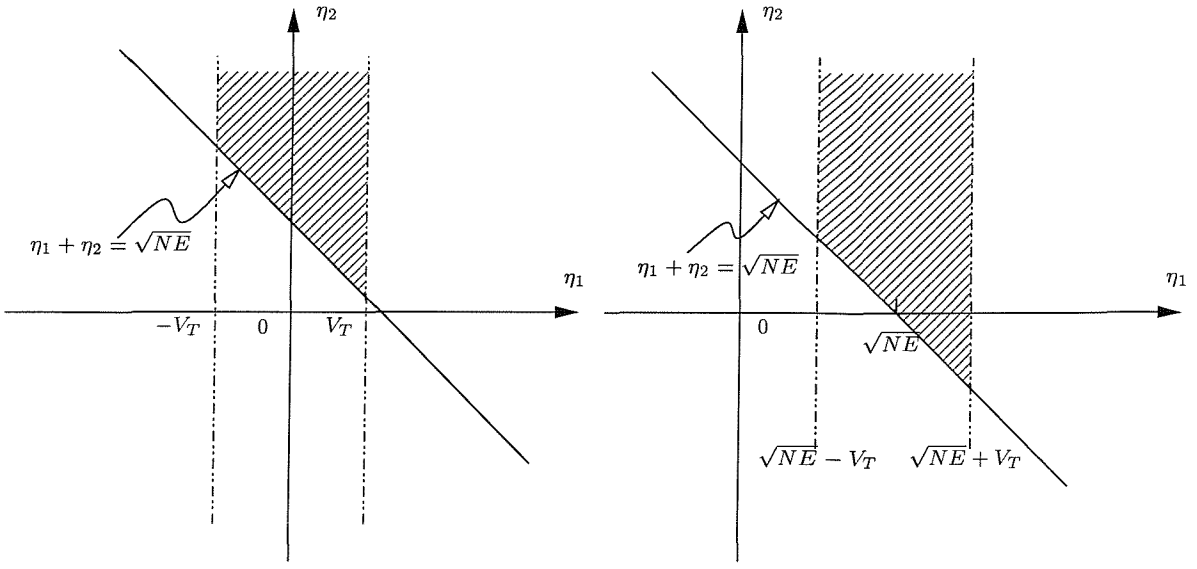

(a) Region 1 (b) Region 2

Figure 6.5: Integration regions for the conditional bit error probabilities associated with the Type III detector: (a) region 1 is for $\mathrm{P}(\eta_1 + \eta_2 > \sqrt{NE},\ |\eta_1| < V_T)$ and (b) region 2 is for $\mathrm{P}(\eta_1 + \eta_2 > \sqrt{NE},\ \sqrt{NE} - V_T < \eta_1 < \sqrt{NE} + V_T)$.

where, again, $\gamma = E/N_o$, and $\upsilon = V_T/\sqrt{NE}$. On the other hand, the conditional BEP, when $\mathbf{d}_1[k]$ falls in the region '0' of Figure 6.3(a) and $\hat{\mathbf{b}}_1[k] < 0$, although $\mathbf{b}_1[k] = -\mathbf{b}_2[k] = +1$, has the same value as $P_e(0|0)$ given in (6.76).

Considering the probability that $\mathbf{d}_1[k]$ falls in the regions of '$\pm$1' in Figure 6.3(a) despite $\mathbf{b}_1[k] = -\mathbf{b}_2[k]$, which was given in (6.32), the bit error probability for the case of $\mathbf{b}_1[k] = -\mathbf{b}_2[k]$, namely when $\mathbf{d}_1[k]$ is expected to fall in the region '0', can be expressed as:

$$P_e(0) = \mathrm{Q}(2\sqrt{\gamma}\upsilon) + \frac{1}{\sqrt{2\pi}} \int_{-2\sqrt{\gamma}\upsilon}^{2\sqrt{\gamma}\upsilon} e^{-\eta^2/2} \mathrm{Q}(2\sqrt{\gamma} - \eta) d\eta\,, \tag{6.77}$$

where the first term is the conditional BEP, when $\mathbf{d}_1[k]$ falls in the region of '+1' or '-1', while the second term is the conditional BEP, when $\mathbf{d}_1[k]$ falls in the region '0'.

By contrast, when $\mathbf{b}_1[k] = \mathbf{b}_2[k] = -1$ or $+1$, bit errors occur (a) when the first stage detection variable $\mathbf{d}_1[k]$ falls in the region '+1' or '-1' of Figure 6.3(a), or (b) when it falls in the region '0' and the second stage detection variable falls in the region of '+1' or '-1'. The probability of case (a), denoted by $P_e(\mp 1|\pm 1)$, was already given in (6.43) as:

$$P_e(\mp 1|\pm 1) = \mathrm{Q}\left(\frac{\sqrt{NE} + V_T}{\sigma}\right) \tag{6.78}$$

$$= \mathrm{Q}(2\sqrt{\gamma}(1+\upsilon))\,, \tag{6.79}$$

where again γ is the SNR per bit and υ is the normalised threshold defined as $\upsilon = V_T/\sqrt{NE}$.

Let us now consider case (b). The associated conditional BEP is denoted by $P_e(0|\pm 1)$, since this corresponds to the scenario, where $\mathbf{d}_1[k]$ falls in the region '0' of Figure 6.3(a), when $\mathbf{d}_1[k]$ is expected to fall in the region '+1' or '-1', depending on the value of $\mathbf{b}_1[k]$. Specifically, when $\mathbf{b}_1[k] = \mathbf{b}_2[k] = -1$, according to (6.21) the first stage detection variable becomes $\mathbf{d}_1[k] = -\sqrt{NE} + \eta_1[k]$, which falls in the region '0' associated with $|\mathbf{d}_1[k]| \leq V_T$, if $(\sqrt{NE} - V_T) < \eta_1[k] < (\sqrt{NE} + V_T)$. In this case a bit error occurs, when $\hat{\mathbf{b}}_1[k] = -\sqrt{NE} + \eta_1[k]$ is positive. Hence, this probability can be expressed as:

$$
\begin{aligned}
P_e(0|-1) &= \Pr(|\mathbf{d}_1[k]| < V_T \mid \mathbf{b}_1[k] = \mathbf{b}_2[k] = -1) \cdot \\
&\quad \Pr(\hat{\mathbf{b}}_1[k] > 0 \mid \mathbf{b}_1[k] = \mathbf{b}_2[k] = -1,\ |\mathbf{d}_1[k]| < V_T) && (6.80)\\
&= \Pr(|\mathbf{d}_1[k]| < V_T,\ \hat{\mathbf{b}}_1[k] > 0 \mid \mathbf{b}_1[k] = \mathbf{b}_2[k] = -1) && (6.81)\\
&= \Pr(|-\sqrt{NE} + \eta_1[k]| \leq V_T,\ -\sqrt{NE} + \eta_1[k] + \eta_2[k] > 0) && (6.82)\\
&= \Pr(\sqrt{NE} - V_T \leq \eta_1[k] \leq \sqrt{NE} + V_T,\ \eta_1[k] + \eta_2[k] > \sqrt{NE}) && (6.83)
\end{aligned}
$$

On the other hand, the conditional BEP $P_e(0|+1)$ of the Type III detector associated with the scenario, where the first stage detection variable $\mathbf{d}_1[k] = +\sqrt{NE} + \eta_1[k]$ falls in the region '0' of Figure 6.3(a), provided that $\mathbf{d}_1[k]$ is expected to fall in the region '+1', since $\mathbf{b}_1[k] = \mathbf{b}_2[k] = +1$ was transmitted, can be formulated following the same approach as for $P_e(0|-1)$ in (6.80), which results in the same value, as $P_e(0|+1)$ of (6.83). Hence, the combined BEP $P_e(0|\pm 1)$ can be expressed as:

$$
\begin{aligned}
P_e(0|\pm 1) &= Pr(\mathbf{b}_1[k] = \mathbf{b}_2[k] = -1 \mid \mathbf{b}_1[k] = \mathbf{b}_2[k]) \cdot P_e(0|-1) \\
&\quad + Pr(\mathbf{b}_1[k] = \mathbf{b}_2[k] = +1 \mid \mathbf{b}_1[k] = \mathbf{b}_2[k]) \cdot P_e(0|+1) && (6.84)\\
&= \frac{1}{2} P_e(0|-1) + \frac{1}{2} P_e(0|+1) && (6.85)\\
&= \Pr(\sqrt{NE} - V_T \leq \eta_1[k] \leq \sqrt{NE} + V_T,\ \eta_1[k] + \eta_2[k] > \sqrt{NE})\,. && (6.86)
\end{aligned}
$$

In order to calculate $P_e(0|\pm 1)$ of (6.86), we need the joint PDF of η_1 and η_2, which is given in (6.71). The integration region, where the bracketed conditions of (6.86) are satisfied, is depicted in Figure 6.5(b). Referring to (6.71) and to Figure 6.5(b), $P_e(0|\pm 1)$ can be expressed as:

$$
\begin{aligned}
P_e(0|\pm 1) &= \Pr(-\sqrt{NE} + \eta_1[k] + \eta_2[k] > 0,\ \sqrt{NE} - V_T < \eta_1[k] < \sqrt{NE} + V_T\} \\
&= \frac{1}{\sqrt{2\pi}} \int_{2\sqrt{\gamma}(1-\upsilon)}^{2\sqrt{\gamma}(1+\upsilon)} e^{-\eta^2/2}\, \mathrm{Q}(2\sqrt{\gamma} - \eta)\, d\eta\,. && (6.87)
\end{aligned}
$$

With the aid of (6.79) and (6.87), the BEP associated with $\mathbf{b}_1[k] = \mathbf{b}_2[k]$ can be expressed as:

$$
P_e(\pm 1) = \mathrm{Q}(2\sqrt{\gamma}(1+\upsilon)) + \frac{1}{\sqrt{2\pi}} \int_{2\sqrt{\gamma}(1-\upsilon)}^{2\sqrt{\gamma}(1+\upsilon)} e^{-\eta^2/2} \mathrm{Q}(2\sqrt{\gamma} - \eta) d\eta\,. \qquad (6.88)
$$

Finally, from (6.77) and (6.88), we can derive the total BEP $P_{e,III}$ of the Type III detector, which

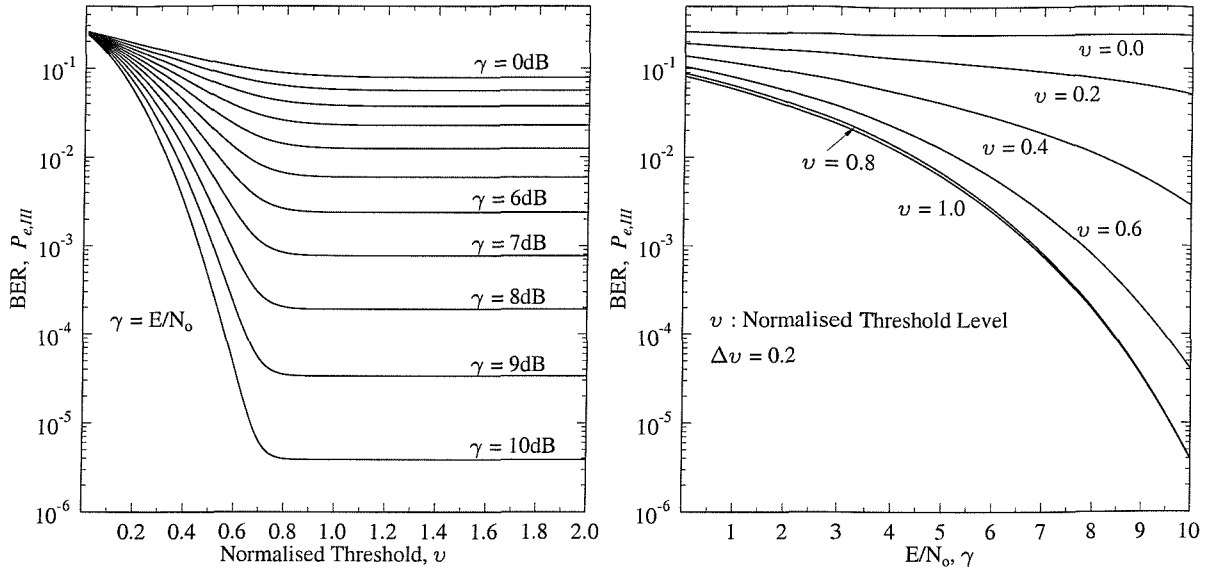

(a) BER versus υ

(b) BER versus γ

Figure 6.6: The bit error probability $P_{e,III}$ of the Type III detector. As the normalised threshold level υ becomes higher, $P_{e,III}$ approaches the BER of the ideal BPSK, which is indistinguishable from the conventional BPSK scheme. However, this is achieved at the expense of an increasing computational costs.

can be expressed as:

$$P_{e,III} = \frac{1}{2}\left\{\mathrm{Q}(2\sqrt{\gamma}\upsilon) + \mathrm{Q}(2\sqrt{\gamma}(1+\upsilon))\right\} + \frac{1}{2\sqrt{2\pi}}\int_{-2\sqrt{\gamma}\upsilon}^{2\sqrt{\gamma}\upsilon} e^{-\eta^2/2}\mathrm{Q}(2\sqrt{\gamma}-\eta)d\eta + \frac{1}{2\sqrt{2\pi}}\int_{2\sqrt{\gamma}(1-\upsilon)}^{2\sqrt{\gamma}(1+\upsilon)} e^{-\eta^2/2}\mathrm{Q}(2\sqrt{\gamma}-\eta)d\eta\,, \quad (6.89)$$

which depends on the normalised threshold level, υ, as well as on the SNR γ.

The bit error probability $P_{e,III}$ of the Type III detector is depicted against the normalised threshold level υ and the bit energy to noise power ratio γ in Figure 6.6. In Figure 6.6(b) we can observe that the BER approaches the ideal BPSK BER curve, as υ approaches unity. In fact, the BER curve associated with $\upsilon = 1$ was indistinguishable from the ideal BPSK BER curve. This implies that the Type III detector has the potential of reducing the required number of calculations without a noticeable performance degradation.

Having analysed the BEP of the Type III detector communicating over an AWGN channel, let us now consider the complexity of the Type III detector. The first stage detection variable $\mathbf{d}_1$ always has to be evaluated according to (6.7) in the Type III detector, requiring $(N/2)^2$ number of multiplications and $(N/2)(N/2-1)$ additions. Additionally, when $\mathbf{d}_1$ falls in the region '0' of Figure 6.3(a) with the probability of $P_{III}(0)$, $\mathbf{d}_2$ has to be evaluated according to (6.8), and then $\hat{\mathbf{b}}_1$ and $\hat{\mathbf{b}}_2$ have to be evaluated according to (6.66) and (6.67), respectively. The former evaluation for $\mathbf{d}_2$ requires the same number of

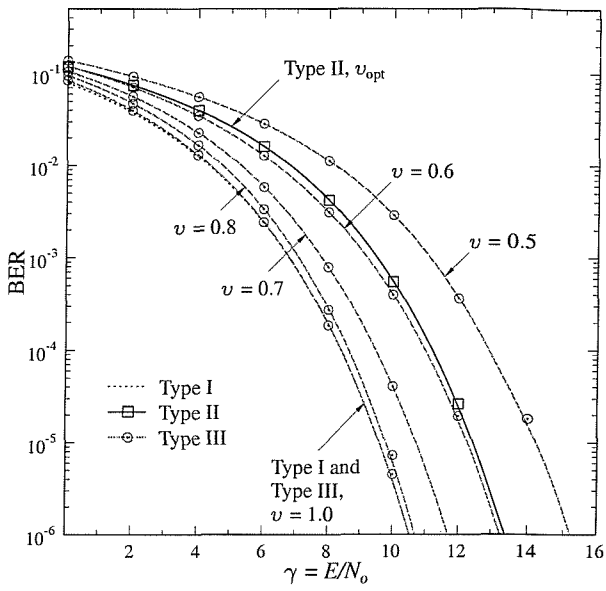

Figure 6.7: The bit error ratio versus γ performance of SPD detectors. The BER performance of the Type I detector is the same as that of a conventional despreading detector or as that of an ideal BPSK detector. The Type II detector exhibits an approximately 3dB disadvantage in terms of the required SNR compared to the Type I detector. The BER curves of the Type III detector shows a wide range of variations, depending on the normalised threshold value, v. The markers represent the corresponding simulation results.

computations as for $\mathbf{d}_1$. On the other hand, the latter evaluation for $\hat{\mathbf{b}}_1$ and $\hat{\mathbf{b}}_2$ requires N number of additions. It is worth noting that the probability, $P_{III}(0)$, of having a $\mathbf{d}_1[k]$ value in the region '0' of Figure 6.3(a) at the first stage detector is the same as $P_{II}(0)$ given in (6.61). Hence, the expression of the required number of multiplications, $N_{III}(\times)$, is the same as $N_{II}(\times)$ given in (6.63) for the Type II detector. The required number of additions, $N_{III}(+)$, becomes slightly different, which can be expressed as:

$$N_{III}(+) = \frac{N}{2} \cdot \left(\frac{N}{2} - 1\right) + P_{III}(0) \cdot \left\{\frac{N}{2} \cdot \left(\frac{N}{2} - 1\right)\right\} + P_{III}(0) \cdot N \tag{6.90}$$

$$= \frac{N(N-2)}{4} + \frac{N(N+2)}{8}\{1 - 2\mathrm{Q}(2\sqrt{\gamma}v) + \mathrm{Q}(2\sqrt{\gamma}(1-v)) - \mathrm{Q}(2\sqrt{\gamma}(1+v))\}, \tag{6.91}$$

where the first and the second terms of (6.90) corresponds to the number of additions required for evaluating $\mathbf{d}_1$ and $\mathbf{d}_2$, respectively, and the last term of (6.90) is that for evaluating $\hat{\mathbf{b}}_1$ and $\hat{\mathbf{b}}_2$, as mentioned before.

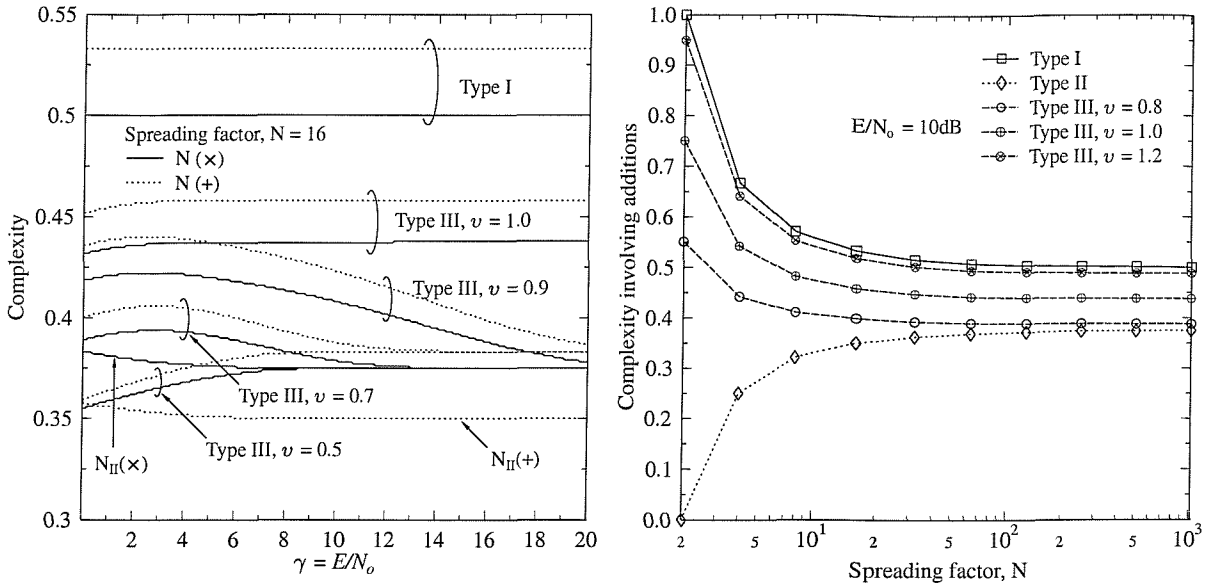

(a) Complexity vs signal strength

(b) Complexity vs spreading factor

Figure 6.8: Relative complexity of SPD detectors to the conventional despreading detector: (a) complexity versus E/N_o for a spreading factor of $N = 16$ (b) complexity versus spreading factor for $E/N_o = 10dB$.

6.4.4 Summary and Discussions

In this section, we analysed the bit error rate of the three different types of SPD detectors in the AWGN channel. The corresponding bit error rate curves are depicted in Figure 6.7. The BER of the Type I detector, as given in (6.25), is identical to that of ideal BPSK. Figure 6.7 shows that the Type II detector has an approximately 3dB SNR disadvantage compared to ideal BPSK and to conventional despreading based detection, while attaining the same bit error rate performance. The optimum threshold level of (6.56) was assumed for the Type II detector. The BER of the Type III detector varies depending on the threshold levels employed. We can observe that the Type III BER was close to that of the Type II detector, when the normalised threshold level υ was set to 0.6 for the Type III detector. At $\upsilon = 0.8$ the BER of the Type III detector approached the ideal BER within about 0.2 dB E/N_o difference. The BER of the Type III scheme was indistinguishable from the ideal BER when $\upsilon = 1.0$ was used.

Figure 6.8 illustrates the implementational complexity of the three types of SPD detectors in terms of the achievable complexity normalised to the conventional full-despreading based detector. The required number of multiplications and additions is N^2 and $N^2 - N$, respectively, for the conventional full despreading based detector, where N is the spreading factor. The implementational complexity of the Type I, Type II and Type III detectors was given in (6.26), (6.27), (6.63), (6.64) and (6.91). Figure 6.8(a) shows the achievable complexity relative to that of the conventional full despreading detector, which are $N_M(\times)/N^2$ and $N_M(+)/(N(N-1))$, where $M = I$, II and III for the spreading factor of $N = 16$.

We can observe in Figure 6.8(a) that the Type I detectors reduce the number of operations required by about a factor two, compared to the conventional detectors. The Type II SPD detectors require 35% of the additions and 37.5% of the multiplications necessary for the conventional full despreading detector. The complexity of the Type III detector falls between those of the Type I and the Type II detectors. As the threshold becomes higher, the complexity of the Type III detector increases. As γ becomes higher, $N_{III}(\times)/N^2$ approaches $3/8$ for $v < 1$, $7/16$ for $v = 1$ and $1/2$ for $v > 1$. Figure 6.8(b) shows the reduction of the required number additions for the three types of SPD detectors as a function of the spreading factor N at $E/N_o = 10$dB . As the spreading factor N increases, the reduction of the required number of additions for the Type I and the Type II detectors approach $1/2$ and $3/8$, respectively. The multiplication reduction factors of the three detectors do not vary, as N changes.

6.5 Effects of Impulse Noise or Narrow Band Jamming

As mentioned in Section 6.2, when the received signal is impaired by impulse noise [158, 159] in the time domain or by a narrow-band interferer / tone-jamming [160] in the frequency domain, some of the time-domain chips or some of the subcarriers in the frequency domain may be corrupted completely and hence the obliteration of the corrupted symbols may result in a better performance. In this section, we assume that lth time domain chip or frequency domain subcarrier is completely lost and the index l is known to the receiver. We refer to this lost chip or subcarrier signal as the lost Walsh transform-domain symbol.

6.5.1 Conventional BPSK System without Spreading

Since there is no spreading involved, for example as in conventional OFDM, the obliteration of the lth symbol results in a bit error with the probability of $1/2$ in conjunction with conventional BPSK schemes. Hence, the average BEP $P_{e,BPSK}$ of conventional BPSK schemes can be expressed as:

$$P_{e,BPSK} = \frac{1}{N}\frac{1}{2} + \frac{N-1}{N}\mathrm{Q}(\sqrt{2\gamma}), \tag{6.92}$$

where the corresponding BER floor is given by $1/(2N)$, since one of the N bits has a 50% BER. The associated bit error rates for the spreading factors of $N = 8, 16, 32$ are depicted in Figure 6.9 .

6.5.2 Conventional Despreading Scheme

When strong single-tone jamming is present in a multi-carrier system, the received subcarrier having the same frequency as the tone jammer or the frequency near the jamming tone exhibits a high power owing to the jamming signal, which results in unreliable detection of the symbol conveyed by the subcarrier [161]. In a WHT/OFDM system, this corrupted high magnitude symbol reduces the reliability of detecting the original bit, since the Signal to Interference + Noise Ratio (SINR) is given as:

$$\mathrm{SINR} = \frac{N\,E}{J + N\,\sigma^2} = \frac{E}{J/N + \sigma^2}, \tag{6.93}$$

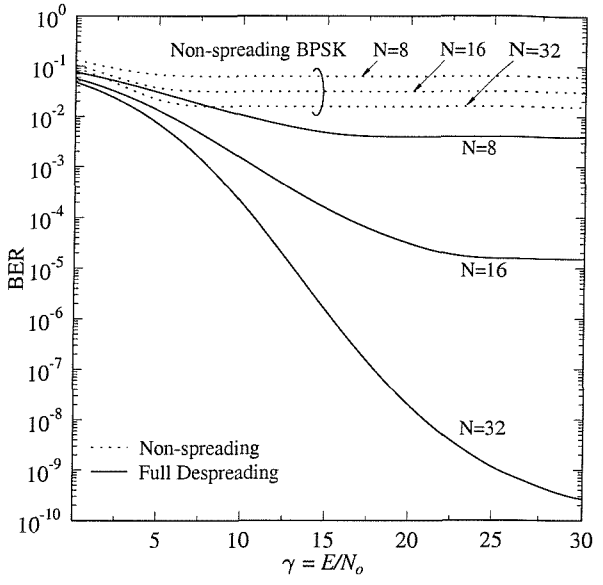

Figure 6.9: The bit error rates of the conventional detectors for transmission over the AWGN channel, when one of N transform-domain symbols is obliterated. The non-spread BPSK scheme has a high irreducible BER of $0.5/N$, while the spread systems have far lower error floor at $1/2^N$.

where N is the spreading factor, E is the signal power, J is the jamming power and σ is the noise variance. While a high value of N reduces the adverse effect of jamming, the SINR may be unacceptably low, when the jamming power J is sufficiently high. In this case, we can improve the SINR by discarding the jamming-contaminated symbol during the despreading process. Please note that this approach is equivalent to the frequency domain notch filtering technique proposed for example in [162] for suppressing the tone-jamming signal. Then the frequency domain received vector, $\hat{\mathbf{s}} = \sqrt{E/N}\,\mathbf{W}_N\,\mathbf{b} + \mathbf{n}$, should be modified to $\hat{\mathbf{s}}'$ such that $\hat{\mathbf{s}}'[l] = 0$ indicating the loss of the lth transform domain symbol. Alternatively, we can model the loss of the lth transform domain symbol by replacing $\mathbf{W}_N$ with $\mathbf{W}'_N$, such that its lth column is replaced by an $N \times 1$-dimensional zero vector. Then, the despread symbol vector $\mathbf{d}$ can be expressed as:

$$\mathbf{d} = \mathbf{W}'_N \hat{\mathbf{s}} \tag{6.94}$$

$$= \sqrt{\frac{E}{N}}\,\mathbf{W}'_N\,\mathbf{W}_N\,\mathbf{b} + \mathbf{W}'_N\,\mathbf{n}\,. \tag{6.95}$$

This equation can be expressed for each vector component $\mathbf{d}[k]$ as:

$$\mathbf{d}[k] = \sqrt{\frac{E}{N}}\,\alpha[k] + \eta[k]\,, \tag{6.96}$$

where the normalised noiseless signal component, $\alpha[k]$, may be expressed using (6.95) as:

$$\alpha[k] = (N-1)\mathbf{b}[k] - \sum_{i=1, i\neq k}^{N} \mathbf{W}_N[k,l]\mathbf{W}_N[l,i]\mathbf{b}[i] \tag{6.97}$$

and the noise component, $\eta[k]$, is given with the aid of (6.95) as:

$$\eta[k] = \sum_{i=1, i\neq l}^{N} \mathbf{W}_N[k,i]\, \mathbf{n}[i]\,, \tag{6.98}$$

where $\eta[k]$ has a zero mean Gaussian distribution with a variance of $(N-1)N_o/2$, since it is a linear sum of $N-1$ Gaussian random variables having the variance of $N_o/2$. It is worth mentioning that the second term at the right hand side of (6.97) is the Multiple Code Interference (MCI) or Multiple User Interference (MUI), which is a consequence of the destroyed orthogonality between the codes owing to the loss of the lth transform-domain symbol.

Let us determine the probability density function (PDF) of $\alpha[k]$, which was defined in (6.97). Assuming that the information bits $\mathbf{b}[i]$ are independent binary random variables, $\alpha[k]$ becomes a binomially distributed random variable, since $\alpha[k]$ is the linear sum of $\mathbf{b}[i]$ [25, 163]. Given a fixed $\mathbf{b}[k]$ value, there are $N-1$ independent $\mathbf{b}[i]$ values in the N-dimensional vector $\mathbf{b}$. If we choose n number of bits $\mathbf{b}[i]$ out of $N-1$ such that $\mathbf{b}[i] = \mathbf{W}_N[k,l]\mathbf{W}_N[l,i]$ yielding n number of '+1's and $N-1-n$ number of '-1's in the summation of the second term in (6.97), then with the aid of (6.97) we have:

$$\begin{aligned}\alpha[k] &= (N-1)\mathbf{b}[k] - \{n - (N-1-n)\} \\ &= (N-1)(\mathbf{b}[k]+1) - 2n\,,\end{aligned} \tag{6.99}$$

which becomes either $2(N-1-n)$ or $-2n$ depending on the bit $\mathbf{b}[k]$ being $+1$ or -1. The probability of choosing n $\mathbf{b}[i]$'s out of $N-1$ is given as $\binom{N-1}{n}(1/2^{N-1})$ [163] and the probability of $\mathbf{b}[k]$ being '+1' or '-1' is $1/2$. Considering that $\binom{N-1}{n} = \binom{N-1}{N-1-n}$ [163], we can represent the PDF $f_C(\alpha)$ of $\alpha[k]$ for the conventional despreading scheme as:

$$\begin{aligned} f_C(\alpha) &= \Pr(\mathbf{b}[k]=+1)\cdot \sum_{n=0}^{N-1} \binom{N-1}{n} \frac{1}{2^{(N-1)}}\, \delta(\alpha - 2(N-1-n)) \\ &\quad + \Pr(\mathbf{b}[k]=-1)\cdot \sum_{n=0}^{N-1} \binom{N-1}{n} \frac{1}{2^{(N-1)}}\, \delta(\alpha + 2n) \qquad (6.100) \\ &= \frac{1}{2^N} \sum_{n=0}^{N-1} \binom{N-1}{n} [\,\delta(\alpha-2n) + \delta(\alpha+2n)\,]\,. \qquad (6.101) \end{aligned}$$

Figure 6.10 illustrates the PDF of the normalised noiseless signal component α for the spreading factor of $N=8$. We can observe that two binomial distributions are superimposed, meeting at zero. Since the expected value of $\alpha[k]$ in (6.97) is $E[\alpha[k]] = (N-1)\,\mathbf{b}[k]$, the two binomial PDFs in (6.10) are centred at $\pm(N-1) = \pm 7$.

Having obtained the statistics of the signal component $\alpha[k]$ as well as those of the noise component $\eta[k]$, let us now consider the BEP of the conventional despreading scheme transmitting over AWGN channels, assuming that one transform domain symbol is lost due to a strong tone-jamming signal. When $\alpha[k] = -2n$ and $\mathbf{b}[k] = -1$, the decision variable $\mathbf{d}[k]$ given in (6.96) has the Gaussian distribution

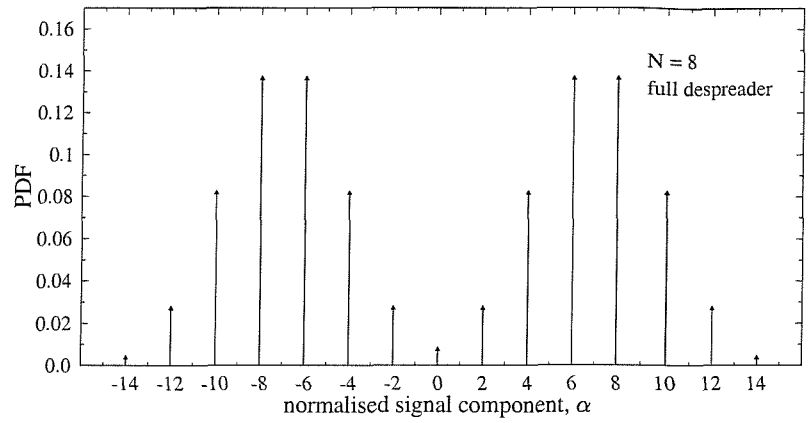

Figure 6.10: The PDF $f_C(\alpha)$ given in (6.101), of the normalised signal component α for the conventional despreading detector when transmitting over AWGN channels under the assumption that one transform-domain is lost due to a strong tone-jamming signal. The spreading factor was $N = 8$, while the PDF is constituted by the superposition of two binomial distributions, as implied by (6.101).

having the mean value of $-\sqrt{E/N}\,2n$ and the variance of $\sigma^2 = (N-1)(N_o/2)$. Hence, the bit error probability $P_{e,C}[\alpha = -2n]$ can be formulated as:

$$P_{e,C}[\alpha = -2n] = \Pr(\alpha = -2n) \cdot \Pr(\mathbf{d}[k] > 0 \mid \alpha = -2n) \tag{6.102}$$

$$= \frac{1}{2^{(N-1)}} \binom{N-1}{n} \cdot \mathrm{Q}\left(\frac{\sqrt{E/N}\,2n}{\sigma}\right) \tag{6.103}$$

$$= \frac{1}{2^{(N-1)}} \binom{N-1}{n} \cdot \mathrm{Q}\left(\frac{2n\sqrt{2\gamma}}{\sqrt{N(N-1)}}\right). \tag{6.104}$$

The BEP corresponding to the scenario of $\mathbf{b}[k] = +1$ can be evaluated in a similar way, yielding the same expression as in (6.104). The probability of $\mathbf{b}[k]$ being $+1$ and -1 is $1/2$ and the BEP given in (6.104) can be used for representing the combined BEP for both scenarios. Referring to (6.101) and (6.104), we can obtain the average BEP $P_{e,C}$ of the conventional despreading detector, which can be expressed as

$$P_{e,C} = \frac{1}{2^{N-1}} \sum_{n=0}^{N-1} \binom{N-1}{n} \mathrm{Q}\left(\frac{2n\sqrt{2\gamma}}{\sqrt{N(N-1)}}\right), \tag{6.105}$$

where γ is the bit energy to noise power ratio, defined as $\gamma = E/N_o$ and N is the spreading factor. The BER floor imposed by the corruption of the lth transform domain symbol is given as $\lim_{\gamma\to\infty} P_{e,C} = 1/2^N$. Figure 6.9 compares the BEP $P_{e,C}$ with that of the non-spreading detectors.

In addition to characterising the detector's performance, we are interested in the required number of operations in the detection process as well. Assuming that the position of the lost transform-domain

symbol is known, the number of operations required is given by:

$$N_C(\times) = (N-1)N \tag{6.106}$$

$$N_C(+) = (N-2)N, \tag{6.107}$$

where $N_C(\times)$ is the number of multiplications required and $N_C(+)$ is the number of additions required for the conventional despreading detector, since the $N-1$ transform-domain symbols except for the lth symbol, are involved in evaluating N number of decision variables $\mathbf{d}[k]$ according to (6.94).

6.5.3 SPD Detectors

Let us now consider the performance of the various SPD detectors. The received transform-domain symbol vector, $\hat{\mathbf{s}}$, may be expressed in its decomposed form, given by:

$$\hat{\mathbf{s}}_1 = \sqrt{\frac{E}{N}}\mathbf{W}_{N/2}\mathbf{b}_1 + \sqrt{\frac{E}{N}}\mathbf{W}_{N/2}\mathbf{b}_2 + \mathbf{n}_1 \tag{6.108}$$

$$\hat{\mathbf{s}}_2 = \sqrt{\frac{E}{N}}\mathbf{W}_{N/2}\mathbf{b}_1 + \sqrt{\frac{E}{N}}\overline{\mathbf{W}}_{N/2}\mathbf{b}_2 + \mathbf{n}_2\,. \tag{6.109}$$

Since the position of the corrupted transform-domain symbol, l, is assumed to be known, we can always identify the received sub-vector, which has not been affected by the corrupted transform-domain symbol, which will be used for the first stage detection. Without loss of generality, let us assume that $l = N/2 + l'$, $0 \leq l' \leq N/2$, *i.e.* the lower-half received sub-vector $\mathbf{r_2}$ contains the lost symbol at the l'th position. Then, after despreading the detection variables $\mathbf{d}_1$ and $\mathbf{d}_2$ become:

$$\mathbf{d}_1 = \mathbf{W}_{N/2}\hat{\mathbf{s}}_1 \tag{6.110}$$

$$= \sqrt{\frac{E}{N}}\frac{N}{2}(\mathbf{b}_1 + \mathbf{b}_2) + \eta_1\,, \tag{6.111}$$

$$\mathbf{d}_2 = \mathbf{W}'_{N/2}\hat{\mathbf{s}}_2 \tag{6.112}$$

$$= \sqrt{\frac{E}{N}}\mathbf{W}'_{N/2}\mathbf{W}_{N/2}(\mathbf{b}_1 - \mathbf{b}_2) + \eta_2\,, \tag{6.113}$$

where $\mathbf{W}'_{N/2}$ is the modified version of $\mathbf{W}_{N/2}$, such that its l'th column was replaced by a $N/2 \times 1$-dimensional zero vector. Furthermore, η_1 in (6.111) is a zero mean Gaussian random variable vector. Its covariance matrix, $\mathrm{Cov}(\eta_1)$, can be calculated as:

$$\begin{aligned}
\mathrm{Cov}(\eta_1) &= \mathrm{E}\{\eta_1\eta_1^T\} \\
&= \mathrm{E}\{\mathbf{W}_{N/2}\,\mathbf{n}_1\,\mathbf{n}_1^T\,\mathbf{W}_{N/2}^T\} \\
&= \mathbf{W}_{N/2}\,\mathrm{E}\{\mathbf{n}_1\mathbf{n}_1^T\}\,\mathbf{W}_{N/2} \\
&= \mathbf{W}_{N/2}\,\frac{N_o}{2}\,\mathbf{I}_{N/2}\,\mathbf{W}_{N/2} \\
&= \frac{N}{2}\,\frac{N_o}{2}\,\mathbf{I}_{N/2}\,.
\end{aligned} \tag{6.114}$$

Hence, the noise samples $\eta_1[k]$ are *iid* and the associated noise variance is $\sigma_1^2 = (N/2)\,(N_o/2)$, where N_o is the noise power associated with each $\mathbf{n}[i]$. The noise contribution of the second detection variable η_2 in (6.113) is also a zero mean Gaussian random variable vector. The associated covariance matrix $\mathrm{Cov}(\eta_2)$, can be evaluated as:

$$\begin{aligned}\mathrm{Cov}(\eta_2) &= \mathrm{E}\{\eta_2 \eta_2^T\} \\ &= \mathrm{E}\{\mathbf{W}'_{N/2}\,\mathbf{n}_1\,\mathbf{n}_1^T\,\mathbf{W}'^{\,T}_{N/2}\} \\ &= \mathbf{W}'_{N/2}\,\mathrm{E}\{\mathbf{n}_1\mathbf{n}_1^T\}\,\mathbf{W}'^{\,T}_{N/2} \\ &= \mathbf{W}'_{N/2}\,\frac{N_o}{2}\,\mathbf{I}_{N/2}\,\mathbf{W}'^{\,T}_{N/2} \\ &= \frac{N_o}{2}\,\mathbf{W}'_{N/2}\,\mathbf{W}'^{\,T}_{N/2}\,, \end{aligned} \tag{6.115}$$

where the diagonal elements of $\mathbf{W}'_{N/2}\,\mathbf{W}'^{\,T}_{N/2}$ have the value of $N/2-1$ and the off diagonal elements are $+1$ or -1 due to the all zero values in the l'th column of $\mathbf{W}'_{N/2}$. Hence, the noise contributions $\eta_2[k]$ are not independent. However, considering that $\sigma_2^2 = (N/2-1)\,N_o/2$ in the diagonal elements of $\mathrm{Cov}(\eta_2)$ grows linearly with N, we can conclude that the noise contributions $\eta_2[k]$ become nearly independent for high spreading factors N.

Having investigated the noise statistics, let us now concentrate on the desired signal component. The kth element of the first stage detection variable, $\mathbf{b}_1[k]$, may be rewritten as:

$$\mathbf{d}_1[k] = \sqrt{\frac{E}{N}}\alpha_1[k] + \eta_1[k]\,, \tag{6.116}$$

where the normalised noiseless signal component $\alpha_1[k]$ is defined as:

$$\alpha_1[k] = \frac{N}{2}(\mathbf{b}_1[k] + \mathbf{b}_2[k])\,. \tag{6.117}$$

Since the first stage detection variable is assumed to be unaffected by the symbol loss, $\alpha_1[k]$ becomes either $\pm N$ or zero with an equal probability of $1/2$.

The modified despreading matrix $\mathbf{W}'_{N/2}$ of (6.113) can be written as $\mathbf{W}'_{N/2} = \mathbf{W}'_{N/2} - \mathbf{L}_{N/2}$, where $\mathbf{L}_{N/2}$ is a $N/2 \times N/2$-dimensional matrix having all zero elements except the l'th column, where the value is the same as that of the despreading matrix $\mathbf{W}_{N/2}$, namely $\mathbf{L}_{N/2}[i,l'] = \mathbf{W}_{N/2}[i,l']$. Hence, the second stage detection variable $\mathbf{d}_2$ of (6.113) can be written as:

$$\mathbf{d}_2 = \sqrt{\frac{E}{N}}\,(\mathbf{W}_{N/2} - \mathbf{L}_{N/2}) \cdot \mathbf{W}_{N/2}(\mathbf{b}_1 - \mathbf{b}_2) + \eta_2 \tag{6.118}$$

$$= \sqrt{\frac{E}{N}}\,\frac{N}{2}\,(\mathbf{b}_1 - \mathbf{b}_2) - \sqrt{\frac{E}{N}}\,\mathbf{L}_{N/2}\,\mathbf{W}_{N/2}\,(\mathbf{b}_1 - \mathbf{b}_2) + \eta_2 \tag{6.119}$$

The kth element of $\mathbf{d}_2$ in (6.119) can be written as:

$$\mathbf{d}_2[k] = \sqrt{\frac{E}{N}}\,\alpha_2[k] + \eta_2[k]\,, \tag{6.120}$$

where the normalised signal component $\alpha_2[k]$ is defined as:

$$\alpha_2[k] = \frac{N}{2}\left(\mathbf{b}_1[k] - \mathbf{b}_2[k]\right) - \sum_{i=1}^{N/2} \mathbf{W}_{N/2}[k,l]\,\mathbf{W}_{N/2}[l,i](\mathbf{b}_1[i] - \mathbf{b}_2[i]) \tag{6.121}$$

$$= \left(\frac{N}{2} - 1\right)\left(\mathbf{b}_1[k] - \mathbf{b}_2[k]\right) - \sum_{i=1, i\neq k}^{N/2} \mathbf{W}_{N/2}[k,l]\,\mathbf{W}_{N/2}[l,i](\mathbf{b}_1[i] - \mathbf{b}_2[i])\,. \tag{6.122}$$

Following a similar approach to that described in the previous section, we can derive the PDF of $\alpha_2[k]$ of (6.122), which is our next objective. For fixed $\mathbf{b}_1[k]$ and $\mathbf{b}_2[k]$ values, we have $N-2$ independent random binary variables $\mathbf{b}_1[i]$ and $\mathbf{b}_2[i]$, where $i \neq k$. The probability of choosing n number of specific $\mathbf{b}_1[i]$ values and/or $\mathbf{b}_2[i]$ values out of $N-2$, such that $\mathbf{b}_1[i] = \mathbf{W}_{N/2}[k,l]\,\mathbf{W}_{N/2}[l,i]$ and $\mathbf{b}_2[i] = -\mathbf{W}_{N/2}[k,l]\,\mathbf{W}_{N/2}[l,i]$, is $\binom{N-2}{n}/2^{N-2}$. Then we have n number of '+1's and $N-2-n$ number of '-1's in the summation of the second term in the right hand side of (6.122), yielding:

$$\begin{aligned}\alpha_2[k] &= \left(\frac{N}{2} - 1\right)\left(\mathbf{b}_1[k] - \mathbf{b}_2[k]\right) - \{n - (N-2-n)\} \\ &= \left(\frac{N}{2} - 1\right)\left(\mathbf{b}_1[k] - \mathbf{b}_2[k]\right) + N - 2 - 2n\,.\end{aligned} \tag{6.123}$$

Depending on the information bits transmitted, we have either Case 1: $\mathbf{b}_1[k] = \mathbf{b}_2[k]$ or Case 2: $\mathbf{b}_1[k] = -\mathbf{b}_2[k]$. For Case 1, $\alpha_2[k]$ of (6.123) becomes $(N-2)(\mathbf{b}_1[k]+1) - 2n$, which is either $2(N-2-n)$ or $-2n$ depending on $\mathbf{b}_1[k]$ being $+1$ or -1, respectively. Considering that $\binom{N-2}{n} = \binom{N-2}{N-2-n}$, we can represent the PDF of $\alpha_2[k]$, $f_{SPD,1}(\alpha_2)$, as:

$$\begin{aligned} f_{SPD,1}(\alpha_2) &= \Pr(\mathbf{b}_1[k] = +1) \cdot \sum_{n=0}^{N-2} \binom{N-2}{n} \frac{1}{2^{N-2}}\,\delta(\,\alpha_2 - 2(N-2-n)\,) \\ &\quad + \Pr(\mathbf{b}_1[k] = -1) \cdot \sum_{n=0}^{N-2} \binom{N-2}{n} \frac{1}{2^{N-2}}\,\delta(\,\alpha_2 + 2n\,) \\ &= \frac{1}{2}\frac{1}{2^{N-2}} \cdot \sum_{n=0}^{N-2} \binom{N-2}{N-2-n}\,\delta(\,\alpha_2 - 2n\,) \qquad (6.124) \\ &\quad + \frac{1}{2}\frac{1}{2^{N-2}} \cdot \sum_{n=0}^{N-2} \binom{N-2}{n} \frac{1}{2^{N-2}}\,\delta(\,\alpha_2 + 2n\,) \qquad (6.125) \\ &= \frac{1}{2^{N-1}} \sum_{n=0}^{N-2} \binom{N-2}{n}\,\{\,\delta(\alpha_2 - 2n) + \delta(\alpha_2 + 2n)\,\}\,. \qquad (6.126) \end{aligned}$$

Figure 6.11(a) shows an example of $f_{SPD,1}(\alpha_2)$ for the spreading factor of $N = 8$, which is again constituted by the superposition of two binomial distributions centered at ± 6, because the expected value of $\alpha_2[k]$ is given by the first term of (6.122), which is $\left(\frac{N}{2} - 1\right)\left(\mathbf{b}_1[k] - \mathbf{b}_2[k]\right) = 6\,\mathbf{b}_1[k]$.

For Case 2, namely when $\mathbf{b}_1[k] = -\mathbf{b}_2[k]$, $\alpha_2[k]$ of (6.123) becomes $N-2-2n$ with the probability

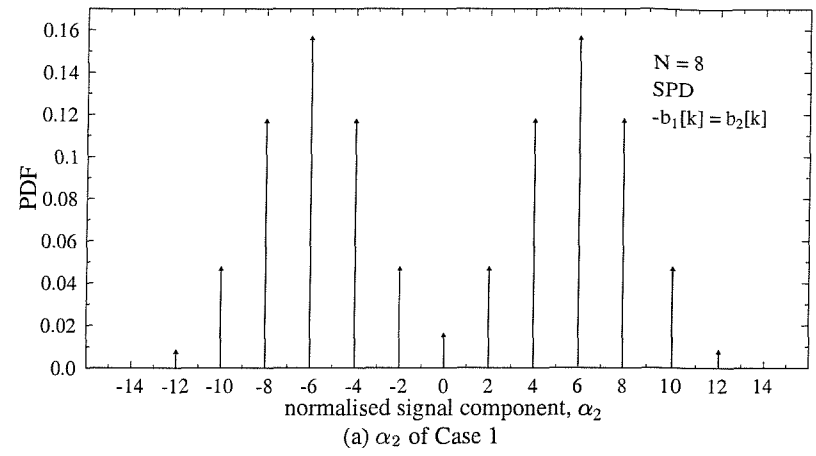

(a) α_2 of Case 1

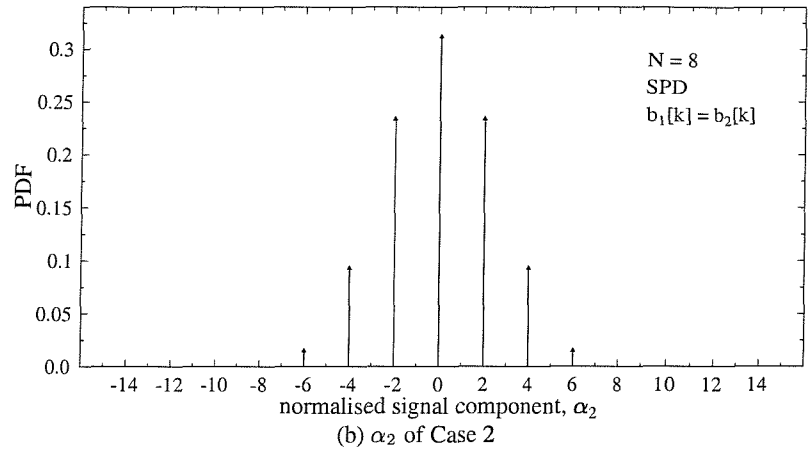

(b) α_2 of Case 2

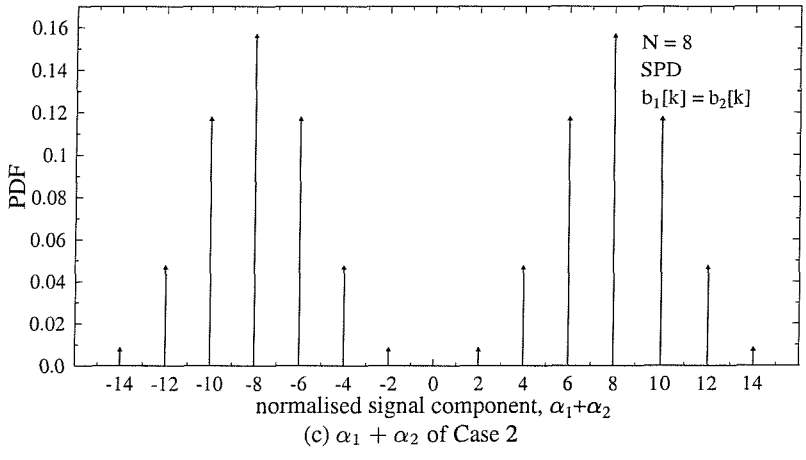

(c) $\alpha_1 + \alpha_2$ of Case 2

Figure 6.11: The PDF of normalised signal component α_1 and α_2 defined in (6.117) and (6.121), respectively, of the SPD detector for transmission over the AWGN channel, when one transform-domain symbol is obliterated. The spreading factor was $N = 8$. Case 1 is for $-\mathbf{b}_1[k] = \mathbf{b}_2[k]$ and Case 2 is for $\mathbf{b}_1[k] = \mathbf{b}_2[k]$.

of $\binom{N-2}{n}$ $(1/2^{N-2})$. Hence, we may express the PDF $f_{SPD,2}(\alpha_2)$ of $\alpha_2[k]$ as:

$$f_{SPD,2}(\alpha_2) = \frac{1}{2^{N-2}} \sum_{n=0}^{N-2} \binom{N-2}{n} \delta(\alpha_2 - (N-2-2n)) \tag{6.127}$$

$$= \frac{1}{2^{N-2}} \sum_{n=0}^{N-2} \binom{N-2}{n} \delta(\alpha_2 - 2n) \tag{6.128}$$

An example of $f_{SPD,2}(\alpha_2)$ is depicted in Figure 6.11(b) for the spreading factor of $N = 8$. Since we now have all the necessary statistics of SPD detection variables, we can analyse the bit error rate performance of the three different types of SPD detectors.

6.5.4 Type I Detector

In the Type I SPD detector, according to (6.13) and (6.13) $\hat{\mathbf{b}}_1$ and $\hat{\mathbf{b}}_1$ are given the sum and the difference of $\mathbf{d}_1$ and $\mathbf{d}_2$. Since $\mathbf{d}_1$ and $\mathbf{d}_2$ are given in (6.116) and Eq. (6.120), the estimates of the original bits become:

$$\hat{\mathbf{b}}_1[k] = \sqrt{\frac{E}{N}}(\alpha_1[k] + \alpha_2[k]) + \eta_1[k] + \eta_2[k] \tag{6.129}$$

$$\hat{\mathbf{b}}_2[k] = \sqrt{\frac{E}{N}}(\alpha_1[k] - \alpha_2[k]) + \eta_1[k] - \eta_2[k] \,. \tag{6.130}$$

Since $\eta_1[k]$ and $\eta_2[k]$ are independent zero-mean Gaussian random variables, the noise term $\eta_1[k] \pm \eta_2[k]$ is also a zero-mean Gaussian random variable with a variance of $(N/2)(N_o/2) + (N/2-1)(N_o/2) = (N-1)(N_o/2)$. We can conclude that the noise statistics of the Type I decision variables are identical to those of the conventional full despreader characterised in (6.98).

For the case of $\mathbf{b}_1[k] = -\mathbf{b}_2[k]$, according to (6.117) $\alpha_1[k]$ becomes zero, and hence according to (6.129) and (6.130) $\sqrt{E/N}\alpha_2[k]$ becomes the mean of the Gaussian random variables $\hat{\mathbf{b}}_1$ and $\hat{\mathbf{b}}_2$. The PDF of $\alpha_2[k]$ for the case of $\mathbf{b}_1[k] = -\mathbf{b}_2[k]$ was given in (6.126).

On the other hand, when $\mathbf{b}_1[k] = \mathbf{b}_2[k]$, according to (6.117) $\alpha_1[k]$ becomes $N\,\mathbf{b}_1[k] = \pm N$ depending on the value of $\mathbf{b}_1[k]$ and $\alpha_1[k]$ becomes:

$$\alpha_2[k] = -\sum_{i=1, i\neq k}^{N/2} \mathbf{W}_{N/2}[k,l]\,\mathbf{W}_{N/2}[l,i](\mathbf{b}_1[i] - \mathbf{b}_2[i]), \tag{6.131}$$

while its PDF was given in (6.128). Then, the mean of $\hat{\mathbf{b}}_1[k]$ given in (6.129) becomes $\sqrt{E/N}(\alpha_2[k] \pm N)$ depending on the actual value of $\mathbf{b}_1[k]$. In this case, the PDF of the effective normalised signal component α defined by $\alpha = \alpha_1 + \alpha_2[k]$, which becomes $\alpha = \alpha_2[k] \pm N$ according to the above argument, can be derived by introducing the variable $\alpha_2[k] = \alpha - N$ with a probability of $1/2$ and $\alpha_2[k] = \alpha + N$ with a probability of $1/2$ in the expression of the PDF of $\alpha_2[k]$ given in (6.127),

yielding:

$$f_{SPD,2}(\alpha) = \frac{1}{2^{N-2}} \sum_{n=0}^{N-2} \binom{N-2}{n} \{\frac{1}{2}\,\delta(\alpha+N-(N-2-2n)) + \frac{1}{2}\,\delta(\alpha-N-(N-2-2n))\}$$

$$= \frac{1}{2^{N-1}} \sum_{n=0}^{N-2} \binom{N-2}{n} \{\delta(\alpha+2(n+1)) + \delta(\alpha-2(N-1-n))\} \tag{6.132}$$

$$= \frac{1}{2^{N-1}} \sum_{n=0}^{N-2} \binom{N-2}{n} \{\delta(\alpha+2(n+1)) + \delta(\alpha-2(n+1))\}\,, \tag{6.133}$$

where we used the relationship of $\binom{N-2}{n} = \binom{N-2}{N-2-n}$ for replacing $\delta(\alpha-2(N-1-n))$ of (6.132) with $\delta(\alpha-2(n+1))$ of (6.133). An example of $f_{SPD,2}(\alpha)$ is given in Figure 6.11(c) for the spreading factor of $N=8$.

Since $\mathbf{b}_1[k]$ and $\mathbf{b}_2[k]$ are independent, the overall PDF of the effective signal component of the Type I SPD detector can be expressed as the sum of the PDFs given in (6.126 and (6.133), yielding:

$$f_I(\alpha) = \frac{1}{2} f_{SPD,1} + \frac{1}{2} f_{SPD,2'} \tag{6.134}$$

$$= \frac{1}{2^N} \sum_{n=0}^{N-2} \binom{N-2}{n} \{\delta(\alpha-2n) + \delta(\alpha+2n)\}$$

$$+ \frac{1}{2^N} \sum_{n=0}^{N-2} \binom{N-2}{n} \{\delta(\alpha-2(n+1)) + \delta(\alpha+2(n+1))\} \tag{6.135}$$

$$= \frac{1}{2^N} \sum_{n=0}^{N-2} \binom{N-2}{n} \{\delta(\alpha-2n) + \delta(\alpha+2n)\}$$

$$+ \frac{1}{2^N} \sum_{n=1}^{N-1} \binom{N-2}{n-1} \{\delta(\alpha-2n) + \delta(\alpha+2n)\} \tag{6.136}$$

$$= \frac{1}{2^N} \sum_{n=0}^{N-1} \binom{N-1}{n} \{\delta(\alpha-2n) + \delta(\alpha+2n)\}\,, \tag{6.137}$$

where we used the relationship of [164]:

$$\binom{N-2}{n-1} + \binom{N-2}{n} = \binom{N-1}{n}\,. \tag{6.138}$$

We can observe that the PDF $f_I(\alpha)$ given in (6.137) is identical to the PDF of $\alpha[k]$ of the conventional full despreader, which was given in (6.101). Hence we can conclude that the bit error rate performance of the Type I detector for transmission over the AWGN channel with one obliterated transform-domain symbol is identical to that of the conventional despreader, given in (6.105). Figure 6.12(a) shows the BER as a function of E/N_o.

Let us now consider the complexity of the Type I SPD detector. Since $\mathbf{d}_1$ is calculated according to

(6.110), the number of operations required is given as:

$$N_{\mathbf{d}_1}(\times) = \frac{N}{2} \cdot \frac{N}{2} = \left(\frac{N}{2}\right)^2 \tag{6.139}$$

$$N_{\mathbf{d}_1}(+) = \left(\frac{N}{2} - 1\right) \cdot \frac{N}{2}. \tag{6.140}$$

On the other hand, $\mathbf{d}_2$ is calculated according to (6.112), exploiting the fact that the l'th transform-domain symbol was obliterated and hence eliminating the unnecessary operations. Hece the number of operations required is given by:

$$N_{\mathbf{d}_2}(\times) = \left(\frac{N}{2} - 1\right) \frac{N}{2} \tag{6.141}$$

$$N_{\mathbf{d}_2}(+) = \left(\frac{N}{2} - 2\right) \frac{N}{2} \tag{6.142}$$

Since the Type I SPD detector only requires additional additions, when evaluating $\hat{\mathbf{b}}_1$ and $\hat{\mathbf{b}}_2$ according to (6.13) and (6.14), respectively, the required number of multiplications $N_I(\times)$ is given as:

$$\begin{aligned} N_I(\times) &= N_{\mathbf{d}_1}(\times) + N_{\mathbf{d}_2}(\times) \\ &= \frac{1}{4}(2N^2 - 2N) \\ &= \frac{1}{2}N_C(\times), \end{aligned} \tag{6.143}$$

where $N_C(\times)$ is the number of multiplications required for a conventional full-despreading detector given in (6.106). By contrast, the required number of additions $N_I(+)$ involved in the evaluation of (6.13) and (6.14) is given as:

$$\begin{aligned} N_I(+) &= N_{\mathbf{d}_1}(+) + N_{\mathbf{d}_2}(+) + N \\ &= \frac{1}{4}(N^2 - 2N + N^2 - 4N + 2N) + \frac{1}{2}N \\ &= \frac{1}{2}N_C(+) + \frac{1}{2}N, \end{aligned} \tag{6.144}$$

where $N_C(+)$ is the number of additions required for a conventional full-despreading detector given in (6.106). The achievable complexity reduction is shown in Figure 6.12(b) and will be discussed in more depth in Section 6.5.7

6.5.5 Type II Detector

In the type II SPD detector, only $\mathbf{d}_1[k]$ is used at the first stage detection. Recall from Section 6.3 that when $\mathbf{d}_1[k]$ falls in the region '0' of Figure 6.3, $\mathbf{d}_2[k]$ is used for the second stage detection assuming that $\mathbf{b}_1[k] = -\mathbf{b}_2[k]$, as described in Section 6.3 on page 163. Since we assumed that $\mathbf{d}_1[k]$ is not affected by the obliterated transform-domain symbol, the BER analysis regarding $\mathbf{d}_1[k]$ given in Section 6.4.2 may be used here without any modifications. The analysis regarding $\mathbf{d}_2[k]$ may be modified considering the

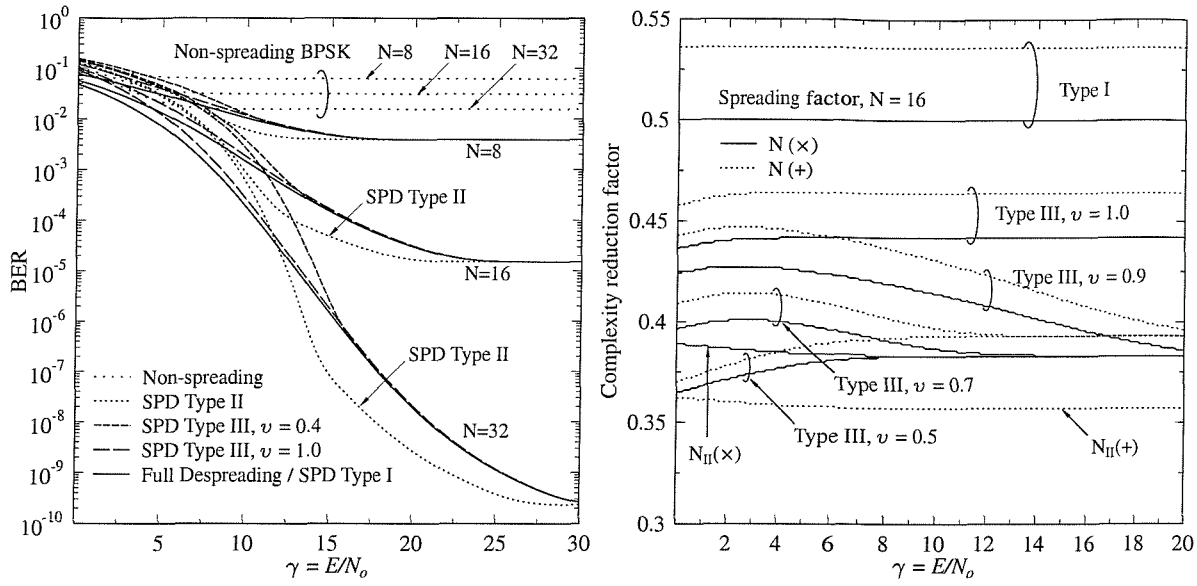

(a) Bit Error Rate

(b) Complexity

Figure 6.12: The performance of various detection for transmission over the AWGN channel, when one of N transform-domain symbol is obliterated. (a) The non-spread BPSK scheme has a high irreducible BER of $0.5/N$, while the spread systems have far lower error floor at $1/2^N$. The Type II SPD Detector shows a superior performance in the high SNR region compared to the conventional despreading method. (b) The complexity of various SPD detectors normalised to that of conventional despreading detector for the spreading factor of $N=16$. The Type II SPD detector requires less than 40% of the computations of that for the conventional despreading

PDF given in (6.126). Specifically, $P_e(0|0)$ of (6.36) has to be modified, which is the bit error probability, when $\mathbf{d}_1[k]$ falls in the region '0' of Figure 6.3(a), provided that $\mathbf{b}_1[k] = -\mathbf{b}_2[k]$ and, hence $\mathbf{d}_2[k]$ has to be used for the final detection. The BEP $P_e(0|0)$ can be formulated as:

$$P_e(0|0) = \Pr(\,|\mathbf{d}_1[k]| \leq V_T \mid \mathbf{b}_1[k] = -\mathbf{b}_2[k]) \cdot P_{e,2} \tag{6.145}$$

$$= \left\{1 - 2\mathrm{Q}\left(\frac{V_T}{\sigma_1}\right)\right\} \cdot P_{e,2}\,, \tag{6.146}$$

where $P_{e,2}$ is the average BEP at the second stage detection based on $\mathbf{d}_2[k]$ of (6.120) when $\mathbf{b}_1[k] = -\mathbf{b}_2[k]$. The PDF of the normalised signal component α_2 of $\mathbf{d}_2[k]$ was given in (6.126) and a specific PDF example for the spreading factor of $N = 8$ was illustrated in Figure 6.11(a). Since $\mathbf{d}_2[k]$ is a Gaussian random variable having the mean of $\sqrt{E/N}\,\alpha_2[k]$ and the variance of $\sigma^2 = (N/2 - 1)\,N_o/2$,

as argued in Section 6.5.3, the BEP $P_{e,2}$ can be expressed using (6.126) as:

$$P_{e,2} = \sum_{n=0}^{N-2} \Pr(\alpha = 2n) \cdot \mathrm{Q}\left(\frac{2n\sqrt{E/N}}{\sigma_2}\right) \tag{6.147}$$

$$= \frac{1}{2^{N-2}} \sum_{n=0}^{N-2} \binom{N-2}{n} \mathrm{Q}\left(\frac{2n\sqrt{E/N}}{\sigma_2}\right) \tag{6.148}$$

$$= \frac{1}{2^{N-2}} \sum_{n=0}^{N-2} \binom{N-2}{n} \mathrm{Q}\left(\frac{4n\sqrt{\gamma}}{\sqrt{N(N-2)}}\right) . \tag{6.149}$$

Since we now have the modified BEP term $P_e(0|0)$, which is given in (6.146) and (6.149), let us express the average BEP $P_{e,II}$ of the Type II detector, when one transform-domain symbol is obliterated. The BEP of the Type II detector was expressed in (6.52) as:

$$P_{e,II} = \frac{1}{2}\{P_e(0) + P_e(\pm 1)\} \tag{6.150}$$

$$P_{e,II} = \frac{1}{2}\{P_e(\pm 1|0) + P_e(0|0) + P_e(\pm 1)\}, \tag{6.151}$$

where $P_e(\pm 1|0)$ and $P_e(\pm 1)$ were given in (6.32) and (6.51), respectively, in Section 6.4.2, while $P_e(0|0)$ was calculated above and was given in (6.146), yielding:

$$P_{e,II} = \frac{1}{4}\left[\mathrm{Q}\left(2\sqrt{\gamma}(1-\upsilon)\right) + \mathrm{Q}\left(2\sqrt{\gamma}(1+\upsilon)\right)\right] + \mathrm{Q}(2\sqrt{\gamma}\,\upsilon)\left[\frac{1}{2} - P_{e,2}\right] + \frac{1}{2}P_{e,2}, \tag{6.152}$$

where $P_{e,2}$ was given in (6.149). The expression for the optimum normalised threshold υ_{opt} given in (6.56) is still valid, when using the modified parameter $\mu = \{1 - 2P_{e,2}\}e^{2\gamma}$. The bit error probability $P_{e,II}$ of the Type II SPD detector exhibits the same BER floor at $1/2^N$, as the conventional full despreading detector or the Type I SPD detector. Figure 6.13(a) depicts the bit error probability as functions of the normalised threshold levels employed for SNR values of $\gamma = 0\text{dB} \sim 25\text{dB}$ and for the spreading factor of $N = 16$. By comparing Figure 6.4(a) and Figure 6.13(a), we can observe that as the lowest BERs approach the BER floor, the regions of the normalised threshold levels where their BERs are maintained become wide. Figure 6.13(b) shows the optimum threshold levels as a function of E/N_o for several values of the spreading factor N. For low spreading factors, the optimum normalised threshold levels turn out to be lower, than those for higher spreading factors. As the spreading factor is increased, the optimum normalised threshold curve approached that valid for the AWGN channel determined without any transform-domain symbol losses.

Let us briefly characterise the computational cost of the Type II SPD detector. Considering that the detector requires $\mathbf{d}_2$ for detection only when $\mathbf{d}_1$ falls in the region '0' of Figure 6.3(a)), the number of multiplications and additions involved in the evaluation of (6.110) and (6.110) can be expressed with the aid of (6.139) to (6.142) as:

$$N_{II}(\times) = N_{\mathbf{d}_1}(\times) + N_{\mathbf{d}_2}(\times)P_{II}(0) = \left(\frac{N}{2}\right)^2 + \frac{N(N-2)}{4}P_{II}(0), \tag{6.153}$$

$$N_{II}(+) = N_{\mathbf{d}_1}(+) + N_{\mathbf{d}_2}(+)P_{II}(0) = \frac{N(N-2)}{4} + \frac{N(N-4)}{4}P_{II}(0), \tag{6.154}$$

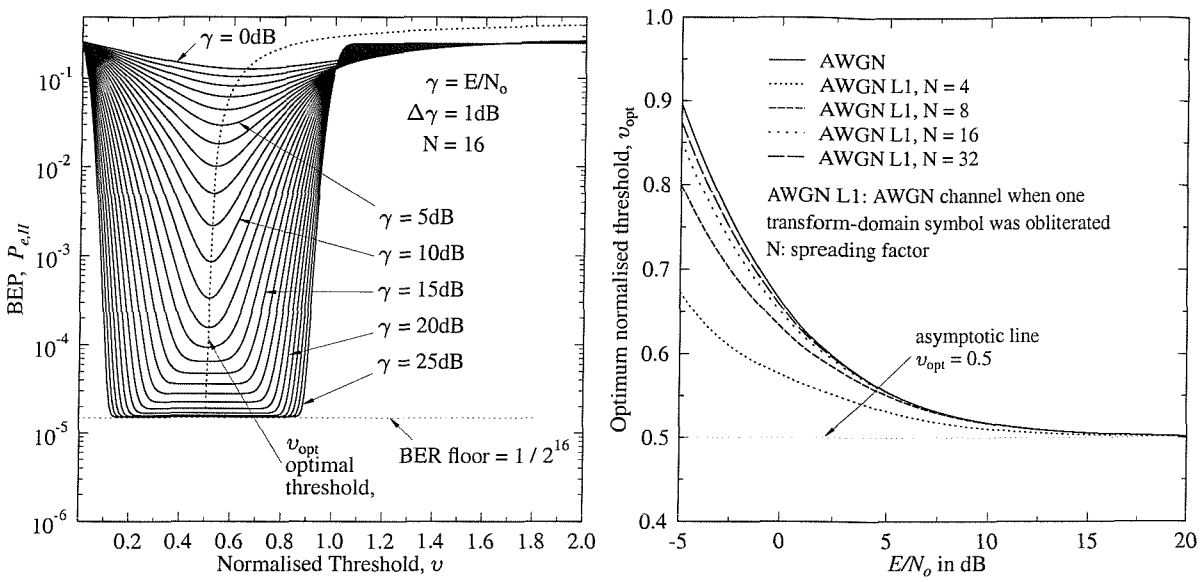

(a) Bit error rates

(b) Optimal threshold level

Figure 6.13: Characteristics of the Type II detector: (a) the BEP of the Type II detector, $P_{e,II}$, against the normalised threshold level, υ, for several E/N_o values. The spreading factor N is 16. (b) the optimum normalised threshold levels, υ_{opt}, versus E/N_o for several values of N. υ_{opt} asymptotically approaches $1/2$ as E/N_o becomes large.

where $P_{II}(0)$ is the probability that $\mathbf{d}_1$ falls in the region '0', given in (6.61). Again, Figure 6.12(b) compares the computational costs involved with those of other detection schemes.

6.5.6 Type III Detector

Finally, let us analyse the bit error ratio performance of the Type III SPD detector for transmission over the AWGN channel, when one transform-domain symbol is totally corrupted. The detection method was introduced in Section 6.3 on page 164. When $\mathbf{d}_1[k]$ of (6.116) falls in the region '0' of Figure 6.3(a), $\hat{\mathbf{b}}_1[k]$ and $\hat{\mathbf{b}}_2[k]$ of (6.129) and (6.130) are used for the detection of $\mathbf{b}_1[k]$ and $\mathbf{b}_2[k]$. Otherwise, the detection process is concluded at the first stage, determining both bits solely based on $\mathbf{d}_1[k]$. The performance analysis given in Section 6.4.3 can be repeated here with some modifications considering the different PDF of $\mathbf{d}_2[k]$ due to the loss of one transform-domain symbol.

Firstly, let us consider the case of $\mathbf{b}_1[k] = -\mathbf{b}_2[k]$ and hence $\mathbf{d}_1[k]$ of (6.116) is expected to fall in the region '0' of Figure 6.3(a) when the noise contribution is not excessive. However, when $\mathbf{d}_1[k]$ of (6.116) falls in the region of '+1' or '-1' of Figure 6.3(a), the Type III SPD detector will assume $\mathbf{b}_1[k] = \mathbf{b}_2[k]$ and will detect one of the bits incorrectly. This error probability, denoted by $P_e(\pm 1|0)$ according to our convention introduced on page 166 of Section 6.4.2, was given in (6.32) and is repeated

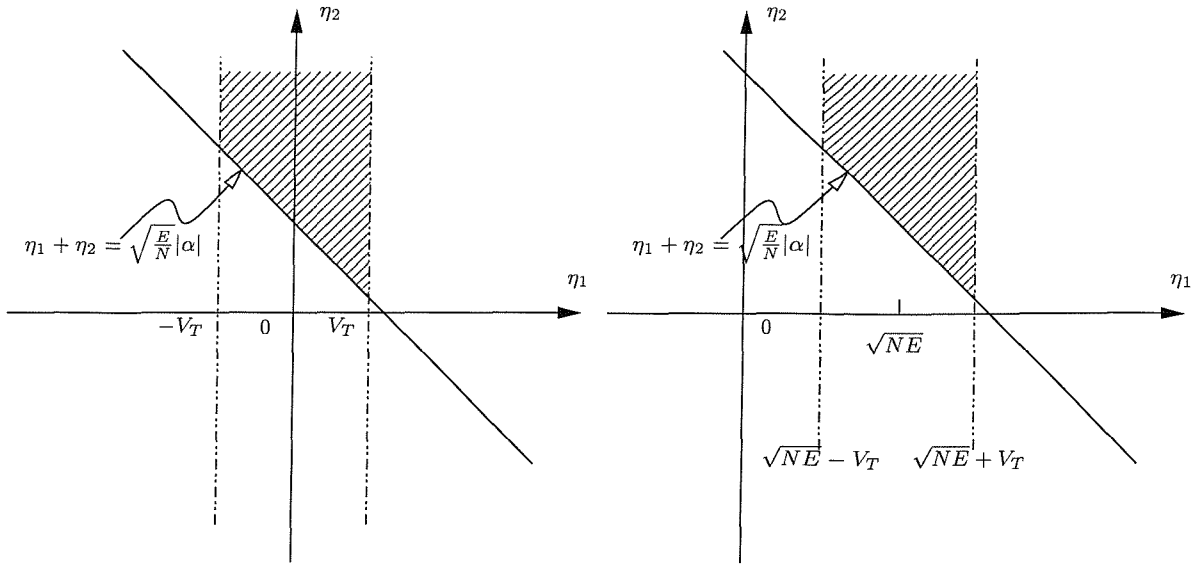

(a) Region 1 (b) Region 2

Figure 6.14: Integration regions for conditional bit error probabilities for the Type III detector in the AWGN channel when one transform-domain symbol was obliterated. (a) Region 1 represents the area satisfying $\mathrm{P}(\eta_1 + \eta_2 > \sqrt{\frac{E}{N}}|\alpha|,\ |\eta_1| < V_T)$ and (b) Region 2 represents that satisfying $\mathrm{P}(\eta_1 + \eta_2 > \sqrt{\frac{E}{N}}|\alpha|,\ \sqrt{NE} - V_T < \eta_1 < \sqrt{NE} + V_T)$.

here for convenience:

$$P_e(\pm 1|0) = \mathrm{Q}(2\sqrt{\gamma}\upsilon)\,. \tag{6.155}$$

It can be inferred from the PDFs seen in Figure 6.3 that a bit error also occurs when $\mathbf{d}_1[k]$ falls in the region '0' and

$$sgn(\,\hat{\mathbf{b}}_1[k]\,) \neq \mathbf{b}_1[k] \tag{6.156}$$

$$\Longleftrightarrow\ sgn(\sqrt{E/N}\alpha[k] + \eta_1[k] + \eta_2[k]) \neq \mathbf{b}_1[k]\,, \tag{6.157}$$

where $sgn(x) = 1$ if $x \geq 0$, otherwise $sgn(x) = -1$ and $\alpha[k]$ is the normalised noiseless signal component defined as $\alpha[k] = \alpha_1[k] + \alpha_2[k]$, which becomes $\alpha_2[k]$ when $\mathbf{b}_1[k] = -\mathbf{b}_2[k]$, according to (6.117) and (6.122). For a given positive $\alpha[k]$, the BEP $P_e(\alpha, 0|0)$ can be formulated, following the argument given in Section 6.4.3, as:

$$P_e(\alpha, 0|0) = \Pr(\hat{\mathbf{b}}_1[k] > 0,\ |\mathbf{d}_1[k]| \leq V_T \mid \mathbf{b}_1[k] = -\mathbf{b}_2[k] = -1)\,. \tag{6.158}$$

Substituting $\hat{\mathbf{b}}_1[k]$ of (6.129) into (6.158) and noting that $\mathbf{d}_1[k]$ of (6.139) becomes $\mathbf{d}_1[k] = \eta_1[k]$, we have:

$$P_e(\alpha, 0|0) = \Pr(-\sqrt{E/N}\alpha[k] + \eta_1[k] + \eta_2[k] > 0,\ |\eta_1[k]| < V_T)\,, \tag{6.159}$$

which can be calculated with the aid of the joint PDF f_{η_1,η_2} of (6.71) having the combined variance of $\sigma^2 = (N-1)\,N_o/2$ and with the aid of the integration region depicted in Figure 6.14(a), yielding:

$$\begin{aligned} P_e(\alpha, 0|0) &= \int_{-V_T}^{V_T} \int_{\sqrt{E/N}\alpha-\eta_1}^{\infty} \frac{1}{2\pi\sigma_1\sigma_2} e^{-\eta_1^2/(2\sigma_1^2)-\eta_2^2/(2\sigma_2^2)} d\eta_2\, d\eta_1 \\ &= \int_{-V_T}^{V_T} \frac{1}{\sqrt{2\pi}\sigma_1} e^{-\eta_1^2/(2\sigma_1^2)}\, \mathrm{Q}\left(\frac{\sqrt{E/N}\alpha-\eta_1}{\sigma_2}\right) d\eta_1 \\ &= \frac{1}{\sqrt{2\pi}} \int_{-2\sqrt{\gamma}\upsilon}^{2\sqrt{\gamma}\upsilon} e^{-\eta^2/2}\, \mathrm{Q}\left(2\sqrt{\gamma}\frac{\alpha}{\sqrt{N(N-2)}} - \sqrt{\frac{N}{N-2}}\,\eta\right) d\eta\,. \end{aligned} \tag{6.160}$$

Since the random variables α and η in (6.160) have symmetric PDFs, the expression of $P_e(0|0)$ given in (6.160) can be used for a negative $\alpha[k]$. Using the PDF of $\alpha[k]$ given in (6.126), $P_e(\alpha, 0|0)$ can be averaged over $\alpha[k]$, yielding:

$$P_e(0|0) = \sum_{n=0}^{N-2} \Pr(\alpha = 2n) \cdot P_e(\alpha = 2n, 0|0) \tag{6.161}$$

$$\begin{aligned} &= \frac{1}{2^{N-2}} \sum_{n=0}^{N-2} P_e(\alpha, 0|0) \binom{N-2}{n} \delta(\alpha - 2n) \\ &= \frac{1}{\sqrt{2\pi}} \frac{1}{2^{N-2}} \sum_{n=0}^{N-2} \binom{N-2}{n} \int_{-2\sqrt{\gamma}\upsilon}^{2\sqrt{\gamma}\upsilon} e^{-\eta^2/2} \mathrm{Q}\left(4\sqrt{\gamma}\frac{n}{\sqrt{N(N-2)}} - \sqrt{\frac{N}{N-2}}\,\eta\right) d\eta\,. \end{aligned} \tag{6.162}$$

From (6.155) and (6.162, we can obtain the total average BEP $P_e(0)$ for the case of $\mathbf{b}_1[k] = -\mathbf{b}_2[k]$, given as $P_e(0) = P_e(\pm 1|0) + P_e(0|0)$.

When $\mathbf{b}_1[k] = \mathbf{b}_2[k]$, there can be two scenarios remiting incorrect detection, one at the first stage detector and another at the second stage combined detector. The bit error probability of the fist stage detector was given in (6.43) and remains the same, since the loss of one transform-domain symbol does not affect the first stage detection variable. For a further reference, we repeat the expression of (6.43) here:

$$P_e(\mp 1|\pm 1) = \mathrm{Q}\left(2\sqrt{\gamma}(1+\upsilon)\right)\,. \tag{6.163}$$

We obtain the BEP $P_e(0|\pm 1)$ at the second detection stage using similar approaches to those involved in Section 6.4.3. Assuming that $\mathbf{b}_1[k] = \mathbf{b}_2[k] = -1$ is transmitted, according to the Type III detection strategy given in Section 6.3 a bit error occurs, when $\mathbf{d}_1[k] = -\sqrt{NE} + \eta_1[k]$ falls in the region '0' of Figure 6.3(a) and $\hat{\mathbf{b}}_1[k] = \sqrt{E/N}\alpha[k] + \eta_1[k] + \eta_2[k]$ is positive. This error probability can be formulated as:

$$P_e(0|\pm 1) = \Pr(|-\sqrt{NE} + \eta_1[k]| < V_T,\ \sqrt{E/N}\alpha[k] + \eta_1[k] + \eta_2[k] > 0)\,. \tag{6.164}$$

With the aid of the joint PDF of $\eta_1[k]$ and $\eta_2[k]$ given in (6.71) and the corresponding integration region

depicted in Figure 6.14(b), the conditional BEP $P_e(\alpha, 0|\pm 1)$ for a fixed value of α can be expressed as:

$$P_e(\alpha,0|\pm 1) = \int_{\sqrt{NE}-V_T}^{\sqrt{NE}+V_T} \int_{\sqrt{E/N}\,|\alpha|-\eta_1}^{\infty} \frac{1}{2\pi\sigma_1\sigma_2} e^{-\eta_1^2/(2\sigma_1^2)-\eta_2^2/(1\sigma_2^2)}\, d\eta_2\, d\eta_1 \tag{6.165}$$

$$= \frac{1}{\sqrt{2\pi}\,\sigma_1} \int_{\sqrt{NE}-V_T}^{\sqrt{NE}+V_T} e^{-\eta_1^2/(2\sigma_1^2)}\, Q\left(\frac{\sqrt{E/N}\,|\alpha|-\eta_1}{\sigma_2}\right) d\eta_1\,, \tag{6.166}$$

where according to (6.114) and (6.115) $\sigma_1^2 = (N/2)(N_o/2)$ and $\sigma_2^2 = (N/2-1)(N_o/2)$. A change of variable according to $\eta_1 = \eta\sigma_1$ in (6.166) yields:

$$P_e(\alpha,0|\pm 1) = \frac{1}{\sqrt{2\pi}} \int_{2\sqrt{\gamma}(1-\upsilon)}^{2\sqrt{\gamma}(1+\upsilon)} e^{-\eta^2/2}\, Q\left(2\sqrt{\gamma}\frac{|\alpha|}{N(N-2)} - \sqrt{\frac{N}{N-2}}\,\eta\right) d\eta\,. \tag{6.167}$$

Then we can arrive at the average BEP $P_e(0|\pm 1)$ by averaging $P_e(\alpha, 0|\pm 1)$ of (6.167) using the PDF of α given in (6.133):

$$P_e(0|\pm 1) = \sum_{n=0}^{N-2} \Pr(\alpha = 2n)\cdot P_e(\alpha = 2n, 0|\pm 1) \tag{6.168}$$

$$= \frac{1}{\sqrt{2\pi}2^{N-2}} \sum_{n=0}^{N-2} \binom{N-2}{n} \int_{2\sqrt{\gamma}(1-\upsilon)}^{2\sqrt{\gamma}(1+\upsilon)} e^{-\eta^2/2} Q\left(4\sqrt{\gamma}\frac{n+1}{\sqrt{N(N-2)}} - \sqrt{\frac{N}{N-2}}\,\eta\right) d\eta\,. \tag{6.169}$$

From (6.163) and (6.169), the total average BEP $P_e(\pm 1)$ for the case of $\mathbf{b}_1[k] = \mathbf{b}_2[k]$ can be expressed as $P_e(\pm 1) = P_e(\mp 1|\pm 1) + P_e(0|\pm 1)$.

Using the above analysis, the BEP of the Type III detector for transmission over the AWGN channel, provided that one transform-domain symbol was obliterated can be summarised as:

$$P_{e,III} = \frac{1}{2} P_e(0) + \frac{1}{2} P_e(\pm 1) \tag{6.170}$$

$$= \frac{1}{2}\left\{P_e(\pm 1|0) + P_e(0|0) + P_e(\mp 1|\pm 1) + P_e(0|\pm 1)\right\}\,. \tag{6.171}$$

Substituting $P_e(\pm 1|0)$, $P_e(0|0)$, $P_e(\mp 1|\pm 1)$ and $P_e(0|\pm 1)$ given in (6.155), (6.162), (6.163) and (6.169), respectively, into (6.171), we have:

$$\begin{aligned} P_{e,III} =& \frac{1}{2}\mathrm{Q}(2\sqrt{\gamma}\upsilon) + \frac{1}{2}\mathrm{Q}(2\sqrt{\gamma}(1+\upsilon)) \\ &+ \frac{1}{\sqrt{2\pi}}\frac{1}{2^{N-1}} \sum_{n=0}^{N-2} \binom{N-2}{n} \int_{-2\sqrt{\gamma}\upsilon}^{2\sqrt{\gamma}\upsilon} e^{-\eta^2/2} Q\left(4\sqrt{\gamma}\frac{n}{\sqrt{N(N-2)}} - \sqrt{\frac{N}{N-2}}\,\eta\right) d\eta \\ &+ \frac{1}{\sqrt{2\pi}}\frac{1}{2^{N-1}} \sum_{n=0}^{N-2} \binom{N-2}{n} \int_{2\sqrt{\gamma}(1-\upsilon)}^{2\sqrt{\gamma}(1+\upsilon)} e^{-\eta^2/2} Q\left(4\sqrt{\gamma}\frac{n+1}{\sqrt{N(N-2)}} - \sqrt{\frac{N}{N-2}}\,\eta\right) d\eta\,. \end{aligned} \tag{6.172}$$

Figure 6.15 shows the bit error rate of the Type III detector for transmission over the AWGN channel,

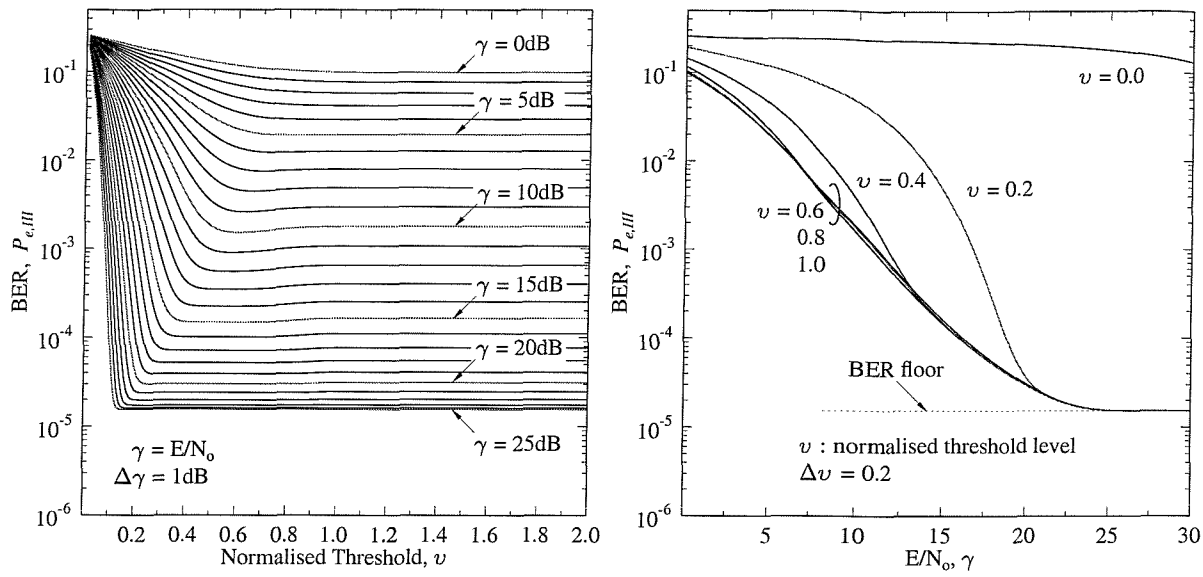

(a) BER vs υ

(b) BER vs γ

Figure 6.15: The bit error probability $P_{e,III}$ of the Type III SPD detector for transmission over the AWGN channel, when one transform-domain symbol was obliterated, for the spreading factor of $N = 16$. (a) Bit error rate versus the normalised threshold level υ. (b) Bit error rate versus the bit energy to noise power ratio $\gamma = E/N_o$. The BER floor is $1/2^N = 1.53 \times 10^{-5}$.

when one transform-domain symbol was obliterated, for the spreading factor of $N = 16$. Comparing Figure 6.15 and Figure 6.6, we can observe that the BER curves in Figure 6.15 become flat at relatively low values of υ and at high bit error rates due to the loss of one transform-domain symbol. The irreducible BER can also be observed in Figure 6.15(a) and Figure 6.15(b). The value of this BER floor is not obvious in (6.172). The first two terms certainly vanish, as γ becomes high. We have to consider the integration region depicted in Figure 6.14 in order to identify which terms approach zero. As the signal energy is increased, the integration region becomes smaller, moving away from the origin, except for the third term when $n = 0$, in which case the integration region covers half of the entire η_1-η_2 plane, as υ is increased. Hence, the BER floor becomes $1/2^N$ again. This analysis is corroborated by Figure 6.15 for the spreading factor of $N = 16$, where the BER approached $1/2^{16} = 1.523 \times 10^{-5}$. In the SNR range of about 10-15dB, the bit error rate is slightly increased as the normalised threshold levels becomes higher, widening the region '0'. This could not be observed in Figure 6.6 of Section 6.4.3. When no symbol was lost in the AWGN channel, the system always resulted in an improved BER when activating the second stage, because the second stage detector was the ideal detector. However, in the scenario we are considering the second stage detector processes the impaired detection variable, since the obliterated symbol is assumed to be in the second subblock. Thus, it is not always better to increase the normalised threshold level in this case. However, as seen in Figure 6.15(b), the BER differences are insignificant.

The Type III SPD detector uses $\mathbf{d}_2$, only when $\mathbf{d}_1$ falls in the region '0' of Figure 6.3(a). Hence, the

expression of the number of multiplications required for the Type III SPD detector is identical to that of the Type II detector, which was given in (6.153). However, N number of extra additions are required for computing the sum and the difference of $\mathbf{d}_1[k]$ and $\mathbf{d}_2[k]$ according to (6.18). The probability $P_{III}(0)$ of requiring the computation of $\mathbf{d}_2$ is identical to $P_{II}(0)$ given in (6.61). From the above argument, the number of additions required by the Type III detector can be expressed as:

$$N_{III}(+) = N_{\mathbf{d}_1}(+) + N_{\mathbf{d}_2}(+)P_{III}(0) + N\,P_{III}(0) \tag{6.173}$$

$$= \frac{N(N-2)}{4} + \frac{N^2}{4}P_{III}(0)\,, \tag{6.174}$$

where $N_{\mathbf{d}_1}(+)$ is the number of additions required for computing $\mathbf{d}_1$ given in (6.140) and $N_{\mathbf{d}_2}(+)$ is that for $\mathbf{d}_2$, which has to be evaluated with the probability of $P_{III}(0)$ given in (6.142).

6.5.7 Summary and Discussions

In Section 6.5 we have investigated a non-spreading BPSK detector, a full despreading based detector and three different types of SPD detectors in the AWGN channel, when one transform-domain symbol was obliterated. The bit error rate curves of the detectors were depicted in Figure 6.12(a). An uncoded OFDM system can be regarded as a non-spread BPSK system in our context. Non-spread systems have a high irreducible bit error rate of $0.5/N$ in the investigated channel scenario. We can conclude that non-spread systems cannot be used in this channel without powerful error correction mechanisms. All the investigated spreading assisted systems have the same BER floor of $1/2^N$, which is considerably lower, than that of the non-spread systems for spreading factor of $N \geq 4$. Amongst the three different types of SPD detectors the Type II detector exhibited a lower bit error rate, than that of the full-despreading aided detectors for bit energy to noise power ratios of $\gamma > 6.5$dB in conjunction with $N = 8$, for $\gamma > 9.0$dB along with $N = 16$ and for $\gamma > 12.0$dB in conjunction with $N = 32$. In Figure 6.12(a) we can observe that the maximum SNR advantage of the Type II SPD detector over a conventional full-despreading based detector is around 3dB, depending on the spreading factor N.

Figure 6.12(b) compares the implementational complexity of the investigated detectors in terms of the required number of operations normalised to that of the conventional full-despreading based detector for the spreading factor of $N = 16$. The Type I SPD detectors have about half the complexity of the conventional detector. The Type II and III SPD detectors require lower number of multiplications and additions, than the Type I detector. It is interesting to see that the Type II detectors exhibits a lower BER as well as a lower complexity in the SNR region spanning from 12dB to 30dB in comparison to those of the conventional full-despreading based detector.

Although we discussed the performance of our SPD detectors in the context of a AWGN channel contaminated by a narrow-band jamming, one of the transform domain symbol may be deliberately obliterated at the receiver. For example the transmitter may choose one transform domain symbol in order to reduce the crest factor studied in Chapter 4 rather than conveying message dependent information and then the transform domain symbol can be discarded at the receiver.

6.6 Summary and Conclusions

The family of novel SPD detectors was introduced utilising a Walsh spreading matrix in the context of fully loaded multi-code CDMA systems, where the number of simultaneous codes L is equal to the spreading factor N, in an effort to reduce the required number of computations. The associated bit error ratio and the complexity of the detectors was analysed when communicating over an AWGN channel in Section 6.4. Our simulation based BER results were also presented, in order to corroborate the results of the analyses. It was found in Section 6.4 that some of these detectors show a near ideal bit error rate performance in an AWGN channel, while requiring less than half the number of multiplications and additions, as it can be seen in Figure 6.7 and Figure 6.8. When the channel impairments are dominated by time-domain impulse noise [165, 166] or frequency-domain narrow band interference [167, 168], the Type II SPD detection scheme was found to perform better, than the conventional full-despreading based detector for the SNR range of 12dB to 30dB for the spreading factor of $N = 32$ in Section 6.5, while requiring less than 40% of the computational efforts of the conventional scheme, as it was evidenced by Figure 6.12(b).

Although we observed the potential of the proposed SPD schemes, when communicating over AWGN channels in terms of reducing the computational efforts in comparison to the conventional full-despreading based scheme, the performance of the SPD schemes over fading channels has to be investigated in the context of joint detection receivers, in order to confirm the feasibility of this technique in practical systems.

Chapter 7

Conclusions and Future Work

Since their initial introduction in 1993 [1, 2, 36, 37], multi-carrier spread-spectrum systems have attracted significant research interest. Existing advanced techniques originally developed for DS-CDMA and OFDM have also been applied to MC-CDMA, while a range of new unique techniques have been proposed for solving various problems specific to multi-carrier CDMA systems. The first three chapters of this thesis reviewed the basic concept of MC-CDMA, the various spreading sequences applicable to MC-CDMA and characterised the performance of MC-CDMA schemes employing various detectors. Then, three specific topics closely related to MC-CDMA were investigated in depth.

Specifically, the peak factor reduction techniques were presented in Chapter 4. While analysing the signal envelope of MC-CDMA in Section 4.5.1, it was found that the aperiodic correlations of the spreading sequences play an important role in determining the associated peak factor. By investigating several orthogonal sequences, in Section 4.5.2.2 it was shown that a set of orthogonal complementary sequences applied to MC-CDMA has the advantageous property of limiting the peak factor of the MC-CDMA signal to 2 or 3dB, when the number of simultaneously transmitting users is less than or equal to four, regardless of the spreading factor. When the MC-CDMA system was 'fully-loaded', *i.e.* supported the highest possible number of users, Walsh codes exhibited the lowest worst-case peak-factor as well as the lowest median peak-factor. The latter property was exploited in terms of limiting the peak factor of 'fully-loaded' MC-CDMA systems having a spreading factor of 15 to a maximum peak factor of 2.5, which is comparable to the peak factor of filtered single carrier signals. This was achieved by employing a peak-factor limiting block code, as was detailed in Section 4.5.2.3. However, our simulation study of MC-CDMA systems employing realistic power amplifier models revealed in Section 4.5.3 that Zadoff-Chu spreading based MC-CDMA outperforms Walsh spreading based MC-CDMA, when transmitting over a Rayleigh fading channel. Investigating this unexpected result further, it was found that Zadoff-Chu spreading based MC-CDMA better exploits the frequency diversity in comparison to Walsh spreading assisted MC-CDMA, since the combined symbol after Zadoff-Chu spreading over each sub-carrier is less likely to have a low value compared to Walsh spread and combined symbols. This suggests that the effects of the frequency-domain peak-factor, in other words the dynamic range of the frequency domain symbols on the achievable diversity gain has to be further investigated. A preliminary idea related to this

idea was presented in Section 4.6.1.

Chapter 5 was devoted to adaptive modulation techniques. After the introduction of a general model of various adaptive modulation schemes in Section 5.3.1, the existing techniques proposed for determining the transceiver mode-switching levels were reviewed in Section 5.4.1, 5.4.2 and 5.4.3, since the performance of adaptive schemes is predetermined by the switching levels employed as well as by the average SNR per symbol. In search of the globally optimum switching levels, the Lagrangian optimisation technique was invoked in Section 5.4.4 and the relationship amongst the different mode-switching levels was found to be independent of the underlying channel scenarios such the Multi Path Intensity (MIP) profile or the fading magnitude distribution. Having established the technique of determining the optimum switching levels, a comprehensive set of performance results was presented for adaptive PSK schemes, adaptive Star QAM schemes as well as for adaptive Square QAM schemes, when they were communicating over a flat Nakagami m fading channel. Since adaptive Square QAM exhibited the highest BPS throughput among the three adaptive schemes investigated, the performance of adaptive Square QAM schemes was further studied, employing two-dimensional Rake receivers in Section 5.5.2 and applying concatenated space-time coding in conjunction with turbo convolutional coding in Section 5.5.5. As expected, in Section 5.5.1, 5.5.2 and 5.5.5, it was found that the SNR gain of the adaptive schemes over fixed-mode schemes decreased, as the fading became less severe. Hence, the adaptive schemes exhibited only a modest performance gain, when (a) the Nakagami fading parameter m was higher than four, (b) the number of diversity antennas was higher than four when MRC diversity combining was used over independent Rayleigh fading channels, or (c) the total number of transmit antennas plus receive antennas was higher than four when space-time coding was used. Specifically, in Section 5.5.5 it was found that ST block coding reduces the relative performance advantage of adaptive modulation as summarised in Figure 5.49(b), since it increases the diversity order and eventually reduces the channel quality variations. When the adaptive modulation schemes were operating over wide-band channels, their SNR gain eroded even in conjunction with a low number of antennas, since the fading depth of wideband channels is typically less deep, than that of narrow-band channels. For transmission over correlated fading channels it is expected that the SNR gain of adaptive schemes over their fixed-mode counterparts erodes less, as the number of antenna increased. However, further investigations are required for quantifying the effects of correlated fading. Even though some channel-coding based results were presented in Section 5.5.5, the investigation of coded adaptive modulation schemes is far from complete. Since our AQAM mode switching levels were optimised for uncoded systems, the performance results presented for the coded adaptive schemes are not optimum. The technique similar to that developed in Section 5.4.4 may be applied, provided that a closed-form mode-specific average BER expression becomes available for channel coded fixed modulation schemes. In addition, the 'spread of BER' has to be quantified by some measure, such as its PDF. This concept arises, since the quality of service experienced by a user may differ for fixed-mode schemes and for adaptive modulation schemes, even if their average BERs are identical. The variance or in other words fluctuation of the instantaneous BER distribution may serve as a useful quality measure. The PDF of this instantaneous BER may be obtained by applying the Jacobian transformation [163] to the PDF of the instantaneous SNR per symbol. It is expected that there may be a

direct relationship between this measure of 'spread of BER' and the required interleaver length of the channel codec associated. More explicitly, it is expected that the distribution of the bit errors becomes less bursty in conjunction with AQAM schemes, since they are capable of near-instantaneously involving a more robust but reduced-throughput AQAM mode, when the channel quality degrades. Hence AQAM schemes may require shorter channel interleavers for randomising the position of channel errors.

In Chapter 6, a Successive Partial Detection (SPD) scheme was introduced. We analysed the BEP performance and the implementational complexity of three proposed SPD detectors, when communicating over the AWGN contaminated by an impulse noise in the time domain or a narrow band interference / a tone jamming signal in the frequency domain, assuming that one transform-domain symbol was obliterated due to a severe corruption. We found that the Type II SPD detector exhibits a lower BEP and requires a lower complexity than those of the conventional full-despreading based detector. This work has to be expanded for transmission over wideband channels. The application of the SPD scheme in the context of a joint-detector is also an interesting future research issue, since it will reduce the complexity of the joint detector.

The thesis concentrated on investigating the MC-CDMA [1, 2, 35] scheme, which is one of the family of three different multi-carrier CDMA techniques [42]. This technique was advocated, because MC-CDMA results in the lowest BER among the three schemes investigated in a similar scenario [42]. Our investigations concentrated on the downlink, because in the uplink stringent synchronisation of the mobile terminals has to be met. Future research should extend the results of Chapter 4 and 5 to both multi-carrier DS-CDMA [36] and to multi-tone (MT) CDMA [37], as well as to the family of more sophisticated adaptive MC-CDMA schemes [169].

Summary and Contributions

The main contributions of this thesis are in three specific topics closely related to Multi-Carrier Code Division Multiple Access (MC-CDMA), which are summarised in this section.

Crest Factor of Multi-Code MC-CDMA Signal

One of the main drawbacks of Orthogonal Frequency Division Multiplexing (OFDM) [13] is that the envelope power of the transmitted signal fluctuates widely, requiring a highly linear RF power amplifier. Finding a solution to this problem has stimulated intensive research. The accrueing advances were critically reviewed in Sections 4.3 and 4.4. Since MC-CDMA [1, 2] schemes spread a message symbol across the frequency domain and employ an OFDM transmitter for conveying each spread bit, their transmitted signal also exhibits a high crest factor (CF), which is defined as the ratio of the peak amplitude of the modulated time-domain signal to its root mean square (RMS) value. Hence, the characteristics of the crest factor of the MC-CDMA signal were studied in Section 4.5, with a view to reduce the associated power envelope variations.

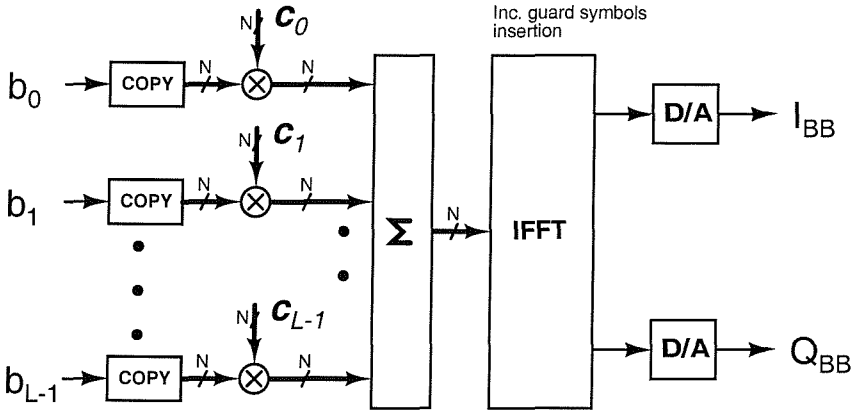

Figure 1: MC-CDMA transmitter model: b_l and $\mathbf{C}_l$ are the l-th message symbol and spreading sequence, respectively.

The simplified transmitter structure of a multi-code MC-CDMA system is portrayed in Figure 1, where L M-ary Phase Shift Keying (MPSK) modulated symbols $\{b_l \mid 0 \leq l < L\}$ are transmitted simultaneously using L orthogonal spreading sequences $\{\mathbf{C}_l \mid 0 \leq l < L\}$. Each of the spreading

sequences is constituted by N chips according to $\mathbf{C}_l = \{c_l[n] \mid 0 \leq n < N\}$, where the complex spreading sequence c_l has a unit magnitude of $|c_l[n]| = 1$. Then, the normalised complex envelope $s(t)$ of an MPSK modulated multi-code MC-CDMA signal is represented for the duration of a symbol period T as:

$$s(t) = \frac{1}{\sqrt{N}} \sum_{l=0}^{L-1} \sum_{n=0}^{N-1} b_l \, c_l[n] \, e^{j2\pi F n \frac{t}{T}} \, .$$

The power envelope $|s(t)|^2$ of this MPSK modulated multi-code MC-CDMA signal was analysed in Section 4.5.1 and it was expressed as [43]:

$$|s(t)|^2 = \frac{2}{N} \mathrm{Re} \left[\sum_{n=0}^{N-1} (A[n] + X[n]) \, e^{j2\pi n \frac{t}{T}} \right] ,$$

where $A[n]$ is the collective aperiodic autocorrelation of the spreading sequences $\{\mathbf{C}_l\}$ defined in the context of Equation (4.38), while $X[n]$ is the collective aperiodic crosscorrelation defined in (4.39).

Having observed that the power envelope of the MPSK modulated multi-code MC-CDMA signal is completely characterised by the collective autocorrelations and crosscorrelations of the spreading sequence employed, a set of various spreading sequences was investigated in quest of the sequences yielding low CF or Peak Factor (PF), where the PF was defined as the square of the CF, namely PF $\triangleq$ CF^2. **It was shown by Theorem 4.5 in Section 4.5.2.2 that a specific version of Sivaswamy's complementary set [105] results in a low CF, bounded by 3dB, in the context of BPSK modulated four-code MC-CDMA systems, regardless of the spreading factor employed, as seen in Figure 2.**

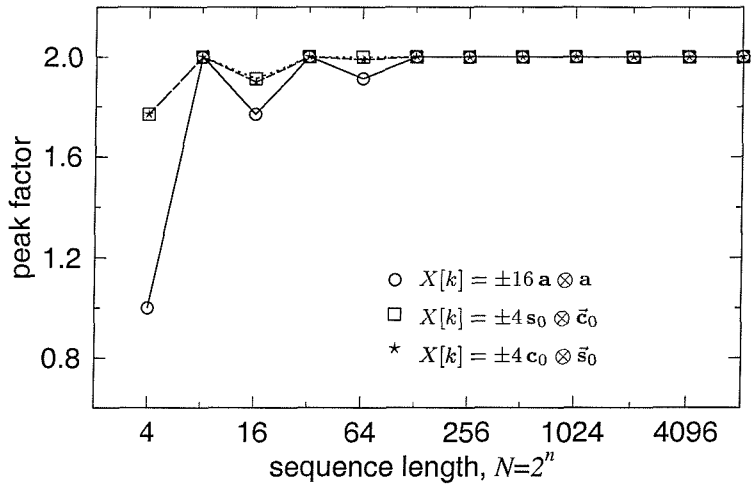

Figure 2: The peak-factors of Sivaswamy's complementary set of sequences. The number of simultaneously used sequences is $L = 4$ and the sequence length of $N = 2^n$ is between $2^2 = 4$ and $2^{13} = 8192$.

Since a similar family of spreading sequences yielding such a low CF could not be found for code sets having more than four codes, *i.e.* for $L > 4$, in Section 4.5.2.3 a crest factor reduction coding scheme [31] was applied instead. We found in Section 4.5.2.3 that the peak factors of BPSK modulated

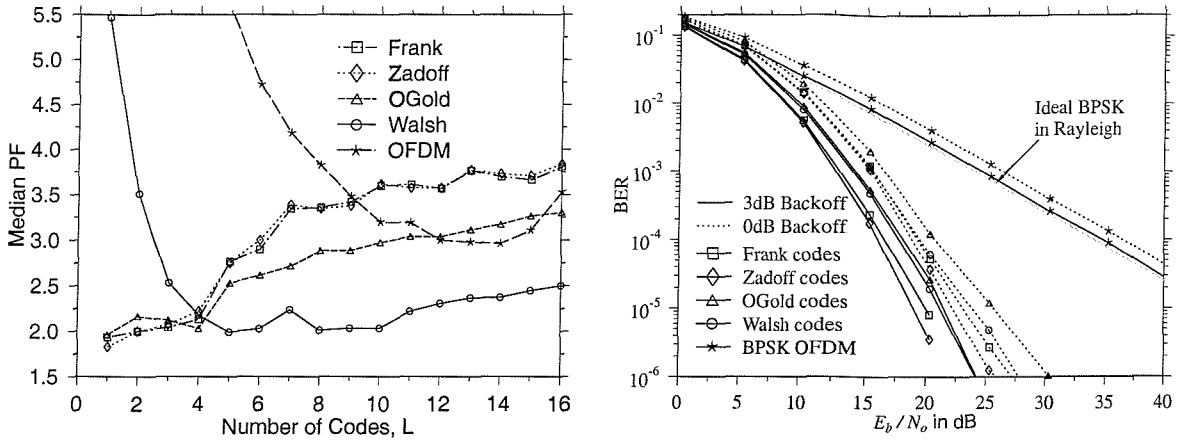

(a) Median Peak Factor

(b) BER performance

Figure 3: Effects of the $(L-1)/L$-rate crest factor reduction coding for the spreading factor of $N = 16$. (a) The worst-case peak factor when using various spreading codes for BPSK modulated MC-CDMA. (b) BER versus E_b/N_o performance of BPSK modulated MMSE-JD MC-CDMA and that of BPSK modulated OFDM, when transmitting over independent Rayleigh channels for each subcarriers.

MC-CDMA employing an appropriate family of spreading codes could be reduced below 2.5, when using the crest factor reduction code proposed in [43], as seen in Figure 3(a). In order to investigate the effects of the modulated signal peak clipping by the non-linear power amplifier, the Bit Error Ratio (BER) performance was studied in Section 4.5.3.3. It was expected that the Walsh spreading based scheme would result in the lowest BER, since it resulted in the lowest worst-case peak factor for 'fully-loaded $(L = N)$' BPSK modulated MC-CDMA employing a Minimum Mean Square Error (MMSE) Block-Decision Feedback Equaliser (BDFE) based Joint Detector (JD) [59], when experiencing independent Rayleigh fading for each subcarriers. However, the Zadoff-Chu based scheme performed better than Walsh based scheme [43]. We found that the Zadoff-Chu spreading based MC-CDMA scheme inflicted less Multiple User Interference (MUI), than the Walsh-spreading based scheme and it utilised the available diversity more efficiently, than the Walsh-spreading based scheme.

Adaptive Modulation

The second field, where novel contributions were made, was in realms of adaptive modulation schemes. Adaptive modulation [13, 111, 113, 114] attempts to provide the highest possible throughput given the current near-instantaneous channel quality, while maintaining the required data transmission integrity. We analysed in Section 5.3.3.1 the performance of adaptive modulation schemes and derived a closed form expression for the average BER and for the average Bits Per Symbol (BPS) throughput [45]. Since the modulation mode switching levels predetermine the average BER as well as the average BPS, it is important to optimise these switching levels for achieving the maximum possible average through-

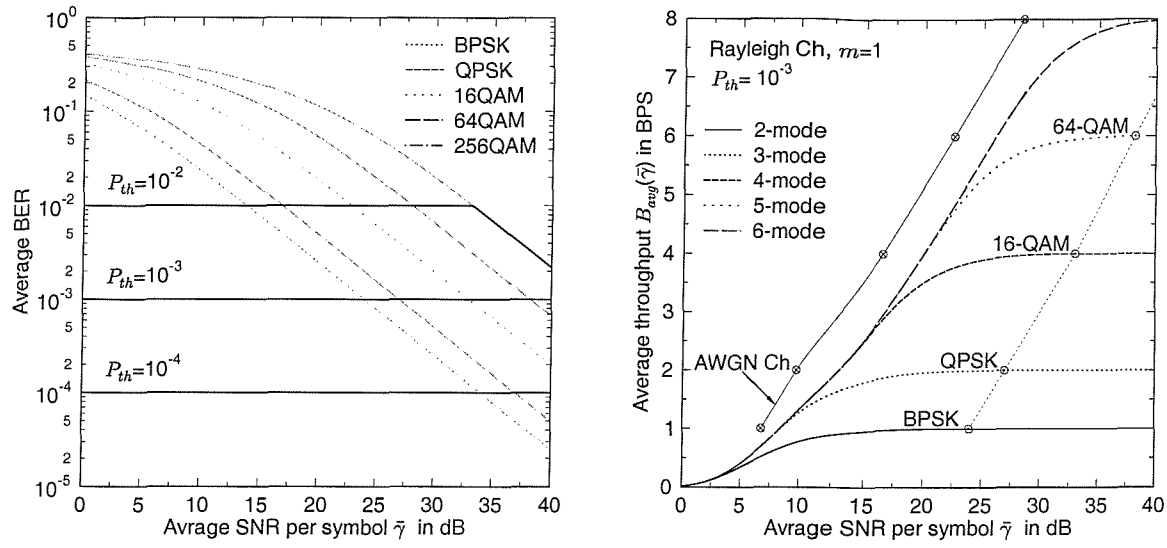

(a) Average BER

(b) Throughput at the BER of $P_{th} = 10^{-2}$

Figure 4: The average BER and average throughput performance of a six-mode adaptive Square QAM scheme for communicating over a flat Rayleigh channel ($m = 1$). (a) The constant target average BER is maintained over the entire range of the average SNR values up the avalanche SNR. (b) The markers '⊗' and '⊙' represent the required SNR of the corresponding fixed-mode Square QAM schemes achieving the same target BER as the adaptive schemes, operating over an AWGN channel and a Rayleigh channel, respectively.

put. Having reviewed the existing techniques of determining the switching levels [113, 132], a per-SNR optimisation technique was proposed in [44], which was based on Powell's multi-dimensional optimisation [58], yielding a constant target BER and the maximum BPS throughput. Since this optimisation procedure was often trapped in local optima, rather than reaching the global optimum, the Lagrangian-based optimisation technique was developed [48] and was subsequently used in Section 5.5 in order to investigate the performance of adaptive modulation schemes employing various modulation modes, namely PSK, Star QAM and Square QAM phasor constellations.

Since our modulation mode switching levels were optimised in order to achieve the highest throughput, while maintaining the target BER, the average BER of our six-mode AQAM scheme remained constant over the entire range of the average SNR values up the avalanche SNR, beyond which it followed the BER of the highest throughput mode, namely that of 256-QAM, as seen in Figure 4(a). On the other hand, the BPS throughput increased steadily, as the average SNR increased, as seen in Figure 4(b). Our optimised AQAM operating over a Rayleigh fading channel required 4dB more SNR, in comparison to fixed-mode QAM operating over an AWGN channel.

Since in Section 5.5.2 receiver antenna diversity has been used for combating the effects of fading, we investigated the performance of Maximal Ratio Combining (MRC) antenna diversity assisted AQAM schemes [45]. As it is seen in Figure 5, the average SNRs required for achieving the target BEP of

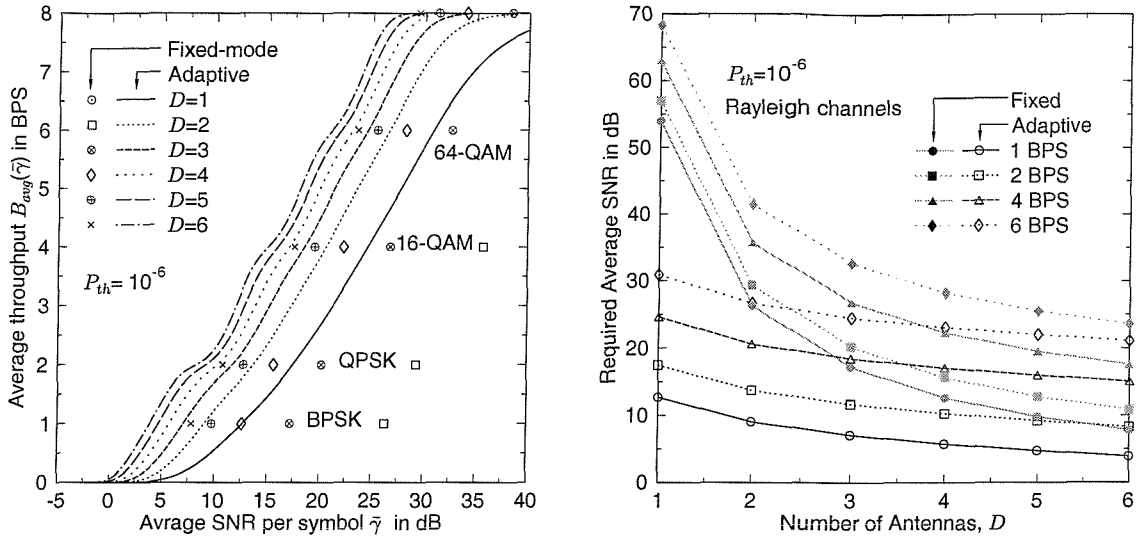

(a) BPS throughput

(b) The SNR required versus the number of antenna D

Figure 5: The performance of the MRC-aided antenna-diversity assisted AQAM scheme operating over independent Rayleigh fading channels at the target average BEP of $P_{th} = 10^{-6}$. (a) The markers represent the corresponding fixed-mode QAM performance. (b) The required SNR achieving the various throughput for the AQAM and fixed-mode QAM schemes.

$P_{th} = 10^{-6}$ for the fixed-mode schemes and that for the adaptive schemes decrease, as the antenna diversity order increases. However, the differences between the required SNRs of the adaptive schemes and their fixed-mode counterparts also decrease, as the antenna diversity order increases.

In Section 5.5.5, the performance of Space-Time (ST) block coded constant-power adaptive multi-carrier modems employing optimum SNR-dependent modem mode switching levels were investigated [46, 47]. As expected, it was found that ST block coding reduces the relative performance advantage of adaptive modulation, since it increases the diversity order and eventually reduces the channel quality variations, as it can be observed in Figure 6(a). **Having observed that 1-Tx aided AOFDM and 2-Tx ST coding aided fixed-mode MC-CDMA resulted in a similar BPS throughput performance, we concluded that fixed-mode MC-CDMA in conjunction with 2-Tx ST coding could be employed, provided that we could afford the associated complexity. By contrast, AOFDM could be a low complexity alternative of counteracting the near-instantaneous channel quality variations.** When turbo convolutional coding was concatenated to the ST block codes, near-error-free transmission was achieved at the expense of halving the average throughput, as seen in Figure 6(b) . Compared to the uncoded system, the turbo coded system was capable of achieving a higher throughput in the low SNR region at the cost of a higher complexity. Our study of the relationship between the uncoded BER and the corresponding coded BER showed that adaptive modems obtain higher coding gains, than that of fixed modems. This was due to the fact that the adaptive modem avoids burst errors even in deep channel fades by reducing the number of bits per modulated symbol eventually to zero.

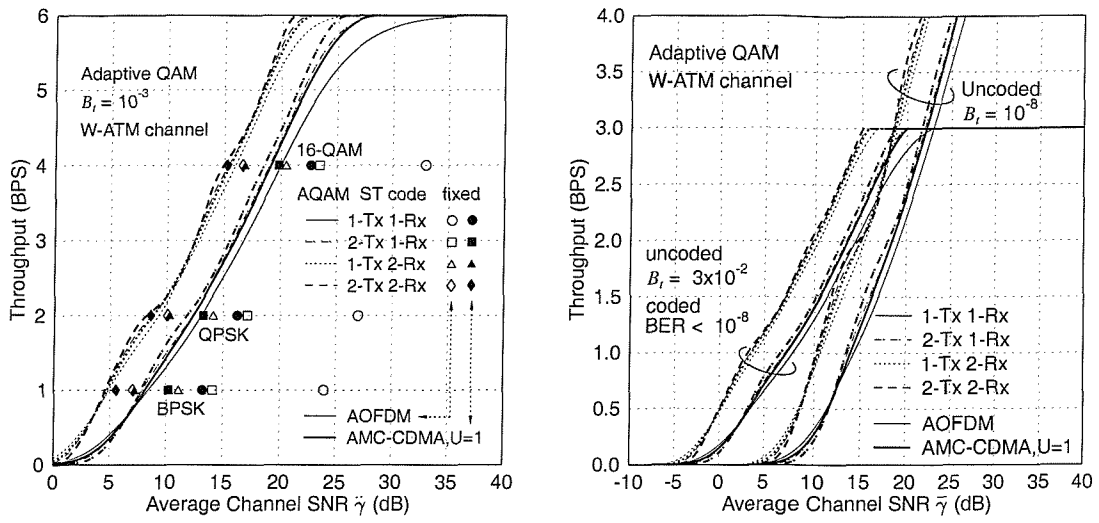

(a) With ST coding

(b) With ST and turbo coding

Figure 6: The BPS throughput performance of five-mode AOFDM and AMC-CDMA for communicating over the W-ATM channel [13, pp.474]. (a) The SNR gain of the adaptive modems decreases, as the diversity of the ST coding increases. The BPS curves appear in pairs, corresponding to AOFDM and AMC-CDMA - indicated by the thin and thick lines, respectively - for each of the four different ST code configurations. The markers represent the SNRs required by the fixed-mode OFDM and MC-CDMA schemes for maintaining the target BER of 10^{-3} in conjunction with the four ST-coded schemes considered. (b) The turbo convolutional coding assisted adaptive modems have SNR gains up to 7dB compared to their uncoded counterparts achieving a comparable average BER.

Successive Partial Despreading

In Chapter 6, a Successive Partial Detection (SPD) scheme was introduced in an effort to reduce the computational efforts involved in despreading in the context of a 'fully loaded' CDMA downlink scenario. We analysed the bit error rate performance and the implementational complexity of three different types of SPD detectors, when communicating over the AWGN channel, contaminated by time-domain impulse noise or frequency-domain tone-jamming. It was found that the Type II SPD scheme resulted in a lower BER, than the conventional despreading scheme in the SNR range of $\gamma > 13dB$, while requiring significantly reduced computational efforts, namely less than 40% in comparison to the conventional scheme, when quantified in terms of the required number of multiplications and additions, as it can be observed in Figure 7.

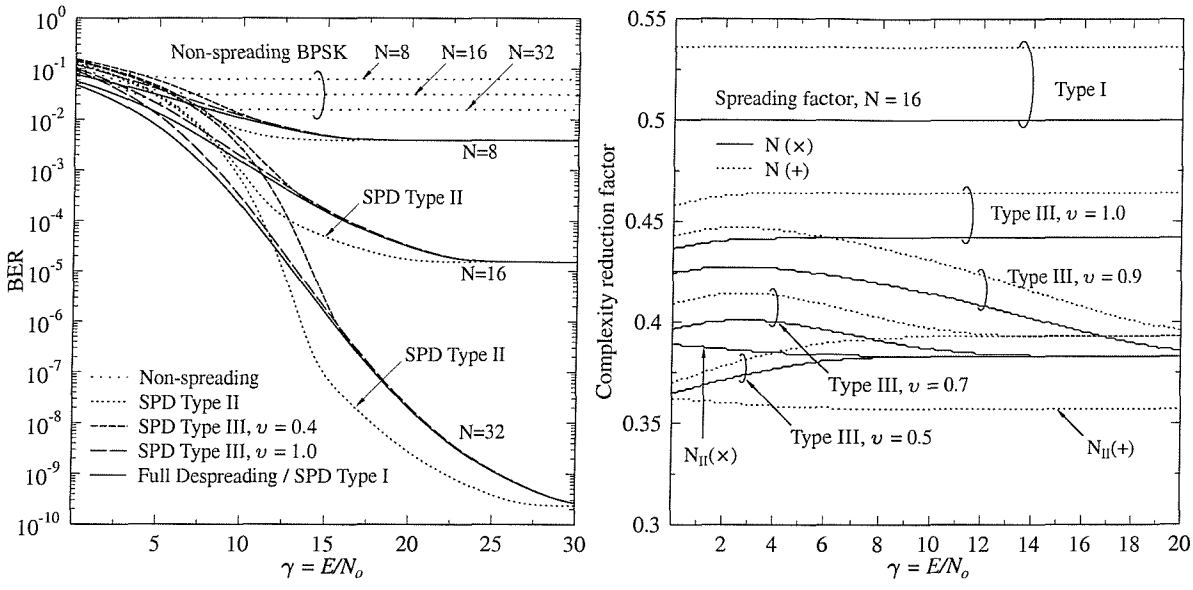

(a) BER (b) Complexity

Figure 7: The bit error rates and complexities of the various SPD detectors and the conventional despreading scheme, where N is the spreading factor. (a) The non-spread BPSK scheme has a high irreducible BER of $0.5/N$, while the spread systems have a significantly lower error floor of $1/2^N$. The Type II SPD Detector shows a superior performance in the high SNR region in comparison to the other schemes. (b) The complexity of three types of SPD detectors quantified in terms of the required number of multiplications and additions, normalised to those of the conventional full-despreading based detector associated with the spreading factor of $N = 16$. The Type II SPD detector requires less than 40% of the operations necessitated by the conventional scheme.

Appendix A

Peak-to-mean Envelope Power Ratio of OFDM Systems

A.1 PMEPR Analysis of BPSK Modulated OFDM

The normalized complex envelope of the BPSK modulated OFDM signal, $s(t)$, is given by

$$s(t) = \frac{1}{\sqrt{N}} \sum_{k=0}^{N-1} c_k \, e^{j2\pi \frac{kt}{T}} , \tag{A.1}$$

where N is the number of carriers, $c_k \in \{-1, +1\}$ is the frequency domain information symbol mapped to the kth subcarrier of the OFDM symbol and T is the OFDM symbol duration. The peak-to-mean envelope power ratio (*PMEPR*) of the given frequency domain samples, $c = \{c_0, c_1, \cdots, c_{N-1}\}$ is defined as

$$PMEPR \triangleq \max_{0 \le t \le T} \frac{|s(t)|^2}{\mathrm{E}\left[\, |s(t)|^2 \right]} , \tag{A.2}$$

where $\mathrm{E}\left[\,\cdot\,\right]$ denotes a time averaging operator.

Using the same technique as described in [68] and assuming $T = 1.0$, $N|s(t)|^2$ can be represented

as:

$$\begin{aligned}
N|s(t)|^2 &= \left(\sum_{k=0}^{N-1} c_k\, e^{j2\pi\frac{kt}{T}}\right)^2 \\
&= \left(\Re\left[\sum_{k=0}^{N-1} c_k\, e^{j2\pi\frac{kt}{T}}\right]\right)^2 + \left(\Im\left[\sum_{k=0}^{N-1} c_k\, e^{j2\pi\frac{kt}{T}}\right]\right)^2 \\
&= \left(\sum_{k=0}^{N-1} c_k \cos(2\pi kt)\right)^2 + \left(\sum_{k=0}^{N-1} c_k \sin(2\pi kt)\right)^2 \\
&= \sum_{k=0}^{N-1} c_k^2 \cos^2(2\pi kt) + 2\sum_{k=0}^{N-2}\sum_{i=k+1}^{N-1} c_k c_i \cos(2\pi kt)\cos(2\pi it) \\
&\quad + \sum_{k=0}^{N-1} c_k^2 \sin^2(2\pi kt) + 2\sum_{k=0}^{N-2}\sum_{i=k+1}^{N-1} c_k c_i \sin(2\pi kt)\sin(2\pi it) \\
&= N + 2\sum_{k=0}^{N-2}\sum_{i=k+1}^{N-1} c_k c_i \cos(2\pi(i-k)t) \\
&= N + 2P_o(t)\,, \qquad \text{(A.3)}
\end{aligned}$$

where $\Re[x]$ and $\Im[x]$ are the real part and the imaginary part of x respectively, and the AC component of the power envelope of the OFDM signal $P_o(t)$ is defined as:

$$P_o(t) = \sum_{k=0}^{N-2}\sum_{i=k+1}^{N-1} c_k c_i \cos(2\pi(i-k)t). \qquad \text{(A.4)}$$

The double summations in Equation A.4 can be replaced with a single summation by combining each term according to its harmonic and $P_o(t)$ becomes

$$P_o(t) = \sum_{k=1}^{N-1} C_k \cos(2\pi kt), \qquad \text{(A.5)}$$

which can be physically interpreted as the sum of cosine harmonics weighted by the aperiodic autocorrelation C_k of the frequency domain information bits, where the aperiodic autocorrelation C_k is defined as

$$C_k = \sum_{i=0}^{N-k-1} c_i c_{i+k}. \qquad \text{(A.6)}$$

Upon using (A.3) and (A.5) the average power of $s(t)$ becomes:

$$\begin{aligned}
\mathrm{E}\left[\,|s(t)|^2\right] &= \mathrm{E}\left[\,1 + \frac{2P_o(t)}{N}\,\right] \\
&= 1 + \frac{1}{N}\mathrm{E}\left[\,2P_o(t)\,\right] \\
&= 1\,. \qquad \text{(A.7)}
\end{aligned}$$

As the average power of $s(t)$ is unity, the *PMEPR* in (A.2), when considering its symmetry with respect to the half symbol time, becomes:

$$PMEPR = \max_{0 \le t \le 0.5} (1 + \frac{2}{N} P_o(t)) , \tag{A.8}$$

where $P_o(t)$ is given in (A.5).

A.2 PMEPR Properties of BPSK Modulated OFDM

It is readily seen from (A.5), (A.6) and (A.8) that the *PMEPR* is completely characterized by the aperiodic autocorrelations, C_k. For the case of $N = 4$ the aperiodic autocorrelation C_k are given by:

$$\begin{aligned} C_1 &= c_0 c_1 + c_1 c_2 + c_2 c_3 \\ C_2 &= c_0 c_2 + c_1 c_3 \\ C_3 &= c_0 c_3 . \end{aligned}$$

Table A.1 presents the values of C_k and the *PMEPR* values for BPSK modulated OFDM in conjunction with $N = 4$. There are six different sets of aperiodic autocorrelation $\{C_k\}$ and three different *PMEPR*

$(Code)_2$	$(Code)_{10}$	C_1	C_2	C_3	*PMEPR*
0000	0	3.0	2.0	1.0	4.00
0001	1	1.0	0.0	-1.0	1.77
0010	2	-1.0	0.0	1.0	1.77
0011	3	1.0	-2.0	-1.0	2.37
0100	4	-1.0	0.0	1.0	1.77
0101	5	-3.0	2.0	-1.0	4.00
0110	6	-1.0	-2.0	1.0	2.37
0111	7	1.0	0.0	-1.0	1.77
1000	8	1.0	0.0	-1.0	1.77
1001	9	-1.0	-2.0	1.0	2.37
1010	10	-3.0	2.0	-1.0	4.00
1011	11	-1.0	0.0	1.0	1.77
1100	12	1.0	-2.0	-1.0	2.37
1101	13	-1.0	0.0	1.0	1.77
1110	14	1.0	0.0	-1.0	1.77
1111	15	3.0	2.0	1.0	4.00

Table A.1: PMEPR values and aperiodic autocorrelations, C_k, of all the 16 different symbols in a 4-carrier BPSK modulated OFDM system

values, namely 1.77, 2.37 and 4.00 in Table A.1. The message symbols can be grouped according to their

PMEPR values. Figure A.1 shows the waveforms of these three groups. Half of the message symbols[1] yield the lowest *PMEPR* of 1.77 . The corresponding sets of C_k values in Table A.1 are $(1, 0, -1)$ and $(-1, 0, 1)$. The power envelope waveforms are shown in the top sub-figure of Figure A.1. One the waveforms is a $0.5T$-shifted version of the other one corresponding to the same *PMEPR*. This is also true for all other envelope power waveforms of different *PMEPR* values, as seen in Figure A.1. This observation can be stated more generally for BPSK modulated OFDM signals, where $P_o(t)$ defined in (A.4) can be represented as:

$$P_o(t) = \Re\left[\sum_{k=1}^{N-1} C_k e^{j2\pi kt}\right] . \tag{A.9}$$

Then, the half symbol-duration time shifted version of $P_o(t)$ by half a symbol time, namely $P'_o(t)$, becomes:

$$\begin{aligned} P'_o(t) &= P_o(t+1/2) \\ &= \Re\left[\sum_{k=1}^{N-1} C_k e^{j2\pi k(t+1/2)}\right] \\ &= \Re\left[\sum_{k=1}^{N-1} C_k e^{j2\pi kt} e^{jk\pi}\right] \\ &= \Re\left[\sum_{k=1}^{N-1} (-1)^k C_k e^{j2\pi kt}\right] \\ &= \Re\left[\sum_{k=1}^{N-1} C'_k e^{j2\pi kt}\right] , \end{aligned} \tag{A.10}$$

where C'_k represents to the aperiodic autocorrelation values obtained from C_k by changing the sign of every C_k for odd k indices. This can be verified for the 4-carrier case using the C_k values and *PMEPR* values in Table A.1 together with Figure A.1 .

It is clear that the *PMEPR* is invariant to the message symbol changes, as long as either $\{C_k\}$ does not change or $\{C_k\}$ becomes $\{(-1)^k C_k\}$. This leads to several transformations[2] that can be applied to $\{c_k\}$, which result in the same *PMEPR*, *i.e.* are invariant in terms of the *PMEPR*. We note that a message symbol set, $\{c_k\}$, can be represented in a polynomial form, defined as:

$$c(z) \triangleq \sum_{k=0}^{N-1} c_k z^k . \tag{A.11}$$

Theorem A.1 *The following three transforms of* $c(z)$ *result in the same* PMEPR*s:*

[1] These sequences are known as Barker sequences [85].

[2] Having completed these derivations, the author found retrospectively that in 1961 Marcel J. E. Golay mentioned these transforms, while he was investigating the properties of complementarty codes in [77]

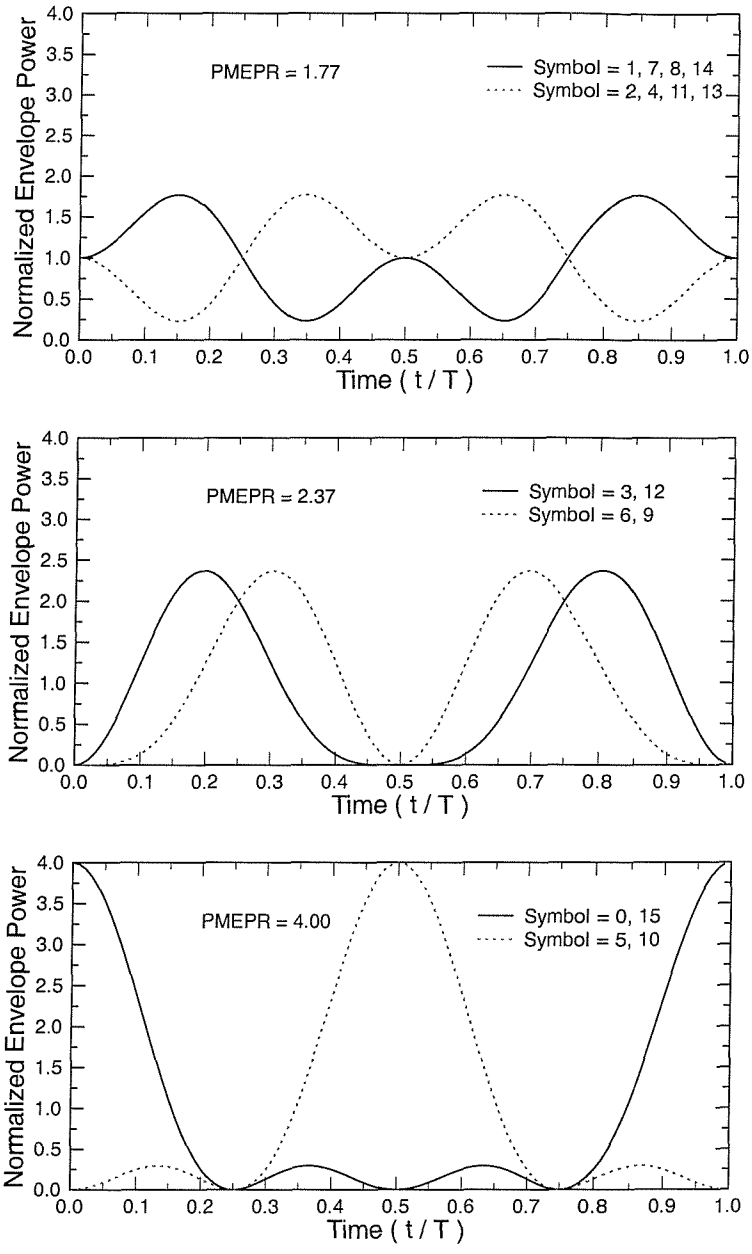

Figure A.1: Normalized envelope power waveforms, $|s(t)|^2$, of 4-carrier BPSK modulated OFDM signals for various frequency domain bits symbol $\{c_k\}$. The frequency domain symbols $\{c_k\}$ are represented using a decimal notation of the bits, for example Symbol $= 7$ in the top sub-figure represents $\{0111\}$ and Symbol $= 14$ $\{1110\}$.

- $T_1[c(z)] = -c(z)$
- $T_2[c(z)] = z^{N-1}c(z^{-1})$
- $T_3[c(z)] = c(-z)$

Proof: It will be shown that $T_1[\bullet]$ and $T_2[\bullet]$ do not change the corresponding aperiodic autocorrelation C_k, while $T_3[\bullet]$ changes the corresponding C_k values to $(-1)^k C_k$. These are sufficient conditions for attaining the same *PMEPR*. The transform $T_1[\bullet]$ replaces each c_i by $c'_i = -c_i$, which corresponds to an exclusive-or operation in terms of their binary representation. Let C'_k represent the new aperiodic autocorrelations after the transform. Using the definition in Equation A.6, C'_k becomes:

$$\begin{aligned} C'_k &= \sum_{i=0}^{N-k-1} c'_i c'_{i+k} \\ &= \sum_{i=0}^{N-k-1} (-c_i)(-c_{i+k}) \\ &= \sum_{i=0}^{N-k-1} c_i c_{i+k} \\ &= C_k \, . \end{aligned}$$

This shows that the application of T_1 does not change C_k.

Applying $T_2[\bullet]$ to $c(z)$ yields

$$\begin{aligned} c'(z) &= T_2[c(z)] \\ &= z^{N-1}c(z^{-1}) \\ &= \sum_{k=0}^{N-1} c_k z^{-k} z^{N-1} \\ &= \sum_{k=0}^{N-1} c_k z^{N-k-1}. \end{aligned}$$

By substituting $N-k-1$ with i, $c'(z)$ becomes

$$\begin{aligned} c'(z) &= \sum_{i=N-1}^{0} c_{N-1-i} z^i \\ &= \sum_{i=0}^{N-1} c_{N-1-i} z^i \, , \end{aligned}$$

which corresponds to the reverse ordering of the bits in the OFDM symbol or to a substitution of c_k with $c'_k = c_{N-1-k}$. Then, using (A.6), C'_k becomes:

$$\begin{aligned} C'_k &= \sum_{i=0}^{N-k-1} c'_i c'_{i+k} \\ &= \sum_{i=0}^{N-k-1} c_{N-1-i} c_{N-1-i-k} \, . \end{aligned}$$

By substituting $N-1-i-k$ as j, C'_k becomes:

$$\begin{aligned} C'_k &= \sum_{j=N-1-k}^{0} c_{j+k}c_j \\ &= \sum_{j=0}^{N-k-1} c_j c_{j+k} \\ &= C_k \, . \end{aligned}$$

Hence the transform T_2 preserves the original C_k.

The result of $T_3\,[c(z)]$, namely $c'(z)$, becomes:

$$\begin{aligned} c'(z) &= \sum_{k=0}^{N-1} c_k(-z)^k \\ &= \sum_{k=0}^{N-1} (-1)^k c_k z^k \, . \end{aligned}$$

This is equivalent to substituting c_k with $c'_k = (-1)^k c_k$. The corresponding aperiodic autocorrelation becomes:

$$\begin{aligned} C'_k &= \sum_{i=0}^{N-k-1} c'_i c'_{i+k} \\ &= \sum_{i=0}^{N-k-1} (-1)^i c_i (-1)^{i+k} c_{i+k} \\ &= \sum_{i=0}^{N-k-1} (-1)^{2i+k} c_i c_{i+k} \\ &= \sum_{i=0}^{N-k-1} (-1)^k c_i c_{i+k} \\ &= (-1)^k C_k \, . \end{aligned}$$

This shows that the application of T_3 results in a circular time shift of the envelope power waveform without changing the maximum value of the waveform. This concludes the proof of Theorem A.1. ¶

By applying the combinations of T_1, T_2 and T_3, we can get eight OFDM message symbols which give the same *PMEPR*. An example of 4-carrier BPSK modulated OFDM is shown in Table A.2. The eight codes in the table are *equivalent* in terms of their *PMEPR*. A closer look at the combinations of T_1, T_2 and T_3 reveals that there are at least four different codes having the same *PMEPR*. The following theorem states this fact in a formal manner.

Theorem A.2 *In BPSK modulated OFDM systems at least four message symbols are equivalent in terms of their PMEPR.*

T	I	T_1	T_2	T_1T_2	T_3	T_3T_1	T_3T_2	$T_3T_2T_1$
$(Code)_2$	0001	1110	1000	0111	0100	1011	0010	1101

Table A.2: The eight message symbols, which yield the same *PMEPR* value of 1.77 in a 4-carrier BPSK modulated OFDM system (T_n is defined in Theorem A.1 and I represents the identical transformation.)

Proof: The sufficient and necessary condition for two message symbols, m_1 and m_2, to be identical is that the corresponding polynomial representations, $m_1(z)$ and $m_2(z)$, satisfy

$$m_1(z) - m_2(z) \equiv 0\,. \tag{A.12}$$

Using this property, $c(z)$, $T_1[c(z)]$, $T_3[c(z)]$ and $T_3T_1[c(z)]$ will be shown to be different from each other. Let us examine $c(z)$ and $T_1[c(z)]$ first, which give:

$$\begin{aligned} c(z) - T_1[c(z)] &= c(z) + c(z) \\ &= 2c(z) \\ &\neq 0 \ \forall\, c(z)\,. \end{aligned} \tag{A.13}$$

Thus, $c(z)$ and $T_1[c(z)]$ are always different. In the same way, $c(z)$ and $T_3[c(z)]$ can be shown to be different as follows:

$$\begin{aligned} c(z) - T_3[c(z)] &= c(z) - c(-z) \\ &= \sum_{k=0}^{N-1} [c_k z^k - c_k(-z)^k] \\ &= \sum_{k=0}^{N-1} [(1-(-1)^k)c_k z^k] \\ &= \sum_{k=0}^{\lfloor N/2 \rfloor - 1} [2c_{2k+1} z^{2k+1}] \\ &\neq 0 \ \forall\, c(z)\,. \end{aligned} \tag{A.14}$$

This shows that $c(z)$ and $T_3[c(z)]$ are always different. Furthermore $c(z)$ and $T_3T_1[c(z)]$ are also different, since:

$$\begin{aligned} c(z) - T_3T_1[c(z)] &= \sum_{k=0}^{\lfloor (N+1)/2 \rfloor - 1} [2c_{2k} z^{2k}] \\ &\neq 0 \ \forall\, c(z)\,. \end{aligned} \tag{A.15}$$

We note that $T_3[c(z)] - T_1[c(z)] = c(z) - T_3T_1[c(z)]$ and that $c(z)$ and $T_3T_1[c(z)]$ always differ. From the argument so far, we conclude that $c(z)$, $T_1[c(z)]$, $T_3[c(z)]$ and $T_3T_1[c(z)]$ are different from each other. Therefore, there are at least four different message sequences, which have the same *PMEPR*. ¶

Theorem A.1 suggests that there may exist eight equivalent message sequences in terms of their *PMEPR*, but theorem A.2 states that the existence of only four different equivalent message sequences is guaranteed. The following theorem resolves this dilemma.

Theorem A.3 *If T_2 satisfies any of the following three conditions for any member in the equivalent code set, then the number of the members in the set becomes four.*

- $T_2 \equiv I$
- $T_2 \equiv T_1$ *for even* N
- $T_2 \equiv T_3$ *for odd* N

Proof: If the number of *PMEPR*-equivalent symbols is less than eight, there exists a number of combined transforms of T_1, T_2 and T_3 defined in Theorem A.1, which are equivalent in terms of producing the same symbol. It has been argued that I, T_1, T_3 and T_3T_1 are different in the proof of Theorem A.2. The remaining possibility is that T_2 becomes equivalent to one of I, T_1, T_3 and T_3T_1. Let us consider these cases individually.

Assume that $T_2 \equiv I$. In this case, $c(z) - T_2[c(z)]$ should be 0, which is confirmed below:

$$\begin{aligned} c(z) - T_2[c(z)] &= c(z) - z^{N-1}c(z^{-1}) \\ &= \sum_{k=0}^{N-1}(c_k z^k - z^{N-1}c_k z^{-k}) \\ &= \sum_{k=0}^{N-1}(c_k z^k - c_k z^{N-1-k}) \\ &= \sum_{k=0}^{N-1}(c_k - c_{N-1-k})z^k \\ &= 0 \text{ (when } c_k = c_{N-1-k}\ \forall k,\ k \in \{0,1,\ldots,N-1\}). \end{aligned}$$

All codes, which are symmetric with respect to the centre of code meet this condition. These elaborations are valid for arbitrary code lengths, however in practical OFDM implementations we tend to favour a code length, which is an integer power of two.

Let us now assume that $T_2 \equiv T_1$. In this case, $T_2[c(z)] - T_1[c(z)]$ should be 0, which is confirmed

below:

$$\begin{aligned} T_2[c(z)] - T_1[c(z)] &= z^{N-1}c(z^{-1}) + c(z) \\ &= \sum_{k=0}^{N-1}(z^{N-1}c_k z^{-k} + c_k z^k) \\ &= \sum_{k=0}^{N-1}(c_k z^{N-1-k} + c_k z^k) \\ &= \sum_{k=0}^{N-1}(c_{N-1-k} + c_k)z^k \\ &= 0 \text{ (when } c_k = -c_{N-1-k}\ \forall k,\ k \in \{0,1,\ldots,N-1\}). \end{aligned}$$

In order for the transforms T_2 and T_1 become identical, c_k should satisfy the above condition, which can be interpreted as requiring odd symmetry of the message sequences in the frequency domain. This condition cannot be met for odd values of N, because there exist a center symbol, which cannot meet the condition imposed.

Assume that $T_2 \equiv T_3$. Then $T_2[c(z)] - T_3[c(z)]$ becomes:

$$\begin{aligned} T_2[c(z)] - T_3[c(z)] &= z^{N-1}c(z^{-1}) - c(-z) \\ &= \sum_{k=0}^{N-1}(z^{N-1}c_k z^{-k} - (-1)^k c_k z^k) \\ &= \sum_{k=0}^{N-1}(c_k z^{N-1-k} - (-1)^k c_k z^k) \\ &= \sum_{k=0}^{N-1}(c_{N-1-k} - (-1)^k c_k)z^k\,. \end{aligned}$$

In order that the transforms T_2 and T_3 become identical, c_k should be equal to $(-1)^k c_{N-1-k}$. Note that this condition cannot be met for even values of N, because it requires $c_0 = c_{N-1}$ and $c_{N-1} = -c_0$ for $k = 0$ and $k = N-1$, respectively.

Finally, let us assume that $T_2 \equiv T_1 T_3$. Then $T_2[c(z)] - T_1T_3[c(z)]$ becomes:

$$\begin{aligned} T_2[c(z)] - T_1T_3[c(z)] &= z^{N-1}c(z^{-1}) + c(-z) \\ &= \sum_{k=0}^{N-1}(z^{N-1}c_k z^{-k} + (-1)^k c_k z^k) \\ &= \sum_{k=0}^{N-1}(c_k z^{N-1-k} + (-1)^k c_k z^k) \\ &= \sum_{k=0}^{N-1}(c_{N-1-k} + (-1)^k c_k)z^k\,. \end{aligned}$$

In order for the transforms T_2 and T_1T_3 to become equivalent c_k should be equal to $-(-1)^k c_{N-1-k}$. For even values of N, this requires $c_0 = -c_{N-1}$ and $c_{N-1} = c_0$ for $k = 0$ and $k = N-1$, respectively.

Thus the condition for the equivalence of T_2 and T_1T_3 cannot be met for the even values of N. In case of odd N, $c_{(N-1)/2}$ should be equal to $-c_{(N-1)/2}$, in order to meet the above condition and it is readily seen that this is impossible. Thus, the assumed case never occurs.

Therefore, the first three cases considered above are the only cases, in which eight possible equivalent message sequences yield only four different ones. ¶

Theorem A.4 *The worst case* PMEPR *of BPSK modulated OFDM over all the message symbols is N, where N is the number of carriers.*

Proof: From (A.8) and (A.4), the worst case *PMEPR* is encountered when $P_o(t)$ is the maximum over range of $t \in [0, 0.5]$ and over all message symbols. The maximum value of C_k, $C_{k,max}$, is $N-k$ according to (A.6). The time dependent term, $\cos(2\pi kt)$ in $P_o(t)$ of (A.5) should be positive and at its maximum of 1, in order to yield the maximum of $P_o(t)$ by constructively combining all positive C_ks. Considering this argument, the worst case *PMEPR*, $PMEPR_{max}$, becomes:

$$\begin{aligned} PMEPR_{max} &= 1 + \frac{2}{N} P_{o,max} \\ &= 1 + \frac{2}{N} \sum_{k=1}^{N-1} C_{k,max} \\ &= 1 + \frac{2}{N} \sum_{k=1}^{N-1} (N-k) \\ &= 1 + \frac{2}{N} \left(N - 1 - \frac{N(N-1)}{2} \right) \\ &= 1 + \frac{2}{N} \frac{N(N-1)}{2} \\ &= N\,. \end{aligned}$$

Thus, the worst case *PMEPR* is N. ¶

Corollary A.5 *In BPSK modulated OFDM systems the number of message symbols, which yield the worst case* PMEPR *is four for all N over* 1 .

Proof: The message symbol, which comprises the all zero sequence results in the maximum values of C_k for all k. By applying $T_1[\bullet]$, $T_3[\bullet]$ and $T_4[\bullet]$, we can obtain the other three message symbols yielding the maximum value of C_k. Note that $T_2 \equiv I$ holds for the all zero sequence and corresponds to a degenerated case, yielding only four different OFDM message symbols. ¶

In BPSK modulated OFDM systems having a high number of carriers, it is observed that sometimes more than eight message sequences yield the same *PMEPR*, which cannot be identified by Theorem A.1. For example, the message sequences represented by 4 and 5 in a 6-carrier BPSK OFDM system exhibit exactly the same *PMEPR* value, while they have totally different envelope power waveforms and, thus,

Theorem A.1 does not detect their equivalence in terms of their *PMEPR*. The modified power envelope waveforms corresponding to the message sequences 4 and 5 in the previously mentioned 6-subcarrier scheme are shown in Figure A.2. Table A.3 presents the aperiodic autocorrelations and the *PMEPR*s for

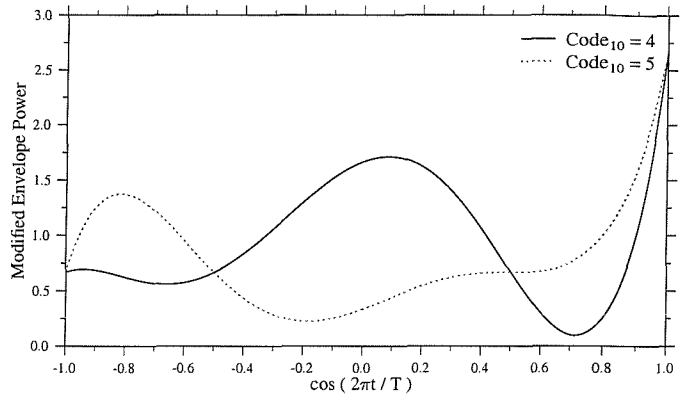

Figure A.2: Modified power envelope waveforms for the message sequences 4 and 5 in 6-carrier BPSK modulated OFDM systems

the message sequences 4 and 5. According to (A.3) the power envelope of OFDM signal corresponding

$(Code)_{10}$	$(Code)_2$	C_1	C_2	C_3	C_4	C_5	*PMEPR*
4	000100	1	0	1	2	1	2.67
5	000101	-1	2	-1	0	-1	2.67

Table A.3: Aperiodic autocorrelations evaluated from (A.6) for the message sequences 4 and 5 in 6-carrier BPSK modulated OFDM system

to the OFDM message symbol $(Code)_{10} = 4$ and $(Code)_{10} = 5$ is given as $|s(t)|^2 = 1 + 2/N\, P_{o,m}(t)$, where $P_{o,m}(t)$ are given by:

$$P_{o,4}(t) = \cos(2\pi t) + \cos(6\pi t) + 2\cos(8\pi t) + \cos(10\pi t) \tag{A.16}$$

$$P_{o,5}(t) = -\cos(2\pi t) + 2\cos(2\pi t) - \cos(6\pi t) - \cos(10\pi t). \tag{A.17}$$

The harmonics of $\cos(2\pi t)$ in (A.16) and (A.17) can be represented using $\cos(2\pi t)$ only and the parametric polynomial representation is obtained by substituting $\cos(2\pi t)$ by α, which varies between -1 and $+1$ as t changes. In this way, the power envelope of OFDM signal corresponding to the message sequences of 4 and 5 were plotted in Figure A.2 and their maximum values of $1+3P_{o,4}(\alpha)$ and $1+3P_{o,5}(\alpha)$ were obtained, which turned out to be exactly the same analytically. Considering that the set of aperiodic autocorrelations $\{C_k\}_5$ for the message sequence 5 shown in Table A.3 can be obtained by applying T_2

and T_3 defined in Theorem A.1 to $\{C_k\}_4$ for the message sequence 4, there may be a rule, which governs this phenomenon, although these considerations are beyond the scope of this treatise.

A.3 PMEPR Calculation of BPSK Modulated OFDM

In order to determine the value of the *PMEPR*, we evaluate (A.8) for $t \in \{0, \Delta, 2\Delta, \cdots, K\Delta\}$, where Δ is much less than 0.5 and K is the smallest integer which satisfies $\lfloor 10K\Delta \rfloor \geq 5$. The value of Δ required for attaining a specified accuracy of the *PMEPR* can be derived using Equation (A.8). Let us consider the worst case scenario, when all the coefficients C_k, $k = 1, \cdots, N-1$ in (A.5) have the maximum possible values and also assume that the derivatives of the cosine functions are all unity. Note that these two worst-case assumptions never occur simultaneously and hence these are very conservative assumptions. With these assumptions, ΔP_o, the worst case error associated with determining $P_o(t)$ and according to (A.8) also the *PMEPR*, is given by:

$$\begin{aligned} \Delta P_o &= \left| P_o\left(t_{max} + \frac{\Delta}{2}\right) - P_o(t_{max}) \right| \\ &\leq \frac{\Delta}{2} \sum_{k=1}^{N-1} k \qquad \text{(A.18)} \\ &= \frac{\Delta}{4} N(N-1)\,, \qquad \text{(A.19)} \end{aligned}$$

where t_{max} is the exact time instant, when $P_o(t)$ has its maximum value, while $t_{max} + \frac{\Delta}{2}$ is the worst case evaluation time. Using (A.8) and (A.18), the worst case error in associated with determining the *PMEPR*, namely $\Delta PMEPR$ is given by:

$$\Delta PMEPR = \frac{N-1}{2}\Delta\,. \qquad \text{(A.20)}$$

As an example, Δ should satisfy the following condition in order to arrive at *PMEPR* values that are accurate up to two decimal places:

$$\begin{aligned} \frac{N-1}{2}\Delta &\leq 0.005 \qquad \text{(A.21)} \\ \Delta &\leq \frac{0.01}{N-1} \qquad \text{(A.22)} \end{aligned}$$

The choice of Δ is important in order to arrive at the correct *PMEPR* values, especially in the context of OFDM having a high number of carriers. In [31, Table 1], several Peak-Envelope-Power (PEP) values are tabulated up to two decimal places, where according to the above analytical results small amendments are necessary. For example, 7.07 should be 7.08 and 9.45 should be 9.48, when using 20 decimal places in the calculations. In conclusion, since the condition imposed by (A.18) and (A.22) is very conservative, the PMEPR values can be determined according to the required accuracy.

A.4 PMEPR Properties of QPSK Modulated OFDM

In QPSK modulated OFDM systems, two message bits are used for modulating each carrier. The *normalized* complex envelope waveform, $s(t)$, becomes [32]:

$$s(t) = \frac{1}{\sqrt{2N}} \sum_{k=0}^{N-1} (c_{2k} + jc_{2k+1})\ e^{j2\pi \frac{kt}{T}}\ , \tag{A.23}$$

where N is the number of carriers, c_{2k} and c_{2k+1} are the in-phase symbol and the quadrature phase symbol respectively, modulating the kth carrier of the OFDM symbol, where we have $c_i \in \{-1, +1\}$, and finally, T is the OFDM symbol duration. Equation A.2 can also be used for defining the *PMEPR* of QPSK modulated OFDM signals. Van Eetvelt, Wade and Tomlinson presented an excellent analysis of QPSK modulated multi-carrier systems and showed that 16 messages form a coset, where the messages belonging to the same coset yield the same *PMEPR*. For a detailed description we refer to [32].

According to the findings of [32], very large number of message sequences yield exactly the same *PMEPR*. Algorithm 2 [32, page 91] was used for generating Table 4 [32, page 94] for QPSK modulated 5-carrier OFDM, suggesting that 192 message sequences yield a *PMEPR* value of 2.859, although we found that the application of Algorithm 2 [32, page 91] resulted in a lower number of such message sequences. In fact, the message symbols represented as 31 and 47 in the associated cosets list in the context of the *PMEPR* value of 4.095 in Table 4 [32, page 94] have slightly different *PMEPR* values, as shown in Figure A.3, which is likely to be a consequence of the more accurate number representation using 20 effective decimal digits in our calculations. The peak values of the power waveforms found for the message symbols represented by 1, 2, 30, 31, 45 and 47 appear identical in the upper graph of Figure A.3. In reality, the power envelope waveforms for the messages corresponding to the decimal notations 1, 2, 30, 45 are truly identical except for a time shift and hence have exactly the same *PMEPR* value. By contrast, the waveforms of the messages represented by 31 and 47 have a different shape and have a slightly different *PMEPR* value, as shown in the lower graph of Figure A.3, which is the enlarged version of the marked rectangle seen in the upper graph. The correct characterisation of the 5-carrier QPSK modulated OFDM messages is presented in Table A.4.

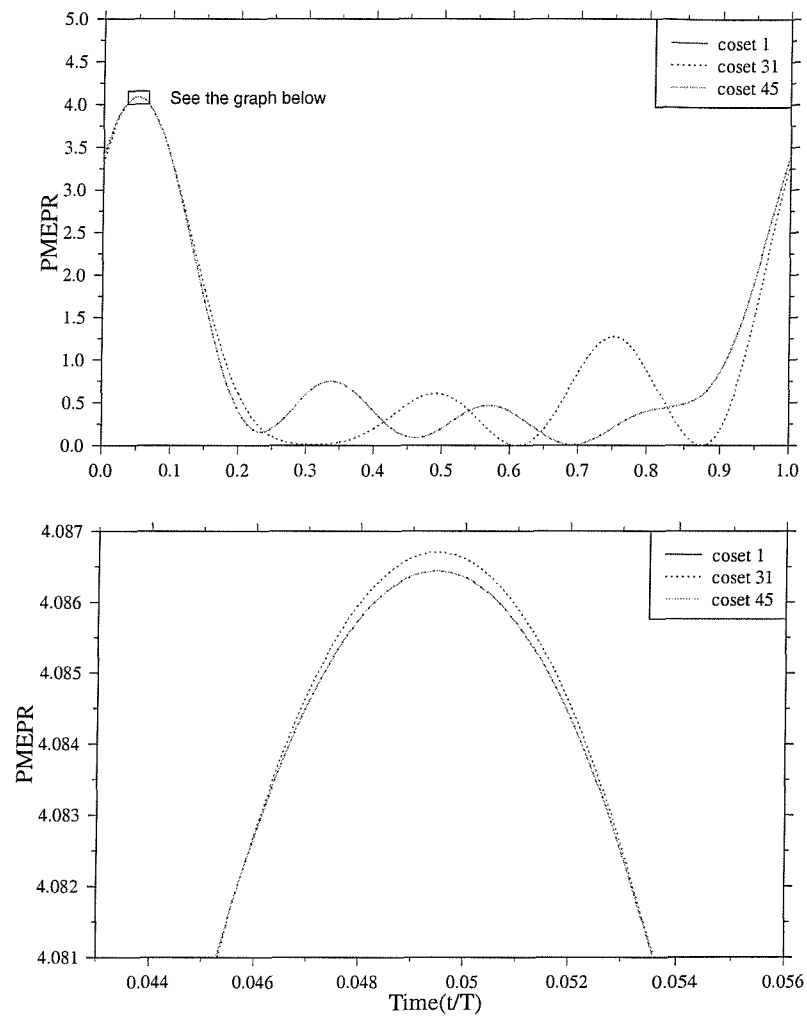

Figure A.3: Power envelope waveforms of three message sequences corresponding to their decimal notations of 1, 31 and 45 in 5-carrier QPSK modulated OFDM systems (waveforms are appropriately shifted in time, in order to compare their shapes and the peak values)

Number of carriers	Number of equivalence classes	Orders of the equivalence classes	Associated cosets	Associated peak factors
5	23	16	0	5.000
		64	5, 10, 21, 42	4.304
		32	23, 43	4.297
		32	31, 47	4.087
		64	1, 2, 30, 45	4.086
		64	4, 8, 52, 56	3.539
		32	7, 11	3.497
		32	16, 32	3.400
		64	17, 34, 61, 62	3.327
		64	22, 41, 54, 57	2.801
		64	26, 37, 53, 58	2.789
		64	20, 24, 36, 40	2.778
		64	29, 46, 49, 50	2.680
		32	15, 63	2.679
		48	28, 44, 60	2.600
		32	55, 59	2.366
		64	13, 14, 18, 33	2.242
		32	19, 35	2.233
		16	48	2.112
		32	3, 51	2.101
		64	6, 9, 25, 38	1.976
		32	27, 39	1.967
		16	12	1.800

Table A.4: Re-calculated equivalent cosets of 5-carrier QPSK modulated OFDM signals

Appendix B

Two-Dimensional Rake Receiver

B.1 System Model

The schematic of our Rake-receiver and D-antenna diversity assisted adaptive Square QAM (AQAM) system is illustrated in Figure B.1. A band-limited equivalent low-pass m-ary QAM signal $s(t)$, having a spectrum of $S(f) = 0$ for $|f| > 1/2\,W$, is transmitted over time variant frequency selective fading channels and received by a set of D RAKE-receivers. Each Rake-receiver [17, 25] combines all the resolvable multi-path components using Maximal Ratio Combining (MRC). The combined signals of the D-antenna assisted Rake-receivers are summed and demodulated using the estimated channel quality information. The estimated signal-to-noise ratio is fed back to the transmitter and it is used for deciding upon the most appropriate m-ary square QAM modulation mode to be used during the next transmission burst. We assume that the channel quality is estimated perfectly and it is available at the transmitter immediately. The effects of channel estimation error and feedback delay on the performance of AQAM were studied for example by *Goldsmith* and *Chua* [122].

The low-pass equivalent impulse response of the channel between the transmitter and the d-th antenna may be represented as [25] :

$$h_d(t,\tau) = \sum_{n=1}^{N} h_{d,n}(t)\ \delta\left(\tau - \frac{n}{W}\right)\ , \tag{B.1}$$

where $\{h_{d,n}(t)\}$ is a set of independent complex valued stationary random Gaussian processes. The maximum number of resolvable multi-path components N is given by $\lfloor T_m W \rfloor + 1$, where T_m is the multi-path delay spread of the channel [25]. Hence, the low-pass equivalent received signal $r_d(t)$ at the d-th antenna can be formulated as :

$$r_d(t) = \sum_{n=1}^{N} h_{d,n}(t) s\left(t - \frac{n}{W}\right) + z_d(t)\ , \tag{B.2}$$

where $z_d(t)$ is a zero mean Gaussian random process having a two-sided power spectral density of $N_o/2$. Let us assume that the fading is sufficiently slow or $(\Delta t)_c \ll T$, where $(\Delta t)_c$ is the channel's coherence time [14] and T is the signaling period. Then, $h_{d,n}(t)$ can be simplified to $h_{d,n}(t) = \alpha_{d,n} e^{j\phi_{d,n}}$ for the

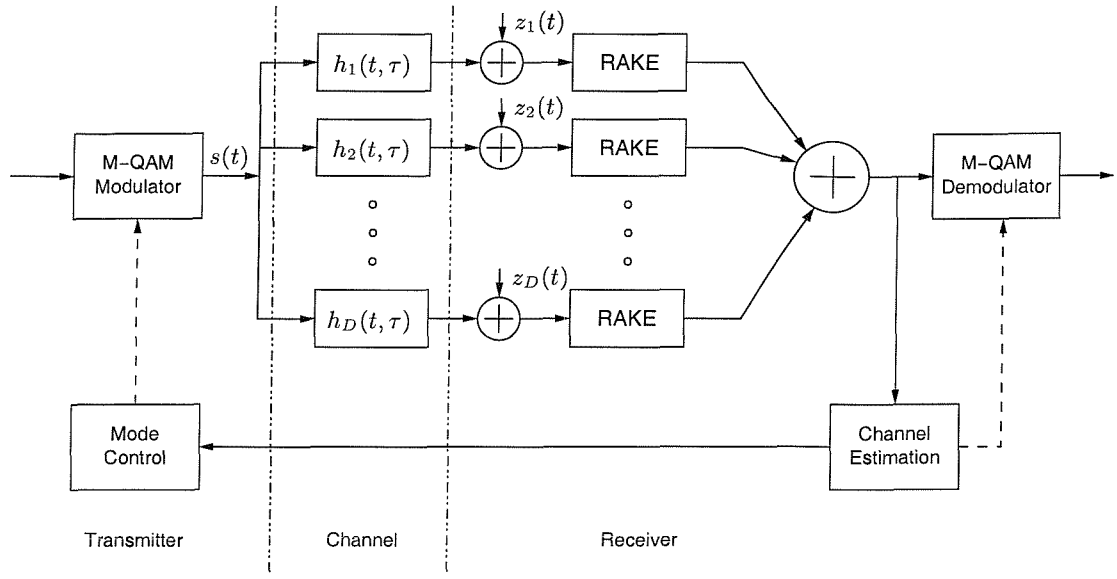

Figure B.1: Equivalent low-pass model of a D-th order antenna diversity based RAKE-receiver assisted AQAM system

duration of signalling period T, where the fading magnitude $\alpha_{d,n}$ is assumed to be Rayleigh distributed and the phase $\phi_{d,n}$ is assumed to be uniformly distributed.

B.2 BER Analysis of Fixed-mode Square QAM

An ideal RAKE receiver [17] combines all the signal powers scattered over N paths in an optimal manner, so that the instantaneous Signal-to-Noise Ratio (SNR) per symbol at the RAKE receiver's output can be maximised [25]. The noise at the RAKE receiver's output is known to be Gaussian [25]. The SNR, γ_d, at the d-th ideal RAKE receiver's output is given as [25] :

$$\gamma_d = \sum_{n=1}^{N} \gamma_{d,n} \ , \tag{B.3}$$

where $\gamma_{d,n} = E/N_o \, \alpha_{d,n}^2$ and $\{\alpha_{d,n}\}$ is assumed to be normalised, such that $\sum_{n=1}^{N} \alpha_{d,n}^2$ becomes unity. Since we assumed that each multi-path component has an independent Rayleigh distribution, the characteristic function of γ_d can be represented as [25, pp 802] :

$$\psi_{\gamma_d}(j\upsilon) = \prod_{n=1}^{N} \frac{1}{1 - j\upsilon\bar{\gamma}_{d,n}} \ , \tag{B.4}$$

where $\gamma_{d,n} = E/N_o \mathsf{E}[\alpha_{d,n}^2]$. Let us assume furthermore that each of the D diversity channels has the same multi-path intensity profile (MIP), although in practical systems each antenna may experience a different MIP. Under this assumption, $\bar{\gamma}_{d,n}$ in (B.4) can be written as $\bar{\gamma}_n$. The total SNR per symbol, γ,

at the output of the demodulator depicted in Figure B.1 is given as :

$$\gamma = \sum_{d=1}^{D} \gamma_d \,, \tag{B.5}$$

while the characteristic function of the SNR per symbol γ, under the assumption of independent identical diversity channels, can be formulated as :

$$\psi_\gamma(j\upsilon) = \prod_{n=1}^{N} \frac{1}{(1 - j\upsilon\bar{\gamma}_n)^D} \,. \tag{B.6}$$

Applying the technique of Partial Fraction Expansion (PFE) [94], $\psi_\gamma(j\upsilon)$ can be expressed as :

$$\psi_\gamma(j\upsilon) = \sum_{d=1}^{D}\sum_{n=1}^{N} \Lambda_{D-d+1,n} \frac{1}{(1 - j\upsilon\bar{\gamma}_n)^d} \,. \tag{B.7}$$

Let us now determine the constant coefficients $\Lambda_{d,n}$. Equating (B.6) with (B.7) and substituting $j\upsilon = -p$, we have

$$\prod_{i=1}^{N} \frac{1}{(1 + p\bar{\gamma}_i)^D} = \sum_{d=1}^{D}\sum_{i=1}^{N} \Lambda_{D-d+1,i} \frac{1}{(1 + p\bar{\gamma}_i)^d} \,. \tag{B.8}$$

Multiplying by $(1 + p\bar{\gamma}_n)^D$ at both sides, (B.8) becomes :

$$\prod_{\substack{i=1 \\ i\neq n}}^{N} \frac{1}{(1 + p\bar{\gamma}_i)^D} = \sum_{d=1}^{D}\sum_{\substack{i=1 \\ i\neq n}}^{N} \Lambda_{D-d+1,i} \frac{1}{(1 + p\bar{\gamma}_i)^d} + \sum_{d=1}^{D} \Lambda_{d,n} \, (1 + p\bar{\gamma}_n)^{d-1} \,. \tag{B.9}$$

Setting the $(d-1)$th derivatives with respect to p and substituting $p = -1/\bar{\gamma}_n$, we have :

$$\frac{d^{d-1}}{dp^{d-1}} \left[\prod_{\substack{i=1 \\ i\neq n}}^{N} (p\,\bar{\gamma}_i + 1)^{-D} \right]_{p\,=\,-1/\bar{\gamma}_n} = (d-1)!\,\bar{\gamma}_n^{(d-1)} \Lambda_{d,n} \,. \tag{B.10}$$

Hence, $\Lambda_{d,n}$ is given as :

$$\Lambda_{d,n} \triangleq \frac{1}{(d-1)!\,\bar{\gamma}_n^{(d-1)}} \, \varphi_{d,n}\left(-1/\,\bar{\gamma}_n\right) \,, \tag{B.11}$$

where $\varphi_{d,n}(x)$ is defined as :

$$\varphi_{d,n}(x) \triangleq \frac{d^{d-1}}{dp^{d-1}} \left[\prod_{\substack{i=1 \\ i\neq n}}^{N} (p\,\bar{\gamma}_i + 1)^{-D} \right]_{p\,=\,x} \,. \tag{B.12}$$

Upon setting the derivatives directly, $\varphi_{d,n}(-1/\,\bar{\gamma}_n)$ of (B.12) can be represented recursively as :

$$\begin{aligned} \varphi_{1,n}(-1/\,\bar{\gamma}_n) &= \pi_n^D \\ \varphi_{d,n}(-1/\,\bar{\gamma}_n) &= \sum_{i=1}^{d-1} \left[C_{d,i}\, D\, \varphi_{d-i,n}(-1/\,\bar{\gamma}_n) \sum_{\substack{j=1 \\ j\neq n}}^{N} \left(\frac{\bar{\gamma}_n\bar{\gamma}_j}{\bar{\gamma}_n - \bar{\gamma}_j} \right)^i \right] \,, \end{aligned} \tag{B.13}$$

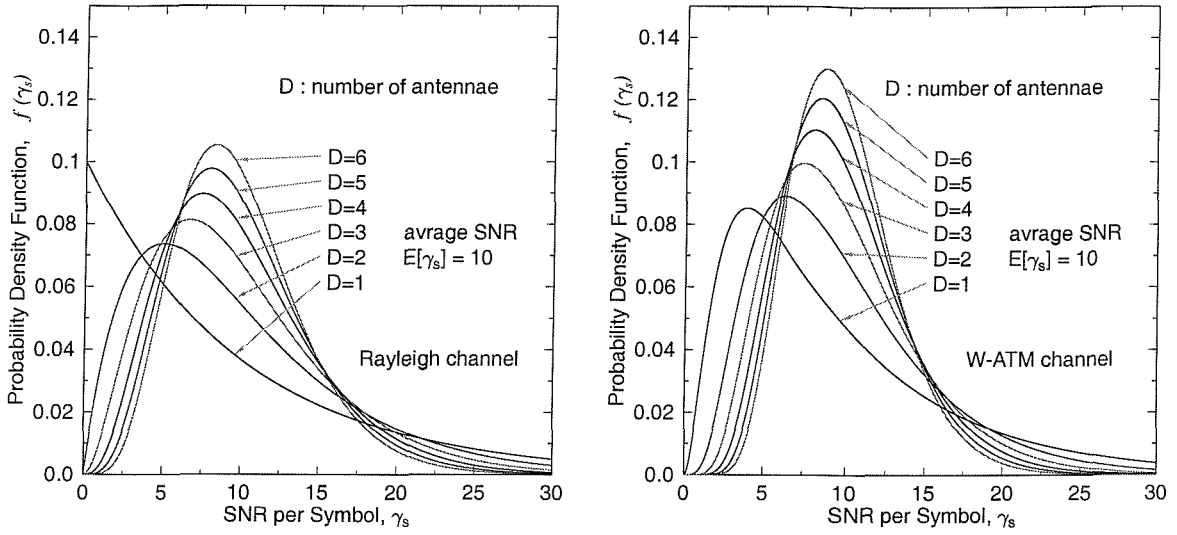

(a) Rayleigh Channel, $L = 1$

(b) W-ATM Channel, $L = 3$

Figure B.2: PDF of γ_s given in (B.16) for an average SNR per symbol of $\mathsf{E}[\gamma_s] = 10\text{dB}$

where π_n is defined as :

$$\pi_n \triangleq \prod_{\substack{i=1 \\ i \neq n}}^{N} \frac{\bar{\gamma}_n}{\bar{\gamma}_n - \bar{\gamma}_i} \tag{B.14}$$

and the doubly indexed coefficient $C_{d,i}$ of (B.13) can also be expressed recursively as :

$$\begin{aligned} C_{d,1} &= -1 && \text{for all } d \\ C_{d,d} &= 0 && \text{for } d > 1 \\ C_{d,i} &= -(i-1)\, C_{d-1,i-1} + C_{d-1,i} && \text{for } d > i\,. \end{aligned} \tag{B.15}$$

The PDF of γ, $f_{\bar{\gamma}}(\gamma)$, can be found by applying the inverse Fourier transform to $\psi_\gamma(j\upsilon)$ in (B.7), which is given by [25, pp 781, (14-4-13)] :

$$f_{\bar{\gamma}}(\gamma) = \sum_{d=1}^{D} \sum_{n=1}^{N} \Lambda_{D-d+1,n}\, \frac{1}{(d-1)!\, \bar{\gamma}_n^d}\, \gamma^{d-1}\, e^{-\gamma/\bar{\gamma}_n}\,. \tag{B.16}$$

Figure B.2 shows the PDF of the SNR per symbol over both a narrow-band Rayleigh channel and the dispersive Wireless Asynchronous Transfer Mode (W-ATM) channel of [13]. Specifically, the W-ATM channel is a 3-path indoor channel, where the average SNR for each path is given as $\bar{\gamma}_1 = 0.79192\bar{\gamma}$, $\bar{\gamma}_2 = 0.12424\bar{\gamma}$ and $\bar{\gamma}_3 = 0.08384\bar{\gamma}$.

Since we now have the PDF $f_{\bar{\gamma}}(\gamma)$ of the channel SNR, let us calculate the average BEP of m-ary square QAM employing Gray mapping. The average BEP P_e can be expressed as [13, 25] :

$$P_e = \int_0^\infty p_m(\gamma) f(\gamma) d\gamma\,, \tag{B.17}$$

where $p_m(\gamma)$ is the BER of m-ary square QAM employing Gray mapping over Gaussian channels [13] :

$$p_m(\gamma) = \sum_i A_i Q(\sqrt{a_i \gamma}) \ , \tag{B.18}$$

where $Q(x)$ is the Gaussian Q-function defined as $Q(x) \triangleq \frac{1}{\sqrt{2\pi}} \int_x^\infty e^{-t^2/2} dt$ and $\{A_i, a_i\}$ is a set of modulation mode dependent constants. For the modulation modes associated with $m = 2, 4, 16$ and 64, the sets $\{A_i, a_i\}$ are given as [13, 123] :

$$\begin{array}{lll} m = 2, & \text{BPSK} & \{(1,2)\} \\ m = 4, & \text{QPSK} & \{(1,1)\} \\ m = 16, & \text{16-QAM} & \left\{\left(\frac{3}{4}, \frac{1}{5}\right), \left(\frac{2}{4}, \frac{3^2}{5}\right), \left(-\frac{1}{4}, \frac{5^2}{5}\right)\right\} \\ m = 64, & \text{64-QAM} & \left\{\left(\frac{7}{12}, \frac{1}{21}\right), \left(\frac{6}{12}, \frac{3^2}{21}\right), \left(-\frac{1}{12}, \frac{5^2}{21}\right), \left(\frac{1}{12}, \frac{9^2}{21}\right), \left(-\frac{1}{12}, \frac{13^2}{21}\right)\right\} . \end{array} \tag{B.19}$$

The average BEP of m-ary QAM in our scenario can be calculated by substituting $p_m(\gamma)$ of (B.18) and $f_{\bar{\gamma}}(\gamma)$ of (B.16) into (B.17) :

$$P_{e,m}(\bar{\gamma}) = \int_0^\infty \sum_i A_i Q(\sqrt{a_i \gamma}) f_{\bar{\gamma}}(\gamma) d\gamma \tag{B.20}$$

$$= \sum_i A_i P_e(\bar{\gamma}; a_i) \ , \tag{B.21}$$

where each constituent BEP $P_e(\bar{\gamma}; a_i)$ is defined as :

$$P_e(\bar{\gamma}; a_i) = \int_0^\infty Q(\sqrt{a_i \gamma}) \, f_{\bar{\gamma}}(\gamma) \, d\gamma \ . \tag{B.22}$$

Using the similarity of $f_{\bar{\gamma}}(\gamma)$ in (B.16) and the PDF of the SNR of a D-antenna diversity-assisted Maximal Ratio Combining (MRC) system transmitting over flat Rayleigh channels [25, pp 781], the closed form solution for the component BEP $P_e(\bar{\gamma}; a_i)$ can be expressed as :

$$P_e(\bar{\gamma}; a_i) = \sum_{d=1}^{D} \sum_{n=1}^{N} \frac{1}{\sqrt{2\pi}} \int_0^\infty \int_{\sqrt{2\gamma}}^\infty e^{-x^2/2} \, \Lambda_{D-d+1,n} \, \frac{1}{(d-1)! \, \bar{\gamma}_n^d} \, \gamma^{d-1} \, e^{-\gamma/\bar{\gamma}_n} \, dx \, d\gamma \tag{B.23}$$

$$= \sum_{d=1}^{D} \sum_{n=1}^{N} \left[\Lambda_{D-d+1,n} \left\{\tfrac{1}{2}(1-\mu_n)\right\}^d \sum_{i=0}^{d-1} \binom{d-1+i}{i} \left\{\tfrac{1}{2}(1+\mu_n)\right\}^i \right] , \tag{B.24}$$

where $\mu_n \triangleq \sqrt{\frac{a_i \bar{\gamma}_n}{2 + a_i \bar{\gamma}_n}}$ and the average SNR per symbol is $\bar{\gamma} = D \sum_{n=1}^{N} \bar{\gamma}_n$. Substituting $P_e(\bar{\gamma}; a_i)$ of (B.24) into (B.21), the average BEP of an m-ary QAM Rake receiver using antenna diversity can be expressed in a closed form.

Let us consider the performance of BPSK by setting D=1 or N=1 . When the number of antennae is one, *i.e.* D=1, $P_{e,2}(\bar{\gamma})$ is reduced to

$$P_{e,BPSK} = \sum_{n=1}^{N} \Lambda_{1,n} \left\{\tfrac{1}{2}(1-\mu_n)\right\} \tag{B.25}$$

$$= \sum_{n=1}^{N} \pi_n \left\{\tfrac{1}{2}(1-\mu_n)\right\} \ , \tag{B.26}$$

which is identical to the result given in [25, (14-5-28), pp 802] . On the other hand, when the channels exhibit flat fading, *i.e.* L=1, our system is reduced to a D-antenna diversity-based MRC system transmitting over D number of flat Rayleigh channels. In this case, $\Lambda_{D-d+1,n}$ of (B.11) becomes zero for all values of d, except for $\Lambda_{1,1}$=1 when d=D, and the average BPSK BEP in this scenario becomes :

$$P_{e,BPSK} = \sum_{d=1}^{D} \left[\Lambda_{D-d+1,1} \left\{ \tfrac{1}{2}(1-\mu_1) \right\}^d \sum_{i=0}^{d-1} \binom{d-1+i}{i} \left\{ \tfrac{1}{2}(1+\mu_1) \right\}^i \right] \tag{B.27}$$

$$= \left\{ \tfrac{1}{2}(1-\mu_1) \right\}^D \sum_{i=0}^{D-1} \binom{D-1+i}{i} \left\{ \tfrac{1}{2}(1+\mu_1) \right\}^i , \tag{B.28}$$

which is also given in [25, (14-4-15), pp781] .

Appendix C

Mode Specific Average BEP of an Adaptive Modulation System

A closed form solution for the 'mode-specific average BER' of a Maximal Ratio Combining (MRC) receiver using Dth order antenna diversity over independent Rayleigh channels is derived, where the 'mode-specific average BER' refers to the BER of the adaptive modulation scheme, while activating one of its specific constituent modem modes. The PDF $f_{\bar{\gamma}}(\gamma)$ of the channel SNR γ is given as [25, (14-4-13)]

$$f_{\bar{\gamma}}(\gamma) = \frac{1}{(D-1)!\,\bar{\gamma}^D}\,\gamma^{D-1}\,e^{-\gamma/\bar{\gamma}}\,,\quad \gamma \geq 0\,, \tag{C.1}$$

where $\bar{\gamma}$ is the average channel SNR. Since the PDF of the instantaneous channel SNR γ over a Nakagami fading channel is given as :

$$f_{\bar{\gamma}}(\gamma) = \left(\frac{m}{\bar{\gamma}}\right)^m \frac{\gamma^{m-1}}{\Gamma(m)}\,e^{-m\gamma/\bar{\gamma}}\,,\quad \gamma \geq 0\,, \tag{C.2}$$

the following results can also be applied to a Nakagami fading channel with a simple change of variable given as $D = m$ and $\bar{\gamma} = \bar{\gamma}\,/\,m$.

The mode-specific average BEP is defined as

$$P_r(\alpha,\beta;\bar{\gamma},D,a) \triangleq \int_\alpha^\beta Q(\sqrt{a\gamma})\,f_{\bar{\gamma}}(\gamma)\,d\gamma \tag{C.3}$$

$$= \int_\alpha^\beta Q(\sqrt{a\gamma})\,\frac{1}{(D-1)!\,\bar{\gamma}^D}\,\gamma^{D-1}\,e^{-\gamma/\bar{\gamma}}\,d\gamma\,, \tag{C.4}$$

where $Q(x) \triangleq \frac{1}{\sqrt{2\pi}} \int_x^\infty e^{-t^2/2}\, dt$. Applying integration-by-part or $\int u\, dv = uv - \int v\, du$ and noting that

$$\begin{aligned} u &= Q(\sqrt{a\gamma}) \\ du &= -\frac{\sqrt{a}}{2\sqrt{2\pi\gamma}}\, e^{-a\gamma/2} \\ dv &= \frac{1}{(D-1)!\,\bar{\gamma}^D}\, \gamma^{D-1}\, e^{-\gamma/\bar{\gamma}} \\ v &= -e^{-\gamma/\bar{\gamma}} \sum_{d=0}^{D-1} (\gamma/\bar{\gamma})^d\, \frac{1}{d!} \end{aligned}$$

(C.3) becomes

$$P_r(\alpha, \beta; \bar{\gamma}, D, a) = \left[e^{-\gamma/\bar{\gamma}}\, Q(\sqrt{a\gamma}) \sum_{d=0}^{D-1} (\gamma/\bar{\gamma})^d \frac{1}{d!} \right]_\beta^\alpha - \sum_{d=0}^{D-1} I_d(\alpha, \beta)\ , \tag{C.5}$$

where

$$I_d(\alpha, \beta) = \int_\alpha^\beta \frac{\sqrt{a}}{2\sqrt{2\pi}}\, \frac{1}{d!}\, (\gamma/\bar{\gamma})^d\, \frac{1}{\sqrt{\gamma}}\, e^{-a\gamma/(2\mu^2)}\, d\gamma \tag{C.6}$$

and $\mu = \sqrt{\frac{a\bar{\gamma}}{a\bar{\gamma}+2}}$. Let us consider I_d for the case of $d = 0$:

$$I_0(\alpha, \beta) = \int_\alpha^\beta \frac{\sqrt{a}}{2\sqrt{2\pi}}\, \frac{1}{\sqrt{\gamma}}\, e^{-a\gamma/(2\mu^2)}\, d\gamma\ . \tag{C.7}$$

Upon introducing the variable $t^2 = a\gamma/\mu^2$ and exploiting that $d\gamma = 2\mu\sqrt{\gamma/a}\, ds$, we have :

$$I_0(\alpha, \beta) = [\mu\, Q(\sqrt{a\gamma}/\mu)\,]_\beta^\alpha\ . \tag{C.8}$$

Applying integration-by-part once to (C.6) yields

$$I_d(\alpha, \beta) = \left[\frac{\mu^2}{\sqrt{2a\pi}}\, \frac{1}{d!}\, (\gamma/\bar{\gamma})^d\, \frac{1}{\sqrt{\gamma}}\, e^{-a\gamma/(2\mu^2)} \right]_\beta^\alpha + \frac{2d-1}{a\bar{\gamma}d}\, \mu^2\, I_{d-1}\ , \tag{C.9}$$

which is a recursive form with the initial value given in (C.8). For this recursive form of (C.9), a non-recursive form of I_d can be expressed as :

$$\begin{aligned} I_d(\alpha, \beta) = &\left[\frac{\mu^2}{\sqrt{2a\pi}}\, \frac{\Gamma(d+\frac{1}{2})}{\bar{\gamma}^d\, \Gamma(d+1)} \sum_{i=1}^{d} \left(\frac{2\mu^2}{a} \right)^{d-i} \frac{\gamma^{i-\frac{1}{2}}}{\Gamma(i+\frac{1}{2})}\, e^{-a\gamma/(2\mu^2)} \right]_\beta^\alpha \\ &+ \left[\left(\frac{2\mu^2}{a\bar{\gamma}} \right)^d \frac{1}{\sqrt{\pi}}\, \frac{\Gamma(d+\frac{1}{2})}{\Gamma(d+1)}\, \mu\, Q(\sqrt{a\gamma}/\mu) \right]_\beta^\alpha\ . \end{aligned} \tag{C.10}$$

By substituting $I_d(\alpha, \beta)$ of (C.10) into (C.5), the regional BER $P_r(\bar{\gamma}; a, \alpha, \beta)$ can be represented in a closed form.

Appendix D

BER Analysis of Type-I Star-QAM

The Star Quadrature Amplitude Modulation (SQAM) technique [13], also known as Amplitude-modulated Phase Shift Keying (APSK), employs circular constellations, rather than rectangular constellation as in Square QAM [170]. Although Square QAM has the maximum possible minimum Euclidean distance amongst its phasors given a constant average symbol power, in some situations Star QAM may be preferred due to its relatively simple detector and for its low Peak-to-Average Power Ratio (PAPR) compared to Square QAM [170]. Since differentially detected non-coherent Star QAM signals are robust against fading effects, many researchers analysed its Bit Error Ratio (BER) performance for transmission over AWGN channels [171], Rayleigh fading channels [171, 172] as well as Rician fading channels [173]. The effects diversity reception on its BER were also studied when communicating over Rayleigh fading channels [174, 175]. The BER of coherent 16 Star QAM was also analysed for transmission over AWGN channels [171] as well as when communicating over *Nakagami-m* fading channels [176]. However, the BER of Star-QAM schemes other than 16-level Star QAM, such as 8, 32 and 64-level Star QAM, has not been studied.

D.1 Coherent Detection

The BER of coherent star QAM schemes employing Type-I constellations [170] when communicating over AWGN channels can be analysed using the signal-space method [131, 171, 176, 177]. The phasor constellations of the various Type-I Star QAM schemes are illustrated in Figure D.1 and D.6. Let us first consider 8-level Star QAM, which is also referred to as 2-level QPSK [170]. In Figure D.1(a), a is the radius of the inner ring, while $a\beta$ is the radius of the outer ring. The ring ratio is given by $a\beta/a = \beta$. The three bits, namely b_1, b_2 and b_3, are assigned as shown in Figure D.1(a), representing Gray coding for each ring using the bits $b_1 b_2$. The third bit, namely b_3 indicates, which ring of the constellation is encountered. The average symbol power is given as:

$$E_s = \frac{4a^2 + 4a^2\beta^2}{8} = \frac{1}{2}a^2(1+\beta^2)\,. \tag{D.1}$$

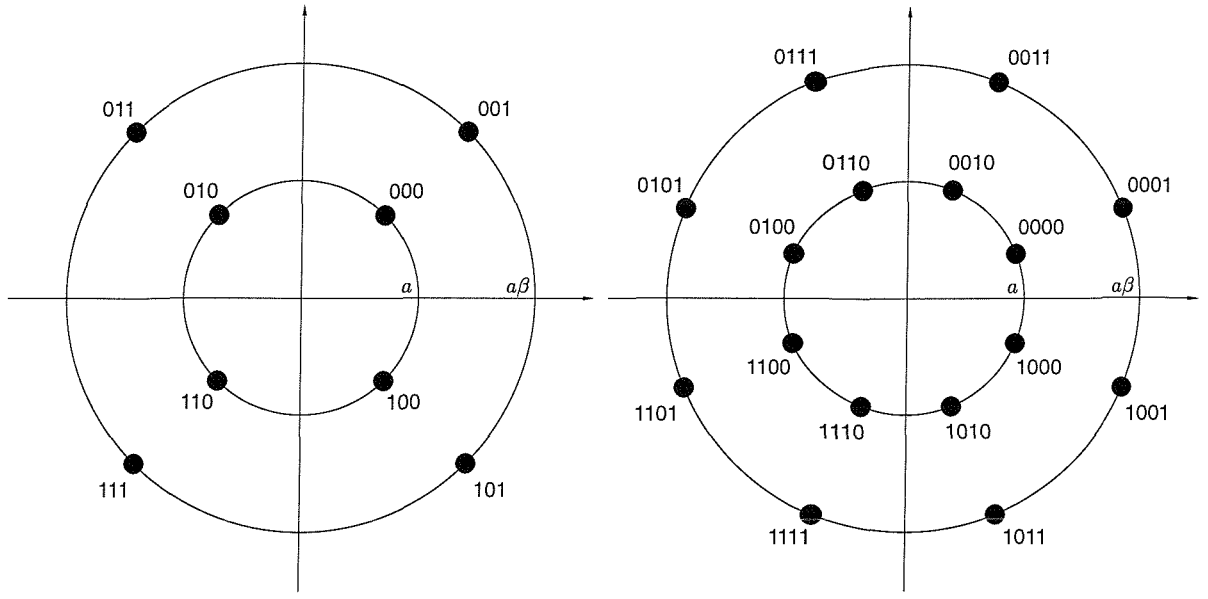

(a) 8-level Star QAM

(b) 16-level Star QAM

Figure D.1: Type-I constellations of Star QAM using two constellation rings

In order to nomalise the constellations so that the average symbol power becomes unity, a should be given as:

$$a = \sqrt{\frac{2}{1+\beta^2}} \,. \tag{D.2}$$

In terms of the signal space, the modulation scheme with respect to b_3 is an Amplitude Shift Keying (ASK) scheme. The decision rule related to bit b_3 is specified in Figure D.2(a). The BER of bit b_3 can be expressed as:

$$\begin{aligned} P_{b_3} &= \frac{1}{2}\left[Q\left(\frac{a(\beta-1)}{2}\sqrt{2\gamma}\right) + Q\left(\frac{a(\beta+3)}{2}\sqrt{2\gamma}\right)\right] \\ &\quad + \frac{1}{2}\left[Q\left(\frac{a(\beta-1)}{2}\sqrt{2\gamma}\right) - Q\left(a(\beta+1)\sqrt{2\gamma}\right)\right] \qquad \text{(D.3)} \\ &\simeq Q\left(\frac{a(\beta-1)}{2}\sqrt{2\gamma}\right) \qquad \text{(D.4)} \\ &= Q\left(\sqrt{\frac{(\beta-1)^2}{1+\beta^2}\gamma}\right), \qquad \text{(D.5)} \end{aligned}$$

where the Gaussian Q-function is defined as $Q(x) = \frac{1}{\sqrt{2\pi}}\int_x^\infty e^{-y^2/2}dy$ and γ is the SNR per symbol. Since bits b_1 and b_2 corresponds to Gray coded QPSK signals, their BER can be expressed as:

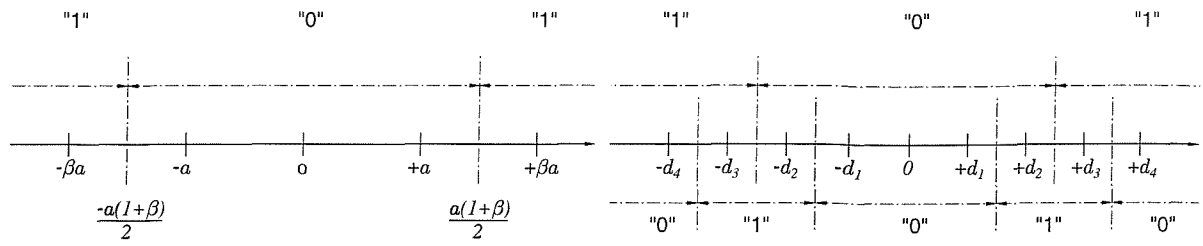

(a) 8- and 16-level Star QAM (b) 32- and 64-level Star QAM

Figure D.2: Magnitude-bit decision regions for various Type-I Star QAM constellations

$$P_{b_1} = P_{b_2} \simeq \frac{1}{2}Q\left(\frac{a}{\sqrt{2}}\sqrt{2\gamma}\right) + \frac{1}{2}Q\left(\frac{a\beta}{\sqrt{2}}\sqrt{2\gamma}\right) \tag{D.6}$$

$$= \frac{1}{2}Q\left(\sqrt{\frac{2}{1+\beta^2}\gamma}\right) + \frac{1}{2}Q\left(\sqrt{\frac{2\beta^2}{1+\beta^2}\gamma}\right) . \tag{D.7}$$

Hence, the average BER of an 8-level Star QAM scheme communicating over an AWGN channel can be expressed as:

$$P_8 = \frac{1}{3}P_{b_1} + \frac{1}{3}P_{b_2} + \frac{1}{3}P_{b_3} \tag{D.8}$$

$$\simeq \frac{1}{3}\left[Q\left(\sqrt{\frac{2}{1+\beta^2}\gamma}\right) + Q\left(\sqrt{\frac{2\beta^2}{1+\beta^2}\gamma}\right) + Q\left(\sqrt{\frac{(\beta-1)^2}{1+\beta^2}\gamma}\right)\right] . \tag{D.9}$$

The BER of (D.9) is plotted in Figure D.3(a) as a function of the ring ratio β for various values of the SNR per symbol γ. We can observe that the BER of 8-level Star QAM reaches its minimum, when the ring ratio is $\beta \simeq 2.4$. This is not surprising, considering that the ring ratio should be $\beta = 1 + \sqrt{2}$ in order to make the Euclidean distances between an inner ring constellation point and its three adjacent constellation points the same. However, the optimum ring ratio β_{opt}, where the BER reaches its minimum is SNR dependent. The optimum ring ratio versus the SNR per symbol is plotted in Figure D.3(b). It can be observed that when the SNR is lower than 8dB, the optimum ring ratio increases sharply. Since the corresponding BER improvement was however less than 0.1dB even at SNRs near 0dB, the fixed ring ratio of $\beta = 1 + \sqrt{2}$ can be used for all SNR values. Figure D.4(a) compares the BER of 8-level Star QAM and 8-PSK. Observe that 8-level Star QAM exhibits an approximately 1dB SNR performance gain, when the SNR is below 2dB, but above this SNR the SNR gain becomes marginal..

Let us now consider 16-level Star QAM. The corresponding phasor constellation is given in Figure D.1(b). Since the average symbol power is the same as that of 8-level Star QAM, Equation D.2 can be used for determining a. The BER analysis for the fourth bit, namely for b_4 is exactly the same as that of 8-level Star QAM and the corresponding value of P_{b_4} is given in (D.5). Since the first three bits, namely b_1, b_2 and b_3, are 8-PSK modulated, their BER can be expressed as:

$$P_{b_1} = P_{b_2} = P_{b_3} = \frac{1}{2}P_{8PSK}(a^2\gamma) + \frac{1}{2}P_{8PSK}(a^2\beta^2\gamma) . \tag{D.10}$$

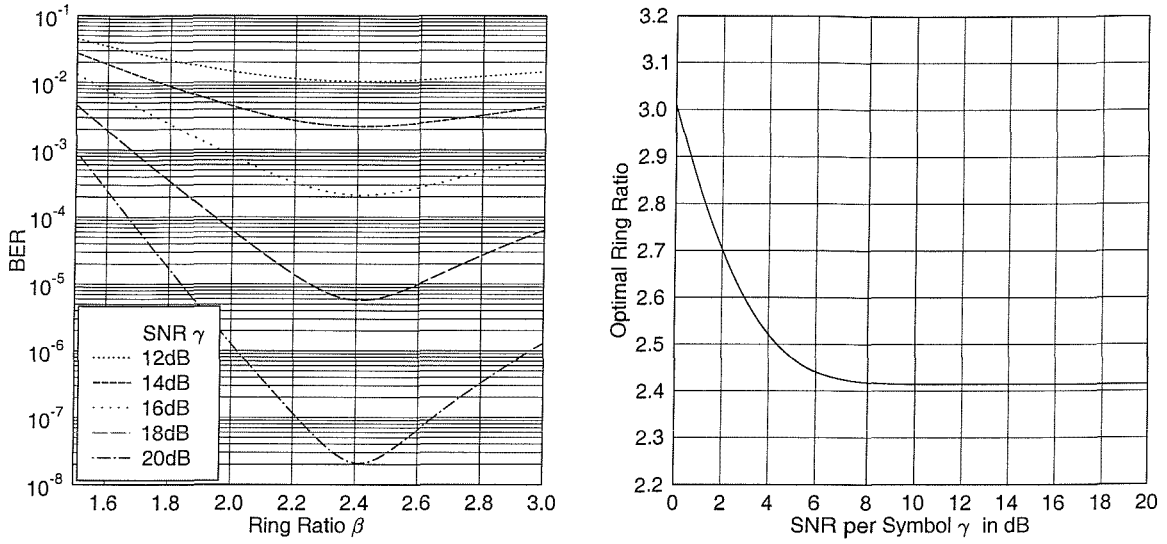

(a) Effect of ring ratio β

(b) Optimum ring ratio β_{opt}

Figure D.3: BER of Gray-mapped 8-level Star QAM for transmission over AWGN channels

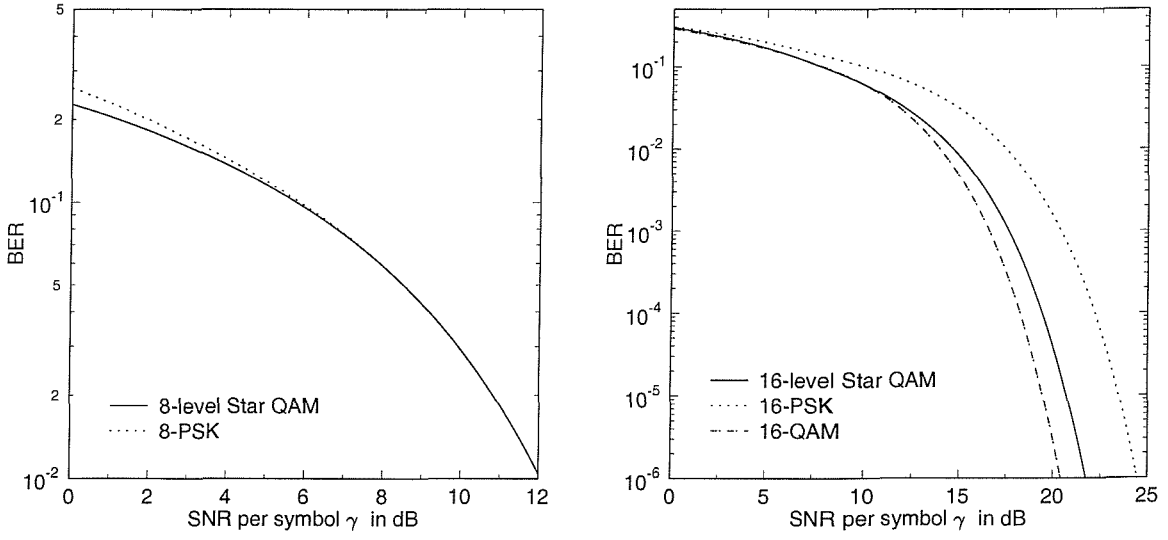

(a) BER of 8-level Star QAM and 8-PSK

(b) BER of 16-ary Schemes

Figure D.4: BER comparison of 8-ary and 16-ary modulation schemes for transmission over AWGN channels

Lu, Letaief, Chuang and *Liou* found an accurate approximation of the BER of Gray-coded MPSK, which is given by [131]:

$$P_{MPSK} \simeq \frac{2}{\log_2 M} \sum_{i=1}^{2} Q\left(\sqrt{2\sin^2\left(\frac{2i-1}{M}\pi\right)\gamma}\right), \tag{D.11}$$

where γ is the SNR per symbol. Hence, the BER of (D.10) can be expressed as:

$$\begin{aligned} P_{b_1} &= P_{b_2} = P_{b_3} \qquad (D.12)\\ &\simeq \frac{1}{3}\left[Q\left(\sqrt{\frac{4\sin^2(\pi/8)}{1+\beta^2}\gamma}\right) + Q\left(\sqrt{\frac{4\sin^2(3\pi/8)}{1+\beta^2}\gamma},\right)\right] \\ &\quad + \frac{1}{3}\left[Q\left(\sqrt{\frac{4\beta^2\sin^2(\pi/8)}{1+\beta^2}\gamma}\right) + Q\left(\sqrt{\frac{4\beta^2\sin^2(3\pi/8)}{1+\beta^2}\gamma}\right)\right]. \qquad (D.13)\end{aligned}$$

Now, the average BER of a 16-level Star QAM scheme for transmission over AWGN channel can be expressed as:

$$\begin{aligned} P_{16} &= \frac{1}{4}P_{b_1} + \frac{1}{4}P_{b_2} + \frac{1}{4}P_{b_3} + \frac{1}{4}P_{b_4} \qquad (D.14)\\ &\simeq \frac{1}{4}\left[Q\left(\sqrt{\frac{4\sin^2(\pi/8)}{1+\beta^2}\gamma}\right) + Q\left(\sqrt{\frac{4\sin^2(3\pi/8)}{1+\beta^2}\gamma},\right) + Q\left(\sqrt{\frac{4\beta^2\sin^2(\pi/8)}{1+\beta^2}\gamma}\right)\right. \\ &\quad \left. + Q\left(\sqrt{\frac{4\beta^2\sin^2(3\pi/8)}{1+\beta^2}\gamma}\right) + Q\left(\sqrt{\frac{(\beta-1)^2}{1+\beta^2}\gamma}\right)\right]. \qquad (D.15)\end{aligned}$$

The BER of (D.15) is plotted in Figure D.5(a) as a function of the ring ratio β for the various values of the SNR per symbol γ. We can observe that the ring ratio of $\beta \simeq 1.8$ minimises the BER of 16-level Star QAM, when communicating over AWGN channels [171]. This is also expected, since the ring ratio should be $\beta = 1 + 2\cos(3\pi/8) = 1.7654$ in order to render the Euclidean distances between an inner-ring constellation point and its three adjacent constellation points the same. The actual optimum ring ratio β_{opt}, where the BER reaches its minimum is plotted in Figure D.5(b). As for 8-level Star QAM, even though the optimum ratio is SNR dependent, the difference between the BER corresponding to the optimum ring ratio and that corresponding to the constant ring ratio of $\beta = 1+2\cos(3\pi/8)$ is negligible. Figure D.4(b) compares the BER of 16-level Star QAM, 16-PSK and 16-level Square QAM. We found that the BER performance of 16-level Star QAM is inferior to that of 16-level Square QAM. Viewing the corresponding performance from the perspective of the required SNR per symbol, the former requires an approxmately 1.3dB high SNR for maintaining the BER of 10^{-6}. By contrast, it requires a 2.7dB lower symbol-SNR, than 16-PSK.

Having considered the family of twin-ring constellations, let us focus our attention on two four-ring constellations. The Type-I constellations of 32-level and 64-level Star QAM scheme are depicted in Figure D.6. The last two bits of a symbol are Gray coded in the 'radial direction' and they are four-level

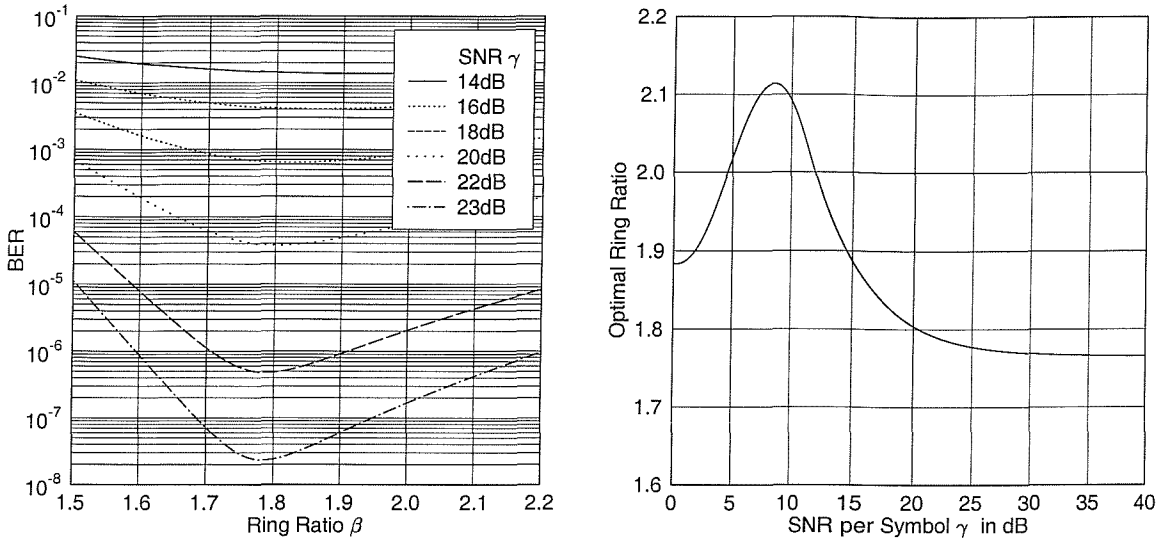

(a) Effect of ring ratio β

(b) Optimum ring ratio β_{opt}

Figure D.5: BER of Gray mapped 16-level Star QAM for transmission over AWGN channels

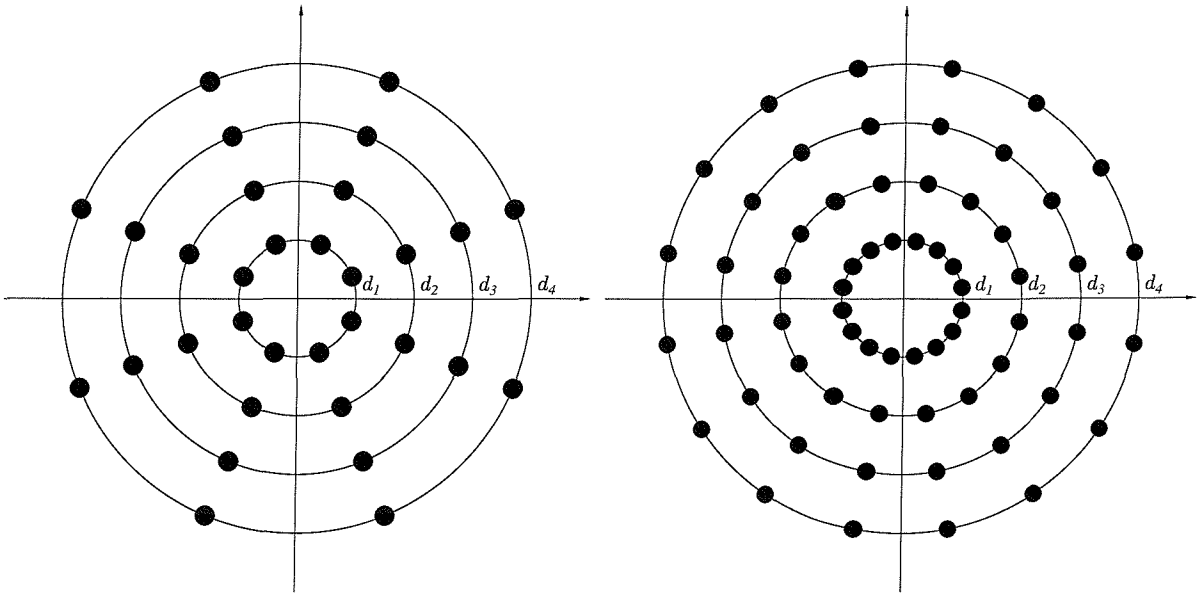

(a) 32-level Star QAM

(b) 64-level Star QAM

Figure D.6: Type-I constellations of Star QAM constellaions having four rings

ASK modulated. Let us assume that the Gray coding scheme for the bits "b_4b_5" of 32-level Star QAM in the 'radial direction' is given as "00", "01", "11" and "10", when viewing it from the inner most ring to the outer rings. The decision regions of these bits were illustrated in Figure D.2(b). The remaining bits are also Gray coded along each of the four rings and PSK modulated. Let us denote the radius of each ring as d_1, $d_2 = d_1\,\beta_1$, $d_3 = d_1\,\beta_2$ and $d_4 = d_1\,\beta_3$, where β_1, β_2 and β_3 are the corresponding ring ratios of each ring. Since the average power per symbol E_s is given as:

$$E_s = \frac{d_1^2 + d_2^2 + d_3^2 + d_4^2}{4} = \frac{d_1^2}{4}(1 + \beta_1^2 + \beta_2^2 + \beta_3^2)\,, \tag{D.16}$$

the value of d_1 required for normalising the average power to unity can be expressed as:

$$d_1 = \sqrt{\frac{4}{1 + \beta_1^2 + \beta_2^2 + \beta_3^2}}\,. \tag{D.17}$$

Inspecting Figure D.2(b), the BER of the fourth bit of 32-level Star QAM can be formulated as:

$$\begin{aligned} P_{b_4} = &\frac{1}{4}\left[Q\left(\frac{d_2 + d_3 - 2d_1}{2}\sqrt{2\gamma}\right) + Q\left(\frac{d_2 + d_3 + 2d_1}{2}\sqrt{2\gamma}\right)\right] \\ &+ \frac{1}{4}\left[Q\left(\frac{d_3 - d_2}{2}\sqrt{2\gamma}\right) + Q\left(\frac{d_3 + 3d_2}{2}\sqrt{2\gamma}\right)\right] \\ &+ \frac{1}{4}\left[Q\left(\frac{d_3 - d_2}{2}\sqrt{2\gamma}\right) - Q\left(\frac{3d_3 + d_2}{2}\sqrt{2\gamma}\right)\right] \\ &+ \frac{1}{4}\left[Q\left(\frac{2d_4 - d_2 - d_3}{2}\sqrt{2\gamma}\right) - Q\left(\frac{2d_4 + d_2 + d_3}{2}\sqrt{2\gamma}\right)\right] \end{aligned} \tag{D.18}$$

$$\begin{aligned} \simeq &\frac{1}{4}\left[Q\left(\sqrt{\frac{2(\beta_1 + \beta_2 - 2)^2}{1 + \beta_1^2 + \beta_2^2 + \beta_3^2}\gamma}\right) + 2\,Q\left(\sqrt{\frac{2(\beta_2 - \beta_1)^2}{1 + \beta_1^2 + \beta_2^2 + \beta_3^2}\gamma}\right)\right. \\ &\left. + Q\left(\sqrt{\frac{2(2\beta_3 - \beta_1 - \beta_2)^2}{1 + \beta_1^2 + \beta_2^2 + \beta_3^2}\gamma}\right)\right]\,. \end{aligned} \tag{D.19}$$

The decision regions depicted in the lower part of Figure D.2(b) are valid for the fifth bit, namely b_5. The

BER of b_5 can be expressed as:

$$\begin{aligned}P_{b_5} = \frac{1}{4}\Bigg[&Q\left(\frac{d_2-d_1}{2}\sqrt{2\gamma}\right)+Q\left(\frac{d_2+3\,d_1}{2}\sqrt{2\gamma}\right)\\&-Q\left(\frac{d_3+d_4-2\,d_1}{2}\sqrt{2\gamma}\right)-Q\left(\frac{d_3+d_4+2\,d_1}{2}\sqrt{2\gamma}\right)\Bigg]\\+\frac{1}{4}\Bigg[&Q\left(\frac{d_2-d_1}{2}\sqrt{2\gamma}\right)+Q\left(\frac{d_3+d_4-2\,d_2}{2}\sqrt{2\gamma}\right)\\&-Q\left(\frac{d_1+3\,d_2}{2}\sqrt{2\gamma}\right)+Q\left(\frac{d_3+d_4+2\,d_2}{2}\sqrt{2\gamma}\right)\Bigg]\\+\frac{1}{4}\Bigg[&Q\left(\frac{2\,d_3-d_1-d_2}{2}\sqrt{2\gamma}\right)+Q\left(\frac{d_4-d_3}{2}\sqrt{2\gamma}\right)\\&-Q\left(\frac{d_1+d_2+2\,d_3}{2}\sqrt{2\gamma}\right)+Q\left(\frac{3\,d_3+d_4}{2}\sqrt{2\gamma}\right)\Bigg]\\+\frac{1}{4}\Bigg[&Q\left(\frac{d_4-d_3}{2}\sqrt{2\gamma}\right)-Q\left(\frac{2\,d_4-d_1-d_2}{2}\sqrt{2\gamma}\right)\\&+Q\left(\frac{d_1+d_2+2\,d_4}{2}\sqrt{2\gamma}\right)-Q\left(\frac{d_3+3\,d_4}{2}\sqrt{2\gamma}\right)\Bigg]\,.\end{aligned}\tag{D.20}$$

The expression of the BER P_{b_5} can be accurately approximated as ;

$$\begin{aligned}P_{b_5} \simeq \frac{1}{4}\Bigg[&2\,Q\left(\sqrt{\frac{2(\beta_1-1)^2}{1+\beta_1^2+\beta_2^2+\beta_3^2}\,\gamma}\right)+Q\left(\sqrt{\frac{2(\beta_2+\beta_3-2\,\beta_1)^2}{1+\beta_1^2+\beta_2^2+\beta_3^2}\,\gamma}\right)\\&+Q\left(\sqrt{\frac{2(2\,\beta_2-1-\beta_1)^2}{1+\beta_1^2+\beta_2^2+\beta_3^2}\,\gamma}\right)+2\,Q\left(\sqrt{\frac{2(\beta_3-\beta_2)^2}{1+\beta_1^2+\beta_2^2+\beta_3^2}\,\gamma}\right)\Bigg]\,.\end{aligned}\tag{D.21}$$

Let us now find the BER of the PSK modulated bits b_1, b_2 and b_3. Since they are 8-PSK modulated, the BER can be expressed using the results of [131] as:

$$P_{b_1} = P_{b_2} = P_{b_3} = \frac{1}{4}P_{8PSK}(d_1^2\gamma)+\frac{1}{4}P_{8PSK}(d_2^2\gamma)+\frac{1}{4}P_{8PSK}(d_3^2\gamma)+\frac{1}{4}P_{8PSK}(d_4^2\gamma)\tag{D.22}$$

$$\begin{aligned}\simeq&\frac{1}{6}\left[Q\left(\sqrt{\frac{8\sin^2(\pi/8)}{1+\beta_1^2+\beta_2^2+\beta_3^2}\gamma}\right)+Q\left(\sqrt{\frac{8\sin^2(3\pi/8)}{1+\beta_1^2+\beta_2^2+\beta_3^2}\gamma}\right)\right]\\&+\frac{1}{6}\left[Q\left(\sqrt{\frac{8\,\beta_1^2\sin^2(\pi/8)}{1+\beta_1^2+\beta_2^2+\beta_3^2}\gamma}\right)+Q\left(\sqrt{\frac{8\,\beta_1^2\sin^2(3\pi/8)}{1+\beta_1^2+\beta_2^2+\beta_3^2}\gamma}\right)\right]\\&+\frac{1}{6}\left[Q\left(\sqrt{\frac{8\,\beta_2^2\sin^2(\pi/8)}{1+\beta_1^2+\beta_2^2+\beta_3^2}\gamma}\right)+Q\left(\sqrt{\frac{8\,\beta_2^2\sin^2(3\pi/8)}{1+\beta_1^2+\beta_2^2+\beta_3^2}\gamma}\right)\right]\\&+\frac{1}{6}\left[Q\left(\sqrt{\frac{8\,\beta_3^2\sin^2(\pi/8)}{1+\beta_1^2+\beta_2^2+\beta_3^2}\gamma}\right)+Q\left(\sqrt{\frac{8\,\beta_3^2\sin^2(3\pi/8)}{1+\beta_1^2+\beta_2^2+\beta_3^2}\gamma}\right)\right]\,.\end{aligned}\tag{D.23}$$

Hence, the BER of 32-level Star QAM can be expressed as:

$$P_{32} = \frac{1}{5}(3P_{b_1}+P_{b_4}+P_{b_5})\,,\tag{D.24}$$

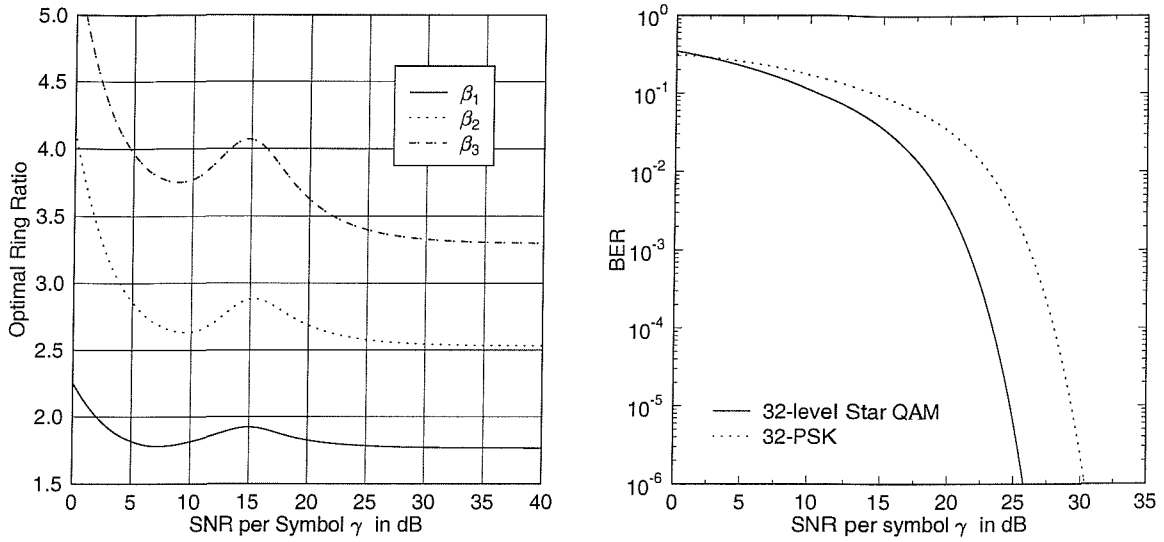

(a) Optimum ring ratios

(b) BER of 32-level Star QAM and 32-PSK

Figure D.7: BER of 32 Star QAM over AWGN channel

where P_{b_1}, P_{b_4} and P_{b_5} are given in Equations (D.23), (D.19) and (D.21), respectively. The optimum ring ratios of 32-level Star QAM are depicted in Figure D.7(a). The optimum ring ratios converge to $\beta_1 = 1.77$, $\beta_2 = 2.541$ and $\beta_3 = 3.318$. Note that the first optimum ring ratio is the same as the optimum ring ratio of 16-level Star QAM and the corresponding distances between the second, the third and the fourth rings are approximately equal, as one would expect in an effort to maintain an identical distance amongst the constellations points. Figure D.7(b) compares the BER of 32-level Star QAM and 32-PSK. We found that the SNR gain of 32-level Star QAM over 32-PSK is 4.6dB at a BER of 10^{-6}.

The BER of 64-level Star QAM can be obtained using the same procedure employed for determing the BER of 32-level Star QAM, considering that now the bits b_1, b_2, b_3 and b_4 are 16-PSK modulated on each ring. The BER of the last two bits, P_{b_5} and P_{b_6} are the same as those given in (D.19) and (D.21), respectively. On the other hand, the BER of the 16-PSK modulated bits of 64-level Star QAM can be

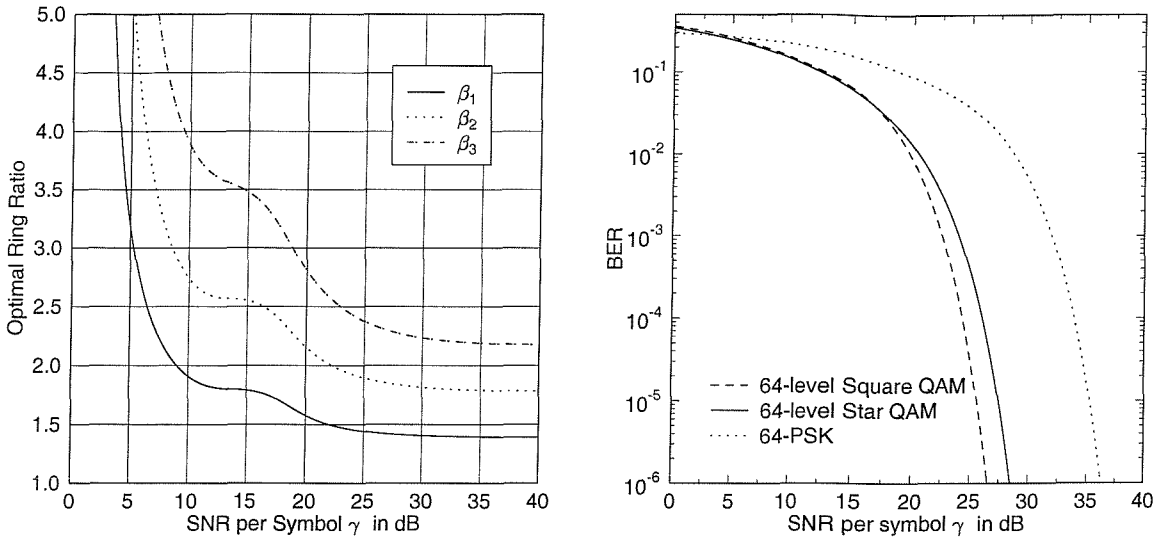

(a) Optimum ring ratios

(b) BER of 64-level Star QAM, 64-level Sqauare QAM and 64-PSK

Figure D.8: BER of 64-level Star QAM for transmission over AWGN channels

expressed as:

$$
\begin{aligned}
P_{b_1} =& P_{b_2} = P_{b_3} = P_{b_4} \\
=& \frac{1}{4} P_{16PSK}(d_1^2\gamma) + \frac{1}{4} P_{16PSK}(d_2^2\gamma) + \frac{1}{4} P_{16PSK}(d_3^2\gamma) + \frac{1}{4} P_{16PSK}(d_4^2\gamma) \qquad \text{(D.25)} \\
\simeq& \frac{1}{8}\left[Q\left(\sqrt{\frac{8\sin^2(\pi/16)}{1+\beta_1^2+\beta_2^2+\beta_3^2}\gamma}\right) + Q\left(\sqrt{\frac{8\sin^2(3\pi/16)}{1+\beta_1^2+\beta_2^2+\beta_3^2}\gamma}\right)\right] \\
&+ \frac{1}{8}\left[Q\left(\sqrt{\frac{8\beta_1^2\sin^2(\pi/16)}{1+\beta_1^2+\beta_2^2+\beta_3^2}\gamma}\right) + Q\left(\sqrt{\frac{8\beta_1^2\sin^2(3\pi/16)}{1+\beta_1^2+\beta_2^2+\beta_3^2}\gamma}\right)\right] \\
&+ \frac{1}{8}\left[Q\left(\sqrt{\frac{8\beta_2^2\sin^2(\pi/16)}{1+\beta_1^2+\beta_2^2+\beta_3^2}\gamma}\right) + Q\left(\sqrt{\frac{8\beta_2^2\sin^2(3\pi/16)}{1+\beta_1^2+\beta_2^2+\beta_3^2}\gamma}\right)\right] \\
&+ \frac{1}{8}\left[Q\left(\sqrt{\frac{8\beta_3^2\sin^2(\pi/16)}{1+\beta_1^2+\beta_2^2+\beta_3^2}\gamma}\right) + Q\left(\sqrt{\frac{8\beta_3^2\sin^2(3\pi/16)}{1+\beta_1^2+\beta_2^2+\beta_3^2}\gamma}\right)\right] . \qquad \text{(D.26)}
\end{aligned}
$$

Hence, the average BER of 64-level Star QAM can be expressed as:

$$P_{64} = \frac{1}{6}(4P_{b_1} + P_{b_5} + P_{b_6}) , \qquad \text{(D.27)}$$

where P_{b_1} is given in (D.26), where P_{b_5} and P_{b_6} are given in (D.19) and (D.21), respectively. The optimum ring ratios of 64-level Star QAM are depicted in Figure D.8(a). The optimum ring ratios converge to $\beta_1 = 1.4$, $\beta_2 = 1.81$ and $\beta_3 = 2.23$. It was observed that the SNR difference between the

optimised BER and that employing the asymptotic ring ratio is at most 1dB in the SNR range of 5dB to 15dB. Figure D.8(b) compares the BER of 64-level Star QAM, 64-level Square QAM and 64-PSK. We found that the SNR gain of 64-level Star QAM over 64-PSK is 7.7dB at the BER of 10^{-6}. The 64-level Square QAM arrangement is the most power-efficient scheme, which exhibits 2dB SNR gain over 64-level Star QAM at the BER of 10^{-6}.

Bibliography

[1] N. Yee, J. P. Linnartz, and G. Fettweis, "Multicarrier CDMA in indoor wireless radio networks," in *Proc. PIMRC'93*, pp. 109–113, 1993.

[2] K. Fazel and L. Papke, "On the performance of convolutionally-coded CDMA/OFDM for mobile communication system," in *Proc. PIMRC'93*, pp. 468–472, 1993.

[3] R. A. Scholtz, "The origins of spread spectrum communications," *IEEE Transactions on Communications*, vol. 30, no. 5, pp. 822–854, 1982.

[4] G. R. Cooper and R. W. Nettleton, "A spread-spectrum technique for high-capacity mobile communications," *IEEE Transactions on Vehicular Technology*, vol. 27, pp. 264–275, November 1978.

[5] O. C. Yue, "Spread spectrum mobile radio, 1977-1982," *IEEE Transactions on Vehicular Technology*, vol. 32, pp. 98–105, February 1983.

[6] M. K. Simon, J. K. Omura, R. A. Scholtz, and B. K. Levitt, *Spread Spectrum Communications Handbook*. New York, USA: McGraw-Hill, 1994.

[7] Y. C. Yoon, R. Kohno, and H. Imai, "A SSMA system with cochannel interference cancellation with multipath fading channels," *IEEE Journal on Selected Areas in Communications*, vol. 11, pp. 1067–1075, September 1993.

[8] K. S. Gilhousen, I. M. Jacobs, R. Padovani, A. J. Viterbi, L. A. Weaver Jr., and C. E. Wheatley III, "On the capacity of a cellular CDMA system," *IEEE Transactions on Vehicular Technology*, vol. 40, pp. 303–312, May 1991.

[9] P. Patel and J. Holtzman, "Analysis of a simple successive interference cancellation scheme in a DS/CDMA system," *IEEE Journal on Selected Areas in Communications*, vol. 12, pp. 796–807, June 1994.

[10] R. Lupas and S. Verdú, "Linear multiuser detectors for synchronous code divison multiple access channels," *IEEE Transactions on Information Theory*, vol. 35, pp. 123–136, January 1989.

[11] P. Jung and J. Blanz, "Joint detection with coherent receiver antenna diversity in CDMA mobile radio systems," *IEEE Transactions on Vehicular Technology*, vol. 44, pp. 76–88, February 1995.

[12] J. S. Thompson, P. M. Grant, and B. Mulgrew, "Smart antenna arrays for CDMA systems," *IEEE Personal Communications Magazine*, vol. 3, pp. 16–25, October 1996.

[13] L. Hanzo, W. T. Webb, and T. Keller, *Single- and Multi-carrier Quadrature Amplitude Modulation.* New York, USA: IEEE Press-John Wiley, April 2000.

[14] R. Steele and L. Hanzo, eds., *Mobile Radio Communications.* New York, USA: IEEE Press - John Wiley & Sons, 2nd ed., 1999.

[15] K. Feher, *Wireless digital communications: Modulation and spread spectrum.* Englewood Cliffs, NJ: Prentice-Hall, 1995.

[16] R. Kohno, R. Meidan, and L. B. Milstein, "Spread spectrum access methods for wireless communication," *IEEE Communications Magazine*, vol. 33, pp. 58–67, January 1995.

[17] R. Price and E. Green Jr., "A communication technique for multipath channels," *Proceedings of the IRE*, vol. 46, pp. 555–570, March 1958.

[18] U. Grob, A. L. Welti, E. Zollinger, R. Kung, and H. Kaufmann, "Microcellular direct-sequence spread-spectrum radio system using n-path rake receiver," *IEEE Journal on Selected Areas in Communications*, vol. 8, no. 5, pp. 772–780, 1990.

[19] P. W. Baier, "A critical review of CDMA," in *Proceedings of the IEEE Vehicular Technology Conference (VTC)*, (Atlanta, GA, USA), pp. 6–10, 28 April–1 May 1996.

[20] Telcomm. Industry Association (TIA), Washington, DC, USA, *Mobile station — Base station compatibility standard for dual-mode wideband spread spectrum cellular system, EIA/TIA Interim Standard IS-95*, July 1993.

[21] A. J. Viterbi, A. M. Viterbi, and E. Zehavi, "Performance of power-controlled wideband terrestrial digital communication," *IEEE Transactions on Communications*, vol. 41, no. 4, pp. 559–569, 1993.

[22] F. Simpson and J. M. Holtzman, "Direct sequence CDMA power control, interleaving, and coding," *IEEE Journal on Selected Areas in Communications*, vol. 11, pp. 1085–1095, September 1993.

[23] S. Ariyavisitakul and L. F. Chang, "Signal and interference statistics of a CDMA system with feedback power control," *IEEE Transactions on Communications*, vol. 41, pp. 1626–1634, November 1993.

[24] S. Ariyavisitakul, "Signal and interference statistics of a CDMA system with feedback power control - Part II," *IEEE Transactions on Communications*, vol. 42, no. 2/3/4, pp. 597–605, 1994.

[25] J. G. Proakis, *Digital Communications.* Mc-Graw Hill International Editions, 3rd ed., 1995.

[26] R. W. Chang, "Synthesis of band-limited orthogonal signals for multichannel data transmission," *Bell Systems Technical Journal*, vol. 46, pp. 1775–1796, December 1966.

[27] B. R. Saltzberg, "Performance of an efficient parallel data transmission system," *IEEE Transactions on Communication Technology*, pp. 805–813, December 1967.

[28] R. W. Chang and R. A. Gibby, "A theoretical study of performance of an orthogonal multiplexing data transmission scheme," *IEEE Transactions on Communication Technology*, vol. 16, no. 4, pp. 529–540, 1968.

[29] L. J. Cimini Jr., "Analysis and simulation of a digital mobile channel using orthogonal frequency division multiplexing," *IEEE Transactions on Communications*, vol. 33, pp. 665–675, July 1985.

[30] S. B. Weinstein and P. M. Ebert, "Data transmission by frequency division multiplexing using the discrete fourier transform," *IEEE Transactions on Communication Technology*, vol. COM–19, pp. 628–634, October 1971.

[31] A. E. Jones, T. A. Wilkinson, and S. K. Barton, "Block coding scheme for reduction of peak to mean envelope power ratio of multicarrier transmission schemes," *Electronics Letters*, vol. 30, pp. 2098–2099, December 1994.

[32] P. V. Eetvelt, S. J. Shepherd, and S. K. Barton, "The distribution of peak factor in QPSK multicarrier modulation," *Wireless Personal Communications*, vol. 2, pp. 87–96, 1995.

[33] T. Pollet, M. V. Bladel, and M. Moeneclaey, "BER sensitivity of OFDM systems to carrier frequency offset and wiener phase noise," *IEEE Transactions on Communications*, vol. 43, pp. 191–193, February/March/April 1995.

[34] H. Sari, G. Karam, and I. Jeanclaude, "Transmission techniques for digital terrestrial TV broadcasting," *IEEE Communications Magazine*, pp. 100–109, February 1995.

[35] A. Chouly, A. Brajal, and S. Jourdan, "Orthogonal multicarrier techniques applied to direct sequence spread spectrum CDMA systems," in *Proceedings of the IEEE Global Telecommunications Conference 1993*, (Houston, TX, USA), pp. 1723–1728, 29 November – 2 December 1993.

[36] V. M. DaSilva and E. S. Sousa, "Performance of orthogonal CDMA codes for quasi-synchronous communication systems," in *Proceedings of IEEE ICUPC 1993*, (Ottawa, Canada), pp. 995–999, October 1993.

[37] L. Vandendorpe, "Multitone direct sequence CDMA system in an indoor wireless environment," in *Proceedings of IEEE SCVT 1993*, (Delft, The Netherlands), pp. 4.1:1–8, October 1993.

[38] R. Prasad and S. Hara, "Overview of multicarrier CDMA," *IEEE Communications Magazine*, pp. 126–133, December 1997.

[39] R. Prasad and S. Hara, "Overview of multi-carrier CDMA," in *Proceedings of the IEEE International Symposium on Spread Spectrum Techniques and Applications (ISSSTA)*, (Mainz, Germany), pp. 107–114, 22–25 September 1996.

[40] D. I. Scott, P. M. Grant, S. McLaughlin, G. J. R. Povey, and D. G. M. Cruickshank, "Research in reconfigurable terminal design for mobile and personal communications," tech. rep., Department of Electrical Engineering, The University of Edinburgh, March 1997.

[41] N. Yee and J. P. Linnartz, "MICRO 93-101: Multi-carrier CDMA in an indoor wireless radio channel," tech. rep., University of California at Berkeley, 1994.

[42] T. Ojanperä and R. Prasad, "An overview of air interface multiple access for IMT-2000/UMTS," *IEEE Communications Magazine*, vol. 36, pp. 82–95, September 1998.

[43] B. J. Choi, E. L. Kuan, and L. Hanzo, "Crest–factor study of MC-CDMA and OFDM," in *Proc. VTC'99 (Fall)*, vol. 1, (Amsterdam, Netherlands), pp. 233–237, IEEE, 19–22 September 1999.

[44] B. J. Choi, M. Münster, L. L. Yang, and L. Hanzo, "Performance of Rake receiver assisted adaptive-modulation based CDMA over frequency selective slow Rayleigh fading channel," *Electronics Letters*, vol. 37, pp. 247–249, February 2001.

[45] B. J. Choi and L. Hanzo, "Performance analysis of Rake receiver assisted adaptive QAM using antenna diversity over frequency selective Rayleigh channels," *Submitted to IEEE Journal on Selected Areas in Communications*, January 2001.

[46] B. J. Choi, T. H. Liew, and L. Hanzo, "Concatenated space-time block coded and turbo coded symbol-by-symbol adaptive OFDM and multi-carrier CDMA systems," in *Proceedings of IEEE VTC 2001-Spring*, p. P.528, IEEE, May 2001.

[47] T. H. Liew, B. J. Choi, and L. Hanzo, "Space-time block coded and space-time trellis coded OFDM," in *Proceedings of IEEE VTC 2001-Spring*, p. P.533, IEEE, May 2001.

[48] B. J. Choi and L. Hanzo, "Optimum mode-switching levels for adaptive modulation systems," in *Submitted to IEEE GLOBECOM 2001*, 2001.

[49] B. J. Choi, M. Münster, L. L. Yang, and L. Hanzo, "Performance of Rake receiver assisted adaptive-modulation based CDMA over frequency selective slow Rayleigh fading channel," in *Submitted to IEEE VTC 2001-Fall*, IEEE, 2001.

[50] R. L. Peterson, R. E. Ziemer, and D. E. Borth, *Introduction to Spread Spectrum Communications*. Prentice Hall International Editions, 1995.

[51] S. W. Golomb, *Shift Register Sequences*. Holden-Day, 1967.

[52] R. Gold, "Optimal binary sequences for spread spectrum multiplexing," *IEEE Transactions on Information Theory*, vol. 13, pp. 619–621, October 1967.

[53] F. Adachi, K. Ohno, A. Higashi, T. Dohi, and Y. Okumura, "Coherent multicode DS-CDMA mobile Radio Access," *IEICE Transactions on Communications*, vol. E79-B, pp. 1316–1324, September 1996.

[54] S. C. Bang, "ETRI wideband CDMA system for IMT-2000," in *Presentation material in 1st IMT-2000 Workshop*, (Seoul, Korea), pp. II–1–1 – II–1–21, KIET, August 1997.

[55] J. Bingham, "Multicarrier modulation for data transmission: an idea whose time has come," *IEEE Communications Magazine*, pp. 5–14, May 1990.

[56] H. Rohling, K. Brüninghaus, and R. Grünheid, "Comparison of multiple access schemes for an OFDM downlink system," in *Multi-Carrier Spread-Spectrum* (K. Fazel and G. P. Fettweis, eds.), pp. 23–30, Kluwer Academic Publishers, 1997.

[57] M. Schnell and S. Kaiser, "Diversity considerations forMC-CDMA systems in mobile communications," in *Proceedings of IEEE ISSSTA 1996*, pp. 131–135, 1996.

[58] W. H. Press, S. A. Teukolsky, W. T. Vetterling, and B. P. Flannery, *Numerical Recipies in C*. Cambridge University Press, 1992.

[59] P. Jung, F. Berens, and J. Plechinger, "Joint detection for multicarrier CDMA mobile radio systems - Part II: Detection techniques," in *Proceedings of IEEE ISSSTA 1996*, vol. 3, (Mainz, Germany), pp. 996–1000, September 1996.

[60] E. L. Kuan, *Burst-by-burst Adaptive Multiuser Detection CDMATechniques*. PhD thesis, University of Southampton, UK, 1999.

[61] M. R. Schroeder, "Synthesis of low-peak-factor signals and binary sequences with low autocorrelation," *IEEE Transactions on Information Theory*, pp. 85–89, 1970.

[62] E. V. der Ouderaa, J. Schoukens, and J. Renneboog, "Peak factor minimization using a time-frequency domain swapping algorithm," *IEEE Transactions on Instrumentation and Measurement*, vol. 37, pp. 145–147, March 1988.

[63] L. J. Greenstein and P. J. Fitzgerald, "Phasing multitone signals to minimize peak factors," *IEEE Transactions on Communications*, vol. 29, no. 7, pp. 1072–1074, 1981.

[64] R. W. Bäuml, R. F. H. Fischer, and J. B. Huber, "Reducing the peak-to-average power ratio of multicarrier modulation by selected mapping," *Electronics Letters*, vol. 32, pp. 2056–2057, October 1996.

[65] X. Li and J. A. Ritcey, "M-sequences for OFDM peak-to-average power ratio reduction and error correction," *Electronics Letters*, vol. 33, pp. 554–555, March 1997.

[66] J. Jedwab, "Comment : M-sequences for OFDM peak-to-average power ratio reduction and error correction," *Electronics Letters*, vol. 33, pp. 1293–1294, July 1997.

[67] C. Tellambura, "Use of m-sequences for OFDM peak-to-average power ratio reduction," *Electronics Letters*, vol. 33, pp. 1300–1301, July 1997.

[68] S. Narahashi and T. Nojima, "New phasing scheme of N-multiple carriers for reducing peak-to-average power ratio," *Electronics Letters*, vol. 30, pp. 1382–1383, August 1994.

[69] M. Friese, "Multicarrier modulation with low peak-to-average power ratio," *Electronics Letters*, vol. 32, pp. 713–714, April 1996.

[70] P. V. Eetvelt, G. Wade, and M. Tomlinson, "Peak to average power reduction for OFDM schemes by selective scrambling," *Electronics Letters*, vol. 32, pp. 1963–1964, October 1996.

[71] J. A. Davis and J. Jedwab, "Peak-to-mean power control and error correction for OFDM transmission using Golay sequences and Reed-Muller codes," *Electronics Letters*, vol. 33, no. 4, pp. 267–268, 1997.

[72] S. Boyd, "Multitone signals with low crest factor," *IEEE Transactions on Circuits and Systems*, vol. 33, pp. 1018–1022, October 1986.

[73] W. Rudin, "Some theorems on Fourier coefficients," *Proc. American Mathematics Society*, vol. 10, pp. 855–859, December 1959.

[74] D. J. Newman, "An L^1 extrimal problem for polynomials," *Proc. of American Mathematics Society*, vol. 16, pp. 1287–1290, December 1965.

[75] B. M. Popović, "Synthesis of power efficient multitone signals with flat amplitude spectrum," *IEEE Transactions on Communications*, vol. 39, no. 7, pp. 1031–1033, 1991.

[76] H. S. Shapiro, "Extremal problems for polynomials and power series," Master's thesis, Massachusetts Institute of Technology, 1951.

[77] M. J. E. Golay, "Complementary series,," *IRE Transactions on Information Theory*, vol. IT-7, pp. 82–87, 1961.

[78] S. J. Shepherd, P. V. Eetvelt, C. W. Wyatt-Millington, and S. K. Barton, "Simple coding scheme to reduce peak factor in QPSK multicarrier modulation," *Electronics Letters*, vol. 31, pp. 1131–1132, July 1995.

[79] C. Tellambura, "Upper bound on peak factor of n-multiple carriers," *Electronics Letters*, vol. 33, pp. 1608–1609, September 1997.

[80] C.-C. Tseng and C. L. Liu, "Complementary sets of sequences," *IEEE Transactions on Information Theory*, vol. 18, pp. 644–652, September 1972.

[81] R. Sivaswamy, "Multiphase complementarty codes," *IEEE Transactions on Information Theory*, vol. 24, pp. 546–552, September 1978.

[82] R. L. Frank, "Polyphase complementary codes," *IEEE Transactions on Information Theory*, vol. 26, pp. 641–647, November 1980.

[83] D. Wulich and L. Goldfeld, "Reduction of peak factor in orthogonal multcarrier modulation by amplitude limiting and coding," *IEEE Transactions on Communications*, vol. 47, no. 1, pp. 18–21, 1999.

[84] R. H. Barker, "Group synchronizing of binary digital systems," *in Communication Theory*, pp. 273–287, 1953.

[85] R. H. Pettit, "Pulse sequences with good autocorrelation properties," *The Microwave Journal*, pp. 63–67, February 1967.

[86] R. Turyn and J. Storer, "On binary sequences," *Proc. American Mathematics Society*, vol. 12, pp. 394–399, June 1961.

[87] S. W. Golomb and R. A. Scholtz, "Generalized Barker sequences," *IEEE Transactions on Information Theory*, vol. 4, pp. 533–537, October 1965.

[88] D. J. G. Mestdagh and P. M. P. Spruyt, "A method to reduce the probability of clipping in DMT-based transceivers," *IEEE Transactions on Communications*, vol. 44, no. 10, pp. 1234–1238, 1996.

[89] D. J. G. Mestdagh, P. M. P. Spruyt, and B. Biran, "Effect of amplitude clipping in DMT-ADSL transceivers," *Electronics Letters*, vol. 29, pp. 1354–1355, July 1993.

[90] S. J. Shepherd, J. Oriss, and S. K. Barton, "Asymptotic limits in peak envelope power reduction by redundant coding in orthogonal frequency-division multiplex modulation," *IEEE Transactions on Communications*, vol. 46, no. 1, pp. 5–10, 1998.

[91] M. Breiling, S. H. Müller-Weinfurtner, and J. B. Huber, "Peak-power reduction in OFDM without explicit side information," in *Proceedings of International OFDM Workshop 2000*, (Hamburg, Germany), September 2000.

[92] S. H. Müller and J. B. Huber, "OFDM with reduced peak-to-mean power ratio by optimum combination of partial transmit sequences," *Electronics Letters*, vol. 33, pp. 368–369, February 1997.

[93] C. Tellambura, "Phase optimisation criterion for reducing peak-to-average power ratio in OFDM," *Electronics Letters*, vol. 34, pp. 169–170, January 1998.

[94] E. Kreyszig, *Advanced engineering mathematics*. John Wiley & Sons, Inc., 7th ed., 1993.

[95] R. C. Heimiller, "Phase shift pulse codes with good periodic correlation properties," *IRE Transactions on Information Theory*, vol. 7, pp. 254–257, October 1961.

[96] R. L. Frank, "Phase shift pulse codes with good periodic correlation properties," *IRE Transactions on Information Theory*, vol. 8, pp. 381–382, October 1962.

[97] R. L. Frank, "Polyphase codes with good nonperiodic correlation properties," *IEEE Transactions on Information Theory*, vol. 9, pp. 43–45, 1963.

[98] D. C. Chu, "Polyphase codes with good periodic correlation properties," *IEEE Transactions on Information Theory*, vol. 18, pp. 531–532, July 1972.

[99] R. L. Frank, "Comments on polyphase codes with good correlation properties," *IEEE Transactions on Information Theory*, vol. 19, p. 244, March 1973.

[100] K. W. Yip and T. S. Ng, "Tight error bounds for asynchronous multicarrier cdma and their application," *IEEE Communications Letters*, vol. 2, pp. 295–297, November 1998.

[101] B. M. Popović, "Spreading sequences for multicarrier CDMA systems," *IEEE Transactions on Comminications*, vol. 47, no. 6, pp. 918–926, 1999.

[102] B. M. Popović, "Comment: Merit factor of Chu and Frank sequences," *Electronics Letters*, vol. 27, pp. 776–777, April 1991.

[103] M. Antweiler and L. Bömer, "Reply: Merit factor of Chu and Frank sequences," *Electronics Letters*, vol. 27, pp. 777–778, April 1991.

[104] M. Antweiler and L. Bömer, "Merit factor of Chu and Frank sequences," *Electronics Letters*, vol. 26, pp. 2068–2070, December 1990.

[105] R. Sivaswamy, "Digital and analog subcomplementary sequences for pulse compression," *IEEE Transactions on Aerospace and Electronic Systems*, vol. 14, pp. 343–350, March 1978.

[106] E. Costa, M. Midrio, and S. Pupolin, "Impact of amplifier nonlinearities on OFDM transmission system performance," *IEEE Communications Letters*, vol. 3, pp. 37–39, February 1999.

[107] G. Santella and F. Mazzanga, "A model for performance evaluation in M-QAM-OFDM schemes in presence of non-linear distortions," in *Proc. IEEE VTC'95*, pp. 830–834, July 1995.

[108] C. Rapp, "Effects of HPA-nonlinearity on 4-DPSK-OFDM-signal for digital sound broadcasting system," in *Proceedings of 2nd European Conference on Satellite Communications*, (Liege, Belgium), ESA-SP-332, October 1991.

[109] P802.11a/D6.0, *Draft supplement to standard for tellecommunications and information exchange between systems - LAN/MAN specific requirements - Part 11: Wireless MAC and PHY specifications: High Speed Physical Layer in the 5 GHz Band*, May 1999.

[110] D. V. Sarwate, "Bounds on crosscorrelation and autocorrelation of sequences," *IEEE Transactions on Information Theory*, vol. 25, pp. 720–724, November 1979.

[111] J. F. Hayes, "Adaptive feedback communications," *IEEE Transactions on Communication Technology*, vol. 16, no. 1, pp. 29–34, 1968.

[112] J. K. Cavers, "Variable rate transmission for rayleigh fading channels," *IEEE Transactions on Communications Technology*, vol. COM-20, pp. 15–22, February 1972.

[113] W. T. Webb and R. Steele, "Variable rate QAM for mobile radio," *IEEE Transactions on Communications*, vol. 43, no. 7, pp. 2223–2230, 1995.

[114] R. Steele and W. T. Webb, "Variable rate QAM for data transmission over Rayleigh fading channels," in *Proceeedings of Wireless '91*, (Calgary, Alberta), pp. 1–14, IEEE, 1991.

[115] M. L. Moher and J. H. Lodge, "TCMP—a modulation and coding strategy for rician fading channels," *IEEE Journal on Selected Areas in Communications*, vol. 7, pp. 1347–1355, December 1989.

[116] J. K. Cavers, "An analysis of pilot symbol assisted modulation for rayleigh fading channels," *IEEE Transactions on Vehicular Technology*, vol. 40, pp. 686–693, November 1991.

[117] S. Sampei and T. Sunaga, "Rayleigh fading compensation for QAM in land mobile radio communications," *IEEE Transactions on Vehicular Technology*, vol. 42, pp. 137–147, May 1993.

[118] S. Otsuki, S. Sampei, and N. Morinaga, "Square QAM adaptive modulation/TDMA/TDD systems using modulation level estimation with Walsh function," *Electronics Letters*, vol. 31, pp. 169–171, February 1995.

[119] W. C. Y. Lee, "Estimate of channel capacity in Rayleigh fading environment," *IEEE Transactions on Vehicular Technology*, vol. 39, pp. 187–189, August 1990.

[120] A. J. Goldsmith and P. P. Varaiya, "Capacity of fading channels with channel side information," *IEEE Transactions on Information Theory*, vol. 43, pp. 1986–1992, November 1997.

[121] M. S. Alouini and A. J. Goldsmith, "Capacity of Rayleigh fading channels under different adaptive transmission and diversity-combining technique," *IEEE Transactions on Vehicular Technology*, vol. 48, pp. 1165–1181, July 1999.

[122] A. J. Goldsmith and S. Chua, "Variable rate variable power MQAM for fading channels," *IEEE Transactions on Communications*, vol. 45, pp. 1218–1230, October 1997.

[123] M. S. Alouini, X. Tand, and A. J. Goldsmith, "An adaptive modulation scheme for simultaneous voice and data transmission over fading channels," *IEEE Journal on Selected Areas in Communications*, vol. 17, pp. 837–850, May 1999.

[124] D. Yoon, K. Cho, and J. Lee, "Bit error probability of M-ary Quadrature Amplitude Modulation," in *Proc. IEEE VTC 2000-Fall*, vol. 5, pp. 2422–2427, IEEE, September 2000.

[125] C. H. Wong and L. Hanzo, "Upper-bound performance of a wideband burst-by-burst adaptive modem," *IEEE Transactions on Communications*, vol. 48, pp. 367–369, March 2000.

[126] E. L. Kuan, C. H. Wong, and L. Hanzo, "Burst-by-burst adaptive joint-detection CDMA," in *Proc. of IEEE VTC'99 Fall*, vol. 2, (Amsterdam, Netherland), pp. 1628–1632, September 1999.

[127] K. J. Hole, H. Holm, and G. E. Oien, "Adaptive multidimensional coded modulation over flat fading channels," *IEEE Journal on Selected Areas in Communications*, vol. 18, pp. 1153–1158, July 2000.

[128] J. M. Torrance and L. Hanzo, "Upper bound performance of adaptive modulation in a slow Rayleigh fading channel," *Electronics Letters*, vol. 32, pp. 718–719, 11 April 1996.

[129] M. Nakagami, "The m-distribution - A general formula of intensity distribution of rapid fading," in *Statistical Methods in Radio Wave Propagation* (W. C. Hoffman, ed.), pp. 3–36, Pergamon Press, 1960.

[130] I. S. Gradshteyn and I. M. Ryzhik, *Table of Integrals, Series and Products*. New York, USA: Academic Press, 1980.

[131] J. Lu, K. B. Letaief, C. I. J. Chuang, and M. L. Lio, "M-PSK and M-QAM BER computation using signal-space concepts," *IEEE Transactions on Communications*, vol. 47, no. 2, pp. 181–184, 1999.

[132] J. M. Torrance and L. Hanzo, "Optimisation of switching levels for adaptive modulation in a slow Rayleigh fading channel," *Electronics Letters*, vol. 32, pp. 1167–1169, 20 June 1996.

[133] T. Keller and L. Hanzo, "Adaptive modulation technique for duplex OFDM transmission," *IEEE Transactions on Vehicular Technology*, vol. 49, pp. 1893–1906, September 2000.

[134] G. S. G. Beveridge and R. S. Schechter, *Optimization: Theory and Practice*. McGraw-Hill, 1970.

[135] W. Jakes Jr., ed., *Microwave Mobile Communications*. New York, USA: John Wiley & Sons, 1974.

[136] "COST 207 : Digital land mobile radio communications, final report," tech. rep., Office for Official Publications of the European Communities, Luxembourg, 1989.

[137] M. K. Simon and M. S. Alouini, *Digital Communication over Fading Channels: A Unified Approach to Performance Analysis*. John Wiley & Sons, Inc., 2000.

[138] C. Y. Wong, R. S. Cheng, K. B. Letaief, and R. D. Murch, "Multiuser OFDM with adaptive subcarrier, bit, and power allocation," *IEEE Journal on Selected Areas in Communications*, vol. 17, pp. 1747–1758, October 1999.

[139] T. Keller and L. Hanzo, "Adaptive multicarrier modulation: A convenient framework for time-frequency processing in wireless communications," *Proceedings of the IEEE*, vol. 88, pp. 611–642, May 2000.

[140] A. Klein, G. K. Kaleh, and P. W. Baier, "Zero forcing and minimum mean square error equalization for multiuser detection in code division multiple access channels," *IEEE Transactions on Vehicular Technology*, vol. 45, pp. 276–287, May 1996.

[141] B. Vucetic, "An adaptive coding scheme for time-varying channels," *IEEE Transactions on Communications*, vol. 39, no. 5, pp. 653–663, 1991.

[142] H. Imai and S. Hirakawa, "A new multi-level coding method using error correcting codes," *IEEE Transactions on Information Theory*, vol. 23, pp. 371–377, May 1977.

[143] G. Ungerboeck, "Channel coding with multilevel/phase signals," *IEEE Transactions on Information Theory*, vol. IT-28, pp. 55–67, January 1982.

[144] S. M. Alamouti and S. Kallel, "Adaptive trellis-coded multiple-phased-shift keying Rayleigh fading channels," *IEEE Transactions on Communications*, vol. 42, pp. 2305–2341, June 1994.

[145] S. Chua and A. J. Goldsmith, "Adaptive coded modulation for fading channels," *IEEE Transactions on Communications*, vol. 46, pp. 595–602, May 1998.

[146] T. Keller, T. H. Liew, and L. Hanzo, "Adaptive redundant residue number system coded multicarrier modulation," *IEEE Journal on Selected Areas in Communications*, vol. 18, pp. 1292–2301, November 2000.

[147] T. Keller, T. Liew, and L. Hanzo, "Adaptive rate RRNS coded OFDM transmission for mobile communication channels," in *Proceedings of VTC 2000 Spring*, (Tokyo, Japan), pp. 230–234, 15-18 May 2000.

[148] T. Liew, C. Wong, and L. Hanzo, "Block turbo coded burst-by-burst adaptive modems," in *Proceedings of Microcoll'99*, (Budapest, Hungary), pp. 59–62, 21-24 March 1999.

[149] C. Wong, T. Liew, and L. Hanzo, "Turbo coded burst by burst adaptive wideband modulation with blind modem mode detection," in *ACTS Mobile Communications Summit*, (Sorrento, Italy), pp. 303–308, 8-11 June 1999.

[150] M. Yee, T. Liew, and L. Hanzo, "Radial basis function decision feedback equalisation assisted block turbo burst-by-burst adaptive modems," in *Proceedings of VTC '99 Fall*, (Amsterdam, Holland), pp. 1600–1604, 19-22 September 1999.

[151] V. Tarokh, N. Seshadri, and A. Calderbank, "Space-time codes for high data rate wireless communication: Performance criterion and code construction," *IEEE Transactions on Information Theory*, vol. 44, pp. 744–765, March 1998.

[152] S. M. Alamouti, "A simple transmit diversity technique for wireless communications," *IEEE Journal on Selected Areas in Communications*, vol. 16, pp. 1451–1458, October 1998.

[153] V. Tarokh, H. Jafarkhani, and A. R. Calderbank, "Space-time block coding for wireless communications: Performance results," *IEEE Journal on Selected Areas in Communications*, vol. 17, pp. 451–460, March 1999.

[154] C. Berrou and A. Glavieux, "Near optimum error correcting coding and decoding: Turbo-codes," *IEEE Transactions on Communications*, vol. 44, pp. 1261–1271, October 1996.

[155] Z. Dlugaszewski and K. Wesolowski, "WHT/OFDM - an imporved OFDM transmission method for selective fading channels," in *Proceedings of IEEE SCVT 2000*, (Leuven, Belgium), pp. 71–74, 19 October 2000.

[156] Z. Dlugaszewski and K. Wesolowski, "Performance of several OFDM transceivers in the indoor radio channels in 17 ghz band," in *Proceedings of IEEE VTC 2001 Spring*, p. P.644, IEEE, May 2001.

[157] S. Verdú, "Minimum probability of error for asynchronous Gaussian multiple-access channel," *IEEE Transactions on Communications*, vol. 32, pp. 85–96, January 1986.

[158] K. M. Wong, J. Wu, T. N. Davidson, Q. Jin, and P. C. Ching, "Performance of wavelet packet-division multiplexing in impulsive and Gaussian noise," *IEEE Transactions on Communication*, vol. 48, no. 7, pp. 1083–1086, 2000.

[159] M. Ghosh, "Analysis of the effect of impulse noise on multicarrier and single carrier QAM systems," *IEEE Transactions on Communications*, vol. 44, no. 2, pp. 145–147, 1996.

[160] Q. Wang, T. A. Gulliver, L. J. Mason, and V. K. Bhargava, "Performance of SFH/MDPSK in tone interference and Gaussian noise," *IEEE Transactions on Communications*, vol. 42, no. 2/3/4, pp. 1450–1454, 1994.

[161] G. E. Atkin and I. F. Blake, "Performance of multitone FFH/MFSK systems in the presence of jamming," *IEEE Transactions on Communications*, vol. 35, no. 2, pp. 428–435, 1989.

[162] L. B. Milstein and P. K. Das, "An analysis of a real-time transform domain filtering digital communication system - Part i: Narrow-band interference rejection," *IEEE Transactions on Communications*, vol. 28, no. 6, pp. 816–824, 1980.

[163] A. Papoulis, *Probability, Random Variables, and Stochastic Processes*. McGraw-Hill, 3 ed., 1991.

[164] M. R. Spiegel, *Mathematical Handbook of Formulas and Tables*. McGraw-Hill Book Company, 1968.

[165] W. X. Zheng, "Design of adaptive envelope-constrained filters in the presence of impulsive noise," *IEEE Transactions on Circuits and Systems II*, vol. 48, pp. 188–192, February 2001.

[166] Y. Zhang and R. S. Blum, "Iterative multiuser detection for turbo-coded synchronous cdma in gaussian and non-gaussian impulsive noise," *IEEE Transactions on Communication Technology*, vol. 49, no. 3, pp. 397–400, 2001.

[167] M. Moeneclaey, M. V. Bladel, and H. Sari, "Sensitivity of multiple-access techniques to narrow-band interference," *IEEE Transactions on Communication Technology*, vol. 49, no. 3, pp. 497–505, 2001.

[168] K. Cheun and T. Jung, "Performance of asynchronous fhss-ma networks under rayleigh fading and tone jamming," *IEEE Transactions on Communications*, vol. 49, no. 3, pp. 405–408, 2001.

[169] L. L. Yang and L. Hanzo, "Blind joint soft-detection assisted slow frequency-hopping multi-carrier DS-CDMA," *IEEE Transactions on Communication*, vol. 48, no. 9, pp. 1520–1529, 2000.

[170] W. T. Webb and L. Hanzo, *Modern Quadrature Amplitude Modulation : Principles and Applications for Fixed and Wireless Channels*. London: IEEE Press, and John Wiley & Sons, 1994.

[171] Y. Chow, A. Nix, and J. McGeehan, "Analysis of 16-APSK modulation in AWGN and rayleigh fading channel," *Electronics Letters*, vol. 28, pp. 1608–1610, November 1992.

[172] F. Adachi and M. Sawahashi, "Performance analysis of various 16 level modulation schemes under Rrayleigh fading," *Electronics Letters*, vol. 28, pp. 1579–1581, November 1992.

[173] F. Adachi, "Error rate analysis of differentially encoded and detected 16APSK under rician fading," *IEEE Transactions on Vehicular Technology*, vol. 45, pp. 1–12, February 1996.

[174] Y. C. Chow, A. R. Nix, and J. P. McGeehan, "Diversity improvement for 16-DAPSK in Rayleigh fading channel," *Electronics Letters*, vol. 29, pp. 387–389, February 1993.

[175] Y. C. Chow, A. R. Nix, and J. P. McGeehan, "Error analysis for circular 16-DAPSK in frquency-selective Rayleigh fading channels with diversity reception," *Electronics Letters*, vol. 30, pp. 2006–2007, November 1994.

[176] C. M. Lo and W. H. Lam, "Performance analysis of bandwidth efficient coherent modulation schems with L-fold MRC and SC in Nakagami-m fading channels," in *Proceedings of IEEE PIMRC 2000*, vol. 1, pp. 572–576, September 2000.

[177] S. Benedetto, E. Biglierri, and V. Castellani, *Digital Transmission Theory*. Prentice-Hall, 1987.

Glossary

Adaptive Modulation	A modulation scheme, where the actual modulation mode of transmitter 'A' is adjusted according to the near-instantaneous channel quality perceived by receiver 'B'
AMQAM	Adatpive M-ary Quadrature Amplitude Modulation, an adaptive modulation scheme which employs an M-ary QAM employing square-shaped constellations as the constitent modulation modes
AOFDM	Adaptive Orthogonal Frequency Division Mulplexing, an OFDM scheme employing adaptive modulation in the frequency domain as well as in the time domain, resulting in so-called two-dimensional adaptive modulation or frequency-time processing
APSK	Adaptive Phase Shift Keying, a PSK modulation scheme where the number of legitimate phases is adaptive chosen according to the near-instantaneous channel condition
ASQAM	Adaptive Star-constellation Quadrature Amplitude Modulation, an adaptive modulation scheme which employs a version of QAM employing Star-constellations as the constituent modulation modes
AWGN	Additive White Gaussian Noise
BCH	Bose-Chaudhuri-Hocquenghem, a class of forward error correcting codes (FEC)
BER	Bit Error Ratio, the ratio of the number of bits received incorrectly to the total number of received bits
BPS	Bits Per Symbol, the number of bits used to generate a modulation symbol
CDMA	Code Division Multiple Access
complementary sequences	A pair of sequences, which satisfies that the sum of of their autocorrelation values result in all zero sequence except at zero offset, also know as complemntary pair or Golay codes

DFT Discrete Fourier Transform, a discrte time version of Fourtier Transform, which converts a time domain signal into the corresponding frequency domain signal

EGC Equal Gain Combining scheme

FDM Frequency Division Multiplexing, a multiplexing technique, where a set of different information is multiplexed using different frequency band

FDMA Frequency Division Multiple Access, a multiple access technique where each user is assigned different frequency band in order to communicate with the base station

FEC Forward Error Correction

FFT Fast Fourier Transform, a computationally efficient version of DFT

Gray Mapping A bit assignment scheme which maps a set of bits to a constellation such that the the number of different bits assigned to any adjacent constellations is one

iBEP Instantaneous Bit Error Probability

IDFT Inverse Discrete Fourier Transform, the inverse transform of DFT, which which converts a frequency domain signal into the corresponding time domain signal

IFFT Inverse Fast Fourier Transform, a computationally efficient version of IDFT, *see also* IDFT

IS-95 Pan-American DS-CDMA cellular communication system developed by Quall-comm, *see also* Narrowd Band CDMA

ISI Inter Symbol Interference

iSNR Instantaneous Signal-to-Noise Ratio

LFSR Linear Feedback Shift Register

MAI Multiple Access Interference

MC-CDMA A version of Multi-Carrier CDMA, which spreads an information symbol over several subcarriers and uses the OFDM structure to transmit the signal, also known as OFDM-CDMA

MC-DS-CDMA A version of Multi-Carrier CDMA, which uses a set of orthogonal subcarriers conveying a time domain spread information signal

MIP Multi-path Intensity Profile, a characteristic of a wide-band fading channel, also known as Channel Impulse Response

MLD	Maximum Likelihood Detection
MMSE-BDFE JD	Minimum Mean Square Error Block Decision Feedback Equalised Joint Detector
MMSEC	Minimum Mean Square Error Combining scheme
MRC	Maximal Ratio Combining scheme, which maximises the SNR at the output of the combiner
MSP	Mode Selection Probability, the probability of selecting a specific constituent modulation mode in a adaptive modulation scheme, *see also* Adaptive Modulation
MT-CDMA	Multi-Tone CDMA, a version of Multi-Carrier CDMA technique, which employs OFDM transmitter to generate a time domain signal and then apply a time domain spreading to the signal
MUI	Multiple User Interference, an interference inflicted by the other users' signal
Multi-Carrier CDMA	A family of CDMA technique employing several number of carriers, *see also* MC-CDMA, MC-DS-CDMA and MT-CDMA
OFDM	Orthogonal Frequency Division Multiplex
OFDM-CDMA	*see* MC-CDMA
OGold	Orthogonal Gold codes
OOB	Out-Of-Band
ORC	Orthogonality Restoring Combining scheme, also known as Zero-Forcing combining scheme
PDF	Probability Density Function
PSAM	Pilot Symbol Assisted Modulation, a technique where known symbols (pilots) are transmitted regularly and the effect of channel fading on all symbols can then be estimated by interpolating between the pilots
QAM	Quadrature Amplitude Modulation
QOS	Quality of Service
RF	Radio Frequency
RMS	Root Mean Square

RRNS	Redundant Residue Number System
RSSI	Received Signal Strength Indicator, commonly used as an indicator of channel quality in a mobile radio network
SINR	Signal to Interference plus Noise ratio, same as signal to noise ratio (SNR) when there is no interference
SPD	Successive Partial Despreading
TCM	Trellis-Coded Modulation
TDMA	Time Division Multiple Access, a multiple access technique where each user is assigned different time slot in order to communicate with the base station
W-ATM	Wireless Asynchronous Transfer Mode
WHT	Walsh Hadamard Transform
ZF	Zero-Forcing, *see also* ORC

Author Index

Index

Z